ISSN 2338-0128
VOLUME 2

PROCEEDINGS BOOK
THE 7TH ANNUAL BASIC SCIENCE INTERNATIONAL CONFERENCE

7-8 March 2017
Ijen Suites Resort and Convention
Malang, Indonesia

Basic Science for Improving Survival & Quality of Life

Sub Topics:
Material Science and Technology
Mathematics, Statistics, and Modelling

BaSiC 2017
INTERNATIONAL CONFERENCE

Faculty of Science
Brawijaya University

ISSN 2338-0128

Volume 2

BaSIC 2017

The 7th Basic Science International Conference

Basics Science for Improving Survival and Quality of Life

7 – 8 March 2017

Ijen Suites Resorts & Convention

Malang, East Java

Indonesia

Proceedings Books

Sub Topics:

- ✓ Material Science and Technology
- ✓ Mathematics, Statistics and Modelling

BRIEF CONTENTS

SCIENTIFIC PAPERS

BASIC 2017 COMMITTEE

Steering Committee

Prof. Dr. Ir. Mohammad Bisri, M.S.
Rector, Brawijaya University

Adi Susilo, M.Si., Ph.D
Dean, Faculty of Mathematics and Natural Sciencess
Brawijaya University

Dr. Agung Pramana Warih Marhendra, M.S.
Vice Dean I, Faculty of Mathematics and Natural Sciences
Brawijaya University

Moh. Farid Rahman, S.Si., M.Si.
Vice Dean II, Faculty of Mathematics and Natural Sciences Brawijaya University

Advisor

Johan A. E. Noor, Ph.D
Department of Physics, Faculty of Mathematics and Natural Sciences, Brawijaya University
Indonesia

Achmad Efendi, Ph.D
Department of Mathematics, Faculty of Matematics and Natural Sciences, Brawijaya University
Indonesia

Dr.Ing Setyawan P. Sakti, M.Eng
Department of Physics, Faculty of Mathematics and Natural Sciences, Brawijaya University
Indonesia

Organizing Committee

Hari Arief Dharmawan, M. Eng., Ph.D
Chairperson
Department of Physics, Faculty of Mathematics and Natural Sciences, Brawijaya University
Indonesia

Chomsin S. Widodo, Ph.D Vice chairperson I
Department of Physics, Faculty of Mathematics and Natural Sciences, Brawijaya University
Indonesia

Dian Siswanto, Ph.D Vice chairperson II
Department of Biology, Faculty of Mathematics and Natural Sciences, Brawijaya University
Indonesia

Dr. Eng. Masruroh, M.Si Secretary
Department of Physics, Faculty of Mathematics and Natural Sciences, Brawijaya University
Indonesia

Dr. Istiroyah, M.Si Treasury
Department of Physics, Faculty of Mathematics and Natural Sciences, Brawijaya University
Indonesia

Surakhaman, S.AP., MM Treasury
Department of Physics, Faculty of Mathematics and Natural Sciences, Brawijaya University
Indonesia

Lisfadiana Ekakurniawati, S.E. Treasury
Faculty of Mathematics and Natural Sciences, Brawijaya University
Indonesia

Sunarti Treasury
Faculty of Mathematics and Natural Sciences, Brawijaya University
Indonesia

Rustika Adiningrum, SE. Treasury
Faculty of Mathematics and Natural Sciences, Brawijaya University
Indonesia

Muhammad Ghufron, M.Si Secretariat Coordinator
Department of Physics, Faculty of Mathematics and Natural Sciences, Brawijaya University
Indonesia

Cholisina Anik Perwira, S.Si, M.Si Secretariat
Department of Physics, Faculty of Mathematics and Natural Sciences, Brawijaya University
Indonesia

Susilo Purwanto Secretariat
Department of Physics, Faculty of Mathematics and Natural Sciences, Brawijaya University
Indonesia

Sahri Secretariat
Department of Physics, Faculty of Mathematics and Natural Sciences, Brawijaya University
Indonesia

Ir. Tjujuk Usmanhadi Secretariat
Faculty of Mathematics and Natural Sciences, Brawijaya University
Indonesia

Trivira Meirany Secretariat
Faculty of Mathematics and Natural Sciences,
Brawijaya University
Indonesia

Dr. Eng. Agus Naba, MT
Web and IT Division Coordinator
Department of Physics, Faculty of Mathematics and Natural Sciences, Brawijaya University
Indonesia

Fransiscus Adi Purwanto Web and IT Division
Faculty of Mathematics and Natural Sciences,
Brawijaya University
Indonesia

Dr. Alamsyah M. juwono, M.Sc.
Program Division Coordinator
Department of Physics, Faculty of Mathematics and Natural Sciences, Brawijaya University
Indonesia

Sukir Maryanto, S.Si.,M.Si.,Ph.D
Program Division
Department of Physics, Faculty of Mathematics and Natural Sciences, Brawijaya University
Indonesia

Zulfaida P. G., Ph.D. Program Division
Department of Biology, Faculty of Mathematics and Natural Sciences, Brawijaya University
Indonesia

Dra. Lailatin Nuriyah, M.Si
Banquet Division Coordinator
Department of Physics, Faculty of Mathematics and Natural Sciences, Brawijaya University
Indonesia

Firdy Yuana, S.Si., M.Si. Banquet Division
Department of Physics, Faculty of Mathematics and Natural Sciences, Brawijaya University
Indonesia

Achmad Hidayat, S.Si., M.Si
Equipment Division Coordinator
Department of Physics, Faculty of Mathematics and Natural Sciences, Brawijaya University
Indonesia

Dr. Sunaryo, S.Si.,M.Si Equipment Division
Department of Physics, Faculty of Mathematics and Natural Sciences, Brawijaya University
Indonesia

Purnomo Equipment Division
Department of Physics, Faculty of Mathematics and Natural Sciences, Brawijaya University
Indonesia

Karyadi Eka Putra, A.Md. Equipment Division
Faculty of Mathematics and Natural Sciencess
Brawijaya University
Indonesia

Agung Kurniawan Equipment Division
Faculty of Mathematics and Natural Sciences
Brawijaya University
Indonesia

Hasan Muhajir Equipment Division
Faculty of Mathematics and Natural Sciences,
Brawijaya University
Indonesia

Suliono Equipment Division
Faculty of Mathematics and Natural Sciences
Brawijaya University
Indonesia

Deny Equipment Division
Department of Physics, Faculty of Mathematics and Natural Sciences, Brawijaya University
Indonesia

Drs. Wasis, MAB
Accomodation Division Coordinator
Department of Physics, Faculty of Mathematics and Natural Sciences, Brawijaya University
Indonesia

Drs. Arinto Yudi Ponco Wardoyo, M.Sc., Ph.D
Accomodation Division
Department of Physics, Faculty of Mathematics and Natural Sciences, Brawijaya University
Indonesia

Dr. Heru Harsono, M.Si.
Funding Division Coordinator
Department of Physics, Faculty of Mathematics and Natural Sciences, Brawijaya University
Indonesia

Ir. Mochammad Djamil, MT Funding Division
Department of Physics, Faculty of Mathematics and Natural Sciences, Brawijaya University
Indonesia

Gancang Saroja, S. Si., MT
Proceeding Division Coordinator
Department of Physics, Faculty of Mathematics and Natural Sciences, Brawijaya University
Indonesia

Mauludi Ariesto Pamungkas, S.Si., M.Si, Ph.D.
Proceeding Division
Department of Physics, Faculty of Mathematics and Natural Sciences, Brawijaya University
Indonesia

Ahmad Nadhir, S.Si., MT., Ph.D.
Proceeding Division
Department of Physics, Faculty of Mathematics and Natural Sciences, Brawijaya University
Indonesia

DR.rer.nat Abdurrouf, S.Si., M.Si
Proceeding Division
Department of Physics, Faculty of Mathematics and Natural Sciences, Brawijaya University
Indonesia

Dr. Drs. Sugeng Rianto, M.Sc
Proceeding Division
Department of Physics, Faculty of Mathematics and Natural Sciences, Brawijaya University
Indonesia

International Scientific Committee

Prof. Dr. Wolfgang Nellen
Institut fur biology, Germany

Dr. Guillaume Mauri
Neuchatel University, Switzerland

Prof. Peter Andrew Lay
Sydney University, Australia

Prof. Tatsuhiko Aizawa
Shibaura Institute of Technology (SIT), Japan

Dr. Ing. Setyawan P. Sakti, M.Eng
Department of Physics, Brawijaya University
Indonesia

Prof. Dr. Agus Suryanto, M.Sc.
Department of Mathematics, Brawijaya University
Indonesia

Local Scientific Committee

Prof. Dr. M. Nurhuda
Scientific Division Coordinator
Department of Physics, Faculty of Mathematics and Natural Sciences, Brawijaya University
Indonesia

Drs. Unggul Pundjung Juswono, M.Sc.
Department of Physics, Faculty of Mathematics and Natural Sciences, Brawijaya University
Indonesia

Dr. Eng. Didik Rahadi Santoso, M.Si.
Department of Physics, Faculty of Mathematics and Natural Sciences, Brawijaya University
Indonesia

Ir. D. J. Djoko H. Santjojo, M.Phill., Ph.D
Department of Physics, Faculty of Mathematics and Natural Sciences, Brawijaya University
Indonesia

Prof. Muhaimin Rifa'I, S.Si., Ph.D..Med.Sc
Department of Biology, Faculty of Mathematics and Natural Sciences, Brawijaya University
Indonesia

Drs. Adi Susilo, M.Si., Ph.D.
Department of Physics, Faculty of Mathematics and Natural Sciences, Brawijaya University
Indonesia

Ir. Retno Mastuti, M.Ag.Sc., D.Agr.Sc
Department of Biology, Faculty of Mathematics and Natural Sciences, Brawijaya University
Indonesia

Dr. Suharjono, MS
Department of Biology, Faculty of Mathematics and Natural Sciences, Brawijaya University
Indonesia

Dr. Dra. Catur Retnaningdyah, M.Si
Department of Biology, Faculty of Mathematics and Natural Sciences, Brawijaya University
Indonesia

Widodo,S.Si., M.Si., Ph.D.Med.Sc
Department of Biology, Faculty of Mathematics and Natural Sciences, Brawijaya University
Indonesia

Masruri, S.Si., M.Si., Ph.D.
Department of Chemistry, Faculty of Mathematics and Natural Sciences, Brawijaya University
Indonesia

Akhmad Sabarudin, S.Si., M.Sc., Dr.Sc
Department of Chemistry, Faculty of Mathematics and Natural Sciences, Brawijaya University
Indonesia

Lukman Hakim, S.Si., M.Sc., Dr. Sc
Department of Chemistry, Faculty of Mathematics and Natural Sciences, Brawijaya University
Indonesia

Dr. rer. nat. Rachmat Triandi Tjahjanto, M.Si
Department of Chemistry, Faculty of Mathematics and Natural Sciences, Brawijaya University
Indonesia

Drs. Abdul Rouf Alghofari, S.Si., M.Si., Ph.D
Department of Mathematics, Faculty of Mathematics and Natural Sciences, Brawijaya University
Indonesia

Achmad Efendi, S.Si., M.Sc., Ph.D
Department of Mathematics, Faculty of Mathematics and Natural Sciences, Brawijaya University
Indonesia

Rahma Fitriani, S.Si., M.Sc., Ph.D
Department of Mathematics, Faculty of Mathematics and Natural Sciences, Brawijaya University
Indonesia

Dr. Adji Achmad Rinaldo Fernandes, S.Si., M.Sc
Department of Mathematics, Faculty of Mathematics and Natural Sciences, Brawijaya University
Indonesia

Dr. Suci Astutik, S.Si., M.Si.
Department of Mathematics, Faculty of Mathematics and Natural Sciences, Brawijaya University
Indonesia

Student Committee

Bagas Adi Saputra
Department of Physics, Faculty of Matematics and Natural Sciences, Brawijaya University
Indonesia

Adwi Arifin
Department of Physics, Faculty of Matematics and Natural Sciences, Brawijaya University
Indonesia

Muhamad Abdullah Faqih, S.Si,
Department of Physics, Faculty of Matematics and Natural Sciences, Brawijaya University
Indonesia

Ully Mamba’atul Mukarromah, S.Si,
Department of Physics, Faculty of Matematics and Natural Sciences, Brawijaya University
Indonesia

Mira Setiana S.Si,
Department of Physics, Faculty of Matematics and Natural Sciences, Brawijaya University
Indonesia

Muhammad Warits Ishari
Department of Physics, Faculty of Matematics and Natural Sciences, Brawijaya University
Indonesia

Lalu Muhammad Shirr Wujudulhaaq
Department of Physics, Faculty of Matematics and Natural Sciences, Brawijaya University
Indonesia

Arin Siska Indarwatin
Department of Physics, Faculty of Matematics and Natural Sciences, Brawijaya University
Indonesia

Ragil Danang Kusuma
Department of Physics, Faculty of Matematics and Natural Sciences, Brawijaya University
Indonesia

Citra Anggun Noorjannah
Department of Physics, Faculty of Matematics and Natural Sciences, Brawijaya University
Indonesia

Pramita Dhealia Larasati
Department of Physics, Faculty of Matematics and Natural Sciences, Brawijaya University
Indonesia

Dimmy Kurniawan Irwanto
Department of Physics, Faculty of Matematics and Natural Sciences, Brawijaya University
Indonesia

Conference Secretariat

Departement of Physics,
Faculty of Mathematics and Natural Sciencess
Brawijaya University
Jl. Veteran, Malang, East Java, Indonesia 65145
Phone: +62 0341 575833
Fax: +62 0341 575834
E-mail: basicsciences2017@gmail.com
Website: http://basic.ub.ac.id

ABOUT BASIC

The Annual Basic Science International Conference is a scientific meeting aimed to promote mutual exchange between scientists and also experts, to discuss innovative ideas in scientific research, and to tackle contemporary problems through the application of knowledge that rise from sciences. The scope of this conference is fundamental and applied research in chemistry, biology, physics, and mathematics. The origin of this conference was initiated in year 2000, by the Faculty of Mathematics and Natural Sciences of Brawijaya University, under the name of Seminar Nasional Kemipaan (National Sciences Conference). Since then, the conference has been organized regularly on annual basis. In 2004, the conference changed its name to Basic Sciences Seminar (BSS) and started to invite international speakers and participants. The conference then expands its scope to international in 2011 and formally adopting the current name. The previous Basic Sciences International Conference was held at Atria Hotel Malang in 2016 with participants from many countries including Australia, Malaysia, Thailand, Japan, UK and Germany.

WELCOME MESSAGE

On behalf of the organizing committee, I would like to welcome you to the 7th Annual Basic Science International Conference.

Firstly, I would like to thank all participants who have spent their time to come and join us for the conference. I believe that we will not be able to hold this conference successfully without participation from all of you. Secondly, I would like to thank the dean of faculty of Mathematics and Natural Sciences, Brawijaya University, because the faculty has provided us supports and facilities. I am thankful to our great keynote and invited speakers for their willingness to join the conference and share their scientific knowledge to all of us. Thanks to our reviewers who have made assessments and suggestions related to the abstracts. I also want to thank the sponsors which have made their contributions to this conference. Finally, I want to thank all members of the committee for their hard work to make this conference successful.

The Basic Science International Conference is held every year since 2010, and always organized by the Faculty of Mathematics and Natural Sciences, Brawijaya University. This conference is a forum that enables us to share our ideas among us. The participants are expected also to take their time and opportunities to know each other during the conference, in order to strengthen their networks and collaborations. In this conference, we have more than 300 participants from counties such as Indonesia, Japan, Australia, Germany, Switzerland, and Thailand. In the conference, we have plenary lectures and sessions for parallel oral presentations as well as poster presentations.

We hope that all participants enjoy all activities during the conference and this proceedings book will be useful for all of us.

Thank you very much.

Best regards,

Hari Arief Dharmawan, Ph.D.

Chairman of BaSIC 2017

WELCOME MESSAGE

On behalf of the Dean of Faculty of Mathematics and Natural Sciences, Brawijaya University, I would like to extend my warmest welcome to all delegates from all over the world. Welcome to Malang, where Malang is one of the educational city in Indonesia. Malang, which is about more than 400 meters above sea level, has many tourist destinations. Malang is like a bowl, surrounded by some volcanoes in the east (Semeru and Bromo), west (Kawi and Kelud) and north (Arjuna and Welirang Complex), and in the south are coastal areas, where we have many beautiful new opening beaches.

We are very pleased to welcome you in the proceedings book of the seventh Annual Basic Science International Conference 2017. I would like to express my gratitude to all of the participants, keynote and invited speakers as well. Many thanks also go to the reviewers and the editorial team for their big effort in supporting this book of abstracts. Last but not least my big appreciation to the steering and organizing committees, in realizing this proceedings book.

Thank you.

Faculty of Mathematics and Natural Sciences,

Dean,

Adi Susilo, Ph.D.

CONFERENCE VENUE

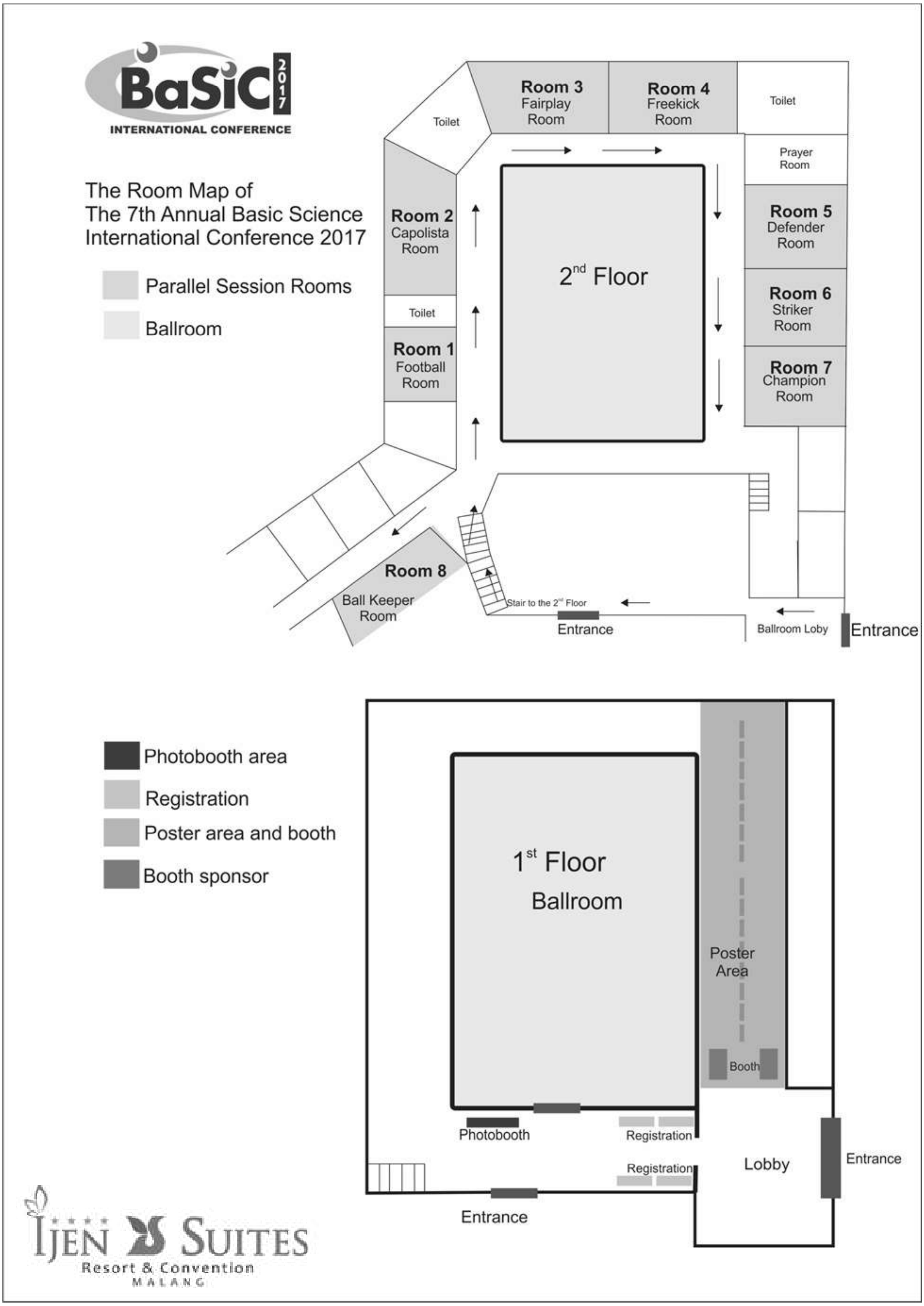

CONFERENCE PROGRAM

Day One: March 7th, 2017

07.30 – 08.30	Registration
08.30 – 09.00	Opening Ceremony
09.00 – 09.45	**Plenary Lecture 1**: *CRISPR/Cas9: Basics and Applications in "gene surgery".* Prof. Dr. Wolfgang Nellen, Institut fur biology, Germany
09.45 – 10.00	Coffee Break
10.00 – 10.45	**Plenary Lecture 2**: *Use of Wavelet Analyses with Potential Field Data in Exploration and Monitoring Studies* Dr. Guillaume Mauri, Neuchatel University, Switzerland
10.50 – 11.35	**Plenary Lecture 3**: *Mathematics for Solving 5G Massive Wireless IoT Networks Problems* Dr. Eng. Khoirul Anwar, S. T., M. Eng., Telkom University
11.35 – 12.30	Lunch
12.30 – 15.00	**Parallel Session 1**
15.00 – 15.30	Poster Session & Coffee Break
15.30 – 17.30	**Parallel Session 2**
17.30 – 19.00	Breaks
19.00 – 21.00	Gala Dinner

Day Two: March 8th, 2017

07.30 – 08.10	Registration
08.10 – 08.55	**Plenary Lecture 4**: *The Roles of Metal Ions in Diabetes – Metal Drugs and Supplements* Prof. Peter Andrew Lay, Sydney University, Australia
09.00 – 09.45	**Plenary Lecture 5**: *Functionalization of Stainless Steels Via Low Temperature Plasma Nitriding* Prof. Tatsuhiko Aizawa, Shibaura Institute of Technology (SIT) , Japan
09.45 – 10.00	Coffee Break
10.00 – 12.00	**Parallel Session 3**
12.00 – 13.00	Lunch
13.00 – 14.30	**Parallel Session 4**
14.30 – 15.00	Coffee Break
15:00 – 16.00	**Parallel Session 5**
16.00 – 16.30	Closing Ceremony & Award Announcement

TABLE OF CONTENTS

Plenary Lectures

Scientific Papers

A. Invited Papers

B. Material Science and Technology

C. Mathematics, Statistics and Modelling

Volume 2

BaSIC 2017

The 7th Basic Science International Conference

Basics Science for Improving Survival and Quality of Life

PLENARY LECTURES

CRISPR/Cas9 – the new gene surgery

Wolfgang Nellen

Kassel University, Germany and Brawijaya University, Malang, Indonesia

Abstract-The new gene editing tool CRISPR/Cas9 allows for easy and efficient targeted changes in the genomes of microbes, plants and animals (including humans). CRISPR/Cas is a prokaryotic immune system that "memorizes" infections by phages and plasmids. The molecular biology and biochemistry of the machinery is very well understood and it has been engineered in different ways to serve specific needs in biotechnology. I will briefly present the origins and biochemistry of bacterial CRISPR/Cas systems, the technical use in gene technology and some applications that have already been achieved and others that are in the pipe-line.

1. SUMMARY

In 2012, a revolutionary paper appeared in the journal Science: Jennifer Doudna and Emmanuelle Charpentier and co-workers published the application of the bacterial CRISPR immune system to modify, delete and insert genes in essentially every living cell.

In bacteria and archaea, CRISPR represents an array of short DNA pieces that were captured from infecting phages or plasmids. Using enzymes encoded by the adjacent Cas locus, the microorganisms can fight subsequent infections. Transcripts of the short DNA pieces (crRNA) serve as guides to direct a nuclease encoded in the Cas locus to the invader and destroy it.

The Cas-nucleases can thus be programmed to cleave any specific sequence in any genome. Out of a plethora of different Cas-nucleases from different bacteria and archaea, the Cas9 enzyme from *Streptococcus pyogenes* proved to be the most convenient enzyme from the family for technical applications. In eukaryotes, the cut in the DNA is reversed by the cellular repair machinery. However, relegation of the cut ends usually results in sequence mistakes by short deletions or short insertions. Consequently, the gene targeted by a synthetic crRNA becomes functionless.

An additional piece of DNA with (partial) homology to the targeted sequence can be introduced to the cell. This will be used as a template and can replace the original sequence around the cut – including large insertions and deletions as well as single nucleotide changes.

CRISPR/Cas can thus be used in any organism to delete, insert or modify genes at a defined target site. The applications are endless and only a few examples will be presented here.

1. Compatibility in bone marrow transplantation: For BMT in leukaemia patients, compatible donors have to be found which have the same surface antigens as the recipient. With CRISPR/Cas9, genes for surface antigens of the donor can be adjusted to the recipient. If the genetic defect in the patient is exactly known, bone marrow cells can be removed, repaired in vitro and reintroduced into the patient.
2. Resistance of crop plants to fungal or viral diseases: In many cases natural resistances of plants against viral and fungal infections were accidentally lost during breeding and selection over the last few hundred years. Resistance genes are still present in some old variants or the wild forms of modern crops. Backcrossing these traits into the modern strains would take decades while introducing the resistance by CRISPR/Cas9 could be done in approximately one year.
3. Animal diseases: The same approach can be used to deal with diseases of farm animals like chicken flu or swine fever, where resistance genes exist in related species and can be transferred to livestock by CRISPR/Cas9
4. Nutritional value: Malnutrition is a substantial problem, though sufficient calories are supplied, in many regions of the world insufficient amounts of vitamins and micro-nutrients are contained in the common staple crops. Multiple genes to construct biochemical pathways for the synthesis e.g. vitamin A can be introduced into plants easily by CRISPR/Cas9.
5. Gene drive: CRISPR/Cas9 can be used for a copying (recombination) mechanism that generates homozygous individuals from heterozygous ones. This is currently being used for spreading infertility genes in disease vectors like Anopheles and Aedes. A realistic aim is to reduce the population of mosquitos by 80 to 90% and thus reduce infection by Malaria, Dengue, Yellow Fever and others.

6. Antibiotic resistant bacteria: it may be feasible to target resistance genes in pathogenic bacteria by CRISPR/Cas9 and thus solve the increasing problem of multi-resistant infections.

The advantages of CRISPR/Cas9 are that it can be universally applied, that the method is quite easy to perform and that it is inexpensive. These advantages could lead to a "democratisation of gene technology", meaning that the method is not only available to large, financially strong companies but also to small companies and even local breeders.

These advantages may also create the risk of intentional or unintentional misuse since any well trained molecular biologist may carry out CRISPR/Cas9 constructions with quite simple and inexpensive equipment.

There are also concerns on ethical issues, e.g. the interference with ecosystems or the genetic modification of human life. Though especially the latter issue requires serious and rational discussion, we are still very far from "designer babies" with specific (complex) traits and behaviour and it is questionable if this can be achieved at all. Rules and regulations on gene technology in general and CRISPR/Cas9 in particular have to be made wisely. In Europe, especially in Germany, legislation has strangled progress in genetic engineering, companies have moved out of the country and innovation is significantly slowing down. Even worse, western political parties and NGOs try to force their anti-science opinion onto developing countries, preventing progress that is so much needed. One should always consider that using a technology requires responsibility. However, prohibiting a technology also requires responsibility. Indonesia should find its own way to make best and responsible use of this new break-through technology. There are many challenges in agriculture, animal breeding, nutrition and human health that can be approached by CRISPR/Cas9. Unfortunately, after more than five years, no university or research institution has yet picked the technology to pursue serious projects.

For further details: there is a huge number of excellent review papers, cartoons, videos, graphs, podcasts and discussions in various languages available on the internet. A reference list would be endless or a very subjective, arbitrary choice. Readers interested in CRISPR/Cas will have no problem to find further material on every level of knowledge.

Use of Wavelet Analyses with Potential Field Data in Exploration and Monitoring Studies

*Guillaume Mauri[1], Ginette Saracco[2]

[1]Center for Hydrogeology and Geothermics, Université de Neuchâtel, Neuchâtel, Switzerland,
[2]CNRS-UMR 7330, CEREGE, Aix-Marseille Université, Aix-en-Provence cedex 4, France,
Corresponding authors: [guillaume.mauri@unine.ch & gmvolcano@yahoo.fr]

1. INTRODUCTION

Developed in the 1980's, first for seismic analyses [1,2,3,4,5], the wavelet method is used since the 1990's to analyses potential field data [6,7,8,9]. The aim of this work is to present some of the benefits when using wavelet analyses on potential field data (e.g., gravity, self-potential) when conducting geothermal exploration and volcano monitoring.

2. METHOD

Wavelets are mathematical equations that allow for analyzing either time series or spatial data set, which are used in a wide variety of domains, which include but not limited to seismic/acoustics [1], image or signal processing [9,10], fluid mechanics (turbulence) [12], archeology [13], volcano monitoring [14], or biology [15].

The wavelets analyses are organized into different categories, such as orthogonal wavelet [16], discrete wavelet analyses [20] and continuous wavelet analyses [5,8,10]. Many wavelet exists and are organized into families [8,9,10,12]. Here, we present the use of the Poisson wavelet family [8,9,13]. Wavelet analysis is a multi-scale analyses method, which is used to determine power and frequency spectrum, and distribution (space, time) of a processed signal [1,9,13,16,17].

3. RESULTS AND DISCUSSION

In 2010, we developed the multi-scale wavelet tomography approach, which use multiple wavelets to better constrain depth of source generating observed potential field anomaly [18]. Later on, we published a wavelet code using Poisson family for potential field data, named MWTmat, based on matlab platform [19]. Since, we have applied MWTmat on several projects that cover volcano monitoring [20,21] and geophysical study for geothermal exploration [18,20,22].

Our results show the usefulness of the MWTmat method that brings information on depths, location and structural shape of the source. We present examples that include but not limited to Kawah Ijen aquifer monitoring (Indonesia) [21], geothermal fluids circulation on Waita volcano (Japan) [18]. Fig. 1 presents an example of MWT method applied on gravity data to better constrain the geological structures affected by increase of fracture density due to fault movement and rock dissolution through karstification processes (study case of Jura range, Switzerland) [22].

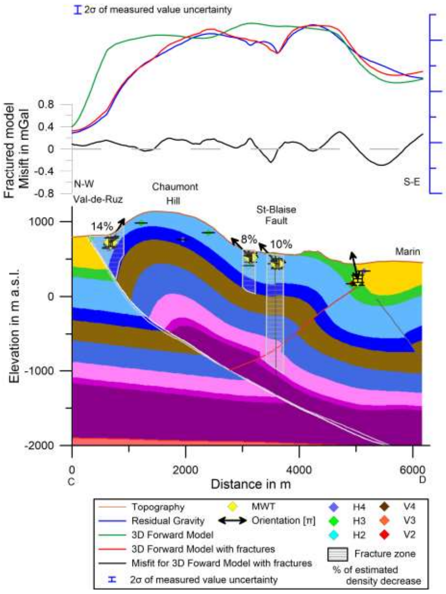

Fig. 1. Example of MWT analyses using Poisson wavelet on gravity data to locate rock density decrease associated to fault and karstification on geothermal exploration [22].

4. REFERENCES

[1]. Morlet, J ; Arens, G ; Fourgeau, E ; Giard, D, Wave-propagation and sampling theory .1 & 2. Complex signal and scattering in multilayered media, geophysics, 47(2), 203-236, doi: 10.1190/1.1441328 & doi:10.1190/1.1441329 (1982).

[2]. Morlet, J, A Decomposition of hardy into square integrable wavelets of constant shape. SIAM J. Math Anal, (1980).

[3]. Saracco G, Grossmann A, Tchamitchian P, Use of wavelet transform in the study of propagation of transient acoustic signals across a plane interface between two homogeneous media, "Wavelets, Time-Frequency methods and Phases Space", eds P. Combes, A. Grossmann, P. Tchamitchian, SPRINGER-VERLAG, Berlin, 139-146 (1989).

[4]. Saracco G, Tchamitchian P, Retrieval of time-dependent source in an acoustic propagation problem. Inverse Problems in Action, Ed. P C Sabatier, Inv Probl Theor Imag Springer-Verlag Berlin Heidelberg, 207-211 (1990)

[5]. Saracco G, Tchamitchian P, Gazahnes C, Transmission of source signals through a plane interface and their reconstruction. J Phys 51(C2):1049-1052 doi: 10.1051/jphyscol:19902246 (1990).

[6]. Saracco G, Propagation of transient waves through a stratified fluid medium: Wavelet analysis of a nonasymptotic decomposition of the propagator. Part I. Spherical waves through a two-layered system. J Acous Soc Am 95(3):1191-1205, doi:10.1121/1.408563 (1994).

[7]. Grossmann A, Morlet J, Decomposition of Hardy functions into square integrable wavelets of constant shape. Soc Int Amer Math J Analysis. 15:723-736 (1984).

[8]. Moreau F, Gilbert D, Saracco G , Filtering non-stationary geophysical data with orthogonal wavelets. Geophys Res Lett 23(4):407-410, doi: 10.1029/96GL00155 (1996).

[9]. Moreau F, Gilbert D, Holschneider M, Saracco G, Wavelet analysis of potential fields. Inv Probl 13(1):165-178 (1997).

[10]. Mallat, SG, A theory for multiresolution signal decomposition - the wavelet representation, Ieee Transactions On Pattern Analysis And Machine Intelligence, 11, 7, 674-693, doi: 10.1109/34.192463, (1989).

[11]. Mallat, SG, Multiresolution Approximations And Wavelet Orthonormal Bases Of L2(R), Transactions Of The American Mathematical Society, 315(1), 69-87, doi: 10.2307/2001373 (1989).

[12]. Farge, M., Wavelet Transforms and Their Applications to Turbulence, Annual Review of Fluid Mechanics, 24, 395-457 (1992).

[13]. Saracco G, Moreau F, Mathe PE, Hermitte D, Michel JM, Multiscale tomography of buried magnetic structures: its use in the localization and characterization of archaeological structures. Geophys J Int 171(1):87-103, doi:10.1111/j.1365-246X.2007.03501.x (2007).

[14]. Saracco G, Labazuy P, Moreau F, Localization of self-potential sources in volcano-electric effect with complex continuous wavelet transform and electrical tomography methods for an active volcano. Geophys Res Lett 31:L12610 doi: 10.1029/2004GL019554 (2004).

[15]. Arneodo, A, Bacry, E, Graves, PV, Muzy, JF, Characterizing long-range correlations in DNA sequences from wavelet analysis. Physical Review Letters, 74(16), 3293 (1995).

[16]. Daubechies, I, Orthonormal bases of compactly supported wavelets, Communications On Pure And Applied Mathematics, 41 (7), 909-996, doi: 10.1002/cpa.3160410705 (1988).

[17]. Fedi M, Primicerin R, Quarta T, Villani AV, Joint application of continuous and discrete wavelet transform on gravity data to identify shallow and deep sources. Geophys J Int 156(1):7-21 (2004).

[18]. Mauri G, Williams-Jones G, Saracco G Depth determinations of shallow hydrothermal systems by self-potential and multi-scale wavelet tomography. J Volcanol Geotherm Res 191(3):233-244 (2010).

[19]. Mauri G, Williams-Jones G, Saracco G, MWTmat - Matlab application of Multi-scale Wavelet Tomography on potential field. Comp Geosci 37(11):1825-1835 (2011).

[20]. Mauri G, Williams-Jones G, Saracco G, A geochemical and geophysical investigation of the hydrothermal complex of Masaya volcano, Nicaragua. J Volcanol Geotherm Res 227:15-31(2012).

[21]. Caudron, C, Mauri, G, Williams-Jones, G, Lecocq, T, Syahbana, dK, De Plaen, R, Peiffer, L, Bernard, A, Saracco, G, New insights into Kawah Ijen hydrothermal system from geophysical data. Special Issue on Volcanic Lakes, Geol. Soc. London, vol. SP437, doi:10.1144/SP437.4 (2016)

[22]. Mauri G, Negro F, Abdelfettah Y, Vuataz F-D, Schill E, Deep geothermal exploration of low enthalpy reservoir in the Neuchâtel Jura (GeoNE project) – Use of gravity survey to validate and improve 3D geological models.10th Swiss Geosciences Meeting, Bern2012,P2-19 (2012).

Mathematics for Solving 5G Massive Wireless IoT Networks Problems

Khoirul Anwar[1*]

[1]Center for Advanced Wireless Technologies (AdWiTech), Telkom University,
Jl. Telekomunikasi No. 1, Terusan Buah Batu, Bandung 40257, Indonesia
*Corresponding author: [anwarkhoirul@telkomuniversity.ac.id]

1. INTRODUCTION

Requirements of the fifth telecommunication generation (5G) aspects expected in 2020, according to the definition of international telecommunications union (ITU), are: (1) data rate beyond 10 Gbps, (2) massive machine-type communications, and (3) latency below 1 milisecond. This talk considers solution to massive machine-type communications, which is expected to serve about 40-50 billion devices connected to the internet, called the internet of things (IoT). Based on the contention-based access mechanism, IoT technologies are divided into four categories: (i) pure ALOHA, (ii) slotted ALOHA, (iii) non-slotted carrier sense multiple access with collision avoidance (CSMA/CA), and (iv) slotted CSMA/CA.

TABLE I
THE SIX MOST IMPORTANT STOPPING SETS.

Set	Graph	$P_o(\cdot)$	$\mathcal{X}(\cdot)$
$\mathcal{S}_1$	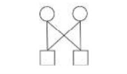	$\frac{M!}{(M-2)!}\frac{\Lambda_2^2}{2!}\frac{2}{(N-1)N}$	$\binom{M}{2}\Lambda_2^2$
$\mathcal{S}_2$	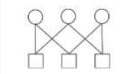	$\frac{M!}{(M-3)!}\frac{\Lambda_2^3}{3!}\frac{8(N-2)}{(N-1)^2N^2}$	$\binom{M}{3}\Lambda_2^3$
$\mathcal{S}_3$	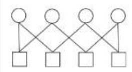	$\frac{M!}{(M-4)!}\frac{\Lambda_2^4}{4!}\frac{288(N-3)(N-2)}{3(N-1)^3N^3}$	$\binom{M}{4}\Lambda_2^4$
$\mathcal{S}_4$	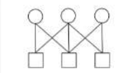	$\frac{M!}{(M-3)!}\frac{\Lambda_2^2\Lambda_3}{2!}\frac{24}{(N-1)^2N^2}$	$\binom{M}{3}\frac{\Lambda_2^2\Lambda_3}{2}$
$\mathcal{S}_5$	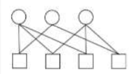	$\frac{M!}{(M-3)!}\frac{\Lambda_2\Lambda_3^2}{2!}\frac{36(N-3)}{(N-2)(N-1)^2N^2}$	$\binom{M}{3}\frac{\Lambda_2\Lambda_3^2}{2}$
$\mathcal{S}_6$	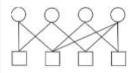	$\frac{M!}{(M-4)!}\frac{\Lambda_2^3\Lambda_3}{3!}\frac{288(N-3)}{(N-1)^3N^3}$	$\binom{M}{4}\frac{\Lambda_2^3\Lambda_3}{6}$

In this talk, we propose new categories of IoT [1]-[6] to provide better probability of success in detection, where collision is even beneficial [1]-[2]. Using the basic concept of mathematics [3]-[4], especially on probability, binomial and exponential distribution (combined with some findings in information theory), we provide better IoT technologies [5]-[6] in terms of: (a) higher throughput (serve more devices), (b) lower packet loss rate , (c) optimizable networks (using extrinsic information (EXIT) chart analysis), and the most important finding, i.e., (d) the theoretical IoT limits given multiple user/devices detection capability per time slot.

2. METHOD, RESULTS AND DISCUSSION

We use EXIT chart analysis to design the rate of each IoT devices. To make it applicable in practice, the time-slot can not be set very large. As a consequence, the stopping set happens causing performance limitation. We derive stopping sets from multinomial distribution. We found 6 stopping sets shown in Table I [4] for the case of no multiuser detection. We found that the probability is accurate enough to predict the performance of massive IoT wireless networks.

3. REFERENCES

[1]. K. Anwar and M. Nur Hasan, “Uncoordinated Transmission in Multiway Relaying Systems,” International ITG Conference on System, Communications and Coding (SCC), Hamburg, Ger- many, Feb. 2015.

[2]. M. Nur Hasan and K. Anwar, “Massive Uncoordinated Multi-way Relay Networks with Simul- taneous

Detections," IEEE International Conference on Communications (ICC) Workshop on Advanced PHY and MAC Techniques for Super Dense Wireless Networks, London, June 2015.

[3]. Khoirul Anwar and Rina Pudji Astuti, "Finite-Length Analysis for Wireless Super-Dense Net- works Exploiting Coded Random Access Over Rayleigh Fading Channels", IEEE Asia Pacific Conference on Wireless and Mobile 2016 (APWiMob 2016), Bandung, Indonesia, 13–15 Sept. 2016.

[4]. Khoirul Anwar, "Decoding for Wireless Super-Dense Networks and Its Finite-Length Analysis for Practical Applications (Invited Paper)", *International Symposium on Electronics and Smart Devices (ISESD)*, Bandung, Indonesia, November 2016.

[5]. Ardimas A. Purwita and K. Anwar, "Vehicular Massive Multiway Relay Networks Applying Graph-Based Random Access'", 2015 IEEE Vehicular Networking Conference (VNC), Kyoto, December 2015.

[6]. Ardimas Andi Purwita and Khoirul Anwar, "Massive Multiway Relay Networks Applying Coded Random Access", *IEEE Transaction on Communications*, Vol. 64. No. 10, October 2016.

The roles of metal ions in diabetes – metal drugs and supplements

*Peter A. Lay[1], Anna Safitri[1,2], Aviva Levina[2]

[1]School of Chemistry, Faculty of Science, University of Sydey, Sydney, Australia
[2]Chemistry Department, Brawijaya University, Malang, Indonesia
*Corresponding auhors: [peter.lay@sydney.edu.au]

1. INTRODUCTION

Metal ions have diverse roles in controlling diabetes, with Cu, Zn and Mn deficiencies known to contribute to the disease through loss of control of oxidative stress, and there is debate about whether vanadium may also be an essential trace element that is involved in both insulin mimetic and insulin enhancing roles [1]. Both vanadium and chromium supplements are consumed widely for glucose metabolism and control of diabetes, and there has been considerable interest in developing anti-diabetic drugs based on these metals and also Mo and W [1]. Recntly, we have shown that it is important to consider speciation of such species in cell media and other biological fluids [2], and that supposedly safe Cr(III) supplements can be oxidized to carcinogenic Cr(VI) and that there are natural pathways to prevent Cr toxicity [3,4]. This and other evidence points to neither a natural role for Cr in diabetes nor safety in its long-term consumption [1-4]. Thus, most evidence is currently focused on vanadium and to a lesser extent Mo and W. These aspects will be discussed in this talk.

2. METHOD

The speciation of metal ions within cells and tissues were investigated with X-ray absorption spectroscopy, EPR spectroscopy and UV/Vis spectroscopy [2], whereas elemental distribution in cells and tissues were measured by X-ray fluorescence microscopy [3]. Various biochemical assays including vibrational spectroscopy and imaging of glucose metabolism in cells, capillary immunoassays of cell signaling and phosphatase inhibition have been studied.

3. RESULTS AND DISCUSSION

The results of the experiments described above throw considerable doubt on the efficacy and safety of widely consumed Cr dietary supplements for the control of glucose metabolism. On the other hand, evidence has been obtained for both a potential essential role for vanadium and insights into the reasons for its efficacy as a drug, which will be discussed.

4. REFERENCES

[1]. Levina, A.; Lay, P. A. *Dalton Trans.* 40, 2011, 40, 11675-11686 (2011).
[2]. Levina, A.; Crans, D. C.; Lay, P. A. *Coord. Chem. Rev.*, in press (2017), doi: 10.1016/j.ccr.2017.01.002.
[3]. Wu, L. E.; Levina, A.; Harris, H. H.; Cai, Z.; Lai, B.; Vogt, S.; James, D. E.; Lay, P. A. *Angew. Chem., Int. Ed.,* 55, 1742–1745 (2016).
[4]. Levina, A.; Pham, T. H. N.; Lay, P. A. *Angew. Chem., Int. Ed.*, 55, 8104-8107 (2016).

Functionalization of Stainless Steels via Low Temperature Plasma Nitriding

Tatsuhiko Aizawa[1*]

[1] Shibaura Institute of Technology, 3-9-14 Shibaura, Minato-City, Tokyo 108-8548, Japan
* Tatsuhiko Aizawa: taizawa@sic.shibaura-it.ac.jp

Abstract – AISI420 type martensitic stainless steels were utilized to experimentally describe the low temperature plasma nitriding behavior with respect to the inner nitriding process in matrix, the lattice expansion and straining process, the strain-induced refinement process and the phase transformation from α'- to γ-phases. The physical modeling was built from these experimental results, which was difficult to explain by the classical nitriding models. This model took account of the inner nitriding process with consideration on the occupation of nitrogen solute with high contents into the vacancy sites in the a'-lattice. The strain induced phase transformation and microstructure refinement was investigated to describe the material model in Fe(Cr) – N system.

1. INTRODUCTION

The plasma-based nitrogen processes have been high-lighted; e.g. the plasma nitriding, the ion implantation, and the plasma immersion ion implantation [1]. In particular, the DC and DC-pulsed plasma nitriding processes have been utilized in industries with the name of ion-nitriding and radical-nitriding [2]. Those conventional plasma nitriding processes are characterized by higher holding temperature than 773 K and longer processing time than 20 ks. The hardening process is also driven by the precipitation strengthening where the synthesized chromium nitride (CrN) precipitates with nano-meter size and large volume fraction in the stainless steel substrates. The inner nitriding process is mainly governed by the nitrogen diffusion; e.g., the nitrided layer thickness is proportional to the square root of nitriding time [2-4]. As pointed out by [5], the high temperature plasma nitriding process for most of stainless steels and tool steels abides by this diffusion-oriented mechanism; the nitrogen solute content makes exponential decrease from the maximum content at the surface to the depth. Besides for the bound nitrogen in content in the form of CrN or Fe_4N, the surface maximum nitrogen solute content is limited by 0.1 mass %, which is equivalent to the maximum nitrogen solubility limit in the phase diagram. In the low temperature plasma nitriding below 673 K, the diffusing nitrogen interstitial atoms never react with the chromium and iron to form CrN or Fe_4N but occupy the vacancy sites in the fcc- and bcc-structured supercells in the stainless steel [6]. Owing to this occupation of vacancies by nitrogen solute, the original fcc- and bcc-structured lattices expand in their c-axis and contact in their a- and b-axes, respectively [7, 8]. In those previous studies, the nitrogen solute content [N] was limited at most by 20 at%; e.g., [N] = 10 at% in case of the ion implantation [9], [N] = 12 at% in case of the glow discharge plasma nitriding [10], and, [N] = 18 at% when using the low temperature plasma nitriding [11].

Authors have developed the high density plasma nitriding process to be working in low temperature [12-15]. In this low temperature plasma nitriding of martensitic stainless steels type AISI420 and austenitic stainless steels type AISI304, the nitrogen interstitials were infiltrated into the stainless steel substrates with significantly high content. Under this condition, the nitrogen interstitials occupy the vacancy sites in the α'-phase bcc structured lattices of martensitic stainless steels, and in the γ-phase fcc structured lattices of austenitic stainless steels, respectively. Due to this occupation of nitrogen solutes in the lattices with high concentration, each constituent grain is refined in the nitrided layer together with high straining by the lattice expansion with and without phase transformation. Hence, the nitrogen solute diffusion process still plays an important role in this low temperature nitriding; the occupation process must be taken into account for description of this process. In the present study, new physical modeling is proposed to describe the inner nitriding process without formation of nitrides as well as the strain-induced phase transformation from α'- to γ-phases. In addition, the strain-induced refinement in microstructure is also discussed to develop the heterogeneous structuring in stainless steels.

2. EXPERIMENTAL PROCEDURE

2.1 High density plasma nitriding

The high density nitriding system has no mechanical matching box with slow response time of 1 s to 10 s to adjust the applied power. Since both the input and output powers are automatically matched by frequency adjustment around 2 MHz, the matching response time is only limited to 1 ms at most. This prompt power control provides to make full use of mesoscopic plasma pressure range over 50 Pa. Figure 1 a) illustrates the standard RF/DC plasma nitriding system. Different from the conventional processes, the vacuum chamber is electrically neutral so that RF-power and DC-bias should be controlled independently from each other. A dipole electrode is utilized to generate RF-plasma; DC bias is directly applied to the specimens. Heating unit is located under this DC-biased cathode plate. In the following nitriding experiments, the specimens are located in the inside of the hollow as shown in Fig. 1 b) before evacuation down to the base pressure of 0.1 Pa. This hollow cathode device is effective to intensify the density of activated nitrogen atoms and NH-radicals as well as electrons toward its outlet of hollow.

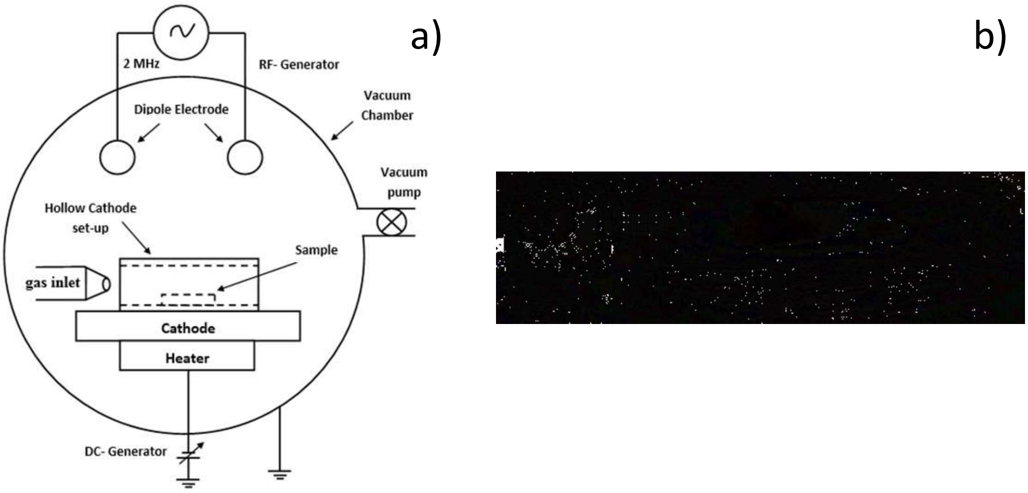

Figure. 1 High density plasma nitriding set-up. a) Standard RF/DC plasma nitriding system, and, b) Hollow cathode device to intensify the plasma density.

2.2 Measurement and observation

The microstructure of the nitrided layer was analyzed by scanning electron microscope (SEM). Energy dispersive spectroscopy (EDS) and electron backscattering diffraction (EBSD; HITACHI SU-70) were employed to make a precise analysis. The phase analysis was also performed by the X-ray diffraction.

3. RESULTS AND DISCUSSION

Figure 2 depicts the SEM image and nitrogen mapping on the cross-section of the nitrided AISI420 substrate at 673 K for 14.4 ks by 70 Pa. The original coarse grains were seen below the nitriding front end in Fig. 2 a); little grain boundaries can be detected even with the trace level in the nitrided layer. This implies that grain size should be significantly reduced during this low temperature plasma nitriding. Highly concentrated nitrogen atoms are present from 31 at% to 10 at% at the vicinity of surface down to 20 □m in depth. The nitrogen contents detected are much higher than the solubility limit of 0.08 at%; no chromium nitride (CrN) precipitates are detected. The high nitrogen concentration at the surface is responsible for driving the nitrogen diffusion process down to the nitriding front end at 80 □m in depth.

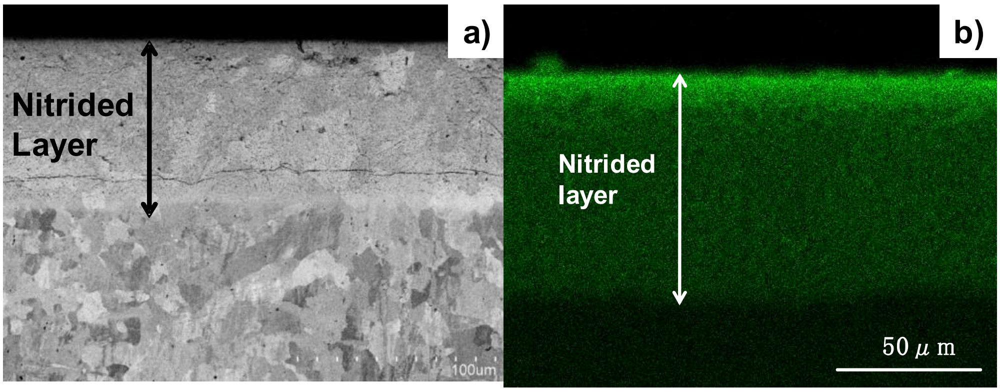

Figure. 2 Cross-sectional view of the plasma nitrided AISI420 specimen at 673 K for 14.4 ks. a) SEM image of cross-section, and, b) Nitrogen mapping by EDX.

Figure 3 depicts the nitrogen content depth profile from the surface to the nitriding front end in correspondence to Fig. 2 b). In the present plasma nitriding, the nitrogen content decreases form the surface to the nitriding front end; however, the plateau of nitrogen content is observed to have almost 9 at% from 20 μm to 80 μm in depth.

In the normal nitrogen diffusion process, the nitrogen content decreases from its maximum solubility limit of 0.1 at% to the nitriding front end exponentially. This essential difference in the nitrogen depth profiles is never explained by the normal diffusion model. The evolution of the nitrided layer thickness (E) is described by the classical Wagner's law where E^2 is proportional to the nitriding duration time (τ). This E^2 of the nitrided AISI420 specimen at the higher temperature than 723 K was proportional to τ; in case of this low temperature nitriding, no proportionality held on between E^2 and τ.

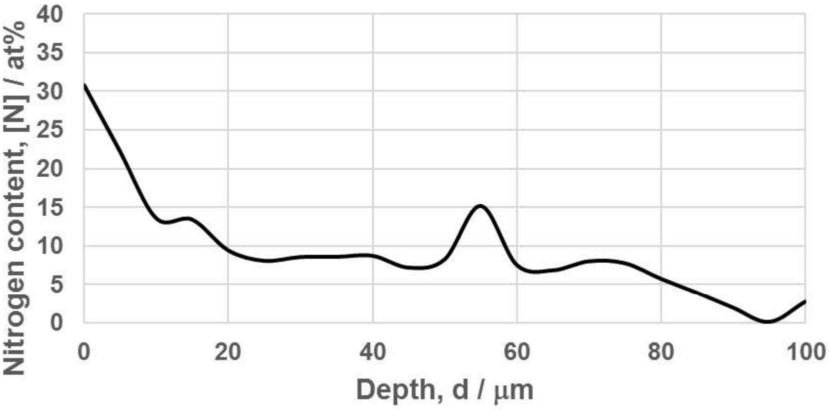

Fig. 3 Comparison of the nitrogen diffusion process between the high temperature and low temperature plasma nitriding treatments.

This nitrogen diffusion process in the low temperature nitriding accompanies with occupation process of nitrogen solute atoms into octahedral vacancy sites in the α'-bcc martensitic lattice structure. This occupation process is detected as an α'-lattice expansion by XRD analysis. As shown in Fig. 4, the original peak for α' (110) shifted itself to α'_N (100) in the lower 2θ direction; this large peak shift reveals that α'-lattice expands by occupation of nitrogen solute into lattice.

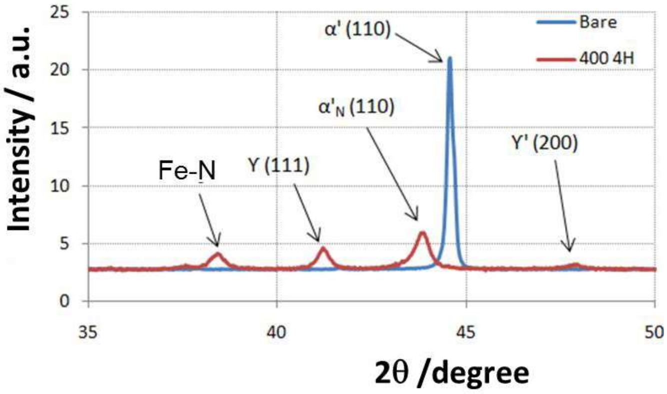

Figure. 4 Comparison of the XRD diagrams before and after nitriding at 673 K for 14.4 ks.

After [16], the original diffusion partial-differential equation is modified by considering this occupation process. The chemical reaction between the vacancies and the diffusing nitrogen atoms is taken into account in formulation; the occupation process is theoretically modeled by the single-step reaction kinetics. For simplicity, the nitrogen content is normalized to be represented by u (t, x) for 0 < u < 1. Then, this new diffusion model is expressed by

$$\frac{\partial u}{\partial t} = \frac{\partial^2 u}{\partial x^2} + \left(au - bu^2\right), \quad a, b > 0 \quad (1)$$

where the second term in its right hand side denotes for the occupation process, and, a and b are material constants. If a and b are assumed to be unity, Eq, (1) reduces to the Fisher – Kolmogorov equation. Hence, this solution of Eq. (1) predicts that the nitriding front end advances in the depth with a wave velocity.

Beside for the α'-lattice expansion, the γ-phase peaks were seen in Fig. 4. The unknown peak around 2θ = 38° was identified to correspond to the Fe – N bonding state; more precise analysis is necessary in future. The physical analysis by EBSD works to describe this phase transformation from α'- to γ-phases during the plasma nitriding. Figure 5 shows the relationship among the crystalline structure, the staining and the phase mapping.

As shown in Fig. 5 b), the highly strained network is formed into the matrix by α'-lattice expansion in each grain. Corresponding to this network, the phase transformation to γ-phase is induced in the network structure in Fig. 5 c). In parallel with this high straining, the grain size is significantly refined to be invisible by EPSD-analysis at the vicinity of the surface in Fig. 5 a).

4. CONCLUSIONS

The low temperature plasma nitriding provides a method to describe the structure of α'- or γ-lattices in the stainless steels in the wider range of nitrogen contents up to 30 at%. Two phase structure such as (α', γ) is induced by high straining during this nitriding. Furthermore, the original coarse grain structure is refined by this high straining to have ultra-fine grain sizes. This low temperature nitriding also becomes a tool to make heterogeneous structuring for functionalization of stainless steels.

ACKNOWLEDGEMENTS

The author would like to express his gratitude to Dr. K. Wasa (TECDIA, Co. Ltd.), Mr. A. Farghari (SIT), Mr. H. Herdianto (University of Brawijaya) and Mr. S. Kurozumi (SIT) for their help in experiments. This study is financially supported in part by the METI (Ministry of Economics, Trades and Industries)-project.

REFERENCES

[1]. R. Wei, J.J. Vajo, J.N. Matossian, P.J. Wilbur, J.A. Davis, D.L. Williamson, G.A. Collins, Surf. Coat. Tech. 83 (1996) 235-242.
[2]. T. Aizawa, Y. Sugita, Res. Rep. SIT 57 (2013) 1-10.
[3]. T. Aizawa, H. Kuwahara, 2003, Mater. Trans., 44 (2003)1303-1310.
[4]. N. Granito, H. Kuwahara, T. Aizawa: J. Materials Science 37 (2002) 835-844.
[5]. Y. Hirota, K. Inoue, Denki-Seiko 80-1 (2010) 15-24.
[6]. D. Santojoyo, T. Aizawa, S. Muraishi, H. Morita, Proc. 9th ICOMM 90 (2014) 1-8.
[7]. C. Blawert, B.L. Mordike, Y. Jiraskova, O. Schneeweiss, Surf. Coat. Technol. 116–119 (1999) 189.
[8]. S.K. Kim, J.S. Yoo, J.M. Priest, M.P. Fewell, Surf. Coat. Technol. 163–164 (2003) 380–385.
[9]. D. Manova, et al., Nucl. Inst. Meth. Phys. Res. B 242 (2006) pp. 285-288.
[10]. I. Alphonsa, A. Chainani, P.M. Raole, B. Ganguli, P.I. John, Surf. Coat. Technol. 150 (2002) 263.
[11]. L.M. Ferreira, S.F. Brunatto, R. O. Cardoso, Mater. Res. 18 (3) (2015) pp. 622-627.
[12]. A. Farghari, T. Aizawa: Mater. Trans. (2017) (in press).
[13]. A. Farghari, T. Aizawa: Proc. 11th SEATUC (2017) (in press).
[14]. T. Aizawa, T. Yoshino, A. Farghari, T. Shiratori: Surf. Coat. Technol. (2017) (to be published).
[15]. T. Aizawa, A. Farghari, T. Yoshino, T. Shiratori: Res. Rep. SIT 60-1 (2017) (to be published).
[16]. C.W. Curtis, D.M. Mortz, Phys. Rev. E 88 (6-2) (2012) pp. 066108-1 to -8.

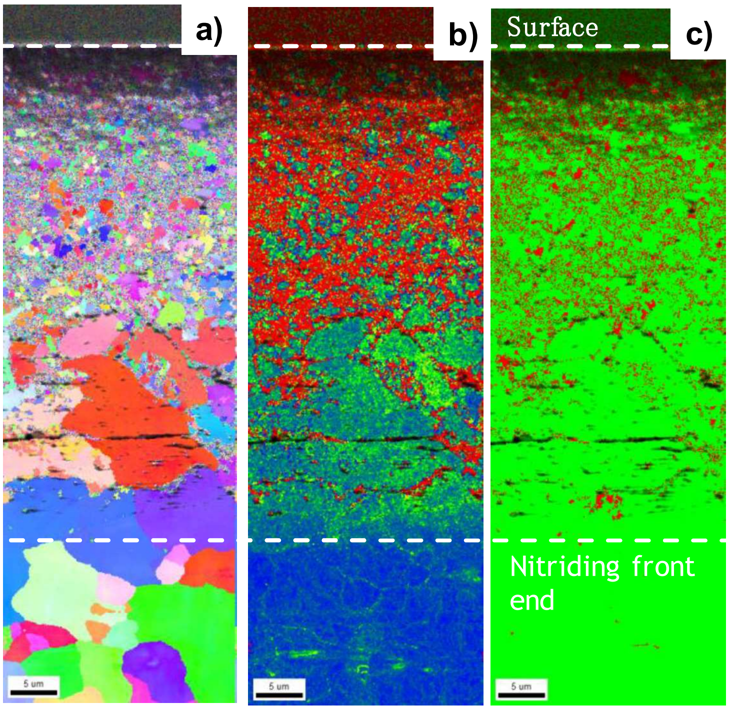

Fig. 5 EBSD analysis. a) IPF-mapping, b) KAM distribution, and c) Phase-mapping.

Volume 2

BaSIC 2017

The 7th Basic Science International Conference

Basics Science for Improving Survival and Quality of Life

Invited Papers

Complexity and Nano Science Approach in Life Sciences: The way to overcome our partial understanding on living system

Sutiman B. Sumitro

[1]Department of Biology, Faculty of Mathematic and Natural Sciences, Brawijaya University, Indonesia
*Corresponding authors: [sutiman@ub.ac.id]

Abstract-Universe is organizational system built from complex interactions and interconnections of components where biological system is complex structure with specific function dedicated to perform normal ordered organizational system. Developing Complexity Science and Nano Biological perspective giving the ideas of interfacing between modern physical and biological sciences into more comprehensive understanding of life system. The ideas initiated for more than 7 decades by physicist Erwin Schrodinger in a 1944 book What is Life? The argument that life feeds on negative entropy or negentropy was asserted and may initiate the way to more comprehensive and better understanding life. We can then develop understanding biological behavior on nano size biological materials and its higher order using modern physics. While other physicist namely Firtjof Capra give another stimulating definition of biological system that enable to apply thermodynamic law. He defined that life is the ceaseless flow of energy and material through complex chemical interaction namely metabolism to perform self organization, perpetuation, regeneration, reparation as well as movement. These ideas are interesting while most people are not even conscious that biologists when they coming into nano size molecular biological discussion, they remain using what is called Newtonian principles respecting the mechanical view of reality when they think and talk. This Newtonian based principles, in order to fulfil the scientific methodologies, many biological scientists including who works in applied sciences such as edical Sciences, they practiced reductionism, reducing things into their parts and examining the parts to understand what made them tick. They reduced life to cells, molecules while the concepts is remain within Newtonian. In the early 20th Century, the certainty of Newton's mechanics was undermined by quantum mechanics and the Uncertainty Principle developed by Werner Heisenberg. This is the new challenges to the old Newtonian view of reality. So some biological scientists began abandoning the Newtonian worldview, while most of them and the ordinary people held on to it.

Surface Modification for Quartz Crystal Microbalance using Polystyrene as a Basis for Biosensor

Setyawan P. Sakti[1*], Akhmad Sabarudin[2], Masruroh[1], Dionysius J.D.H. Santjojo[1]

[1]Department of Physics, Faculty of Mathematic and Natural Sciences, Brawijaya University, Indonesia
[2]Department of Chemistry, Faculty of Mathematic and Natural Sciences, Brawijaya University, Indonesia
*Corresponding authors: [sakti@ub.ac.id]

Abstract – Surface modification of the Quartz Crystal Microbalance is one importance factor in the application of the sensor as a biosensor. The property of the surface physically must not affect the performance of the sensor. It is indicated by a minimal damping of the sensor, while biochemically the sensor surface must be able to bind or adsorb the biomolecules being immobilized as a sensitive layer of the biosensor. Polystyrene is one from many materials which can be used as a sensor coating for the basis of the biosensor as the polystyrene can be used as a matrix for immobilizing antigen or antibody. Polystyrene coating on top of the QCM sensor can be done by using spin coating, airbrush spray coating, and ultrasonic spray coating. Those different methods result in a different surface structure. Good coating using glassy material will not increase the electrical impedance of the sensor. Therefore it is suitable to be used as a mass sensitive biosensor. In addition, modification of the polystyrene surface can be done to alter the surface hydrophobicity. UV radiation and plasma treatment can effectively alter the polystyrene surface hydrophobicity without affecting the electrical impedance of the QCM sensor which can be influenced by the acoustic impedance characteristic of the coating layer. Surface hydrophobicity plays an important role in the used of the QCM biosensor which detects the viscosity and density of the target molecule in liquid. Polystyrene surface with hydrophilic surface decreases the resonance frequency of the QCM biosensor in contact with liquid more than the decreasing resonance frequency on a hydrophobic surface.

1. INTRODUCTION

Since the first Quartz Crystal Microbalance has been used, the application of the quartz crystal microbalance can be found in many areas. The interesting aspect of the sensor is its ability to works in gas and liquid. The sensor responds to physical, chemical and biological quantity results in a frequency change or impedance change. The wide use of the QCM sensor for chemical and biological sensors are mostly based on the sensor responds to mass change on its surface, and it responds to viscosity and or density of contacting material on the sensor surface 1. The first respond is described by Sauerbrey equation 2 and the second respond by Kanazawa and Gordon 3.

The electrical behavior of the QCM sensor and its coating and loading can be modeled as an electrical circuit model (RLC model) 4,5. The model is well known as a Butterworth van Dyke (BvD) model. The electrical model is presented in Figure 1a. The right part of the model is the electromechanical equivalent model of the piezoelectric property of the sensor, while the capacitance in the left is the capacitance of the sensor as a parallel plate capacitor with the quartz as the dielectric material.

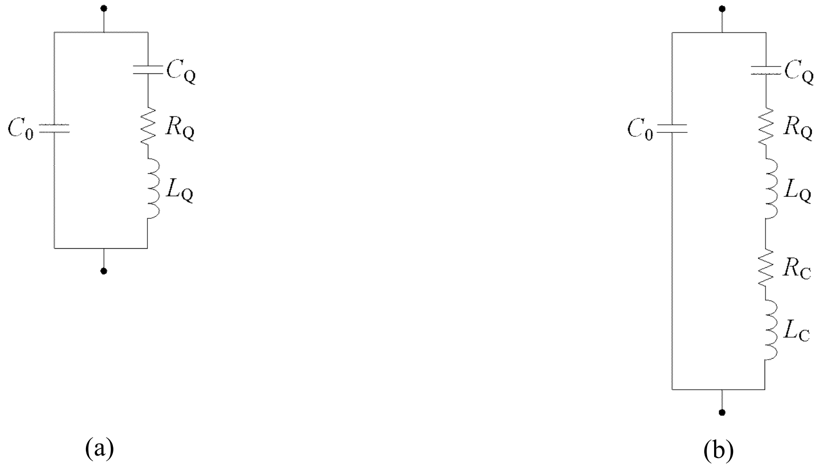

(a) (b)

Figure 1. Electrical equivalent model of the QCM sensor without coating (a) and with coating (b)

The coating layer and liquid behaviour is also modelled as a resistive and inductive elements in the extended BVD model 6. The model is depicted in Figure 1b. The load contribution of the coating layer can also be expressed in an RLC model. The resistive part of the model shows a dissipative behavior of the sensor and the coating material. A glassy coating material does not contribute to the resistance equivalence value, and those the value of the resistive element is close to zero. The coating material behaves only as a rigid mass on top of the sensor which can be expressed only by an inductor element. In the impedance spectrum of the sensor, the glassy coating material causes the series resonance frequency of the sensor goes down, and the minimum impedance of the sensor at the series resonance remains. In contrast, a rubbery coating material lowers the series resonance frequency of the sensor together with an effect of increasing minimum impedance of the series resonance sensor and decreasing maximum impedance at the parallel resonance. It was studied that the glassy and rubbery property of the coating material is determined by the shear moduli of the coating material. Also, the thickness of the coating material affects the property of the material. A very thin coating most likely behaves as a glassy material at high frequency, for example at 10MHz.

The rubbery coating material is not preferred to be used for QCM sensor because it contributes an additional damping to the sensor indicates by the increasing impedance of the coated sensor at series resonance. In the worst condition, the additional damping causes the sensor to stop oscillating. Therefore it is importance to maintain the low damping caused by the coating materials. The low damping is indicated by a non-significant or zero increase of the sensor impedance at series resonance.

Polystyrene is one from many polymers which can be used as a coating material for QCM biosensor 7–9 The polystyrene up to view micrometer thickness still behaves as a glassy material. Therefore polystyrene coating does not contribute additional damping to the sensor. The surface property of the polystyrene can be modified by physical and chemical modification. Method to deposit the polystyrene on top of the QCM sensor affects the surface roughness of the sensor. UV radiation to the polystyrene coating alters the hydrophobicity of the polystyrene surface. Plasma treatment can also change the hydrophobicity.

2. COATING FOR MASS SENSITIVE BIOSENSOR

Those indicated that the polystyrene coating is a good matrix layer to immobilized sensitive biomolecule for QCM biosensor. The high shear moduli of the polystyrene make the polystyrene coating behaves as a glassy coating material. Those it is expected that a polystyrene coating on QCM sensor does not add damping to the sensor. The sensor surface needs to be modified to make the sensor responds only to a specific quantity target. Surface modification of the QCM sensor using polystyrene can be done easily and targeted for many difference applications. The polystyrene coating on the sensor can be used as immobilization matrix for a biomolecule to be used as an immunosensor for various target molecules such as insulin, human serum albumin, a specific protein of cow milk, matrix metalloproteinase-3 (MMP-3) antibody and many others.

The simple method of coating development using polystyrene on top of the QCM sensor is done by spin coating, air pressure spray coating, and ultrasonic spray coating. Proper selection of the coating method results in a homogeny coating thickness with no damping contribution to the QCM sensor. However, come condition of the inhomogeneous coating exists caused by preparations and coating process. Inhomogeneous coating thickness raises the minimum impedance at series resonance of the QCM sensor.

Spin coating is the simplest method to make a polystyrene coating on top of the QCM sensor with HC-49U form. Rotation speed, concentration, and solvent selection can be done to achieve the desired film thickness and surface roughness 10. The surface roughness of the polystyrene which was deposited using spin coating method is affected by the solvent. Polystyrene coating which was deposited using spray coating (airbrush) resulted in more roughness. However, optimization of some parameter of the coating such as solvent, pressure, and the distance between the nozzle and the sensor surface need to be optimized to get a homogeneous surface. The same action is also required when the deposition is done using an ultrasonic deposition method.

The surface roughness of the coating, however, does not contribute any additional damping to the sensor. Inhomogeneity of the coating deposition can add damping to the sensor. By measuring the electrical impedance of the sensor, one can identify whether the coating layer is electromechanically good or bad. A good coating layer will not add additional impedance in the measured impedance spectrum, while a bad coating results in an increasing minimum impedance of the sensor at series resonance.

Figure 2 shows impedance curves of a QCM sensor before and after coating. Both were coated using polystyrene. In the left figure, the minimum impedance of the sensor at series resonance after coating dows not increase. Before and after coating the minimum impedance is around 10Ω. On the right side, the impedance of the sensor with the coating is around 38Ω. The frequency change of both sensors caused by the coating layer is around 27KHz. The increasing minimum impedance of the sensor in the right figure is caused by inhomogeneity of the coating.

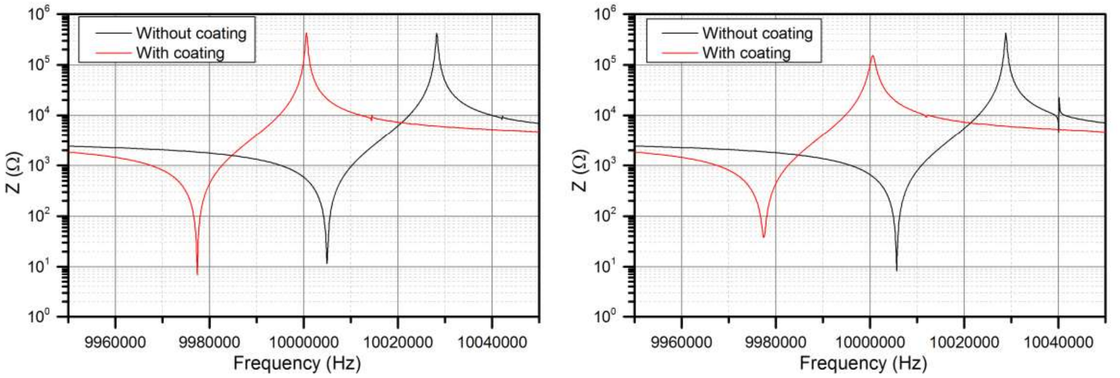

Figure 2. Impedance spectrum of QCM sensor with coating with no additional damping (left) and with additional damping (right)

Immobilized The surface roughness of the coating, however, does not contribute any additional damping to the sensor. Inhomogeneity of the coating deposition can add damping to the sensor. By measuring the electrical impedance of the sensor, one can identify whether the coating layer is electromechanically good or bad. A good coating layer will not add additional impedance in the measured impedance spectrum, while a bad coating results in an increasing minimum impedance of the sensor at series resonance.

3. COATING FOR LIQUID VISCOSITY AND DENSITY CHANGE

Hydrophobicity of the polystyrene surface affects the loading properties of the liquid to the sensor response. This result in a different frequency change of the sensor at the same viscosity caused by different hydrophobicity. Biological sensor by detecting viscosity change of the sample liquid caused by interaction between the substance in the liquid and target molecule was demonstrated for endotoxin detection using QCM sensor 11. In those works, the change in the hydrophobicity of the surface resulted in a significant effect on the sensor response. A higher signal was obtained using a hydrophilic surface.

For the application where the detected target sample will result in viscosity and density change of the liquid on top of the QCM sensor, the surface property of the coating layer needs to be modified to effectively couples the liquid and the sensor. The good coupling is required to transfer the energy of the vibrating quartz to the liquid. The surface property of the sensor should be modified to minimize the slip effect of the liquid 12,13. The mechanical coupling between the surface and the liquid affects the frequency change of the sensor caused by the liquid viscosity and density change as described by Kanazawa and Gordon.

Different surface hydrophobicity can be achieved using many different approaches. One can use different materials or by modifying the surface property of the material by chemical or physical treatment. Polystyrene is one material where its surface hydrophobicity can be changed physically and chemically. The surface hydrophobicity of the polystyrene can be change to be more hydrophilic by UV radiation or by using plasma treatment. Both modifications do not change the bulk property of the polystyrene coating. Therefore the modulus elasticity of the polystyrene coating remains. Figure 3 shows an example of impedance curve of a QCM sensor with polystyrene coating before and after UV radiation. It can be seen that the minimum impedance of the sensor remains.

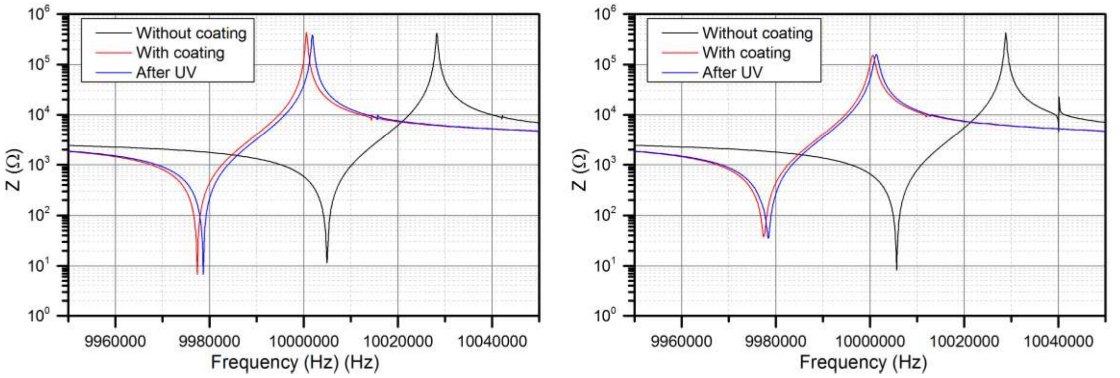

Figure 3. Impedance spectrum of QCM sensor with coating with no additional damping (left) and with additional damping (right) before and after UV radiation

A significant change of the impedance curve can be observed when the sensor surface is in contact with water. The minimum impedance of the sensor in contact with water increases significantly after the Polystyrene coating treated with UV radiation and become a hydrophilic surface (Figure 4). When the polystyrene surface become hydrophilic, the shift of the resonance frequency is higher, and the minimum impedance increases. Therefore for a biosensor which uses a liquid viscosity and density change of the water-based solution needs a hydrophilic surface to get a higher signal change.

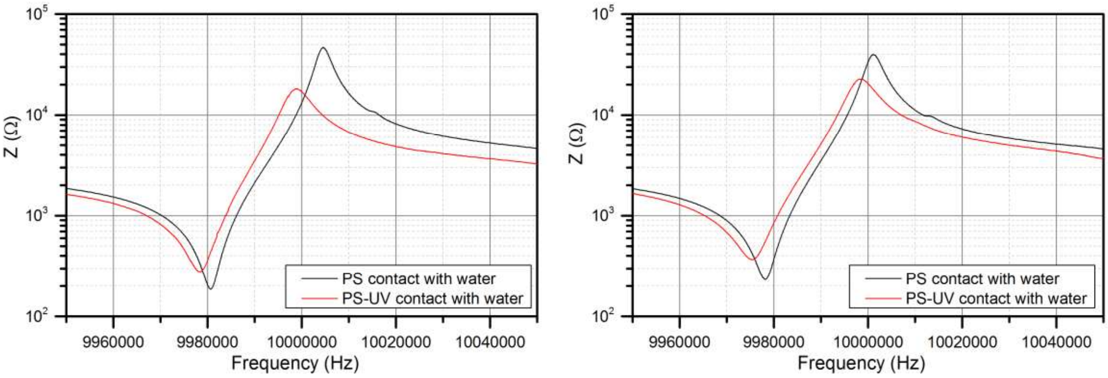

Figure 4. Impedance spectrum of QCM sensor in contact with water

4. CONCLUSIONS

Polystyrene can be used as a coating material for QCM sensor. The mechanical property of the polystyrene as a glassy material gives an advantage to the polystyrene coating which does not add additional damping to the sensor. Meanwhile, the surface property of the polystyrene can be modified to make the surface as a good matrix for biomolecule immobilization and to make a better coupling between the sensor and water solution containing target molecule.

5. REFERENCES

[1]. U. Latif, S. Can, O. Hayden, P. Grillberger, and F.L. Dickert, 2013, *Sensors Actuators B Chem.*, **176**, 825.
[2]. G. Sauerbrey, 1959, *Zeitschrift Für Phys.*, **155**, 206.
[3]. K. Keiji Kanazawa and J.G. Gordon, 1985, *Anal. Chim. Acta*, **175**, 99.
[4]. S.J. Martin, V.E. Granstaff, and G.C. Frye, 1991, *Anal. Chem.*, **2281**, 2272.
[5]. H. Muramatsu, E. Tamiya, and I. Karube, 1988, *Anal. Chem.*, **60**, 2142.
[6]. A. Arnau, 2008, *Sensors*, **8**, 370.
[7]. M.Z. Atashbar, B. Bejcek, A. Vijh, and S. Singamaneni, 2005, *Sensors Actuators B Chem.*, **107**, 945.
[8]. N. Iqbal, G. Mustafa, A. Rehman, A. Biedermann, B. Najafi, P.A. Lieberzeit, and F.L. Dickert, 2010, *Sensors*, **10**, 6361.
[9]. S.P. Sakti, F. Wahyuni, U.P. Juswono, and Aulanni'am, 2013, *Sensors and Transducers*, **149**, 143.
[10].S.P. Sakti, E. Rahmawati, and F. Robiandi, 2016, *AIP Conf. Proc.*, **1719**, 16.
[11].S.P. Sakti, R. Lucklum, P. Hauptmann, F. Bühling, and S. Ansorge, 2001, *Biosens. Bioelectron.*, **16**, 1101.
[12].J. Pye, C. Wood, and J.C. Burton, 2016, *24th Int. Congr. Theor. Appl. Mech.*, TS.FM06.
[13].M. V. Voinova, M. Jonson, and B. Kasemo, 2004, *Spectroscopy*, **18**, 537.

Structure and Dynamics of Water: An Insight from Molecular Simulation

Lukman Hakim[1*], Irsandi Dwi Oka Kurniawan[1], Irwansyah Putra Pradana[1],
Masakazu Matsumoto[2], Hideki Tanaka[2]

[1] Department of Chemistry, Faculty of Science, Brawijaya University, Indonesia, 65145
[2] Graduate School of Natural Science and Technology, Okayama University, Japan, 700-8530
*Corresponding author: lukman.chemist@ub.ac.id

ABSTRACT-While being termed as the "matrix of life", in which the majority of important biochemical reactions took place, water is the most puzzling substance and does not share many properties with other liquids [1]. Upon cooling and/or pressurized, water has at least 14 crystalline polymorphs in pure state [2]. This number increases with the presence of small hydrophobic molecules that can be encaged in a network of water molecules that are connected by hydrogen bonds [3,4]. A deep understanding on the structure and dynamics of water is of paramount importance in life science, cryobiology, climate prediction, and material design. Molecular simulation methods provide an access to experimentally difficult conditions such as extreme temperature and pressure or metastable state; thus provides possibilities to discover novel phenomena and peculiar character of a chemical system [5–7]. The methods enable a systematic investigation at nanoscale level with a great numerical detail. In the absence of technical difficulty in preparing certain material, molecular simulation methods facilitate creative minds to tweak the system with more freedom, and the results are useful to interpret the nature and to design innovative materials. Here we will introduce a number of our molecular simulation works in attempt to unravel the structures and dynamics of a water dominated system.

REFERENCES

[1]. P. Ball, Chem. Rev. **108**, 74 (2008).
[2]. E. Sanz, C. Vega, J. Abascal, and L. MacDowell, Phys. Rev. Lett. **92**, 23 (2004).
[3]. L. Hakim, T. Yagasaki, M. Matsumoto, and H. Tanaka, Rev. High Press. Sci. Technol. **24**, 265 (2014).
[4]. L. Hakim, K. Koga, and H. Tanaka, Phys. Rev. Lett. **104**, 115701 (2010).
[5]. K. Himoto, M. Matsumoto, and H. Tanaka, J. Phys. Soc. Japan **81**, SA023 (2012).
[6]. K. Koga, G. T. Gao, H. Tanaka, and X. C. Zeng, Nature **412**, 802 (2001).
[7]. T. Yagasaki, M. Matsumoto, and H. Tanaka, Phys. Rev. E - Stat. Nonlinear, Soft Matter Phys. **89**, (2014).

Electrochemical Sensor for Industry and Medical

*Fredy Kurniawan[1], Liana Ari Widyanti[1], Kartika A. Madurani[1]

[1]Department of Chemistry, Faculty of Mathematics and Natural Sciences, Institut Teknologi Sepuluh Nopember, Surabaya, Indonesia
*Corresponding authors: [fredy@chem.its.ac.id]

Abstract-Electrochemical sensor had been developed for many purposes. This type sensor mostly can be easily adopted to solve the problem in industry and medical with a high degree of accuracy, precision, sensitivity and selectivity. This study we review a highlight recent in the using of electrochemical sensor for industry and medical. We developed a spicy sensor based gold nanoparticle for industry, which can be used for spicy analysis of any kind food. Both of anodic and cathodic can be used for spicy measurement with limit of detection of the sensor at about 0.500 µM. The sensitivity at anodic and cathodic is 0.102 and -0.268 $\mu A.\mu M^{-1}.mm^{-2}$ respectively. The spicy sensor has been applied to detect the quantity of capsaicin at the seed and fruit of red pepper. We also fabricate and utilize the extract of Maja (*Aegle marmelos*) leaves and pulp to modify silver electrode for medical biosensor. The maja leaf extract modified silver electrode gives a good performance as a urea biosensor at pH 13 with LOD and sensitivity are 2.299 µM and 19.781 $\mu A.\mu M^{-1}.mm^{-2}$ (for anodic) and 5.165 µM and 38.177 $\mu A.\mu M^{-1}.mm^{-2}$ (for cathodic) respectively. Whereas, the maja pulp extract modified silver electrode can be used as glucose biosensor. The biosensor has a good LOD and sensitivity for glucose detection, i.e., 1.920 µM and 1.222 $\mu A.\mu M^{-1}.mm^{-2}$ (for anodic) and 1.701 µM and 1.522 $\mu A.\mu M^{-1}.mm^{-2}$ (for cathodic) respectively. The urea and glucose biosensors were also proven have good selectivity.

1. INTRODUCTION

Jaroslav Heyrovsky, Czech scientist discovered voltammetry which is a form of electrochemistry in 1920s. This technique can analyze a samples by measuring current as a function of the applied potential [1]. In recent years, the sensor technology was developed using electrochemical technique. This sensor commonly used because it was relatively fast, simple and low-cost. Therefore, the electrochemical sensor have been widely applied in industry and medical [2–6].

Improvement of selectivity and sensitivity of the sensor can be conducted by modify the electrode surface using definite material. Most of the electrodes that modified are platinum, gold and silver. The modification on the electrode surface give general result in the:

1. Transfer of physicochemical properties of the modifier to the electrode
2. Enhanced electrocatalytic activity due to the use of materials with large surface area which in turn allows better sensitivity
3. Selectivity towards analyte due to immobilized functional groups and dopents
4. Fast diffusion kinetics in case of some materials
5. Extraction and accumulation of an analyte at the electrode surface [7].

Based on the above explanation, the scientist already modify many electodes to increase the sensor performance [8–12]. In this article, we reviewed our electrode modification as a sensor for industry and medical purpose. Our sensor was proven have a good limit of detection (LOD), selectivity and sensitivity. For industry purpose, we develop a gold nanoparticles for spicy sensor. We also utilize the Indonesian original plant (i.e., Maja (*Aegle marmelos*)) to modify silver electrode for urea and glucose biosensor. The performance of our modified electrode will be compared with another works.

2. APPLICATION ELECTROCHEMICAL SENSOR FOR INDUSTRY

2.1 SPICY SENSOR

Chili is one of important commodity in the world, include Indonesia. In the period 2000-2014, Indonesia is able to export an average of 8.38% per year for fresh chili and 31.74% per year for processed chili such as sauce. Determination of the pungency level of chili is needed, especially in the export-import industry. The pungency level of chili is related to the presence of capsaicinoid compounds [10,13–16]. Monitoring of this compound is important because excessive intake of capsaicinoid may be harmful to health [15,17]. In fact, the Council of Europe has recommended a certain limit to the total capsaicinoid content permitted in a few categories, for instance, 5 ppm as the general limit for food and beverages, 10 ppm for spicy food and beverages, 20 ppm for hot sauces, and 50 ppm for tobacco, harissa, pimento hot oil, and so forth [15].

Conventional methods used to determine the pungency level or capsaicin concentration are using tongue by a panel of tasters (Scouville Organoleptic test method). This test is leveled in Scouville, which is the spiciness measurement of 30 chilies or its derivatives. Pure capsaicin itself has 16 million Scouville. Currently, the industrial Scouville test measurement becomes the standard of spicy flavor, but it is less accurate due to its subjectivity [18]. Quantitative methods such as spectrophotometry and high performance liquid chromatography (HPLC) has been used for the detection of capsaicinoid. HPLC results are reported in spicy ASTA units (15 multiple converted into Scouville) and claimed more reproducible than the conventional method. Unfortunately, this technique requires high cost and complex preparation. Therefore, a simple and accurate technique is still needed to detect and determine capsaicinoid.

Electrochemical method have been reported for fast, simpler and accurate technique. The first claimed of this method for capsaicin analysis is reported on the patent number WO 2009/115840A1. The active material used is double walled carbon nanotubes. Fabrication double walled carbon nanotube is relatively difficult since it requires relatively expensive. We provides another alternative active material that work in the similar system but using simpler process, i.e., composite polyamide 11 and gold nanoparticles. Synthesis of gold nanoparticles was done using wet method, which is simpler than the making of double walled nanocarbon active materials.

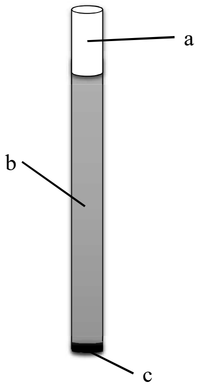

Fig 1. Polyamide composite electrode-gold nanoparticle.

In general, the composition of our modified electrode can be seen at Fig. 1. The surface of gold electrodes was coated by gold nanoparticles (Fig. 1a). The edge of the gold electrodes was isolated (Fig. 1b) and make the bottoms were opened. Deposition of polyamide 11 on the gold electrode surface is carried out using LbL (Layer by Layer) technique. Solution of polyamide 11 appeared by dissolving 0.2 grams powdered polyamide 11 with 7 mL of concentrated H2SO4. Gold electrodes immersed for 5 seconds in a solution of polyamide 11 and was directly included in the distilled water to rinse. The electrode was dipped in the suspension of gold nanoparticles for 24 hours (Fig. 1c), then rinsed again with distilled water. The electrodes are ready to analyze, after dried. The characterization of electrode surface by microscope optic was presented at Fig. 2.

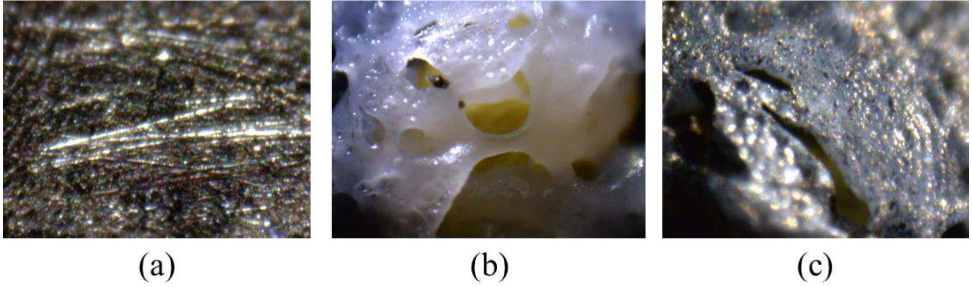
(a) (b) (c)

Fig 2. Gold electrode surface before (a) and after deposited by polyamide 11 (b), and the surface of modified gold electrode with polyamide 11-gold nanoparticles.

The combination of polyamide and gold nanoparticles are able to oxidize capsaicin, which cannot be done by gold electrodes. The peak of oxidation and reduction are observed at 0.439 V and 0 V, respectively. The detection limit (LOD) of electrode polyamide 11 gold nanoparticles at 0.439 V reaches up to 0.5 µM. Linear concentration range that can be used as a calibration curve is in the region of concentration 220 µM. In linear regression equation of the calibration curve obtained y = 6.75 + 0.08 x with a value of R of 0.99468, so the sensitivity of electrodes polyamide/gold nanoparticles was 0.102 μM^{-1} $\mu A.mm^{-2}$. A calibration curve in this concentration range can be seen in Fig. 3. Besides the oxidation current, the reduction current can also be used to determine the concentration of capsaicin. This regularity is observed at a potential of 0 V. Detection limit of reduction current on the electrode polyamide 11 gold nanoparticles is 0.5 µM. The reduction current detection limit has the same value as oxidation currents. The range of linear concentration was 230 µM. The calibration curve in the concentration range of 230 µM can be seen in Fig. 4. From linear regression, calibration curve equation y = -16.69 - 0.21x the value of R for -0.97535 can be obtained. Based on the linear equation, it can be seen that the sensitivity of the electrode is equal to -0.268 mA $\mu M^{-1}.mm^{-2}$, where the negative value indicates reduction current, while the value exhibits positive oxidation current.

Comparison with the patent number WO 2009/115840A1 indicates that the polyamide11-gold nanoparticles modified gold electrode has nearly the same value of LOD (Table 1). Thus, the polyamide11-gold nanoparticles modified gold electrode is demonstrated as an alternative spicy sensor for industrial purposese

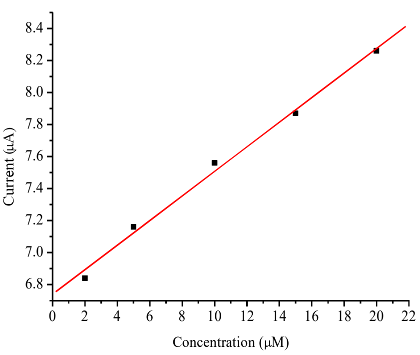

Fig 3. Calibration curve of anodic..

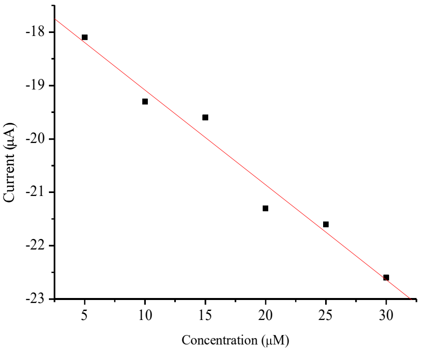

Fig 4. Calibration curve of cathodic

Table 1. Performance comparison of spicy sensor.

Electrode	Linear range (µm)	LOD (µM)	Sensitivity ($\mu A.\mu M^{-1}.mm^{-2}$)	Reference
Modified MWCNTs	0.5-35	0.45	-	[19]
Modified gold	2-20 (anodic) and 5-30 (cathodic)	0.500 (for anodic and cathodic)	0.102 (anodic) and -0.268 (cathodic)	This work

2.2 APPLICATION ELECTROCHEMICAL SENSOR FOR MEDICAL

Since medical analysis in laboratory are expensive and time-consuming process, more measurements of analytes are performaed in various locations, including hospital point-of-care setting, by caregivers in non-hospital settings and by patients at home. Today one of main challenges is the development of methods to perform these rapid ‘in situ’ analysis. These methods must be sensitive and accurate, and able to determine various substances with different properties in ‘real-life’ samples. Electrochemical sensors for the measurement of analytes of interest in medical analysis are ideally suited for these new application, due to their high sensitivity and selectivity, portable field-based size, rapid response time and low-cost. We already develop and use the extract of leaves and pulp of Maja (*Aegle marmelos*), Indonesian original plant, to modify the silver electrode and used it as urea and glucose biosensors. Similar with spicy sensor, we also provide a simpler process to urea and glucose detection.

2.2.1 UREA SENSOR

Urea is widely distributed in nature and its analysis is of considerable interest in clinical and agricultural chemistry. It is known to be an important marker for evaluating uremic toxin levels. The normal level of urea in serum is from 15 to 40 mg/dl (2.5–7.5 mM/l). In patients suffering from renal insufficiency, urea concentrations in serum vary from 180 to 480 mg/dl and, at elevated levels above 180 mg/dl, hemodialysis is required [8,12]. Hence, urea detection is important. In our study, we presented another alternative method for urea detection, that is electrochemical non-enzymatic biosensor using the extract of Maja leaf [5].

The composition of the electrode was reported in our previous paper [5]. The response of electrode was presented at Fig 5. It shows that the Maja leaf extract-modified silver electrode can detect urea without any interference from glucose. This result prove that the electrode have a good selectivity. The cathodic and anodic current signals are appears at 0.4 V and 0.625 V, respectively. The performance of the electrode also proven with LOD and sensitivity. According to Table 2, our Maja leaf extract-modified silver electrode is better that the other studies.

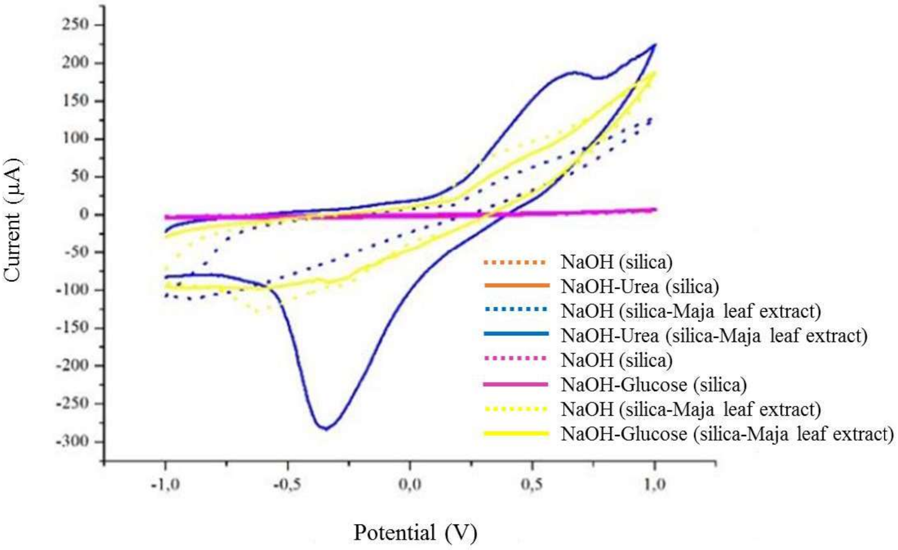

Fig 5. Response comparison between silica gel and silica gel/Maja leaf extract to glucose solution and urea at pH 13 condition.

Table 2. Comparison of the non-enzymatic urea biosensors.

Electrode	Linear range (µM)	LOD (µM)	Sensitivity ($\mu A.\mu M^{-1}.mm^{-2}$)	Reference
Modified Pt	80-1440	40	1.11	[8]
NiO/cellulose/CNT	10-1400	7	371	[12]
Ni-MOF/MWCNT	10-1120	3	685	[20]
Modified silver	1-6 (anodic) and 2-7 (cathodic)	2.299 (anodic) and 5.165 (cathodic)	19.781 (anodic) and 38.177 (cathodic)	This work

2.2.2 GLUCOSE SENSOR

Development of simple, reliable and fast methods for glucose detection is important, especially for medical diagnostics. The methods usefull to determination of glucose in the blood for diabetes screening and treatment. Many researcher reported and develop the electrochemical glucose sensors and biosensors both in enzymatic or non-enzymatic form. Enzymatic sensors normally have a short life due to the properties of the enzyme, which is very easy to decompose. Therefore, we used Maja pulp extract to modify silver electrode for non-enzymatic glucose biosensor [4].

The composition of the electrode was reported in our previous paper [4]. The response of electrode was presented at Fig 6. It shows that the Maja pulp extract-modified silver electrode can detect glucose. The signals of cathodic and anodic current discovered at 0.38 V and -0.25 V, respectively. There is no interference signal from urea and ascorbic acid. The performance of our Maja pulp extract-modified silver electrode was compared with other studies, which summarized at Table 3. It justifice that our electrode show a better performance than other research.

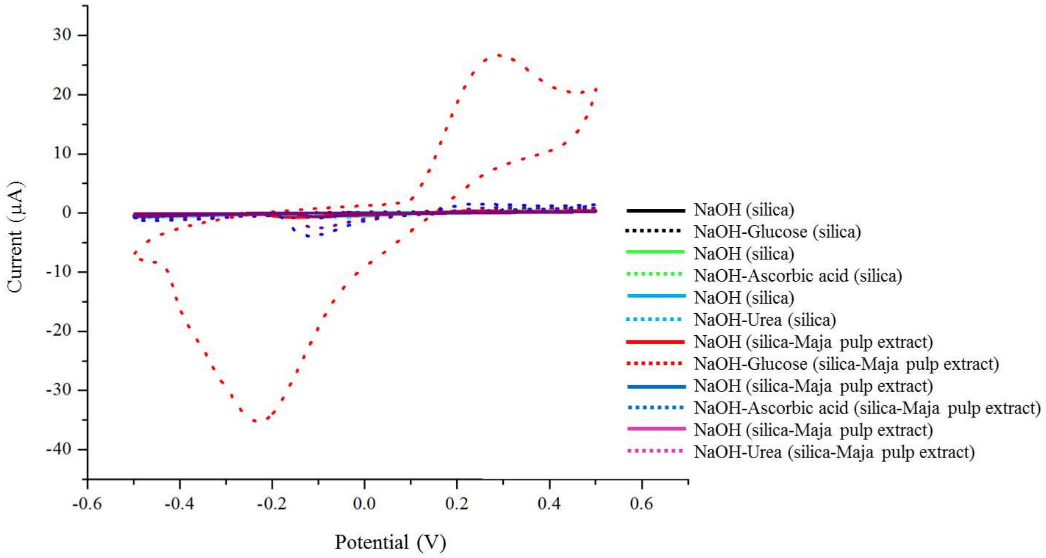

Fig 6. Response comparison between silica gel and silica gel/Maja pulp extract to glucose solution and urea at pH 13 condition.

Table 3. Performance comparison of the non-enzymatic glucose biosensors.

Electrode	Linear range (µM)	LOD (µM)	Sensitivity	Reference
Nanoporous Au	1000-18000	3	0.002 µA.µM^{-1}.mm^{-2}	[21]
ZnO/MWCNT/GCE	1000-10000	820	0.0064 µA.µM^{-1}.mm^{-2}	[22]
Micro/nano hybrid structured	55.6-13890	9	0.0749 µA.µM^{-1}.cm^{-2}	[23]
Modified silver	0-4 (anodic and cathodic)	1.920 (anodic) and 1.701 (cathodic)	1.222 (anodic) and 1.522 µA.µM^{-1}.mm^{-2} (cathodic)	This work

3. REFERENCES

[1]. N. Jadon, R. Jain, S. Sharma, K. Singh, Recent trends in electrochemical sensors for multianalyte detection – A review, Talanta. 161 (2016) 894–916. doi:10.1016/j.talanta.2016.08.084.

[2]. F. Kurniawan, V. Tsakova, V.M. Mirsky, Analytical Applications of Electrodes Modified by Gold Nanoparticles: Dopamine Detection, J. Nanosci. Nanotechnol. 8 (2008) 1–6. doi:10.1166/jnn.2008.013.

[3]. F. Fitriyana, F. Kurniawan, Polyaniline-Invertase-Gold Nanoparticles Modified Gold Electrode for Sucrose Detection, Indones. J. Chem. 15 (2015) 226–233.

[4]. T.P.H. Hutapea, Y. Triana, F. Kurniawan, Silica Gel / Maja (Aegle marmelos) Pulp Extract Paste Electrode for Glucose Detection, in: Proceeding 6th Annu. Basic Sci. Int. Conf., Faculty of Mathematics and Sciences Brawijaya University, Malang, East Java, Indonesia, 2016: pp. 476–478.

[5]. Y. Triana, T.P.H. Hutapea, F. Kurniawan, Maja Leaf Extract (Aegle Marmelos) and Silica Gel for Urea Detection by Using Cyclic Voltammetry, in: Asea Uninet Sci. Plenary Meet. 2016, ASEA-UNINET, Udayana University, Bali, 2016: pp. 20–27.

[6]. F. Kurniawan, N.S. Al Kiswiyah, K.A. Madurani, M. Tominaga, Single-Walled Carbon Nanotubes-Modified Gold Electrode for Dopamine Detection, ECS J. Solid State Sci. Technol. 6 (2017) M3109–M3112.

[7]. M. Sajid, M.K. Nazal, M. Mansha, A. Alsharaa, S.M.S. Jillani, C. Basheer, Chemically modified electrodes for electrochemical detection of dopamine in the presence of uric acid and ascorbic acid: A review, TrAC Trends Anal. Chem. 76 (2016) 15–29. doi:10.1016/j.trac.2015.09.006.

[8]. S. Mondal, M.V. Sangaranarayanan, A novel non-enzymatic sensor for urea using a polypyrrole-coated platinum electrode, Sens. Actuators B Chem. 177 (2013) 478–486. doi:10.1016/j.snb.2012.11.031.

[9]. N. Lu, C. Shao, X. Li, F. Miao, K. Wang, Y. Liu, CuO nanoparticles/nitrogen-doped carbon nanofibers modified glassy carbon electrodes for non-enzymatic glucose sensors with improved sensitivity, Ceram. Int. 42 (2016) 11285–11293. doi:10.1016/j.ceramint.2016.04.046.

[10].D.-H. Kim, W.-Y. Lee, Highly sensitive electrochemical capsaicin sensor based on graphene-titania-Nafion composite film, J. Electroanal. Chem. 776 (2016) 74–81. doi:10.1016/j.jelechem.2016.06.035.

[11].S. Wang, C. Wang, G. Wei, H. Xiao, N. An, Y. Zhou, C. An, J. Zhang, Non-enzymatic glucose sensor based on facial hydrothermal synthesized NiO nanosheets loaded on glassy carbon electrode, Colloids Surf. Physicochem. Eng. Asp. 509 (2016) 252–258. doi:10.1016/j.colsurfa.2016.08.076.

[12].N.S. Nguyen, H.H. Yoon, Nickel oxide-deposited cellulose/CNT composite electrode for non-enzymatic urea detection, Sens. Actuators B Chem. 236 (2016) 304–310. doi:10.1016/j.snb.2016.05.165.

[13].R. Mohammad, M. Ahmad, L.Y. Heng, Chilli hotness determination based on optical capsaicin biosensor using stacked immobilisation technique, Sens. Actuators B Chem. 190 (2014) 593–600. doi:10.1016/j.snb.2013.09.023.

[14].M.I. Sabela, T. Mpanza, S. Kanchi, D. Sharma, K. Bisetty, Electrochemical sensing platform amplified with a nanobiocomposite of L-phenylalanine ammonia-lyase enzyme for the detection of capsaicin, Biosens. Bioelectron. 83 (2016) 45–53. doi:10.1016/j.bios.2016.04.037.

[15].R. Mohammad, M. Ahmad, L.Y. Heng, Amperometric capsaicin biosensor based on covalent immobilizationof horseradish peroxidase (HRP) on acrylic microspheres for chillihotness determination, Sens. Actuators B Chem. 241 (2017) 174–181. doi:10.1016/j.snb.2016.10.077.

[16].Y. Wang, B. Huang, W. Dai, J. Ye, B. Xu, Sensitive determination of capsaicin on Ag/Ag2O nanoparticles/reduced graphene oxide modified screen-printed electrode, J. Electroanal. Chem. 776 (2016) 93–100. doi:10.1016/j.jelechem.2016.06.031.

[17].M.A. Dkhil, S. Al-Quraishy, Effects of extensive consumption of hot red pepper fruit on liver of rabbit, J. Od Med. Plants Res. 4(23) (2010) 2533–2538.

[18].W.L. Scoville, Note Capsicum, J. Am. Pharm. Assoc. (1912) 453.

[19].R.G. Compton, G.G. Wildgoose, R.T. Kachoosangi, Method of electrochemically detecting a capsaicinoid in a sample, WO2009115840 A1, n.d.

[20].T.Q.N. Tran, G. Das, H.H. Yoon, Nickel-metal organic framework/MWCNT composite electrode for non-enzymatic urea detection, Sens. Actuators B Chem. 243 (2017) 78–83. doi:10.1016/j.snb.2016.11.126.

[21].L.Y. Chen, X.Y. Lang, T. Fujita, M.W. Chen, Nanoporous gold for enzyme-free electrochemical glucose sensors, Scr. Mater. 65 (2011) 17–20. doi:10.1016/j.scriptamat.2011.03.025.

[22].A. Tarlani, M. Fallah, B. Lotfi, A. Khazraei, S. Golsanamlou, J. Muzart, M. Mirza-Aghayan, New ZnO nanostructures as non-enzymatic glucose biosensors, Biosens. Bioelectron. 67 (2015) 601–607. doi:10.1016/j.bios.2014.09.063.

[23].C.-W. Hsu, F.-C. Su, P.-Y. Peng, H.-T. Young, S. Liao, G.-J. Wang, Highly sensitive non-enzymatic electrochemical glucose biosensor using a photolithography fabricated micro/nano hybrid structured electrode, Sens. Actuators B Chem. 230 (2016) 559–565. doi:10.1016/j.snb.2016.02.109.

Polyaniline-Modified Zeolite NaY: A New Sorbent for Dispersive Solid Phase Extraction of Multiclass Pesticides

Rodjana Burakham[1*], Prapha Arnnok[1], Nopbhasinthu Patdhanagul[2]

[1]Materials Chemistry Research Center, Department of Chemistry and Center for Innovation in Chemistry, Faculty of Science, Khon Kaen University, Khon Kaen 40002 THAILAND
[2]Department of General Science, Faculty of Science and Engineering, Kasetsart University, Chalermphrakiat Sakon Nakhon Province Campus, Sakon Nakhon 47000 THAILAND
*Corresponding authors: [rodjbu@kku.ac.th]

1. INTRODUCTION

Pesticide residues are highly concerned as one of contaminants in environment, foods and agricultural products since their applications are continually expanding and their consumptions are ever increasing. Trace analyses of these substances require analytical techniques for the detection of the greatest number of compounds possible, with the fewest number of extraction and clean-up steps. The analytical techniques for these trace residues usually consist of sample preparation and quantification using analytical instruments. Our work is intended to developed new materials for preconcentration of chemical residues as well as to propose a sample preparation procedure [1]. A novel polyaniline (PANI)-modified zeolite NaY was proposed as sorbent for the dispersive solid-phase extraction (DSPE) of diverse pesticide residues [2].

2. METHOD

The PANI-coated zeolite NaY sorbent was created via oxidative polymerization of aniline onto the surface of the zeolite. The sorbent was applied for DSPE of commonly used pesticides belonging to five different chemical groups, including carbamate, organophosphate, sulfonylurea, pyrethroid and neonicotinoid. To perform the DSPE, 150 mg sorbent was added to 125 mL of sample. A suspension was then shaken for 4 min to promote the sorption of the analytes onto the sorbent before transferring to the SPE eluting column. The column was washed with 10 mL water before eluting with an appropriate eluent. The final extract was analyzed by HPLC-PDA.

3. RESULTS AND DISCUSSION

The applicability of synthesized PANI-modified zeolite NaY as a sorbent for multiclass pesticides extraction was investigated. An average sorption capacity of 833 mg kg^{-1} sorbent was reached. The experimental conditions of the DSPE procedure were optimized. The coupling of DSPE and HPLC resulted in an efficient method for multiresidue analysis of pesticides. The preconcentration factor of up to 42 was observed. The LODs and LOQs of the proposed method were found in the ranges of 0.001–1.00 mg L^{-1} and 0.005–2.50 mg L^{-1}, respectively. The method was successfully applied to the determination of pesticide residues in environmental and food samples. The satisfactory recoveries were obtained.

4. REFERENCES

[1]. P. Arnnok, N. Patdhanagul, R. Burakham, 2015, *Chromatographia*, **78**, 1327.
[2]. P. Arnnok, N. Patdhanagul, R. Burakham, 2017, *Talanta*, **164**, 651.

Mathematical Model of a Growing Tumor and Its Interaction with Immune System: The role of dendritic cell in controlling the immune system

Trisilowati[1*] and D.G. Mallet[2]

[1]Department of Mathematics, Faculty of Mathematics and natural Sciences, University of Brawijaya, Malang, Indonesia
[2]Mathematical Sciences School, Faculty of Sciences, Queensland University of Technology, Brisbane, Australia
[*]trisilowati@ub.ac.id; dg.mallet@qut.edu.au

1. INTRODUCTION

Immune system such as natural killer (NK) cells and cytotoxic T cells are capable of recognizing and killing tumor cells. In recent years, it is found that dendritic cells (DCs) also have a potential role in controlling a tumor growth, besides their function as a regulator of immune system [1]. This talk relates to a mathematical model of a growing tumor and its interactions with the immune system that is emphasized in the role of dendritic cells in controlling immune system. First, we construct a mathematical model in the form of system of ordinary differential equation. Then, existence of the equilibrium point and their stability are analyzed. We also investigate which parameters that play important role in this model. Second, we develop a hybrid cellular automata model that can describe the system in more detail, including cell-cell interactions of every single cell in the system. Besides providing more detail of the immune system, this model also include the chemokine which function to activate dendritic cells. Furthermore, to include the effect of chemokine, we use a partial differential equation to describe the concentration of chemokine.

2. METHOD

First, we construct the model based on some assumptions stated in [2]. This model consists of tumor cells, NK cells, cytotoxic T cells, DCs and chemokine in the form of system of nonlinear ordinary differential equations. The stability analysis is done by linearizing the system near equilibrium points and Routh-Hurwitz creterion is then used. In the second model, we combine the numerical solution of partial differential equation model with the discrete cellular automata used to model individual cells [3]. Finally, some numerical simulations are conducted to illustrate the behavior of the solution of both models.

3. RESULTS AND DISCUSSION

Based on analysis result, the first model has two equilibrium points which exist and asymptotically stable under certain conditions. It is also obtained that the parameters such as tumor growth, NK cells tumor cell kill rate, death rate of NK cells and source term of NK cells play important role in the growth of tumor.

Hybrid cellular automata model can describe the evolution of the tumor cells both in space and in time. From simulation, increasing the concentration of DCs will decrease the concentration of tumor cells.

4. REFERENCES

[1]. N. Larmonier, J. Fraszack, *et al.*, 2010, *Cancer Immunology Immunotherapy*, **59**, 1-11
[2]. L.G. de Pillis and A.E Radunskaya, 2003, *Comp. Fluid and Solid Mechanics*, 1661-1668
[3]. D.G. Mallet and L.G. de Pillis, 2006, *J. of Theoretical Biology*, **239**, 334-350

Spatial Panel Dynamic Econometrics Model of Land Value, Land Use Externalities and Their Dynamic: Case Study of the Jakarta's Fringe

*Rahma Fitriani[1], Eni Sumarminingsih[1], Suci Astutik[1]

1Departmen of Mathematics, Faculty of Science, Brawijaya University, Indonesia, 65145
*Corresponding author: [rahmafitriani@ub.ac.id]

Abstract-Land value is the product of past decision of its use leading to its value. It is also affected by the local characteristic and the observed surrounded land use (externalities) from the previous period. The effect of each factor on land value has dynamic and spatial virtues. An empirical land value model with a spatial panel dynamic setting is appropriate to capture them. The model will be useful to estimate the extent of land use externalities on land value in the short run as well as in the long run. It serves as a basis to formulate an effective urban growth management's policy. The objective of this paper is to derive the indirect effects – externalities on land value and their dynamic. The result will be applied to analyze the significance of land use externalities on land value in the fringe of Jakarta Metropolitan. There is some evidence about the significance of neighborhood urban activity – negative externalities, the previous land value and local accessibility on land value. The effects are accumulated dynamically over years, but they will fully affect the land value after 5 until 6 years.

How Data Science Shapes Personalized Medicine Revolution

Setia Pramana[1*]

[1]Institute of Statistics, Jakarta
*Corresponding authors: [setia.pramana@stis.ac.id]

Abstract-Personalized Medicine coined firstly in 1969 is defined as tailoring of medical treatment to the individual characteristics. This field has made significant progress with key discoveries boosted by rapid development of new biotechnologies such as Microarray Chip and Next Generation Sequencing (NGS).

From the completion of Human Genome Project 2003 scientist in this field have produced billions of data points on properties, structure and functions of genes, proteins and other molecules are compiled in enormous databases and systematically studied. As the price is getting cheaper, the growth of the data on genomes, proteins and cells would be unstoppable by approximately 25 petabyte/year worldwide.

Dealing with this “big data” requires a different approach and poses challenges for data scientist in retrieving, managing, visualizing, analyzing, interpreting and presenting the data. Conventional statistical approaches can no longer be used. Numerous advanced statistical techniques have been proposed to understand and extract more insight and information of the biological data.

The objective of this article is to review and describe the role and increasing importance of data scientist in the research of personalized medicine, as well as discuss the challenges and some current topics.

Furthermore, this article would discuss the development of various advanced statistical techniques from simple to the latest implemented in Bioinformatics in shaping the revolution of personalized or precision medicine. Wide range approaches in classification and clustering techniques used in Microarray and NGS would be presented. Future development and research direction would be discussed as well.

In conclusion, data scientists not only have major role in all aspects of discovering precision medicine but also would be able to speed up the translation of all findings to the clinical practice.

Volume 2

BaSIC 2017

The 7th Basic Science International Conference

Basics Science for Improving Survival and Quality of Life

Material Science and Technology

Synthesis of Textile Natural Colorants from Cassava Peel Waste Fermented by Monascus purpureus

*Ikhwanul Muslim [1], Ika Natalia Mauliza [1], Mohamad Widodo [1]

[1]Department of Textile Chemistry, Politeknik STTT Bandung, Bandung, Indonesia
* Corresponding authors: ikhwanul_01@yahoo.com

Abstract – The use of synthetic colors for dyeing textiles avoided because it is dangerous to human life. Users began switching to natural dyes because of its more environmentally friendly. Natural dyes are selected not only from nature, but it must be sustainable, easily processed, high yield, and does not lead to negative effects during cultivation. Therefore, the use of natural dyes for textiles from mold begins to investigate. The Objectives of this study to determine the quality of the textile natural dyes derived from fermented cassava peel by Monascus purpureus. Initially, the mold cultured on PDA and inoculated in the flour of cassava peels with parameter variation of nutrients and moisture contents. Inoculation was observed for 14 days. At the end of the inoculation process, cassava peels flour dried and characterized: color, yield, and the preliminary study of dyeing ability on silk. The results showed that moisture content gave the effect on the quality of color. Without the addition of nutrients, flour of cassava peels fermented by Monascus purpureus have capacity to produce the dyes. The highest influence actually seen from varying moisture content in the flour of cassava peels. The higher the water content, the higher yield of the dye. The results of the initial dyeing on silk showed that the dye has the ability to dye silk, so it is recommended to be further investigated.

1. INTRODUCTION

The use of natural dyes today is more advisable for the textile dyeing process because it is considered more environmentally friendly. Monascus development as textile natural dyes mentioned by Velmurugan (2013) which states that Monascus has the potential to be used as a natural dyestuff for textile materials [1].

Monascus purpureus are micro fungal which can produce colorants. Monascus product has been established as “angkak” in Indonesia. “Angkak” made from rice fermented by Monascus purpureus. Through its fermentation process, Monascus produce six pigments, they are rubropunctatin and monascorubrin (orange pigment), monascin and ankaflavin (yellow pigment), monascorubramine and rubropunctamine (red dyes). Production of colorants can be obtained in two conditions, solid state and submerged. Most research used solid state fermentation because it is easier and yields a better quality of colorants [2].

Monascus red dye production is influenced by several factors, including the chemical content of the substrate, especially carbon and nitrogen. Carbon derived from carbohydrates contained in the substrate, while nitrogen is produced from protein. To increase the production of dye through the modification of the nitrogen content in the substrate, done in various ways, such as adding a nitrogen-containing compound such as monosodium glutamate. [3].

In addition, the production of dyes is influenced by environmental conditions such as moisture content. Maximum dyes production reached at water content of 50% [3]. The highest the water content cause the substrate become aggregates. It causes the lowering distribution fungal mycelium. Various natural materials have been used as a substitute for rice in the production of Monascus red dye, such as cassava, sugar cane bagasse, cassava bagasse, and corn cobs [2]. One of the potential substrates to produce Monascus dyes is cassava peel waste.

The cassava peel can be used as a fermentation medium of Monascus [4]. Cassava peel waste itself is easily available in large quantities from the rest of the cassava processing industry. This is reinforced by the content of substances that are owned by the skin of cassava in the form of carbohydrates, protein, water, starch and minerals needed for Monascus growth.

Based on the source, textile dyes broadly divided into two parts, namely natural and synthetic. Natural dye that has been widely used among indigofera, curcuma and carmine. Along with advances in technology and the needs of increasingly diverse colors, the synthetic dyes began to shift the natural dyes in textile materials.

Cassava is a plant that lives in the tropics. Cassava is widely used as a staple food instead of rice. According to data from the Agriculture Agency of Indonesia, cassava production in Indonesia reached 20.8 million tons per year. Percentage of the number of cassava peel generated inside is 8-15% of the total weight of fresh cassava. If the production of cassava per year in Indonesia amounted to 20.8 million tons, it will produce cassava peel approximately 1.66 to 3.12 million tons per year. Cassava peel has relatively high carbohydrate content. A Composition of carbogidrate in the cassava peels about 4.55% [5]. The high carbohydrate content of cassava peel may be used as an energy source for microorganisms [6]. This study was conducted to obtain natural dyes for textile from Monascus growth in cassava peel media.

2. METHODS

2.1 Chemicals

Monascus obtained from the Laboratory of Chemical Engineering FTI, ITB. Fungus then cultured on agar media / PDA. Cassava peel obtained from cassava processing industry in Bandung.

2.2 Procedures

Monascuss grown on adar medium to obtain ready to grow Monascuss. Cassava peel processed first, by washing, cutting, soaking and drying. Washing is done using warm water for 30 minutes then cassava peel cut into the size of 1 cm^2. Continued with soaking for 24 hours and then dried under the sun for 48 hours. The dried cassava peel then finely ground into flour and filtered in order to obtain a uniform size. 5-gram flour cassava peel inserted into the bottle fermentation that has been sterilized. Fungal spores are then transferred to a medium peel cassava flour and added 9 ml of distilled water to obtain a suspension of spores Monascus. Monascus fungus grows in media cassava peel at 30 ^{o}C for 14 days. Fermented cassava peel then extracted with 25 ml of ethanol then stirred to 200 rpm for 1 hour and allowed 30 minutes to settle and then filtered through filter paper. Filtrates then characterized its absorbance values with the help of UV-VIS spectrophotometer. The Monascus dyes then applied to silk fabrics to make sure that it can be used as textile colorants.

3. RESULTS AND DISCUSSION

Before doing the main research, cassava peels were characterized as shown in the Table 1.

Table 1 Cassava Peel Characterization

No.	Characterization item	Cassava Peel (%w/w)
1	Water content (gravimetry method)	74
2	Starch content (Luff Schoorl method)	6,8
3	Protein content (Kjeldahl method)	6,7

Table 1 described that cassava peel contains a lot of water. Based on previous research, too much moisture content will disrupt the fermentation process. Recommendation of moisture content should not more than 50%. Cassava peels contain carbon and nitrogen sources as a starch and protein as shown at the Table 1. Starch is the main source of food in order to grow the fungus. The protein content of cassava peel is relatively large. This will affect the speed of fungal growth up to the adult stage. The more protein source would produce good maturity of Monascus mold in order to obtain the desired red color.

The Fermentation process of Monascus can be seen in the Figure 1.

Figure 1 Fermentation process of Cassava Peel Waste using Monascus purpureus

Figure 1 shows that the Monascus fermentation in cassava peel flour media can run well and as expected. This can be seen in color resulting from starting on day 1 to day 12. At Day 1, the growth of the Monascus been clearly shown. It is seen from the color of the cassava peel media still has not changed from the beginning. On Day 6, began to appear whitish on the cassava peel media. This indicates that the Monascus already in the early stages of growth so that it can be said fermentation process in line with expectations. On Day 12, most of the colors red and yellow skin redness already dominate media cassava. This indicates, most of the Monascus fungus had grown so well that it is in the adult fungus stage. It proves that the fermentation process is going according to plan so that the results are as expected.

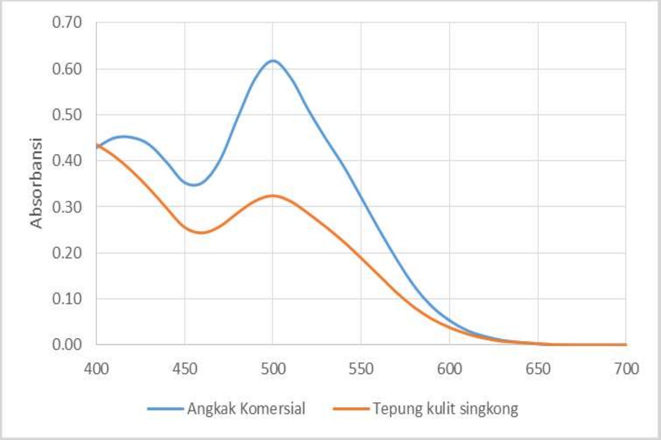

Figure 2 Colour measurement of angkak extract and cassava peel extract

Based on absorbance data in Figure 2, it can be seen that commercial Angkak has maximum absorbance value at a wavelength of 500 nm. Similarly, the cassava peel has the same maximum absorbance value at a wavelength of 500 nm. This indicates that both of the commercial angkak and cassava peel produce the same red color. It also indicates that the maturity level of the Monascus on the cassava peel has the same value with Monascus on commercial Angkak.

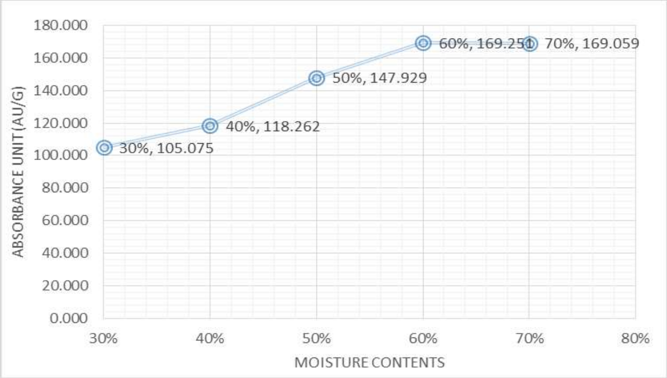

Figure 3. Color measurement results on a wide range of moisture content

The process parameter in this study is moisture content of the media. Variations in water contents used 30% - 70% with 10% interval. The results can be seen in Figure 3. Data of color measurements taken at a wavelength of 500 nm. Change of moisture content in the media gives the dye yield significant changes up to 60% an increase of dye yield.

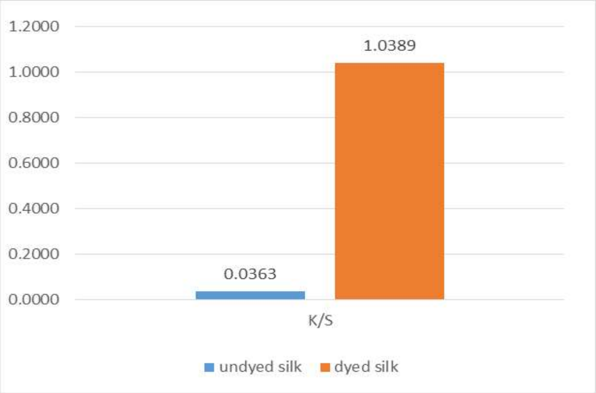

Figure 4 Colour measurement of silk before and after dyed

Figure 5 Dyeing silk using cassava peel extract

To ensure that the extract of Monascus can dye textile fibers, the dyeing is done in silk. Dyeing results can be seen in Figures 4 and 5. Those figures show that the silk fabrics dyed with extracts of Monascus red dyes and the K/S value of dyed silk is greater than the value of K / S undyed silk. This indicates that the silk fabric can be colored by the dyes from fermented cassava peel using Monascus purpureus.

4. CONCLUSIONS

Based on the results of research can be concluded that cassava peel waste produce sufficient nutrition for Monascus growth and given the red color in the silk fabrics.

5. REFERENCES

[1]. Velmurugan, Palanivel, dkk (2013). The Use of Cochineal and Monascus purpureus as Dyes for Cotton Fabric. *Coloration Technology, Society of Dyers and Colourists*,**129**: 246-251

[2]. Pattanagul, P, dkk. (2007) : Review of Angkak Production (MonascusPurpureus). *Chiang Mai J Sci*, **34(3),** 319-328.

[3]. Carvalho, J.C., C.R. Soccol, S. Babitha, A. Pandey, dan A.L. Woiciechowski, (2007) : Production of Pigments. Current Developments in Solid State Fermentation. Asiatech Publisher, inc. New Delhi.

[4]. Afiandiningsih, Depi, (2013). Pengaruh Konsentrasi Inokulum (Monascuspurpureus) terhadap Produksi Pigmen pada Substrat Tepung Kulit Singkong (Manihot esculenta). Skripsi program Sarjana, Universitas Pendidikan Indonesia.

[5]. Marjoko, Agus. (2010). Daya Terima dan Kadar Alkohol pada Tape Kulit Singkong Berdasarkan Variasi Jumlah Ragi. Dalam Undergraduate Theses Universitas Muhammadiyah Semarang. Semarang

[6]. Muhiddin, N., N. Juli, dan I.N.P. Aryantha. (2000). Peningkatan Kandungan Protein Kulit Umbi Ubi Kayu Melalui Proses Fermentasi. *Jurnal Matematika dan Sains*, **Vol. 6**, hal.1-12

An Analysis of Temperature Substrat Effect and Nitrogen Gas Pressure on Aluminum Nitride Crystal Growth Using Reactive Sputtering Method

Dianita Wardani[1], Diah Susanti[1], Agung Purniawan[1], Trimardji Atmono[2]

[1]Department of Material and Metalurgical Engineering, Faculty of Technology Industry,
[1]Institut Teknologi Sepuluh Nopember (ITS), Surabaya, Indonesia
[2]National Nuclear Energy Agency (BATAN), Yogyakarta, Indonesia

Abstract - Today's semi-conductor technology continues to develop, both in terms of material discovery, manufacturing technique, as well as implementation and the development. In this research, the researcher will utilize the AlN synthesis with a reactive sputtering method on the substrate SiO2 that has done with variation substrate temperature of (200, 250, 300^{o}C), and the nitrogen gas pressure of 10, 15 and 20 mBar. This study successfully synthesizes nanomaterial AlN with a hexagonal crystal system and shows the wurtzite phase is formed. While, morphology AlN formed composed of particles - spherical shaped particles. From this research it is known that raising the temperature of the substrate produces more uniform morphology and homogeneous, the surface roughness is formed from 15,4 to 84 nm and obtained the crystal size is 64-87 nm. While the addition of nitrogen gas pressure causes the better crystallinity. The research obtained AlN with Optical Transversal wave type at a wavenumber of 600-670 cm-1. While, the growth of AlN crystal growth of AlN is best obtained on the parameters of the substrate temperature 290 °C and nitrogen gas pressure of 20 mbar.

Keywords: Semiconductors, aluminum nitride (AlN), SiO2, Reactive Sputtering, OpticalTransversal

1. INTRODUCTION

One of semi-conductor materials that attract today's attention is Aluminum nitride (AlN). AlN is an important member of the group III-V with the highest bandgap of around 6.2 eV. It is a promising advanced ceramic material with many interesting properties, such as high electrical resistivity ($>10^{14}$ Ωcm), high thermal conductivity (285 W/(m K)[1]. Therefore, AlN is a potential candidate for many applications in solar cells, transparent conductive coatings, gas sensors, semiconductor materials well as electro and photoluminescence, Several methods of physical and chemical synthesis to produce AlN with a 1-dimensional nanostructures have been developed, including vapor phase method such as thermal evaporation, chemical vapor deposition, deposition of metal-organic vapor phase (MOCVD), electrodeposition and synthesis methods such solutions soles gel, solution deposition, hydrothermal synthesis, microemulsion technique, as well as direct growth 2 the solution of alcohol-aqueous[2], has been made to the process of formation of AlN, for example, the growth of product AlN can occur at temperatures 1300oC at a rate of 10 ° C / min, using the technique of Vapor Liquid Solid (VLS) and using a stream of nitrogen gas [3]one of them is using the reactive sputtering method. This method has several advantages such as simple crystal growing technique, the deposition of low temperature and easy to control the experiment parameters[4].

2. METHOD

2.1 Materials and Tools Research

Silicon dioksida (SiO_2) (100), Material target Aluminium , Material target Au, Larutan Etanol, Larutan aseton, argon (Ar), nitrogen (N_2), *diamond cutting tool, Sputtering PSTA-Batan, Fourier Transform Infra Red* (FTIR) and *Transmission Electron Microscope* (TEM) were used to characterized AlN.

2.2 Sputtering Process SiO_2 dan Growing AlN on Substrates

SiO_2 as the substrate sputtered by sputtering using a Au catalyst uniform AlN growth on SiO_2 substrates for 10 minutes. Time variable can be used in a sputtering tool, among others, 1 minute or 2 minutes, depending on the needs. The function of the sputtering Au to give SiO_2 layer on the substrate so that the ions of aluminum plates and nitrogen gas can attach and grow as a nanomaterial aluminum nitride. SiO_2 substrates incorporated into the PVD chamber and placed in a holder that is prepared at the anode, while for the plates Au and Al is placed on the plate cathode. Furnace chamber and in setting the sputtering deposition of SiO_2 with Au, is then subjected to vacuum for 15 minutes with great pressure Barr $4x10^{-2}$ .Vacuum deposition substrate SiO_2/Au conducted over 10 minutes. After the tool gives a chance for the target sputtering material pure aluminum (75 mm) to the substrate surface SiO_2 / Au with a deposition time of 15 minutes, without removing the substrate and the target material to remain in vacuum conditions. The devices are set to rise 10° C / min to a temperature of 200, 250 and 300°C, then shatter the chamber is opened when the plasma is formed, then purged with nitrogen gas pressure variations nitrogen10, 15 and 20 mBar.

3. RESULT AND DISCUSSION

3.1 Testing Results Fourier Transform Infra Red (FTIR)

The purpose of testing Fourier Transform Infra Red (FTIR) is to identify a compound based on functional clusters. To determine the infrared absorption AlN compound that can be used in the application light emitted diode (LED). In this study, spectra of graphs showing different characteristics. FT-IR testing is done by using Shimadzu 8400S test data obtained from the top of the chart is at wavenumber range between 400- 4000 cm^{-1}.

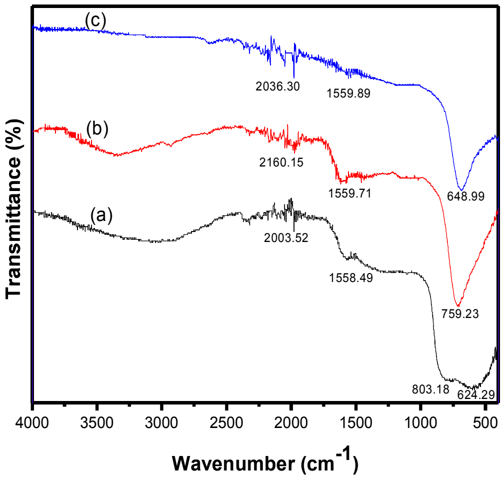

Figure 3.1 The results of Fourier Transform Infrared Spectroscopy (FT-IR) on the AlN substrate temperature to 250°C and pressure of nitrogen (a) 10 mBar (b) 15 mBar (c) 20 mBar

Figure 3.1 shows that at a temperature of 250°C from the test results FT-IR peak have varied from 97-99% transmittance in the range of 600-800 cm-1 are almost the same as the previous variation which indicates the downward peak beam then forwarded and absorbed the higher. According to the results of testing of FTIR, AlN compounds generated in this study can be applied to light emitted diode (LED). AlN compound capable of transmitting visible light at a wavelength of 600-800 cm-1. Wave AlN compounds are inorganic compounds (Fei et al, 2012). Is known that there wavenumber dominated at intervals of 600-800 cm^{-1}. In wavenumber interval 600-670 an optical transverse force active infrared and visible AlN compound produces infrared optical properties of the active transverse to the parameter variations in temperature to 250°C in nitrogen pressure 20 mBar.

By characterisation LED that can emit electromagnetic waves, the compounds can be applied in a window AlN layer of the LED. At the peak absorption region of 2000-2200 cm-1, there are other weak peaks were observed that the vibration mode of bonds N-Al-N, it further confirms that growth over SiO2 is stoichiometric AlN substrate [5]. For the C-O bond bending measured the impurities from the air were identified during the measurement process. It also deals with the homogeneity of crystals that can improve the optical properties where the target is deposited uniformly and relatively the same, making the level of crystallinity the better, so as to boost the value of transmission [6].

3.2 Characterization Analysis of Transmission Electron Microscope (TEM)

Testing Transmission Electron Microscope (TEM) was used to analyze the morphology, crystal structure, and composition of the specimen. TEM provides higher resolution than SEM and can facilitate the analysis of the size of the nanomaterial. TEM testing in this study was conducted using a JEOL JEM-1400 and conducted at the Laboratory of Chemistry, University of Gajah Mada, Yogyakarta.

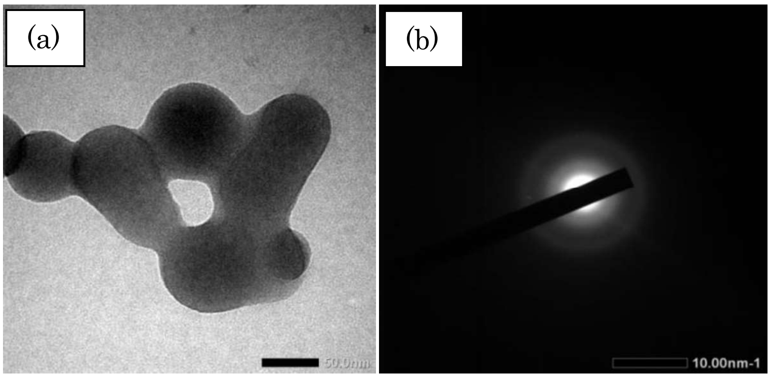

Figure 3.2 The results of TEM imaging at 300ºC Substrate Temperature Variation and Nitrogen pressure 20 mBar (a) Magnification Scale 30.000x with 50nm and (b) Test Results SAED pattern Diffraction Ring.

TEM imaging results in Figure 3.2 (a) show that AlN formed a nanomaterial with magnification scale of 100 nm and 20 nm, for parameter 300ºC substrate temperature and nitrogen pressure 20 mBar on measurements obtained ± 64-87 nm size. On the results of the previous morphological observations performed with the SEM imaging shows the morphology of AlN obtained less clear. In the picture TEM imaging can we know that the round-shaped particles which tend to merge so that oval and elongated. Figure 3.2 (b) shows the test results SAED, for analysis of the results diffraction pattern obtained one point in the ring, after the calculation of the value of d-spacing. The results of the calculations show that the value of diffraction d-spacing is 1.38163 in the notation field (200). The result is worth almost the same as the value of d-spacing of XRD test results is 1.35653 in the field (200).

4. CONCLUSIONS

Based on the research that has been done, it can be concluded that the synthesis of compounds of aluminum nitride (AlN) has been successfully performed using reactive sputtering over SiO_2 substrate. Of the various substrate temperature and nitrogen pressure this study we concluded that AlN compound of testing Fourier Transmission Infrared (FTIR) showed wavenumber 600-800 cm^{-1}, for the FTIR results wavenumber of 600-670 cm^{-1} is the Optical Transversal. TEM results of the tests show that AlN formed a nanomaterial size 64- 87 nm

5. REFERENCES

[1]. Shi, Zhongqi Shi (2014). “Combustion synthesis of AlN nanowhiskers with differentmetallic catalysts” *Journal of Crystal Growth,* 323:286-289.

[2]. Yoon, Jong-Hwan. (2014). “Alternative vapor-liquid-solid process in Au-assisted growth of silica nanowires”. *Materials Letters*, 123:131-134.

[3]. Yu, Leshu, Lv, Y., Zhang, X., Zhang, Y., Zou, R., dan Zhang, F. (2011). “Vapor-liquid-solid growth route to AlN nanowires on Au-coated Si substrate by direct nitridation of Al powder”. *Journal of Crystal Growth*, 334:57-61.

[4]. Wei, Z.Q., Zhang, (2014). “Effects of sputtering pressure on nanostructure and nanomechanical properties of AlN films prepared by RF reactive sputtering”, **Vol 2**, 2845−2855.

[5]. Mortet, V dkk (2003). “Aluminium nitride films deposition by reactive triode sputtering for surface acoustic wave device applications”. *Surface Coatings and Technology*. 176:88–92

[6]. Planck Van, R. P. Devaty, and W. J. Choyke,(2009) “Infrared reflectance of thin aluminum nitride films on various substrates”, *Appl. Phys. Lett.,* **vol. 62**, pp. 750-752.

Nanosilica (SiO_2) From Pyrophyllite Ores Make Hydrophobic Banknotes

Fithrotun Nisa’[1], Abdulloh Fuad[1]*, Sunaryono, Subakti[1]

Department of Physics, Faculty of Mathematics and Natural Sciences, Universitas Negeri Malang
(State University of Malang), Jl. Semarang No. 5, Malang 65145, Indonesia
* Corresponding authors: abdulloh.fuad.fmipa@um.ac.id

Abstract – The number of banknotes which are unfit for circulation in Indonesia keeps increasing and spends Rp 475 billion annually on security paper import. The author was interested in imitating natural hydrophobic symptoms as can be seen on the leaves of lotus flower (*Nelumbo nucifera*) and optimizing its functional characteristic which is potential in the industrial field, especially paper industry. The hydrophobic, transparent, and adhesive banknotes or printing paper have been successfully obtained through spraying the hydrophobic nano silica spray and 5% TMCS/ethanol.

1. INTRODUCTION

Circulated banknotes in Indonesia are often found mutilated, stained by ink, etc. [1]. The Law Number 6 of 2009 set that the missions of Bank of Indonesia which relate with money circulation are to fulfill the society need of money in the sufficient nominal value, appropriate denominations, punctual manner, and in the condition of fit for circulation. Besides, according to Law Number 7 of 2011 on currency and Bank of Indonesia Regulation Number 15/10/PBI/2013 on rupiah currency management, that in principle, money which is unfit for circulation is subject to destruction.

The superhydrophobic character of nano silica layering on a glass substrate has been successfully observed before [2]. Moreover, there are numerous research on hydrophobic characteristic conducted to various materials [3-11]. However, there are still limited case studies on paper hydrophobicity. The properties and characteristics of paper are distinct from other materials.

The above studies did not mention the adhesive power of hydrophobic nano silica particle on paper. Moreover, there is also a lack of explanation about kinds and characteristics of paper which can be produced as hydrophobic paper. Therefore, research on the addition of adhesive substances, such as epoxy resin layer, is necessary to improve the nano silica adhesive power on paper and to study its effects on paper hydrophobicity, especially on banknotes.

2. METHODS

2.1 Chemicals

The required materials are as: Pyrophyllite materials, distilled water with pH of 7, 5M H_2SO_4, 5M NaOH, alcohol, *trimethylchlorosilane* (TMCS), samples of banknotes and printing paper, ethanol, acetone, epoxy resin of *diglycidyl ether bisphenol-A* (DGEBA), and resin hardener.

2.2 Procedures

The research procedures included the following phases.

1. **Nanosilica synthesis via coprecipitation method**

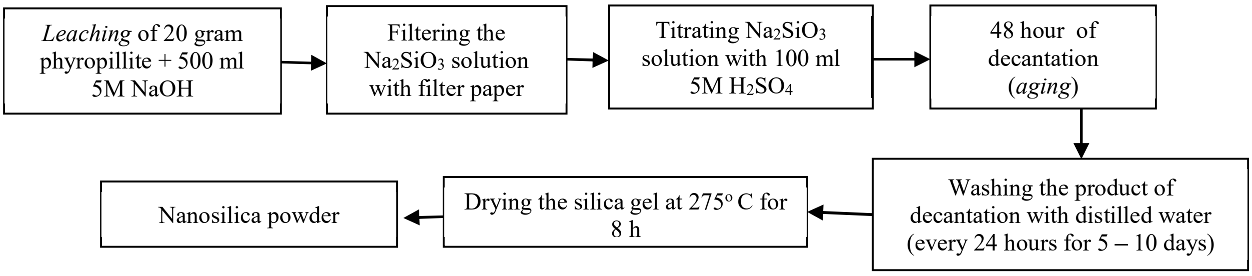

2. Nanosilica characterization through the means of XRF and SEM

The nano-silica was characterized by using X-Ray Fluorescence (XRF) to identify the nano silica purity and its percentage of impurity. Then, the nano silica was tested by using Scanning Electron Microscope (SEM) to identify the size distribution of nano silica powder and morphology of banknotes.

3. Modification of hydrophilic nano silica into hydrophobic

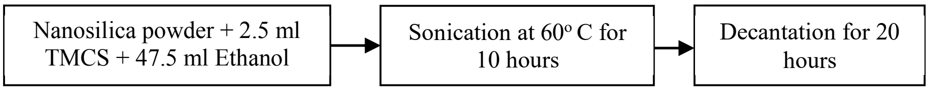

The amount variations of nano silica powder mixed into TMCS/5% ethanol are 1, 2, and 3 grams.

4. Production of epoxy resin layer

The production of resin solution by mixing acetone, DGEBA epoxy resin, and resin hardener with the comparison of 10: 1: 0.5. The solution was stirred until it became a homogeneous solution and then moved to the spray bottle.

5. Resin layering and hydrophobic nano silica spray

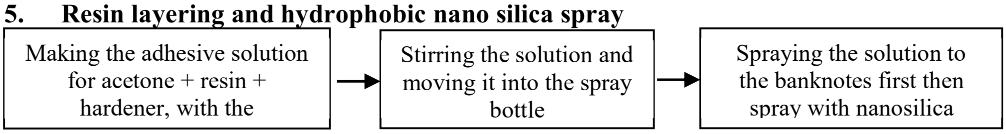

3. RESULTS AND DISCUSSION

3.1 Results of XRF Characterization

Nanosilica with the purity level of 98.6% was obtained, as shown in Table 1. The high purity level of the nano silica affected the formed hydrophobicity. The higher the purity level of nano silica obtained, the higher the hydrophobicity of the nano silica [8, 12].

Table 1. Results of XRF Characterization

Oxide	Percentage (%)
SiO_2	**98,6**
K_2O	0,16
CaO	0,63
TiO_2	0,13
Cr_2O_3	0,060
Fe_2O_3	0,22
NiO	0,084
CuO	0,056
Yb_2O_3	0,05

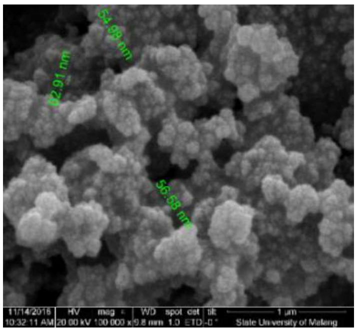

Figure 1. SEM Results of HydrophobicNanosilica

Results of SEM Characterization

Based on Figure 1, it can be identified that the average distribution of silica particle size in this research was 58.16 nm. It is already in conformance with the purpose of the research, namely to synthesize nano-sized silica. The researcher [12] has studied the use of nano silica for 25 nm nano silica fabrication.

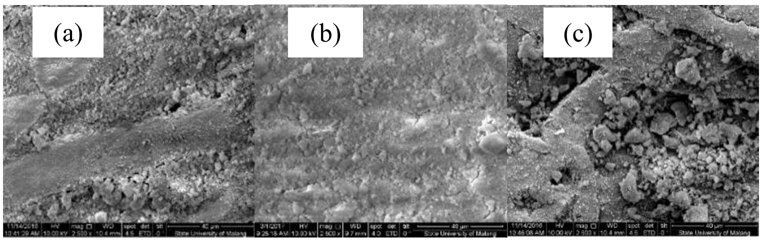

Figure 2. SEM Results of Banknote surface with (a) 1 gram, (b) 2 grams, (c) 3 gram nanosilica in 2500x zoom

According to Figure 2, it can be seen that the addition of concentration or the amount of nanosilica has an influence on the roughness and the production of nanosilica agglomeration on banknote surface. The material roughness and nanosilica agglomeration have a big influence on the paper hydrophobicity [12].

3.2 Test Results on Water Contact Angle via a Digital Microscope

~50 µL of water was dropped in the form of droplets by using a syringe on three spots on a banknote surface. The water contact angle was observed using a digital microscope with 100x zoom. The results of water contact angle test are presented in Table 2, and the water droplets are shown in Figure 5.

Table 2. Results of Water Contact Angle Test

Remark	Droplet position	Water Contact Angle (°)					
		U1R	**U2R**	**U3R**	**K1R**	**K2R**	**K3R**
With Resin	**a**	114,8	110,9	102,9	101,5	102,6	119,3
	b	107,8	110,5	114,3	100,9	115,3	117,3
	c	95,5	99,3	108,1	101,6	119,4	117,3
Average		**106,0**	**106,8**	**108,5**	**101,3**	**112,4**	**117,9**
Remark	**Droplet position**	**U1NR**	**U2NR**	**U3NR**	**K1NR**	**K2NR**	**K3NR**
Without Resin	**a**	122,9	104,4	129,6	127,0	123,0	140,1
	b	115,9	129,7	136,7	118,6	128,1	150,3
	c	106,2	116,4	126,9	111,0	116,4	121,5
Average		**115,0**	**116,8**	**131,1**	**118,9**	**122,5**	**137,3**

Definitions:

UnR	(n sample banknote with Resin)
UnNR	(n sample banknote without Resin)
KnR	(n sample paper with Resin)
KnNR	(n sample paper without Resin)

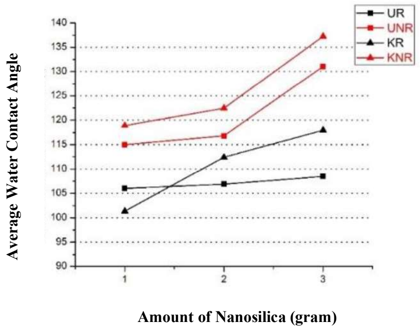

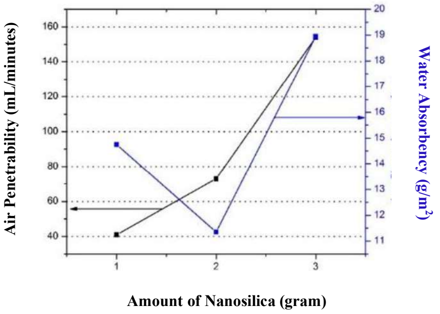

Figure 3. Graphic of Nanosilica and WCA Correlation

Figure 4. Graphic of Nanosilica and DTU and DSA Correlation

Figure 3 shows that the increasing amount of nano silica can increase the formed water contact angle. Either banknote or printing paper without resin has larger water contact angle rather than those with resin. Resin has potential to reduce the formed water contact angle since it has a hydrophilic property [19-21]. However, the resin can improve the nano silica adhesive power on the surface of the paper.

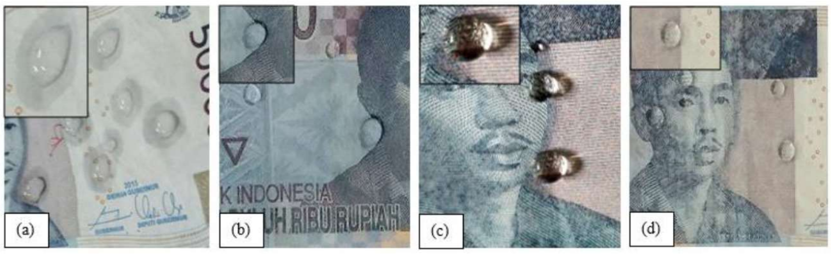

Figure 5. Water droplets on banknote surfaces (a) without nano silica, (b) with 1 gram, (c) 2 gram, and (d) 3 gram nano silica

3.3 Results of Air Penetrability and Water Absorbency Tests

Figure 4 show the graphic of correlation between Air Penetrability (DTU) and water absorbency (DSA) made in BBPK Bandung. More nano silica layering led to higher air penetrability. The high air penetrability showed a large number of nano silica aggregation in the banknote surface and numerous void spaces among individual nanoparticles. Such aggregation results in surface roughness [12, 22]. Hence, the sample with 3-gram nano silica had the highest air penetrability and the highest level of surface roughness in accordance with the results of SEM characterization. Meanwhile, there is nonconformity between the results of water absorbency test and the theory. According to the theory, a high nano silica amount will reduce water absorbency. However, the test results of the 3rd sample show a discrepancy. It was probably due to different pressure during the milling process of water absorbance test since it is performed by a human (human error) and hydrophobic nano silica became to its original characteristic as a good water adsorbent.

4. CONCLUSIONS

The smaller size and larger amount of nano silica can increase banknotes hydrophobicity. The banknote roughness is determined by the number of nano silica aggregation so that it produces higher air penetrability. The average water contact angle also increases along with the increased amount of nano silica, because of the more hydrophobic banknote surface, so that the force that acts between the banknote surface and water becomes smaller than the water molecule cohesive force. Meanwhile, the formed water absorbency decreases in accord with the increased number of nano silica layers, since paper surfaces with a large amount of nano silica would create more hydrophobic banknotes which tend to resist water. The addition of DGEBA epoxy resin layers as the adhesive substances can increase the nano silica adhesive property on paper, yet it can reduce the water contact angle and the formed hydrophobicity. Such fact is found since the epoxy resin is a hydrophilic polymer which tends to absorb water so that it reduces the banknote hydrophobicity.

5. REFERENCES

[1]. R. Dedi, 2014, (http://www.merdeka.com), accessed on 11 March 2016.
[2]. G. Elsandika, A. Fuad, 2016, *AIP Conference Proceedings*, **172**, 050016.
[3]. S. Mahadik, F. Pedraza, R. Vhatkar, 2015, *J. Alloys and Compounds*, **663**, 487-493.
[4]. X. Shi, Z. Suo, 2012, *Surf. and Coating Tech*, **206**, 3700.
[5]. H. Yang, P. Pi, 2016, *Appl. Surf. Sci*, 0169-4332.
[6]. Y. Ye, C. Zhang, 2015, *J. Phy. Chem*, 102.
[7]. C. Du, J. Wang, 2014, *Appl. Surf. Sci*, 28026.
[8]. C. Su, J. Li, 2006, *Appl. Surf. Sci*, 253, 2633-2636.
[9]. S. Liu, S. Latthe, *Ceramics Int*, 15.
[10].A. Gurav, Q. Xu, S. Latthe, 2014, *Ceramics Int*, 14.
[11].Siswanto, M. Hamzah, 2012, *Prosiding InSINas*, 56-59.
[12].H. Ogihara, J. Xie, 2012, *Langmuir*, **28**, 4605-4608.
[13].B. Balu, D. Hess, 2008, *Langmuir*, **24**, 4785.
[14].C. Quan, O. Werner, 2009, *J. Supercritical Fluids*, **49**, 117-124.
[15].H. Yang, Y. Deng, 2008, *J. Colloid and Int. Sci,* **325**, 588-593.
[16].W. Zhang, P. Lu, H. Xiao, 2014, *J. Chem. Eng*, **250**, 431-436.
[17].S. Li, S. Zhang, X. Wang, 2008, *Langmuir*, **24**, 5585.
[18].D. Nystrom, J. Lindqvist, E. Ostmark, 2006, *J. Royal Society of Chem*, 3594-3596.
[19].H. Berahim, K. Sirait, 2003, *Int. Conf. of Properties and Applications of Dielectric Materials*.
[20].J. Marczak, M. Kargol, M. Psarski, G. Celichowski, 2016, *Appl. Surface Sci*, 0169-4332.
[21].A. Syakur, I. Novia, 2011, *J. Teknik*, **32**, 0852-1697.
[22].X. Tang, S. Nan, 2013, *J. Royal Society of Chem.*

Solar Cells Characterization polycrystalline with SUN SIMULATOR System Using Light HALOGEN BULB

Soni Prayogi[1*],Yoyok Cahyono[1], Ahmad Sholih[1], Fitria Silviana[1], Darminto[1]

Departement Physics-FMIPA Institute Technology Sepuluh Nopember
Corresponding authors: [prayogi.sp@gmail.com]

Abstract-Current-voltage characteristic curves of solar cells provide information about the efficiency of solar cells to convert sunlight directly into electricity. The effect of temperature, irradiation levels, as well as a raw material manufacturer will cause changes in the characteristic curve. Sun simulator that uses a halogen lamp is used as a substitute function but the sun as well as the source of irradiation used halogen lamp as the light source and is focused on the box that all sides made the dark. By varying the distance and the amount of irradiated radiation that falls on the solar cell, solar cell characterization. Retrieved suitability output measurement results in the form of solar cell characteristics I_{sc}, V_{oc}, P_{max}, I_{maks}, and V_{max} with the product factory specification. From the results obtained $V_{oc=}$8,59V, I_{sc}=0,00539A and P_{max}=0,0217008W in light intensity is 24,6Watt / m^2.

Keywords: Sun Simulator, Solar Cells, Halogen Bulb

1. INTRODUCTION

Solar cells are one of the electronic devices that can convert solar radiation energy directly into electrical energy. The solar cell is an energy source that will never run out, as long as the sun emits light to the earth. It is estimated that solar cells will become the mainstay of electricity generation sources in the future because of their use very practical, especially for energy supply in remote areas difficult to reach by PLN. Moreover, the energy source is environmentally friendly because the conversion process produces no pollutants at all.

Work solar cells can be measured by looking at the output power generated from the solar cell. Solar cells work is influenced by several things such as the materials used, internal resistance, temperature and solar radiation levels. Research on the characterization of solar cells is still being conducted to date, including the results of measurements of current and voltage (I-V) on a solar cell that is by varying the distance irradiation and the amount of irradiation falling on the solar cells as well as the characterization of solar cells, obtained suitability output measurement results cell characteristics solar form of I_{sc}, V_{oc}, P_{max}, I_{max} and V_{max} with the product factory specification.

The indispensable system equipment in research activities related to the development of solar cells is a system of measuring the characteristics of solar cells and the procedure determination the parameters of the characteristics of solar cells based on existing data for measuring results he gets. Through this research has made the development of measuring system parameters characteristic of the solar cell and the procedures determination the parameters of solar cell characteristics under irradiation conditions.

2. METHODS

The method used in this study is an experiment, using an electronic circuit as shown in Figure 1.

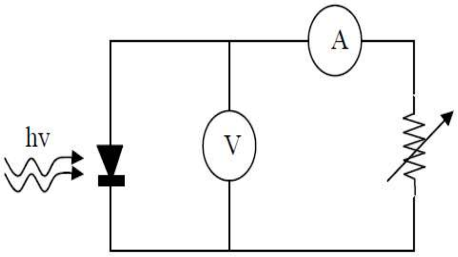

Figure 1. The circuit will be used to measure the characteristics when irradiated

For the measurement of I-V characteristics of solar cells in both the irradiated and without irradiated state, has been developed a system of simple equipment. The design of the characteristic parameter measurement system solar cells is fabricated and used as is shown in Figure 2. The measuring system is made of aluminum material with size (16x16x35) cm^3 and connected with an electronic circuit. At the top of the lamp is placed to measure the I-V characteristics in a state by irradiation.

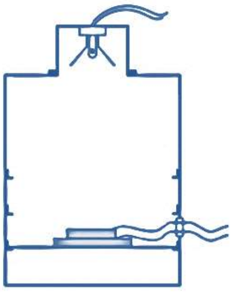

Figure 2. The design of the measuring system of solar cell characteristics

Data were obtained by firing light from the halogen lamp directly to the solar module and carried in the box reflector. The intensity of the incoming light is absorbed and converted into a solar module output in the form of current and voltage.

Current-voltage relationship for a solar cell can be determined as shown in the equation (1) as a follows:

$$I = \frac{V-IR_s}{R_{sh}} + I_{0R}\left(exp\left(\frac{q(V-IR_s)}{2kT}\right) - 1\right) + I_{0D}\left(exp\left(\frac{q(V-IR_s)}{kT}\right) - 1\right) \quad (1)$$

Where IL is the light generated electrical current, its value does not depend on the voltage. With this formula, the I-V characteristics of solar cells under these conditions appeared similar to the I-V characteristics in dark conditions but translated into four quadrants. The main parameters that can be determined from the behavior of solar cells when irradiated are Voc (open circuit voltage), Isc (short circuit current), FF (Fill Factor), and η (conversion efficiency). Fill Factor value determined by the equation:

$$FF = \frac{I_m V_m}{I_{sc} V_{oc}} \quad (2)$$

Where Im and Vm are the electric current and voltage to the optimum working point, is that produces maximum output power. While the equation calculates the conversion efficiency (η):

$$\eta = \frac{FFV_{oc}I_{sc}}{P_{in}} x\ 100\% \quad (3)$$

3. RESULT AND DISCUSSION

The measurement results of I-V characteristics of the irradiation and different spacing showed changes in efficiency that are interconnected. When the intensity of the halogen lamp of 24.6 W/m^2 at a distance that changed between the 25cm, 20cm and 15cm, indicating that the greater the distance irradiation, I_{sc} and V_{oc} generated will be smaller. This is because when the solar cells subjected to a halogen lamp, the intensity of irradiation received by the solar cell becomes greater.

Characteristics measurement results of solar cells using sun simulator at the source intensity of 24.6 W/m^2 with variations distance is:

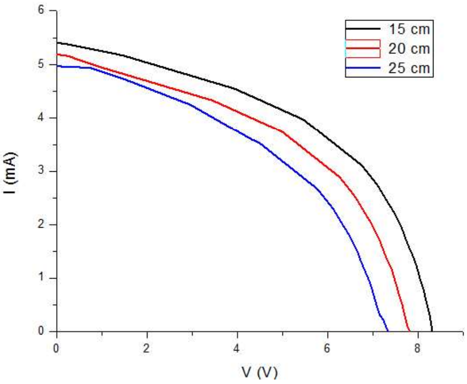

Figure 3. Characteristics measurement results of solar cells with variations distance

Characterization of I-V solar cells under irradiation based on the measurement results are shown in Figure 4. Based on the images obtained by the I_{sc}=0,00539A and V_{oc}=8,59V. While V_m and I_m respectively voltage and current at the optimum operating point. I_mV_m value obtained from the maximum area under the curve I-V as shown in Figure 4. Based on the calculation, the value of V_mI_m=0.0217008 Watt. The value of the fill factor (FF) and efficiency (η) is then determined from the equation (2) and (3).

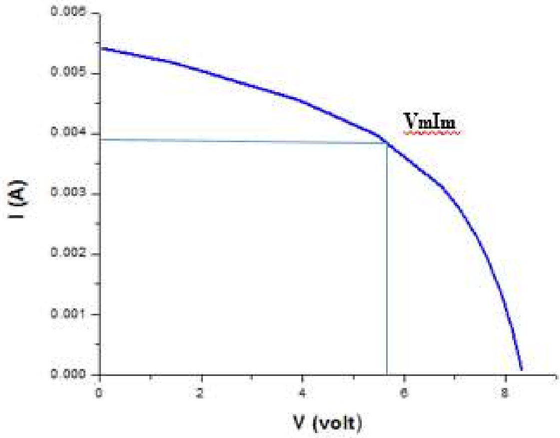

Figure 4. I-V characteristic curves of solar cells in a state of irradiation

The value of the fill factor (FF), which is the ratio of maximum power (V_mI_m) produced by solar cells on the multiple of I_{sc} and V_{oc} obtained at 0.4686, and the value of a conversion efficiency of 12.25%. The value of the acquired solar cell efficiency is considered feasible for solar cells based on polycrystalline silicon material, based on the studies that have been performed on polycrystalline silicon, the efficiency of the measured range (12 to 13.6) %.

From the test results of XRD is known that the constituent materials are polycrystalline solar panels, it is evident from the peak is formed only one because the characteristics of polycrystalline XRD test is when the peak is formed only one or more but still in the same family.

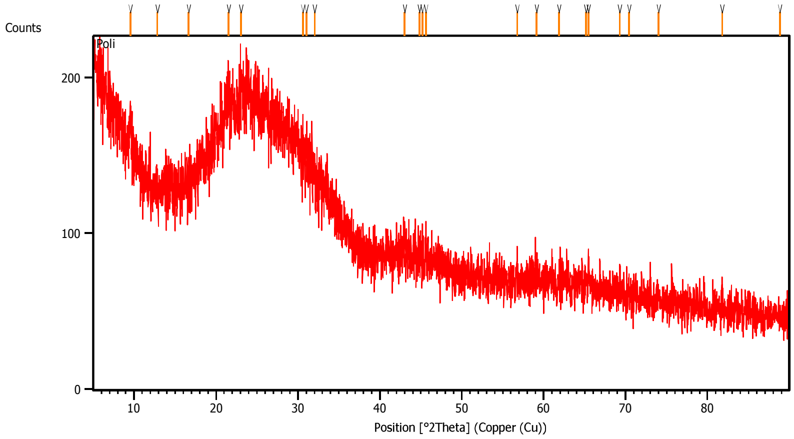

Figure 5. Curve XRD results

For the test results Optical Microscopy clearly visible crystals making up solar panels in the form of plural crystals that are arranged randomly and irregularly.

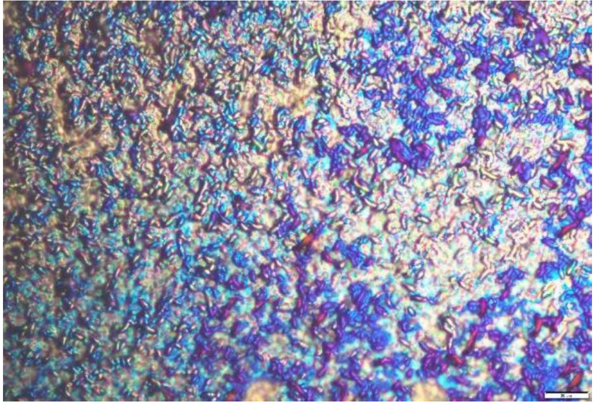

Figure 6. Results optical microscopy

These results indirectly suggest that systems developed equipment and procedures determine the parameters of the characteristics of solar cells have been used quite well and has the potential to be used as a measurement system for lab activities and research related to solar cell characterization.

4. CONCLUSION

The parameters of silicon solar cell characteristics were obtained based on the measurement of the irradiation conditions obtained values of I_{sc}=0.00539 Ampere, V_{oc}=8,59 Volt, FF = 0.4686, and η = 12.25%. These values are very close values of parameter characteristics of polycrystalline silicon solar cells. This shows that the system of measurement equipment developed to have a good potential to be used as a practical tool and a research tool.

5. ACKNOWLEDGMENT

Author S.P. thanked the Ministry of Finance of the Republic of Indonesia, through the Institute of Management Education Fund (LPDP), which has provided financial support through scholarships Master of Indonesia from 2015 to 2017. Also the author would like to thank the team of solar cell material physics research department of physics Institute of Technology (ITS) Surabaya.

6. REFERENCES

[1]. E. Purwandari and T. Winata, "Optimasi Tekanan Deposisi dalam Simulasi Efisiensi Sel Surya Berbasis Material a-Si:H," *GRADIEN*, **vol. 8**, no. 1, pp. 716–721, 2012.

[2]. F. Dimroth and S. Kurtz, "High-Efficiency Multijunction Solar Cells," *MRS Bull.*, **vol. 32**, no. 3, pp. 230–235, Mar. 2007

[3]. I. Martil and G. G. Diaz, "Determination of the dark and illuminated characteristic parameters of a solar cell from I-V characteristics," *Eur. J. Phys.*, **vol. 13**, no. 4, p. 193, 1992.

[4]. I. Usman and T. Winata, "Pengaruh Ketebalan Lapisan Aktif terhadap Karakteristik Sel Surya Berbasis a-Si:H yang Ditumbuhkan dengan Teknik HWC-VHF-PECVD," *J. Mat. Sains*, **vol. 13**, no. 4, pp. 109–113, Dec. 2009.

[5]. J. Poortmans and V. Arkhipov, *Thin Film Solar Cells: Fabrication, Characterization and Applications*. John Wiley & Sons, 2006.

[6]. J. Y. Huang, C. Y. Lin, C.-H. Shen, J.-M. Shieh, and B.-T. Dai, "Low-cost High-efficiency amorphous silicon solar cells with improved light-soaking stability," *Sol. Energy Mater. Sol. Cells*, **vol. 98**, pp. 277–282, Mar. 2012.

[7]. K. Surana, "Towards silicon quantum dot solar cells?: comparing morphological properties and conduction phenomena in Si quantum dot single layers and multilayers," PhD thesis, Université Grenoble Alpes, 2011.

[8]. K. Takahashi and M. Konagai, "Amorphous silicon solar cells," Jan. 1986.

[9]. P. Mialhe and J. Charette, "Experimental analysis of I–V characteristics of solar cells," *Am. J. Phys.*, **vol. 51**, no. 1, pp. 68–70, Jan. 1983.

[10].S. Guha, J. Yang, and B. Yan, "High efficiency multi-junction thin film silicon cells incorporating nanocrystalline silicon," *Sol. Energy Mater. Sol. Cells*, **vol. 119**, pp. 1–11, Dec. 2013.

[11].S. Manan, "Energi Matahari Sumber Alternatif yang Efisien, Handal dan Ramah Lingkungan Indonesia," *Gema Teknol.*, 2009.

[12].S. M. de Nicolas, "a-Si?: H/c-Si heterojunction solar cells?: back side assessment and improvement," phdthesis, Université Paris Sud - Paris XI, 2012.

[13].S. Nacer and A. Aissat, "Simulation of InGaN p–i–n double heterojunction solar cells with linearly graded layers," *Opt. - Int. J. Light Electron Opt.*, **vol. 126**, no. 23, pp. 3594–3597, Dec. 2015.

[14].W. Shockley and H. J. Queisser, "Detailed Balance Limit of Efficiency of p-n Junction Solar Cells," *J. Appl. Phys.*, **vol. 32**, no. 3, pp. 510–519, Mar. 1961.

The Effectiveness Sap of *Avicennia alba* as Antimicrobial that Inhibits Bacteria Growth in *Streptococcus mutans*

Okta Efriyadi[1], Devi Ayu Novita[2]

Institut Agama Islam Negeri (IAIN) Syekh Nurjati Cirebon
email: okta.11@yahoo.com

Abstract- Api-api tree (*Avicennia alba*) is a pioneer manifold mangrove habitat which protected marsh along the coast. The Api-api trees have a sap that contains active anti-bacterial compounds such as *alkaloids, flavonoids, saponins* and *tannins*. Active anti-bacterial compound that can inhibit the bacteria *Streptococcus mutants*. *Streptococcus mutants* is a Gram-positive bacteria which non-motile (not moving) belong to the facultative anaerobic bacteria. Those bacteria are found in human teeth are hollow cavities and bacteria are the most conducive in causing caries on tooth enamel. The purpose of this study to determine the antimicrobial activity of api tree's sap and to determine which concentration that the most effective in inhibiting the bacteria of *Streptococcus mutants*. The method that using in this research is Laboratory Experiment which completely randomized design (CRD) with a concentration of 5%, 10%, 25%, 50%, 75% and 100%. The result of this study indicated that the activity of the antimicrobial from the sap of the api tree can inhibit the growth of *Streptococcus mutants* at a concentration of 5% with inhibitory zone 2mm, 10% concentration with inhibitory zone 4mm, a concentration of 25% with inhibitory zone 10mm, concentration of 50% with zone inhibitory 20mm, concentration 75 % with inhibitory zone 30mm and a concentration of 100% with inhibitory zone 40mm. In this case, the sap concentration of api-api tree is the most effective in inhibiting the growth of *Streptococcus mutants* which is 5%.

Keyword: Sap of *Avicennia alba*, Antimicrobial, *Streptococcus mutans*

1. INTRODUCTION

Mangrove plant has many various types, one of them is api-api. Api-api (*Avicennia alba*) is mangrove plant manifold pioneer which the habitat in an swamp which is covered as long as the edge of the beach which located in the coast. According to Kusmana et al (2008) *Avicennia alba* shaped grove or the tree that grow spread with a height of 25 m. Tree stands *Avicennia alba* form a horizontal root system and root complex breath. The roots of breath usually thin, finger-shaped or pencil covered by lntisel. The outer bark is grayish or dark brown, some overgrown small protrusions, while others sometimes have a smooth surface. On the trunk of the old, sometimes found a thin powder. *Avicennia alba* is a pioneer species in the mangrove swamp habitat in a location sheltered beach, also in the saltier along riverbanks that are tidally influenced, as well as along the shoreline. *Avicennia alba* liked the front of the bay. Roots binding sediments and can help accelerate the process of land formation.

Api-api in addition to many utilized trunk as community timber, Api-api can also be utilized the fruit and sap. The sap is one form of secondary metabolites produced by plants mangrove *Avicennia alba* types. The secondary metabolites is a self-defense mechanism of the organism for instance a plant. The secondary compound metabolites highly variable number and type of each plant and the compound is essential for the survival and potential as anticancer, antiviral, antibacterial, antioxidant and antifungal (Sudiro, 1998). According to Markham (1988) in Handayani Silvia (2013) Api-api is containing steroid compounds, saponin, flavonoid and tannins. Flavonoid is the typical content of greenery located at the plant, including the leaves, roots, woods, barks, flowers, polar because it contains a number of hydroxyl not tersulih or sugar ". The content of the active compounds can inhibit the growth of *Streptococcus mutants* bacteria that cause tooth pain because it has antibacterial properties.

The antimicrobial is a substance that can inhibit the growth of microbes. The number of infectious diseases suffered by some people more of needs for antibiotics. At this time in reality, the patient sometimes does not pay attention to the use of antibiotics that lead to antibiotic-resistant microbes. The use of antibiotics is not rational can make microbial pathogens resistant (Rahmi, 2013).

Streptococcus mutants is a bacteria of gram positif (+), non-motile (not moving), 1-2 μm in diameter, facultatively anaerobic bacteria. Have a rounded or oval shape, arranged like a chain (Samaranayake, 2002). *Streptococcus mutants* is a bacterium that is most important in the process of dental caries (Sidarningsih, 2000) *Streptococcus* *mutants* is usually found in human teeth cavity which wounds and be most conducive bacteria that cause caries to the enamel of teeth (Ari, 2008).

2. METHODS

This research was conducted in the Laboratory of Microbiology Institut Agama Islam Negeri (IAIN) Syekh Nurjati Cirebon to determine the effectiveness of api-api's sap (*Avicennia alba*) against *Streptococcus mutants* using completely randomized design (CRD) with a concentration of 5%, 10%, 25 %, 50%, 75% and 100%.

2.1 Chemicals

The materials used in this research is a sample of tree sap api-api (*Avicennia alba*), Nutrient Agar blood, isolated bacteria of *Streptococcus mutants*, and aquades.

The tools used in this research is the reaction tube, hot plate, oven, autoclave, Erlenmeyer flask, glass Bekker, a pipette, an incubator, a petri dish, a ruler, a cotton bud, a Bunsen, the perforator, camera documentation and stationery.

2.2 Procedure

2.2.1 Sterilization Equipment and materials used

To prevent contamination at the time of planting the bacteria of *Streptococcus mutants* test conducted sterilization of tools and materials used beforehand. The sterilization process using an oven with a temperature of 100 0 C for 1 hour. Sterilization material using an autoclave at a temperature of 1210C pressure of 2 atm for 15 minutes.

2.2.2 Making Blood Agar Medium

The media MH-blood agar made by the standard procedure of making the media Agar, starting with the media dissolves the MH agar with 100 ml aquades, and adding 5 ml goat's blood. The media that has been made of this sterility is maintained and ready to use in the cultivation of *Streptococcus mutants* thoroughly.

2.2.3 Bacterial Isolates of *Streptococcus mutants* Rejuvenation

To obtain a pure Streptococcus mutants isolates conducted rejuvenation, ie from stock *Streptococcus mutants* taken several colonies carved into media MH-blood agar and incubated for 24 hours at 37 0C overnight. The next day the colonies obtained small, soft translucent color.

2.2.4 Suspension of bacteria *Streptococcus mutants*

Streptococcus mutants Suspension of prepared from colonies grown on media blood agar MH. From these colonies were taken using a needle ose to be inoculated. The colonies streaked into a new media blood agar. Then let stand a few minutes.

2.2.5 Testing of Antimicrobial Activity

Testing the antimicrobial activity of *Avicennia alba* sap was conducted by using sumuran method. In each of the blood Agar that has been inoculated with the bacteria of *Streptococcus mutants* created a hole by using a perforator size 1cm hereinafter condition with tree sap api-api (Avicennia alba) at a concentration of 5%, 10%, 25%, 50% , 75% and 100%. Each treatment was made two replications. Then incubated at 37°C for 24 hours. Further observation in a way inhibition zone diameter was measured by using a ruler.

2.2.6 The Measurement of Inhibition Zone

Medium samples were incubated for 24 hours in the measuring inhibitory zone using a ruler. Each hole contained clear color zones measured in diameter.

3. RESULT AND DISCUSSION

Based on the test results of the inhibition of *Avicennia alba* sap to the bacteria *Streptococcus mutants* by pitting method, conveniently indicates the sample sap inhibition against the bacteria *Streptococcus mutants*. Activities resulting inhibition seems that the clear zone around the hole in wells containing latex solution *Avicennia alba*. According Pratama (2005) in Octavian (2013) "clear zone around the paper disc showed activity antibacterial". The following table inhibition zone measuring results *Streptococcus mutants*.

Table 1. Inhibition Zone Diameter bacteria *Streptococcus mutants*

Bacteria	Treatment	Inhibition Zone Diameter (mm) Repetition 1	2	Average (mm)
Streptococcus mutans	Concentration 5%	1,7	2,3	2
	Concentration 10%	3,5	4,5	4
	Concentration 25%	8,6	11,4	10
	Concentration 50%	19,4	20,6	20
	Concentration 75%	30,5	29,5	30
	Concentration 100%	47,6	33,4	40

Based on Table 1 the results obtained from testing the antimicrobial activity. Tree sap api-api (*Avicennia alba*) indicates the existence of barriers to bacteria, the testing of the bacteria *Streptococcus mutants* showed the average diameter of inhibitory zone every different concentration, that is concentration of 5% has an average diameter of inhibitory zone 2 mm, concentration 10% have an average diameter of 4 mm zone of inhibition, concentration of 25% has an average diameter of 10 mm zone of inhibition, concentration of 50% has an average diameter of 20 mm zone of inhibition, concentration of 75% has an average diameter of 30 mm zone of inhibition and a concentration of 100% have an average diameter of 40 mm zone of inhibition. This shows that the greater the concentration used, then the larger zone of inhibition produced.

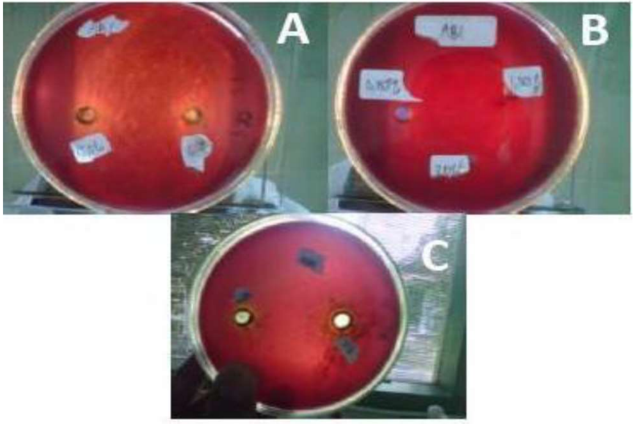

Figure 1. Zone of Inhibition of *Streptococcus mutants* bacteria with wells Method

Based on Figure 1. A is a zone of inhibition of bacterial concentration of 5% and 10%, B is a zone of inhibition of bacterial concentrations of 25% and 50%, and C is a zone of inhibition of bacterial concentrations of 75% and 100%. From the observation of the wells that contain sap *Avcennia alba* showed positive results in the formation of inhibition zones around the wells. This is because their secondary metabolites which influenced the growth of test bacteria. Mechanism of action of tannins as an antibacterial agent is inhibiting the enzyme reverse transcriptase and DNA opoisomerase that bacterial cells can not be formed (Nuria et al., 2009). Tannin has an antibacterial activity that is related to its ability to inactivate microbial cell adhesin also inactivate the enzyme and disrupt protein transport in the inner layer of cells (Cowan, 1999). According to Sari (2011), tannins also have targets in polypeptide cell wall so that the formation of the cell wall becomes less than perfect. This causes the bacterial cells into lysis due to osmotic pressure and physically so that the bacterial cell will die.

The mechanism of action of flavonoids as antibacterial compound was formed a complex with extracellular proteins and soluble so that may damage the cell membrane of bacteria and is followed by the release of intracellular compounds (Cowan, 1999). According to Cushnie et al. (2005), in addition to a role in the inhibition of the synthesis of DNA - RNA by intercalation or hydrogen bonds with the buildup of nucleic acid bases, flavonoids also play a role in inhibiting energy metabolism. These compounds would disrupt energy metabolism in a similar manner to inhibit the respiratory system, because it takes energy to active absorption of various metabolites and for the biosynthesis of macromolecules.

Mechanism of action of saponin as antibacterial lower the surface tension resulting increase in permeability or leakage of the intracellular cell and lead compounds going out (Nuria et al. 2009). According to Cavalieri et al. (2005), this compound diffuses through the outer membrane and the cell wall are vulnerable, and then binding the cytoplasmic membrane and disrupt and reduce the stability. This causes the cytoplasm to leak out of the cell resulting in cell death. Antimicrobial agents that disrupt the cytoplasmic membrane is bactericidal.

4. CONCLUSION

Based on the results and discussion, it can be concluded that the sap of the tree api-api inhibits the growth of *Streptococcus mutants*, demonstrated by the inhibition zone on the media culture. The antibacterial activity can be seen at a concentration of 5%. The concentration of tree sap fires is most effective in inhibiting the growth of *Streptococcus mutants* which is 5%. Therefore sap, bark api-api (*Avicennia alba*) can be used as an alternative as a cure toothache caused by the bacterium *Streptococcus mutants*.

5. REFERENCES

[1]. Ari, W. 2008. *Streptococcus Mutans,* Si Plak Dimana-mana, Available from: http://mikrobia.files.wordpress.com/2008/05/streptococcus-mutans 31.pdf [Senin 13 Maret 2017].

[2]. Cavalieri, et al. 2005. Manual of Antimicrobial Susceptibility Testing. *American Society for Microbiology*, USA.

[3]. Cowan, M.M. 1999. Plant Products as Antimicrobial Agents. *Clinical Microbiology Reviews*. **12**: 564 – 582.

[4]. Cushnie, T.P.T., dan A.J. Lamb. 2005. Antimicrobial Activity of Flavonoids. *International Journal of Antimicrobial Agents*. **26**: 343 – 356.

[5]. Handayani, Silvia. 2013. Kandungan Flavonoid Kulit Batang Dan Daun Pohon Api-Api (Avicennia Marina (Forks.)Vierh) Sebagai Senyawa Aktif Antioksidan. *Skripsi*. Departemen Teknologi Hasil Perairan Fakultas Perikanan Dan Ilmu Kelautan Institut Pertanian Bogor.

[6]. Kusmana, C., et al. 2008. *Manual Silvikultur Mangrove di Indonesia*. Departemen Kehutanan Republik Indonesia dan Korea International Cooperation Agency (KOICA).

[7]. Nuria, M.C., et al. 2009. Uji Antibakteri Ekstrak Etanol Daun Jarak Pagar (Jatropha cuircas L) terhadap Bakteri Staphylococcus aureus ATCC 25923, *Escherichia coli* ATCC 25922, dan *Salmonella typhi* ATCC 1408. *Jurnal Ilmu – ilmu Pertanian*. **5**: 26 – 37.

[8]. Oktavianus, Satria. 2013. Uji Daya Hambat Ekstrak Daun Mangrove Jenis *Avicennia Marina* Terhadap Bakteri *Vibrio Parahaemolyticus. Skripsi.* Jurusan Ilmu Kelautan. Makassar : Fakultas Ilmu Kelautan Dan Perikanan Universitas Hasanuddin.

[9]. Sari, F.P., et al. 2011. Ekstraksi Zat Aktif Antimikroba dari Tanaman Yodium (Jatropha multifida Linn) sebgai Bahan Baku Alternatif Antibiotik Alami. Semarang: Fakultas Teknik Universitas Diponegoro.

[10].Sidarningsih. 2000. Kadar Anti bodi IgA Sekretori terhadap Antigen I/II *Streptococcus mutants* dalam Saliva Subyek Bebas Karies dan Karies Aktif, Dent J, 33(3), page 99-102.

[11].Rahmi, Adila. 2013. Uji Antimikroba Curcuma spp. Terhadap Pertumbuhan Candida albicans, Staphylococcus

[12].Aerous dan Escherichia coli. *Jurnal Biologi Universitas Andalas* **Vol 2** No. 1

Making of Ecofriendly Fiber from Recycled Polyethylene Plastic Bag Waste

Asril Senoaji Soekoco[1*], Noerati[2], Maya Komalasari[3], Kurniawan[4], Agus Hananto[5]

[1-5] Politeknik STTT Bandung, Jl. Jakarta No 31, Bandung, Indonesia
*Corresponding authors: [asrilsenoaji@gmail.com, noeratikemal@yahoo.com]

Abstract – Plastic bag waste is a potential alternative material for many things, include textile fiber. Recycling plastic bag waste into textile fiber has not developed yet. This research will focus on producing eco-friendly fiber made from recycled polyethylene to overcome plastic bag waste and serve as an alternative process of producing textile fiber material using lab scale melt spinning equipment. Proper processing temperature and take-up axial velocity are the main parameters. Melt spinning equipment with a single orifice of a spinning nozzle can produce recycled textile fiber in processing temperature of 147 °C. The usage of 15 mm diameter barrel and 2 mm of diameter orifice to process plastic bag waste can produce 74.03 dTex textile fiber.

1. INTRODUCTION

World plastic bags consumption shows increasing trend and tends to lead a serious problem of plastic waste. Plastic bag waste commonly is made from 2 groups of polyethylene polymer, low-density polyethylene (LDPE) and high-density polyethylene (HDPE). Efforts to overcome plastic bag waste have been developed, one of them is through thermal degradation technology to convert polymer chain into the shorter chain and enable to use it as materials for alternative fuel. To conduct this effort requires energy and creates air pollution, therefore another effort to solve plastic bag waste problem need to be discovered. Since plastic bag waste material is thermoplastic, recycle is the most interesting challenge.

Polyethylene is a thermoplastic polymer, this material can be processed into the fiber through melt spinning and gel spinning. The most suitable method to recycle plastic bag waste into textile fiber for the thermoplastic polymer is melt spinning, considering production cost and environment aspect [1]. The basic principle of melt spinning is by melting materials and then extruding it through the small orifice of a spinning nozzle to form fibers [2]. Fiber take-up velocity can influence mechanical properties and diameter of the fiber [3]. Fiber diameter can be arranged as its application. For apparel, commonly needs smaller fiber diameter.

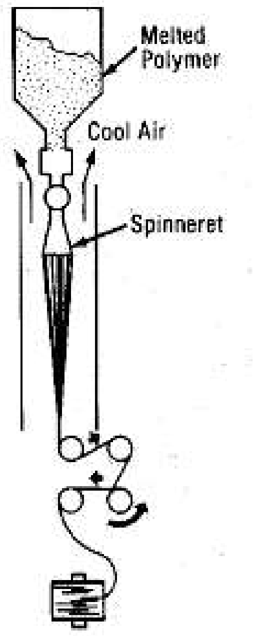

Figure 1 Melting Spinning Basic Principle

2. METHODS

2.1 Materials

The plastic bag waste cleaned before melt spinning process. The plastic bag waste was classified by color to reach more similar material properties, this research used three colors plastic bag waste. Fourier Transform Infra Red (FTIR) analysis was conducted on Shimadzu to identify the polymer of each color. FTIR spectra showed all these plastic bags waste were polyethylene according to their fingerprints. Thermal analysis of the material was performed with thermogravimetric analysis (TGA) and acknowledged the melting temperature of the material was 140 ^{0}C.

Figure 2 Polyethylene bags waste

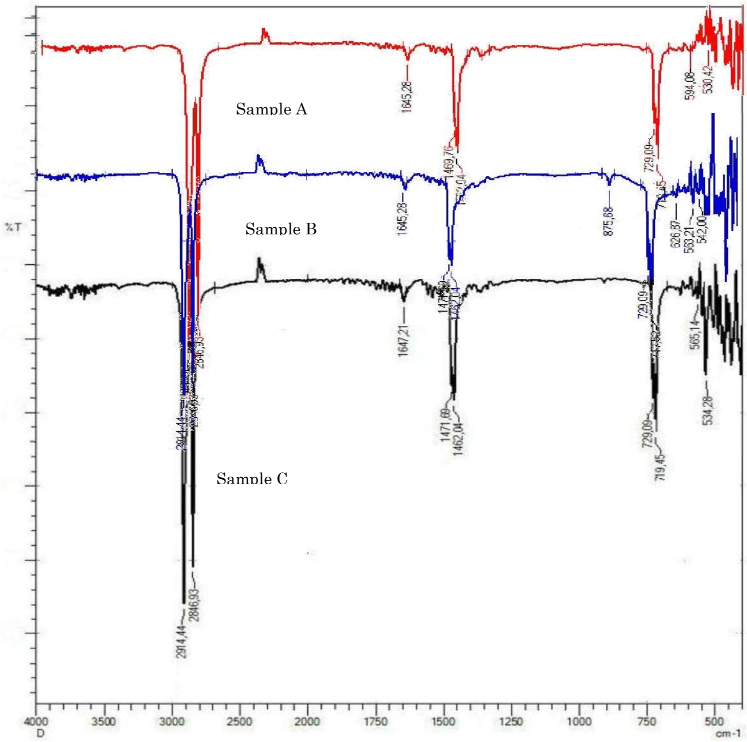

Figure 3 Thermal properties of plastic bags waste

2.2 Melt Spinning Equipment

This research developed a melt spinning equipment with plunger system. A single small orifice design was chosen to provide the easiest operational control and produce more uniform fiber [4]. This experiment conducted using laboratory scale melt spinning equipment. This melt spinning equipment has a single orifice of a spinning nozzle with a maximum processing temperature of 347 ºC from 1500 watt heater. The processing temperature was controlled by a type-K thermocouple at the lower side of the barrel. The orifice diameter is 2 mm and the barrel diameter is fixed at 15 mm. The plunger and take-up velocity can be adjusted as demand to produce variations in produced fiber diameter.

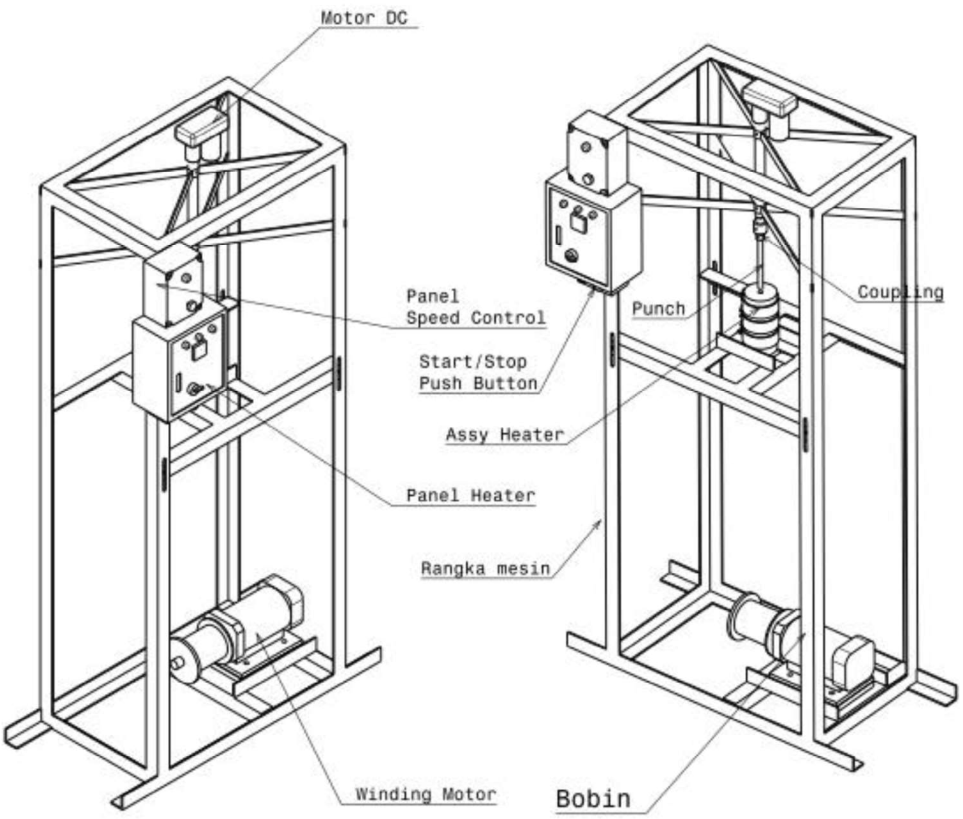

Figure 4 Laboratory scale melt spinning equipment

2.3 Procedures

Plastic bag waste inserted into the barrel after cleaning process to avoid dirt and contamination. Proper processing temperature and take-up axial velocity are the main parameters in this research. The processing temperature adjusted according to TGA result, the processing temperature of this material was 147 ^{0}C due to a thermal loss in the heating unit. The resident time in this process was 20 minutes after processing temperature reached to get the uniform phase of the material. The plunger velocity adjusted at 12 mm/minute to force melted polymer pass through the orifice. Melted polymer solidified after had contacted with room air and then pulled by a take-up roll. Higher axial take-up velocity leads to lower fiber diameter, the increment of take-up velocity caused spin-line breakage [4]. A Precise take-up velocity is obviously needed to produce expected fiber diameter with the lowest fiber breakage. The optimum take-up velocity is 18.5 m/minute.

3. RESULTS AND DISCUSSION

Melt spinning equipment with a single orifice of a spinning nozzle can produce recycled textile fiber in processing temperature of 147 ºC. A single orifice design was proven to provide easy operational control due to simple fiber breakage monitoring. Plunger system is very suitable for laboratory melt spinning equipment due to its minimum material feeding, it was possible to process only by using 2 grams of material. The usage of 15 mm diameter barrel and 2 mm of diameter orifice to process plastic bag waste can produce 74.03 dTex textile fiber. The optimum plunger velocity is 12 mm/minute and the take-up axial velocity is 18.5 m/minute. The cross section of recycled fiber is circular taking the shape of the orifice with a diameter of 150 micrometers. Fiber diameter can be arranged as its application. For apparel, commonly needs smaller fiber diameter.

Figure 5 Recycled plastic bag waste fiber

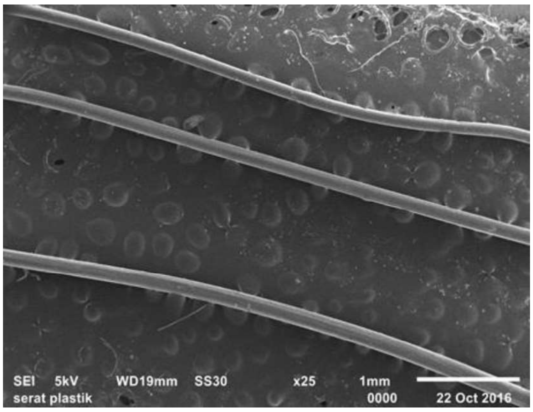

Figure 6 Cross section of recycled plastic bag waste fiber

The cross section of recycled fiber is circular taking the shape of the orifice with a diameter of 150 micrometers. Fiber diameter can be arranged as its application. For apparel, commonly needs smaller fiber diameter.

4. CONCLUSIONS

Plastic bag waste has a great potential as environment-friendly material for textile fiber. Ecofriendly fiber can be made through laboratory scale melt spinning equipment with Noun string plunger system. A single orifice design was proven to provide easy operational control due to simple fiber breakage monitoring. 15 mm diameter barrel and 2 mm of diameter orifice can produce 74.03 dTex textile fiber with the take-up axial velocity is 18.5 m/minute. Further study is needed to produce high mechanical properties of recycled polyethylene using plastic bag waste.

5. REFERENCES

[1]. Fambri Luca, Izabela D, Ceccato R, 2014, Melt Spinning and Drawing of Polyethylene Nanocomposite Fiber with Organically Modified Hydrotactile, *Journal of Applied Polymer Science*, 10
[2]. T Nakajima, 2009, Advanced fiber spinning technology, 150.
[3]. Young P Jeon, 2009, Simulation of Multifilament Semicrystalline Polymer Fiber Melt-Spinning,1.
[4]. Jun Jia, 2010, Melt Spinning of Continuous Filaments by Cold Air Attenuation, 49.
[5]. Dong Zhang, 2014. Advances in Filament Yarn Spinning of Textiles and Polymer, 3.

Characterization Argon Plasma on DC Bias Discharge by using Comsol Multiphysics Simulation and The Effect of Voltage Variation

Muhammad Ghufron[1]*, E.E Yunata[2], T. Aizawa[2]

[1]Department of Physics, Faculty of Science, Brawijaya University, Malang, Indonesia
[2]Department of Physics, Shibaura Institute of Technology, Tokyo, Japan
*Corresponding authors: [mghufron@ub.ac.id]

Abstract – 1D simulation of Argon Plasma DC Bias has been conducted by using Comsol Multiphysics. The plasma generated by DC Bias Voltage -200 V to -400 V, T=400K and P=70 Pa. When the bias voltage applied to electrode then electric field appear in the chamber and the neutral Argon gas become ionized. Simulations show that the plasma formed near the cathode that indicated by the high value of the electric potential distribution, electrons density, ions density and electron temperatures distribution. The distribution of electron density from the cathode increasing exponentially from 10^9 m^{-3} until 10^{18} m^{-3} near cathode with average value 1,37 x 10^{15} m^{-3}. The electron temperature increasing exponentially with maximum value 9.93 eV and decrease very fast due the collision between electrons with the other species in the chamber. The more high bias voltage applied than the more electron density, ions density and the electron temperature increase.

1. INTRODUCTION

Plasma is known as the fourth phase after solid, liquid and gas phase and describes as an ionize material that has quasi-neutral properties. Plasma technology has been widely used in the industry such as plasma nitriding for improving material hardness [1], ashing material in the large area [2] and even in the medical field such as plasma for killing mycobacteria [3]. However plasma has unique properties and needs to explore further related with the characterization of plasma such as electron density (n_e), ion density (n_i) and electron temperature (T_e) that representative of their energy. Up until now there is a few people concern in this topic and still limited result due to the properties of plasma.

The advantage of using plasma technology could be improved by understanding the plasma behaviors and characteristics. A variety of ways has been used to generate plasma such as using radio frequency [4], microwave frequency [5], and DC glow discharge [6]. Simulation simulation is one of the solutions to measure the plasma properties like electric potential distribution, electron density (n_e), ion density (n_i) and electron temperature (T_e) distribution in the chamber during the proses ionization of gas. This work will discuss about the characterization of Argon plasma generated by DC Bias Discharge -200 V, 300 V and -400 V, T=400K and P=70 Pa using Comsol Multiphysics. One dimensional axisymmetric simulation used in this work to simplify the problem.

2. METHODS

2.1 Model Definition

Figure 1 shows a cross section model used in this simulation. The model has two conductors where the inner conductor is used as a negative electrode (cathode) while the outer conductor grounded. Based on the cross-section, measurements direction can be done in the z-axis by using 1D axisymmetric to simplify the problem.

Model is used to represents the presence of ionization near cathode (the purple color). When Bias voltage applied to the cathode (inner conductors) then high electric field occur in the chamber. The high electric field will make free electrons accelerate and cause a collision with neutral gas. Gas become ionized and the result is positive ion and secondary electron. Positive ions accelerate towards cathode and electron is moving away from cathode due to Coulomb law. The result of ionization is generated more ions and electrons. These electrons will take an apart in new ionization which creates new couple ion-electron until electrons lost their energy and cannot cause more ionization. Gas discharge follows Poisson equation and ideal gas fluid in this system. The model uses a Scharfetter-Gummel upwind scheme to eliminate numerical instabilities in the number density of charged particles associated with finite element method.

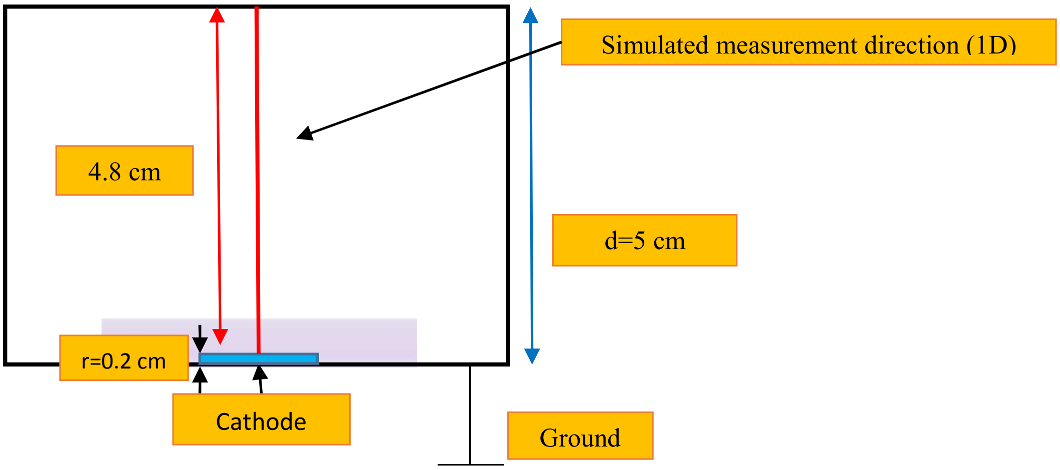

Figure 1: Cross section model of DC Bias Discharge plasma. Negative applied voltage input on the cathode (blue plate) and the other conductor (the black chamber) was grounded.

The electron density is figured out by solving drift-diffusion equations. Convection of electron due to fluid motion is neglected. The equation for the electron number density:

$$\frac{\partial}{\partial t}(n_e) + \nabla.[-(\mu_e.\boldsymbol{E})n_e - \boldsymbol{D}_e.\nabla n_e] = R_e \qquad (1)$$

Where $\boldsymbol{E}$ is the electric field (V/m), μ_e denotes the electron mobility ($m^2/(V.s)$), n_e is electron density (m^{-3}), $\boldsymbol{D}_e$ denotes the electron diffusivity, and $\boldsymbol{R}_e$ is the electron rate expression ($1/m^3.s$). For a Maxwellian electrons energy distribution function, there is relationship hold:

$$\boldsymbol{D}_e = \mu_e T_e, \mu_\varepsilon = \left(\frac{5}{3}\right)\mu_e, \boldsymbol{D}_\varepsilon = \mu_\varepsilon T_e \qquad (2)$$

Where T_e is electron “temperature” which is correlated with electron energy[7].

2.2 Boundary Condition

The boundary condition in the model is related with sustaining the discharge near the cathode. The mechanism for sustaining the discharge is secondary electrons. The electrons are accelerated by the applied high voltage in the cathode where they have energy to initiate ionization. The electron is lost to the wall due to random motion within a few mean free path of the wall and gained due to secondary emission effects. Ions are lost to the wall and excited Argon gas lost their energy due to surface reactions.

3. RESULTS AND DISCUSSION

The first observation in this simulation is to know that the plasma occurs in the system. Simulation set up at fixed gas temperature 400 K, DC Bias -400 V and gas pressure 70 Pa. ion densities, electron densities, electric potential and electron temperature is the characteristic of plasma.

Figure 2(a) show electric potential as a function of time in the cathode and ground. Voltage in the cathode shows a rapid rise around $t = 10^{-4}$ s then become constant at $t > 7x10^{-3}$ s, however the ground state always zero. Figure 3(b) evidence that electric potential occurs near the cathode, indicate ionization take place around cathode and plasma is formed. When DC Bias -400V applied to the inner conductor, the highly mobile electrons are accelerated towards the ground leaving a positively charged gas (ion Ar^+) near the cathode. At the same time the positive charges are accelerated to the cathode. The electric potential value except near cathode shows small value in the whole chamber that indicate there is a few charges (electron densities and ion densities) or have the similar value.

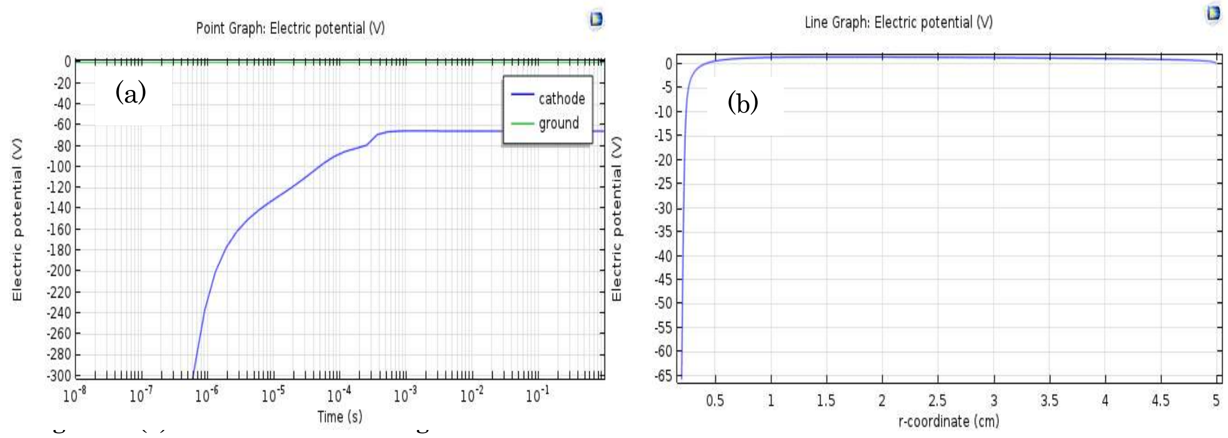

Figure 2. Function of distance

Figure 3 show a distribution of electron and ion density in the z direction from the edge of the cathode to the outer conductor. Ion and electron density rise up significantly near the cathode until maximum at 2.6 x 10^{18} m^{-3} (r = 0.92 cm) then decrease until 1.36x10^{15} m^{-3} for electron and 3.60x10^{15} m^{-3} (r = 5.00 cm) for ion density like sinusoidal profile. Electrons and ions having relatively low densities compared to neutral atoms ~ 10^{21} atom/m^3 at P = 70 Pa. As we can see the ion and electron density have the same value and this proves that the plasma is quasi-neutral (ne=ni). Figure 3b (insert) show that the ion density has a higher value (approximately two order of magnitude) than electron density which proves that after ionization resulting ion-electron pair, ions mobile to the cathode and electron push away from cathode under high electric field.

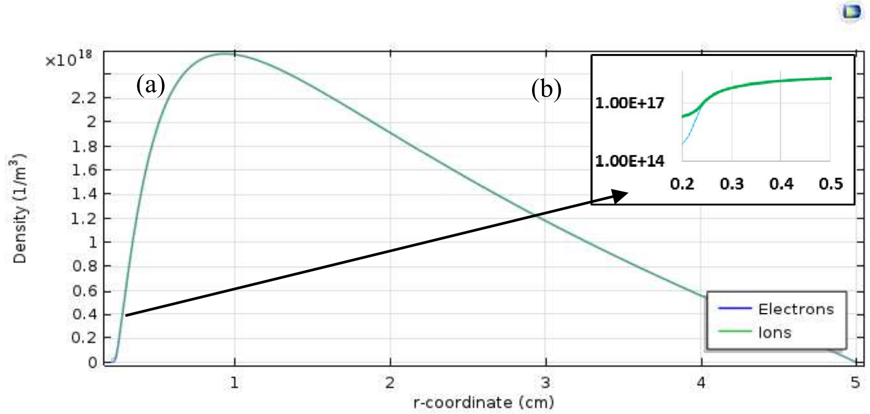

Figure 3. (a) Plot of the electron (blue) and ion (green) number density at the end of the simulation (t = 0.1s) and (b) insert plot on log scale only in the near cathode.

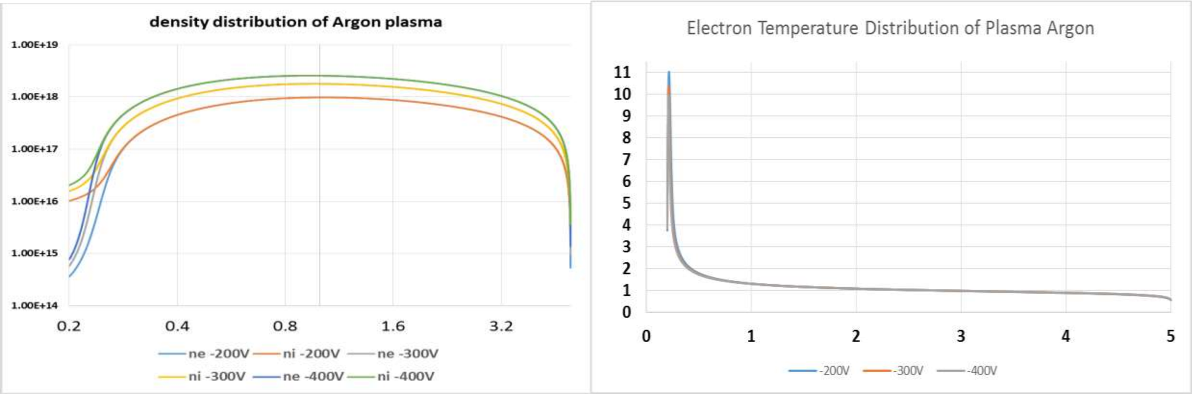

Figure 4. (a) Log scale of n_e and n_i distribution of plasma in the chamber (b) Electron Temperature as a function of the distance at the end of the simulation (t = 0.1 s) with voltage variation from -200 V until -400 V.

The high voltage accelerates an electron from the cathode to the outer conductor, so the electron gets energy from electric potential and changes it to kinetic energy. The kinetic energy of electron correspondence to electron temperature due to the average of electron velocity (figure 4b). Electron lost their energy due to collision with neutral argon gas and resulting ion-electron pair during migration. Figure 4(b) show that electron lost their energy from around 10 eV near cathode until 1.4 eV (r = 1 cm) for all of the variation of voltage during simulation. With decreasing voltage applied on cathode result the increase of electrons temperature near cathode (figure 4(b)).When the kinetic energy of the electrons decreases reducing electrons capability to ionize neutral gas as a consequence there more residual energy. This indicates that most of the reaction of ionization take place here. Electron temperature nearly constant during migration and then lost their energy after reach outer conductor. With increasing negative potential (figure 4(a)), ion bombardment and ionization on the cathode surface increase, which results in more secondary electrons, ionizing more neutral atoms again and the result is more ion and electron densities. Figure 4a show that increasing voltage from -200 V, -300 V and -400 V causing an increase electron densities by 1.8 times for -300 V and 2.57 times for -400V.

4. CONCLUSIONS

Argon plasma occurs in the simulation 1D simulation of DC Bias by the measure of electric potential distribution, electron densities, ion densities and electron temperature distribution. The higher negative potential applied in the plasma system result the higher densities of ion and electron in the whole chamber and decrease the electron temperature near the cathode and have the similar value in the whole chamber.

5. REFERENCES

[1] M. Naeem, et. al., 2017, Materials Letters, 189, 213.

[2] Seungryul Yoo et.al., 2011, Thin Solid Films, 519, 6746.

[3] Georg Daeschlein et. al., 2017, Clinical Plasma Medicines, 5. 1.

[4] Sohbatzadeh, Farshad., et al., Characterization of diamond-like carbon thin film synthesized by RF atmospheric pressure plasma Ar/CH4 jet. *Superlattices and Microstructures*. **Vol. 89** pp. 231-241

[5] Bolshakov, et al., High-rate growth of single crystal diamond in microwave plasma in CH4/H2 and CH4/H2/Ar gas mixtures in presence of intensive soot formation. *Diamond and Related Materials*. **Vol. 62**. Pp. 49-57

[6] Yan, Xiao.et. Al., Removal of p-chlorophenol in mist by DC corona discharge plasma. *Chemical Engineering Journal*. **Vol. 245**. pp. 41-46. 2014

[7] G.J.M. Hagelaar and L.C. Pitchford, “Solving the Boltzmann Equation to Obtain Elektron Transport Coefficients and Rate Coefficients for Fluid Models,” *Plasma Sources Science and Technology*, **Vol. 14**, pp. 722–733, 2005

The Characteristics of Optical and Magnetic Properties of $Zn_{0.75}Mn_{0.25}O$ Nanoparticles

Heru Harsono1*, Zahratul Jannah AR[2]

[1]Department of Physics, Faculty of Mathematics and Natural Sciences, University of Brawijaya, Malang, Indonesia
[2]Department of Mechanical Engineering, Malang State Polytechnic, Malang, Indonesia
* Corresponding authors: [heru_har@ub.ac.id]

Abstract – In this present report, Mn2+ ions were introduced into ZnO in the form of Zn0.75Mn0.25O by means of coprecipitation method at low temperature using Zn(CH3COO)2·2H2O, Mn(CH3COO)2·4H2O, HCl, and NH4OH as starting materials. Ultra Violet Visible Spectrophotometry 1601 Shimadzu, and Vibrating Sample Magnetometer (VSM) have been conducted to characterize the produced Zn0.75Mn0.25O samples. The result of optical characterization of Zn0.75Mn0.25O nanoparticles using Ultra Violet Visible Spectrophotometry 1601 Shimadzu 6 shows a decrease in the size of energy gap from 3.50 eV to 3.20 eV and Vibrating Sample Magnetomater test results shows that the sample Zn0.75Mn0.25O have paramagnetic behavior.

1. INTRODUCTION

Magnetic nanoparticles are interesting materials because of their unique properties and important potential applications. Researchers have studied magnetic nanoparticles because they have different physical and chemical properties than the bulk material. Differences in physical and chemical properties are related to the existence of quantum size effects in the material [1].

A special quality possessed by magnetic nanoparticles is the ability to behave as superparamagnetic. Superparamagnetic behavior appears on materials with a single magnetic domain. Because of its small size, the material is highly reactive to an external magnetic field, but if the effect of the external magnetic field is removed, the material will have paramagnetic behavior. [2].

The synthesis of ZnO and transition metal ions-doped ZnO, in recent years, has occurred worldwide in the field of nanotechnology [3] by means of many routes, e.g. mechanical milling [4], mechanochemical [5], sol–gel [6], and coprecipitation [7]. Among all those methods, coprecipitation and sol-gel routes provide sufficient control on the size and morphology of nanometer-sized particles. Furthermore, coprecipitation is also recognized as one of the simple, low cost, and environmentally friendly synthetic method for fine production of nanoparticles [8].

In the present work, we report a simple coprecipitation method to fabricate $Zn_{0.75}Mn_{0.25}O$ nanoparticles. The effects of Mn-doping concentration on optical and magnetic properties of the produced $Zn_{0.75}Mn_{0.25}O$ nanoparticles were investigated.

2. METHODS

1.1 Materials

The chemicals used were zinc acetate dihydrate $Zn(CH_3COO)_2.2H_2O$ (Merck,≥99%), manganese (II) acetate tetrahydrate $Mn(CH_3COO)_2.4H_2O$ (Aldrich Chemestry,≥99%), 37% HCl (Merck) and NH_4OH 25% (Merck).

1.2 Procedures

The synthesis of Zn0.75Mn0.25O nanoparticles is conducted by co-precipitation method. The starting materials making up the Zn0.75Mn0.25O nanoparticles are zinc acetate dihydrate powder (CH3COO)2.Zn.2H2O and manganese (II) acetate tetrahydrate or (CH3COO)2.Mn.4H2O weighted according to the molar composition of compound. The molar composition is changed into weight ratio adjusted for characterization purposes.

1.3 Characterization

The sample of $Zn_{0.75}Mn_{0.25}O$ nanoparticles generated from the experiment were characterized by Ultra Violet Visible Spectrophotometry 1601 Shimadzu. Analysis of the magnetic properties is done by using Vibrating Sample Magnetometer (VSM Oxford VSM1.2H).

3. RESULTS AND DISCUSSION

The result of optical characterization of $Zn_{0.75}Mn_{0.25}O$ nanoparticles using *Ultra-Violet Visible Spectrophotometry* 1601 Shimadzu 6 shows a decrease in the size of energy gap from 3.50 eV to 3.20 eV (Fig.1). The decrease in the size of energy gap indicates that Mn^{2+} ion doping has succeeded in influencing the optical properties of ZnO nanoparticles and also indicates that Mn^{2+} ions have been successfully substituted into the ZnO lattice. The larger the width of the band gap, the greater the energy needed for the excitation of electrons from the valence band to the conduction band.

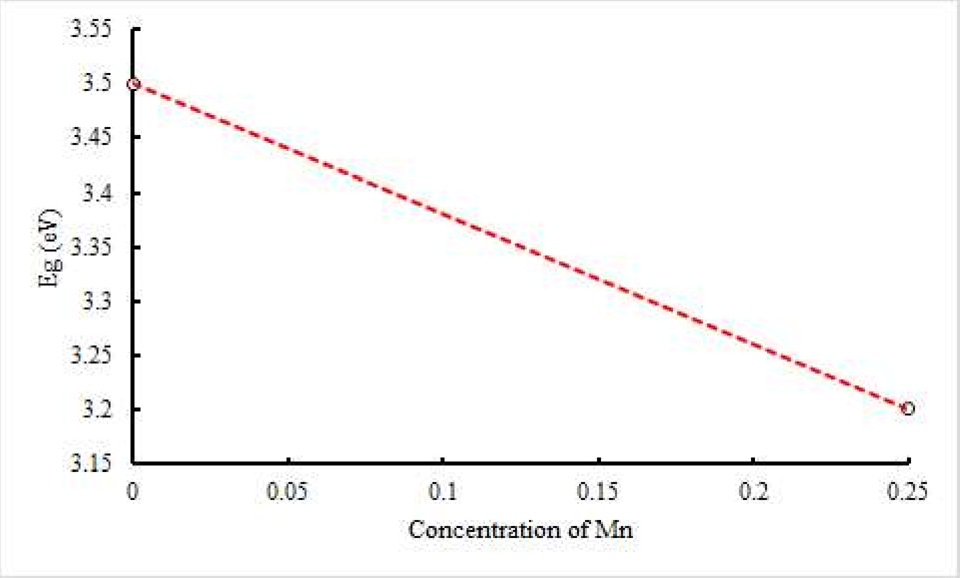

Figure.1 : Mn atom concentration curve of the energy gap

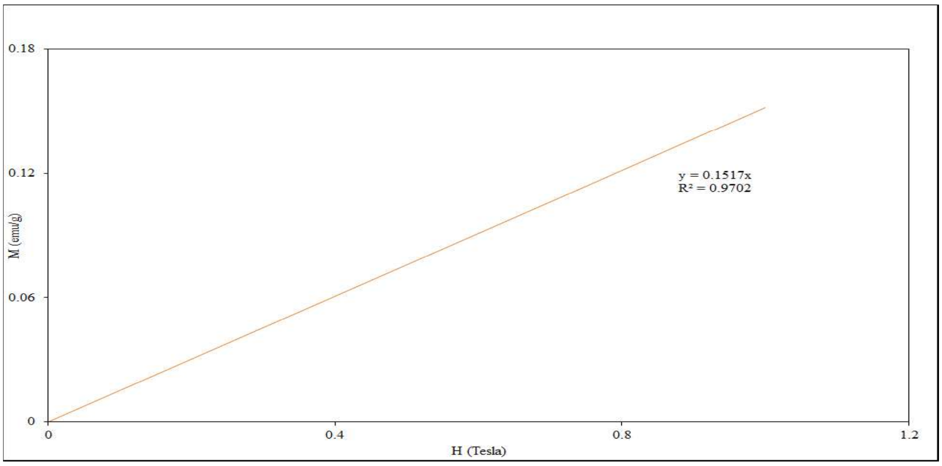

Figure. 2 : Vibrating sample magnetometer results for sample $Zn_{0.75}Mn_{0.25}O$ nanoparticles produced by co-precipitation method, under a magnetic field 1 tesla at room temperature

Based on the vibrating sample magnetometer results in Fig. 2 a linear shaped curve which indicates the paramagnetic properties of the sample is obtained. The same pattern of magnetic curves is also reported by Abdel Hakeem et.al. [9]. It is presumed that the paramagnetic properties are due to the formation of mn cluster which is caused by little solubility of Mn in ZnO [10]. Mera et.al. assumption is supported by the research result of Sharma et.al. [11] which states that mn cluster with stands the on set of ferromagnetic phase and give a great paramagnetic effect on mn doped zno. in addition, according to O.D. Jayakumar et.al [12], the appearance of $ZnMn_2O_4$ impurity phase is not likely to cause ferromagnetic properties since this impurity phase has ferrimagnetic properties with Tc≈15 K.

4. CONCLUSIONS

The result of optical characterization of $Zn_{0.75}Mn_{0.25}O$ nanoparticles shows a decrease in the size of energy gap from 3.50 eV to 3.20 eV and Vibrating Sample Magnetomater test results shows that the sample $Zn_{0.75}Mn_{0.25}O$ have paramagnetic behavior.

5. REFERENCES

[1]. Gubin,S.P., Y.A. Koksharov, G.B. Khomutov, G.Y. Yurkov, *Russian Chemical* Reviews **74 (6),** 489-520, (2005).

[2]. Wu,A., P. Ou, L. Zeng, *Nano*, **Volume 5**, No.5, 245-270, (2010).

[3]. M.E. Abrishami, S.M. Hosseini, E.A. Kakhki, A. Kompany, M. Ghasemifard, 2010, *International Journal of Nanoscience*, **9**, 19–28.

[4]. L.C. Damonte, Z. Mendoza, B.M. Soucase, M.A.H. Fenollosa, 2004, *Powder Technology*. **148**, 15-19.

[5]. R. He, R.K. Hocking, T. Tuzuki, 2013, *Journal of the Australian Ceramic Society.* **49(1)**, 70–75.

[6]. B.N. Dole, V.D. Mote, V.R. Huse, Y. Purushotham, M.K. Lande, K.M. Jadhav , S.S. Shah, 2011, *Current Applied Physics*, **11**, 762-766.

[7]. T. Liang, Tong, W.L. Chin, S.B.A. Hamed, 2014, *Journal of Nanomaterials.* 1-6.

[8]. F. Chekin, S. Bagheri, S.B.A. Hamid, 2012, *Analytical Methods.* **4**, 2423-2428.

[9]. A.M. Abdel Hakeem, *Journal of Magnetism and Magnetic Materials* 322, 709, (2010).

[10].J. Mera, C. Cordoba, J. Benavidez, O. Paredes, J. Doria, A. Gomez, C. Sanchez, C. Paucar, O. Moran, 2010, *Journal of Mater Science* **45**, 5398.

[11].P. Sharma, A. Gupta, K.V. Rao, F.J. Owens, R. Sharma, R. Ahuja, J.M. Osorio, B. Johansson, G.A. Gehring, 2003, *Nature Matter* **2**, 673.

[12].O.D. Jayakumar, H.G. Salunke, R.M. Kadam, M. Mohapatra, G. Yaswant, S.K. Kulshreshtha, 2006, *Nanotechnology* **17**, 1278.

Austempering Process At Low Temperatures In Production Of Wear Resistant Steel With Structured Carbide Free Bainite

Faisal Manta[1*], Suwarno[2]

[1]Department of Mechanical Engineering, Faculty of Industrial Technology, University of Institut Teknologi Sepuluh Nopember, Surabaya, Indonesia
[2] Department of Mechanical Engineering, Faculty of Industrial Technology, University of Institut Teknologi Sepuluh Nopember, Surabaya, Indonesia
* Corresponding authors: [faisalmanta@gmail.com]

Abstract – (This study focused on obtaining wear-resistant by a local material with required heat treatment to produce characters that are comparable to imported materials. The material used in this study is a steel 1CcrMnSi (A) and 0.6CcrMnSi (B) taking into account existing reference and alloying elements that support the character of the material is expected. The heat treatment used in the research is austempering produce a free bainite structure with a good hardness and good toughness properties. After the heat treatment process, several tests is performed toward the material including hardness test, toughness test and microstructural observation. This research obtain maximum hardness by austempering temperatures 150ºC and holding time 160 hours is 53 HRC but it has the lowest impact toughness 0.5 Kgm because has martensite phase. The better properties get when austempering temperature 200ºC and holding time 320 hours because the microstructures suspected is fine bainit

1. INTRODUCTION

In 1930 Daveport and Bain discovered a new phase which is different from the perlite or martensite transformation. This “new phase” transformed at higher temperature point than martensite start. People named it bainite. Bainite has a variety of structures that makes many researchers interested to examine it. Transformation temperature very influences the morphology of bainite. Lower bainite (LB) on the low transformation has a high density of dislocation and fine structures which are providing good mechanical properties. Upper bainite (UB) on the higher temperature transformation has poor mechanical properties. In traditional bainite transformation, we will discover the presence of carbides, where the bainites are classified based on the carbide based distribution. For UB carbide distributed in the grain boundary carbide grains whereas in LB distributed in other location than in the grain boundary including at the ferrite grain of bainite. In 1964 Grosmaann and Bain did research on high-carbon steel and it is obtained that an austempered steel has better toughness than the quench-tempered steel at the same hardness point. In 1980 a new kind of bainite “carbide free bainite” was discovered. This kind of bainite has both high strength and toughness, making it widely researched in its use in industries such as bearing and railway lines. Carbide free bainite had a phase structure of ferrite and retained austenite, which is obtained by adding the element capable of inhibiting the formation of carbides such as Si and Al. In 2013 Bhadeshia and his colleagues studied high-carbon steel to produce the fine structure of pearlite, bainite and martensite. It is found that Bainite has the best wear resistance than the other phases. In 2014 X.Y Long did research on a medium carbon steel with a martensite start temperature (Ms) 310 °C, to obtain materials with bainite structure at various temperatures. It is found that the maximum impact is achieved at austempering temperature 310-320°C which is very close to Ms temperature of the steel, indicating that bainite at low temperatures has better performance on low temperature. Where it is obtained a thinner bainite lath structure and retained austenite. So, in this study a formation of bainite is applied to obtained an adequate level of impact toughness and hardness point.

2. METHODS

2.1 Material & Experimental

The material is steel 1C; 1.5Si; 2Mn; 1Cr (%) and 0.6C; 2Si; 2Mn; 1Cr(%) casted with an electric furnace and forged at forging ratio 3, spectrometry tested and Ms temperature calculated using formulas and programs. The sample size is 100 x 30cm and each sample was heated for 1 hour at 1000°C and furnace cooled to 200°C and then air cooled to room temperature. The austempering process aimed to obtain bainite which is consist of austenitization at 1000°C for 1 hour and then rapidly cooled in a liquid salt bath with a temperature variation of

150, 200, and 250 °C, 160 and 320 hours holding time variation and air cooled to room temperature. The salt bath is consist of KNO3 and NaNO2 with 4: 6 ratio. The microstructure observations test was performed to a 20x10x10(mm) steel before and after heat treatment process with nital 2% HNO3 as etching agent and Olympus Digital Microscope. Hardness test also was performed to 20x10x10(mm) steel before and after heat treatment using Rockwell (HRC) method with a load of 150 kPa. Impact test conducted on steel before and after heat treatment based on JIS Z 2242 standard using the Charpy method and Frank test machine with a load of 30 Kg.

3. RESULTS AND DISCUSSION

3.1 Material & Experimental

In these experiments calculations of temperature bainite star (Bs), martensite start (Ms) is performed, A1 and A3 of steel to determine the temperature parameters of the study. Temperature Bs and Ms is approached in two ways, using the method of calculation by Van Bohemen [1] and the program Map Steel Muc46 by Bhadeshia [2]. In Table 4.1 attached to the value of Bs and Ms results of calculation and the computer program of experimental steel. Then austempering temperatures chosen was 150, 200, 250 °C with holding time is 160 and 320 hours.

Table 1. Ms dan Bs Temperatures by program and calculation

Stee	Alloy (% berat)									Program (°C)		Calculation (°C)	
	C	Si	Mn	Cr	P	S	Ni	Mo	B	Bs	Ms	Bs	Ms
Target A	1	1.6	2	1	-	-	-	-	-	260	137	386	180
Baja A	0.78	1.66	1.89	1.24	0.03	0.01	0.05	0.01	-				
Target B	0.6	2	2	1	-	-	-	-	-	240	84	380	160
Baja B	0.65	2.01	1.84	1.27	0.02	0.01	0.04	0.01	-				

3.2 Material & Experimental

Presented the results observation microstructure of steel 0.6CCrMnSi (A) and 1CCrMnSi (B) to temperature and the holding time variation before and after treatment.

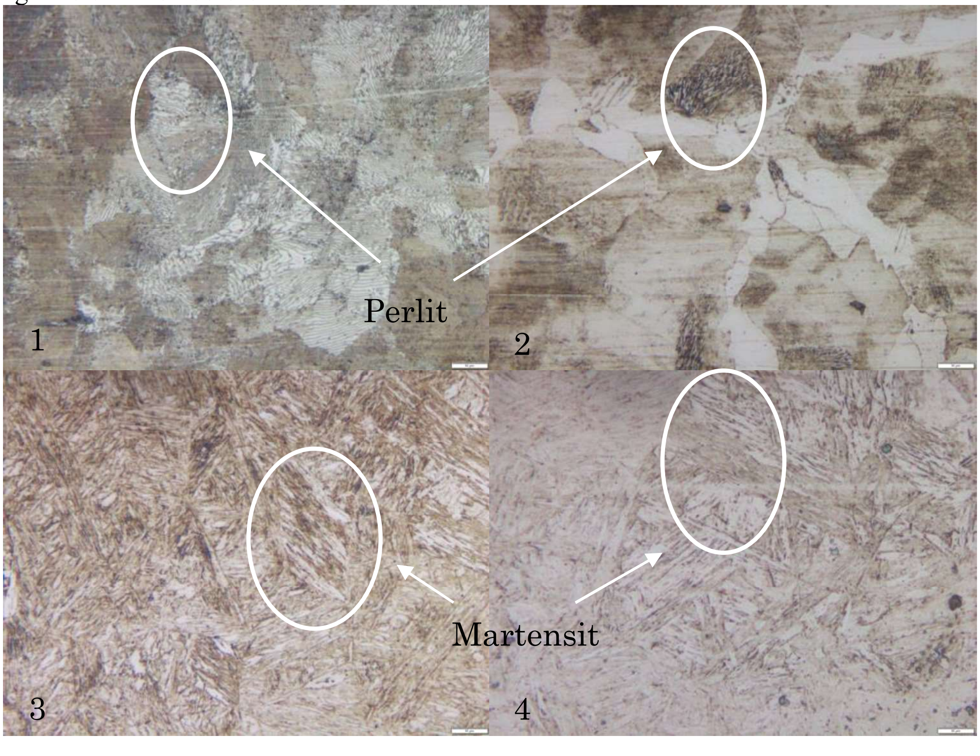

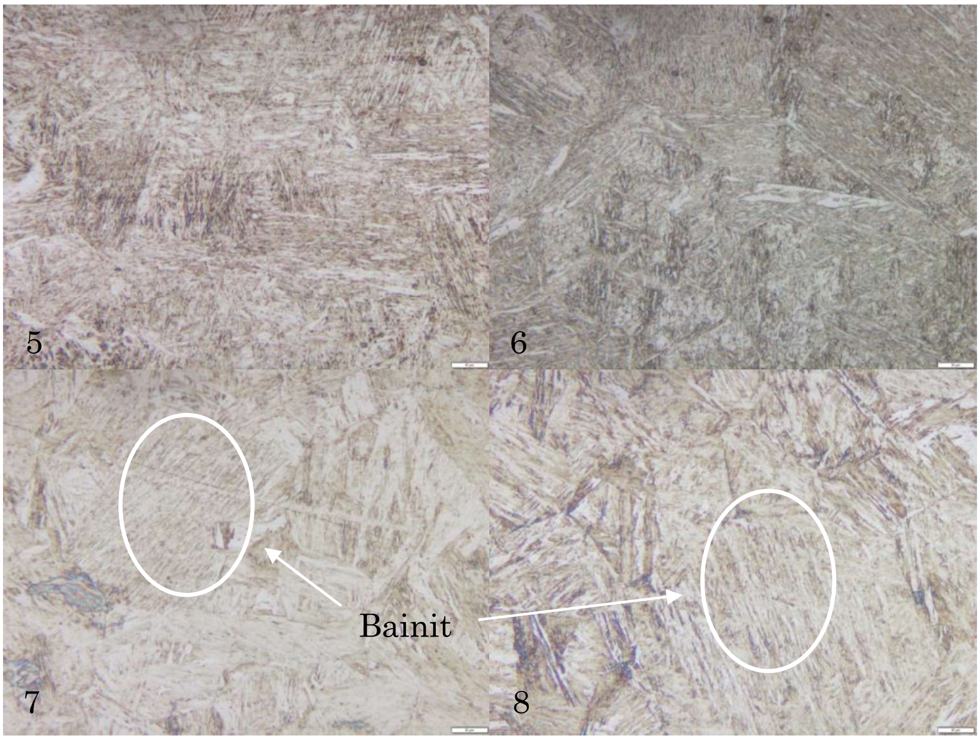

Figure 1. Microstructures result from 0.6CCrMnSi (1;3;5;7) and 1CCrMnSi steel (2;4;6;8). 1 and two steel before treatment, 3 and four austempering temperature 150 °C and holding time 160 hours, 5 and six austempering temperature 200 °C and holding time 160 hours, 7 and eight austempering temperature 250 °C and holding time 320 hours

The untreated steel is suspected of having the pearlite structure for both types of steel. Austempering at temperatures of 150°C and 200°C suspected to have martensite structure for all the holding time. Bainite is suspected to obtained at austempering temperatures 250°C with a holding time of 320 hours.

3.3 Mechanical Properties

Presented the results of testing hardness (HRC) and the impact of the steel 0.6CCrMnSi (A) and 1CCrMnSi (B) before and after heat treatment.

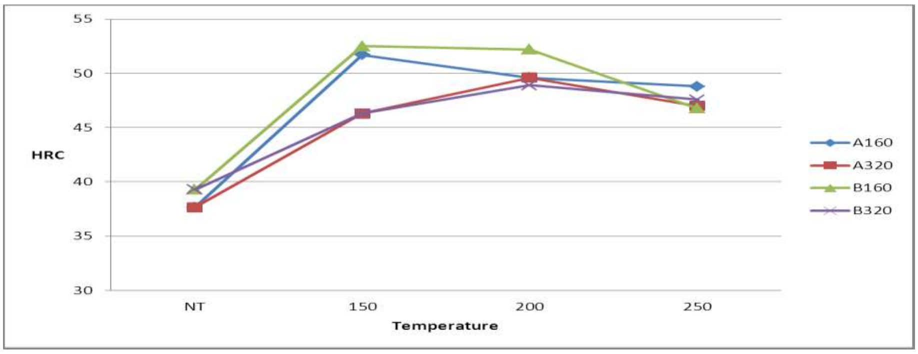

Figure 2. Hardness (HRC) to austempering temperatures and holding time variation on 0.6CCrMnSi (A) and 1CCrMnSi (B)

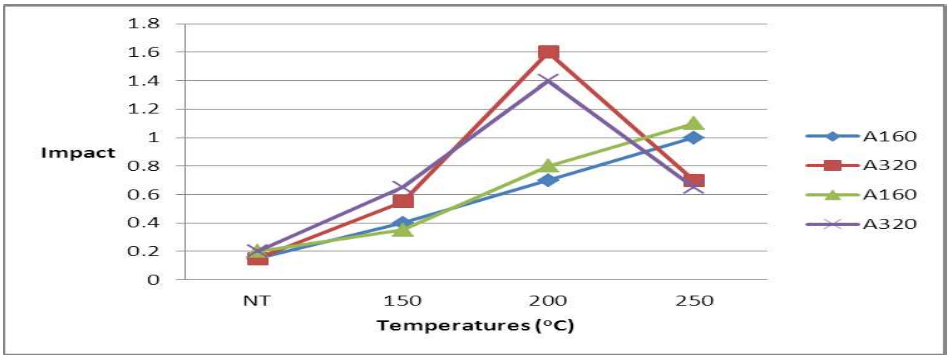

Figure 3. Impact toughness to austempering temperatures and holding time variation on 0.6CCrMnSi (A) and 1CCrMnSi (B)

Hardness values decrease with rising temperature austempering and maximum hardness is achieved at the holding time of 160 hours for all kinds of steel. The impact value increases with rising temperature austempering, but at holding time of 320 hours, maximum value in 200 ºC temperature austempering

4. CONCLUSIONS

The maximum hardness value is achieved at a low austempering temperature and the short holding time is suspected due to the presence of martensitic structure, and in general the hardness level is decreasing along with increased holding time. This phenomenon is suspected to happened due to more carbon is distributed from the martensite phase to form carbide-free. Hardness value is decreasing along with increasing austempering temperature and is suspected due to bainite formation and softerretained austenite. Low impact value suspected because of segregation of alloy elements and casting defects.

5. REFERENCES

[1]. Van Bohemen (2012),"Bainite and Martensite Start Temperature Calculated With Exponential Carbon Dependence",Materials Science and Technology

[2]. Bhadeshia, H.K.D.H., "Phase Transformation Group", Department of Material Science and Metallurgy, University of Cambridge

The Effect of Cr_2O_3 Addition on the Phase Stability of $Tl_{2x}Cr_xBa_2CaCu_2O_{8-\delta}$ Superconductor

Syahrul Humaidi[1*], Marhaposan S[1], Eddy Marlianto[1] and Roslan Abd-Shukor[2]

1Physics Department, FMIPA, Universitas Sumatera Utara
2School of Applied Physics, FST, Univ. Kebangsaan Malaysia, Kuala Lumpur
* Corresponding authors: [humaidi2009@gmail.com]

Abstract – The phase stability of High Temperature Superconductor $Tl_{2-x}Cr_xBa_2CaCu_2O_{8-\delta}$ (x= 0.0, ..., 0.4) via solid state reaction method with $BaCO_3$ as precursor has been observed by addition of Cr_2O_3. The powders were sintered at 900°C for 24 hours with twice grounding. The powders were then pressed into pellets of 13 mm diameter and 2 mm thickness under a load of 7 metric tons using hydraulic press for 10 minutes. The pellets were sintered at 900°C in a quarz tube in oxygen flow for 4-5 mins followed by furnace cooling. The van der Pauw method with silver paste contact has been employed to study the resistance of materials. The resistance and temperatur dependence were conducted in the range of 300K-30K using Edwards Cryogenics 8200 and CTL-Cryogenics model 22 compressor and X-ray powder diffraction has been employed to identify the Tl-2212 phase occurence with $2\Theta = 0^o - 60^o$. The critical temperature was in the range of 92K-96K , indicated that all of our samples were high temperature superconductors.. The volume fraction of Tl-2212 phase wiithout Cr_2O_3 was 50% and it was increase up to 88,23 % mole when 0.1 %mole and 94.11% when 0.2% mole Cr_2O_3 has been addeed-in.

Keywords: superconductors, critical temperature, Tl-2212, cryogenics and phase stability

1. INTRODUCTION

Superconductors material have attracted the researches and being developed rapidly in few decades. Some base materials like Bismuth [4] and Thallium [5] have been intensively explored in order to find the higher critical temperature. As we know, the critical temperature of superconductor is still far below the room temperature. That is why, this material is limited in practical use.High temperature superconductor (HTSC) Tl-Ba-Ca-Cu-O (Tl-HTS) is one of the attractive material nowadays due to its multi phases. Most of the superconducting phases have a Tc above 100K [1]. Some of the phases have been investigated and showed superconductivity phenomenon at 110K (Tl-1212) [5], Tl-1201 has Tc at 70K [11], Tl-1234 at 114K [12]. Some phases have been investigated, like Tl-1212 with Tc around 110K [5], Tl-1201 with Tc 70K and Tl-1234 with Tc of 114K [12]. However, the preparation of Thallium based superconductor is not easy to do [3]. Beside the powder is toxic, thallium also volatile.

Most of the precursor material for CuO based superconductor have a certain multi layers structure and high anisotropic degree. This multi layers structure is also known as CuO layer. CuO layer usually is in 2 dimensional and plays an important role in superconductivity properties of material. According to Nobumasa et al. [7], an extra ordinary condition occurs between CuO_2 layers when the critical temperarature, T_c was achieved. The T_c is inversely proportional to the Cu-Cu distance. If the Cu-Cu distance decreases, then the interaction between CuO increases. Thus the increasing in T_c. For $T_c < 50K$, the distance between Cu-Cu is greater than 6 A°. Meanwhile, if $50K < T_c < 125K$, then the distance is less than 4 A°. CuO based high temperature superconductor for thallium system has 3 main phases: Tl-2201(T_c:80K), Tl-2212 (T_c:108K) dan Tl-2223 (T_c:125K).
The homolog serie has a formula of $Tl_2Ba_2Ca_{n-1}Cu_nO_{4+2n}$, with n= 1, 2 and 3. For technical applied, Tl-2212 can be applied for microwave application compared to other two phases [8]. For thallium system superconductor material, the T_c increases when the number of CuO layer increases. However, the homolog serie of thallium system, $Tl_2Ba_2Ca_{n-1}Cu_nO_{4+2n}$, the T_c increases when CuO_2 layer increases. It is known that if the CuO_2 layer is more than 3 layers, the T_c decreases [9]. This is encouraging us to explore the Tl-2212 to produce 2 layers CuO_2. The addition of Cr_2O_3 is aimed to enhance critical temperature and to stabilize the Tl-2212 phase occurrence.

2. METHODS

2.1 Sample Preparation

All the samples were prepared via solid state reaction (stoichiometric). The starting precursor material BaO (99,99%) in powder form was mixed with $BaCO_3$ powder (99.99%), CaO powder (99.95%) and CuO powder (4N) according to mole%. The precursor was then grained in porcelen mortar for 1 hour before sintering at 900°C for 18 hours. The powder was then grained for 1 hour and sintered at the same temperature for 6 hours. This stepwork has been done to get a precursor material. The next step is addition of thallium oxide (99,99%) and chromium oxide (99.95%) according the mole-%. The pellet with diameter of (2-3) mm and 13 mm diameter was then produced using palletizing machine under the stress of 7 ton for 10 minutes. The pellet was sintered at 900°C with oxygen flow for 4 minutes. Chemically, the stoichiometric reaction can be written as [10]:

$$2BaCO_3 + CaO + 2CuO \dashrightarrow Ba_2CaCu_2O_5 + 2CO_2$$

The sintering step can be illustrated in Figure 1:

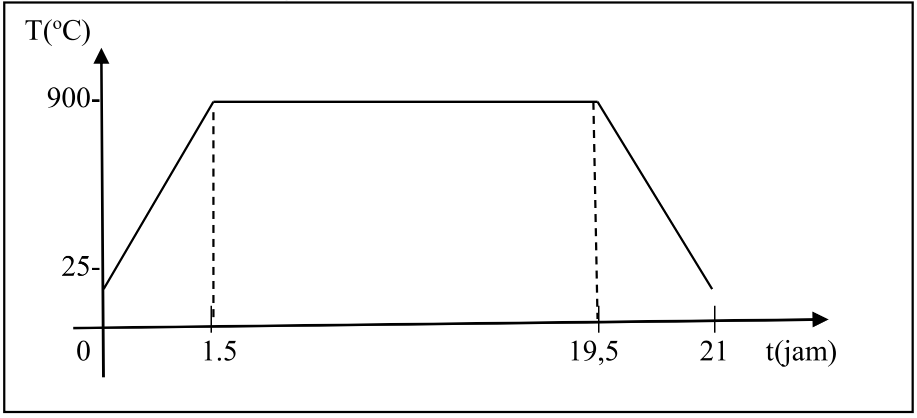

Figure 1: Sintering process of $Ba_2CaCu_2O_5$ precursor

The next step is the second sintering process for 6 hours at 900°C and furnace cooling to room temperature. The pellet was produced by palletizing machine under 7 ton of pressure with the addition of Tl_2O_3 and Cr_2O_3 powder according to mole%, chemically can be illustrated as follow:

$$Tl_2O_3 + Cr_2O_3 + Ba_2CaCu_2O_5 \dashrightarrow Tl_2Cr_2Ba_2CaCu_2O_{8-\delta}$$

In this our research, x is in the range of 0.0 to 0.4. The occurrence of Tl-2212 phase was confirmed by using XRD analysis (Eva program).

2.2 T_c Measurement

The resistance of the pellet was measured by multimeter before characterized in a vacuum pump of model Edwards Cryogenics 8200 Compressor and CTL Cryogenesis Model 22 Refrigenator Controller model Lakeshore 325 autotuning temperature controller. The initial temperature was room temperature and the final temperature was 30K using liquid Helium. The four point probe method was used to measure the sampel resistance minute to minute with silver paste as ohmic contact. A 220-Programmable Current Source and Keithley 2000 Autoranging Microvolt DMM was used with 20 mA current source. From the graph of temperature versus voltage produced, we can determine the resistance graph with critical temperature of the sample. The occurrence of Tl-2212 phase was analized using XRD powder method with $2\theta = 5^0$ to 60^0. The XRD pattern was recorded by Bruker model D8 diffractometer with CuKα radiation. The analyse was done with Eva software.

3. RESULTS AND DISCUSSION

Figure 2 shows the resistance versus temperature for x=0.0 to x=0.2. From the Figure 1, it can be seen that all the samples show a metal-like characteristic at normal state. The critical temperature as can be noted from Figure 2(a) were: 93K/105K (x=0), 94K/110K (x=0.1) and 96K/116K (x=0.2). In the composition of x=0.3 and x=0.4 as can be seen in Figure 2(b), the critical temperature were 92K/110K and 83K/106K. respectively. As such, all the samples are in high temperature class of superconductor[6].

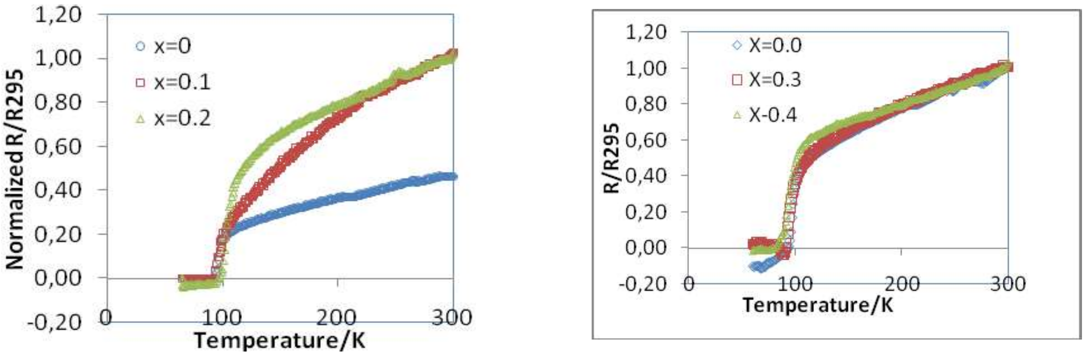

(a) (b)

Figure 2: Resistance versus temperature for sample with x=0.0–0.2 (a) and x=0.0-0.4 (b)

Figure 3 shows the XRD pattern of the pure samples. As it can be seen, first three maximum peaks: (105), (107) and (110) are in between $25 < 2\Theta < 35$. This indicated that the occurrence of Tl-2212 phase.

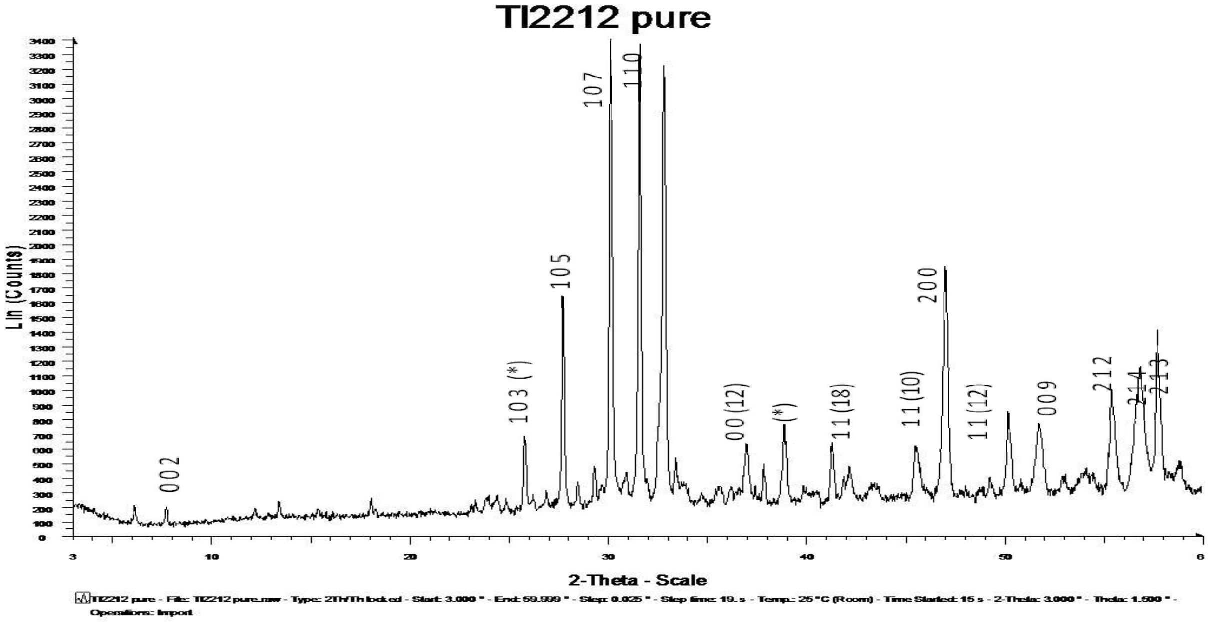

Figure 3: XRD pattern for $Tl_2Ba_2CaCu_2O_{8-\delta}$ sample

Some lines with multi indexes have been observed such as: (103) for Tl-2201, (109) for Tl-2234. This is indicated that the Tl-2212 phase was not stable, the volume fraction was about 50%. The volume fraction of Tl-2212 phase increased up to 88% when 0.1 mole-% Cr_2O_3 was added in. The addition of 0.2 mole% Cr_2O_3 produced the highest volume fraction (94%) as can be presented in Table 1. However, when the amount of Cr_2O_3 was increased up to 0.3 mole%, the volume fraction of Tl-2212 phase decreased to 72%. Thus, it can be concluded that the addition of few moles of Cr_2O_3 has increased the critical temperature as well as the stability of Tl-2212 phase in $Tl_2Ba_2CaCu_2O_{8-\delta}$ system.

Table 1: Phase occurrence of Tl-2212 with Cr content.

Series	Tl-2212 Phase	Tl-1212 Phase	Tl-1223 Phase	Tl-2223 Phase	Tl-2201 Phase	Tl-2234 Phase	Other Phase
$Tl_2Ba_2CaCu_2O_{8-\delta}$	50%	8%	0	0	27%	0	0
$Tl_{1.9}Cr_{0.1}Ba_2CaCu_2O_{8-\delta}$	83%	6%	0	6%	0	6%	0
$Tl_{1.8}Cr_{0.2}Ba_2CaCu_2O_{8-\delta}$	88%	6%	0	0	0	6%	0
$Tl_{1.7}Cr_{0.3}Ba_2CaCu_2O_{8-\delta}$	68%	4%	4%	12%	0	4%	Tl-1234 (4%)
$Tl_{1.6}Cr_{0.4}Ba_2CaCu_2O_{8-\delta}$	46%	4%	4%	4%	0	15%	Tl-1234 (15%)

4. CONCLUSION

High temperature superconductor $Tl_{2-x}Cr_xBa_2CaCu_2O_{8-\delta}$ has been prepared via solid state reaction. The addition of Cr_2O_3 as a Cr source in the system of superconductor enhanced the critical temperature and phase stability. The highest volume fraction of Tl-2212 for 94% has been achieved when 0.2 mole-% Cr_2O_3 had been introduced to the $Tl_{2-x}Cr_xBa_2CaCu_2O_{8-\delta}$ system. The composition of x=0.2 can be referred as a starting material in the future work.

5. REFERENCES

[1]. Michael P. Siegal, Donald L. Overmyer, Eugenee L. Venturini, Richard P. Padhilla and Paula N. Provencio, 1999, Remarkable Properties of Tl-Ba-Ca-Cu-O Thin Films Following Post-Growth High Temperature Annealing, IEEE Transaction on App.Supercond., Vol. **9**, No. 2, June 1999

[2]. M. Fatmasari · R. Abd-Shukor, 2012, Formation of Tl-1212 Phase in Bi- and Cr-Substituted $(Tl_{0.5}Pb_{0.5-x}M_x)Sr_2CaCu_2O_7$ Superconductor, J Supercond Nov Magn DOI 10.1007/s10948-011-1335-x.

[3]. Faizah M Salleh, A K Yahya, I Hamadneh and R Abd-Shukor,2002, " Effects of Ag Addition and Propertiesof Tl-2212 Superconductors", Solid State Science and Tech., Vol.**10** No 1 & 2, 30-36

[4]. Nasri A-Hamid dan R Abd-Shukor, 1999, Fabrication and Characterization of Ag-Sheatled $Bi_2Sr_2CaCu_2O_8$, Solid State Science and Technology, vol. **7**, No. I , 113-119

[5]. R Abd-Shukor, Baharuddin Yatim & Lau R S L, 1997, Formation of Tl-1212 phase in $(Tl_{0.8}M_{0.2})Sr_2(Ca,Cr)Cu_2O_7$ (M: Cd and Sc) High-Tc Superconductor, Journal of Materials Science Letters**16**: 818-820]

[6]. R Abd-Shukor, 2004, Introduction to Superconductivity in Metals, Alloys & Cuprates, Penerbit University Pendidikan Sultan Idris, Tanjong Malim

[7]. Nobumasa H., Shimizu K., Kwai T.. 1990. Correlation between the Superconducting Transition Temperature and The Spacing of Cu-O_2 sheet in the Copper-oxide Superconductor. *Physics C* **167**: 515-519.

[8]. Paranthaman M. et al. 1994. Synthesis and magnetic characterization of $(Tl_{0.5}Pb_{0.5})Sr_2Ca_2Cu_3O_9$ and $Tl_2Ba_2CaCu_2O_8$ bulk superconductors. *Physcia C* **219:** 413-419.

[9]. Sheng Z. Z., Hermann A. M., 1988. Superconductivity in the rare-earth free Tl–Ba–Cu–O system above liquid nitrogen temperature. *Nature* **332**: 55–58.

[10].Syahrul Humaidi, Awan Maghfirah and Tua Raja Simbolon, 2012, The Preparation of Thallium Cupric Oxide $(Tl_2Ba_2CaCu_2O_{8-\delta})$ Superconductor Precursor, Research Report, LP USU.

[11].Kikuchi, M , Ohshima, E, Ohninshi, N, Muraoka, Y, Nakajima, S, Aoyagi, E, Ogawa, M, Akimitsu, J, Oku, T, Hiraga, K & Syono, Y, 1994, Synthesis and superconductivity o f oxycarbonates of the Tl-1201 phase. *Physica C* **219** (1-2): 200-204.

[12].Ogborne, D, M, & Weller, M, T, 1994, Oxygen non-stoichiometry in the (Tl,Pb)-Sr-Ca-Cu-O 1212 system, *Physica C* **220**: 389-395

The Influence of KOH Concentration of the Chemical Activation on The Production of Active Carbon Made of Agave Fiber by Combined Activation Method

Gancang Saroja[1]*, Lailatin Nuriyah[1], Yogi Fernandus[1]

[1]Department of Physics, Faculty of Science, University of Brawijaya, Malang, Indonesia
*Corresponding authors: [saroja@ub.ac.id]

Abstract-Agave fiber is a natural fiber with primarily contain are cellulose, hemicellulose, and lignin. Therefore, Agave fiber is highly potential used as the material of active carbon. The process of active carbon production is divided into three steps: dehydration, carbonization, and activation process. The dehydration process was performed by using the oven to get rid of the water content. The carbonization process was done by heating at 400 ºC. Furthermore, the chemical activation process was carried out with KOH solution at concentrations 25 %, 27%, 29%, and 31%. After that, it was done the physical activation process by heating at 700 0C. The active carbon resulted from the process was characterized by Scanning Electron Microscopy (SEM) to see the morphology and the size of pores, and with the method of blue methylene absorption for measuring the large of the surface area. The measurement result shows that chemical activation process with 27 % concentration of KOH gives the widest surface of the carbon, about 570,1 m^2/g. Based on the SEM image, the pores of the carbon have a size in macroporous scale.

1. INTRODUCTION

East Java province is one of the regions in Indonesia where have the potential for cultivation of natural fiber, such as Cotton, Ramie (*Boehmeria Nivea*), Kenaf (*Hibiscus Cannabinus L.*), and Agave [1]. Natural fibers are a substance that can be renewable and environmentally friendly. They contain three primarily components: cellulose, hemicellulose, and lignin. The amount of matter contained in the fiber is influenced by the type of fiber, the age of the plant, and extraction method. One of fibers that most useful is Agave fiber.

Agave fiber is natural fiber which has cellulose content until 74% of the content total [2]. The chemical composition of Agave fiber has investigated by researchers. Ansell (1971) found that Agave fiber contains cellulose, lignin, hemicellulose, wax, and ash as much as 78%, 8 %, 10%, 2%, and 1% respectively. Meanwhile, Rowell (1992), revealed that Agave contains 43-56% cellulose, 7-9% lignin, 21-24 pentose, and 0,6-1% ash. According to Joseph (1996), Agave fiber contains the cellulose about 85-88% [3]. The variant of the chemical composition in some results of research is caused by the different of the plant come from, the age, and the method used. Research by Chand and Hashmi show that the amount of the cellulose and lignin contained in Agave depend on the age of Agave plant [4].

Because of the cellulose content of Agave fiber is high, it potentially becomes the raw material for active carbon. The active carbon has very many pores than ordinary carbon, so the sum of surface area is very big [5]. To achieve the condition, we need to activate a carbon by physical and chemical activation process. Based on references, the chemical activation using KOH as the activating reagent is very promising because of its lower activation temperature and well-defined micropore size distribution [6].

2. METHODS

In this research, it was used three steps of the process to produce the active carbon from Agave fiber: dehydration, carbonization, and activation. In the first step, the process was initiated by extracting of Agave Leafs to obtain the fibers. Then, the fibers were cut to be shorter for making the carbonization process easier. After that, the fibers were washed with aquades and then the fibers were dried naturally. The heating by the oven at 110 ºC was given to the fibers for dehydration process. The process was done in about an hour. The second step is carbonization. The carbonization process was done by the oven machine at 400 ºC for 2 hours in the air-tight condition. This process would result in the carbon. The last step of the process is activation. The chemical activation was done by KOH solutions with concentration: 25, 27, 29, and 31 %. Then, the carbon was activated physically by heating at 700 ºC in the air-tight condition. The result of the process is active carbon. The investigation of the active carbon properties did by SEM testing for seeing the structure and by the method of blue methylene absorption for measuring the large of the surface area.

3. RESULTS AND DISCUSSION

The preparation and dehydration process will produce the dry fiber that is ready for carbonization process. The carbonization process was done in the oven. The result of this process produces black carbon which shows in Figure 1.

Figure 1. The carbon resulted by carbonization process

Figure 2. Final result, the active carbon made from Agave fiber

The next step is reducing the size of carbon become carbon powder. Furthermore, the powder was activated chemically by KOH solutions with concentration 25, 27, 29, and 31 % for 24 hours long. Then, the carbon powder was washed and dried, the carbon powder was heated by the oven at 700 ºC in the air-tight condition for 1,5 hours and produce the active carbon. The result of the process is shown in Figure 2. The active carbon has a powder form and black in color.

The active carbon was characterized using SEM to see the morphology and the size of pores, and with the method of blue methylene absorption to measure the large of the surface area.

The measured surface area by the blue methylene shows the influence of chemical activation to the surface area of carbon (see Table 1). When the concentration of KOH solution is increased from 25 % to 27 %, the surface area will be raising as well. However, when concentration rises from 27 % to 29 %, there is no significant change of the result. On the other hand, the surface area is decreasing when we use the 30% KOH solution in the activation process. The largest surface area of the carbon is found in this research about 570 m^2/g. This value is still under the ideal surface area of active carbon, that is 1000 m^2/g.

Table 1. The surface area of active carbon based on calculation of the blue methylene absorption

No	The KOH concentration used in chemical activation process (%)	The surface area (m^2/g)
1	25	566,3
2	27	570,1
3	29	570,0
4	31	566,3

The result of SEM testing shows that the carbon has the pores, as shown in Figure 4. Based on the images, it can be seen that there is a difference of porous size of the active carbon that influenced by the chemical activation process. From the resulted images, we have information about the size of pores wide. The collection of pores size which shown from images is presented in Table 2.

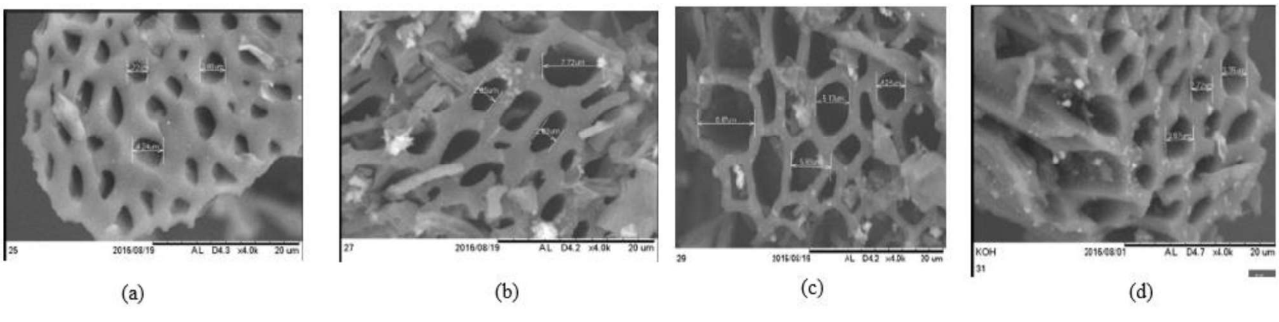

(a) (b) (c) (d)

Figure 4. The SEM image of the carbon by chemical activation using KOH (a) 25% (b), 27%(c), 29%, and (d) 31%

Table 2. The pores size of active carbon on SEM image as function of chemical activation

No	Concentration of KOH (%)	wide (μm)			Average of size (μm)
		d_1	d_2	d_3	
1	25	2,72	3,48	4,24	3,48
2	27	2,85	7,72	2,53	4,37
3	29	8,67	5,13	4,24	6,01
4	31	3,67	2,72	3,35	3,25

Note; d_1, d_2, and d_3 are wide of pores that presented by SEM at three different location in an image

There is an increasing of porous size when the KOH solution concentration is increased from 25% to 29%. However, when the KOH solution concentration used in the experiment is up to 31%, the porous size decreased from the size before. The structure of pores has a size in micrometer scale, so the carbon is categorized as macropores.

4. CONCLUSIONS

Based on the results of the research, it can be concluded as follows.

a) The active carbon has successfully synthesized from Agave fibers with the chemical activation process using KOH solution and carbonization process at temperature of 700 ºC .
b) Based on the SEM examination, the porous has a size more than 50 nm which categorized as a macropores scale.

5. REFERENCES

[1]. Potensi Jawa Timur sebagai Penghasil Serat Alam untuk Berbagai Agro Industri, *Sinar Tani*, edition 12 – 18 April 2006 (*downloaded* 29 March 2016)

[2]. Kalia, S, Kaith, B.S., and Kaur, I., *Cellulose Fibers: Bio-and Nano-Polymer Composites*, Springer 2011

[3]. Adhi Kusumastuti, Aplikasi Serat Sisal sebagai Komposit Polimer, *Jurnal Kompetensi Teknik*, **Vol. 1**, No. 1, November 2009

[4]. Chand, N. & Hashmi, S.A.R. *Journal of Materials Science* (1993) **28**: 6724.doi:10.1007/BF00356422

[5]. Deithorn, Robert T. & Mazzoni, Anthony F. 2015. *Activated Carbon; Properties of Activated Carbon*. Oakdale. TIGG

[6]. Leimkuehler, Eric Paul. 2010. *Production, Characterization, and Application of Activated Carbon*. Thesis. The Faculty of Graduate School University of Missouri.

Effect of Various Amount of Sucrose on the Properties of Zeolite-X Templated Carbon and CO_2 Adsorption Capacity

Ibnu Muhariawan Restuaji[1], Nurul Widiastuti[2]*

[1,2]Department of Chemistry, Faculty of Mathematics and Natural Science, Institut Teknologi Sepuluh Nopember, Surabaya, Indonesia
*Corresponding author: [nurul_widiastuti@chem.its.ac.id]

Abstract - Zeolite-X templated carbons (ZTC-X) have been synthesized by impregnation method using sucrose as a carbon source and zeolite-X as a template for CO_2 adsorption. The mass ratio of sucrose/zeolite-X was varied at 0.5; 0.75; 1; and 1.25. The properties of ZTC-X was characterized by XRD and N_2 isotherm analysis by Brenauer-Emmet-Teller (BET) method. XRD result of ZTC-X shows that all the samples have a sharp peak at $2\theta = 6°$, attributing to the ordered zeolite-like structure of ZTC-X. The intensity of ZTC-X 0.5 to 1.25 at $2\theta = 6°$ was decreasing (650 – 645 counts). The result of N_2 isotherm analysis by BET method shows that the surface area of ZTC-X 0.5 to 1.25 was increasing (442.827 – 576.338 m^2/g). However, the micropore volume of ZTC-X 0.5 to 1.25 was decreasing (0.149 – 0.097 cm^3/g). The result of characterization was indicating that ZTC-X 0.5 has high an ordered zeolite-like structure and also high microporosity. It has a good agreement with CO_2 adsorption data which ZTC-X 0.5 shows higher adsorption capacity than other samples (33.55 %wt). ZTC-X 0.75; 1; and 1.25 have adsorption capacity at 3.82; 27.23; and 26.48 %wt, respectively.

1. INTRODUCTION

The CO_2 emissions in the atmosphere lead a climate change coupled with an increase in the air temperature and an increasing of sea level. The CO_2 emissions were generated by the combustion of fossil fuels such as petroleum, coal, and natural gas [1]. Various materials for adsorbing CO_2 have been suggested. The common material is microporous materials, such as carbons, metal-organic frameworks, polymers, zeolitic materials, etc [2]. Among the best known microporous solids, the zeolite-X has the advantages like high stability, low cost and ordered structures [4].

The adsorption capacity of CO_2 on Faujasite-X zeolite was about four mmol/g [4]. The CO_2 selectivity of zeolite-X is affected by regular pore structure and uniform. However, the surface area of zeolite-X is relatively low. Lee [3] has reported, carbon materials have larger of the specific surface area than zeolite and mesoporous silica. Besides, both of zeolite-X and carbon have the ease of operation and low cost. Therefore in this study, zeolite-X and sucrose were used as template and carbon source to produce zeolite-X templated carbon (ZTC-X) for CO_2 adsorption.

In a recent study, ZTC is synthesized by various methods such as impregnation, chemical vapor deposition (CVD), casting, and carbonization [5]; [6]; [7]. The impregnation is one of the most simple methods and does not require complex equipment. In this method, the carbon precursor (sucrose) was added to the template and then polymerized by carbonization. To obtain the best condition of synthesis, it needs to vary the mass ratio of sucrose/zeolite-X. This paper reports properties of ZTC-X at various amount of sucrose and its performance in CO_2 adsorption.

2. METHODS

2.1 Chemicals

The chemicals used in this research were $NaAl_2O_3$, Na_2SiO_3, NaOH (99% p.a), sucrose (98%, Fluka), H_2SO_4 (98% p.a), high purity N_2 gas (99,99% N_2), HCl (37%, SAP), HF (48% p.a), demineralisation water, and CO_2 gas.

2.2 Procedures

Synthesis of ZTC-X was prepared by the impregnation method, which divided into three stages, namely, impregnation of sucrose to zeolite-X with various amount of sucrose at 5; 7.5; 10; and 12.5 g, carbonization of sucrose/zeolite-X composite, and removal of the zeolite-X template by acid. According to mass ratio sucrose/zeolite-X, the samples were denoted as ZTC-X 0.5; ZTC-X 0.75; ZTC-X 1; and ZTC-X 1.25. The materials were characterized by XRD and N_2 sorption isotherms by Brenauer-Emmet-Teller (BET) method. The

CO_2 adsorption capacity test was conducted by gravimetric method. The sample weight was recorded every minute until no additional mass. It was carried out at a temperature of 30 °C and pressure of 1 bar.

3. RESULTS AND DISCUSSION

The structure of the synthesized ZTC-X by varying the mass ratio of sucrose/zeolite-X was characterized by XRD. For comparison, Fig. 1 shows the XRD patterns for zeolite-X and carbon/zeolite-X composite before template removal is included. Fig. 1b shows that the XRD patterns of carbon/zeolite-X composite exhibit similar to characteristic peak of zeolite-X. It suggests that carbon has already formed pore structure zeolite-X-like without affecting or damaging the crystal structure of zeolite-X. Fig. 1c shows that the zeolite-X template was successfully removed. Besides, the ZTC-X sample shows a sharp peak at $2\theta = 6°$. It is believed originating from the (111) plane of zeolite-X, indicating that some of the structural regularity exists in carbons.

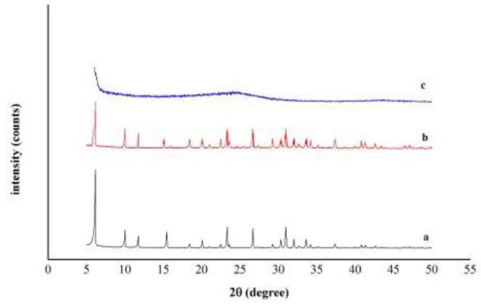

Figure 1. XRD patterns of (a) zeolite-X, (b) sucrose/zeolite-X composite before template removal, (c) ZTC-X after treated by acid

Fig. 2a shows all of the carbon samples have a similar characteristic peak at $2\theta = 6°$ which indicating ordered structure zeolite-X-like. Furthermore, two broad and weak peaks are observed at around 25 and 45°, attributing to the (002) and (100) plane from turbostratic carbons, respectively. Turbostratic carbon is regarded as a variant of h-graphite which is stacked up by disordered graphene layer [8]. It is obtained by the high-temperature process. It is also generated from carbon which is not deposited onto pore zeolite template. Besides, Fig. 2a. Shows that ZTC-X 0.5 and ZTC-X 0.75 have a weak sharp peak at 35°, indicating that some Al from zeolite-X were not clearly removed. It is probably raised by a high composition of zeolite-X on the composite samples. Fig. 2b shows that intensity of ZTC-X 0.5 to 1.25 at $2\theta = 6°$ was decreasing. ZTC-X 0.5 shows higher intensity of $2\theta = 6°$ at 650 counts. It indicates that mass ratio sucrose/zeolite-X 0.5 was effectively replicated with high ordered zeolite-like structure.

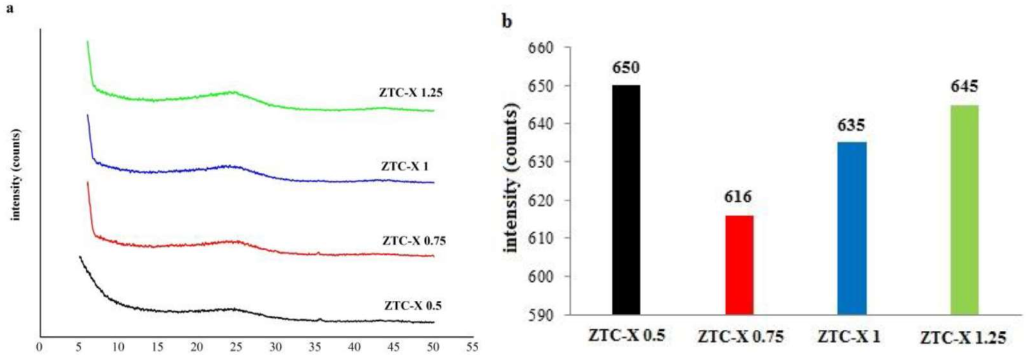

Figure 2. XRD patterns for ZTC-X (a) and intensity of ZTC-X at $2\theta = 6°$ (b)

The N_2 sorption isotherms by BET method and pore size distribution curves of ZTC-X are represented in Fig. 3. The results show that all the samples are mainly typed I, as depicted in Fig. 3a. It is indicating that large numbers of N_2 molecules are adsorbed by carbons at low-pressure range ($P/P_0 < 0.1$) and it exhibits a micropores character of carbons. The presence of micropores is consistent with the observed ordered structure zeolite-X-like in the XRD patterns of carbons. The hysteresis loop is obvious exists at wide pressure range ($P/P_0 > 0.4$), attributing to the presence of mesopores channel in carbons. The isotherm curve of ZTC-X 0.5 shows a narrow hysteresis loop which indicating the more presence micropores in this sample. It exhibits that ZTC-X 0.5 more effectively replicating a high microporosity ordered structure zeolite-X than other samples.

The pore size distribution curves for ZTC-X obtained by Hovarth-Kawazoe (HK) method are presented in Fig. 3b. All the carbons exhibit pore size distribution centered at below 1.2 nm. The pore size distribution of ZTC-X 0.75; ZTC-X 1; and ZTC-X 1.25 are centered at 1.017; 1.018; and 1.017 nm, respectively. Whereas, the ZTC-X 0.5 possess a narrow pore size distribution which centered at 0.15 nm. It consistents with BET data which indicating a high microporosity character of ZTC-X 0.5. These larger micropores may be generated due to an effectiveness pore filling in the zeolite-X by a carbon with a mass ratio of sucrose/zeolite-X 0.5.

Structural properties summarized in Table 1 provide further information about the porosity of ZTC-X. The surface area of ZTC-X 0.5; ZTC-X 0.75; ZTC-X 1; and ZTC-X 1.25 are 444.827; 392.539; 493.564; and 576.338 m^2/g, respectively. It shows that the surface area of ZTC-X is smaller than ZTC in the previous study. It suggests that rather than a collapse of the ZTC-X framework, a pore-blocking during the impregnation process, and the presence of turbostratic carbons. Meanwhile, Table 1 shows that ZTC-X 0.5 has higher micropore volume (0.149 cm^3/g) than other samples. It also shows a small average pore size (2.558 nm) which are in excellent agreement with XRD and BET data.

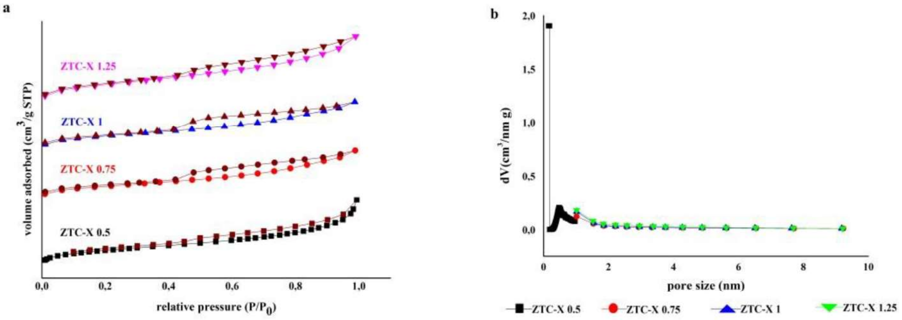

Figure 3. N_2 sorption isotherms by BET method (a) and pore size distribution curves by HK method (b) for ZTC-X 0.5; ZTC-X 0.75; ZTC-X 1; and ZTC-X 1.25

Table 1. Structural Properties and CO_2 Adsorption Capacity of ZTC-X with Various Mass Ratio of Sucrose/Zeolite-X

Sample	Surface Area BET (m^2/g)	Total pore volume (cm^3/g)	Micropore volume (cm^3/g)	Average pore size (nm)	CO_2 adsorption capacity (%wt)
ZTC-X 0.5	444.827	0.5665	0.149	2.558	33.55
ZTC-X 0.75	392.539	0.4366	0.065	4.449	3.82
ZTC-X 1	493.564	0.4798	0.108	3.888	27.23
ZTC-X 1.25	576.338	0.6128	0.097	4.253	26.48

The CO_2 adsorption capacity of ZTC-X obtained by the gravimetric method at 30 °C and pressure of 1 bar are shown in Fig. 4 and Table 1. As a result, ZTC-X 0.5 shows a high CO_2 adsorption capacity (33.55 %wt). The CO_2 adsorption capacity of ZTC-X 1 and ZTC-X 1.25 are 27.23 and 26.48 %wt, respectively. Meanwhile, ZTC-X 0.75 exhibits a low CO_2 adsorption capacity (3.82 %wt). This result indicates the CO_2 adsorption capacity of ZTC-X have correlated to average pore size and microporosity.

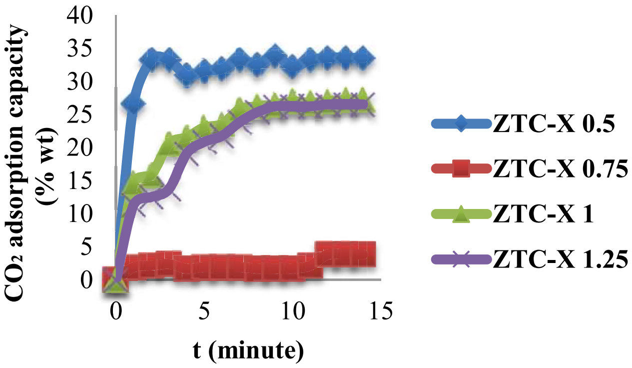

Figure 4. CO_2 adsorption capacity of ZTC-X at 30 °C and pressure of 1 bar

4. CONCLUSION

Based on the results presented in this study, it can be concluded that various amount of sucrose on ZTC-X was effecting properties and CO_2 adsorption capacity of ZTC-X. XRD patterns of ZTC-X 0.5 to 1.25 shows a decreasing peak at $2\theta = 6°$ (650 – 645 counts) which indicating ZTC-X 0.5 was higher ordered zeolite-like structure than other samples. N_2 sorption isotherm results show that the surface area of ZTC-X 0.5 to 1.25 was increasing (444.827 – 576.338 m^2/g). The micropore volume of ZTC-X 0.5 to 1.25 was decreasing (0.149 – 0.097 cm^3/g). ZTC-X 0.5 shows high microporosity and have a good performance for CO_2 adsorption at 30 °C, 1 bar of pressure reaches up 33.55 %wt. ZTC-X 0.75; 1; and 1.25 have an adsorption capacity at 3.82; 27.23; and 26.48 %wt, respectively.

5. REFERENCES

[1]. Leung, D.Y.C., Caramanna, G., Maroto-Valer, M.M. 2014. *Renew. Sustain. Energy Rev*. **39**, 426–443.

[2]. Mondal, M.K., Balsora, H.K., Varshney, P. 2012. *Energy Exergy Model. Adv. Energy Syst*. **46**, 431–441.

[3]. Lee, S.-Y.,Park, S.-J. 2015 . *J. Ind. Eng. Chem*. **23**, 1–11.

[4]. Li, L., Zhao, N., Wei, W., Sun, Y. 2013. *Fuel* 108, 112–130.

[5]. Ducrot-Boisgontier, C., Parmentier, J., Faour, A., Patarin, J., Pirngruber, G.D. 2010. *Am. Chem. Soc*. **24**, 3595–3602.

[6]. Anggarini, U. 2013. Tesis Magister. Institut Teknologi Sepuluh Nopember. Surabaya

[7]. Cai, J., Yang, M., Xing, Y., Zhao, X. 2014. *Colloids Surf. Physicochem. Eng. Asp.* **444**, 240–245.

[8]. Li, Z.Q., Lu, C.J., Xia, Z.P., Zhou, Y., Luo, Z. 2007. *Carbon* **45**. 1686 - 1695

Study on Physical Properties and Mineralogy of Pumice and Scoria From Mount Kelud Blitar To Evaluate Their Potential As Geotechnical Material

Andre Primantyo Hendrawan[1*], Heri Suprijanto[1], Emma Yuliani[1], Muhammad Nurjati Hidayat[1]

[1] Department of Water Resources Engineering, Brawijaya University, Malang, Indonesia
* Corresponding authors: [aphendra05@yahoo.com]

Abstract –Two series of laboratory tests were carried out on pumice and scoria from the lava flow of Mount Kelud eruption at Kali Putih River, Blitar Regency, East Java Province, to evaluate their physical and mineralogy characteristics as geotechnical materials. Tests on physical characteristics include grain size distribution analysis and the determination of specific gravity (Gs), density and void ratio index. Analysis of Scanning Electron Microscope, X-Ray Diffraction and X-Ray Fluorescence were also conducted to evaluate the microscopic aspect and mineral properties of pumice and scoria. By using USCS standard, pumice and scoria granules can be classified as SP (poorly graded clean sand) and SW (well graded clean sand), respectively. By using AASHTO standard, both pumice and scoria granules can be classified as A-3 (sand with the fine grain). The mean specific gravity (Gs) of pumice and scoria are 2.878 and 2.781, respectively. The value of void ratio of pumice is higher than scoria. It indicates that pumice has a higher volume of pores or cavities than scoria. From SEM analysis, it is seen that pumice and scoria have inter-connected vesicular forms with varied pore sizes, however scoria has cavities smaller than pumice. From XRD analysis it is observed that the dominant compound (more than 90%) in pumice and scoria is anorthite ($Ca\ Al_2\ Si_2\ O_8$). From XRF analysis, it is found that the dominant elements in pumice and scoria are an element of total iron (Fe), calcium (Ca), silica (Si) and aluminum (Al).

1. INTRODUCTION

Pumice and scoria are pyroclastic rocks which can be found in many places around the world where volcanic activities have appeared. In nature, pumice is derived from acidic lavas and it has a very low density caused by its large amount of vesicular voids. Scoria is created from basic lavas and it also consists of highly vesicular voids having a much higher density than pumice. Pumice and scoria are found in some areas of lava flow around active volcanoes in Indonesia [1]. The large deposit of pumice and scoria has been found at Kali Putih River, Blitar Regency, East Java Province as resulted from Mount Kelud eruption as seen in Fig. 1 (a). From site observation (Fig. 1 (b)), these two materials have almost similar appearance; however, usually scoria is denser and darker in color than pumice. The similar observations have been also reported by many investigations [2].

For centuries, pumice and scoria have been widely used in the world in many industrial applications, for example, as lightweight aggregates, adsorbents, fillers, filtering media [3]. However, their application in geotechnical engineering as embankment materials for dikes, subgrades and parts of hydraulic structures are still limited. As natural materials, pumice and scoria have different physical characteristics when compared with silica sand. These differences are low grain strength, but high in friction angle grain, void ratio and compressibility [4]. To evaluate their potential as geotechnical materials, it is important to study the physical properties, mineralogy aspects and other geotechnical aspects of pumice and scoria.

The important aspect of pumice materials are characterized by the vesicular voids of their particles. Each particle contains a dense network of fine holes, some of which may be interconnected and open to the surface, while others may be entirely isolated inside the particles [5]. The schematic of such voids is presented in Fig. 2. The volume of surface voids was observed to be much greater than that of internal voids [5]. It is also observed that pumice particles have fragile structure because they have many voids (porous) and very angular in nature [6].

(a) (b)

Figure 1 Deposit of scoria and pumice:(a)Kali Putih River near Mount Kelud (b)Visualization of scoria (dark color) and pumice (light color)

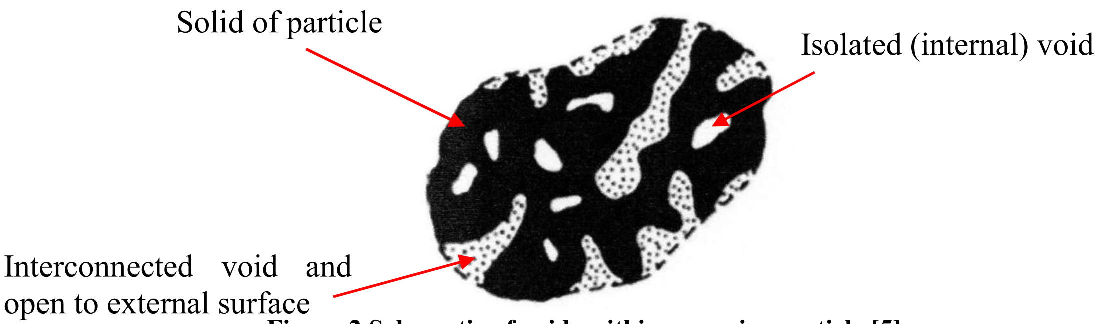

Figure 2 Schematic of voids within a pumice particle [5]

2. METHODS

2.1 Samples

Pumice and scoria in this study were collected from Kali Putih River, Blitar Regency, East Java Province, Indonesia. The natural condition of pumice and scoria in the site are rock materials, which then were crushed to simulate their size as embankment materials. These materials are found along the river and they originated from the eruption of Kelud volcano in 2014. By the power of explosion and airborne transport which were followed by river stream and debris flow transport, the pumice and scoria materials were distributed and mixed with other materials such as silica sands in this river.

2.2 Procedures

Two series of laboratory tests were carried out on pumice and scoria to evaluate their physical and mineralogy characteristics as embankment materials. First, tests on grain size distribution (sieve test) and determination of specific gravity (Gs), density and void ratio index were conducted to investigate the physical characteristics of these materials. All of these previous tests were conducted following ASTM standards. Then, analysis of Scanning Electron Microscope, X-Ray Diffraction and X-Ray Fluorescence were also conducted to determine the microscopic aspect and mineral properties of pumice and scoria. The main focus of the research was to investigate the physical properties, mineralogy aspects and other geotechnical aspects of pumice and scoria and to explore their potential applications as embankment materials.

3. RESULTS AND DISCUSSION

From the result of sieve analysis, crushed pumice and scoria from Mount Kelud were dominated by a medium to coarse sand fraction; 53.7% for pumice and 52% for scoria. It appears that they have similar gradation with natural silica sand from the same location. By using the picnometer method, the mean specific gravity (Gs) of pumice is 2.878, while the scoria has a mean value of Gs of 2,781 (Table 1). The values of specific gravity of pumice and scoria can be varied due to their different chemical and mineralogical elements, and their volcanic process. It is reported that pumice and scoria from Tanzania and Kenya have a specific gravity of 2.5 and in a range of 2.81 – 3.03, respectively [3]. It has been investigated that specific gravity of scoria from Mount Fuji Japan was 2.722 [7] and specific gravity in a range of 1.95 to 2.38 was found from pumice sand of Waikato River, New Zealand [8].

For soil classification, pumice granules can be classified as SP by the standard of USCS (poorly graded clean sand), whereas from AASHTO standard can be classified as A-3 or sand with the fine grain. Scoria is classified as SW (well graded clean sand) by USCS method while according to AASHTO standard can be evaluated as A-3 that has a fraction of sand with the fine grain. However, it can be noted that the gradation of these materials can be designed to a certain range of gradation.

Also, void ratio is an important soil property in geotechnical engineering. This parameter can be related to packing density which is also associated with volume change tendency and particles movement. From this study, it is found that the value of void ratio of pumice is higher than scoria (Table 1). It indicates that pumice has a higher volume of pores or cavities than scoria. The similar results have been reported from many investigators. Agustian and Goto reported the minimum and maximum void ratio of scoria from Mount Fuji, Yamanashi Prefecture Japan was 0.956 and 1.407, respectively [7]. Orense et al [8] found that pumice sand from Waikato River, New Zealand had minimum and the maximum void ratio of 1.76 and 2.584, respectively. Again, it can be assumed that the chemical and mineralogical elements and the volcanic process play an important role to characterize the unique vesicular voids of pumice and scoria particles. Pumice particles are highly crushable, compressible and lightweight as a result of the vesicular nature and the presence of internal voids [8]. Due to these characteristics, it can be assumed that pumice particles are problematic from a geotechnical engineering point of view.

Table 1 Physical property indices of pumice and scoria from Mt. Kelud

Parameter	Pumice	Scoria
Specific gravity (Gs)	2.878	2.781
Maximum void ratio (e_{max})	1.537	1.377
Minimum void ratio (e_{min})	1.137	1.150
Maximum dry density, $\gamma_{d\ max}$ (gr/cm^3)	1.347	1.293
Minimum dry density, $\gamma_{d\ min}$ (gr/cm^3)	1.134	1.170

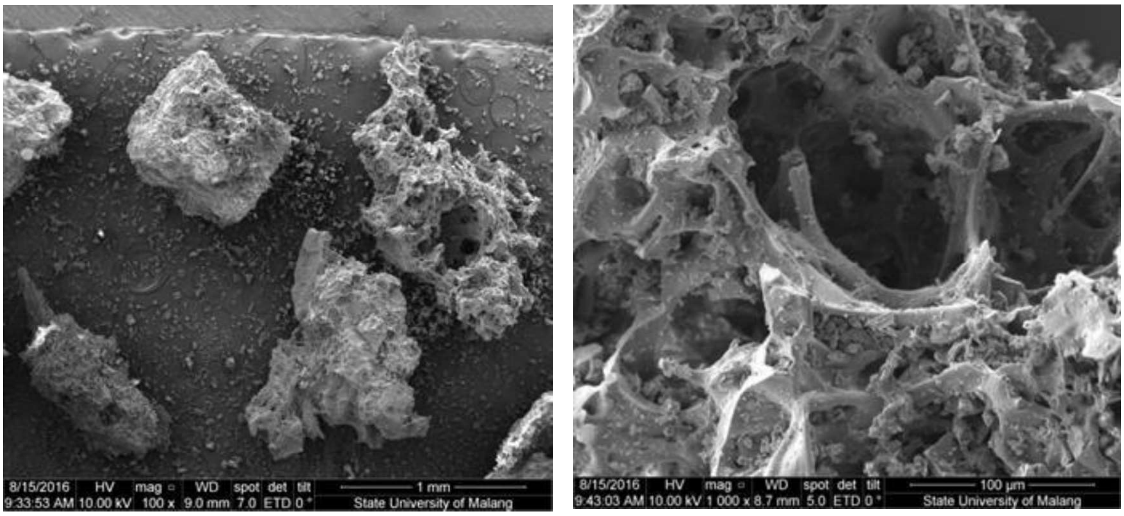

(a) 100x **(b) 1000x**

Figure 3 SEM images of crushed pumice

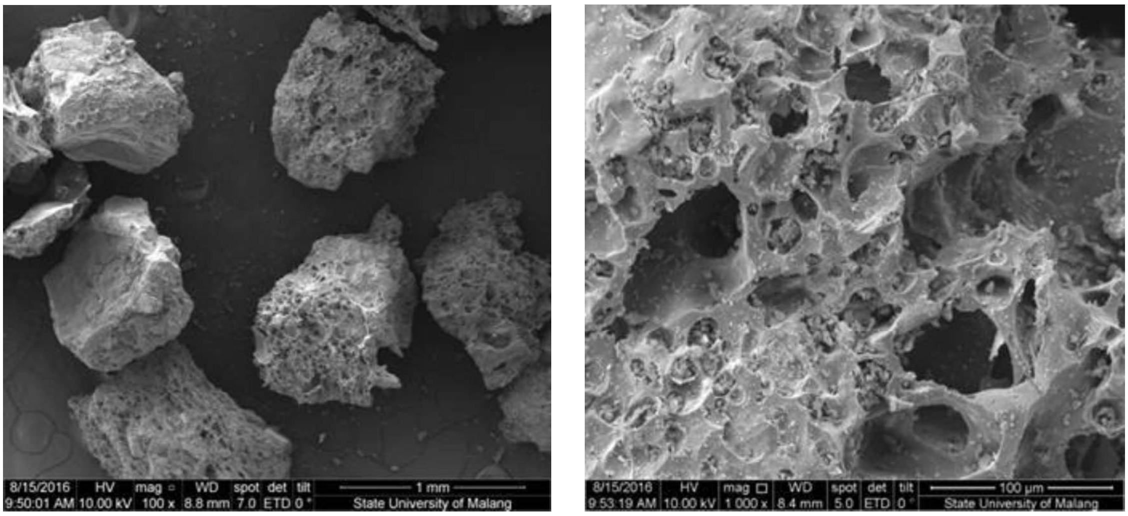

(a)100x **(b) 1000x**

Figure 4 SEM images of crushed scoria

From SEM analysis (see Fig. 3 and 4), it is observed that pumice and scoria have inter-connected vesicular forms with varied pore sizes, however scoria has cavities smaller than pumice. It is seen that some of the voids may be interconnected and related to the surface, while others may be entirely isolated inside the particles. For pumice, it is clearly observed that the volume of surface voids was much greater than that of internal voids.

From XRD analysis it is observed that the dominant compound (more than 90%) in pumice and scoria is anorthite ($Ca\ Al_2\ Si_2\ O_8$). From XRF analysis, it is found that the dominant elements in pumice and scoria are an element of total iron (Fe), calcium (Ca), silica (Si) and aluminum (Al).

4. CONCLUSIONS

The physical and mineralogical properties of crushed pumice and scoria from Mount Kelud Blitar Regency have been investigated by performing a series of laboratory tests. The major conclusions from this paper are as follows:

- Crushed granular of pumice and scoria have some potentials as alternative embankment materials. However, their behaviors are different due to the presence of voids or pores in grains and interconnecting between pores. Comparing with natural soil, this can cause differences in the physical and volumetric parameters as well as in the mechanical behavior of these materials.
- It can be observed that pumice and scoria have inter-connected vesicular forms with varied pore sizes, however scoria has cavities smaller than pumice. Each particle contains many voids, some of which may be interconnected and open to the surface, while others may be isolated inside the particles.
- The important aspect of pumice materials is characterized by the vesicular voids of their particles. The volume of surface voids was observed to be much greater than that of internal voids.
- From XRD analysis it is observed that the dominant compound (more than 90%) in pumice and scoria is anorthite ($Ca\ Al_2\ Si_2\ O_8$). Finally, from XRF analysis, it is found that the dominant elements in pumice and scoria are an element of total iron (Fe), calcium (Ca), silica (Si) and aluminum (Al).

5. REFERENCES

[1] H. Suseno, 2013, *Jurnal Rekayasa Sipil*, **7** (2), 149 (in Indonesian).

[2] D. F. Lapidus, 1990, *Dictionary of Geology*, HarperCollins Publishers, UK.

[3] E. J. Evans, S. J. D. Inglethorpe, P. D. Wetton, 1999, *Evaluation of Pumice and Scoria Samples from East Africa as Lightweight Aggregates*, British Geological Survey, UK.

[4] M. Yildiz, A. S. Soganci, 2015*, Scientia Iranica A*, **22** (1), 81.

[5] L. Wesley, 2001, *Geotechnical Testing Journal*, **24 (4)**, 418.

[6] N. Kikkawa, R. P. Orense, M. J. Pender, 2013, *Canadian Geotechnical Journal*, **50(11),** 1109.

[7] Y. Agustian, S. Goto, 2008, *Soils and Foundations,* **48 (6)**, 851.

[8] R. P. Orense, M. J. Pender, A. S. O'Sullivan, 2012, *Liquefaction Characteristics of Pumice Sands*, University of Auckland, New Zealand.

Metal Coat Spray Distance Analysis of AISI Steel 1045 to Corrosion Resistance with Stainless Steel as Lamination

Ipick Setiawan[1*], Sunardi[1], Budiman[1]

[1] Mechanical Engineering Department, Universitas Sultan Ageng Tirtayasa
* Corresponding authors: [ipicks@untirta.ac.id]

Abstract – The process of surface coating by using electric arc spray is an effort to improve the quality of the metal surface. To protect base metals from damaging environmental conditions, it is required that layer results should have feasible harshness, corrosion resistance, and layer strength. This research was aimed to find out the effect of spray distance toward harshness, corrosion resistance, and layer strength. Electric arc wire spraying used twin wires which were fed into the heat flow. An arc would arise between the ends of two wire feeds (316 stainless steel*)* and the heat formed would melt the ends of both wires. High-pressure gas (6 bars) was streamed to take the liquid metal to the substrate surface. The substrate surface was cleaned and roughened first by using grit blasting before being coated with the first layer of 95%Ni5%Al and the second layer of 316 stainless steel by varying the spray distance (10 cm, 20 cm, 30 cm). This technique is commonly used to coat the surface of steel roller, roller, and plastic roller and reclaim hydraulic rams, piston, axis, and pad. The test result showed higher harshness after being coated with the maximum amount of 332 VHN, acquired at 20 cm spray distance. Lower corrosion rate with the best amount of 1.1526 mpy was acquired at 30 cm spray distance. Maximum coating strength is obtained at 30 cm spray spacing at 4071.94 psi.

1. INTRODUCTION

Thermal spraying is a process in which metal and non-metal materials are heated and converted from the atom form into its basic form. The materials are originally in the form of wire, rod, or powder. The materials are heated until they reach plastic or liquid state by oxyfuel gas flame, electric arm or plasma, the detonation of the gas mixture. In thermal spraying process*,* the temperature of the coating material to be fed to the spray gun will gradually rise and reach the substrate surface in the form of a particle. Next, the layer on the surface of the substrate will be shaped. The density of this layer depends on the materials, temperature when it reaches the substrate, and energy with its impact*.* The adhesion between the layer and the substrate depends on several factors; including the condition of the substrate surface (it must be clean and rough). The rough surface of the substrate can be obtained by shot blasting or rough machining process.

Takeshi Kobayashi and Toru Maruyama (2003) conducted research on the characteristics of pure aluminum and zinc layer by the flame spraying method. The test results showed that the tensile strength of the aluminum coating materials tends to decrease with the increase of spray distance since the particle of the coating materials is not sufficiently diffused on the base material. The tensile strength of the zinc coating material decreases as the spray distance is reduced due to the number of oxides formed on the layer surface. The closer spray distance leads to the increase of harshness due to the rapid cooling rate.

2. METHODS

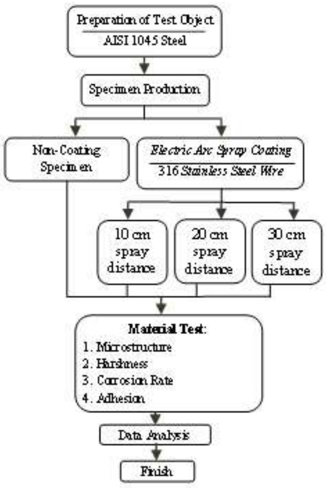

Figure 1. Flowchart of Research

3. RESULTS AND DISCUSSION

3.1 Result of Metallography Test

3.1.1 Metallography of Surface Layer

Figure 2, shows the microstructure of the coating with a variation range of 10, 20, and 30 cm with the stainless steel coating of 316L PMET 730.

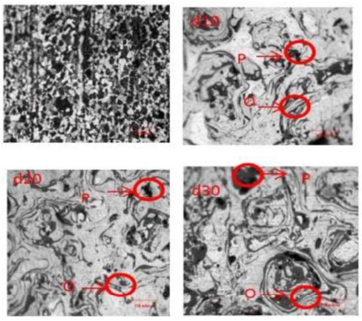

Figure 2. Microstructure. P) Porosity, O) Oxides

As seen in Figure 2, there were some black dots indicating the porosity occurring during the coating. However, the porosity was still below the standard. By using the planimetric method, it was revealed that the magnitude of porosity diameter was of 19 µm with a porosity area of 31,2% at 10 cm spray distance, 15% and 22 µm at 20 cm spray distance, and 17% and 16 µm at 30 cm spray distance. Farther spray distance allowed wider diffusion, causing the porosity to increase. The emersion of oxides was the reaction between oxygen with chromium or nickel during the spraying process. As seen in d10 and d20 specimen, the oxides formed were almost as many, while the oxides in d30 specimen were less than the two and dominated by the porosity, causing the lower harshness in d30 compared to d10 and d20 specimen. The oxides were more grayish and lengthy, appearing in the layer which was parallel to the substrate. The oxides formed were due to the insufficient evaporation on the layer. The humid condition resulted in the liquid particle during the spraying process to react with the oxygen, which formed the oxides. The more oxides formed, the higher the harshness.

3.1.2 Metallography of Layer Limit and Raw Materials

The metallography on the inside of the materials was aimed to analyze the coating results in the layer limit and the raw materials to estimate the strength of the adhesion of the coating results.

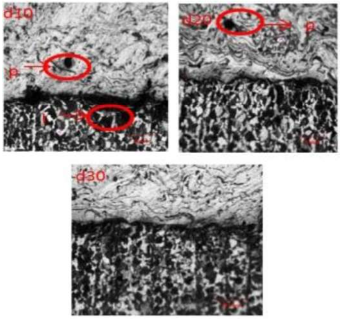

Figure 3. Metallography in the layer limit. P) Porosity, I) Internal Defect

The internal defect is a defect which occurs between layer limit and raw materials. The internal defect may be one of the indications which cause the growing extent of crack, resulting in a lack of adhesion of the coating. Based on the observation, it was revealed that the internal defect occurred in the coating at 10 cm spray distance and almost did not take place at 20 cm and 30 cm spray distance. The internal defect can reduction of the coating adhesion at 10 cm spray distance due to the crack indication which could widely spread.

3.2 Result of Harshness Test

The test on harshness was carried out by using Vickers method with a load of 10 HV. In the test of each specimen, there were 5 points of stamping on the surface. Figure 3, shows that with 10 cm spray distance, the harshness acquired was of 324 VHN. While for 20 cm and 30 cm spray distance, the harshness acquired was respectively of 332 VHN and 303 VHN. The harshness as the result of the coating was above the harshness of raw materials. The result of harshness test is shown in Table 1 and Figure 3.

Table 1 Result of Harshness Test (VHN)

Sample				
Rm	Ss316	d10	d20	d30
183	254	324	332	303

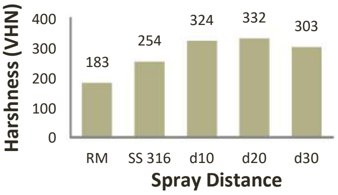

Figure 3. Graphic of Relation between Harshness and Spray Distance

Overall, the harshness after being coated increased compared to the raw materials (183 VHN). However, the harshness differed at each variation of the spray distance. The highest harshness was at 20 cm spray distance with the amount of 332 VHN, while the lowest was at 30 cm spray distance with the amount of 303 VHN. The harshness may occur due to the different spray distances, resulting in the focal point of powder diffusion on different nozzles. The harshness would affect the density of the spray powder attached to the layer, as seen in the porosity percentage and porosity diameter.

At 10 cm spray distance by using the ASTM E-562 method, it was revealed that the porosity diameter on d10 layer surface in ASTM E-112 table was of 19 µm. This amount was still below the average of the maximum amount of porosity determined by CFM56 (2002), which is of 30 µm. The percentage of porosity at 10 cm distance was of 31,2%. This amount did not exceed 50% of the layer surface. Thus, the coating was considered to meet the standard.

At 20 cm spray distance with the same method, it was revealed that the porosity diameter decreased to 16 µm, while the porosity area fell back to 17%. The two of the amount affected the harshness of d20 which was higher compared to d10. The lower porosity extent and diameter allowed the avoidance of porosity to be affected by the indenter in the process of harshness test.

At 30 cm spray distance, the porosity area fell back to 15%. However, the porosity diameter increased to 25 µm. At 30 cm spray distance where the harshness decreased, the indenter might affect the porosity, causing the indenter to have an effect on the softer raw materials.

The porosity in the coating might affect the nature of the harshness. The higher the percentage of the layer porosity, the lower the harshness, and vice versa. The porosity was due to the effect of the melting state, and as mentioned earlier, the oxides affected at the materials level. The harshness would be higher if there were more oxides formed.

3.3 Result of Corrosion Rate Test

The method used was a three-electrode cell by using NaCl liquid at the level of 3%.

Table 2 Result of Corrosion Rate

No.	SAMPEL	E COOR (Mv)	I COOR (uA/cm2)	COOR RATE (mpy)
1	RM	-498,05	3,88	1,7915
2	d 10	-495,56	3,77	1,7404
3	d 20	-499,03	3,13	1,4475
4	d 30	-498,05	2,5	1,1526

To make the reading easier, the result of corrosion rate is shown in the following graphic:

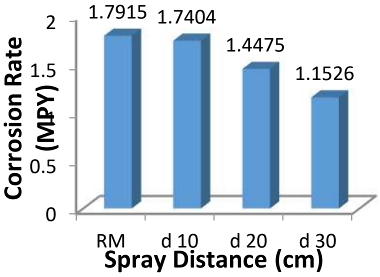

Figure 4. Graphic of Relation between Spray Distance and Corrosion Rate (mpy)

It was indicated that the raw materials had the highest corrosion rate. The high corrosion rate showed a lack of material resistance toward the corrosion. After being coated, the corrosion rate decreased more, indicating the resistance toward the corrosion which experienced an increase. It turned out that the variation of spray distances had an effect on the corrosion rate. The farther the spray distance, the better the corrosion rate.

The porosity had an effect on the corrosion rate. The extent of porosity area was directly proportional to the corrosion rate. The following is the amount of corrosion rate compared to the extent of the porosity area, depicted in Figure 5.

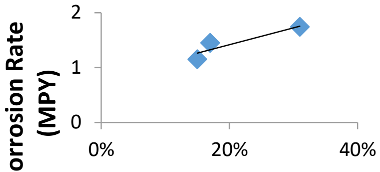

Figure 5. Graphic of Relation between Extent of Porosity Area and Corrosion Rate

3.4 Relation between Harshness and Corrosion

The harshness of metal is the measure of material resistance toward deformation. The material can be easily or hardly corroded by the environment. The following is the relation between the harshness and the corrosion rate.

Table 3. Relation between Harshness and Corrosion

No.	Sample	Harshness (HVN)	Corrosion Rate (mpy)
1	RM	183	1,7915
2	d 10	324	1,7404
3	d 20	332	1,4475
4	d 30	303	1,1526

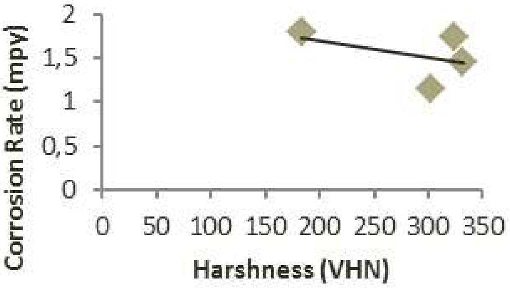

Figure 6. Graphic of Relation between Harshness and Corrosion Rate

The graphic above shows the relation between harshness and corrosion rate. Based on the graphic, it can be seen that the higher the harshness of material, the lower the corrosion rate. That means the higher the harshness of material, the better the resistance toward the corrosion. The harshness is related to the density of the surface (porosity). The low porosity causes favorable corrosion rate and increasing harshness.

4. CONCLUSIONS

1. The harshness after being coated with 316 SS experienced an increase, compared to the raw materials. However, it was no higher than the harshness of 316 SS. This was due to the porosity occurring on the layer surface. The maximum amount of harshness was acquired at 20 cm spray distance, which was of 332 VHN.
2. The corrosion rate experienced a decrease in the materials of layer result, compared to the raw materials. The farther the spray distances, the lower the corrosion rate. The minimum amount of corrosion rate was acquired at 30 cm spray distance, which was of 1.1526 mpy.

5. REFERENCES

[1]. Azizpour, M.J., Norouzi, S., dan Madj, H.M., 2012, Effect of Spray Stand-off on Hardness of Thermally Sprayed Coatings, World Academy of Science, *Engineering and Technology*, **vol. 61**.

[2]. Kobayashi, T., Maruyama, T., and Kano, M., 2003, Characterization of Pure Aluminium and Zinc Sprayed Coatings Produced by Flame Spraying, Department of Material Science and Engineering, Faculty of Engineering, Kansai University, Suita 564-8680, Japan.

[3]. Sarikaya, O., 2004, Effect of some parameters on microstructure and hardness of alumina coatings prepared by the air plasma spraying process, Department of Mechanical Engineering, Faculty of Engineering, Sakarya University, Turkey.

Magnetic Susceptibility and Mineralogy of Deposited Sediment in Eastern Part of Sentani Lake

Dian Sisinggih[1*], Zem Dhani[1], Siti Zulaikah[2], Yusuf Bungkang[3] and Sri Wahyuni[4]

[1] Department of Water Resources Engineering, University of Brawijaya, Malang, Indonesia
[2] Department of Physics, State University of Malang, Malang, Indonesia
[3] Department of Physics, University of Cendrawasih, Papua, Indonesia
[4] Department of Civil Engineering, University of Jember, Jember, Indonesia
* Corresponding authors: [singgih@ub.ac.id]

Abstract – Accelerated erosion of fine-grained sediment is an environmental problem. The urban developing in surrounding Sentani Lake is increasing and it tends to accelerate the sedimentation rate of Sentani Lake. To conserve the sustainability of Lake functions it is necessary to understand the processes of transportation of sediment by identifying the characteristics of its potential sources. The micromorphology, magnetic susceptibility and mineralogy are used to assess the characteristics and the provenance of recently deposited sediment in the eastern part of Sentani Lake.

1. INTRODUCTION

The Sentani Lake is located in Jayapura regency, West-Papua province, Indonesia. It is part of the Cycloop basin with an area of approximately 245,000 ha. The lake is lying about 70 meters above mean sea level. The surface area of Lake is about 9,630 ha with depth varies from 6 to 140 meters. The land cover of the catchment is dominated by tropical rain forest with an average temperature of 27 degree Celsius. There are also 14 large and small rivers flows to the lake as shown in Fig.1. Sentani Lake is functioned as the main source of various needs such as irrigation, fisheries, tourism, transport and the domestic water. As the significant increasing of urban development and not being coupled yet with watershed conservation activities it may bring a future potential problem of lake sedimentation. Recently, increasing the sedimentation rate of the Sentani Lake threatens its sustainability. To conserve the sustainability of Lake functions it is necessary to understand the processes of transportation of sediment by identifying the characteristics of sediment.

Sediment fingerprinting is commonly used for sediment provenance studies in lakes. Mineralogy and rock magnetism are widely used techniques to characterize the sediment source and their mixing patterns under a variety of depositional environments. This paper is exploring the linkages of the micro-morphology, sediment grain size, magnetic and mineralogy attributes of sediment with the provenance of sediments.

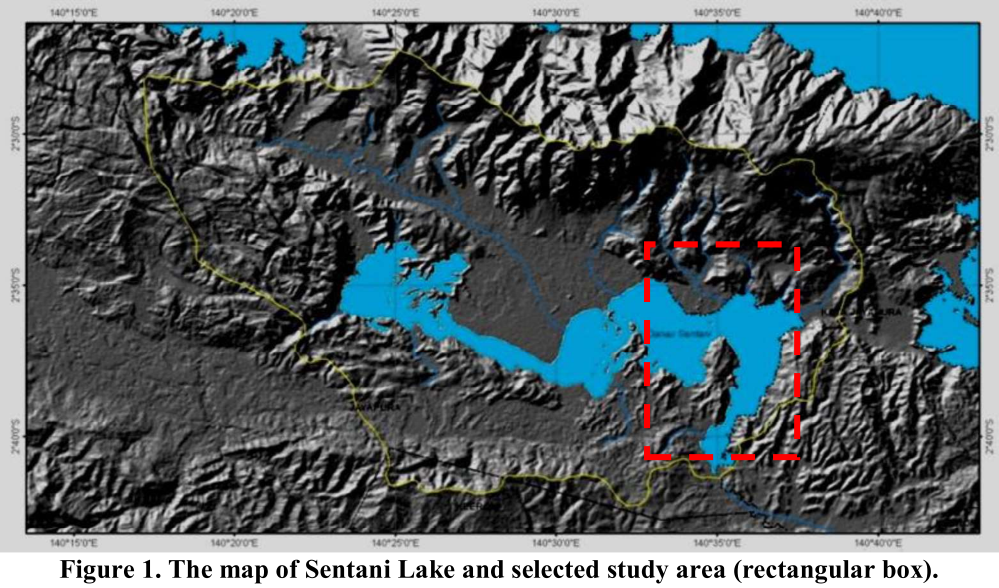

Figure 1. The map of Sentani Lake and selected study area (rectangular box).

2. METHODS

2.1 Material Sediment

The 32 samples of sediment were collected from 8 sampling sites along tributary rivers (Hubay and Kamp Wolker Rivers) as well as and its outlets in the eastern part of Sentani Lake. The detail of sampling sites is shown in Fig.2.

River	Sampling Point	Lat	Long
Hubay	K1	2°34'24.24"S	140°37'31.27"E
	K2	2°34'40.95"S	140°37'23.38"E
	K3	2°35'22.64"S	140°37'01.65"E
	K4	2°35'26.90"S	140°36'56.93"E
Kamp Walker	B1	2°34'27.94"S	140°39'03.58"E
	B2	2°34'51.74"S	140°38'43.13"E
	B3	2°35'20.73"S	140°38'12.44"E
	B4	2°36'03.30"S	140°37'31.66"E

Figure 2. The sampling sites, coordinates and collected sediments.

2.2 Analysis Procedures

The magnetic susceptibility (MS) of sediment samples were measured by the Bartington magnetic susceptibility meter (MS2B). The scanning electron microscopy and the dispersive spectroscopy (SEM/EDAX) were used to identify the micro-morphology, sediment grain size and the elements dissolved in representative samples of sediment. Further the X-Ray Fluorescence (XRF) was conducted to study the qualitative and quantitative analysis of the elements. Finally, the provenance of recent sediment and surface transport processes were reconstructed by cluster analysis based on the similarities of their attributes. The main step of analysis procedures was figured out in Fig. 3.

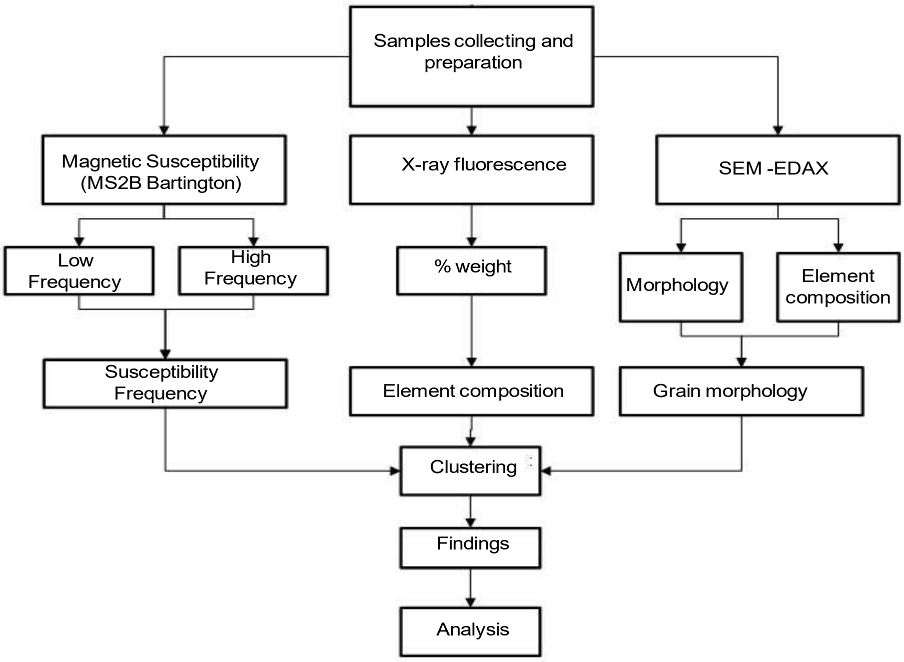

Figure 3. Flowchart of the main steps in data analysis.

3. RESULTS AND DISCUSSION

The low field magnetic susceptibility (χ_{lf}) for the sediment of Wolker Kamp River is ranging from (11.105-24.958)x10^{-6} kg/m^3, while Hubay River is about (4.561-16.926)x10^{-6} kg/m^3. This suggests the higher ferromagnetic concentration of uniform source for Wolker Kamp River compared to Hubay River. The frequency-dependent susceptibility (χ_{fd}) for sediments of Wolker Kamp River is about 0,031% – 0,367% while at Hubay River is about 0,104% - 1,033%. The lower value of χ_{fd} < 2% indicated the magnetic grains was natural and almost no grain of superparamagnetic. They are associated with milder topography that does not allow scour occurs in magnetic minerals due to sediment transport and influences of human activities surrounding the river. In contrast, there is bed scouring processes in Hubay River as its steep topography environment.

The results of SEM-EDAX analysis also support that the magnetic constituent is dominated by ferromagnetic due to the existence of Fe-Ni elements. The X-RF results on the samples indicated that there are 12 dominant elements with Fe, Si, Al, Cr, Ca, P, Ni, Ti, Mn, K, Zn and Mg. Fe (48.05% - 67.38%) and Si (17.00% - 29.00%) respectively. Along the Hubay river the percentage value of Fe became lower following the increasing its rate of natural erosion processes. Fe has been played as important roles in the carrier magnetic properties of sediment. Meanwhile, in the Wolker Kamp River the percentage of Fe is gradually increasing toward downstream that was likely due to anthropogenic factors. Scanning Electron Microscopy imaging results of material in the Wolker Kamp River show that morphologically it is irregularly thin-sheets that indicated a low rate of erosion processes during transportation of sediment. In the Hubay River the sorting in grain size of sediment revealed more erosion processes here. The summaries of sediment transport along those rivers are as outlined in Fig.4 and Fig.5 below.

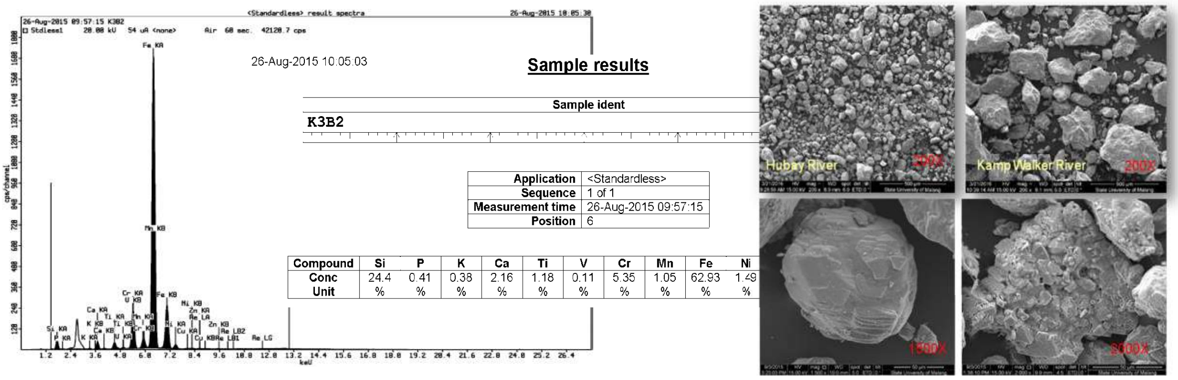

<Standardless> result spectra

26-Aug-2015 10:05:03

Sample results

Sample ident
K3B2

Application	<Standardless>
Sequence	1 of 1
Measurement time	26-Aug-2015 09:57:15
Position	6

Compound	Si	P	K	Ca	Ti	V	Cr	Mn	Fe	Ni
Conc	24.4	0.41	0.38	2.16	1.18	0.11	5.35	1.05	62.93	1.49
Unit	%	%	%	%	%	%	%	%	%	%

Figure 4. XRF and SEM imaging results of material sediments.

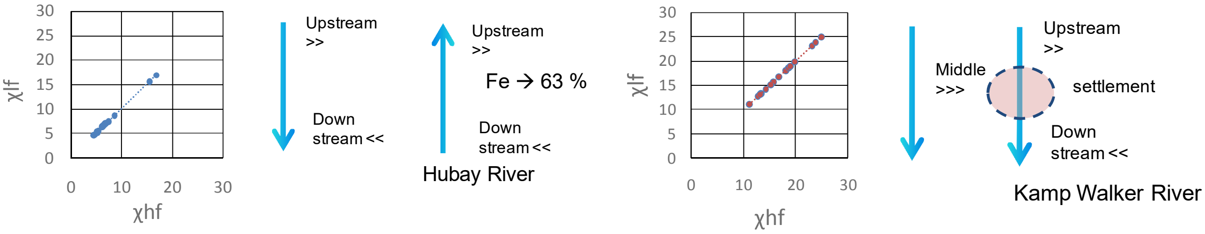

Figure 5. Magnetic susceptibility and associated the sediment transport processes.

Based on the similarity of the characteristics of the constituent elements and the magnetic susceptibility between river and lake sediment samples, the cluster analysis shows there are grouped into two clusters as indicating their provenance. In conclusion, the magnetic susceptibility and mineralogy approaches may distinguish the origin of lake sediment input. Findings from this study suggest that the upland conservation of Hubay River basin should be given priority to conserve the eastern part of Sentani Lake. In the Wolker Kamp River basin, the monitoring and preservative woks are urgently established.

Table 1. The element attributes of sediment samples and magnetic susceptibility.

Sampel	Fe	Si	Al	Cr	Ca	P	Ni	Ti	Mn	K	Zn	Mg	Re	Cu	V	Pb	Ta	xlf
K1A1	65,11	20	5,3	2,02	2,02	0,46	1,9	1,15	0,89	0,46	0,09	0	0,2	0,1	0,093	0	0	5,299
K1B1	63,94	22,2	5,5	1,68	1,64	0,43	1,62	1,06	0,85	0,45	0,07	0	0,2	0,2	0,09	0	0	6,186
K2A1	55,83	29	5,5	2,87	2,49	0	1,27	1,21	0,76	0,4	0,06	0	0,2	0,3	0,089	0	0	6,87
K2B1	67,38	17	4,1	4,88	1,26	0,31	1,28	1,22	0,85	0,23	0,09	0	0,2	0,2	0,099	1	0	16,82
K3A1	57,45	27,5	4,9	2,49	2,13	0,5	1,73	1,17	1	0,48	0,09	0	0,2	0,2	0,087	0	0	5,218
K3B2	62,93	24,4	0	5,35	2,16	0,41	1,49	1,18	1,05	0,38	0,1	0	0,2	0,2	0,11	0	0	4,484
K4A2	63,66	21,5	5,9	2,15	1,68	0,57	1,75	1,14	1,04	0,36	0	0	0	0,2	0,085	0	0	4,297
K4B2	63,21	24,3	0	2,2	1,7	0,43	2,04	0,95	1,23	0,34	0,09	0	0,3	0,2	0,067	0	0	4,245
B1A1	48,05	25,9	4	1,96	5,2	0,59	3,33	0,61	0,84	0,64	0,05	8,1	0,3	2	0,69	0	0,2	15,68
B1B2	49,26	25,8	0	1,45	5,46	0,57	3,2	0,53	0,74	0,61	0,07	12	0,3	0,3	0,05	0	0	15,16
B2A1	52,61	22,5	2,8	1,97	3,19	0,6	3,77	0,35	0,74	0,27	0,1	11	0,2	0	0,03	0	0	23,15
B2B1	48,5	26,4	3,2	1,58	2,96	1	4,1	0,51	0,81	0,31	0,1	9,99	0,3	0,3	0,063	0	0	18,02
B3A1	54,22	23,4	3,2	3,3	3,96	0,51	2,46	0,34	0,84	0,4	0,09	6,9	0,2	0,2	0,048	0	0	24,95
B3B1	52,35	23,5	3,4	3,9	4,18	0,41	2,34	0,52	0,75	0,38	0,06	7,8	0,2	0,2	0,067	0	0	18,6
B4A1	55,26	23,2	0	4,78	5,44	0,46	1,97	0,46	0,88	0,22	0,07	6,6	0,3	0,2	0,078	0	0	13,28
B4B2	57,55	23,8	0	2,96	5,8	0,41	1,7	0,78	0,82	0,48	0,08	5	0,3	0,2	0,078	0	0	13,14

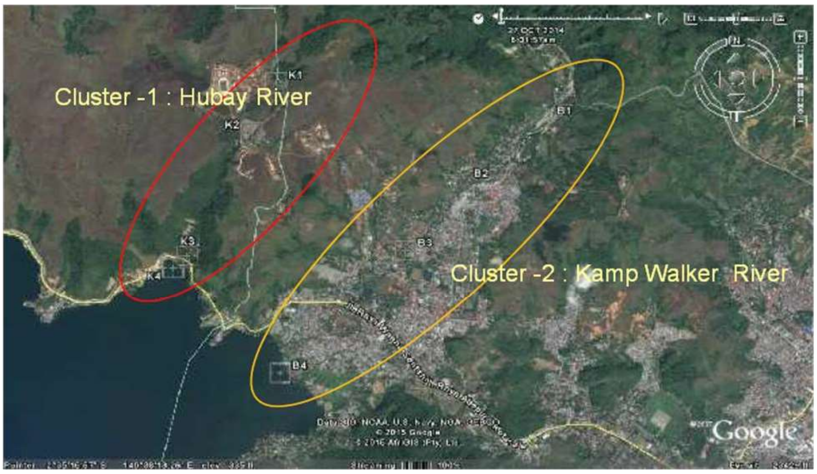

Figure 6. Major clusters of potential sediment sources in the eastern part of Sentani Lake.

4. CONCLUSIONS

The sediment in the eastern part of Sentani Lake is successfully characterized by MS, XRF and SEM-EDAX. Mass susceptibility value of Hubay River is gradually lowering as associated with environmental processes (higher rate of surface erosion, on-stream erosion). Meanwhile in the Kamp Walker River, the order of MS is higher from upstream to downstream, but slightly higher in the middle part as affected by human activity (residence). The XRF results indicate that almost of the element of sediment samples are dominated by Fe (iron) followed by Quartz (Si), Aluminium (Al), Chrom (Cr), Calcium (Ca), Phosphor (P), Nickel (Ni), Titanium (Ti), Mangan (Mn), Kalium (K), Zink (Zn), Magnesium (Mg). SEM imagining results also reveal that the catchment area of Hubay River is subject to surface erosion. The sediment in the eastern part of Sentani Lake is grouped into two clustering according to the sediment attributes. Based on findings of this study, the proposed preventive measures to reduce sedimentation rate in Eastern part of Sentani Lake are by controlling upland erosion in Hubay river catchment and regulate the sedimentation induced by human activities in the middle of Kamp Walker River. Further, more samples/cores are required to be collected for the sediment fingerprinting.

5. REFERENCES

[1] Pozza, M. R., J. I. Boyce dan W.A. Morris, 2004, *J. Applied Geophysics*., **57**. pp 23-41.
[2] Wang, H., Huo, Y., 5 Zeng, L.,Wu, X. And Cai, Y., 2008, *J. Paleolimnol*, **40**, pp. 897–921.
[3] Canbay, M., Aydin, A., & Kurtulus, C. 2009, *J. Applied Geophysics*. **70.** pp 46-57.
[4] Tamuntuan, G., Satria Bijaksana, ., Gaffar, Eddy., Russel, James., Safiuddin, La Ode & Huliselan, Estevanus. 2010, *ITB J. Sci, (Online),* **42**A, pp 31- 48.
[5] Bungkang, Y. 2014. Theses-Disertation. Universitas Brawijaya Malang.

Effect of Addition of Malic Acid and Sodium Alginate Biopolymer to The Poly(vinyl) Alcohol Membrane on TG-DTA Thermogram

Andayani, U.[1*], Mardiana, D.[1]

[1] Department of Chemistry, Faculty of Mathematic and Science, University of Brawijaya, Malang, Indonesia
* Corresponding authors: [ulfa_suryadi@yahoo.co.id]

Abstract – Poly(vinyl alcohol), PVA, is selected as the basic membrane because it has a high water permeation properties and capable of forming a characteristic film layer. PVA is easily inflated, so it is necessary to add crosslinking agents which can reduce the swelling. Malic acid (MA) be used as crosslinking agents. Therefore, it is necessary to investigate how far the effect of adding the crosslinking agents to decrease swelling and permeation rate. Increasing the rate of permeation can be done by adding an active group that is able to form a hydrogen bond with sample. The active groups being learned are the carboxyl and hydroxyl functional groups. Both of the functional groups are owned by the biopolymer with the types of sodium alginate (NaAlg). The aim of this research is study the effect of the addition of crosslinking agents and biopolymers on physicochemical properties of the membrane. Variables on the optimization of membrane covered the composition of the PVA mixture-biopolymers (NaAlg)-crosslinking (MA). Each variable was characterized by thermogravimetric-differential thermal analysis (TG-DTA). Based on the thermogram, from all kinds of membranes were studied, there were three main areas marked with the weight loss in TG thermogram and were supported by the appearance of three peaks in the DTA thermogram. From the DTA thermogram, the 3 types of membranes had significantly different thermal stability. The thermal stability of PVA-MA had a higher thermal stability compared to the PVA-NaAlg and PVA. Pure PVA membrane decomposed at 200 °C, the PVA-MA membranes decomposed at a higher temperature of around 480 °C, while the decomposition temperature for the blended membrane of PVA-NaAlg-MA was between PVA-MA and PVA. Thus, the addition of crosslinking agents can increase the thermal stability of PVA membrane, whereas the addition of biopolymers NaAlg might decrease the stability of the membrane, thereby it reduced the tensile strength of the membrane.

1. INTRODUCTION

Poly(vinyl alcohol), PVA, is selected as the basic membrane because it has a high water permeation properties and capable of forming a characteristic film layer. PVA is easily inflated, so it is necessary to add crosslinking agents which can reduce the swelling. Malic acid (MA) be used as crosslinking agents. Therefore, it is necessary to investigate how far the effect of adding the crosslinking agents to decrease swelling and permeation rate. Increasing the rate of permeation can be done by adding an active group that can form a hydrogen bond with the sample. The active groups being learned are the carboxyl and hydroxyl functional groups. Both of the functional groups are owned by the biopolymer with the types of sodium alginate (NaAlg). The aim of this research is to study the effect of the addition of crosslinking agents and biopolymers on physicochemical properties of the membrane, e.i on TG-DTA thermogram.

2. METHODS

2.1 Chemicals

The chemicals was used in this research from Merck with analysis quality (unless mentioned specifically): acetone, ethanol, n-butanol, NaOH, akuabides (Laboratory of Analytical Chemistry, University of Brawijaya), NaAlg (production Aldrich, W201502) BM: 20-50 kDa, poly vinyl alcohol (PVA) BM: 15-22 kDa, malic acid, and filter paper.

2.2 Procedures

The blended membrane is prepared by mixing NaAlg to 10,0 mL PVA 2%. The mole ratio of a component of blended membrane PVA-NaAlg-AM can be seen in Table 4.1. After stirring until homogeneous, add malic acid with a mole ratio of PVA: malic acid (n) to be crosslinked as shown in Table 2, then stirred for one day.

Tabel 1. Composition of PVA–NaAlg with malic acid as crosslinker malat

Perbandingan mol (PVA: NaAlg)	Volume $_{\text{PVA 2\%}}$ (mL)	W $_{\text{NaAlg}}$ (g)	W $_{\text{asam malat}}$ (g)
1:½	10,0	0,0023	0,0053
1:1	10,0	0,0047	0,0053
1:2	10,0	0,0094	0,0053

Tabel 2. The addition of malic acid as crosslinker agent for PVA membrane

n	V $_{\text{PVA 2\%}}$ (mL)	Asam malat (g)
60	10,0	0,0079
90	10,0	0,0053
120	10,0	0,0039
150	10,0	0,0032

The membrane is mixed in a petri dish with a diameter of 5 cm. Membrane drying is done with 3 steps of heating:

1. room temperature for 24 hours
2. 80° C for 6 hours.
3. 40° C for 24 hours.

Changes in molecular weight and modulus of the membrane are influenced by the composition of the membrane, which can be measured using an instrument Thermogravimetric and Differential Thermal Analysis (TG-DTA). Methods for analysis of TG-DTA in this study refers to the method that is used by Corcione and Frigione (2012).

3. RESULTS AND DISCUSSION

The number of cross-linked monomers will affect the physical properties of the resulted membrane. A large number of monomers cross-linked to the PVA-MA membrane achieved the highest flux at n = 90. The higher cross-density or the smaller value of n, the smaller rate of permeation produced. Membranes PVA-NaAlg-MA with n < 90 produced the lower permeation rate of ethanol, due to the low density of the cross, thus allowing the membrane became more expanded, and the selectivity of membrane became lower.

The addition of biopolymers could increase the value of permeation flux. That was proved by the membrane flux values of PVA-NaAlg-MA were higher than the PVA and PVA that was cross-linked by MA. Biopolymer NaAlg has hydroxide group (OH) and carboxylic (COOH) that are capable of forming bond with other molecules that have similar groups, such as compounds of alcohol. The membrane of PVA-NaAlg-MA mixture generates the optimum composition in the mole ratio of PVA: NaAlg = 1:½ (for permeation of ethanol).

The result of the weight loss is shown in Figure 1 and Table 3. Figure 1(A) show that thermogravimetric (TG) is a type of characterization tests carried out on a material to determine changes in weight-losses in connection with changes in temperature. TG carried out at a temperature range of 30-900 ° C with an increase of 10 ° C / min. Each sample to be analyzed is determined the initial weight and calculated reduction in weight in any change in temperature. Based on the thermogram, from all kinds of membranes that were studied, there were three main areas marked with the weight loss in TG thermogram and were supported by the appearance of three peaks in the DTA thermogram.

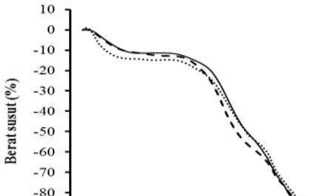

Figure 1 (A) Thermogram TG of membranes (a) PVA 2%, (b) PVA 2% by crosslinking MA for n = 90 (PVA-MA) and (c) blended membrane PVA-NaAlg mole ratio of PVA: NaAlg = (1: 2) with the crosslinking MA for n = 90 (PVA-NaAlg-MA)

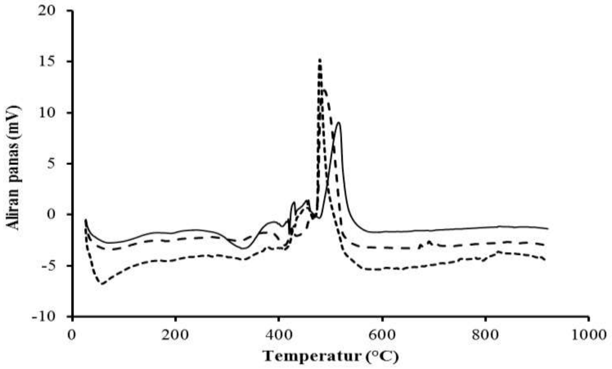

Figure 1 (B) Thermogram DTA of membranes (a) PVA 2%, (b) PVA 2% by crosslinking MA for n = 90 (PVA-MA) and (c) blended membrane PVA-NaAlg mole ratio of PVA: NaAlg = (1: ½) with the crosslinking MA for n = 90 (PVA-NaAlg-MA)

The amount of energy is needed to break bonds that occur within a membrane can be determined based on the peak area of the resulting thermogram. The wider the peak, the higher the energy is needed. In Figure 1 (B) we can estimate the DTA thermogram peak area by drawing a straight line between two points by the peak to determine a baseline peak. The sequence is based on the peak area of the vast thermogram: PVA, PVA-biopolymer-MA then PVA-MA.

Table 3. Weight loss of membrane materials of 2% PVA, PVA-MA (n = 90) and PVA-NaAlg (1: ½)-MA (n = 90)

Membrane Type	Initial Weight (mg)	Range of Weight Loss (%)		
		Area I	Area II	Area III
PVA	13,539	8	42	98
PVA–MA	4,878	10	42	92
PVA–NaAlg–AM	9,652	5	40	96

In principle, the TG of the sample has three main areas weight loss appear as the three peaks in the DTA curve.

The first area at a temperature of 30-130 ° C due to evaporation of water bound physically till the strong bonded chemically. Weight loss that occurs about 10%. Heating is used to remove the water molecules present in the membrane.

The second transition region around 250-350 ° C due to the thermal degradation of the polymer membrane. Heating at 250 ° C resulted in the release of water molecules due to the loss of atom Hydrogen and group hydroxide that contained in the blended membrane. Weight loss that occurs is about 40-80%. Heavy depreciation in the third stage is at a temperature range of 350-500 °C which is carbonation reaction. Thermal decomposition that occurs attacks the main chain of carbon (C-C) that contained in the blended membrane PVA-biopolymer.

From the DTA thermogram, the three types of membranes had significantly different thermal stability. The thermal stability of PVA-MA had a higher thermal stability compared to the PVA-NaAlg and PVA. Pure PVA membrane decomposed at 200 °C, the PVA-MA membranes decomposed at a higher temperature of around 480 °C, while the decomposition temperature for the blended membrane of PVA-NaAlg-MA was between PVA-MA and PVA. Thus, the addition of crosslinking agents can increase the thermal stability of PVA membrane, whereas the addition of biopolymers (NaAlg) might decrease the stability of the membrane, thereby it reduced the tensile strength of the membrane.

Pure PVA membrane shrinkage at 200 ºC. PVA membrane is biodegradable membrane because it has bonds between molecules. PVA–MA membrane decompose at higher temperatures of around 480 °C, because in addition to the bonds between the molecules also are crosslink between PVA with malic acid, thus requiring greater energy than the energy is needed for the decomposition of pure PVA membrane. The amount of the decomposition temperature of the blended membrane PVA-NaAlg-MA is between PVA-MA and PVA. Thus it can be said that the blended membrane PVA-NaAlg-AM has a higher thermal stability than the pure PVA, but lower when compared with PVA crosslinked with malic acid. The addition of crosslinker agents can increase the thermal stability of PVA membrane.

Heating the membrane above 500 ° C no longer cause severe shrinkage with the rest of the heating of about 5-10% by weight of the sample. Usually the rest of the samples were not decomposed is an inorganic mineral that can't be decomposed. DTA thermogram shows a similar pattern for all membrane compared (PVA, PVA and PVA-NaAlg-MA), but each has different thermal stability significantly. The highest thermal stability possessed by PVA-MA, followed by PVA-NaAlg-MA and the lowest is PVA.

The result of ABE permeation used three membranes to compare; PVA, PVA-pectin-GA and PVA-NaAlg-MA respectively showed in Figure 2.

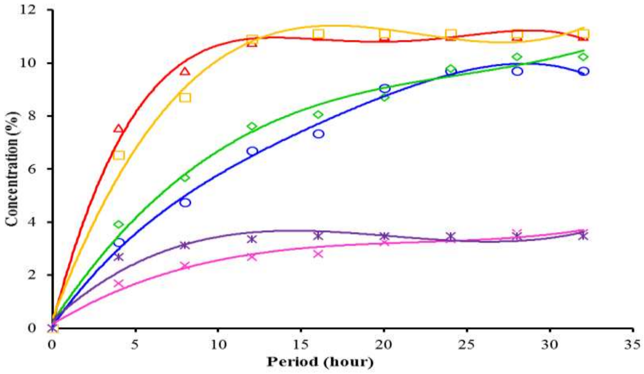

Figure 2. Comparison of flux on permeation of acetone (O), n-butanol (×) and ethanol (◇) using PVA membrane and acetone (Δ), n-butanol (✳) and ethanol (□) using membrane blended of PVA-NaAlg-MA

The flux calculation result of those three membranes are presented in Table 4.

Table 4. Comparison of flux value between PVA-biopolymer-crosslinker membrane to PVA membrane

Membrane	Flux (L/m^2.hour)		
	Acetone	n–Butanol	Ethanol
PVA	0,522	0,107	0,332
PVA–NaAlg–MA	0,746	0,232	0,594
x_2	1,428	2,180	1,788

Description: x is the ratio of the value of the mixture membrane flux cross-linked to PVA membranes.

Permeation equilibrium was reached when the permean concentration in the feed phase was equal or nearly equal to the permean concentration in the recipient phase. If it is seen from the speed of permeation, both of PVA–NaAlg–MA membrane, the acetone sample had permeation rate almost similar to ethanol, followed by n-butanol. Although ethanol and acetone had concentrations of the same feed phase, which was 20%, both of them had different flux values. Another factor that could cause different flux values is hydrophilic/ hydrophobic properties of those three solvents. Hydrophilic/ hydrophobic properties were influenced by the polarity of the solvent.

4. CONCLUSIONS

Based on the research that had been done, it can be concluded: (1) PVA membrane can be cross-linked with malic acid. The addition of crosslinking agents can reduce the permeability/flux, but increase the stability of the membrane; (2) PVA can form a blended membrane with NaAlg and crosslinked with malic acid. The addition of NaAlg can increase the permeability/flux, but lower the stability of the membrane; (3) Optimum condition of blended membrane PVA-NaAlg-MA at a mole ratio of PVA: NaAlg = (1 ½) with addition crosslinker MA at n = 90

5. REFERENCES

[1]. Baker, R. W., 2004, *Membrane Technology and Application* (Second Ed.), John Wiley & Sons, Ltd., Chichester, England.

[2]. Bhat, S. D., dan Aminabhavi, T. M., 2007, Pervaporation Separation Using Sodium Alginate and Its Modified Membranes - A Review, *Sep. Purif. Rev.*, **36(3-4)**, 203–229

[3]. Kalyani, S., Smitha, B., Sridhar, S., dan Krishnaiah, A., 2008, Pervaporation Separation of Ethanol–Water Mixtures Through Sodium Alginate Membranes, *Desalination*, **229(1)**, 68–81.

[4]. Kurkuri, M. D., Toti, U. S., dan Aminabhavi, T. M., 2002, Syntheses and Characterization of Blend Membranes of Sodium Alginate and Poly(vinyl alcohol) for The Pervaporation Separation of Water - Isopropanol Mixtures, *J. Appl. Polym. Sci.*, **86(14)**, 3642–3651

[5]. Amaley, S. H., Sapkal, R. S., dan Sapkal, V. S., 2015, Pervaporation : A Novel Process for Ethanol Separation using Fermentation, *IJER*, **4(2)**, 64–68.

Nitrided Austenitic AISI 316L by RF-DC Plasma Nitriding

Istiroyah[*], D.J. Santjojo

Department of Physics, Faculty of Science, University of Brawijaya, Malang, Indonesia

* Corresponding authors: [istiroyah@gmail.com]

Abstract – Austenitic Stainless Steel—ASS plays an important role in industrial sector but its application was limited by its low mechanical and tribological properties. Plasma nitriding is one of surface treatment techniques for improving its properties; this process has a low temperature below 500ºC. In this paper, plasma nitriding of AISI 316L steels was performed at temperature 400, 450, and 480 ºC, using RF-DC plasma nitriding system with a gas mixture of 70% N_2: 30% H_2 for 7.2, 1.44 and 28.8 ks. Both RF- and DC bias voltages were used to keep high-density plasma state. Various properties of the nitrided sample were investigated through micro-hardness measurement and X-ray diffraction analysis. The results show that nitriding rate constant (Kp) is 0,22 $\mu m^2/s$, three times higher than the DC Plasma nitriding.

1. INTRODUCTION

Austenitic stainless steel-ASS- has excellent corrosion resistant behavior so it was widely used in the corrosive industrial environment, such as in the chemical, food and beverage industries [1,2]. However its relatively low hardness and wear resistance. Therefore its application that requires wearing resistant was limited. Many efforts have been made to improve its properties through surface treatment techniques such as nitriding and coating [3].

Among these techniques, plasma nitriding is one of the most versatile nitriding processes with many advantages over the conventional salt-bath and the gas nitriding. In particular, the low-temperature process by plasma nitriding is one of the preferable advantages and is appropriate to increase the surface hardness and wear resistant of austenitic stainless steel [4]. On the other hand, the author has been concerned with research and development of new type plasma nitriding processing system: high-density RF-DC plasma nitriding [5]. By combining the RF and DC sources the capability of RF field to create extended plasmas is used together with the enhanced sputtering and biasing effect of the DC source.

In this present study, AISI 316L was used as a substrate. The present nitriding obtains high surface hardness at relatively low temperature.

2. METHODS

2.1 Experimental Apparatus

High-density plasma state is activated by both RF- and DC- plasmas. Each power supply independently controls the RF- and DC- plasmas. Dipole electrode is used to produce RF Plasma, while DC bias voltage is directly applied to the cathode plate.

In this experiment, nitrogen plasma was used for presputtering process before nitriding to make in-situ cleaning, to remove oxide layer and to activate the substrate surface. The nitriding treatment was performed by using the mixed gas of nitrogen and hydrogen.

2.2 Sample Preparation and Characterization

Austenitic stainless steel AISI 316L steel was used as the substrate. The disc-shaped specimen has 2 cm in diameter and 0,4 cm in thickness, respectively. The samples were degreased to remove surface surfactants and other dirt. Ultrasonic cleaner system with the alkali solution (industrial soap) was used for degreasing.

Presputtering was carried out in nitrogen plasma for 900 s, to remove oxide layer and to activate the surface before plasma nitriding process. Nitriding was conducted at 753 K or 480 ºC, in 70 Pa, using 200 V RF-voltage and -400 V DC-bias. The mixed gas contents were 70% nitrogen-30% hydrogen by controlling the flow rate.

The hardness of nitride sample was measured by Vickers micro-hardness testing, while the phases formed in the nitride layer were characterized by XRD (Phillips diffractometer) using Cu-Kα radiation with the conventional Bragg-Brentano method.

3. RESULTS AND DISCUSSION

There are significant changes on the sample surface. This change proves that the nitride layer should be formed on the surface of samples. Furthermore, this nitriding took place in relatively short duration time; 7.2 ks. This prompt nitriding process is one of the most attractive features for high-density plasma nitriding.

Figure 1 Comparison of AISI-316L specimen before and after plasma nitriding. (a): sample before nitriding, and, (b) after nitriding at 480 °C for 7.2 ks.

Plasma nitriding was driven by nitrogen atom (solute in the matrix) diffusion into the depth of matrix. Then, hardness must be enhanced in this nitride layer at the vicinity of the sample surface. Figure 2 shown surface hardness for the nitrided specimen. Increasing nitriding temperature and nitriding times increase the surface hardness of nitrided specimen. The nitrided specimen has surface hardness value three times till almost five times higher than the un-nitrided substrate.

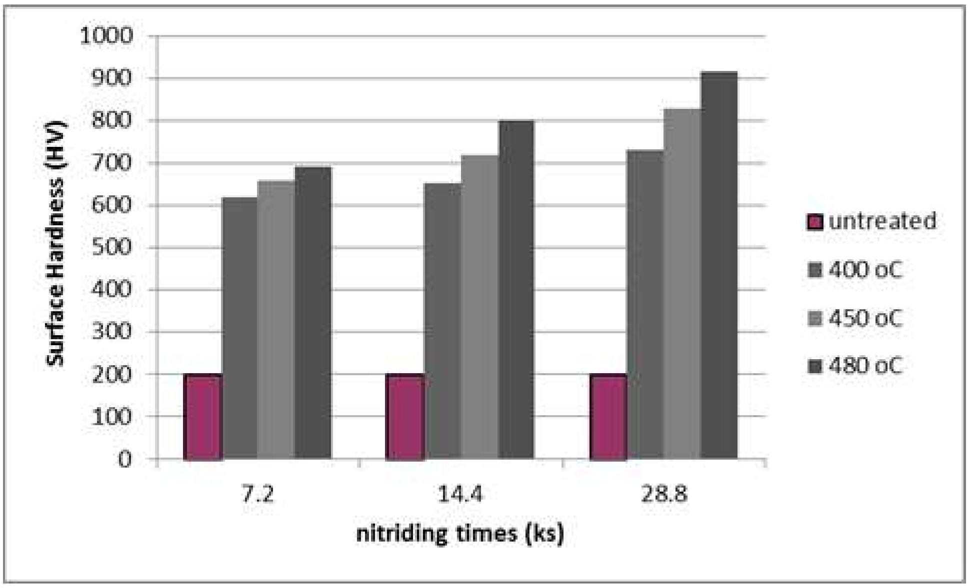

Figure 2. Surface Hardness-nitriding times relation for various nitriding temperature

Classical theory was employed to describe the nitriding process. That theory assumes that one-dimensional nitrogen diffusion process should govern the nitriding process and that reaction should take place only at the nitriding front end. Under this assumption, the nitriding rate is estimated by using Wagner's equation:

$$E^2 = K_p t$$

where E^2 is the squared thickness of the nitrided layer, Kp, the growth rate of nitrided layer during plasma nitriding, and t, the nitriding duration time.

The nitriding rate in the present nitriding was 0,22 μm^2/s while the Kp's of Fe-19 Cr alloy nitrided by conventional DC plasma nitriding, was 0,078 μm^2/s. That is, the nitriding rate by the present plasma nitriding is enhanced three times faster than DC-plasma nitriding. This result reveals that the nitriding rate should be enhanced by high-density RF-DC plasmas. Just as had been pointed out in [6,7], the capability of RF-field to generate the extended plasmas is combined in the present plasma state with the enhanced sputtering and biasing effect of the DC source. Enhancement of nitriding rate is first explained by this combination effect in the plasma state. Also, NH radicals as well as activated nitrogen atoms and ions must activate the external nitriding process as a solute source for nitriding.

These two processes might be responsible for the improvement of the diffusion process of nitrogen atoms into the substrate. Hence, enhancement of plasma state by increasing the electron density and enrichment in NH radical population is expected to improve the plasma nitriding process.

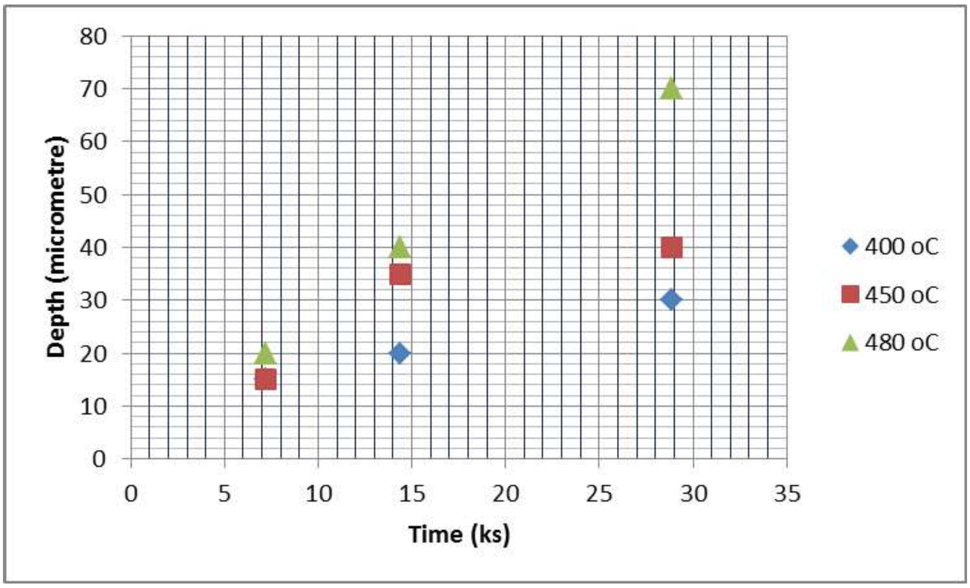

Figure 3 Relationship between the depth of the nitrided layer and nitriding time of AISI 316L.

Hardening process of AISI-316L is directly affected by solid solution and precipitation behavior of nitrides synthesized and formed during the nitriding process. A typical XRD profile was shown in Fig. 4. At high temperature (480 ºC), both γ'Fe4N and CrN nitrides predominate the nitriding reaction without formation of the brittle phase nitrides like ε-Fe_2N. However, at low nitriding temperature (400 ºC), no precipitation observed in the nitrided specimen. The similar result had been reported by [8]. Advancement of high hardness distribution into the depth of samples must be driven by fine and homogeneous N solid solution or precipitation of γ'Fe4N and CrN nitrides in the matrix.

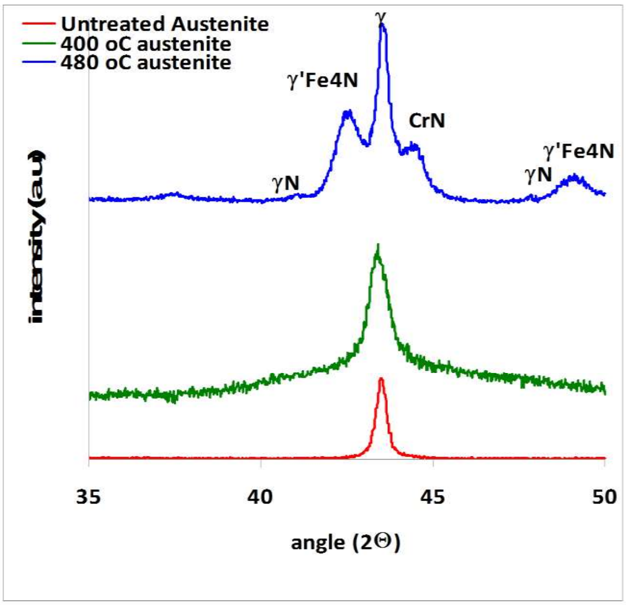

Figure 4 X-ray diffraction pattern of nitrided AISI 316L specimen

4. CONCLUSIONS

High-density RF-DC plasma nitriding system works effectively to harden AISI-316L substrates in a shorter time and with the nitriding rate three times higher than the conventional DC plasma nitriding processes. This fast-rate nitriding must be driven by enhancement of plasma states via a combination of RF- and DC-plasmas and by enrichment of NH radicals in the external nitriding process.

5. REFERENCES

[1]. ASM International, 1999, ASM Specialty Handbook: Stainless Steels.

[2]. Oliviera, A.M., Riofano, R.M.M, Casteletti, L.C., Tremiliosi, G.F., and Bento, C.A.S., *Revista Brassileira de Aplicacoes de vacuo*, **22**, 2, 63-66, 2003.

[3]. Menthe, E., Rie, K.T, *Surface and Coatings Technology*, 116-119, 199-204, 1999.

[4]. Aoki K., Kitano, K., *Surface Engineering* **18**, 429-432, 2002.

[5]. Aizawa, T., Sugita, Y., Development of RF-DCplasma system for nitriding of aluminum alloys, abstract of ICMCTF, 2011.

[6]. Cebulla, R., Wendt, and K. Ellmer, *J. Appl. Phys*. **83**, 1087,1998.

[7]. Dinescu, G., Aldea, E., Musa, G., M van de Sanden, M.C., A de Graaf, Ghica,C., Gartner, M., Andrei, A., , *Thin Solid Films*, **325**, Issues 1–2, P. 123–129, 1998.

[8]. Minggolo, N., Tschiptschin, A.P, Pinedo, C.E., *Surface and Coatings Technology*, doi: 10.1016/j.surfcoat.2006.08.060.

Effect of Horizontal Pegs Distance To The Shear Strength of Beams Bamboo Lamination

Zulmahdi Darwis, ST., M.Eng[1*], Soelarso, ST., M.Eng[2], Ipick Setiawan[3].

Civil Engineering Department Faculty of Engineering Sultan Ageng Tirtayasa University
Jl. General Sudirman km. 03 Cilegon, Banten
*Corresponding Author: [zulmahdi@untirta.ac.id]

Abstract - The use of laminated bamboo beams to be an alternative as one of the elements of building materials. Such laminates techniques can be used to form the building materials used as construction materials in large sizes. Previous studies have extensively covered the beam strength of laminated bamboo, type and pattern collapse crack. Some testing of the shear strength with the use of the adhesives labour 60 # MDGL, resulting in partial fracture or shear fracture between bamboo material and not occur in the adhesives. The objective of this research, to find out the effect of pegs margin on the block against the shear strength of laminated bamboo. Comparison between high beam size and the stripe are two to one size (120 mm x 60mm). Further tested the strength of the beam to the shear capacity with four variations within pegs margin 10 cm, 15 cm, and 20. For laminated bamboo using bamboo outer skin on the surface of the beam, use of adhesives labur 60 # MDGL. The results showed that there was no significant difference in shear strengths. Testing the beam flexible with distance pegs 10 cm, 15 cm, and 20 cm produce shear strength by an average of 3.48, 3.82 and 3.47 Mpa. This strength is mapped out their blueprints word than the strength of the wood beams in general where the strong wood shear stress of class II.

Keywords: *capacity sliding, peg distance variations, highway*

1. INTRODUCTION

Bamboo is one of several material/construction materials that have been long known in the community. The use of bamboo as one of the elements of the building materials for this is still secondary to the interests of the making of scaffold/ bekisting, appropriate range of roof and limited to the necessity of furniture. Morisco (1999) testing strong pull the bamboo skin ori with the result is quite high which is nearly 5000 kg/cm 2 or approximately two times the voltage melted steel is strong pull the average bamboo highway is also higher than the voltage melted steel. Only one specimen of bamboo highway that has a strong pull the lower than the voltage melted steel. Previous studies Ibn Arqam laya (2007) have many comments on the strength of the beam bamboo laminated type of collapse and pattern of cracks. Some testing against the strong slide with the use of tape labur 50#MDGL, acquired happened fracture partially or fracture slide between the bamboo material and not occur on the tape. The results of the research that has been done previously (Zulmahdi, 2009) acquired the use of type labur 30#MDGL, 40#MDGL and 60#MDGL on the beam bamboo laminated no significant difference to the strength of the slide and stiffness. Use of the latch on the making of the blades of laminated bamboo reduces the tape and the time of the implementation of the creation. Previous research (zulmahdi, 2016) the research that has been done can be drawn some conclusions among others as follows: testing the beam flexible with distance latch 10 cm, 15 cm, and 20 cm produce flexible strength by an average of USD 25,739 berututan Mpa, 35,041 Mpa, and 28,027 Mpa. The results of the test are there is a significant difference is the existence of the influence of the use of remote variations latches toward the strong elastic beam laminated bamboo. The research that will be proposed is making the beam bamboo laminated with the blades of joined by using the variation of the distance latch, so we can get the use of a distance of latch to have the optimum strength and economically in the making of . Comparison of the size or dimensions of the beam between the high beam and breadth is 2 : 1 size (12 cm x 6 cm). Then tested the strength of the beam on the strength of the slide and flexible with four fruit variation of distance latch 10 cm, 15 cm and 20 cm.

2. METHODS

This research will be conducted by making laminated blades using the outer skin and variation of distance latch 25 cm, 30 cm, 40 cm and 50 cm, research results obtained distance latch with the strength of the slide on the optimum.

2.1 Research Material

The materials used in this research is as follows:

1. Bamboo Highway

   Bamboo is used for the beam material laminated and making latch taken in the middle of the barcode and wore the outer skin,

2. Materials Tape

   The adhesive material used is the type of tape *thermoset* type cold settings or can be hardening in room temperature namely *Polyvinyl Asetate (PVAC)*.

2.2 Research Equipment

Research equipment is divided into two, namely equipment for the creation of test objects and equipment for testing the test objects, both physical characteristics and mechanical nature.

1. Making Equipment Test Objects

   The tools used for creating test objects namely:

   a. Chainsaw wood *(Circular Panel saas).*

   b. Penyerut machine *(planner)*

2. The tools complement other: Gauges/ruler measuring cup, wire, balance/weights, the clamp tweezers, steel channel (C), tape container with a stirrer (), tang cut stick, lock screws, axs, chainsaws and a cutter blade.

3. Physical testing equipment and mechanics:

   a. Mechanical testing machine UTM *(Universal Testing Machine)* used to test the nature of the beam lamina mekanika.

   b. The appliance for flexible testing and slide the beam laminated *Multiensayo brands* include the *loading frame* and *load controller*. This appliance is equipped with a set of LVDT (*Linear Variable Differential Transformers*) and *data* to the recorder reading lendutan logger and style.

2.3 Test objects

Bamboo mekanika behavior on the place and influential season, then on the first and second year need to test introduction. The size of the test objects for testing the physical characteristics and the nature of bamboo mekanika follow ISO standards *(International Standard Organization)* 3129-1975.

2.4 Laminated Beams Testing

The beam tests done on the object are simple laminated (joints of the roller brush) with one point of imposing. Lateral restraint provided to prevent the contribution of the influence of the bend lateral torque. From these settings expected the collapse of elastic. Loading frame first prepared with two objects and one lateral pengekang among load point and roller brush. After that the beam test was placed above the object, along with the beam profile to be used as the point of imposing. And the load cell. The Load cell is connected with the hydraulic jack and transducer indi digital cator to know the greatness of the burden that works. After it is installed a dial gauge amid landscape a pointer has been set to zero. Imposing done gradually and done record lendutan happens. During charging observed progress damage occurs on the test objects.

2.5 The way the Analysis

The analysis is done with how to connect the data to the results of the study of literature with its application to the structure of the building construction. The data has been analyzed with attention to the mutual relationship between the attributes owned bamboo with the structure of the construction occurred, until there is a conclusion.

2.6 External Expected

The success of this research are measured based on the achievement of indicators of success as follows:

1. The use of distance latch ideal and economic acquired the balance of power between the bamboo material with the strength of the latch.
2. The technique of making the beam bamboo laminated that efficient and can be made by small and medium-sized businesses, so that it can be produced with the price that competes with wooden beams class II.

3. RESULT AND DISCUSSION

3.1 Density

Table 3.1 Test Results Density

Test objects	The average
The end of the	0.66%
The middle part of the	0.60%
The Stem	0.50%

Prayitno (1996:46) stated that for the classification of wood density less than 0.4 g/cm ^{3} including the softwood wood density less than 0.55% g/cm ^{3} including timber and wood density less than 0.72 hkd g/cm ^{3} including heavy timber.

3.2 The strength of the beam Bamboo Laminated

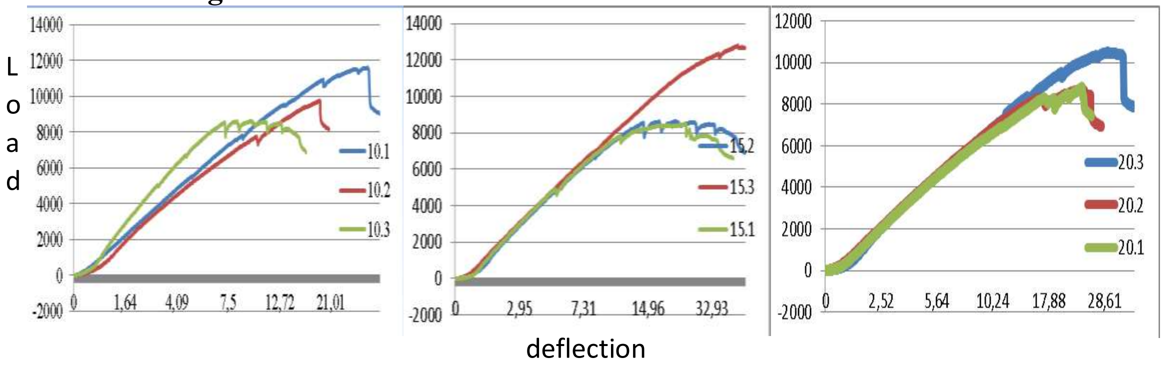

Figure 4 Load and Deflection Graph Distance Variations Latch 10 cm, 15 cm and 20 cm.

The results obtained from the analysis process shows that between the moment the external and internal moments had to meet the conditions of the balances in the style of the structure must be the same with the style of the outside. The difference value that occurs probably caused by the factor of factors namely:

1. The use of the outer skin on the surface of the beam bamboo laminated add rigidity and strength to the burden of the average working with the same lendutan on the beam laminated rose 24%. Morisco (2006) to test the strength of the bamboo the outside (skin) and part in satisfying results bamboo the outside have strength far higher than on bamboo part in. This high-strength obtained from the skin of bamboo. The results obtained the value of the average strong pull the bamboo highway 97 Mpa and the outside of the 285 MPa. Comparison of acquired the strength of bamboo drop-down the outside of the three times stronger than a bamboo part in. Based on this we do the calculation of the use of laminated beams the use of the outer skin on the beam bamboo laminated.
2. The nature of physics and mekanika lamina lamina of bamboo building blocks of laminated beams forebears k homogeneous.

3.3 Slide the voltage

Table 3.2 Strong slide beam laminated bamboo highway

Test objects 60#MDGL	Shear Strength (MPA)	The average	The wood The Class
A1	4,01	3.48	Above the Class II
A2	3.30		
A3	3.13		
B1	3.81	3,82	Above the Class II
B2	3.13		
B3	4.43		
C1	3.75	3.47	Above the Class II
C2	3.45		
C3	3,20		

As a comparison, research results zulmahdi (2011) shows the pattern of damage that is happening on the joint closest to the placement of the connection that was placed on the flexible voltage more flexible voltage both small and bigger does not give impact on the strength of the slide. The beam is used in this research using the tape labur MDGL #60 with width dimension 6 0 mm, high 1 20 mm and the length of the landscape 90 cm.

Table 3.3 Strong Slide Comparison (zulmahdi darwis, 2011)

Test objects 60#MDGL	Slide the voltage	The average
	Mpa	
30A	3.17	3.24
30B	3,44	
30C	3.1	
40A	3.17	3.24
40B	3.45	
40C	3.1	
50A	3.52	3.41
50B	3.32	
50C	3.4	
60A	4.45	3.67
60B	3.07	
60C	3.48	

4. CONCLUSIONS

Based on the discussion and purpose of the research that has been done can be drawn some conclusions among others as follows:

1. The value of the average block testing slide 60#MDGL sequence is 1.63 Mpa, 1.93 Mpa, 1.93 Mpa, 3.00 Mpa, 2,41 Mpa, 2.26 Mpa, and 3,21 Mpa. The results of the test are not obtained significant differences.
2. The behavior of the test of the strength of the slide the beam laminated observed on when it reaches the cracks first burden decline. The beam to do with lendutan resistance so that the load up to the tautness of the maximum burden.
3. The use of the outer skin on the surface of the beam laminated stiffness on the beam bamboo is laminated.
4. Seen from the results of the test of the strength of the slide, obtained strong wood above the class II.

5. ACKNOWLEDGEMENT

We would like to acknowledge to Ministry of Research, Technology, and Higher Education, Indonesia for the research grant in 2016.

6. REFERENCES

[1]. Ibn Arqam Laya, (2007), the *capacity of the Slide Retrofitting Beam Bamboo Laminated Bamboo Highway I Profile* , Thesis S-2, Technique Faculty of the University of Gadjah Mada University in Yogyakarta (not published).

[2]. Morisco, 2006, *Bamboo Technology* , Course Material, the Graduate School of Gadjah Mada University in Yogyakarta (not published).

[3]. Zulmahdi D, 2009, the *influence of the glueAgainst Strong Slide Beam Bamboo laminated* Journal Teknika, July 2009, Cilegon, 11-20

[4]. Zulmahdi D, 2011, Shear Capacity of Bamboo Laminated for used pegs with Variation wash adhesive. *SINAR BAMBOO 2011*, Yogyakarta.

[5]. Zulmahdi D, 2016, The effect of Length Variation of pegs on the flexural strength of laminated Bamboo Beam (Dendrocalamus Asper), International Conference On Engineering and Science For Research and Development (ICESRED), Banda Aceh, 199-204.

Synthesis and Characterization of Alginate Bioplastic Based on Sargassum sp.

Lailatin Nuriyah[1*], Muhammad Ghufron[1], Agesta D. Widyanugraha[2]

1 Department of Physics, Faculty of Science, Brawijaya University, Malang, Indonesia
2 Graduated Student of Department of Physics, Faculty of Science, Brawijaya University, Malang, Indonesia
* Corresponding authors:

Abstract – The production of conventional plastics was exceeded more than 300 million tons every year. Plastic is known as polymers material for packaging application and very hard to degrade in the environment. Bioplastic is a polymer material that could be a solution to this problem because this material can be degraded in the different environment easily. The main ingredient of bioplastics was made from one of the natural polymers, known as alginate which was derived from sargassum sp. This research studied the effect of type and concentration of plasticizers toward alginate bioplastics and the factors that influenced the biodegradation. Plasticizers used were sorbitol and glycerol. There were three stages in manufacturing bioplastics, namely preparation of wet seaweed, alginate extraction and blending. Mixing alginate with a plasticizer, the concentration is varied as follows, 0.5%; 0.75%; 1%; and 1.25% of the total volume. The characterization of bioplastics could be known by the tensile test, percent of elongation, Young's modulus, the resistance of air test and biodegradability test. Results of the research showed that the bioplastics with a plasticizer of sorbitol had a better characterization than bioplastic from glycerol. The best bioplastics alginate was obtained by using sorbitol with concentrations 0,75% which had a value of tensile strength (2,19 ± 0,569) MPa, percent elongation (17,81 ± 2,89) %, Young's modulus (17,17 ± 6,65) MPa, resistant to the environment for two months and degraded on the 5th day. Type and concentration of plasticizers were factors that influence the biodegradation.

1. INTRODUCTION

The production of conventional plastics was exceeded more than 300 million tons every year [1] Plastics known as polymers material for packaging application are very hard to degrade in the environment. However, Bioplastic, which is polymers material, could be a solution to this problem because this material can be degraded in the different environment easily [2]. A natural material such as plants (starch, cellulose, lignin, and alginate) and animals (casein, chitin, chitosan) could be used to make bioplastics as a polymer compound [3]. Sargassum sp, is classified as Phaeophyta division. This species can grow to a length of 12 meters. Its body was brown, yellow-green, with a body structure divided into a Holdfast that serves as a basal structure, a stipe or pseudo stem, and a leaf-shaped frond. Its carbohydrates is stored mostly in the form of polysaccharide of glucose [4]. Based on the previous research such as, physical and mechanical characteristics of bioplastics (Studies Concentration of Tapioca and Comparative Mixture of plasticizer) [5], the mechanical properties and morphology of biodegradable plastics from waste parched rice and tapioca flour using glycerol as plasticizer [6], and the effect of adding sorbitol plasticizer for the manufacturing of bioplastics from cassava husk starch [7]. These studies have shown that the mechanical properties of starch bioplastics still unable to approach the mechanical properties of conventional plastics such as polyethylene. Therefore, researchers are motivated to research bioplastics with different base materials. To see the best results, this work will discuss synthesis and characterization of alginate bioplastic using Sargassum sp. as raw material, glycerol and sorbitol as plasticizer

2. METHODS

2.1 Preparation of Wet Seaweed

This preparation aims to lighten the seaweed extraction stage. First, the preparation of dried seaweed was cleaned of dirt. By soaked dried seaweed in distilled water, wet seaweed was produced. Soaking seaweed was made by inserting the entire portion of dried seaweed in a container contained of distilled water with a ratio of dry seaweed and distilled water were 1: 3. The seaweed was soaked in distilled water for 1 hour until the seaweed looked fresh and light green.

2.2 Alginate Extraction

Alginate extraction carried out in four main stages, namely mixing, crushing, heating, extorting and filtering (as one stage). A mixture of wet seaweed were produced by mixed wet seaweed with a solution of acetic acid. Then, the mixture were blended until smooth. To improve the effectiveness of extraction the seaweed porridge were heated up in 85 - 90 ° C. Ten minutes later, the porridge was extorted and filtered at the same time.

2.3 Bioplastics Synthetize

Bioplastics Synthetize was begun by measuring the volume of alginate and plasticizer in accordance with the necessary variations as shown in Tables 1 and 2. These variations obtained after a preliminary study that refers to the reference. Alginate and plasticizer were mixed and put in a Teflon tray. Furthermore, the liquid was dried using a dryer cabinet at 70 ° C for 6 hours with a hot air discharge (5.0 + 0.1) m3 / min. After drying, the samples were left at room temperature for 24 hours. The bioplastic sheet ready for testing.

Table 1. Mixture Quantity of Alginate with Glycerol

Alginate (mL)		Glycerol (mL)	
%	mL	%	mL
99,5	199,00	0,5	1,00
99,25	198,50	0,75	1,50
99	198,00	1	2,00
98,75	197,50	1,25	2,50

Table 2. Mixture Quantity of Alginate with Sorbitol

Alginate (mL)		Sorbitol (mL)	
%	mL	%	mL
99,5	199,00	0,5	1,00
99,25	198,50	0,75	1,50
99	198,00	1	2,00
98,75	197,50	1,25	2,50

2.4 Observation

The observed variables are tensile strength, percent elongation, Young's modulus, Resistance to air and biodegradability.

3. RESULTS AND DISCUSSION

3.1 Bioplastic

This research resulted bioplastics in the form of thin elastic sheet. Measured by AMT-15, the average thickness of bioplastic were 282 μm. Bioplastics from seaweed Sargassum sp. had a little bit smell and greenish brown color. The smell of bioplastics is the natural smell of seaweed Sargassum sp. itself.

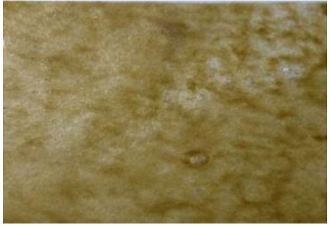

Figure 1. Bioplastic based on *Sargassum sp.*

3.2 Mechanical Properties of Bioplastics

The mechanical properties are defined as a measure of the material ability to resist external forces without damage. The mechanical properties of bioplastics was affected by the chemical bonds between the constituent. The strength of chemical bonds was dependent on the composition of the materials. One way to know the mechanical properties, were by performing a tensile test. Tensile test is a form of testing to determine the response due to the tensile force which was given to the sample so that the mechanical properties could be analyzed through tensile strength and percent elongation.

Table 3 (Mechanical Properties of Bioplastic with Glycerol (G) and Sorbitol (S) Plasticizer)

Bioplastic Sample				Tensile Strength (kPa)		Elongation (%)		Modulus Young (kPa)	
Alginate		Plasticizer							
mL	%	mL	%	G	S	G	S	G	S
199.00	99.50	1.00	0.50	1,090	1,750	12.24	15.52	89.7	126.3
198.50	99.25	1.50	0.75	1,290	2,190	15.34	17.81	85.0	171.7
198.00	99.00	2.00	1.00	800	1,530	16.31	16.32	49.6	97.0
197.50	98.75	2.50	1.25	430	1,350	15.89	24.34	31.7	29.5

Tensile strength is the maximum force which was given to break up bioplastics. As shown in table 3, plasticizer sorbitol in every various concentration produces higher tensile strength than using glycerol. These are because the plasticizer glycerol has a higher tendency to decrease the interaction between the molecules compared to sorbitol, therefore the higher the concentration of glycerol resulted in a decrease in the tensile strength of bioplastics [8]. It appears that both of the plasticizer at concentration of 1% have lower tensile strength values than plasticizers at concentrations of 0.75%. High concentration of plasticizers would cause a decrease in the value of tensile strength in bioplastics [9]. Elongation is defined as the length of the initial length of bioplastic before broken off while was given a tensile force. As shown in the Table 3, glycerol plasticizers at concentration of 0.50% to 1.00% showed an increase in elongation from 12.24 % to 16.31 %. The increase in elongation occurs because glycerol interfere the tensile force between polymer molecules (intermolecular) and decreasing the interactions. Elongation was affected by the plasticizer concentration, the higher of the plasticizers concentration the more elongation it could get [9]. On the other hand, the used of sorbitol concentration at 1.00% shows a slight decrease of elongation 16.32 %. At concentration of 1.25%, increased again with much higher percentage (24.34%). The downturn in elongation might be due to the differences in the thickness of bioplastic sheet. Modulus young is elasticity of a material which indicates the stiffness of a material. Elasticity is also a ratio of elongation and tensile strength before broken up [10]. According to Table 3, alginate bioplastic using sorbitol produces higher modulus young than using glycerol. The highest modulus young is owned by bioplastics alginate using sorbitol 0.75% in amount 171.7 kPa. This is because the sorbitol has lower intermolecular interaction than glycerol [8]. Glycerol molecule has a higher ability to disrupt the cohesiveness of polymers material by lowering the intermolecular interactions and increase the mobility of the polymer, flexibility, and extensibility. This condition will be affected by the changes in mechanical properties such as tensile strength and elasticity [11].

Figure 2. Bioplastic on Resistance of Air Testing

3.3 Air Resistance

The influence of the environment is an important factor in prevention of bioplastics. Based on its function as packaging, the resistance of air (environment) testing is needed to be done to determine the effect of foreign component toward bioplastics. The number of foreign components in the air will affect the physical properties of bioplastics, especially its texture and physical form. This bioplastic air resistance testing was carried out for 2 months with an interval of observation within 2 days. Figure 5 shows that environmental influences during the two months have not changed the physical properties, mechanical and biological bioplastics. The absence of these environmental influences, probably due to the difficulty of moisture to penetrate into the cracks of bioplastic polymer bond at room temperature (27°C). How quickly moisture could enter a material was influenced by the chemical nature, structure constituent materials and environmental conditions such as humidity and temperature [12].

Table 3. Mixture Quantity of Alginate with Sorbitol

Procedure		Mass (gram)					
		Day-0	Day-1	Day-2	Day-3	Day-4	Day-5
Glycerol	0.50%	0.09	0.05	0.04	0.06	0.04	0.04
	0.75%	0.13	0.08	0.06	0.06	0.05	0.07
	1,00%	0.12	0.07	0.06	0.04	0.05	0.07
	1.25%	0.12	0.08	0.06	0.04	0.04	0.05
Sorbitol	0.50%	0.11	0.07	0.07	0.04	0.06	0.07
	0.75%	0.11	0.08	0.07	0.06	0.05	0.03
	1,00%	0.09	0.06	0.05	0.05	0.04	0.04
	1.25%	0.11	0.08	0.06	0.04	0.05	0.08

Biodegradability testing in bioplastics was conducted with soil burial method for 5 days. By conducting two methods such as mass measurement method and visual observation method an observations could be done. Parameter of measurement method is the sample mass loss. Loss of mass in the sample indicates the level of damage to the sample. The value of mass reduction of bioplastics which tested were presented in Table 3. As shown in the Table 3, it can be seen that on day 1 the mass of all samples decreased dramatically compares to day 0 with the value of an average decline of 0.4 g. This mass reduction was caused by microbes which unravel bioplastic composition. This analysis was supported by previous research which stated that bioplastics can be degraded, by bacteria, by cutting the polymer chains into a monomer-monomer. Another test that was used to amplify the sample mass measurement result was a visual observation or a visual method to determine changes in the physical properties of bioplastics [13]. The parameters of this method include changes in the physical form of the sample. All bioplastics had been damaged either crushed or broken until the 4th day. This damage was due to microbes that cut the bond structure of bioplastics during the decomposition process. Another research was also stated that bioplastics will change the chemical structure due to the influence of microbes such as bacteria and fungi [14].

4. CONCLUSIONS

Summing up as follows:

1) Bioplastics alginate by using plasticizer sorbitol has better characteristics than the use of glycerol.
2) The concentration of plasticizer affects tensile strength, percent elongation, Young's modulus, biodegradation but does not affect the environmental resistance of bioplastics alginate up to 2 months. Bioplastics 0.75% alginate by using sorbitol has better characteristics than others with tensile strength values 2.190 kPa, percent elongation 17.81%, Young's modulus 171.7 kPa, resistant to the environment for about 2 months and degraded on the 5th day.
3) The type and concentration of plasticizer affects the speed of degradation of the alginate bioplastics.

5. REFERENCES

[1]. Mekonnen, T., Mussone, P., Khalil, H., Bressler, D., 2013. *Mater. Chem*. **A 1**, 13379

[2]. S. Mehdi Emadian, Turgut T. Onay, Burak Demirel ,2017, *Wate Management*, **59**, 526-536

[3]. Averous, L., 2004. Biodegradable Multiphase System Based on Plasticized Starch: A Review, *Journal of Macromolecular Science*, United Kingdom.

[4]. Guiry, M. D., 2007. Algae Base version 4.2. World-wide electronic publication (online). National Universty of Ireland, Galway, Ireland.

[5]. Harsojuwono, B.A. Dan I W Arnata, 2015. Karakteristik Fisik Dan Mekanik Bioplastik (Studi Konsentrasi Tapioka Dan Perbandingan Campuran Pemlastis). *Media Ilmiah Teknologi Pangan*. **Vol.3**, No. 1, Maret 2016. Hal 1-7.

[6]. Kumoro, A.C. dan A. Purbasari. 2014. Sifat Mekanik Dan Morfologi Plastik Biodegradable Dari Limbah Tepung Nasi Aking Dan Tepung Tapioka Menggunakan Gliserol Sebagai Plasticizer. *Jurnal Teknik Kimia ISSN 0852-1697*, Universitas Diponegoro

[7]. Nurseha, D., 2012. Pengaruh Penambahan Plasticizer sorbitol untuk Pembuatan Bioplastik dari Pati Kulit Singkong. http://digilib.uin-suka.ac.id/10808/1/bab%20i,%20v,%20 daftar%20pustaka.pdf. diakses pada tanggal 9 Agustus 2016.

[8]. Gontard, N. S., Guilbert, and J. L. Cuq. 1993. Water and Glycerol as Plasticizer effect mechanical and Water Vapor Barrier Properties of an Edible Wheat Gluten Film. *J.Food Sci*., **Vol. 58**, No. 1, 206-211.

[9]. Harris, Helmi. 1999. Kajian Teknik Formulasi terhadap Karakteristik *Edible Film* dari Pati Ubi Kayu, Aren, dan Sagu untuk Pengemas Produk Pangan Semi Basah. Desertasi. Program Pasca Sarjana. Institut Pertanian Bogor. Bogor.

[10].Setiani, W., T. Sudiarti dan L. Rahmindar. 2013. Preparasi Dan Karakterisasi Edible Film Dari Poliblend Pati Sukun-Kitosan. *Jurnal Kimia Valensi* **Vol. 3** No. 2, November 2013 (100-109) ISSN : 1978 – 8193. Jurusan Kimia Fakultas Sains dan Teknologi UIN Sunan Gunung Djati Bandung

[11].Khoramnejadian, S., 2011, Converting Non-Biodegradable Plastic to Biodegradable by Using Natural Polymer to Help Environment Conservation, *Journal of Food, Agriculture & Environment,* **9 (2)** : 477-479.

[12].Krochta, J.M.; E.A. Baldwin and M.Nisperos-Carriedo (Eds.). 1994. *Edible Coatings and Films to Improve Food Quality.* Technomic Pub. Co., Inc Lancaster.

[13].Huda, T., dan F. Firdaus, 2007, Karakteristik Fisikokimiawi Film Plastik Biodegradable dari Komposit Pati Singkong-Ubi Jalar, *Jurnal Penelitian dan Sains "Logika",* **4 (2)**: 3-10.

[14].Firdaus, Feris dan Chairil Anwar. 2004. Potensi Limbah Padat-Cair Indutri Tepung Tapioka sebagai Bahan Baku Film Plastik Biodegradabel. *Jurnal LOGIKA*. **Vol. 1**. No. 2. Hal. 38-44. ISSN 1410-2315

The Effect of Addition of Activated Carbon Made from Oil Palm Empty Fruit Bunch and Iron Powder on Ceramic Membrane Characteristics

Sisnayati[1*], Muhammad Said[2], Subriyer Nasir[2], and Dwi Putro Priadi[3]

[1]Doctor Candidate of Environmental Science Doctoral Program Study, Graduate School, Universitas Sriwijaya - Palembang INDONESIA
Chemical Engineering Department, Faculty of Engineering, Universitas Taman Siswa - Palembang INDONESIA
[2]Chemical Engineering Department, Faculty of Engineering, Universitas Sriwijaya - Palembang INDONESIA
[3]Agronomy Department, Faculty of Agriculture, Universitas Sriwijaya - Palembang INDONESIA
*Corresponding Author: sisnayati75@gmail.com

Abstract – The purpose of this study is to determine the effect of the addition of an activated carbon made from oil palm empty fruit bunch as an additive on the characteristics of ceramic membranes. The sintering temperature effects to visible pores and surface texture of the membrane. More addition of the activated carbon OPEFB content, the pore will be more numerous, asymmetric and random. Decreasing of activated carbon content in the ceramic membrane will decrease average pore diameter and porosity of the ceramic membrane, but the surface area of the ceramic membrane will be increased. The ceramic membranes produced in this study is characterized by microfiltration membranes type

1. INTRODUCTION

Sustainable development is an effort and approach in the utilization of natural resources. Polluted water or wastewater resulted by human activity or industry should be treated before entering the environment. One of some technologies to treat polluted water or wastewater is the application of ceramic membrane [1]. Porous ceramic membranes with their various advantages, such as better thermal, chemical and mechanical resistance, controllable microstructure and little pollution to our environment [2]. With the increase in activated carbon concentration in the membrane composition, the membranes exhibited excellent characteristics [3]. Activated carbon can be made from oil palm empty fruit bunch (OPEFB).

2. METHOD

2.1 Chemical

Chemical substances used in this works were oil palm empty fruit bunch (OPEFB), clay and iron powder (IP), aquabidest, aquadest, $ZnCl_2$, HCl,

2.2 Procedures

Preparation of Activated Carbon from OPEFB: OPEFB were washed with distilled water and then dried using sunlight for six days. Carbonization of OPEFB was carried out in a furnace at a temperature of 700 ºC for 1 hour. Then, samples sieved with a 400 mesh sieve to obtain uniformity of shape and size. The activation process was done by immersing samples of carbonization in a solution of $ZnCl_2$ 50% for two days. Then it was washed with HCl and aquabidest then dried in the oven at a temperature of 105 ºC for one day. Morphological characterization of the surface of activated carbon OPEFB was determined by the analysis of Scanning Electron Microscopy (SEM) and the characterization of the elements contained in the activated carbon OPEFB was carried out by using an analysis Energy Disperse Spectroscopy (EDS). Activated carbon OPEFB was put in a planetary ball mill to get a finer particle size again for 30 and 50 hours. The particle size was then analyzed using Particle Size Analyzer (PSA).

Manufacture of ceramic membrane: Clay thinly was sliced and dried for two days. Then it was sieved with a 400 mesh sieve size. Iron powder was sieved at 400 mesh sieve. Clay, activated carbon OPEFB and iron powder thoroughly mixed with a ratio of 77.5%: 20%: 2.5% ; 82.5%: 15%: 2.5% ; and 87.5% : 10% : 2.5%. Add a little water to the dough constituents of the membrane to form a paste (gel). Then it was molded with a molding tool of ceramic membrane. Once molded, the dough was removed from the mold membrane, then dried at room temperature for seven days. After drying, the membrane was burned (sintered) at a temperature of 900⁰C for 9 hours. Finally, the ceramic membrane was characterized by SEM, EDS and BET.

Figure 1 showed the schema of manufacturing of (a) activated carbon from OPEFB, and (b) ceramic membrane respectively.

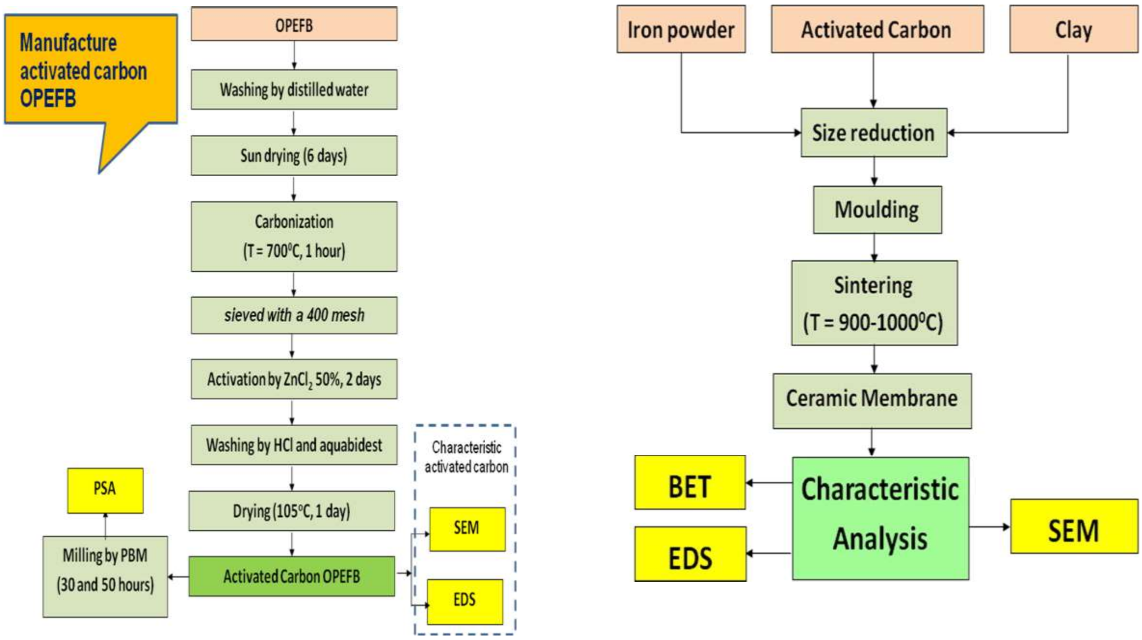

(a) (b)

Figure 1 Schema of manufacturing of (a) activated carbon from OPEFB, and (b) ceramic membrane

3. RESULTS AND DISCUSSION

Figure 2 shows the characterization of Scanning Electron Microscopy (SEM) activated carbon OPEFB (a), characterization of Energy Dispersive Spectroscopy (EDS) of activated carbon OPEFB (b) and Spot sampling of the levels of carbon in the charcoal OPEFB (c).

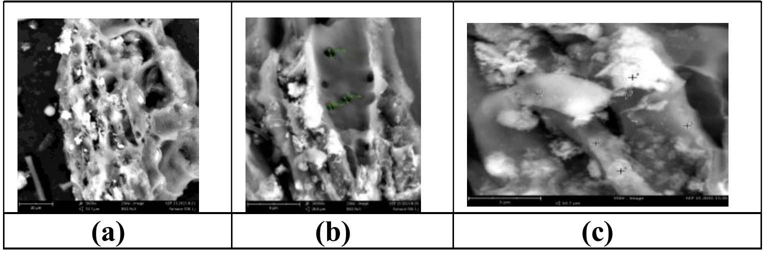

(a) **(b)** **(c)**

Figure 2 (a) SEM, (b) EDS activated carbon OPEFB and, (c) Spot sampling of the levels of carbon in the charcoal OPEFB

The Figure 2a shows the results of the analysis of SEM (Scanning Electron Microscopy) with 5000x magnification. The morphology of the surface of this activated carbon from OPEFB by using $ZnCl_2$ has a porous surface morphology. This is very important because it is closely related to the nature of adsorption. The Figure 2b indicates that the activated carbon from OPEFB after activated with a solution of $ZnCl_2$ has a diameter size of micropores.The pore distribution almost evenly, wherein the pore size is almost the same with each other. The activation process has been done at a temperature of 700°C, so that the pores on the surface of the activated carbon OPEFB are open. By activating solution of $ZnCl_2$, it can reduce hydrocarbon coating on the surface of activated carbon from OPEFB. The Figure 2c represents the spot sampling of the levels of carbon in the charcoal OPEFB and gives the carbon, silicon, oxygen, calcium and aluminum contents as shown in Table 1 as following:

Table 1 The concentration of active element in activated carbon OPEFB in each spot

Element Number	Element Name	Concentration, % wt							Error
		Spot 1	Spot 2	Spot 3	Spot 4	Spot 5	Spot 6	average	
6	Carbon (C)	52.6	51.5	62.6	50.5	60.0	53.4	55.1	0.8
14	Silicon (Si)	5.5	-	6.2	4.3	2.7	-	3.12	4.5
8	Oxygen (O)	38.0	48.5	26.9	45.2	34.6	46.6	39.97	4.0
20	Calcium (Ca)	4.0	-	-	-	-	-	0.67	4.1
13	Aluminium (Al)	-	-	4.3	-	2.7	-	1.17	4.8

Based on Table 1 above, the results of EDS analysis showed that the main elements of OPEFB charcoal are carbon (C) with the percentage of the average weight of 55.1% wt. The existence of the elements oxygen, aluminum, calcium and silicon can also be observed from the analysis of the composition on the surface of activated carbon OPEFB but that have a very low weight percentage

Table 2 represents the properties of activated carbon OPEFB particles in the process. It appears that the nature of activated carbon OPEFB particles has varying diameters. The longer time ball mill process will produce smaller particle (smooth). This proves that during the process ball mill cavitation phenomenon which has occurred rupture of microparticles into nano because of the influence of friction and collisions between particles.

Table 2 the properties of activated carbon OPEFB particles in the process

Size Reduction Time in Ball mill	30 hours		50 hours	
Property	Median	Average	Median	Average
Circle equivalent diameter	2.21 μm	2.5 μm	234.33 nm	361.33 nm
Major axis	3.04 μm	3.42 μm	345 nm	525.67 nm
Minor axis	2.19 μm	2.2 μm	195 nm	255 nm
Area	5.99 μm^2	6.73 μm^2	500.73 nm^2	810.67 nm^2
Volume by area	11 μm^3	14.7 μm^3	765.47 nm^3	3.19 μm^3

Figure 3 shows the BET analysis of ceramic membrane. The average pore diameter of the membrane A, B and C were 487 nm, 365 nm, and 298 nm respectively. So, the ceramic membranes produced this study was characterized by microfiltration membranes type. Porosity is decreased by the reduction of activated carbon content in the membrane. It appears that there is an increasing membrane surface area with a reduction of activated carbon OPEFB content. Porosity is decreased by the reduction of activated carbon content in the membrane.

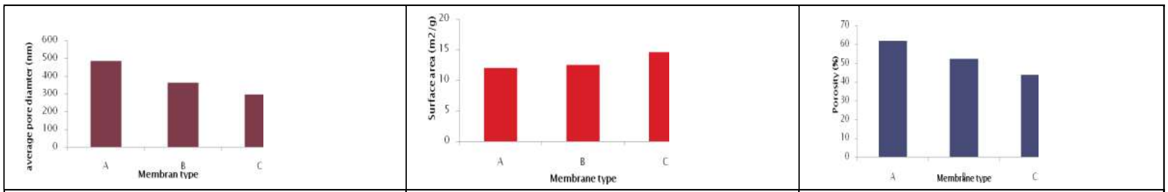

(a) average pore diameter Vs composition

(b) surface area Vs composition

(c) porosity Vs composition

Figure 3 BET Analysis of membrane type.

4. CONCLUSIONS

The conclusion of this work are as following:

a. The sintering temperature effects to visible pores and surface texture of the membrane. More addition of the activated carbon OPEFB content, the pore will be more numerous, asymmetric and random.

b. Decreasing of activated carbon content in the ceramic membrane will decrease average pore diameter and porosity of ceramic membrane, but the surface area of the ceramic membrane will be increased.

c. The pore diameter of the membrane A, B and C were 487 nm, 365 nm, and 298 nm respectively. So, the ceramic membranes produced in this study is characterized by microfiltration membranes type

5. REFERENCE

[1]. Amin, Sh.K., H. A. M. Abdallah, M. H. Roushdy, S. A. El-Sherbiny, 2016, *International Journal of Applied Engineering Research* ISSN 0973-4562 , **11** (12), 7708-7721,.
[2]. Wu, P., Y. Xua, Z. Huang, and J. Zhang, 2015, *Journal of Ceramic Processing Research*, **16** (1), 102-106
[3]. S. Velu, K. Rambabu, L. Muruganandam, 2014, *International Journal of Chem Tech Research*, **6** (**1**), 565-577.

Study on Contamination Detection of Rhodamine B in *Capsicum annum L* Based on The Electrical properties of Materials

Chomsin SW[1*], Unggul PJ[1], Bambang[1]

[1] Dept. of Physics, Faculty of Sciences, Brawijaya University. Veteran Street, Malang, Indonesia.
* Corresponding authors: [chomsin@ub.ac.id]

Abstract –The study was conducted to determine the electrical characteristics of *Capsicum annum L* which have been added Rhodamine-B by using the dielectric method (LCR Meter) at low frequencies (100 – 1000 Hz). The Results show that the electrical capacitance of *Capsicum annum L* decreases with increasing frequency. The addition of rhodamine-B increases the capacitance value and dielectric constant value of the sample.

1. INTRODUCTION

Each biological material has electrical properties that are affected by metabolism that occur in the biological material [1]. Measurements for testing the quality of agricultural products is generally carried out chemically or destructive laboratory testing. The characterization of the electrical properties of the foodstuffs is widely used as a reference for assessing the quality and purity of these ingredients in a rapid, non-destructive and more efficient [2].

The study was conducted to determine the electrical characteristics of *Capsicum annum L* which have been added Rhodamine-B by using the dielectric method at low frequencies. A Randles circuit is an equivalent electrical circuit that consists of an active electrolyte resistance R_S in series with the parallel combination of the double-layer capacitance C_{dl} and an impedance of a faradaic reaction.

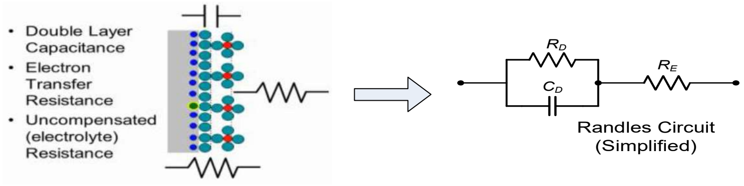

Figure 1 A Randels circuit

2. METHODS

The electrical properties of the material being measured are electrical capacitance and dielectric constant. Capacitance measurement using a capacitor plate made of a copper plate with a size of 20 x 10 mm with 5 mm distance between plates. At the center of the plate in place of *Capsicum annum L* and connected to the LCR meter INSTEK GW-816 series with a double probe L and H, while the dielectric constant capacitance value is obtained from the calculation. Capacitance measurements performed with a frequency range of 100 - 2000 Hz. Rhodamine-B is added to *Capsicum annum L* from 0 mg, 7 mg, 11 mg, 15 mg, 19 mg, 23 mg, 27 mg, and 31 mg per 10 g.

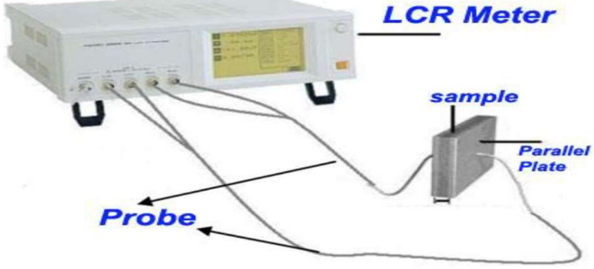

Figure 2 System Acquisition Data of Impedance Measurement

3. RESULTS AND DISCUSSION

In general, the results show that the electrical capacitance of *Capsicum annum L* decreases with increasing frequency as shown in Figure 3. Overall the trend curves provide a logarithmic trend because the total impedance value of the solution is affected by the resistance and capacitance components of the medium in accordance with the Randle model. Addition of rhodamine-B increases the capacitance value and dielectric constant value of sample. Rhodamine-B contains chlorine, lead (Pb) and arsenic (As) [3]. Chlorine is an insulator while the lead (Pb) and arsenic (As) is a conductor.

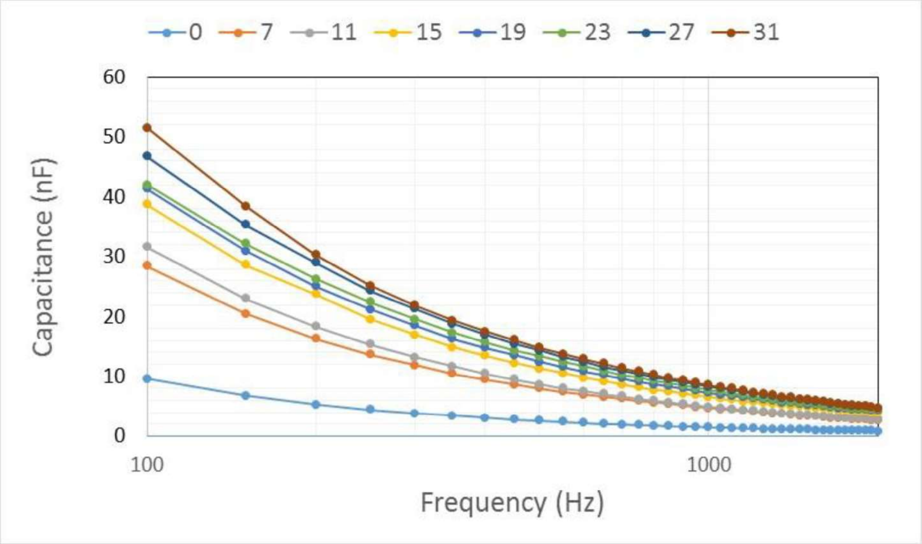

Figure 3. Electrical capacitance of *Capsicum annum L* at various mass of Rhodamine-B

So, the more conductors are added to the dielectric material, in this case, the addition of rhodamine-B, the value of the dielectric constant of the material will increase. Rhodamine-B which has conductive properties will enhance the strengthening of the internal electric field.

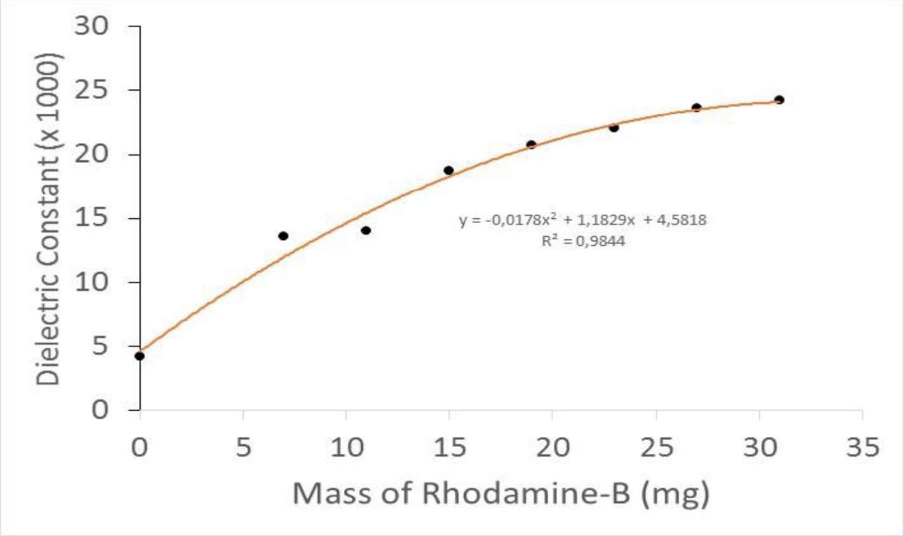

Figure 4. Dielectric Constant of *Capsicum annum L* at various mass of Rhodamine-B at frequency 1000 Hz.

Cases of economically motivated adulteration, where it has been illegally used to impart color to a red chili (*Capsicum annum L)* powder, have come to the attention of food safety regulators.

4. CONCLUSIONS

The electrical capacitance of *Capsicum annum L* decreases with increasing frequency. Addition of rhodamine-B increases the capacitance value and dielectric constant value of sample. The value of the dielectric constant at a frequency of 1000 Hz correlated second-order polynomial.

5. REFERENCES

[1] M. R. Hidayat, C. S. Widodo, and G. Saroja, "Kajian Karakteristik Biolistrik Kulit Ikan Lele (Clarias Batrachus) Dengan Metode Dielektrik Frekuensi Rendah," *Phys. Student J.*, vol. 2, no. 1, p. pp.11-14, 2014.

[2] C. S. Widodo, D. R. Santoso, and U. P. Juswono, "DOUBLE LAYER IMPEDANCE ANALYSIS ON THE ELECTRICAL IMPEDANCE MEASUREMENT OF SOLUTION USING A PARALLEL PLATE," *J. Environmental Eng. Sustain. Technol.*, vol. 3, no. 1, pp. 65–69, 2016.

[3] S. Subandi, "Penentuan Kadar Arsen dan Timbal dalam pewarna Rhodamine B dan Auramine secara Spektrofotometri: Suatu Penelitian Pendahuluan," *MIPA dan Pembelajarannya*, vol. 28, no. 1, 2009.

The Role of Boltzmann Temperature on Short Pulse Molecular Alignment

Abdurrouf

Department of Physics, Brawijaya University, Malang, Indonesia
Corresponding author: [abdurrouf@ub.ac.id]

Abstract – Nowadays, the interaction between molecules and intense short laser pulse has attracted tremendous interest in molecular physics and non-linear optics due mainly to its advantages as a probe of molecular dynamics, as well as a tool for molecular imaging. As molecules have anisotropic polarizability, the laser pulse will rotates and aligns them, expressed in dynamic alignment degree. To get more information, it is convenient to Fourier transform the alignment degree, and obtains the spectrum in frequency domain. This paper is aimed to analyze the role of Boltzmann temperature on molecular alignment, especially on alignment degree, the corresponding Fourier spectrum, and the molecular axis distribution.

1. INTRODUCTION

The molecular alignment can be achieved by subjecting an intense short laser pulse to molecular ensemble in gas phase. Before interaction, the molecular ensemble is assumed to be in thermal equilibrium, characterized by Boltzmann temperature T. This interaction creates a superposition of coherently excited rotational wave functions $\left|\Psi(t_d)\right\rangle$, where t_d is the delay time since entering laser pulses. These rotational wave functions evolve, rotate, and align molecules under field-free conditions [1]. The signature of Boltzmann temperature in molecular alignment is printed out on the molecular axis distribution [1-2], the dynamic expectation value of alignment degree [2-3], and the corresponding Fourier spectrum [2,4].

2. METHODS

The system of interest is a molecular gas of N_2 interacting with a linearly polarized laser pulse with peak intensity of $0.5x10^{14}\,\mathrm{W/cm^2}$ and pulse duration of 40 fs. The properties of N_2 are displayed in Tab. 1. The molecular wave functions are obtained by solving Schrodinger equation by using fifth order Runge-Kutta integration. Having molecular wave functions, one can calculate molecular axis distribution

$$P(t_d,\theta)=\left|\Psi(t_d,\theta)\right|^2, \tag{1}$$

where θ is the relative angle between molecular axis and laser polarization. The average value of θ is then expressed in the dynamic alignment degree

$$\left\langle\left\langle\cos^2\theta\right\rangle\right\rangle(t_d)=\left\langle\left\langle\Psi(t_d)\right|\cos^2\theta\left|\Psi(t_d)\right\rangle\right\rangle. \tag{2}$$

In above, the double brackets stand for the expectation value on the rotational wave packets (inner brackets) and that on the Boltzmann distribution (outer brackets). Finally by Fourier transforming alignment degree we obtain spectrum in frequency domain.

Table 1. Molecular properties of N_2: B is rotational constant of molecule, whereas α_{par} and α_{perp} are parallel and perpendicular polarizability, respectively.

Properties	Values	Ref.
$B\left(\mathrm{cm}^{-1}\right)$	2.0	[5]
$\alpha_{par}\left(\mathrm{angstrom}^3\right)$	2.38	[6]
$\alpha_{perp}\left(\mathrm{angstrom}^3\right)$	1.45	[7]

3. RESULTS AND DISCUSSION

First, we calculate alignment degree by using Eq. (2), The calculated alignment degrees for various Boltzmann temperatures are shown in Fig. 1. From the calculated results, it was obtained that molecules with lower Boltzmann temperature have higher alignment degree, means that they are easier to align in the direction of pulse polarization. It can be understood as follow. Consider that initially the molecule is in a state $\left|J_0 M_0\right\rangle$. The laser interaction will change the rotational state as $\left|J_0 M_0\right\rangle \rightarrow \left|J = J_0 \pm 2, M = M_0\right\rangle$. Unlike an up transition where the molecule can find any J states, there is a restriction for a down transition so that $J \geq M_0$. As a result, the new wave packet would consist of states with higher $J > M_0$ (meaning that the vector of rotational angular momentum tends to lie in plane perpendicular to laser polarization direction). Since the rotational angular momentum is perpendicular to the molecular axis in diatomic molecules, the condition $J > M_0$ means that the molecular axis would tend to align in the direction of the laser polarization. This is the reason why the alignment angle after the laser interaction is always smaller than one before the interaction. In other words, the alignment degree after the laser interaction is always higher than the one before the interaction. For a lower initial temperature we have lower initial M_0 so that the ratio J to M_0 is higher. As consequences, for lower initial temperature the $\left\langle\left\langle \cos^2\theta \right\rangle\right\rangle(t_d)$ values are higher. It means that for lower initial temperature, molecule is easier to align.

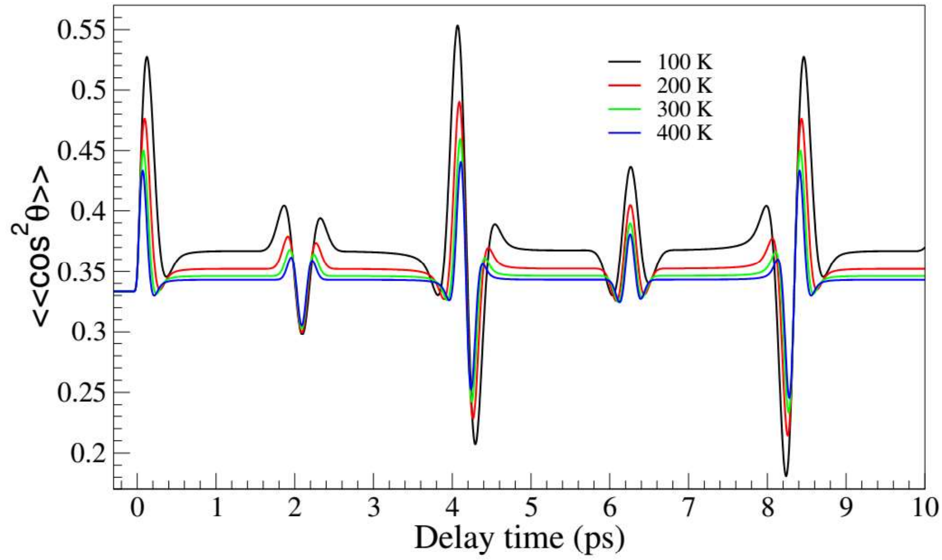

Figure 1 Dynamic alignment $\left\langle\left\langle \cos^2\theta \right\rangle\right\rangle(t_d)$ of N_2 subject to pulse with peak intensity of $0.5x10^{14}$ W/cm^2 and pulse duration of 40 fs, for various Boltzmann temperatures.

A better and clearer understanding of the role of Boltzmann temperature can be obtained by investigating the spectrum in the frequency domain. It that can be obtained by Fourier transforming the dynamic signal (t_d - dependence) and plotting the Fourier amplitude as a function of its frequency in units of Bc, where B is rotational constant of molecules. The calculated Fourier spectrum is shown in Fig. 2. From the figure, it was obtained that the Fourier spectrum appears in two series, which are (6, 14, 22, 30 ….) *Bc* and (10, 18, 26, 34 ….) *Bc*. In general both series follow $(4J+6)Bc$, where the first series is generated by even *J*, whereas the second one is generated by odd *J*. The intensity of series I is twice bigger than that of series II, reflecting nuclei statistics of N_2, where $g_{even} : g_{odd} = 2:1$.

The formulae $(4J+6)Bc$ are easily understood to arise from the *F.T.* of the $\left\langle\left\langle \cos^2\theta \right\rangle\right\rangle(t_d)$ which vanishes unless $\Lambda J = 0,\pm 2$, produces a sequence of lines $\Lambda E = \left(E_{J+2} 2_{-J}\right) = \|4J+6\| Bc$. Fig. 2 also shows that Fourier spectrum reaches maximum at specific value of J called as $J_{\max}$.The value of $J_{\max}$ is sensitive to Boltzmann temperature, where the higher Boltzmann temperature gives higher $J_{\max}$. This dependence $J_{\max}$ on Boltzmann temperature provides a sensitive method for determining temperature of molecular ensemble. In addition, it is also worthwhile to compare $J_{\max}$ with J_{theo} obtained by maximized Boltzmann formulae $P(J)=(2J+1)\exp\left(-\frac{BJ(J+1)}{kT}\right)$. The discrepancy between $J_{\max}$ and J_{theo} should be interpreted as due to the molecular heating by laser pulses. This idea is also supported by the dynamic of calculated rotational energy, whose value after pulse interaction is always greater than that before interaction.

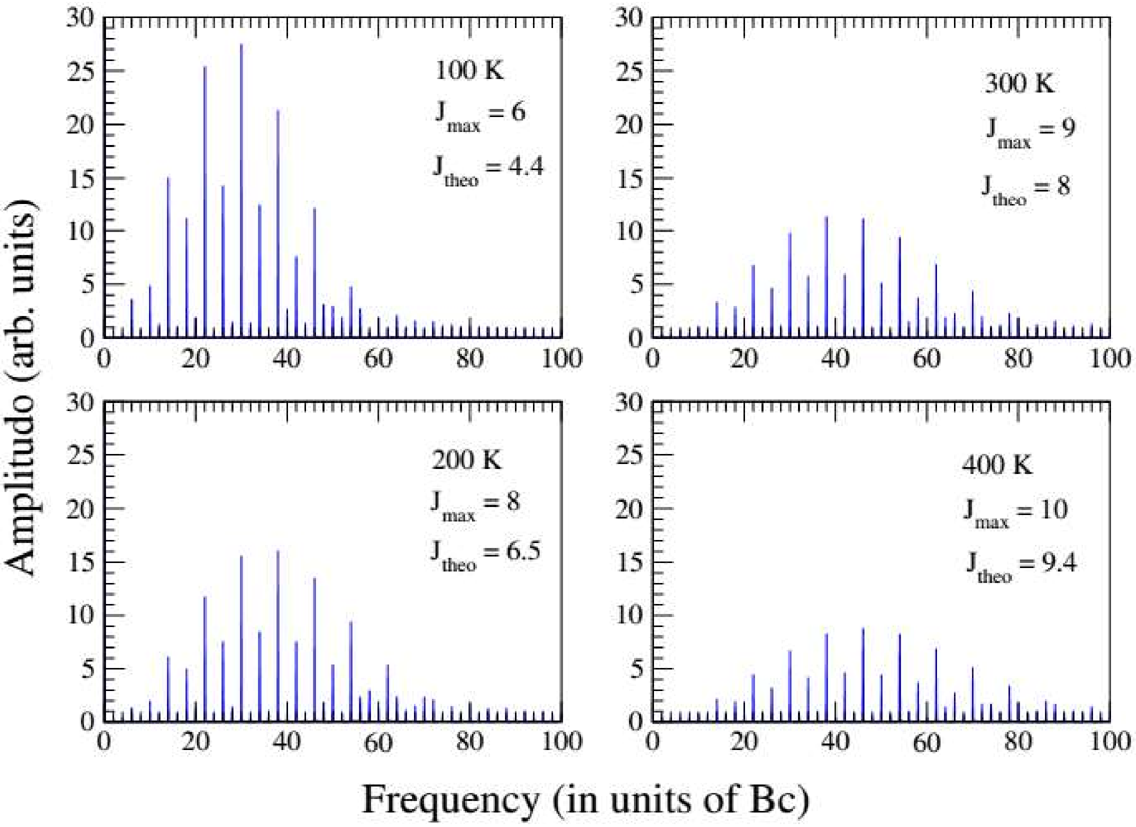

Figure 2. The Fourier spectrum of dynamic signal presented in Fig. 2

To understand the origin of temperature dependence of alignment degree, we also calculate the molecular axis distribution as a function of alignment angle θ. Fig. 3 shows the calculated molecular axis distribution for top alignment, i.e. when its alignment degree reaches maximum. . It is clear that molecules tend to align in molecular axis direction ($\theta = 0^0$), giving the higher alignment degree. As Boltzmann temperature become higher, the percentage of molecules in molecular axis direction become smaller, and reduces the alignment degree.

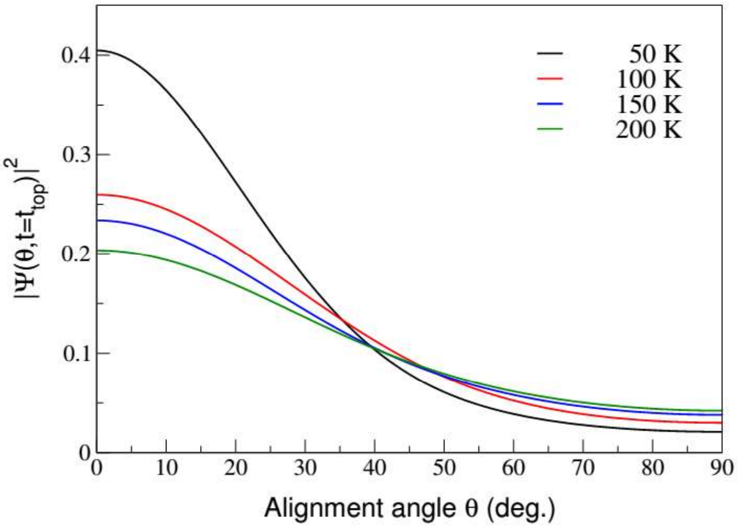

Figure 3. The molecular-axis distribution of N_2 at top alignment. The pulse parameters are similar to that in Fig. 1.

4. CONCLUSIONS

To conclude, we have show the role of Boltzmann temperature in molecular alignment, as printed out in alignment degree, Fourier spectrum, and molecular axis dsitribution.

5. REFERENCES

[1]. K. Miyazaki, M. Kaku, G. Miyaji, A. Abdurrouf, and F.H.M. Faisal., 2005, Phys. Rev. Lett., **95**(24): 243903
[2]. A. Abdurrouf and F.H.M. Faisal, 2009, Phys. Rev. A, **79**, 023405
[3]. F.H.M. Faisal, A. Abdurrouf, K. Miyazaki, and G. Miyaji, 2007, Phys. Rev. Lett., **98**, 143001
[4]. K. Yoshii, G. Miyaji and K. Miyazaki, 2010, JLMN **5**(2), 121
[5]. J.O. Hirschfelder, C.F. Curtis, and R.B. Bird, 1954, *Molecular Theory of Gases and Liquids*, Wiley, New York
[6]. W.L. Jorgensen and L. Salem, 1973, *The Organic Chemist's Book of Orbital*, Academic Press, New York
[7]. S-F Zhao *et al.*, Phys. Rev. A, 2010, **81**, 033423

Volume 2

BaSIC 2017

The 7th Basic Science International Conference

Basics Science for Improving Survival and Quality of Life

Mathematic, Statistics, and Modelling

Forecasting Analysis Using Poverty Level Multiple Regression Analysis

Warnia Nengsih[1*], Juni Nurma Sari[2],

[1] Politeknik Caltex Riau, Umbansari street Rumbai Pekanbaru Riau Indonesia
[2] Politeknik Caltex Riau, Umbansari street Rumbai Pekanbaru Riau Indonesia
* Corresponding authors: [warnia@pcr.ac.id]

Abstract – Poverty is a classic problem in every region. The success of a region is strongly influenced by how big this poverty can be overcome. So that poverty reduction becomes a priority for both central and local government. Various programs and policies began to be formulated to reduce and minimize the problem. The decision for the formulation of policy or program should have been formulated long time ago and refers to the percentage of the poverty line and poor people in the region. However, the difficulty in knowing the level of poverty in the future becomes an obstacle to generate a formulation that is structured. It needs a functioning forecasting analysis predicted poor conditions so as to provide knowledge and reference for the government in making policies and new programs. Forecasting model using multiple regression especially as one of predictive modeling. The result obtained line equation Y = -9.007518374 + 1,10492E-05.325221 + 10,93860947.3,8 = 36.152481626. Equation line formed will be learning to perform forecasting analysis using variable value in the year to predict. So that the predictive value of the number of poor people in 2017 amounted 36.152481626 people with a percentage increase of 3.85% Percentage of poverty statistics shows an increase from the previous year. The predictive value will be a reference for the administration to prepare the programs and policies in alleviating poverty.

1. INTRODUCTION

The problem of poverty became a thing that becomes the focus of attention of the government. Poverty can theoretically be defined as a condition that describes the life of people below the level of prosperity, the difficulty in obtaining rights and basic services to the eligibility status is good. The success of a region can one measure of success in poverty reduction, community prosperous and equitable spread of development.

Various programs and policies began to be formulated to reduce and minimize the problem. The decision for the formulation of a program or policy should have been formulated long ago, and refers to the percentage of the poverty line and poor people in the region. But the difficulty in knowing the level of poverty in the future becomes an obstacle to realizing the formulation. It needs a functioning forecasting analysis predicted the conditions of poverty in the future so as to providing knowledge and reference for the government in making policies and new programs.

Poverty is an area can be seen by calculating the poverty line and the percentage of poor people. These two indicators can determine the number of poor people. Forecasting model using multiple regression especially as one of predictive modeling to estimate the number of poor people in particular. Knowledge in the form of predictions is used as a basis in the policy for reducing poverty in the region.

2. METHODS

2.1 Poverty Level

Poverty is a condition that weakens the welfare of society and the difficulty of access in different ways, particularly basic needs. There are several categories of poverty in the region. Category poverty is particularly vulnerable, poverty illustrates people's lives below the national poverty line so that the public although not classified as poor but vulnerable to poverty. The next category of poverty based on income. Extent of poverty based on income so that poverty can not describe the restrictions and difficulties in accessing basic services such as access to services, education, and health.

Martin Luther King [1960] "We are not going to be a great nation if the majority of the people are still poor and weak. So to become a great nation majority of the people should not live in poverty and vulnerable. Indeed, poverty is not a new problem in this country. A century before the independence of the Dutch colonial government began to fret over poverty in Indonesia [Java]. At that time the only visible indicator of poverty is a rapid population growth [Soejadmoko, 1980]. Hari Susanto [2006] said that general instruments used to determine whether a person or a group of people in these communities is poor or not can not be monitored by using the size of the increase in income or consumption level of the person or the group of people. However, the nature of poverty can be seen from a variety of factors such as socio-cultural, economic, political, and law.

Poverty alleviation policies according to Gunawan Sumodiningrat (1998) can be categorized into 2 (two), namely the policy of indirect and direct policy. Indirect policy covers (1) efforts to create peace and stability of the economic situation, social and political; (2) Control of the population; (3) Preservation of the environment as well as preparing poor people through training.

2.2 Multiple Regression Analysis

Multiple regression analysis is one method of data mining. This method is part of a regression technique using predictive models. This method predicts a value based on the patterns formed on the processed data.

Multiple regression using more than two because of the variables that affect the causal variables. This method will form a line equation by first have to find the value of the gradient and constants. The equation can be illustrated by:

$$\mathbf{Y = a + BX1 + BX2 + BXN}$$

Where Y = a = constant dependent variables b1, b2 = gradient x1, x2 = independent variable Here is an equation to find the value of the gradient and constants.

$$\sum Y = an + b_1 \sum X_1 + b_2 \sum X_2$$

$$\sum X_1 Y = a \sum X_1 + b_1 \sum X_1{}^2 + b_2 \sum X_1 X_2$$

$$\sum X_2 Y = a \sum X_2 + b_1 \sum X_1 X_2 + b_2 \sum X_2{}^2$$

Gradient value calculated as the variable x is used, the calculation process refers to the auxiliary table that has been formulated.

3. RESULTS AND DISCUSSION

The following is an analysis flow forecasting in general.

Figure 1. Flow Forecasting Analysis

Poverty data from the years 2006-2016 Pekanbaru government used as training data using a variable poverty line (x1), he percentage of poor people (x2), the number of poor (y). The data is processed using multiple regression method to get the forecasting analysis in 2017.

Diagram multiple regression analysis shown in Figure 2:

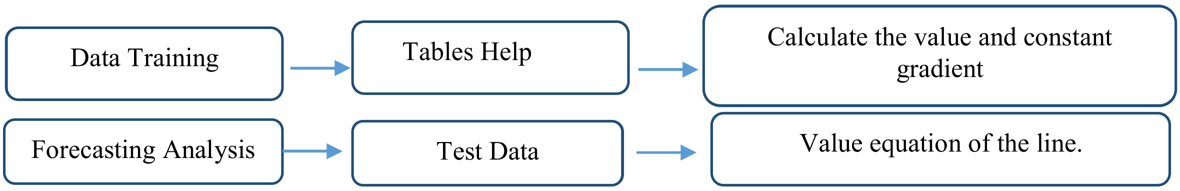

Figure 2. Multiple Regression Analysis

Training data is ready to be processed then determined based on the gradient and the constant auxiliary table that has been created to get the equation of the line. If the equation of the line has been formed, the next step is to test the data with the new gradient value using a variable using the poverty line (x1), percentage of poor people (x2) to get a prediction of the number of poor (y) in 2017.

Here is the result of forecasting using multiple regression analysis

Table 1. Table aids poverty data

Record	x1	x2	y	x1y	x2y	x1x1	x2x2	x1x2
1	183900,00	2,16	16,30	2997570,00	35,21	33819210000,00	4,67	397224,00
2	198361,00	2,24	17,70	3510989,70	39,65	39347086321,00	5,02	444328,64
3	241428,00	3,63	29,74	7180068,72	107,96	58287479184,00	13,18	876383,64
4	32667,00	4,20	38,20	1247879,40	160,44	1067132889,00	17,64	137201,40
5	32667,00	4,20	38,20	1247879,40	160,44	1067132889,00	17,64	137201,40
6	357200,00	3,38	32,70	11680440,00	110,53	127591840000,00	11,42	1207336,00
7	357200,00	3,38	32,70	11680440,00	110,53	127591840000,00	11,42	1207336,00
8	381287,00	3,27	32,50	12391827,50	106,28	145379776369,00	10,69	1246808,49
9	391006,00	3,21	32,30	12629493,80	103,68	152885692036,00	10,30	1255129,26
10	396770,00	3,50	32,50	12895025,00	113,75	157426432900,00	12,25	1388695,00
11	324564,00	3,60	32,30	10483417,20	116,28	105341790096,00	12,96	1168430,40
12	325221,00	3,80	36,15	-	-	-	-	-
11,00	2897050,00	36,77	335,14	87945030,72	1164,73	949805412684,00	127,20	9466074,23

Table 1 shows the auxiliary table of data on poverty, this table contains eleven training data records using a variable which uses the poverty line (x1), percentage of poor people (x2) to get a prediction of the number of poor (y). Auxiliary table used as a reference in the calculation of the gradient and constants.

Table 2. Calculation of gradient values and constants

	y	a	b1	b2
(1)	335,14	11,00	2897050,00	36,77
(2)	87945030,72	2897050,00	949805412684,00	9466074,23
(3)	1164,73	36,77	9466074,23	127,20

Calculation of gradient and the constant value can be seen in Table 2, wherein the table above shows one constant value and the second value of the gradient. Gradient value theoretically searched a total amount of variable x is used.

Table 3. Equation Value

A	**b1**	b2
-9,007518374	1,10492E-05	10,93860947

Table 3 shows the results obtained for the equation of a line is Y = a + BX1 + BX2 where Y = -9.007518374 + 1,10492E-05.325221 + 10,93860947.3,8 = 36.152481626. From the equation of a line is formed, further forecasting analysis uses variable value in the year to predict. So that the number of poor predictive value in 2017 amounted 36.152481626 the percentage increase from the previous year by 3.85%.

4. CONCLUSIONS

Forecasting function analysis was used to predict the conditions of poverty in the future so as to provide knowledge and as a basis for the government in making policies and new programs. Poverty data from the years 2006-2016 Pekanbaru government used as training data using a variable poverty line (x1), percentage of poor people (x2), the number of poor (y). The data is processed using multiple regression method to get the forecasting analysis. Forecasting analysis using test data from variables in the year so that the number of poor predictive value in 2017 amounted 36.152481626 the percentage increase from the previous year by 3.85%.

5. REFERENCES

[1]. Sumodiningrat, Gunawan.1998. Membangun Perekonomian Rakyat, Pustaka Pelajar, Yogyakarta
[2]. Riau dalam angka. Badan Pusat Statistik.
[3]. Andono, Ari Widi, 2011. Analisis Faktor Penentu Dan Tingkat Ketimpangan Ketimpangan Kemiskina Antar Wilayah Di Indonesia Periode 2007-2009. SKRIPSI Universitas Sebelas Maret, Surakarta. Badan Pusat Statistik, Sumatera Utara dalam Angka 2013
[4]. Beasley T.M. 2008. Seemingly Unrelated Regression (SUR) models as a solution to path analytic models with

correlated errors. Multiple Linear Regression Viewpoints, Vol. 34(1), Hal 1-7

[5]. Zellner, A. 1962. An Efficient Method of Estimating Seemingly Unrelated Regressions and Tests For Aggregation Bias. Journal of American Statistical Association Vol. 57, No. 298, pp. 348-368.

[6]. Beasley T.M. 2008. Seemingly Unrelated Regression (SUR) Models as a Solution to Path Analytic Models With Correlated Errors. Multiple Linear Regression Viewpoints, Vol. 34, 1-7

[7]. Culpepper, S. A. 2008. Conducting external profile analysis with multiple regression. Practical Assessment, Research & Evaluation, Vol 13, No 1. ISSN 1531-7714.

[8]. Nengsih, Warnia.2015.A Comparative Study on Market Basket Analysis and Apriori Association Technique , IEEE.

[9]. Syofyan, I. 2007. Estimasi Parameter Regresi dengan Menggunakan Model Residual Bootstrap. Skripsi. Tidak dipublikasikan. Yogyakarta: Prodi Stat FMIPA UGM

[10]. F. Nhita,Adiwijaya,U.N.Wisesty,andI.Ummah,2015 “Planting Calendar Forecasting System Using Evolving Neural Network” For East Journal of Electronics and Communications,vol.14,no 2,pp 81-92.

Solving a System of Nonhomogeneous Fourth Order Ordinary Differential Equtions by Using Diagonalization Matrix

Tjang Daniel Chandra[1*]

[1] Mathematics Department – State University of Malang – Jalan Semarang 5 Malang
* Corresponding authors: [tjang.daniel.fmipa@um.ac.id]

Abstract – This paper discusses a method to solve a system of nonhomogeneous fourth order ordinary differential equations $\boldsymbol{x}^{(4)} = A\boldsymbol{x} + \boldsymbol{f},$ where A is a 3 x 3 matrix. To solve this system, matrix A will be diagonalized by using $J = P^{-1}AP$, where P is a matrix with eigenvectors of A as its columns and J is a diagonal matrix with the entries of main diagonal are the eigenvalues of matrix A. Introducing a new variable y where $\boldsymbol{y} = P^{-1}\boldsymbol{x}$ and differentiating this equation will transform the original system into a new system $\boldsymbol{y}^{(4)} = J\boldsymbol{y} + P^{-1}\boldsymbol{f}$. This new system can be solved by using undetermined coefficients. Therefore, the solution of the original system can be obtained from the equation $\boldsymbol{x} = P\,\boldsymbol{y}$. If the matrix A can not be diagonalized, then the Jordan form of matrix A must be determined. An example of the system with all of eigenvalues of matrix A are equal is given.

1. INTRODUCTION

A system of second order ordinary differential equations to model a spring-mass system was discussed by Nagle[1]. This system was solved by involving sine and cosine functions. Meanwhile An and Yukun [2] discussed a system that consist of second and fourth order of ordinary differential equations. This paper generalizes the above systems, that is, discuss a method to solve a system of nonhomogeneous fourth order ordinary differential equations.

2. METHODS

Consider the following system of nonhomogeneous fourth order ordinary differential equations

$$x^{(4)} = Ax + f, \tag{2.1}$$

where

$$\boldsymbol{x}^{(4)} = \begin{bmatrix} x_1^{(4)} \\ x_2^{(4)} \\ x_3^{(4)} \end{bmatrix}, \quad A = \begin{bmatrix} a_1 & a_2 & a_3 \\ b_1 & b_2 & b_3 \\ c_1 & c_2 & c_3 \end{bmatrix}, \quad \boldsymbol{x} = \begin{bmatrix} x_1(t) \\ x_2(t) \\ x_3(t) \end{bmatrix}, \quad \boldsymbol{f} = \begin{bmatrix} f_1(t) \\ f_2(t) \\ f_3(t) \end{bmatrix},$$

The method to solve the system (2.1) is following the method that is developed by Dettman [3] to solve a system of first order ordinary differential equations. At first, matrix A will be diagonalized by determining eigenvalues of matrix A and its corresponding its eigenvectors. Using these eigenvectors, form a matrix P which is a matrix with eigen vector of A as its columns determine its inverse matrix P-1. Then we obtain a matrix diagonal J by using the equation

$$J = P^{-1}AP.$$

Now, we introduce a new variable $\boldsymbol{y}$ where $\boldsymbol{y} = P^{-1}\boldsymbol{x}$, and $\boldsymbol{y} = \begin{bmatrix} y_1(t) \\ y_2(t) \\ y_3(t) \end{bmatrix}$.

Differentiating both sides of the above equation four times, we have a new system as follows

$$\begin{aligned} \boldsymbol{y}^{(4)} &= P^{-1}\boldsymbol{x}^{(4)} \\ &= P^{-1}(A\boldsymbol{x} + \boldsymbol{f}) \\ &= P^{-1}A\boldsymbol{x} + P^{-1}\boldsymbol{f} \\ &= P^{-1}APP^{-1}\boldsymbol{x} + P^{-1}\boldsymbol{f} \end{aligned}$$

Since $J = P^{-1}AP$ and $\boldsymbol{y} = P^{-1}\boldsymbol{x}$, we obtain

$$\boldsymbol{y}^{(4)} = J\boldsymbol{y} + P^{-1}\boldsymbol{f} \qquad (2.2)$$

By solving the system (2.2), we will have $\boldsymbol{y}$. Finally, the solution of the original system (2.1) can be obtained by applying the equation $x = P\boldsymbol{y}$. Note that if we can not diagonalize matrix A, then we have to determine the Jordan form of matrix A

3. RESULTS AND DISCUSSION

In this section an example will be discussed where all of the eigenvalues of matrix A are equal. Consider the following system of differential equations

$$\begin{aligned} x_1^{(4)} &= 5x_1 + x_3 + \sin(t), \\ x_2^{(4)} &= x_1 + x_2 + \cos(t), \qquad (3.1) \\ x_3^{(4)} &= -7x_1 + x_2 + \sin(t). \end{aligned}$$

To solve the above system, we rewrite the system into a matrix equation as follows:

$$\boldsymbol{x}^{(4)} = A\boldsymbol{x} + \boldsymbol{f}, \text{ where} \qquad (3.2)$$

$$\boldsymbol{x}^{(4)} = \begin{bmatrix} x_1^{(4)} \\ x_2^{(4)} \\ x_3^{(4)} \end{bmatrix}, A = \begin{bmatrix} 5 & 0 & 1 \\ 1 & 1 & 0 \\ -7 & 1 & 0 \end{bmatrix}, \boldsymbol{x} = \begin{bmatrix} x_1 \\ x_2 \\ x_3 \end{bmatrix}, \quad \boldsymbol{f} = \begin{bmatrix} \sin(t) \\ \cos(t) \\ \sin(t) \end{bmatrix}.$$

The eigenvalues of matrix A are $\lambda = 2$, $\lambda = 2$, $\lambda = 2$, and its corresponding eigenvector is

$$\begin{bmatrix} 1 \\ 1 \\ -3 \end{bmatrix}.$$

Since there is only one eigenvector, we can not diagonalize matrix A. Therefore, we have to determine the Jordan form of matrix A, that is,

$$J = \begin{bmatrix} 2 & 1 & 0 \\ 0 & 2 & 1 \\ 0 & 0 & 2 \end{bmatrix}.$$

By letting

$$P = \begin{bmatrix} 1 & a & d \\ 1 & b & e \\ -3 & c & f \end{bmatrix}.$$

and using the equation $AP = PJ$ to obtain the following system of linear equations:

$$\begin{cases} 3a + c &= 1 \\ a - 3d - f &= 0 \\ a - b &= 1 \\ b - d + e &= 0 \\ 7a - b + 2c &= 3 \\ c + 7d - e + 2f &= 0 \end{cases}$$

Solving the above linear system yields matrix P and its inverse as follow:

$$P = \begin{bmatrix} 1 & 0 & 0 \\ 1 & -1 & 1 \\ -3 & 1 & 0 \end{bmatrix}, \text{ and } P^{-1} = \begin{bmatrix} 1 & 0 & 0 \\ 3 & 0 & 1 \\ 2 & 1 & 1 \end{bmatrix}.$$

Now, we can solve the system

$$\boldsymbol{y}^{(4)} = J\boldsymbol{y} + P^{-1}\boldsymbol{f},$$

or

$$\begin{bmatrix} y_1^{(4)} \\ y_2^{(4)} \\ y_3^{(4)} \end{bmatrix} = \begin{bmatrix} 2 & 1 & 0 \\ 0 & 2 & 1 \\ 0 & 0 & 2 \end{bmatrix} \begin{bmatrix} y_1 \\ y_2 \\ y_3 \end{bmatrix} + \begin{bmatrix} 1 & 0 & 0 \\ 3 & 0 & 1 \\ 2 & 1 & 1 \end{bmatrix} \begin{bmatrix} \sin(t) \\ \cos(t) \\ \sin(t) \end{bmatrix}$$

Or

$$\frac{d^4 y_1}{dt^4} = 2y_1 + y_2 + \sin(t),$$

$$\frac{d^4 y_2}{dt^4} = 2y_2 + y_3 + 4\sin(t), \qquad (3.3)$$

$$\frac{d^4 y_3}{dt^4} = 2y_3 + 3\sin(t) + \cos(t).$$

At first, we solve the third equation of the system (3.3) by using undetermined coefficient to obtain :

$$y_3(t) = E_1 e^{\sqrt[4]{2}\,t} + E_2\, e^{-\sqrt[4]{2}\,t} + E_3 \sin(\sqrt[4]{2}\ t) + E_4\cos(\sqrt[4]{2}\ t) - 3\sin(t) - \cos(t). \qquad (3.4)$$

Next, we substitute Equation (3.4) into the second equation of the system (3.3). In a similar way, We can find $y_2(t)$ as follow :

$$y_2(t) = D_1 e^{\sqrt[4]{2}\,t} + D_2\, e^{-\sqrt[4]{2}\,t} + D_3 \sin(\sqrt[4]{2}\ t) + D_4\cos(\sqrt[4]{2}\ t) - \sin(t) + \cos(t)$$

$$+ \frac{E_1}{4\sqrt[4]{8}}t\, e^{\sqrt[4]{2}\,t} - \frac{E_2}{4\sqrt[4]{8}}t\, e^{-\sqrt[4]{2}\,t} - \frac{E_4}{4\sqrt[4]{8}}t\sin(\sqrt[4]{2}\ t) + \frac{E_3}{4\sqrt[4]{8}}t\cos(\sqrt[4]{2}\ t). \qquad (3.5)$$

Finally, by substituting Equation (3.5) into the first equation of system (3.3) and applying the undetermined equation, we have

$$\mathrm{y1(t)} = \mathrm{C1}\, e^{\sqrt[4]{2}\,t} + \mathrm{C2}\, e^{-\sqrt[4]{2}\,t} + \mathrm{C3}\sin(\sqrt[4]{2}\ \mathrm{t}) + \mathrm{C4}\cos(\sqrt[4]{2}\ \mathrm{t}) - \cos(\mathrm{t}) +$$

$$\left(\frac{16D_1 - 3E_1}{64\sqrt[4]{8}}\right)\mathrm{t}\, e^{\sqrt[4]{2}\,t} + \frac{E_1\sqrt{2}}{128}\,\mathrm{t2}\, e^{\sqrt[4]{2}\,t} +$$

$$\left(\frac{-16D_2 + 3E_2}{64\sqrt[4]{8}}\right)\mathrm{t}\, e^{-\sqrt[4]{2}\,t} + \frac{E_2\sqrt{2}}{128}\,\mathrm{t2}\, e^{-\sqrt[4]{2}\,t} +$$

$$\left(\frac{-16D_4 + 3E_4}{64\sqrt[4]{8}}\right)\mathrm{t}\sin(\sqrt[4]{2}\ \mathrm{t}) - \frac{E_3\sqrt{2}}{128}\,\mathrm{t2}\sin(\sqrt[4]{2}\ \mathrm{t}) +$$

$$\left(\frac{16D_3-3E_3}{64\sqrt[4]{8}}\right) t\cos(\sqrt[4]{2}\,t) - \frac{E_4\sqrt{2}}{128}\, t2\cos(\sqrt[4]{2}\,t).$$

Now, we can determine the solution of the original system (3.5) by applying the equation $X = PY$, to obtain

$$x_1(t) = y_1(t),$$

$$x_2(t) = y_1(t) - y_2(t) + y_3(t),$$

$$x_3(t) = -3y_1(t) + y_2(t).$$

4. CONCLUSIONS

A method to solve a system of nonhomogeneous fourth order ordinary differential equations of the form

$$\boldsymbol{x}^{(4)} = A\boldsymbol{x} + \boldsymbol{f}$$

has been discussed by diagonalizing matrix A or finding a Jordan form of matrix A. An example is given with the case where all of the eigenvalues of matrix A are equal.

5. REFERENCES

[1]. Nagle,R.K, 2012, Fundamentals of Differential Equations – 8th edition. Addision – Wesley, Boston.
[2]. An, Yukun, 2008, Ambrosetti-Prodi Type Results In A System Of Second And Forth-Order Ordinary Differential Equations, Electronic Journal of Differential Equations, Vol. 2008, pp. 1–14.
[3]. Dettman, J.U., 1986, Introduction to Linear Algebra and Differential Equations. Dover Publications, Inc, New York.

The Properties Pringheim and Regular Convergence of Doubel Series and Its Application

Moch. Aruman Imron[1]*

[1] Department of Math, Faculty of Mathematics and Sciences of Universitas Brawijaya, Malang, Indonesia
* Corresponding authors: [maimr@ub.ac.id]

Abstract – Wilansky introduced three convergence definitions, which are respectively, Pringsheim, Sheffer and regular convergence. A double series of complex numbers $\{a_{ij}\}$ is said to converges in Pringsheim if the finite the limit of its rectangular partial sums of double series $\{a_{ij}\}$, moreover if single series converges, then the double series $\{a_{ij}\}$, is said to converge regularly. We shall study the properties of Pringsheim convergence and Regular convergence of Double series and its Application.

1. INTRODUCTION

Let $\{a_{ij}\}$ be double sequence of complex numbers and cosider the double sine series

$$\sum_{i=1}^{\infty}\sum_{j=1}^{\infty} a_{ij}\sin ix\sin jy \tag{1}$$

The double sequence of real numbers $\{a_{ij}\}$ is said to be decreasing monotone if

$$\Delta_{10}a_{ij} \geq 0, \Delta_{01}a_{ij} \geq 0, \Delta_{11}a_{ij} \geq 0, i,j = 1,2,3,\ldots$$

Where

$$\Delta_{10}a_{ij} = a_{ij} - a_{i+1,j}, \qquad \Delta_{01}a_{ij} = a_{ij} - a_{i,j+1},$$

$$\Delta_{11}a_{ij} = \Delta_{10}(\Delta_{01}a_{ij}) = \Delta_{01}(\Delta_{10}a_{ij}) = a_{ij} - a_{i+1,j} - a_{i,j+1} + a_{i+1,j+1}.$$

As corresponding the convergence of double series, Wilansky [1] introduced three convergence definition, which are respectively, Pringsheim, Sheffer and regular convergence. Definition of Pringsheim and regular convergence will be given as follows.

Definition 1. *A double series $\sum_{i=1}^{\infty}\sum_{j=1}^{\infty} a_{ij}$ of complex numbers $\{a_{ij}\}$ is said to converges in Pringsheim if the finite the limit of its rectangular partial sums*

$$\sum_{j=1}^{m}\sum_{k=1}^{n} a_{ij}$$

exist as m and n tend to infinity independently of each other, moreover if $\sum_{i=1}^{\infty} a_{in}, n = 1,2,3,\ldots$ *and* $\sum_{j=1}^{\infty} a_{mj}$, $m = 1,2,3,\ldots$ converges, then the double series $\sum_{i=1}^{\infty}\sum_{j=1}^{\infty} a_{ij}$ is said to converge regularly .

Related to double sine series of (1), Imron et. al. [6] introduced regular convergence of double sine series under condition classes of p-Supremum Bounded Variation Double Sequences of first type and p-Supremum Bounded Variation Double Sequences of second type. Furthermore similar to the theorem of Chaundy and Jollife [2], [12], Zak and Sneider proved the following Theorem [9], [10], [11].

Theorem 2. *Suppose that $\{a_{ij}\} \subset \mathbb{R}_+$ is decreasingly tending to zero. Necessary and sufficient conditions for the uniformly regular convergence of the series (1) if and only if $ija_{ij} \to 0$ as $i + j \to \infty$.*

The coefficients of the series (1) are supposed to be member of class of general monotone double sequences to investigate the uniform convergence of double sine series. Imron [7] have introduced class $\mathcal{SBVDS}1_p$ (*p-supremum bounded variation double sequences of first type*) and $\mathcal{SBVDS}2_p$ (*p-supremum bounded variation sequences of second type*), respectively, to extend Theorem 2 stated in the following Definition.

Definition 3. *Let $\alpha = \{a_{ij}\}$ and $\beta = \{\beta_{ij}\}$ be two double sequences of complex and non-negative numbers, respectively. A couple (α, β) is said to be element of class of p-supremum bounded variation double sequences first type, written $(\alpha,\beta) \in \mathcal{SBVDS}1_p$, if there exists $C > 0$ and integer $\lambda \geq 2$ and $\{b_1(l)\}, \{b_2(l)\}, \{b_3(l)\}$, each one converges to infinity, all of them depend only $\{a_{ij}\}$ such that*

$$\text{(i)}\quad \left(\sum_{i=m}^{2m-1}|\Delta_{10}a_{in}|^p\right)^{1/p} \le \frac{C}{m} \max_{b_{1(m)}\le M\le \lambda b_1(m)} \sum_{i=M}^{2M}\beta_{in}, m \ge \lambda, n \ge 1,$$

$$\text{(ii)}\quad \left(\sum_{j=n}^{2n-1}\left|\Delta_{01}a_{mj}\right|^p\right)^{1/p} \le \frac{C}{n} \max_{b_2(n)\le N\le \lambda b_2(n)} \sum_{j=N}^{2N}\beta_{mj}, m \ge 1, n \ge \lambda,$$

$$\text{(iii)}\quad \left(\sum_{i=m}^{2m-1}\sum_{j=n}^{2n-1}\left|\Delta_{11}a_{ij}\right|^p\right)^{1/p} \le \frac{C}{mn} \sup_{M+N\ge b_3(m+n)} \sum_{i=M}^{2M}\sum_{j=N}^{2N}\beta_{ij},$$

$$m, n \ge \lambda,$$

for $1 \le p < \infty$.

Definition 4. *Let* $a = \{a_{ij}\}$ *and* $\beta = \{\beta_{ij}\}$ *be two double sequences of complex and non-negative numbers, respectively. A couple* (a, β) *is said to be element of class of p-supremum bounded variation double sequences of second type, written* $(a, \beta) \in \mathcal{SBVDS}2_p$, *if there exist C > 0 and integer* $\lambda \ge 1$ *and* $\{b(l)\}$, *converging to infinity, depending only* $\{a_{jk}\}$ *such that*

$$\text{(i)}\quad \left(\sum_{i=m}^{2m-1}|\Delta_{10}a_{in}|^p\right)^{1/p} \le \frac{C}{m} \sup_{M\ge b(m)} \sum_{i=M}^{2M}\beta_{in},\quad m \ge \lambda,\quad n \ge 1,$$

$$\text{(ii)}\quad \left(\sum_{j=n}^{2n-1}\left|\Delta_{01}a_{mj}\right|^p\right)^{1/p} \le \frac{C}{n} \sup_{N\ge b(n)} \sum_{j=N}^{2N}\beta_{mj},\quad m \ge 1,\quad n \ge \lambda,$$

$$\text{(iii)}\quad \left(\sum_{i=m}^{2m-1}\sum_{j=n}^{2n-1}\left|\Delta_{11}a_{ij}\right|^p\right)^{1/p} \le \frac{C}{mn} \sup_{M+N\ge b(m+n)} \sum_{i=M}^{2M}\sum_{j=N}^{2N}\beta_{ij},$$

$$m, n \ge \lambda,$$

for $1 \le p < \infty$.

Theorem 5. *If* $1 \le p < \infty$, *then* $\mathcal{SBVDS}1_p \subseteq \mathcal{SBVDS}2_p$.

For single series, Imron et. al. [4], [5] introduced theorem 6 as follows.

Theorem 6. *Let* $(a, \beta) \in \mathcal{SBVS}2_p$, *if* $n^{1-1/p} \sup_{m\ge b_n} \sum_{k=m}^{2m}\beta_{kj} = o(1)$, *for* $1 \le p < \infty$, *then series (3) converges uniformly on* $(0, 2\pi]$.

For double series, Imron [8] introduced Theorem 7 as follows.

Theorem 7. *Let* $(a, \beta) \in \mathcal{SBVDS}2_p$. *If* $(m, n) \in \mathbb{N}X\mathbb{N}$ *and*

$$\left\{ (mn)^{2-\frac{1}{p}} \sup_{M+N\ge b(m+n)} \sum_{j=M}^{2M}\sum_{k=N}^{2N}\beta_{jk} \right\}$$

converges to 0 for $m + n \to \infty$. *then*

$$mn\sum_{j=m}^{\infty}\sum_{k=n}^{\infty}\left|\Delta_{11}a_{jk}\right| \le C(mn)^{2-\frac{1}{p}}\left(\sup_{M+N\ge b(m+n)} \sum_{j=M}^{2M}\sum_{k=N}^{2N}\beta_{jk}\right),$$

holds for p, $1 \le p < \infty$.

In the present paper, by an idea about some convergence definition and combining by definition of p-supremum bounded variation double sequences [7], we investigate convergence of double cosine series related to Pringsheim and regular uniformly convergence.

2. METHODS

This research was done by study of literature both books and the supporting scientific journals to get a well understanding then develop the results related to the research that has been published in the journal. The results of this research are communicated in a seminar. the method of the research are studying the class p-supremum bounded variation double sequences of first type ($\mathcal{SBVDS}1_p$) and second type ($\mathcal{SBVDS}2_p$) with $1 \le p < \infty$, which is hold for $n \ge \gamma$, with $\gamma \ge 1$ to prove the convergent of double cosine series.

3. RESULTS AND DISCUSSION

In this section, we prove some results class of p-supremum bounded variation double sequences related to Pringsheim and regular convergence of double cosine series. In the next discussion, let $n \in \mathbb{N}$ and $\beta = \{\beta_{ij}\}$ be sequences non-negative numbers.

Let $\{a_{ij}\}$ be double sequence of complex numbers and cosider the double sine series

$$\sum_{i=1}^{\infty}\sum_{j=1}^{\infty} a_{ij}\cos ix\cos jy, \tag{2}$$

$$\sum_{i=1}^{\infty} a_{ij}\cos ix, \tag{3}$$

$$\sum_{j=1}^{\infty} a_{ij}\cos jy \tag{4}$$

Theorem 8. *Let* $(a,\beta) \in \mathcal{SBVDS}2_p$, $1 \le p < \infty$. *If condition Theorem 6 and Theorem 7 is satisfied then the series (2) is convergence regular uniformly at (x,y) for all* $0 \le x, y \le \pi$ *if and only if* $\sum_{i=1}^{\infty}\sum_{j=1}^{\infty} a_{ij}$ *is convergence regularly*

Proof.

(i) We show that the double series $\sum_{i=1}^{\infty}\sum_{j=1}^{\infty} a_{ij}$ is convergence regularly. Let series (2) convergence regular uniformly. For $(x,y) = (0,0)$ we have series (2) $\sum_{i=1}^{\infty}\sum_{j=1}^{\infty} a_{ij}\cos 0\cos 0 = \sum_{i=1}^{\infty}\sum_{j=1}^{\infty} a_{ij}$. It can be concluded that the series $\sum_{i=1}^{\infty}\sum_{j=1}^{\infty} a_{ij}$ is regular convengence.

(ii) Let the double series $\sum_{i=1}^{\infty}\sum_{j=1}^{\infty} a_{ij}$ is regular convergence. Following an idea from Moricz [3], we represent the rectangular partial sums

(iii)

$$S_{mn}(x,y) = \sum_{j=1}^{m}\sum_{k=1}^{n} a_{jk}\cos jx\cos kx\,,\quad m,n \ge 1,$$

of series (2) to perform a double summation by part yields

$$S_{mn}(x,y) = \sum_{j=1}^{m}\sum_{k=1}^{n} D_j(x)D_k(y)\Delta_{11}a_{jk} + \sum_{k=1}^{n} D_m(x)D_k(y)\Delta_{01}a_{m+1,k} + a_{m+1,n+1}D_m(x)D_n(y) \tag{5}$$

where D_n Dirichlet kernel defined as

$$D_n(x) = \frac{1}{2} + \sum_{k=1}^{n}\cos kx = \frac{\sin(n+\frac{1}{2})x}{2sin\frac{1}{2}x}, n \ge 0$$

and $|D_n(x)| \le \frac{\pi}{2x}$ for $x \in (0,\pi]$.

By Theorem 7, we obtained

$$\sum_{j=1}^{\infty}\sum_{k=1}^{\infty}\left|\Delta_{11}a_{jk}\right| < \infty$$

Thus

$$\sum_{j=1}^{\infty}\sum_{k=1}^{\infty}\left|D_j^*(x)D_k^*(y)\Delta_{11}a_{jk}\right| < \infty \tag{6}$$

By condition, the series $\sum_{i=1}^{\infty}\sum_{j=1}^{\infty} a_{ij}$ is convergence, we have

$$\left|a_{jk}\right| \to 0, \text{ for } j+k \to \infty \tag{7}$$

Further

$$\Delta_{10}a_{j,n+1} = \sum_{k=n+1}^{\infty}\Delta_{11}a_{jk}.$$

and

$$\sum_{j=1}^{\infty}\left|\Delta_{10}a_{j,n+1}\right| \le \sum_{j=1}^{\infty}\sum_{k=n+1}^{\infty}\left|\Delta_{11}a_{jk}\right| \to 0 \text{ as } n \to \infty.$$

This implies that, for all $0 < x, y \le \pi$

$$\sum_{j=1}^{m} D_j^*(x)D_n^*(y)\Delta_{10}a_{j,n+1} \to 0 \text{ as } n \to \infty, \tag{8}$$

uniformly in m. Similarly, for all $0 < x, y \le \pi$

$$\sum_{k=1}^{n} D_m^*(x)D_k^*(y)\Delta_{01}a_{m+1,k} \to 0 \text{ as } m \to \infty, \tag{9}$$

uniformly in n. By (7)

$$a_{m+1,n+1}D_m^*(x)D_n^*(y) \to 0 \text{ as } m+n \to \infty. \tag{10}$$

Consequently by (5), (6), (8), (9) and (10)

$$S_{mn}(x,y) \to 0, \text{as } m+n \to \infty.$$

For single cosinus series (3) and (4), by Theorem 6, we have uniform convergence . By Definition 1 it can be concluded that series (2) is convergence regular uniformly at (x, y) for all $0 \leq x, y \leq \pi$.. From (i) and (ii) the proof is complete.

Theorem 9. *Let* $(a, \beta) \in \mathcal{SBVDS}_p$, $1 \leq p < \infty$. *If condition Theorem 7 and is satisfied then the series (2) converges in Pringsheim sense at* (x, y) *for all* $0 \leq x, y \leq \pi$ *if and only if that the series* $\sum_{i=1}^{\infty}\sum_{j=1}^{\infty} a_{ij}$ *is convergence in Pringsheim sense*

Proof. *The proof is similar to proof of Theorem 8, we have series (2) converges in Pringsheim sense at* (x, y) *for all* $0 \leq x, y \leq \pi$ *if only if that the series* $\sum_{i=1}^{\infty}\sum_{j=1}^{\infty} a_{ij}$ *is convergence in Pringsheim sense.*

4. CONCLUSIONS

In this paper we have introduced the class of $\mathcal{SBVDS}2_p$. We have investigated that:

(i) Let $(a, \beta) \in \mathcal{SBVDS}2_p$, $1 \leq p < \infty$. If condition Theorem 6 and Theorem 7 is satisfied then the series (2) is convergence regular uniformly at (*x,y*) for all $0 \leq x, y \leq \pi$ if and only if $\sum_{i=1}^{\infty}\sum_{j=1}^{\infty} a_{ij}$ is convergence regularly.

(ii) *Let* $(a, \beta) \in \mathcal{SBVDS}_p$, $1 \leq p < \infty$. If condition Theorem 7 and is satisfied then the series (2) converges in Pringsheim sense at (x, y) *for all* $0 \leq x, y \leq \pi$ if and only if that the series $\sum_{i=1}^{\infty}\sum_{j=1}^{\infty} a_{ij}$ is convergence in Pringsheim sense

5. ACKNOWLEDGEMENTS

The authors gratefully acknowledge the support of the Department of Mathematics FMIPA UB and FMIPA UB.

6. REFERENCES

[1]. A. Wilansky, On the convergence of double series, *Bull Amer. Math. Soc*, 53, no. 8 793-799, 1947.

[2]. A. Zygmund, *Trigonometric Series,* Vol I, II, Second ed, Cambridge Univ. Press, 1959.

[3]. F. Moricz, On Integrability and L^1-convergence of Double Trigonometric Series, *Studia Math.* 98 (3), 1991.

[4]. M, A. Imron, C. R Indrati and Widodo, On uniform convergence of trigonometric series under *p*-supremum bounded variation condition**,** *Proceeding of the third Basic International Conference*, , FMIPA, UB, Malang. M041-M043, 2013

[5]. M.A. Imron, C. R. Indrati and Widodo, Some properties of class of p-Supremum bounded Variation sequences, *Int.Journal of Math. Analysis,* Vol 7, no.35, 1703-1713, 2013.

[6]. M.A. Imron, C. R. Indrati and Widodo, on uniform convergence of double sine series under condition of *p*-supremum bounded variation double sequences, *Int.Journal of Math. Analysis,* Vol 7, no.51, 2535-2548, 2013.

[7]. M, A. Imron, A New Condition of p-Supremum Bounded Variation Double Sequences, *Proceeding of the sixth Basic International Conference*, FMIPA, UB, Malang. 317-320, 2016

[8]. M.A. Imron, Some convergence of double sine series and convergence *p*-Supremum bounded variation double sequences, *American Institute of Physics*, 2017.

[9]. P. Korus, Remark On the uniform and L^1-Convergence Of Trigonometric Series, *Acta Math. Hungar*, 128(4), 2010.M. P. Brown and K. Austin, Appl. Phys. Letters **85**, 2503–2504 (2004).

[10]. P. Korus, On the uniform Convergence Of Double sine series with generalized monotone coefficients, *Periodica Math. Hungar*, 63, 205-214, 2011.

[11]. P.Korus and F. Moricz, On the uniform convergence of Double sine series, *Studia Math*., 193 79-97, 2009.

[12]. T.W. Chaundy and A.E. Jollife, The Uniform Convergence of certain class trigonometric series, Proc. London, Soc. 15, 214-116, 1916.

SFH (Smart Floating Harbour): Smart Harbour With Harbour-Tourism Concept Based On Graph Analysis Of Simpang 5 Semarang

Rezki S.[1*]

[1] Diponegoro University, Semarang
* Corresponding authors: [rezkisuryadinata@gmail.com]

Abstract – There are many applications of graph theory, like in schedule, transportation, and others. Harbour is one of an important element of water transportations. There is some research about floating harbour in Indonesia, however there should be more research especially about optimized design of harbour. Simpang 5 Semarang is located in the center city of Semarang. Simpang 5 is a road that connects with some area in Semarang. For example, if someone want to go to area in Semarang he can pass Simpang 5. Simpang 5 can be transformed into the graph form then giving the analysis of Simpang 5. From the analysis of simpang 5, the result will be applied in Smart Floating Harbour, the design of SFH will be created from the analysis of Simpang 5 graph. Graph simpang 5 has a six vertices which is strongly connected or there is a walk which connects one vertice to the other vertice. Representation of the analysis that SFH will have strongly connected and there is a center vertice which connected to every vertices of the graph. From the design there is a conclusion that floating harbour is not impossible building to build. Graph theory was also used in case to locate the SFH in Indonesia

1. INTRODUCTION

History had recorded that far away before there was Indonesia, Sriwijaya castle has been a transit of International cruise. Indonesia is known as a maritime country, this is the only a simple example of sweet history of Indonesia that in fact, Indonesia has been a maritime country.

The government of Indonesia has been giving the focus in the maritime sector, which is looked from Indonesia masterpiece and Nawacita program of Mr. Joko Widodo. However, there are less of implementation of this program.

Building harbor is one of an effective solution to create a maritime country, harbor is one of the asset which has given maximum foreign exchange to Indonesia because of vital condition of itself. Indonesia should imitate harbour of the other country. For example from Hamburg, which is not located near to the sea, but could be the wealthiest country in the Germany with the foreign exchange 50.000 euros each year from the harbor.

Floating harbour is a harbour which is located in the water and not in the land. This is a new generation of transshipment, and transit in the cruise [1]. Transshipment is one of main function of the harbour, and if the harbor location on the sea so there are less cost, and there are some efficient result like efficient of time, fuel, etc. Finally floating harbour will increase some income to fisherman, and for Indonesia itself.

In the graph analysis, first of all, we transform the maps to graph form, and following action is counting vertices, line or arch, and some characters of graph, like euler graph, or strongly connected graph, etc. Design of SFH has similiar number of vertices, and character from itself.

This paper is divided into four main sections and organized as follows: in section 3.1 we have the special analysis of simpang 5 graph collect the data from google maps and satellite record. In section 3.2 we create the SFH design from the analysis in section 3.1, and in section 3.3 we have SFH location in Indonesia use a minimum spanning tree.

2. METHODS

The Method of this research is a literature study research, the research made according to the research before with the floating harbour theme, or with the graph study instead. Some literature that used in this research are mentioned in the references below, for example for the graph research writer use Tero Harju book with the title “Lecture Notes on Graph Theory” from this book we use the definition of graph, and do the analysis regarding this book.

The procedure of research are first we convert the simpang 5 map into the graph form, which has 6 vertices, then we do the analysis, like count vertices from the graph, what kind of graph (euler, or hamilton, etc.), after performing the analysis, we design SFH based on the analysis before, It's inspired by an architect when design a bridge sometime using body from some animal, so the architect can also get any inspired for design. There are some considerations like endurance, the capacity of the building. After that we do the graph analysis again and from the second analysis we can find similiar character from the SFH graph analysis with Simpang 5 analysis because we made the design from simpang 5 graph analysis. Finally choose the location of SFH with consideration of international cruise, wave, earthquake potential, tourism, wind condition.

3. RESULTS AND DISCUSSION

3.1 Analysis Graph of Simpang 5 Semarang

Simpang 5 Semarang is located in the center of Semarang city in center of java, the function of simpang 5 is not for road in Semarang, the other function is for tourism, market, and other activity, which is this function will be implicated in SFH. Before we go to the graph analysis the graphic below is maps of Simpang 5 Semarang

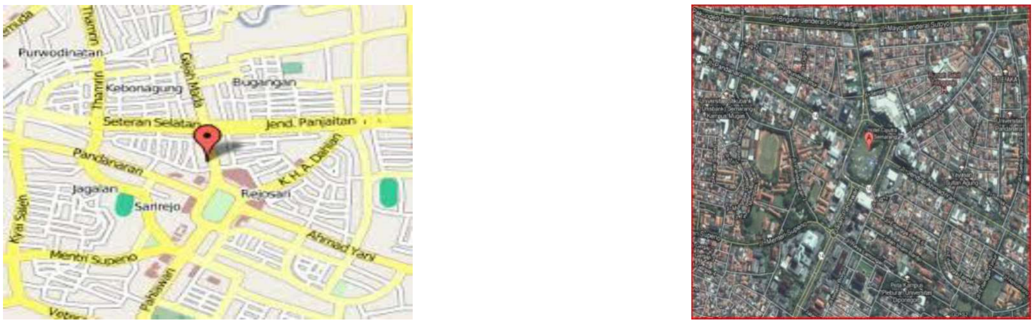

(a) (b)

Figure 1. (a) Maps of Simpang 5 Semarang from google maps (b) Maps of Simpang 5 Semarang from satellite record

From the figure 1 we get the information that there is 5 way from simpang 5 street which is why its called simpang 5 or five ways, the other information is simpang 5 is connected 5 big roads in Semarang. That is KH. A. Dahlan street, Pandanaran street, Ahmad yani street, Pahlawan street, and Gajah mada street. The other data of Simpang 5 is even there are 5 way in Simpang 5, there are less traffic in Simpang 5 although there are many transportation choose simpang 5 to reach some place in Semarang.

There should be something special from Simpang 5 so we are analize the graph of Simpang 5 Semarang, to transform maps of Simpang 5 we need some element of graph itself, like vertices and line. As we know that one graph call connected if there is a line between 2 vertices [2]. Technique of transform the maps into the graph, first pick one of area like street or building in Simpang 5 area and that area will be vertices in the graph. And an arrow of the road will be an arch in graph. This analysis has been done by pick vertices and arch by the real condition of the road from the satellite record and from google maps. Figure below is a graph of Simpang 5

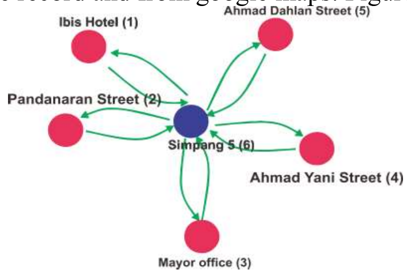

Figure 2. Graph of Simpang 5 Area

Let the graph above be an A digraph, and from the graph above the result are:

1. There are 6 vertices from the digraph, A= {1,2,3,4,5,6}
2. There are 10 arch in digraph A
3. For 1,2,3,4,5 vertices there are 1 arch in, and 1 arch out
4. For the 6 vertice there are 5 arch in, and 5 arch out
5. For every vertices in A there are a walk which is connected one vertices to the other vertices, example: although verice 1 and 2 is not connected with an arch, but there are a walk from 1 to 2, one of them is 1-6-2.

6. From the fifth point we get that A is strongly connected graph
7. From the third and fourth point we get that A is Euler digraph (for every vertices in A, degree in = degree out)

If digraph A representated into the adjacent matrix get the result below

$$A = \begin{pmatrix} 0 & 0 & 0 & 0 & 0 & 1 \\ 0 & 0 & 0 & 0 & 0 & 1 \\ 0 & 0 & 0 & 0 & 0 & 1 \\ 0 & 0 & 0 & 0 & 0 & 1 \\ 0 & 0 & 0 & 0 & 0 & 1 \\ 1 & 1 & 1 & 1 & 1 & 0 \end{pmatrix} \qquad (1)$$

From the matrix we get that there is a “center vertice” from the graph which is connected with every vertices beside itself there is 6 vertice. This matrix ease the analysis of the graph and the result will use to consider the design of smart floating harbour.

3.2 Smart Floating Harbour Design Based on Graph Analysis

The analysis before will be aplicated in SFH design, SFH is a floating harbour with harbour and tourism concept. The harbour has 2 function as a harbour, and as a tourism building. As a harbour SFH has a main function there are transhipment, cargo, international cruise transit, etc. And as a tourism building SFH will be one of tourism destination specially for the people who transit in SFH. Figure below is a design of SFH.

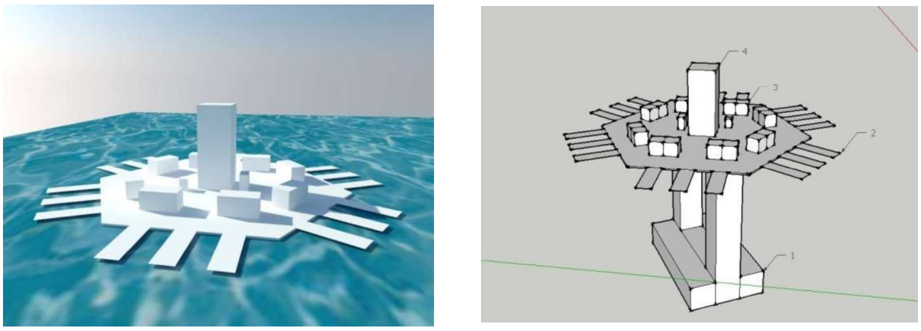

Notes:
1. Pile jacket foundation
2. Dock
3. Cargo
4. Main building

(a) (b)

Figure 3. (a) Design of SFH up section (b) design all of part from SFH

SFH has been made using analysis of graph A before, and let SFH be graph B, from the design we get:

1. There are 19 vertices from B, B={1, 2, 3, 4, 5, 6, 7, 8, 9, 10, 11, 12, 13, 14, 15, 16, 17, 18, 19}
2. B has a center point which is 19 vertice
3. B are strongly connected graph
4. B are graph euler (every vertice in B has even number)

That prove that graph could be aplicated in design of building (in this case the building is a harbour), by the analysis before design can fulfill the need as a harbour and as a tourism building, and the most important SFH is a floating harbour so it can located in the sea [3].

From the design in figure 3 that is mention that the SFH use pile jacket technique on foundation, which is inspirated from the offshore. As we know the offshore usually located in the middle of ocean surface, so this foundation can hold ocean wave. As mention before SFH has a floating structure and designed from analysis of simpang 5 graph. SFH has a 18 dock, which divided into 6 part, for every part has 3 dock instead. Every part has some function for international transit, for ship of local fisherman, for ship of sea patrol, etc. 18 dock is an optimum number to fulfill the ship needs. Harbour use a corrosive protector with anodic method, because consideration from the price, efficient, etc.

3.3 Location of the SFH

SFH will be placed in Indonesia, and to choose the location we use the graph theory specially for minimum spanning tree algorithm. Choice of SFH location is most important in this case, because if SFH will use in international transit, so the location have to support international cruise itself. Location choosen with consideration from ocean wave of Indonesia, and also from a cost to build the harbour itself, by the consideration before we get three best location of SFH. The result will be presented in figure below

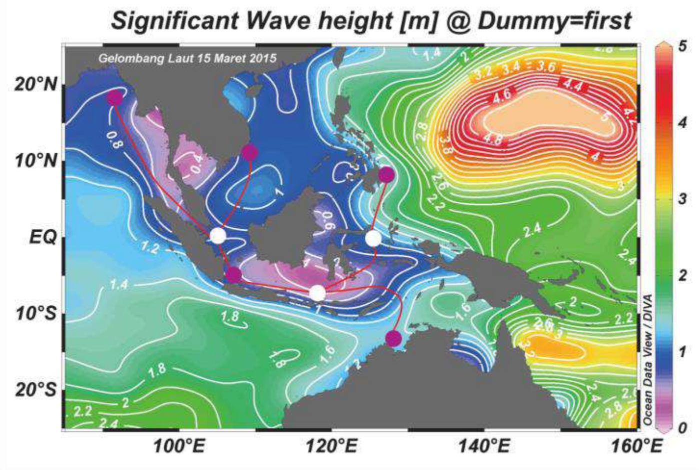

Figure 4. Location of SFH in Indonesia ocean

Location of SFH represent with the white dot in the figure 4, From the figure above there are 3 strategic location of Smart floating harbour, there are located on North Batam Sea, Sulawesi sea, and Sawu Sea, Flores. From the figure 4 SFH location presented in white vertices. From the spanning tree above, the tree location is a strategic location to SFH specially with harbour and tourism concept. Tree location above has a beautiful view of nature, and also with harbour itself because the condition of the wave is the most possible to build SFH. The othe consideration from location is the location support international cruise transit, when the cruise start from Australia, sailor can took a route Australia, Flores, Tanjung priok, Batam, and goes to the north to the Asia.

Potential from build 3 harbour come from the income of harbour activity, from the data of PT. Pelindo II harbour in Indonesia will get income around 2 trillion for 1 year, the income will increase because it comes from other aspect like harbour and tourism. So SFH is great business, to Indonesia.

4. CONCLUSIONS

SFH made inspired by the graph analysis of Simpang 5, it is inspired by an architect when designing a bridge sometime using the body of an animal, so the architect can also get any inspired for design. This research shows the similar character between graph analysis of design SFH and Simpang 5 Semarang, because of the design SFH we consider the graph analysis from Simpang 5 Semarang. From the design in figure 3, it is mentioned that the SFH use pile jacket technique on foundation, which is inspired from the offshore. As we know the offshore usually located in the middle of ocean surface, so this foundation can hold ocean wave. As mention before, SFH has a floating structure and designed from analysis of simpang 5 graph. SFH has a eighteen docks which are divided into six parts, for every part has three docks. Each part has some function for international transit, for a ship of local fisherman, for ship of sea patrol, etc. Eighteen docks is an optimum number to fulfill the ship needs Harbour use a corrosive protector with the anodic method, because of consideration from the price, efficient, etc.

Location of SFH represent with the white dot in the figure 4, From the figure above there are three strategic locations of Smart floating harbour, there are located on North Batam Sea, Sulawesi sea, and Sawu Sea, Flores. From the figure 4 SFH location presented in white vertices. From the spanning tree above, the tree location is a strategic location to SFH especially with harbour and tourism concept. Three locations above have beautiful views of nature, and also with harbour itself because the condition of the wave is the most possible to build SFH. The other consideration from location is the location support international cruise transit, when the cruise start from Australia, sailor can took a route Australia, Flores, Tanjung priok, Batam, and goes to the north to the Asia.

5. REFERENCES

[1] T. Harju, 2011, *Lecture Notes on Graph Theory*, Turku University press, Finland
[2] G.J. Macfarlane, 2015, *The Floating Harbour Transhipper: New-Generation Transhipment Of Bulk Ore Products*, Canada.
[3] R.J. Ballantyne, G.J.Macfarlane, S.E.Ballantyne, and T. Lilienthal, 2012, *The Floating Harbour Transhipper – An Operationally Effective Solution For Military and Emergency Response Duties, Proc. of the Pasific 2012 Int. Maritime Conference*, Australy

Segmentation of Leaf Spot Disease on Apples Plants by Using Fuzzy C-Means Algorithm

Syaiful Anam[1*]

[1] Department of Mathematics, Faculty of Mathematics and Natural Sciences,
Brawijaya University, Malang, Indonesia
* Corresponding authors: [syaiful@ub.ac.id]

Abstract – Apple is an identity of Batu and Malang Cities. Especially, Batu City has many apple industries, such as apple porridge, apple vinegar, apple chips, and other products from apple. They employ more than 100,000 workers. Leaf spot disease on the apple tree is one disease that often appears on the apple tree in Batu City. It causes a decrease in apple production significantly. Early detection of this disease will increase the quality and number of the apple production. The usage of drones to detect the leaf spot disease is an alternative to prevent the apple production in the large area. For detecting the leaf spot disease of the apple plant, the apple leaf image taken by the drone needs to be segmented into infected and healthy leaves. In this paper studied how to segment leaf spot disease on apple leaf by Fuzzy C-means Algorithm. Fuzzy C-means Algorithm has demonstrated the advantage over crisp clustering algorithms in dealing with the challenges posed by large collections of vague and uncertain. It is a well-known unsupervised clustering method, which can be used for unsupervised image segmentation. The first step in the proposed method is that the image of the leaves is converted from RGB format to format CIE L*a*b. The reddish-greenish and yellowish-bluish components of the format CIE L*a*b are taken. The last step is that the color channels of the image are segmented by using Fuzzy C-means Algorithm. For evaluating the performance of this method, we use the image of the apple leaves infected by leaf spot disease. The number of the leaves used is six varied imagery. From the experimental results, it can be seen that the proposed method can segment the leaf spot disease successfully. The experiments show that the Fuzzy C-means Algorithm successfully segment leaf spot disease for almost all the images used.

1. INTRODUCTION

Apple is an identity of Batu and Malang Cities. Especially, Batu City has many apple industries, such as apple porridge, apple vinegar, apple chips, and other products from apple. They employ more than 100,000 workers. Leaf spot disease on the apple tree is one disease that often appears on the apple tree which causes a decrease in apple production significantly. Early detection of the leaf spot disease will increase the quality and number of the apple production. The usage of drones to detect the leaf spot disease is an alternative to prevent the apple production in the large area. For detecting the leaf spot disease of the apple plant, the apple leaf image taken by the drone. The next step that the apple leaf images are segmented into infected and healthy leaves.

Image segmentation method could be applied for segmenting leaves into infected and healthy leaves. The goal of image segmentation is to partition an image into a set of disjoint regions with uniform and homogeneous attributes such as intensity, color, tone or texture, etc [1]. According to reference [2], the image segmentation approaches can be divided into four categories: thresholding, edge detection, region extraction and clustering. The thresholding method has some disadvantages, such as highly dependent on peaks and spatial details are not considered [3]. While the region extraction method is an expensive method in terms of time and memory [3]. Edge detection method is sensitive to noise and produces inaccurate result [4]. For this reason, a clustering based method for image segmentation will be considered in this paper.

Clustering is the process of grouping objects based on its characteristics, so that all members of each cluster has a certain similarity based matrix. The clustering methods are divided into two categories: the conventional hard clustering and the fuzzy clustering. The conventional hard clustering method restricts each point of the dataset to exclusively just one cluster. As a consequence, with this approach the segmentation results are often very crisp, i.e., each pixel of the image belongs to exactly just one class. However, in many real situations, for images, issues such as limited spatial resolution, poor contrast, overlapping intensities, and noise and intensity in homogeneities variation make this hard segmentation a difficult task [5]. Due to the fuzzy, set theory [6] was proposed, which produced the idea of partial membership of belonging described by a membership function, fuzzy clustering as a soft segmentation method has been widely studied and successfully applied in image segmentation. Among the fuzzy clustering methods, fuzzy c-means (FCM) algorithm [7] is the most popular method used in image segmentation. The Fuzzy C-Means algorithm (FCM), as one of the best known and the most widely used fuzzy clustering algorithms, has been utilized in a wide variety of applications. It has robust characteristics for ambiguity and can retain much more information than hard segmentation methods [8]. For this reason, this paper proposes Fuzzy C means to segment leaf spot disease on the apple leaf.

2. METHODS

In this paper proposes a method for segmenting leaf spot disease on apple leaf by using Fuzzy C-means Algorithm. The flowchart of the proposed method can be seen in Figure 1.

2.1 Convert Image from RGB Format in CIE L*a*b Format

We use the image data of leaves infected by leaf spot disease. The image has a format RGB (Red, Green, Blue). After analyzing the image of the RGB format, each component of R, G or B cannot distinguish the leaves infected by leaf spot disease and healthy leaves. Grayscale images from the RGB image of the leaf also cannot differ the leaf infected by leaf spot disease and healthy leaf. The other format for representing an image is CIE L*a*b format. It aspires to perceptual uniformity, and its L component closely matches human perception of lightness. After analysis, we obtain the reddish-greenish components on the image of leaf format CIE L * a * b which can distinguish the image of leaves infected with the image of healthy leaves. Hence the image of leaf format RGB needs to be converted to image format CIE L * a * b. CIE L * a * b has an element L (Luminance), a (range from green to red) and b (range from blue to yellow). The first step in the proposed method is that the image of the leaves is converted from RGB format to format CIE L*a*b. Figure 2 shows each component CIE L*a*b image. The reddish-greenish (Figure 2(b)) and yellowish-bluish (Figure 2(c))components of the format CIE L*a*b can differ the healthy area and infected area. For this reason, we take these components for segmentation in the next step. The last step is that the color channels of the image are segmented by using Fuzzy C-means Algorithm.

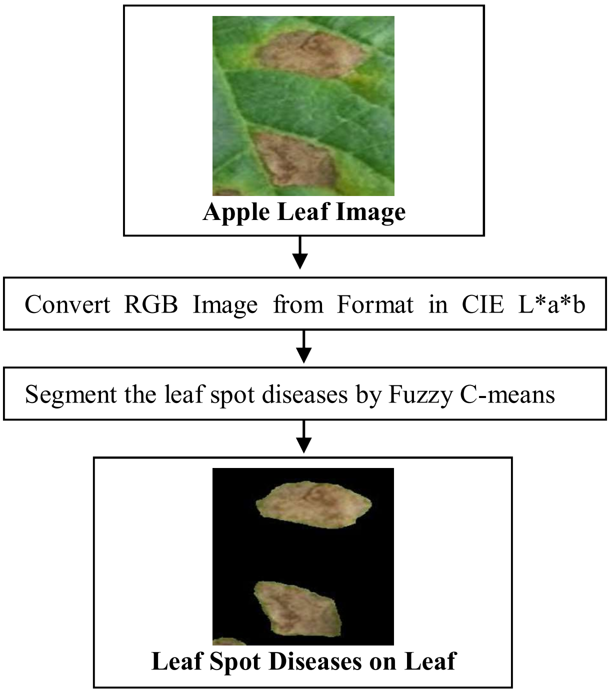

Figure 1 Flowchart of the proposed method

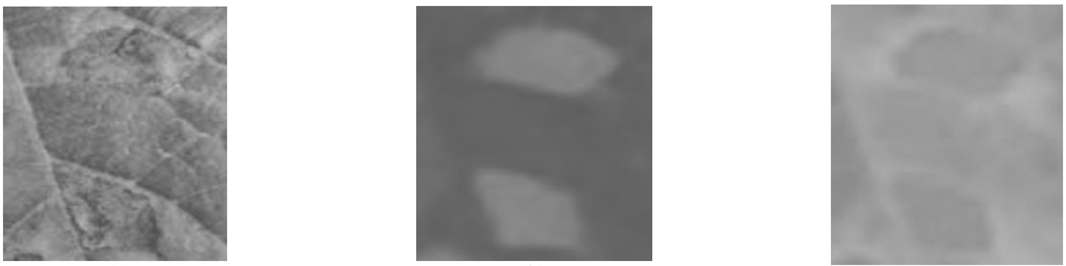

(a) (b) (c)

Figure 2 CIE L*a*b Image. (a) L Component. (b) a Component. (c) b Component.

2.2 Segment the leaf spot diseases by Fuzzy C-means

The next step is that the leaf spot disease in apple plant is segmented by using Fuzzy C-means algorithm. The algorithm can be seen in the following.

Input : X (matrix n x m), where *n* is the number of pixels in the leaf image and *m* is the number of components
image (the reddish-greenish and yellowish-bluish components).
c (≥ 2) is the number of cluster. We use c=2 because we want to segment into two areas (the healthy area and infected area) and $w = 2$ (weighted)
MaxIt (Maximum iteration)
ξ (Termination Criteria)

Output : V (Cluster Center)
U (Partition Matrix)

Step in Fuzzy C-means Algorithm

1. {Initialization}
   t=1; Δ=1.
2. Generate partition matrix, U^0.
3. While ($\Delta \geq \xi$ and t<MaxIt) do
    4. Calculate cluster center (*V*) for each cluster by using Equation (1).
$$v_{ij} = \frac{\sum_{k=1}^{n}(\mu_{ik})^{w}\, x_{kj}}{\sum_{k=1}^{n}(\mu_{ik})^{w}} \tag{1}$$
    5. Calculate distance each data to each cluster center (d_{ik}) by using Equation (2).
$$d_{ik} = d(x_k, v_i) = \sqrt{\sum_{j=1}^{m}\left(x_{kj} - v_{ij}\right)^2}. \tag{2}$$
    6. Update the membership degree for each object on each *cluster* (update partition matrix) by using Equation (3).
$$\mu_{ik} = \left[\sum_{j=1}^{c}\left(\frac{d_{ik}}{d_{jk}}\right)^{1/(w-1)}\right]^{-1}. \tag{3}$$
    7. Calculate objective function by using Equation (4).
$$J_w(U, V; X) = \sum_{k=1}^{n}\sum_{i=1}^{c}(\mu_{ik})^{w}\, d_{ik}, \tag{4}$$
       with constrained
$$\sum_{i=1}^{c}\mu_{ik} = 1, 1 \leq k \leq n.$$
    8. Calculate the difference of partition matrix on the current iteration with the previous iteration, by using Equation (5).
$$\Delta = \|U^{t} - U^{t-1}\|. \tag{5}$$
    9. $t = t + 1$.

3. RESULTS AND DISCUSSION

For evaluating the performance of the proposed method, we use the six images of the apple leaves infected by leaf spot disease. The various apple leaf images for evaluating are shown in Figure 3 (a)- 3 (f). Figure 2 (b) and Figure 2 (c) display redness-greenish and yellowish-bluish components of the image in Figure 2 (a) respectively. It can be seen that the reddish-greenish and yellowish-bluish components can differentiate between areas infected by spot diseases and healthy areas. Compared the yellowish-bluish component, the reddish-greenish component can distinguish between the areas infected by spot diseases and healthy areas better. Figure 2(b) shows that the areas affected by leaf spot are shown by bright area and healthy areas are shown by a dark area.

The images of Figures 3 (g) - 3 (l) show the segmentation results by using the fuzzy C-means algorithm. Figures 3(g)- 3 (l) show that the proposed method successfully segments between the areas infected by spot diseases and healthy areas for almost all images. However, this method fails to differ the areas infected by the spot diseases and healthy areas in several area as shown in Figure 3 (i). It is caused by the reddish-greenish component cannot differ the areas infected by spot diseases and healthy areas well as shown in Figure 4 (a). Since some healthy areas have similar color

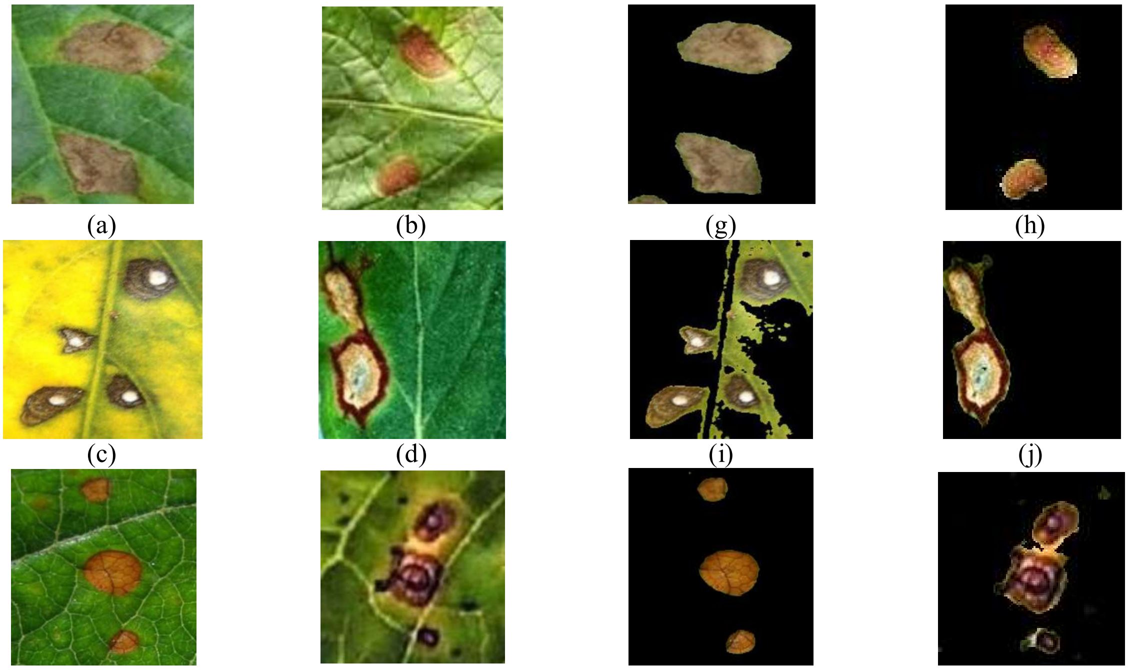

(a) (b) (g) (h)
(c) (d) (i) (j)
(e) (f) (k) (l)

Figure 3 (a)-(f). Image before segmentation. (g)-(l) Image segmented by Fuzzy C-means algorithm.

(a) **(b)**

Figure 4. (a) The reddish-greenish component of Figure 3 (c). (b) The yellowish-bluish component of Figure 3 (c).

intensity with the infected areas which is caused by the variations of the image luminance, it causes missed classification. To solve this problem, it needs to try other operation to reduce the variations of the image luminance.

4. CONCLUSIONS

The reddish-green and yellowish-bluish components of the leaf images in the CIE L*a*b format are able to distinguish between leaves infected by leaf spot disease and healthy leaf. The fuzzy C-means algorithm successfully segments leaf spot disease for almost all of the images used.

5. REFERENCES

[1]. V. Hlaváč, M. Šonka, R. Boyle, 1999, Image Processing, Analysis and Machine Vision.
[2]. Y. Yang, S. Huang, 2007, *Computing and Informatics*, **26**, 17–31.
[3]. D. Kaur, Y. Kaur, 2014, Int. *J. of Computer Science and Mobile Computing*, **3 (5)**, 809-814.
[4]. Y. Yang, C. Zheng, and P. Lin, 2005, *Opto-Electronics*, **13(4)**, 309–315.
[5]. L.A. Zadeh, 1965, *Inform. and Control*, **8**, 338–353.
[6]. J. C. Bezdek, 1981, Pattern Recognition with Fuzzy Objective Function Algorithms, Plenum Press.
[7]. D. Pham, 2001, *Computer Vision and Image Understanding*, **84 (2)**, 285–297.
[8]. J. Bezdek, L. Hall, and L. Clarke, 1993, *Medical Physics*, **20 (4)**, 1033–1048.

Developing Programming of A Quantum Walks Algorithm Using MATLAB

Lila Yuwana *1, Agus Purwanto 1

1 Department of Physics, Faculty of Mathematics and Science, Institut Technology of Sepuluh Nopember, Surabaya 60111, Indonesia
* Corresponding authors: [lila@physics.its.ac.id]

Abstract – There are numerous ideas that have been provided by quantum walks for new quantum algorithms. In this paper, we surveyed the discrete quantum walk to study a step of quantum walk. Moreover, we transformed the step into a programming algorithm. Finally, a MATLAB programming was developed to generate rapid and accurate calculation of a quantum walk problems.

1. INTRODUCTION

An efficiency is a key to sustaining quantum information researches. The consequence of that is from a few decades, researchers have been pursuing cutting-edge methods in order to solve hard problems.

One of interesting quantum algorithms is quantum walks algorithm. Quantum walk coined by Aharonov in 1993 as a quantum random walk that was utilized in a quantum-optics application [1]. In 2003, Kempe [2] revealed that quantum walk has an essential role in quantum computation, hence will be deployed to provision breakthrough and fast algorithms. Therefore, those algorithms could be run on a quantum computer. This paper also showed valuable information of quantum random walks introduction, the contrast differences to classical walks, and developments of the quantum walk in quantum information science. Inspired by tremendous achievements of random walk and Markov chain methods (quantum walk's counterpart in a classical walk) in the development of classical algorithms [3], Nayak and Vishwanath [3] presented quantum walks on an interesting graph. They described the pattern of quantum walks on the line by plotting probability distributions after deployed Fourier analysis of Hadamard walk. Excitingly, the main role of quantum computation, that are able to carry out problems faster than a classical computer, was proofed by Childs et al. [4]. They have successfully solved a hard problem exponentially faster on a quantum computer than on a classical computer. Furtherer, research in the quantum walk still continues, e.g. the paper delivered by Dheeraj et al. that presented alternative approach by defining two different ways: discrete-time and continuous-time quantum walks (DTQWs and CTQWs) [6]. The other important work was delivered by Ambainis [7] who explained about the algorithmic application. More detail about the algorithmic application will be shown in the next section. This paper aimed to construct MATLAB programming based on the algorithmic application. In addition, the programming comprises both numerical and visual results.

2. DISCRETE QUANTUM WALK CALCULATION

Suppose a quantum process which has initial basis states$|n\rangle$, n $\in Z$. A unitary transformation lead to [7]

$$|n\rangle \rightarrow a|n-1\rangle + b|n\rangle + c|n+1\rangle \tag{1}$$

Equation (1) indicates the position moves left, moves right, or holds the current state with probability $|a|^2$, $|c|^2$, and $|b|^2$, respectively. By utilizing a "coin" state, the position can be evaluated the position after n steps. There are two operations applied at each step:

A "coin flip transformation" or C

$C|n,0\rangle = a|n,0\rangle + b|n,1\rangle$,

$$C|n,1\rangle = c|n,0\rangle + d|n,1\rangle. \tag{2}$$

1. Shift or S

$$S|n,0\rangle = |n-1,0\rangle,\ S|n,1\rangle = |n+1,1\rangle. \tag{3}$$

Operator C is a unitary matrix. Consider if C is Hadamard transformation

$$\begin{pmatrix} a & b \\ c & d \end{pmatrix} = \begin{pmatrix} \frac{1}{\sqrt{2}} & \frac{1}{\sqrt{2}} \\ \frac{1}{\sqrt{2}} & -\frac{1}{\sqrt{2}} \end{pmatrix} \tag{4}$$

Substituting eq. (4) to (2) yields

$$C|n,0\rangle = \frac{1}{\sqrt{2}}|n,0\rangle + \frac{1}{\sqrt{2}}|n,1\rangle,$$

$$C|n,1\rangle = \frac{1}{\sqrt{2}}|n,0\rangle - \frac{1}{\sqrt{2}}|n,1\rangle. \tag{5}$$

Eq. (5) shows probabilities of the state after Hadamard transformation is $\frac{1}{2}$ each. It is easy to understand classically that a state after C operation has the same probability of moving left or right. Surprisingly, the results are not similar to our prediction. The derivations below are first four steps of quantum walk after two operations, S and C, are applied with initial state $|0,0\rangle$ (eq. (3) and (5) are involved in this calculation).

\# 1st step: $SC|0,0\rangle = S[\frac{1}{\sqrt{2}}|0,0\rangle + \frac{1}{\sqrt{2}}|0,1\rangle] = \frac{1}{\sqrt{2}}\ |-1,0\rangle + \frac{1}{\sqrt{2}}\ |1,1\rangle$

\# 2nd step: $SC[\frac{1}{\sqrt{2}}|-1,0\rangle + \frac{1}{\sqrt{2}}|1,1\rangle] = \frac{1}{2}|-2,0\rangle + \frac{1}{2}|0,1\rangle + \frac{1}{2}|0,0\rangle - \frac{1}{2}|2,1\rangle$

\# 3rd step: $SC[\frac{1}{2}|-2,0\rangle + \frac{1}{2}|0,1\rangle + \frac{1}{2}|0,0\rangle - \frac{1}{2}|2,1\rangle] =$

$$\underbrace{\frac{1}{2\sqrt{2}}|-3,0\rangle + \frac{1}{2\sqrt{2}}|-1,1\rangle + \frac{1}{2\sqrt{2}}|-1,0\rangle - \frac{1}{2\sqrt{2}}|1,1\rangle + \frac{1}{2\sqrt{2}}|-1,0\rangle + \frac{1}{2\sqrt{2}}|1,1\rangle - \frac{1}{2\sqrt{2}}|1,0\rangle + \frac{1}{2\sqrt{2}}|3,1\rangle}_{2^3=8}$$

\# 4th step: $SC\left[\frac{1}{2\sqrt{2}}|-3,0\rangle + \frac{1}{2\sqrt{2}}|-1,1\rangle + \frac{1}{2\sqrt{2}}|-1,0\rangle - \frac{1}{2\sqrt{2}}|1,1\rangle + \frac{1}{2\sqrt{2}}|-1,0\rangle + \frac{1}{2\sqrt{2}}|1,1\rangle - \frac{1}{2\sqrt{2}}|1,0\rangle + \frac{1}{2\sqrt{2}}|3,1\rangle\right] =$

$$= \frac{1}{4}|-4,0\rangle + \frac{3}{4}|-2,0\rangle + \frac{1}{4}|-2,1\rangle - \frac{1}{4}|0,0\rangle + \frac{1}{4}|0,1\rangle + \frac{1}{4}|2,0\rangle - \frac{1}{4}|2,1\rangle - \frac{1}{4}|4,1\rangle$$

By performing the similar calculation, we can obtain next steps. The first two steps show that the amplitude of each state is the same. Meanwhile, at the third step and after, the amplitudes is not uniform. This is because there are quantum interferences among the same states. In other words, the amplitudes of the same states can be doubled or vanish. That is why, e.g. at the fourth step, the number of states should be 2^4 states or 16 states. However, at the last calculation, the number of states are reduced to eight states. The probabilities of those states can be easily examined by calculating $|a_i|^2$, where a_i is amplitude of each state, then we have

$$\frac{1}{16}\ |-4,0\rangle + \frac{10}{16}\ |-2,0\ and\ 1\rangle + \frac{1}{8}|0,0\ and\ 1\rangle + \frac{1}{8}|2,0\ and\ 1\rangle + \frac{1}{16}|4,1\rangle$$

Finally, the states can be reduced again after examining probabilities of each state, because each state involves both state 0 and 1.

3. DEVELOPING MATLAB PROGRAMMING

Considering involving immense states when we examine quantum walk after next steps, it will be helpful to employ numerical programming to support calculations. Firstly, we show the main stages of the entire programming (Figure 1).

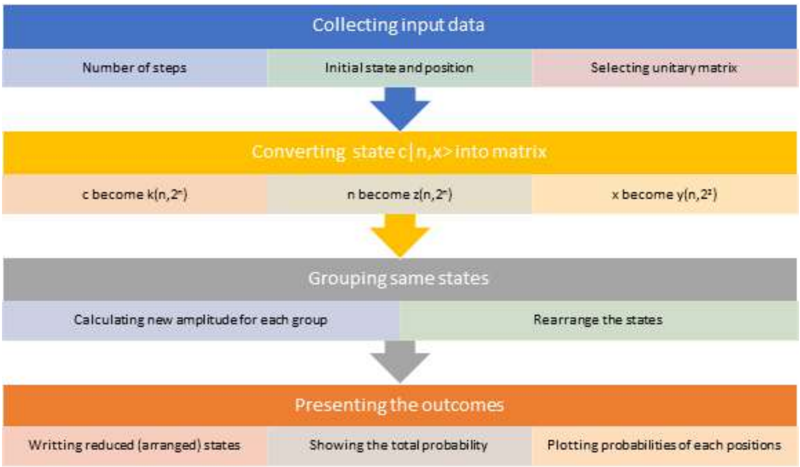

Figure 1. Diagram block of the entire programming

b. Collecting input data

```
disp('=============================
=============');
disp('           SC - Transformation
');
disp('=============================
=============');
disp('');
n=input('Number of Steps: ');
s1=input('Initial   State   (0   or
1) :');
p1=input('Initial Position (x) :');
a=1/sqrt(2); b=1/sqrt(2);
c=1/sqrt(2); d=-1/sqrt(2);
fprintf('\nInitial    State    and
Position: |%1.0f,%1.0f>\n',p1,s1);
fprintf('\n');
```

Output on the screen:

```
    ===============================
    ====
        SC - Transformation
    ===============================
    ====
    Number of Steps: 20
    Initial State (0 or 1) :0
    Initial Position (x) :0
    Initial State and Position: |0,0>
```

c. Converting state c|n,x> into matrix and grouping same states

```
for r=1:n
    for s=1:2^r
        if(mod(s,2)==0) y(r,s)=1;
        else y(r,s)=0; end
        if((r==1))
            if(s1==0)
                if(s==1) k(r,s)=a;
                else k(r,s)=b; end
            else if(s==1) k(r,s)=c;
            else k(r,s)=d end
            end
        else t=t+1;
        if(t==1)
          k(r,s)=a*k(r-
1,round(s/2));
        else if(t==2)
        k(r,s)=b*k(r-1,round(s/2));
        else if(t==3)
        k(r,s)=c*k(r-1,round(s/2));
        else if(t==4)
        k(r,s)=d*k(r-1,round(s/2));
        end end end end
        if(t==4) t=0; end end
        if(r==1)
        if(y(r,s)==0) z(r,s)=p1-1;
        else z(r,s)=p1+1; end
        else if(y(r,s)==0)
        z(r,s)=z(r-1,round(s/2))-1;
        else
        z(r,s)=z(r-1,round(s/2))+1;
end
    end end end
[m,bin]=             histc(z(n,:),
unique(z(n,:)));
multiplez=find(m>1);
indexz=find(ismember(bin,multiplez)
);
[bz,nz]=size(indexz);
[bz,mz]=size(multiplez);rz=2; nz;
zz(n,1)=z(n,1); zz(n,2)=z(n,2^n);
yy(n,1)=y(n,1); yy(n,2)=y(n,2^n);
kk(n,1)=k(n,1); kk(n,2)=k(n,2^n);
rz1=rz; kz=0;
for r=2:2^n-1
rz1=rz1+1; zz(n,rz1)=z(n,r);
yy(n,rz1)=y(n,r);kk(n,rz1)=k(n,r);
end
rzz=rz; pk=0; qk=0;
for i=1:mz
indexz1=find(ismember(bin,multiplez
(i))); kkz(i)=z(n,indexz1(i));end
for i=1:mz
rzz=rzz+1;
for j=(rz+1):2^n
if(yy(n,j))==0
if(zz(n,j))==kkz(i)  pk=pk+kk(n,j);
end
else if(yy(n,j))==1
if(zz(n,j))==kkz(i) qk=qk+kk(n,j);
end end end end
zz(n,rzz)=kkz(i); yy(n,rzz)=0;
kk(n,rzz)=pk; zz(n,rzz+1)=kkz(i);
yy(n,rzz+1)=1; kk(n,rzz+1)=qk;
pk=0; qk=0; rzz=rzz+1; end
```

These parts have a main role in the programming, because in this stage enormous number of states can be reduced in much simple form. In this case, the desired number of step is 20, hence the total states involved in calculations are 2^{20} states or 1,048,576 states. After attempting to group same states and recalculating each amplitudes, 1,048,576 states become 21 states.

d. Presenting the outcomes

```
fprintf('Output State: \n');
for s=1:rzz
fprintf('%s|%1.0f,%1.0f>\n',num2str
(kk(n,s)),zz(n,s),yy(n,s));
k2(n,s)=(abs(kk(n,s)))^2;
p=p+k2(n,s);
end
fprintf('\nTotal
Probability=%1.4f\n',p);
kkz=rz;
nrzz=(rzz-2)/2+2;pzz(n,1)=zz(n,1);
pzz(n,nrzz)=zz(n,2);pk2(n,1)=abs(kk
(n,1))^2;pk2(n,nrzz)=abs(kk(n,2))^2
;
for s=2:nrzz-1
    kkz=kkz+1;pzz(n,s)=zz(n,kkz);
pk2(n,s)=abs(kk(n,kkz))^2+abs(kk(n,
kkz+1))^2; kkz=kkz+1;
end
fprintf('\nThe  Probability  at  any
position: \n');
fprintf('=====================
\n');
fprintf('Position  Probability\n');
fprintf('---------------------
\n');
for s=1:nrzz

fprintf('   %1.0f       %1.8f\n',pzz
(n,s),pk2(n,s));
end
plot(pzz(n,1:nrzz),pk2(n,1:nrzz))
```

Output on the screen:

Output State:

```
 0.00097656     |-         -0.12305 |0,0>
 20,0>                     0.12305 |0,1>
 -0.00097656               0.12305 |2,0>
 |20,1>                    -0.12305 |2,1>
 0.018555 |-18,0>          -0.13672 |4,0>
 0.00097656     |-         0.095703 |4,1>
 18,1>                     0.13672 |6,0>
 0.13184 |-16,0>           -0.027344 |6,1>
 0.016602 |-16,1>          -0.082031 |8,0>
```

```
0.41504 |-14,0>
0.10059 |-14,1>
0.47266 |-12,0>
0.24121 |-12,1>
-0.12891 |-10,0>
0.11328 |-10,1>
-0.19141 |-8,0>
-0.19922 |-8,1>
0.25391 |-6,0>
0.089844 |-6,1>
-0.20508 |-4,0>
0.027344 |-4,1>
0.15039 |-2,0>
-0.095703 |-2,1>
```

```
-0.089844 |8,1>
-0.042969 |10,0>
0.19922 |10,1>
0.11816 |12,0>
-0.11328 |12,1>
0.073242 |14,0>
-0.24121 |14,1>
0.014648 |16,0>
-0.10059 |16,1>
0.00097656
|18,0>
-0.016602 |18,1>
```

Total Probability = 1.0000

```
The Probability at any position:
====================
Position  Probability
------------------------------------
  -20     0.00000095
-18     0.00034523
-16     0.01765633
-14     0.18237495
-12     0.28158665
-10     0.02944946
-8     0.07632446
-6     0.07254028
-4     0.04280472
-2     0.03177643
0     0.03028107
2     0.03028107
4     0.02785110
6     0.01943970
8     0.01480103
10     0.04153442
12     0.02679539
14     0.06354713
16     0.01033211
18     0.00027657
20     0.00000095
```

This result is very exciting because the number of state reduction is very effective, from 2^{20} states or 1,048,576 states become 21 states. Figure 2 shows the probabilities in each reduced states. We have to concern that the total probability must be 1. If the total probability is not 1 or becomes 'explosively', it indicates that the selected matrix is not unitary, then choose another matrix which is really unitary.

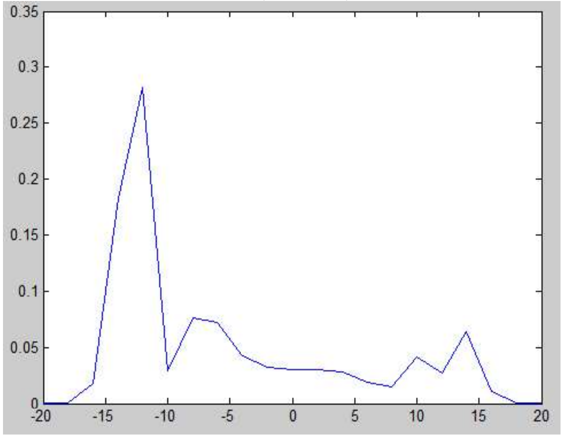

Figure 2. The probabilities of each state in any positions after 20 steps

4. CONCLUSIONS

In this paper we have examined quantum walks obtained by applying Hadamard transformation and shift of position and convert the algorithmic application into MATLAB programming. The results provide numerical values and a graph represents probabilities in each state and positions. The strong good point is that the programming is able to simplify an enormous number of states significantly. In addition, the programming also can identify if a matrix selected is unitary or not.

5. REFERENCES

[1]. Aharonov, L. Davidovich and N. Zagury, "Quantum random walks," *Physical Review A,* vol. 48, pp. 1687-1690, 1993.

[2]. J. Kempe, "Quantum random walks: An introductory overview," *Contemporary Physics,* pp. 307-327, 2003

[3]. R. Motwani and P. Raghavan, Randomized Algorithms, 1st ed., New York: Cambridge University Press, 1995

[4]. N. Ashwin and V. Ashvin, "Quantum walk on the line," Center for Discrete Mathematics & Theoretical Computer Science, New York, 2000.

[5]. A. M. Childs, R. Cleve, E. Deotto, E. Farhi, S. Guttman and D. A. Spielman, "Exponential algorithmic speedup by quantum walk," in *Proc. 35th ACM Symposium on Theory of Computing (STOC 2003)*, San Diego, 2003.

[6]. D. M. N and T. A. Brun, "Continuous limit of discrete quantum walks," *Physical Review A,* vol. 91, no. 6, 2015.

[7]. A. Ambainis, "Quantum walks and their algorithmic applications," *International Journal of Quantum Information,* p. 507, 2003

Spatio Temporal Dynamic Modeling of Dengue Fever Infectious Disease in Bandung

I GN Mindra Jaya[1*] , Budi Nurani Ruchjana [2], Atje Setiawan Abdulah[3], Eddy Hermawan[4]

[1]Department of Statistics, University of Padjadjaran, Bandung, Indonesia
[2]Department of Mathematics, University of Padjadjaran, Bandung, Indonesia

[3]Department of Computer Science, University of Padjadjaran, Bandung, Indonesia
[4]Center for Application of Atmospheric Sciences and Climate of National Institute of Aeronautics and Space (LAPAN) Bandung, Indonesia

* Corresponding authors: [mindra@unpad.ac.id]

Abstract – Dengue fever (DF) is an infectious disease which gives very bad impact on public health and potentially causes death. The spread of DF is very fast as carried because of the spreading by mosquitoes which have flight distance far enough and high population mobility [1]. Dengue cases become a serious problem for every year, especially in rainy season time. Modeling the factors that affect the high number of DF cases is needed to control the increasing prevalence rate and Spread of DF. Spatio temporal dynamic modeling (STDM) can be used to modeling relative risk of DF which not only including spatial variation but also temporal variation. The dynamic modeling is including not only spatial lag dependence but also time lag dependence [2]. We use integrated nested Laplace approximation (INLA) to estimate the parameters STDM. We applied STDM model to build dengue fever model in Bandung. Our research provides a good model to predict relative risk of dengue fever in Bandung. We found the population density and healthy hosing index are two factors that influence the relative risk of dengue fever in Bandung city.

Keyword: Dengue Fever, Dynamic, INLA, Spatio temporal

1. INTRODUCTION

Dengue fever (DF) is an infectious disease which gives very bad impact on public health and potentially causes death. The spread of DF is very fast as carried because of the spreading by mosquitoes which have flight distance far enough and high population mobility [1]. Dengue cases become a serious problem for every year, especially in rainy season time. Indonesia is a tropical country which has a longer rainy season time.

The World Health Organization in 2009 noted Indonesia as the country with the highest DF incidence in Southeast Asia from 1968 to 2009. The case-fatality rate of dengue fever cases in Indonesia was approximately1% [1]. The total number of DF cases in Indonesia increased by 12.65% between 2008 and 2009: from 137,569 in 2008 to 154,855 in 2009. Based on the publication of Health Ministry of RI on 2010, the number of patients who died during that period grew from 1187 to 1384 or by 16.60%; the case fatality rate (*CFR*) reached 1.384% in 2009.

Bandung is a city in West Java has a serious problem with dengue fever disease. The number incidence decreased from 2009 to 2014 however the CFR increased.

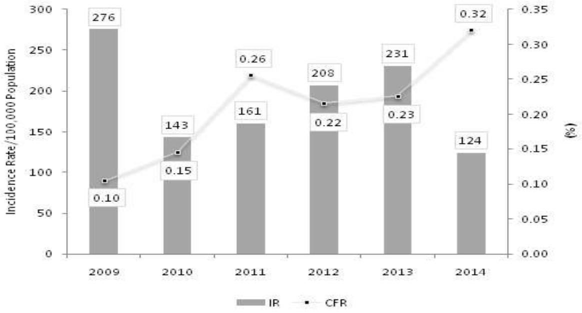

Figure 1. The statistics of dengue fever incidence in Bandung City 2009-2014

We need to develop early warning system as early detection of the spread of dengue fever disease. This is an important step to control the spreading and the impact. The spreading of dengue fever disease has two main characteristics are depended on by location and time [3-2]. We proposed STDM model as a model that can be used explain the pattern of the spreading of DF cases by spatial and temporal aspects. This model also can be used to explain the factors (i.e.: rainfall, humidity, temperature, population density, healthy housing index, healthy index) that have a significant effect on the dengue fever cases. The dynamic model is a model that includes the time lag dependence in the model. The time lag dependence is needed to predict the number of cases in the next period. We propose to use Bayesian approach to estimate the STDM parameters model.

2. METHODS

2.1 Spatio Temporal Modeling

We proposed a spatio temporal dynamic model area level linear mixed model involving spatially correlated and temporally autocorrelated random effects. Spatio temporal data we observe are indexed by $Y(s,t) \equiv \{y(s,t),(s,t) \in D \subset \mathbb{R}^2 \times \mathbb{R}$, with D represent area level Spatio temporal data [4]. In this research the set spatial location $(s_{11},..,s_{nT})$ were used to examine the spatio temporal pattern of number of dengue fever cases over Bandung City. The observed number of dengue fever cases data was represented as $\boldsymbol{y(s)} = \{\boldsymbol{y(s_{11})},\ldots,\boldsymbol{y(s_{NT})}\}$. Let $\{y_{it}: i = 1,\ldots,N, and\ t = 1,\ldots,T\}$ be the Dengue Fever count data collected for sub district i at time point t, where $N = 30$ spatial sub district and $T = 60$ time point representative of the months January, 2009 through December, 2013. Number of cases y_{it} is assumed to follow a Poisson distribution with parameter $\lambda_{it} = E_{it}\theta_{it}$ with $E_{it}$the expected incidence and $\theta_{it}$the relative risk. Let $\eta_{it} = \log(\theta_{it})$. Then, the comprehensive spatio temporal model can be written as follows:

$$\eta_{it} = \rho \sum_{j=1}^{n} w_{ij}\eta_{jt} + \gamma\eta_{it-1}\beta_{0_{it}} + \sum_{k=1}^{K} \beta_{k_{it}}\mathrm{x}_{kit} + \omega_i + \upsilon_i + \phi_t + \psi_t + \delta_{it} \tag{1}$$

where x_{kit} is the kth covariate at location i and time t; κ_i, υ_i, ϕ_t and $\psi_t$are spatially structured, spatially unstructured, temporally structured and temporally unstructured random effects, respectively, and δ_{it}captures space -time interaction. Space and time coefficients may be spatially structured or vary randomly. We assume that the spatially structured area follows a Conditional Autoregressive (CAR)[5-6]. The CAR prior for the random effect ω is given by

$$\omega_i|\omega_{-i} \sim N\left(\frac{\sum_{j=1}^{n} w_{ij}\omega_j}{\sum_{i=1}^{n} w_{ij}}, \frac{\tau_\omega^2}{\sum_{i=1}^{n} w_{ij}}\right) \tag{2}$$

where w_{ij} is the $i\,j\,th$ element of the spatial weights matrix **W**. We use queen spatial contiguity matrix to present **W**. The τ_ω^2 denotes a hyperparameter related to the conditional variance of ω_i given the values of the other elements of ω.We assume a Random Walk model for ϕ and for the unstructured random components υ and ψ we assume normal distribution with mean 0 and variance σ^2. The limitations caused by small sample size or over-dispersion can be handled by means of a Bayesian approach.

2.2 Integrated Nested Laplace Approximation: INLA

Spatio temporal dynamic model (STDM) can be estimated based on Bayesian hierarchical models with three stages processes. The first stage defines the observational model $\boldsymbol{\pi(y|x)}$, where $\boldsymbol{y}$ denotes the number of incidence dengue fever. The second stage defines the latent Gaussian field (GMRF) with precision matrix $\boldsymbol{Q}$ and the third stage defines controlling hyperparmeter model. To define the spatial dependence we use BYM model [5]. Let the number of cases y_{it}, $i = 1,2,..,n$; $t = 1,2,..,T$ of disease is observed over time period for a site of n areas. The intrinsic GMRF of the following form is often assumed for the spatially structured component:

$$\pi(\omega|\kappa_\omega) \propto \kappa_\omega^{\frac{n-1}{2}} \exp\left(-\frac{\kappa_\omega}{2}\sum_{i\sim j}\left(\boldsymbol{\omega}_i - \boldsymbol{\omega}_j\right)^2\right) \forall\, t \tag{3}$$

where κ_ω is the unknown precision parameter. Two district i and j are defined to be neighbours, $i{\sim}j$, if they are adjacent. Further $\boldsymbol{\omega}$ are independent zero mean normal with unknown precision parameter κ_ω.

The BYM model is a hierarchical GMRF model, with $y_{it} \sim P(E_{it}\exp(\eta_{it}))$ at the first stage. At the second stage the GMRF is $\boldsymbol{x} = (\boldsymbol{\eta}^T, \boldsymbol{\omega}^T)^T$. The unknown precision $\boldsymbol{\kappa} = (\kappa_u, \kappa_v)$ constitute the third stage. Note that we have reparameterised the GMRF using $\boldsymbol{x} = (\boldsymbol{\eta}^T, \boldsymbol{u}^T)^T$ instead of $\boldsymbol{x} = (\boldsymbol{v}^T, \boldsymbol{\omega}^T)^T$. The posterior [7]

$$\pi(x,\kappa|y) \propto \kappa_v^{\frac{n}{2}}\kappa_{\boldsymbol{\omega}}^{\frac{n-1}{2}}\, exp\left(-\frac{1}{2}\boldsymbol{x}^T\boldsymbol{Q}\boldsymbol{x}\right) exp(\textstyle\sum_{i=1}^{n} \boldsymbol{y}_i\mathbf{x}_i - \boldsymbol{E}_i\exp(\mathbf{x}_i))\pi(\boldsymbol{\kappa}) \tag{4}$$

Where $\boldsymbol{y_i} = [y_{1i}, y_{2i},..,y_{Ti}]'$; $\mathbf{x_i} = [\mathrm{x}_{1i}, \mathrm{x}_{2i},..,\mathrm{x}_{Ti}]'$ and $\mathbf{E_i} = [\mathrm{E}_{1i}, E_{2i},..,\mathrm{E}_{Ti}]'$. The $2n \times 2n$ precision matrix for the GMRF, Q is

$$\boldsymbol{Q} = \begin{pmatrix} \kappa_v I & -\kappa_v I \\ -\kappa_v I & \kappa_{\boldsymbol{\omega}} R + \kappa_v I \end{pmatrix} \tag{5}$$

The main goal is to estimate the marginal posterior distribution of all component of the GMRF

$$\pi(\mathbf{x}_i|\boldsymbol{y}) = \int_\theta \pi(\boldsymbol{x}_i|\boldsymbol{\theta},\boldsymbol{y})\,\pi(\boldsymbol{\theta}|\boldsymbol{y})d\boldsymbol{\theta} \tag{6}$$

Where $\boldsymbol{\theta} = (\sigma_i^2, \sigma_t^2, \sigma_v^2, \sigma_\omega^2, \sigma_\phi^2, \sigma_\psi^2, \sigma_\delta^2)$. The marginal posterior density $\pi(\boldsymbol{\theta}|\boldsymbol{y})$ of the hyperparameters $\boldsymbol{\theta}$ can be approximated using Laplace Approximation

$$\tilde{\pi}(\boldsymbol{\theta}|\boldsymbol{y}) \propto \frac{\pi(x_i, \boldsymbol{\theta}, \boldsymbol{y})}{\tilde{\pi}_G(x_i|\boldsymbol{\theta}, \boldsymbol{y})}|_{x=x^*(\boldsymbol{\theta})} \tag{7}$$

3. RESULTS AND DISCUSSION

We used monthly data of dengue fever cases and also the covariates. The data take from 2009 until 2013. The number cases of dengue fever in Bandung city vary from very small (0) to very high number incidents (102). The temperature in average nearby 23.4^{0}C for every month, rainfall and humidity nearby 215 mm and 78.2% respectively. The statistics descriptive of the variables also found that there are districts that have healthy housing index and hygiene index lower that 50%. The lowest of healthy housing index was found that in Batununggal, and the lowest of hygiene index was found in Cibeunying Kaler district.

Next, we estimate the parameters model using Bayesian numerical approach or INLA. We assume the covariate population density, larvae free home index, healthy housing index and hygiene index have the same value for every month in a year but different in every year. Because the survey of those covariates were done one time in a year. In Table 1 we present the best model with four covariates based on DIC, MPL, and MSE comparison.

Table 1. Parameter Estimate of STDM

Parameters	Spatio Temporal Model	
	Estimate	Standard Deviation
Intercept (β_0)	-0.5263092	0.2612170
Temporal Lag (γ)	0.0087234	0.0010139*
Rainfall (β_2)	0.0000507	0.0000712
Population Density (β_4)	0.0000594	0.0000210*
Healthy Housing Index (β_6)	-0.0040834	0.0013712*
Spatial Lag (ρ)	0.1188800	0.0072093*

DIC = 10202.45 MPL= -5349.227 MSE = 34.94857

*) significant in level α=0.05

We found all the covariates have a significant effect in level α=0.05 to the relative risk, except the rainfall. The model can be written as:

$$\hat{\eta}_{it} = -0.5263 + 0.0087234\hat{\eta}_{it-1} + 0.1188800 \sum_{j=1}^{n} w_{ij}\hat{\eta}_{jt} + 0.0000507x_{2it} + 0.0000594x_{4it} - 0.0040834x_{6it}$$

The positive effect of the temporal and spatial lag dependence mean that the relative risk in the previous period and in neighborhood districts influence the current relative risk in district *i*. The increasing rainfall and population density worsen the condition of dengue fever in the city of Bandung because of covariates have a positive effect. The Healthy Housing Index has a negative effect on the relative risk which means the increasing healthy behavior will decrease the relative risk of dengue fever.

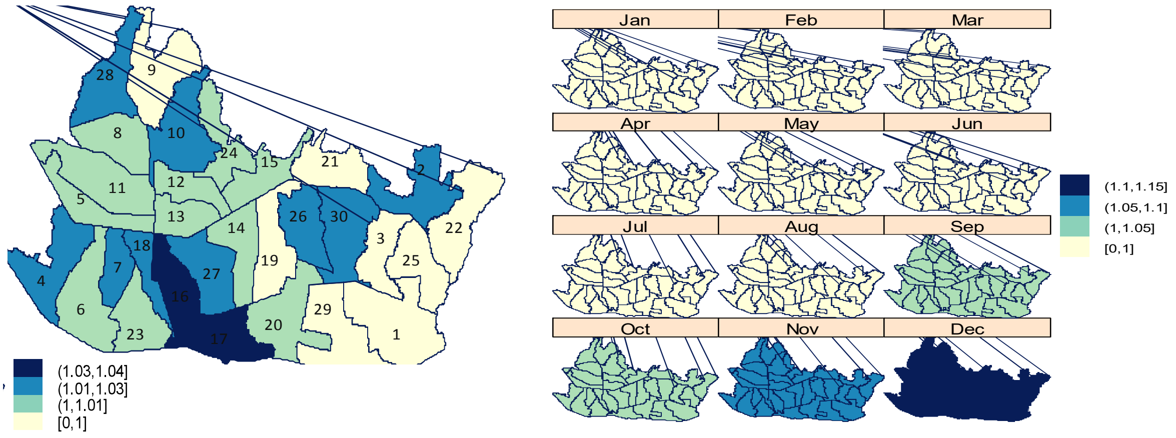

(a) Spatial Effect (b) Temporal Effect

Figure 2. Spatial and Temporal Effect

Figure (a) shows spatial structure effect. Sub-districts of Bandung in the west generally have a high spatial effect and result in high numbers relative risk. Figure (b) shows the temporal effects increase exponentially at the end of the year. This is in accordance with the characteristics of the higher rainfall at the end of the year. So the relative risk figures tend to be higher at the end of the year

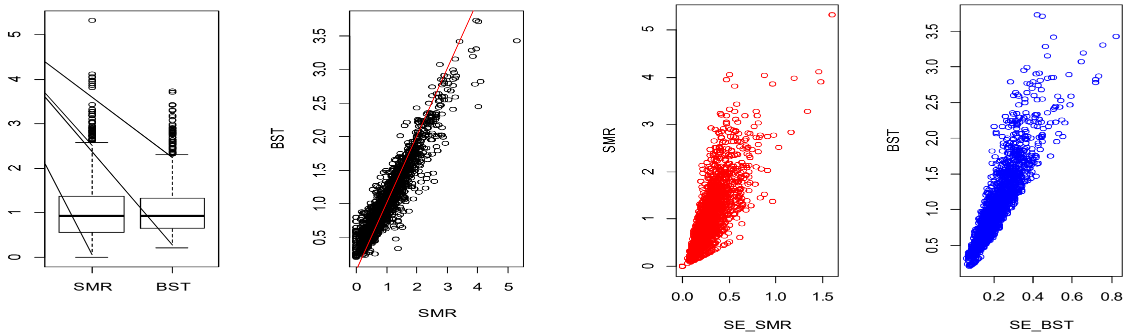

(a) Relative Risk Estimate (b) Relative Risk Standard Error Estimate

Figure 3. A Comparison of STDM Model with SMR

Figure 3 shows the STDM has the smallest variation of the relative risk compared than the SMR. It means the STDM more robust than SMR.

4. CONCLUSIONS

The STDM adequately captures the spatio temporal characteristics of the distribution of Dengue Fever whereas the STDM produces smoother (more robust) relative risk estimates than SMR. We found that temporal lag dependence has a significant effect on the relative risk of dengue fever in Bandung. It means the relative risk of Dengue Fever at time *t* is influenced by the relative risk in the previous period. The hypothesis testing also informs that the spatial lag dependence is significant too. It means the relative risk in area *i* is influenced by the relative risk in neighboring areas. Our analyses found the covariates population density and also have a significant effect on the relative risk. The population density has a positive effect which means increasing population density will increase the relative risk. The healthy house index has a negative effect. Which suggest that we have to increase the percentage of the healthy house index in every time to decrease the relative risk of dengue fever in Bandung city. Finally we can predict that every month, some districts in northern Bandung and some districts in southern Bandung have a high relative risk of dengue fever.

5. ACKNOWLEDGMENT

The work reported in this paper is supported by the Directorate General of Higher Education, Ministry of Research, Technology and Higher Education, Republic of Indonesia, through *Penelitian Kerjasama Luar Negeri dan Publikasi Internasional 2017*

6. REFERENCES

[1]. WHO. Using Climate to Predict Infectious Disease Epidemics. Geneva: WHO. (2005)
[2]. Chen, D., Moulin, B., & Wu, J.. Introduction to Analyzing and Modeling Spatial and Temporal Dynamics of Infectious Diseases. In D. Chen, B. Moulin, & J. Wu, Analyzing and Modeling Spatial and Temporal Dynamics of Infectious Diseases (pp. 3-17). New Jersey: John Wiley & Sons. (2015)
[3]. Jaya, IGN., Abdullah, A. S., Hermawan, E., & Nurani R, B.. Bayesian Spatial Modeling and Mapping of Dengue Fever: A Case Study of Dengue Fever in The City of Bandung, Indonesia. *International Journal of Applied Mathematics and Statistics*, **54 (3)**, 94-103(2016)
[4]. Blangiardo, M., Cameletti, M., Baio, G., & Rue, H. (2012). Spatial and Spatio-Temporal Model with INLA. Spatial and Spatio-Temporal Epidemiology , **4**, 33-49
[5]. Elhorst, J. P. Spatial Econometrics From Cross-Sectional Data to Spatial Panels. New York: Springer. (2014)
[6]. Besag, J., & Newel, J. (1991). The Detection of Clusters in Rare Diseases. *Royal Statistical Society* , 143-155.
[7]. Lee, D. (2013). CARBayes: An R Package for Bayesian Spatial Modeling with Conditional Autoregressive Priors.
[8]. Ugarte, M. D., Adin, A., Goicoa, T., & Militino, F. A. (2014). On fitting spatio-temporal disease mapping models using approximate Bayesian inference. *Statistical Methods in Medical Research* , 507–530

A Comparison of MCMC and DMC Approach For Seemingly Unrelated Regression Model With Application Gross Regional Domestic Product

A.B. Santosa[1], N. Iriawan[2], Setiawan[2] and M. Dokhi[3]

[1]PhD Student of Statistics Department, Institut Teknologi Sepuluh Nopember (ITS), Surabaya
[2]Department of Statistics, Institut Teknologi Sepuluh Nopember (ITS), Surabaya
[3]Institute of Statistics (STIS), Jakarta, Indonesia
Corresponding author: [agusbs_gdg@yahoo.com ; agus_10@mhs.statistika.its.ac.id]

Abstract – Seemingly unrelated regression (SUR) is an econometric model that is widely used in solving some of the regression equation in which each equation has its own parameters and it appears that each equation is not related (seemingly unrelated). Markov Chain Monte Carlo (MCMC) is a method often used by many researchers for analyzing SUR models using the Bayesian approach. Direct Monte Carlo (DMC) method, on the other hand, was claimed as a more efficient developed method for estimating the SUR parameters model. This paper would compare the accuracy of these two methods for SUR modeling and analysis applied to the model of the Gross Regional Domestic Product (GRDP) of East Java. This model would involve four influencing factors, i.e. amount of labor, labor wage, domestic investment, and foreign investment. These two methods was synchronously reported that (1) a number of labors have the highest elasticity on the GRDP model of three main sectors (agriculture sector, manufacturing industrial sector, and the trade, hotel and restaurants sectors); (2) Foreign investment has the lowest elasticity model GDP of agricultural sector; and (3) In GRDP model of the manufacturing industry sector and trade, hotels and restaurants sector, domestic investment have the lowest elasticity. Based on the selection criteria models and computational time consuming show that DMC approach is better and more efficient than MCMC approach.

Keywords: Gross Regional Domestic Product, Seemingly Unrelated Regression, Bayesian, Elasticity, Markov Chain Monte Carlo , Direct Monte Carlo.

1. INTRODUCTION

GRDP is defined as the total value added generated by all business units within a region or the total value of goods and services produced by all economic units. In addition as an important indicator in determining the success of the economic growth of such region that has been achieved, GRDP can also be used as a basis for determining the direction of the future region development. The higher the GRDP will always be associated with the better economic phenomena in society. To understand the phenomenon of the economy, there has been developed some economic theories which attempt to determine the relationship between economic variables in such mathematical formulation.

Seemingly unrelated regression (SUR) is one of an econometric model that is widely used for representing the relationship between economic variables with some correlated error in the model. Some discussions and researches on the SUR models have been conducted by researchers after Zellner had succeeded to introduce the Generalized Least Square (GLS) as an efficient method for estimating SUR models [5,6]. Bayesian approach for parameter estimation SUR models has been carried by Zellner [7] using Markov Chain Monte Carlo (MCMC), which later became one of the most well-known methods in the Bayesian analysis. Geweke [2] had proposed DMC as a new method for calculating posterior of SUR models. Zellner [10] had succeeded to demonstrate this DMC method for estimating parameters SUR model to forecast the growth rates of real sales in several sectors of the Japanese economy. This paper had succeeded to show that DMC is more accurate and faster in computational time-consuming in Bayesian SUR modeling of GDRP in East Java, than MCMC approach.

2. METHODS

2.1 Data

This research used a secondary data obtained from the BPS-Statistics Indonesia for the period 1991-2010. The data is selected for East Java Province consisting of the GRDP (Y), amount of labor (X_1) and labor wage (X_2), and the data on investment (i.e. domestic (X_3) and foreign (X_4)) for each of main sectors (i.e. agriculture (Y_1), manufacturing industry (Y_2) and trade, hotel and restaurant (Y_3)). These variables are also used by Bappenas [1].

2.2 The Seemingly Unrelated Regression (SUR) Model Using MCMC

The general linear SUR model can be written as

$$y_m = X_m\beta_m + \mu_m,\ m = 1,2,...,M, \tag{1}$$

where $\mathrm{E}\left[\mu_m\mu_n^{'}\right] = \begin{cases}\omega_{mn}\mathrm{I}\left(m \neq n\right)\\ \omega_m^2\mathrm{I}\left(m = n\right)\end{cases}.$

As displayed in the model (1), the equations of the model have dissimilar independent variables and error term variances. In matrix form, the SUR model in (1) is written as

$$\mathbf{y} = \mathbf{X\beta} + \mathbf{u}\ \ ;\ \mathbf{u} \sim N\left(0, \mathbf{\Omega}\otimes\mathbf{I}\right), \tag{2}$$

which has the likelihood function

$$L\left(\boldsymbol{\beta},\boldsymbol{\Omega}|y,X\right) = \frac{1}{\left(2\pi\right)^{nm/2}\left|\boldsymbol{\Omega}\right|^{n/2}}\left\{exp\left[-\frac{1}{2}\left(y - X\beta\right)^{'}\left(\boldsymbol{\Omega}^{-1}\otimes \boldsymbol{I}\right)\left(y - X\beta\right)\right]\right\} = \frac{1}{\left(2\pi\right)^{nm/2}\left|\boldsymbol{\Omega}\right|^{n/2}}\left\{exp\left[-\frac{1}{2}tr\left(\mathrm{S}\,\boldsymbol{\Omega}^{-1}\right)\right]\right\}, \tag{3}$$

where the ij^{th} elements of $m \times m$ matrix $\mathbf{S} = \left(\mathbf{s_{ij}}\right)$ is $\mathbf{s_{ij}} = \left(\mathbf{y_i} - \mathbf{X_i\beta_i}\right)'\left(\mathbf{y_j} - \mathbf{X_j\beta_j}\right)$.

One of the most widely used non-informative priors is Jeffreys' invariant prior [3,4]:

$$p\left(\boldsymbol{\beta},\boldsymbol{\Omega}\right) = p\left(\boldsymbol{\beta}\right)p\left(\boldsymbol{\Omega}\right) \propto \left|\,\boldsymbol{\Omega}\,\right|^{-(\mathbf{m}+1)/2}, \tag{4}$$

which, as is well known, is proportional to the square root of the determinant of the Fisher information matrix. The joint posterior density function for the parameters is then:

$$p\left(\boldsymbol{\beta},\boldsymbol{\Omega}\,|\,\mathbf{y},\mathbf{X}\right) \propto \left|\boldsymbol{\Omega}\right|^{-(\mathbf{n}+\mathbf{m}+1)/2}\, exp\left[-\frac{1}{2}tr\left(\mathrm{S}\,\boldsymbol{\Omega}^{\text{-}1}\right)\right]. \tag{5}$$

So, the conditional posterior $\left(\boldsymbol{\beta}\,|\,\boldsymbol{\Omega},\mathbf{y},\mathbf{X}\right)$ and $\left(\boldsymbol{\Omega}\,|\,\boldsymbol{\beta},\mathbf{y},\mathbf{X}\right)$ are given by:

$$\beta|\boldsymbol{\Omega}, y, X :\ N\left(\hat{\boldsymbol{\beta}},\hat{\boldsymbol{\Omega}}_{\boldsymbol{\beta}}\right)\ \text{ and }\ \boldsymbol{\Omega}|\beta, y, X :\ \mathrm{IW}\left(\mathbf{S},\mathbf{n}\right), \tag{6}$$

with $\hat{\beta} = \left(X'(\boldsymbol{\Omega}^{-1}\otimes \boldsymbol{I})X\right)^{-1}X'(\boldsymbol{\Omega}^{-1}\otimes \boldsymbol{I})y$ and $\hat{\boldsymbol{\Omega}}_\beta = \left(X'(\boldsymbol{\Omega}^{-1}\otimes \boldsymbol{I})X\right)^{-1}$.

2.3 The Seemingly Unrelated Regression (SUR) Model Using DMC

In order to generate DMC procedure, we reformulate the standard SUR model (1) as:

$$\begin{aligned} y_1 &= X_1\beta_1 + e_1\\ y_2 &= X_2\beta_2 + \rho_{21}\mu_1 + e_2\\ &\vdots\\ y_M &= X_M\beta_M + \sum_{m=1}^{M-1}\rho_{Mm}\mu_M + e_M. \end{aligned} \tag{7}$$

The equation (7) is a direct calculation of re-parameterization. This model is frequently used also in a simultaneous equation [8,9], which can be written as:

$$\begin{aligned} &y_1 = X_1\beta_1 + e_1 \equiv Z_1b_1 + e_1,\\ &y_m = X_m\beta_m + \sum_{n=1}^{m-1}\rho_{mn}\left(y_n - X_n\beta_n\right) + e_m \equiv Z_mb_m + e_m,\ \text{with } m = 2,3,...,M,\ \text{and}\\ &E\left[e_me_n^{'}\right] = \begin{cases} 0\left(m \neq n\right)\\ \sigma_m^2\mathrm{I}\left(m = n\right)\end{cases}\ \text{and } \Sigma = diag\left\{\sigma_1^2,\sigma_2^2,...,\sigma_M^2\right\}, \end{aligned} \tag{8}$$

where the $n\times(p_m + m - 1)$ matrices Z_m are as the function of $\beta_{m-1},\beta_{m-2,...,}\beta_1$, and $b_1 = \beta_1$ and $b_m = \beta_m, \rho_{j1,}\rho_{j2},...,\rho_{jJ-1.}$.

The likelihood function of equation (8) is

$$L\left(y,X\mid \mathbf{b},\mathbf{\Sigma}\right)=\prod_{m=1}^{M}\left(2\pi\right)^{-\frac{1}{2}}\left(\sigma_m^2\right)^{-\frac{1}{2}}\left\{\exp\left[-\frac{1}{2\sigma_m^2}\left(y_m-Z_m b_m\right)^{'}\left(y_m-Z_m b_m\right)\right]\right\}. \qquad (9)$$

Jeffreys' s prior for the density function of $\left\{\mathbf{b},\mathbf{\Sigma}\right\}$ suppose could be [3,4]:

$$\begin{aligned} p\left(\mathbf{b},\mathbf{\Sigma}\right) &\propto \left|\Omega\left(\mathbf{b},\mathbf{\Sigma}\right)\right|^{\frac{M+1}{2}}\times\left|J\right| \\ &\propto \prod_{m=1}^{M}\left(\sigma_m^2\right)^{\frac{M+1}{2}}\times\prod_{m=1}^{M-1}\left(\sigma_m^2\right)^{M=m}=\prod_{m=1}^{M}\left(\sigma_m^2\right)^{\frac{M-2m-1}{2}}, \end{aligned} \qquad (10)$$

where $\left|J\right|$ is a Jacobian transformation.

Based on the equation (9) and (10), the joint posterior density can be written as follows:

$$p\left(\mathbf{b},\mathbf{\Sigma}\mid y,X\right)\propto\prod_{m-1}^{M}\left(\sigma_m^2\right)^{-(T-M+2m+1)/2}\times\left\{\exp\left[-\frac{1}{2\sigma_m^2}\left(y_m-Z_m b_m\right)^{'}\left(y_m-Z_m b_m\right)\right]\right\}. \qquad (11)$$

Thus, the full conditional posterior of parameter $\mathbf{b}$ is

$$b_m\mid b_{m-1},b_{m-2},\ldots,b_1,\sigma_m^2,y,X\sim N\left(\hat{b}_m,\sigma_m^2\left(Z_m{'}Z_m\right)^{-1}\right),\ \text{with}\ \hat{b}_m=\left(Z_m{'}Z_m\right)^{-1}Z_m{'}y_m, \qquad (12)$$

and the full conditional posterior distribution of parameter $\mathbf{\Sigma}=\operatorname{diag}\left\{\sigma_1{}^2,\sigma_2{}^2,\ldots,\sigma_M{}^2\right\}$ could be expressed as

$$\begin{aligned} &\sigma^2{}_m\mid b_{m-1},\ldots,b_2,b_1,y,X\sim IG\left(A,B\right), \\ &\text{where}\ A=\frac{1}{2}\left(T-M+p_m+m\right),\ B=\frac{1}{2}\left(y_m-Z_m\hat{b}_m\right)^{'}\left(y_m-Z_m\hat{b}_m\right). \end{aligned} \qquad (13)$$

3. RESULTS AND DISCUSSION

The contribution of all of three main sectors is about 72 percent of the total East Java's GRDP. Therefore, these three main sectors are frequently used as an indicator of economic development in this province. Base on the equation(1), SUR models used for GRDP data in East Java are:

$$\begin{aligned} y_{1t}&=\beta_{10}+\beta_{11}X_{1t,1}+\beta_{12}X_{1t,2}+\beta_{13}X_{1t,3}+\beta_{14}X_{1t,4}+u_{1t} \\ y_{2t}&=\beta_{20}+\beta_{21}X_{2t,1}+\beta_{22}X_{2t,2}+\beta_{23}X_{2t,3}+\beta_{24}X_{2t,4}+u_{2t} \\ y_{3t}&=\beta_{30}+\beta_{31}X_{3t,1}+\beta_{32}X_{3t,2}+\beta_{33}X_{3t,3}+\beta_{34}X_{3t,4}+u_{3t}. \end{aligned}$$

Estimation parameter SUR models with MCMC and DMC methods have been done in R package program and the result is shown in Table 1. All estimated parameter are positive, both for the GRDP model of agriculture, manufacturing industry and trade, hotels and restaurants. These results are consistent with economic theory which states that the higher the increasing amount of labor, labor wages, domestic investment and foreign investment, the greater the increasing amount of GRDP. While the partial test shows that there is only one variable, namely investment domestic (X23), which is not significant in affecting the GRDP of the manufacturing sector.

SUR models using Bayesian MCMC method on the model of the agricultural sector GRDP, total employment has the highest level of elasticity is 0, 2848. This means that the growth of total employment by one percent, the GRDP of the agricultural sector in East Java would grow 0.2848 percent. Similarly, DMC approach report that the number of workers has the highest level of elasticity on the agricultural sector value 0.6557. Likewise in the agricultural sector, MCMC and DMC methods in the modeling of industrial sector and trade, hotel and restaurant sectors, are synchronously showed that the amount of labor in this sector also has the highest level of elasticity, but in a different level. MCMC reports 0.4563 for the elasticity of number worker in industry sectors and 0.7910 for trading sectors, while DMC reports for 0.3912 and 1.3452 for each sector respectively.

Table 1 Comparison of Parameter Estimation for MCMC and DMC Approach

Estimation	MCMC				DMC			
Parameter	Mean	2,50%	97,50%	Elasticity	Mean	2,50%	97,50%	Elasticity
β_{10}	24.124,57	14.700,00	33.470,00		8.322,75	-7.432,39	24.230,63	
β_{11}	1,55	0,32	2,79	0,2848	3,57	1,46	5,70	0,6557
β_{12}	18,62	15,48	21,71	0,1199	16,96	13,52	20,51	0,1093
β_{13}	9,25	0,05	19,72	0,0108	17,01	1,23	32,84	0,0198
β_{14}	40,75	15,34	67,81	0,0158	48,91	9,83	87,63	0,0189
β_{20}	17.693,25	-4.958,00	40.880,00		20.669,33	-707,70	41.485,46	
β_{21}	13,03	0,67	24,67	0,4563	11,17	0,36	22,30	0,3912
β_{22}	25,33	14,29	37,01	0,1789	25,17	14,09	36,03	0,1778
β_{23}	0,18	-0,14	0,52	0,0220	0,30	-0,09	0,69	0,0366
β_{24}	4,39	2,26	6,65	0,0697	4,74	2,74	6,74	0,0752
β_{30}	-8.259,73	-39.160,00	19.970,00		-38.327,40	-78.895,67	11.056,65	
β_{31}	15,44	5,39	26,71	0,7910	26,26	7,82	41,35	1,3452
β_{32}	39,26	21,02	56,88	0,2652	25,12	2,60	52,26	0,1697
β_{33}	6,36	1,11	12,18	0,0243	10,84	2,95	18,62	0,0414
β_{34}	55,40	30,80	81,34	0,0507	56,55	15,94	95,50	0,0518

Source: Data analysis using R

Some selection criteria, i.e. Root Mean Square Error (RMSE), Mean Absolute Deviation (MAD) and Mean Absolute Percentage Error (MAPE), DMC approach shows a better value than MCMC approach. Figure 1 shows this comparison. The duration of the computing time processes is also used as an indicator of whether a method is more efficient than the other. In this application, we generated 100.000 posterior samples using the DMC approaches. The total number of Gibbs sampling iterations is chosen to be 110.000, of which the first 10.000 iterations are discarded. The computational time of DMC method for estimating the model was, 239.91(seconds), which is much smaller than when MCMC is employed, 412.16 (seconds).

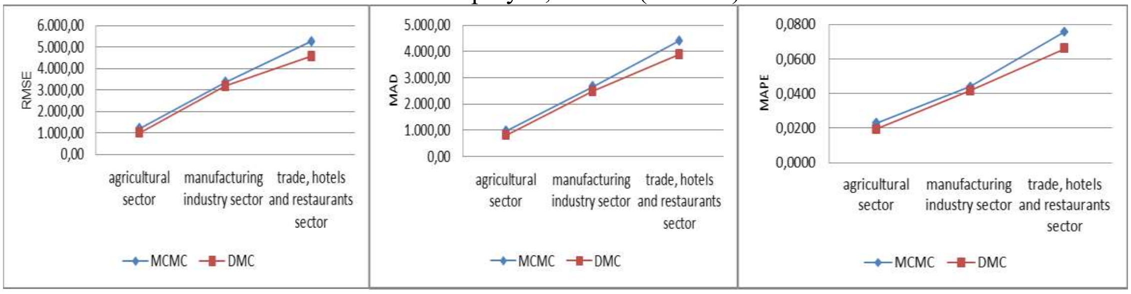

Figure1. Some of the selection criteria models for MCMC and DMC Approach

4. CONCLUSIONS

Parameter estimation results using DMC and MCMC approach show almost the same level of elasticity, the amount of labor has the highest elasticity in figuring the East Java's GRDP model of agriculture, manufacturing industry and trade, hotels and restaurants sectors. However, comparing the goodness of a model based on several criteria for selecting a model (RMSE, MAD and MAPE) shows that the DMC approach is better than the MCMC approach. Similarly, the lengthy process of computing time of DMC approach is more efficient than the approach MCMC.

5. REFERENCES

[1]. Bappenas, 2006, Report of Study Preparation, Jakarta.
[2]. Geweke, J., 2005, Contemporary Bayesian Econometrics and Statistics, Wiley, New York.
[3]. Jeffreys, H., 1946, Proceedings of the Royal Society of London, Series A 196, 453–461.
[4]. Jeffreys, H., 1961, Theory of Probability, 3rd ed. Oxford University Press, Oxford.
[5]. Zellner, A., 1962, Journal of the American Statistical Association 57, 348–368.
[6]. Zellner, A., 1963, Journal of the American Statistical Association 58, 977–992.
[7]. Zellner, A., 1971, an Introduction to Bayesian Inference in Econometrics. Wiley, New York.
[8]. Zellner, A., Bauwens, L., and Van Dijk, H.K., 1988, *Journal of Econometrics* 38, 39–72.
[9]. Zellner, A., and Chen, B., 2001, Macroeconomic Dynamics 5.
[10].Zellner, A., and Ando, T., 2010, *Journal of Econometrics* Vol 159, 33 – 45.

An Explisit Formula for Angles between Subspaces of an n-Inner Product Space

M. Nur 1*, H. Gunawan 2, O. Neswan 3

[1,2,3] Analysis and Geometry Group, Faculty of Mathematics and Natural Sciences, Bandung Institute of Technology, Jl. Ganesha 10, Bandung 40132
* Corresponding authors: [nur_math@yahoo.com]

Abstract – We discuss angles between two subspaces of an inner product space. This paper is an extension of the work by Gunawan et al [7]. We present an explicit formula for angles between two subspaces of an n-inner product space. Moreover, we study its connection with angles in an inner product space.

Keywords: angles, inner product space, n-inner product space.

1. INTRODUCTION

In an inner product space, we can calculate angles between two subspaces. Since the $1950'$s, the concept of angles between two subspaces of the Euclidean space $\mathbb{R}^d$ has been studied by many researchers [2]. Application of angles between two subspaces in an inner product space can be found in the fields of computing and statistics. For example, measuring the similarity of images of three-dimensional objects is invariant under the displacement of the object and the physic of the camera [8]. In statistics, the angle between two subspaces is related to canonical (or principal) angles which are measures of dependency of one set of random variables on another [1]. In 2001, Risteksi and Trencevski [10] introduced a definition of angles between two subspaces of $\mathbb{R}^d$ using determinant Gram and explained their connection with canonical angles. Gunawan *et al.* [6,7] refined their definition and gave the formulas for angles between two subspaces in an inner product space of arbitrary dimension. They also explained the connection with canonical angles by using elementary calculus and linear algebra and some application examples.

Let $(X, \langle\cdot,\cdot\rangle)$ be a real inner product space. If $U = span\{u\}$ is a 1-dimensional subspace and $V = span\{v_1, \cdots, v_q\}$ is a q-dimensional subspace of X, then the angle between subspaces U and V is defined by θ with $0 \le \theta \le \frac{\pi}{2}$ and $\cos^2\theta = \frac{\langle u, u_V\rangle^2}{\|u\|^2\|u_V\|^2}$. In formula, u_V denotes the (orthogonal) projection of u on V and $\|\cdot\| = \langle\cdot,\cdot\rangle^2$. Gunawan *et al* [7] showed that the value of $\cos\,\theta$ is equal to the ratio between the length of the projection of u on V and the length of u $\left(\cos^2\theta = \frac{\|u_V\|^2}{\|u\|^2}\right)$. Likewise, if $U = span\{u, w_2, \cdots, w_p\}$ and $V = span\{v, w_2, \cdots, w_p\}$ are p-dimensional subspaces of X that intersects on $(p-1)$-dimensional subspace $W = span\{w_2, \cdots, w_p\}$ with $p \ge 2$ then the value of $\cos\,\theta$ is equal to the ratio between the volume of the p-dimensional parallelepiped spanned by the projection of $u, w_2, \cdots, w_p$ on V and the volume of the p-dimensional parallelepiped spanned by $u, w_2, \cdots, w_p$ [7].

In this paper, we will give some explicit formulas for angles between two subspaces in various cases of an inner product space of arbitrary dimension. This research is a further development of the work of Gunawan *et al*. In the next section, we will formulate angles in an n-inner product space and will show the connection between angles in an inner product space and in an n-inner product space.

2. METHODS

We have a method to obtain the result in this research. The first study, we study about angles between subspaces in an inner product space and give some explicit formulas. After that, we will formulate angles in an n-inner product space. To obtain the result, we use norm equivalent for showing the connection between angles in an inner product space and in an n-inner product space.

3. RESULTS AND DISCUSSION

3.1 Angles between subspaces in an inner product space

In this subsection, we will discuss angles between subspaces in an inner product space. Let $(X, \langle\cdot,\cdot\rangle)$ be an inner product space and consider the standar n-inner product

$$\langle x_0, x_1 | x_2, \ldots, x_n\rangle = \begin{vmatrix} \langle x_0, x_1\rangle & \langle x_0, x_2\rangle & \cdots & \langle x_0, x_n\rangle \\ \langle x_2, x_1\rangle & \langle x_2, x_2\rangle & \cdots & \langle x_2, x_n\rangle \\ \vdots & \vdots & \ddots & \vdots \\ \langle x_n, x_1\rangle & \langle x_n, x_2\rangle & & \langle x_n, x_n\rangle \end{vmatrix}$$

as in [4,9]. Then, the following function $\|x_1, \ldots, x_n\| := \langle x_1, x_1 | x_2, \ldots, x_n\rangle^{\frac{1}{2}}$ defines the standard n-norm. Geometrically, $\|x_1, \ldots, x_n\|$ represents the volume of the n-dimensional parallelepiped spanned by $x_1, \ldots, x_n$ (see[4,5]. Using definition in [7], we will determine an formula for the cosine of the angle between subspaces U and V that intersects on subspaces W of $(X, \langle\cdot,\cdot\rangle)$ as follows.

Proposition 1. Let $(X, \langle\cdot,\cdot\rangle)$ be a real inner product space. If $U = span\{u, w_1, \cdots, w_r\}$ is a $1 + r$-dimensional subspace and $V = span\{v_1, \cdots, v_q, w_1, \cdots, w_r\}$ is a $(q + r)$-dimensional subspace of X that intersects on r-dimensional subspace $W = span\{w_1, \cdots, w_r\}$ with $q, r \geq 1$ then the angle between subspaces U and V is θ with $\overset{2}{cos}\,\theta = \frac{\|(u^V)_W^{\perp}\|^2}{\|u_W^{\perp}\|^2}$ where $(u^V)_W^{\perp}$ and $u_W^{\perp}$ are the orthogonal complement of $u^V$and u, respectively, on W.

Proof. The projection of u on V is u^V. Next, we may write $u^V = (u^V)_W + (u^V)_W^{\perp}$ where $(u^V)_W$ is the projection of u^V on W and $(u^V)_W^{\perp}$ is the orthogonal complement of u^V on W. In line with this, we may write $u = u_W + u_W^{\perp}$ where u_W is the projection of u on W and $u_W^{\perp}$ is the orthogonal complement of u on W. Using the standard $(1 + r)$-norm, we obtain

$$\cos^2\theta = \frac{\|u^V, w_1, \cdots, w_r\|_{1+r}^2}{\|u, w_1, \cdots, w_r\|_{1+r}^2} = \frac{\|(u^V)_W + (u^V)_W^{\perp}, w_1, \cdots, w_r\|_{1+r}^2}{\|u_W + u_W^{\perp}, w_1, \cdots, w_r\|_{1+r}^2}$$

$$= \frac{\|(u^V)_W^{\perp}, w_1, \cdots, w_r\|_{1+r}^2}{\|u_W^{\perp}, w_1, \cdots, w_r\|_{1+r}^2} = \frac{\|(u^V)_W^{\perp}\|^2}{\|u_W^{\perp}\|^2}.$$

This formula tells us that the value of $\overset{2}{cos}\,\theta$ is equal to the ratio between the length of the orthogonal complement of u^V on W and the length of the projection of u on W. More generally, the angle that intersects on subspaces $W = span\{w_1, \cdots, w_r\}$ of X is poured in following theorem:

Theorem 2. *Let* $(X, \langle\cdot,\cdot\rangle)$ *be a real inner product space. If* $U = span\{u_1, \cdots, u_p, w_1, \cdots, w_r\}$ *is a* $(p + r)$-*dimensional subspace and* $V = span\{v_1, \cdots, v_q, w_1, \cdots, w_r\}$ *is a* $(q + r)$-*dimensional subspace on* X *with* $p \leq q$ *that intersects on* r-*dimensional subspace* $W = span\{w_1, \cdots, w_r\}$ *with* $r \geq 1$ *then the angle between subspaces* U *and* V *is* θ *with*

$\overset{2}{cos}\,\theta = \frac{\|(u_1^V)_W^{\perp}, \cdots, (u_p^V)_W^{\perp}\|_p^2}{\|(u_1)_W^{\perp}, \cdots, (u_p)_W^{\perp}\|_p^2}$, *where* $(u_i^V)_W^{\perp}$ *and* $(u_i)_W^{\perp}$ *are the orthogonal complement of* u_i^V *and* u_i, *respectively, on* W *for* $i = 1, \cdots, p$.

Proof. The projection of u_i on V is u_i^V. Next, we may write $u_i^V = (u_i^V)_W + (u_i^V)_W^{\perp}$ where $(u_i^V)_W$ is the projection of u_i^V on W and $(u_i^V)_W^{\perp}$ is the orthogonal complement of u_i^V on W. In line with this, we may write $u_i = (u_i)_W + (u_i)_W^{\perp}$ where $(u_i)_W$ is the projection of u_i on W and $(u_i)_W^{\perp}$ is the orthogonal complement of u_i on W for $i = 1, \cdots, p$. Using the standard $(p + r)$-norm, we obtain

$$\cos^2\theta = \frac{\|u_1^V, \cdots, u_p^V, w_1, \cdots, w_r\|_{p+r}^2}{\|u_1, \cdots, u_p, w_1, \cdots, w_r\|_{p+r}^2} = \frac{\|(u_1^V)_W + (u_1^V)_W^{\perp}, \cdots, (u_p^V)_W + (u_p^V)_W^{\perp}, w_1, \cdots, w_r\|_{p+r}^2}{\|(u_1)_W + (u_1)_W^{\perp}, \cdots, (u_p)_W + (u_p)_W^{\perp}, w_1, \cdots, w_r\|_{p+r}^2}$$

$$= \frac{\|(u_1^V)_W^{\perp}, \cdots, (u_p^V)_W^{\perp}\|_p^2 \|w_1, \cdots, w_r\|_r^2}{\|(u_1)_W^{\perp}, \cdots, (u_p)_W^{\perp}\|_p^2 \|w_1, \cdots, w_r\|_r^2} = \frac{\|(u_1^V)_W^{\perp}, \cdots, (u_p^V)_W^{\perp}\|_p^2}{\|(u_1)_W^{\perp}, \cdots, (u_p)_W^{\perp}\|_p^2}.$$

3.2 Angles between subspaces in an n-inner product space

In this subsection, we will discuss angles between subspaces in an n-inner product space and its connection with angles in an inner product space. Let $(X, \langle\cdot,\cdot | \cdot, \ldots, \cdot\rangle)$ be a real n-inner product space with $n \geq 2$. Fix a linearly independent set $\{a_1, \ldots, a_n\}$ in X with respect to $\{a_1, \ldots, a_n\}$, define the function $\langle\cdot,\cdot\rangle^*$ by

$$\langle x, y\rangle^* = \sum_{\{i_2,\ldots,i_n\}\subseteq\{1,\ldots,n\}} \langle x, y | a_{i_2}, \ldots, a_{i_n}\rangle$$

for each $x, y \in X$. According to [3], the function $\langle x, y\rangle^*$ defines an inner product on X. Moreover $\|x\|^* = \left[\sum_{\{i_2,\ldots,i_n\}\subseteq\{1,\ldots,n\}} \|x, a_{i_2}, \ldots, a_{i_n}\|^2\right]^{\frac{1}{2}}$ defines a norm that corresponds to an inner product $\langle\cdot,\cdot\rangle^*$ pada X. Next, using an inner product $\langle\cdot,\cdot\rangle^*$, we have a new standard n-inner product $\langle\cdot,\cdot | \cdot, \ldots, \cdot\rangle^*$ on X, namely

$$\langle x_0, x_1 | x_2, \ldots, x_n \rangle^* = \begin{vmatrix} \langle x_0, x_1\rangle^* & \langle x_0, x_2\rangle^* & \cdots & \langle x_0, x_n\rangle^* \\ \langle x_2, x_1\rangle^* & \langle x_2, x_2\rangle^* & \cdots & \langle x_2, x_n\rangle^* \\ \vdots & \vdots & \ddots & \vdots \\ \langle x_n, x_1\rangle^* & \langle x_n, x_2\rangle^* & \cdots & \langle x_n, x_n\rangle^* \end{vmatrix}$$

and a new standard n-norm $\|x_1, \ldots, x_n\|^* := (\langle x_1, x_1 | x_2, \ldots, x_n\rangle^*)^{\frac{1}{2}}$. Furthermore, one may also use an inner product $\langle\cdot,\cdot\rangle^*$ and its induced norm to study the angle between subspaces in an n-inner product space. As in [7] with the new standard n-norm, we define the angle between subspaces in an n-inner product space.

Definition 3. *Let $(X, \langle\cdot,\cdot \mid \cdot,\ldots,\cdot\rangle)$ be a real n-inner product space. If $U = span\{u_1, \cdots, u_p\}$ is a p-dimensional subspace and $V = span\{v_1, \cdots, v_q\}$ is a q-dimensional subspace of X with $p \le q$, then the angle between subspaces U and V is defined by θ with $cos^2\theta = \frac{\left(\|u_1^V,\cdots,u_p^V\|_p^*\right)^2}{\left(\|u_1,\cdots,u_p\|_p^*\right)^2}$, where u_i^V denote the projection of u_i on V for each $i = 1, \cdots, p$ and $\|\cdot, \cdots, \cdot\|_p^*$ denotes the standard p-norm on $(X, \langle\cdot,\cdot\rangle^*)$.*

According to Definition 3, for case $p = q$, we have an explisit formula the cosine of the angle θ that can be obtained as follows.

Proposition 4. Let $(X, \langle\cdot,\cdot \mid \cdot,\ldots,\cdot\rangle)$ be a real n-inner product space. If $U = span\{u_1, \cdots, u_p\}$ and $V = span\{v_1, \cdots, v_p\}$ are p-dimensional subspaces of X then the angle between subspaces U and V is θ with $\cos^2\theta = \frac{\left(det\left[\langle u_i, v_j\rangle^*\right]\right)^2}{\left(\|u_1,\cdots,u_p\|_p^*\right)^2\left(\|v_1,\cdots,v_p\|_p^*\right)^2}$.

Proof. The projection of u_i on V for $i = 1, \cdots, p$ may be expressed as $u_i^V = \sum_{k=1}^p \alpha_{ik}\, v_k$. Observe that

$$\langle u_i^V, u_j^V\rangle^* = \langle u_i, u_j^V\rangle^* = \textstyle\sum_{k=1}^p \alpha_{ik}\, \langle u, v_k\rangle^*$$

for $i, j = 1, \cdots, p$. Hence we have

$$\left(\|u_1^V, \cdots, u_p^V\|_p^*\right)^2 = \begin{vmatrix} \sum_{k=1}^p \alpha_{1k}\, \langle u_1, v_k\rangle^* & \cdots & \sum_{k=1}^p \alpha_{pk}\, \langle u_1, v_k\rangle^* \\ \vdots & \ddots & \vdots \\ \sum_{k=1}^p \alpha_{1k}\, \langle u_p, v_k\rangle^* & \cdots & \sum_{k=1}^p \alpha_{pk}\, \langle u_p, v_k\rangle^* \end{vmatrix}$$

$$= \begin{vmatrix} \langle u_1, v_1\rangle^* & \cdots & \langle u_1, v_p\rangle^* \\ \vdots & \ddots & \vdots \\ \langle u_p, v_1\rangle^* & \cdots & \langle u_p, v_p\rangle^* \end{vmatrix} \begin{vmatrix} \alpha_{11} & \cdots & \alpha_{p1} \\ \vdots & \ddots & \vdots \\ \alpha_{1p} & \cdots & \alpha_{pp} \end{vmatrix}.$$

Because of $\langle u_i, v_i\rangle^* = \langle u_i^V, v_i\rangle^*$ with $i = 1, \cdots, p$, we obtain

$$\begin{vmatrix} \langle u_1, v_1\rangle^* & \cdots & \langle u_1, v_p\rangle^* \\ \vdots & \ddots & \vdots \\ \langle u_p, v_1\rangle^* & \cdots & \langle u_p, v_p\rangle^* \end{vmatrix} = \begin{vmatrix} \alpha_{11} & \cdots & \alpha_{1p} \\ \vdots & \ddots & \vdots \\ \alpha_{p1} & \cdots & \alpha_{pp} \end{vmatrix} \begin{vmatrix} \langle v_1, v_1\rangle^* & \cdots & \langle v_1, v_p\rangle^* \\ \vdots & \ddots & \vdots \\ \langle v_p, v_1\rangle^* & \cdots & \langle v_p, v_p\rangle^* \end{vmatrix}.$$

Consequently, we have

$$\frac{\left(\|u_1^V,\cdots,u_p^V\|_p^*\right)^2}{\left(\|u_1,\cdots,u_p\|_p^*\right)^2} = \frac{\begin{vmatrix} \langle u_1, v_1\rangle^* & \cdots & \langle u_1, v_p\rangle^* \\ \vdots & \ddots & \vdots \\ \langle u_p, v_1\rangle^* & \cdots & \langle u_p, v_p\rangle^* \end{vmatrix}^2}{\left(\|u_1,\cdots,u_p\|_p^*\right)^2\left(\|v_1,\cdots,v_p\|_p^*\right)^2} = \frac{\left(det\left[\langle u_i, v_j\rangle^*\right]\right)^2}{\left(\|u_1,\cdots,u_p\|_p^*\right)^2\left(\|v_1,\cdots,v_p\|_p^*\right)^2}.$$

Next, we will determine a formula for the cosine of the angle between subspaces U and V that intersects on subspaces W of $(X, \langle\cdot,\cdot \mid \cdot,\ldots,\cdot\rangle)$. The formula for the angle $U = span\{u, w_1, \cdots, w_r\}$ and $V = span\{v_1, \cdots, v_q, w_1, \cdots, w_r\}$ can be obtained as follows.

Proposition 5. Let $(X, \langle\cdot,\cdot \mid \cdot,\ldots,\cdot\rangle)$ be a real n-inner product space. If $U = span\{u, w_1, \cdots, w_r\}$ is a $(1 + r)$-dimensional subspace and $V = span\{v_1, \cdots, v_q, w_1, \cdots, w_r\}$ is a $(q + r)$-dimensional subspace on X that intersects on r-dimensional subspace $W = span\{w_1, \cdots, w_r\}$ with $r \ge 1$ then the angle between subspaces U and V is $(0 \le \theta \le \frac{\pi}{2})$, with $\cos^2\theta = \frac{\left(\|(u^V)_W^\perp\|^*\right)^2}{\left(\|u_W^\perp\|^*\right)^2}$ where $(u^V)_W^\perp$ and $u_W^\perp$ are the orthogonal complement of u^V and u, respectively, on W.

Proof. Writing $u^V = (u^V)_W + (u^V)_W^\perp$ and $u = u_W + u_W^\perp$ and using the new standard $(1 + r)$-norm, we obtain

$$\cos^2\theta = \frac{(\|u^V, w_1, \cdots, w_r\|_{1+r}^*)^2}{(\|u, w_1, \cdots, w_r\|_{1+r}^*)^2} = \frac{(\|(u^V)_W + (u^V)_W^\perp, w_1, \cdots, w_r\|_{1+r}^*)^2}{\|u_W + u_W^\perp, w_1, \cdots, w_r\|_{1+r}^2}$$

$$= \frac{(\|(u^V)_W^\perp, w_1, \cdots, w_r\|_{1+r}^*)^2}{(\|u_W^\perp, w_1, \cdots, w_r\|_{1+r}^*)^2} = \frac{(\|(u^V)_W^\perp\|^*)^2}{(\|u_W^\perp\|^*)^2}.$$

More generally, using Definition 7 and following the proof of Theorem 4, the angle $U = span\{u_1, \cdots . u_p, w_1, \cdots, w_r\}$ and $V = span\{v_1, \cdots, v_q, w_1, \cdots, w_r\}$ with $p \le q$ can be obtained as follows.

Theorem 6. *Let* $(X, \langle\cdot,\cdot \mid \cdot, \dots, \cdot\rangle)$ *be a real* n*-inner product space. If* $U = span\{u_1, \cdots, u_p, w_1, \cdots, w_r\}$ *is a* $(p + r)$*-dimensional subspace and* $V = span\{v_1, \cdots, v_q, w_1, \cdots, w_r\}$ *is a* $(q + r)$*-dimensional subspace on* X *with* $p \le q$ *that intersects on* r*-dimensional subspace* $W = span\{w_1, \cdots, w_r\}$ *with* $r \ge 1$ *then the angle between subspaces* U *and* V *is* $(0 \le \theta \le \frac{\pi}{2})$, *with* $cos^2\theta = \frac{\left(\|(u_1^V)_W^\perp, \cdots, (u_p^V)_W^\perp\|_p^*\right)^2}{\left(\|(u_1)_W^\perp, \cdots, (u_p)_W^\perp\|_p^*\right)^2}$, *where* $(u_i^V)_W^\perp$ *and* $(u_i)_W^\perp$ *are the orthogonal complement of* u_i^V *and* u_i, *respectively, on* W *for* $i = 1, \cdots, p$.

Before we discuss the connection between angles in an inner product space and in an n-inner product space, we have equivalent norm on $(X, \langle\cdot,\cdot\rangle)$ with norm $\|\cdot\|^*$ where $\{a_1, \dots, a_n\}$ are an orthonormal set on $(X, \langle\cdot,\cdot \mid \cdot, \dots, \cdot\rangle)$ as follows.

Proposition 7. *[6] Norm* $\|\cdot\|^*$ *equivalent with the norm that corresponds to the inner product* $\|\cdot\|$ *on* $(X, \langle\cdot,\cdot\rangle)$. *Namely, ,* $\|x\| \le \|x\|^* \le \sqrt{n}\|x\|$ *for every* $x \in X$.

From this proposition, we have the connection between angles in an inner product space and in an n-inner product space, namely

Theorem 8. *If* θ *is the angle between subspaces* U *and* V *of* $(X, \langle\cdot,\cdot\rangle)$ *and* θ^* *is the angle between subspaces* U *and* V *of* $(X, \langle\cdot,\cdot \mid \cdot, \dots, \cdot\rangle)$ *with* $dim\ U = 1 + r$, $dim\ V = q + r$ *for* $q \ge 1$ *and* $dim\ (U \cap V) = r$ *for* $r \ge 1$ *then*

$$\frac{1}{n} cos^2\theta \le cos^2\theta^* \le n cos^2\theta.$$

Proof. Writing $U = span\{u, w_1, \cdots, w_r\}$, $V = span\{v_1, \cdots, v_q, w_1, \cdots, w_r\}$ and $U \cap V = span\{w_1, \cdots, w_r\}$. Next, using Proposition 7, we have

$$\frac{\|(u^V)_W^\perp\|^2}{n\|u_W^\perp\|^2} \le \frac{(\|(u^V)_W^\perp\|^*)^2}{(\|u_W^\perp\|^*)^2} \le \frac{n\|(u^V)_W^\perp\|^2}{\|u_W^\perp\|^2},$$

with $(u^V)_W^\perp$ and $u_W^\perp$ are the orthogonal complement of u^V and u, respectively, on W. According to Proposition 1 and 3, we have $\cos^2\theta^* = \frac{\left(\|(u^V)_W^\perp\|^*\right)^2}{\left(\|u_W^\perp\|^*\right)^2}$ and $\cos^2\theta = \frac{\|(u^V)_W^\perp\|^2}{\|u_W^\perp\|^2}$. Hence, we obtain $\frac{1}{n}\cos^2\theta \le \cos^2\theta^* \le n\cos^2\theta$.

By Theorem 8 for $= 1$, the value of $\cos^2\theta^*$ is equal to the value of $\cos^2\theta$. Nevertheless, the upper bound of $\cos\ \theta^*$ for $n \ge 2$ is inappropriate because its value is greater than 1. If $\cos\ \theta = 1$ then the lower bound of $\cos\ \theta^*$ is $\frac{1}{n}$.

4. CONCLUSIONS

We have given a formula for angles between two subspaces U and V that intersects on subspaces W of an inner product space of arbitrary dimension. Moreover, we have given a formula for angles in an n-inner product space. Using this result, we have proved the connection between angles between two subspaces U and V in an inner product space and in an n-inner product space where $\mathrm{dim\ U = 1 + r}$, $\mathrm{dim\ V = q + r}$ for $\mathrm{q \ge 1}$ and $\mathrm{dim\ (U \cap V) = r}$ for $\mathrm{r \ge 1}$. Acknowledgement. The research is supported by ITB Research and Innovation Program 2017.

5. REFERENCES

[1]. T. W. Anderson, 1958, An Introduction to Multivariate Statistical Analysis, *John Wiley* & *Sons, Inc*., New York

[2]. C. Davis and W. Kahan, 1970, The rotation of eigenvectors by a perturbation, *III. SIAM J. Numer. Anal*., **7**,1-46.

[3]. H. Gunawan, 2002, Inner Products On n-Inner Products Spaces, *Soochow Journal of Mathemathics*, **28(4)** 389-398.

[4]. H. Gunawan, 2002, On n-Inner products, n-Norms, and The Cauchy-Schwarz Inequality, *Sci. Math. Jpn*., **55**, 53-60.

[5]. H. Gunawan and M. Mashadi, 2001, On n-Normed Spaces, *Int. J. Math. Sci*., **27**, 321-329.

[6]. H. Gunawan and O. Neswan, 2005, On Angles Between Subspaces of Inner Product Spaces, *J. Indo. Math. Soc*., **11**

[7]. H. Gunawan, O. Neswan and W. Setya-Budhi, 2005, A Formula for Angles between Two Subspaces of Inner Product Spaces, *Beitr. zur Algebra und Geometrie Contributions to Algebra and Geometry*, **46(2)**, 311-320.

[8]. Y. Igarashi and K. Fukui, 2010, 3D Object Recognition Based on Canonical Angles between Shape Subspaces, *Springer ACCV'10* ***Volume Part IV***, 580-591.

[9]. A. Misiak, 1989, n-Inner Product Spaces", *Math. Nachr*., **140**, 299-319.

[10]. I.B. Risteski and K.G. Trencevski, 2001, Principal Values and Principal Subspaces of Two Subspaces of Vector Spaces with Inner Product", *Beitr. Algebra Geom*., **42**, 289-300.

Risk Identification on Food Safety for Fish Supply Chain with Pareto Diagram

Hana Catur Wahyuni[1*], Wiwik Sumarmi[2]

[1,2]Industrial Engineering, Universitas Muhammadiyah Sidoarjo, Indonesia
*Corresponding authors: [hanacatur@umsida.ac.id]

Abstract-Risk analysis in food safety is important because the early identification of risks in the supply chain is able to increase market share and improve the competitiveness of food industry in the global market for food products. One form of food that has a high risk for perishables in the supply chain is fish. This study aims to (1) identify food safety risks of fish at every stage of the supply chain, (2) determining the priority of risk in the supply chain of fish. The object of research is the fresh fish distribution system located in the district of Sidoarjo. Data processing is done by using Pareto diagram to determine the amount of activity that is a potential risk. The results showed identified 11 risky activities on food safety, namely feeding on fish, system management cleanliness of the pool / pond, the process of harvesting the fish, how to spawning fish, the way of sorting the fish, how tow fish storage, how to marketing of fish, the type of vehicle used for the delivery of fish , how safe when shipping fish, how to move fish , the way handling unsold fish, how to handle the fish is not worth selling. And, the most high-risk activities on food safety are fish storage, how to market of fish, the type of vehicle used for the delivery of fish and how safe when shipping fish.

Keyword: supply chain, food safety, risk identification, pareto diagram.

1. INTRODUCTION

Food safety is one of important for people’s life. Therefore, everyone (consumer) wants to make sure that the food they buy and eat quality, safe when produced and throughout the supply chain [1]. Various phenomena of events caused by the food unsafe for consumption have occurred in various parts of the world. In United Stated, The Center for Disease Control and Prevention (CDC) estimates that 76 million people contract a food borne illness and about 5000 die annually [2]. In Malaysia, an increase in diseases caused by cholera, food poisoning and hepatitis A in the range of the year 2009-2011 [3]. According to WHO estimates, in Africa there will be 91 000 people falling ill and more than 137 000 people die each year as a result of food contamination [4]. In Indonesia, during 2015 the 84 incidents of poisoning caused by food [5].

Based on this phenomenon, it is important to identify the risks posed by food. Risk identification is important because it is able to increase market share and improve the competitiveness in the global market for food products. Therefore, to ensure food safety, the identification of risk needs to be carried out along the supply chain products. Because risk in the supply chain is not always a negative effect, but can be positive [6]. Risks involved in the supply chain can be sourced from internal (nature, political system, competitor and market) and external (available capacity, internal operation, information system) [7]. By identifying risks along the supply chain, it can be arranged strategies to avoid or reduce the impact of such risks.

In the context of food safety risks in the supply chain, the factors considered are all activities in the supply chain risky foods alter the product to be unsafe for consumption. Identify the activities in the food supply chain at high risk on food Security settings need to maintain product quality and consumer trust. One form of food that has a high risk for perishables in the supply chain (capture, process the handling, distribution and marketing) is fish (seafood) [8]. It is triggered because food security in Indonesia for seafood focuses on traditional surveillance pattern where the emphasis of quality control and food safety made by testing the final product has not entered a risk factor for them [9].

Several studies of fish in Indonesia have been done by previous researchers, among others, the quality of fish [10, 11], and the fish supply chain [12, 13]. However, the research does not yet explain about food safety risks inherent in the supply chain of fish. This study aims to (1) identify food safety risks of fish at every stage of the supply chain, (2) determine the priority of risk in the supply chain of fish.

3. METHODS

The object of research is the fresh fish distribution system located in the district of Sidoarjo. Techniques of data retrieval are done through survey, observation and questionnaire. Supply chain distribution system used in this study consists of a source, make, deliver and return.

Data processing is done by using Pareto diagram to determine the amount of activity that is potentially risky. In this study, the stages of preparing the Pareto diagram are:

a. Identifying food safety risks in fish along the supply chain.

b. Specifying the period of time to make observations to those risks.

c. Determining the frequency based on value of likelihood, impact and detection for each of the risky activity. The scale used to determine the likelihood, impact and detection refers to a tabulation Gazpers [14].

d. Developing a Pareto diagram by multiplying the value of possibilities, and the impact of such detection. The multiplication result is defined as the value of the RPN (risk priority number)

4. RESULT AND DISCUSSION

The results showed the structure of the supply chain to the fish farmers, traders / distributors and retailers. Each of these actors in these structures a risk of contaminated fish resulted in harmful ingredients that are not safe to eat. The results also identifies that there are 11 activities that risk in the system supply chain, namely: feeding on fish, system management cleanliness of the pool / pond, the process of harvesting the fish, how to spawning fish, the way of sorting the fish, to store fish, how to market of fish, the type of vehicle used for the delivery of fish , how safe when shipping fish, how to move fish , the way handling unsold fish, how to handle the fish is not worth selling.

Table 1. RPN Value for each activity

	Risk event	RPN	Rank
1	Feeding on fish	126	5
2	System management cleanliness of the pool / pond	90	6
3	The process of harvesting the fish	144	4
4	How to spawning fish	343	2
5	How to fish storage	448	1
6	How to marketing of fish	448	1
7	The type of vehicle used for the delivery of fish	448	1
8	How safe when shipping fish	448	1
9	How to move fish	294	3
10	The way of handling unsold fish	126	5
11	How to handle the fish is not worth selling	126	5

Table 1 shows the value of the RPN for each risk event in the fish supply chain. Furthermore, the results of table 1 will be used to construct the Pareto diagram.

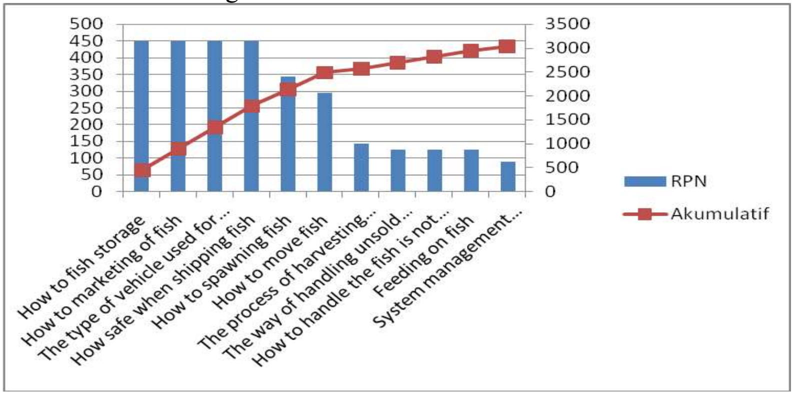

Figure 1. Pareto diagram risk food safety supply chain

Figure 1 shows the Pareto diagram for the risk event in the fish supply chain. Based on Pareto diagram can be seen that there are four activities that have risk food safety is highest in the supply chain of fish, namely: how to fish storage, how to the marketing of fish, the type of vehicle used for the delivery of fish and how safe when shipping fish. The second highest risk food safety contained on activities how to spawning fish. How to move fish are activities that have potential risk food safety third highest. Whereas the fourth highest is the process of harvesting the fish. The highest food safety risks to five are the way of handling unsold fish, How to handle the fish is not worth selling, feeding on fish and the sixth highest food safety risks is a management system cleanliness of the pool / pond.

This condition indicates that there must be an improvement in the fish storage, marketing, types of transport and how irregularities during transmission. In these activities, there is a risk food safety, which is contaminated with bacteria that lead to fish is not safe for consumption. One type of bacteria that can contaminate fish is Escherichia bacterium, sourced from the water and the handling is not good, so that cleanliness should be maintained throughout the distribution chain, because the fish is perishable foodstuffs from the other [15].

5. CONCLUSION

The results of field observations indicate that there are four main activities are at highest risk, namely how to fish storage, how to the marketing of fish, the type of vehicle used for the delivery of fish and how safe when shipping fish. The results of these studies were described in Pareto diagram. The results are the important information because food industry are often unaware of the risks until such risks emerge and become a problem for the company, so it takes a lot of resources to get it done, but the early risk identification in supply chain management is able to increase the market share of industry [3]. Thus, by knowing the risks that would occur, then food industry can develop strategies to avoid or reduce the risks that possibly arise.

6. REFERENCE

[1]. Olsson A, Skjoldebrand C, 2008, Risk Management And Quality Assurance Through The Food Supply Chain- Case Studies In The Swedish Food Industry, *The Open Food Science*, **2**, pp 49-56.

[2]. Subramanian V.C., Gaukler G.M., 2015, Product Contamination In A multi-Stage Food Supply Chain, *European Journal Of Operational Research*, **244**, pp 164-175.

[3]. Mutalib A.M., Syafikaz A.N., Sakai K., Shirai Y., 2015, An overview of foodborne illness and food safety in Malaysia*, International Food Research Journal* **22 (3),** pp 896-901.

[4]. WHO. Website: who.int/foodsafety/en/. Date: 12 Februari 2017.

[5]. Sentra Informasi Keracunan Nasional, BPOM RI. Website: ik.pom.go.id. Date:12 Februari 2017.

[6]. Florian G.L., Constangiora A., 2014, The Impact Of Risk In Supply Chain On Organizational Performance: Evidence From Romania, *Economia,Seria Management*, **Vol 17**, iss 2.

[7]. Olson D.L., Dash Wu D., 2010, A Review Of Enterprise Risk Management In Supply Chain, *Kybernetes*, **Vol 39** No 5, pp 694-706.

[8]. Nurani TW., Astarini JE., Nareswari M., 2011, Sistem Penyediaan Dan Pengendalian Kualitas Produk Ikan Segar di Hypermarket, *Jurnal Pengolahan Hasil Perikanan Indonesia*, **Vol XIV**, No 1, hal 56- 62.

[9]. Trilasani W., Bintang M., Monintja D.R., Hubies M., 2010, Analisis Regulasi Sistem Manajemen Keamanan Pangan Tuna di Indonesia dan Nagara Tujuan Ekspor, *Jurnal Pengolahan Hasil Perikanan Indonesia*, **Vol XIII**, No 1, hal 58- 75.

[10].Swastawati F., Surti T., Agustini T.W., Riyadi P.H., 2013, Karakteristik Kualitas Ikan Asap Yang Diproses Dengan Menggunakan Metode dan Jenis Ikan Berbeda, *Jurnal Aplikasi Teknologi Pangan*, **Vol 2** No 3.

[11].Mardiana N., Waluyo S., Ali M., 2015, Analisis Kualitas Ikan Sembilang Asap Di Pengolahan Ikan "Mina Mulya" Kecamatan Pasir Sakti, Lampung Timur, *Jurnal Teknik Pertanian Lampung*, **Vol 3** No 3, hal 283-290.

[12].Triyanti R., Yusuf R, 2015, Analisis Manajemen Rantai Pasok Lobster (Studi Kasus Di Kabupaten Simeulue Aceh, *Jurnal Sosek KP*, **Vol 10**, No 2, hal 203-216.

[13].Tompodung E., Worang F.G., Roring F., 2016, Analisis Rantai Pasok Ikan Mujair Di Kecamatan Eris Kabupaten Minahasa, *Jurnal EMBA*, **Vol 4** No 4, September, hal 279-290.

[14].Gazpersz V.,2012, "All In One Management Toolbook", PT Percetakan Penebar Swadaya, Jakarta

[15].Francesca H.L., Lohoo J.H.L., Mewengkang W.H., 2014, Identifikasi Bakteri Escherichia Pada Ikan Selar Bakar Di Beberapa Resto Di Kota Manado, *Jurnal Media Teknologi Hasil Perikanan*, **Vol 2** No 1, Februari.

Power Quality Improvement Caused by Electric Arc Furnace Using Unified Power Quality Conditioner

Wahyuni Martiningsih[1*], Rocky Alfanz[1], Rizky[2]

[1] Department of Electrical Engineering, Faculty of Engineering, Sultan Ageng Tirtayasa University
Jl.Jendral Sudirman Km. 03, Cilegon city, Banten
* Corresponding authors: [y_martiningsih@untirta.ac.id]

Abstract – Electric arc furnace (EAF) is a non-linear load that causes power quality problems at the voltage in the power system, especially the distribution system, voltage sag will occur that could disturb the quality of the voltage when EAF operations. In this research it is proposed the use of compensation unified power quality conditioner (UPQC) to dampen voltage sag. The UPQC using three phase voltage source converter (VSC) with control of amplitude and phase angle of the three-phase sinusoidal voltage at the fundamental frequency. The control approach is based on synchronous reference frame theory. The results of the simulation with a load EAF before voltage compensation system 90.96% after voltage compensation system becomes 99.92% on the nominal voltage of 24 kV distribution system and power factor before compensation 81.88% after compensation becomes 99.98%. The performance of UPQC is quite reliable because it is able to compensate time quickly to changes in the value of the voltage.

Keywords: power quality, UPQC, EAF

1. INTRODUCTION

Electrical disturbance problem often occurs on the distribution system, especially in industrial areas. Electrical disturbances associated with power quality, which include power factor, harmonics, sags, swells, interruptions and unbalanced conditions [1][2][3][4].

The term power quality is a concept which gives an idea of good or poor quality electrical power as a result of some kind of disturbance in the electrical system. Power quality is any problem in the form of electric power deviation of voltage, current or frequency that lead to failure or error in the operation of the equipment that occurred in the electrical energy consumers [4][5].

Electric Arc Furnace (EAF) is a typical furnace used in steel making company. Three fundamental changes in the operation of the electric arc furnace, which can produce disturbances voltage at the power system, i.e. short-circuit conditions, open circuit condition, and normal operation [6]. The operation of EAF causes electric short circuit internally between phase and steel. This process then decreases the quality of electricity.Voltage sags and swells frequently occur. High harmonic distortions may also appear due to the internal process of EAF. Power transformers may be overheating, dips on lighting systems, or failure if the dip voltage is deeper than 35%. In this research, a compensator was designed to improve power quality which is called unified power quality conditioner (UPQC).

Voltage sag is according to the IEEE 1159-1995 standard. IEEE recommended practice for monitoring electric power quality. The definition of sag is a decrease in rms value of voltage or current at the power frequency for 0.5 cycles (0.01 sec) to 1 min, and a voltage change from 0.1 to 0.9 pu to the rms value of voltage or current [7]. Voltage sag is usually associated with an error or disturbance of the system, but can also occur because of filtering against a load with a large consumption of electrical energy. As an example of the burden of the electric arc furnace (EAF), reactive power is absorbed. EAF will have a major impact on the supply voltage and during operation will create a voltage drop[8].

2. METHODS

2.1 Design system of load EAF

In this research the electrical network distribution system was designed at a voltage of 150 kV. A 100 MVA transformer was connected to each100 MVA to change the voltage to 30 kV and connected to the distribution system. A 93.5 MVA will change the voltage to 850 V and is connected load EAF. Figure 1 shows the electric distribution system in the steel industry.

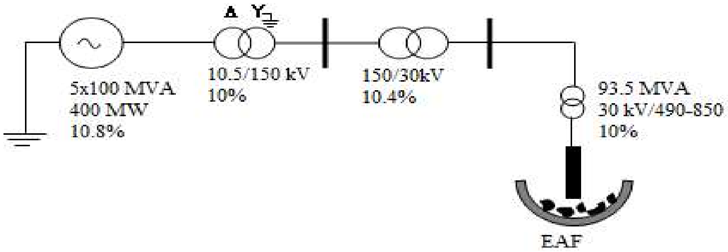

Figure 1. Electrical systems were observed in this research

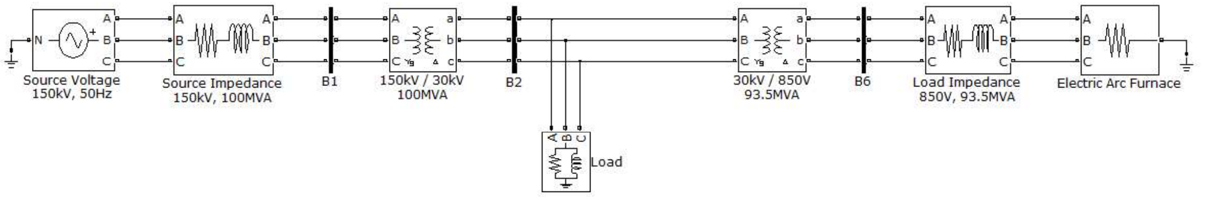

Figure 2. The design of the distribution system of figure 1.

2.2 Design of UPQC

UPQC consists of two voltage source converters (VSC) with the construction which is connected in series and shunt the distribution network to compensate voltage and load current. The main component is UPQC VSC, controller, filter and capacitor.

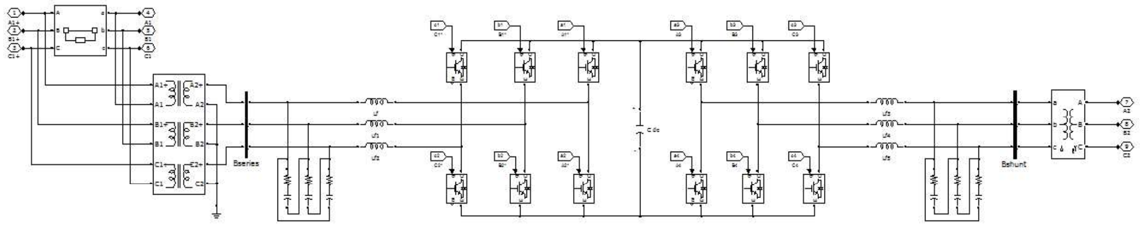

Figure 3. Design of UPQC

3. RESULTS AND DISCUSSION

In this research it has been designed and modeled 30 kV electrical system with electrical arc furnace as a load. The disturbance of power quality that is caused by the load EAF can be mitigated using UPQC. Power quality including voltage sag and power factor is of concern in this research. Compensator UPQC was used for improvement.

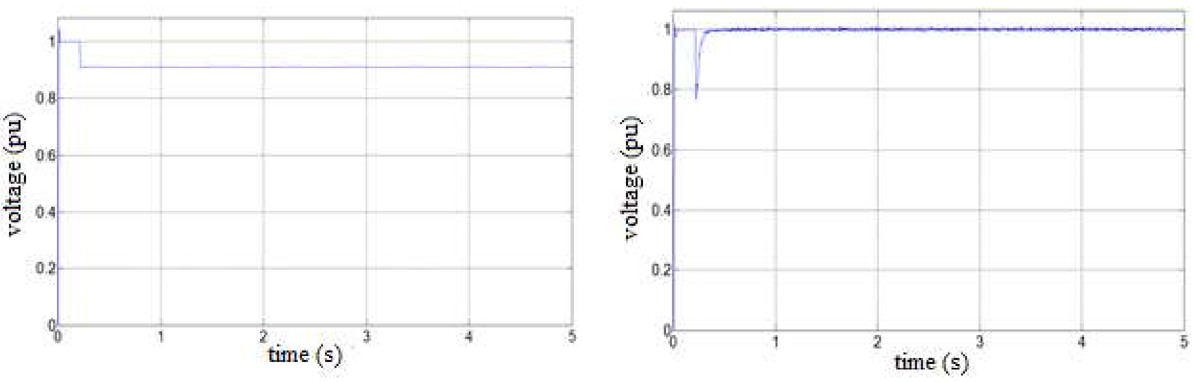

(a) (b)

Figure 4. (a) Voltage without UPQC, (b) Voltage with UPQC

The results of simulations showed that in the distribution system, voltage disturbances occurred during the 4.79 seconds and started at time 0.21 second as seen in figure 4 (a). There was voltage drop of 0.0904 pu and voltage distribution system decrease to 0.9096 pu. When UPQC was connected to the distribution system, disturbance of voltage can be improved at 0.9992 pu as seen in figure 4(b).

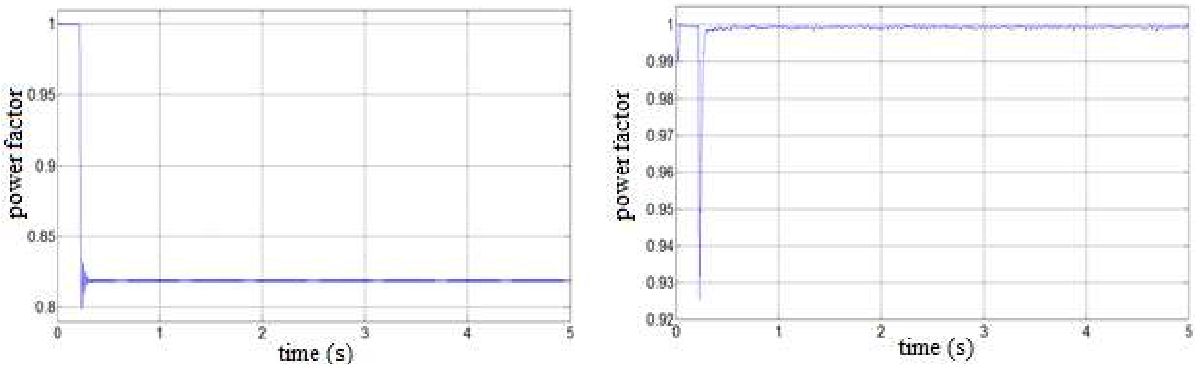

(a) (b)

Figure 5. (a) Power factor without UPQC, (b) Power Factor with UPQC

In the distribution system with EAF load, before compensated with UPQC, the power factor value is 0.8188 and after compensated with UPQC, the power factor value is 0.9998. Figure 5(b) shows the system power factor value after UPQC compensation. Compensator UPQC provides capacitive reactive power that can reduce the reactive power consumed by the load. Comparison of real power to apparent power is the power factor value.The apparent power and active power are separated by an angle which is the angle between the voltage and current. With the reactive power compensation using UPQC then the angle is smaler and the apparent power will be closer to the active power. The power factor improvement may occur with UPQC compensation distribution system installed. Apparent power can be increased due to the EAF which is non-linear. Reactive power can also be influenced by non-linear loads which have resulted in increased consumed reactive power. So UPQC provides capacitive reactive power compensation system, and the amount of reactive power consumed by the load can be reduced so that the system has improved power factor. Figure 6 is the magnitude of the active power and reactive power on the distribution system with a load of EAF. The installation of UPQC causes reactive power change.

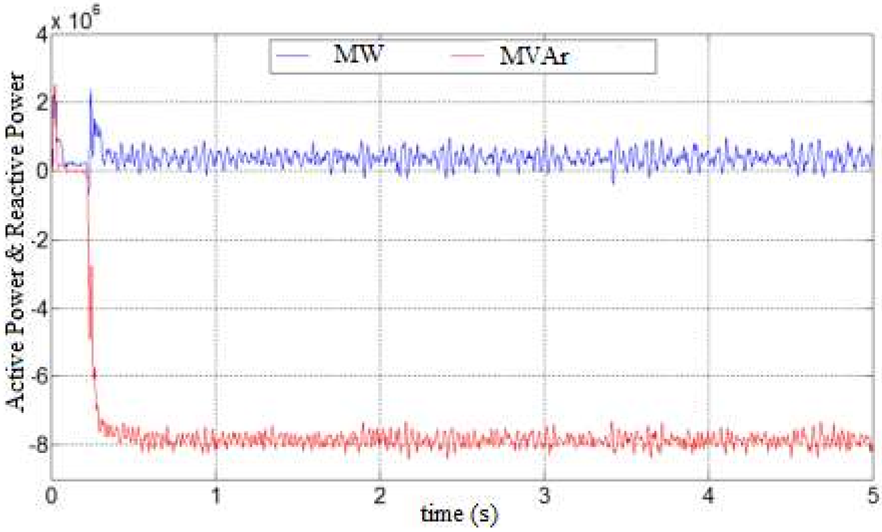

Figure 6. Active and Reactive Power of UPQC

Table 1. Comparison between before and after installed UPQC

Parameter	Without UPQC	With UPQC
Sag Voltage	0.9096	0.9992
Power Factor	0.8188	0.9998
VAR	-	-7,9 MVAR

4. CONCLUSIONS

1. Problems of voltage sag in the distribution system can be improved by using the UPQC. The system voltage after compensation rose to 0.9992 pu from 0.9096 pu. with a nominal voltage of 24 kV system.
2. Power factor improvement was also achieved with compensation UPQC and the use of EAF load power factor. Before compensation it is 0.8188 and after rising, it is 0.9998.
3. In improving the voltage sag, UPQC injects a capacitive reactive power of -7.9 MVAR

5. REFERENCES

[1]. S. Chattopadhyay, M. Mitra, and S. Sengupta, “Sag, Swell, Interruption, Undervoltage and Overvoltage,” *Electr. Power Qual. Dordr. Springer Neth.*, pp. 39–42, 2011.

[2] Wahyuni Martiningsih, Mochamad Ashari, Adi Soeprijanto, and Dian Sawitri, “Sag Voltage Identification on 30 kV Systems Affected By Electric Arc Furnace using Wavelet Transformation Method,” *J. Theor. Appl. Inf. Technol.*, **vol. 61**, no. 2, pp. 352–357, Mar. 2014.

[3] S. Mishra, C. N. Bhende, and B. K. Panigrahi, “Detection and Classification of Power Quality Disturbances Using S-Transform and Probabilistic Neural Network,” *IEEE Trans. Power Deliv.*, **vol. 23**, no. 1, pp. 280–287, Jan. 2008.

[4] A. M. Gaouda, S. H. Kanoun, M. M. A. Salama, and A. Y. Chikhani, “Pattern recognition applications for power system disturbance classification,” *IEEE Trans. Power Deliv.*, **vol. 17**, no. 3, pp. 677–683, Jul. 2002.

[5] Bincy K Jose, “Evaluation of Power Quality in Arc Furnace using Iec Flicker Meter,” *Int. J. Emerg. Technol. Adv. Eng. IJETAE*, **vol. 3**, no. 9, Sep. 2013.

[6] A. A. Gomez, J. J. M. Durango, and A. E. Mejia, “Electric arc furnace modeling for power quality analysis,” 2010, pp. 1–6.

[7] 1159-1995, “IEEE Recommended Practice for Monitoring Electric Power Quality,” IEEE Inc., New York, 1995.

[8] Ahmad Esfandiari, Mostafa Parniani, and Hossein Mokhtari, “Power Quality Impact of an Electric Arc Furnace and Its Compensation,” *J. Electr. Eng. Technol.*, **vol. 1**, no. 2, pp. 153–160, 2006.

Optimal Control Applied to The Spread of HIV/AIDS

Marsudi[1*]

[1] Department of Mathematics, Faculty of Science, University of Brawijaya, Malang, Indonesia
*Corresponding authors: [marsudi61@ub.ac.id]

Abstract – The Human Immunodeficiency Virus (HIV) is the etiological agent of Acquired immunodeficiency Syndrome (AIDS) and has become one of the major public health problems worldwide. This virus has been killing people for more than three decades and will continue doing so if no advances are made towards the better condition. We formulate an optimal control problem and the necessary conditions for the disease control in order to determine the role of unaware infective in the spread of HIV/AIDS using the condom, screening of unaware infective and antiretroviral therapy are used as the control items using optimal control theory and Pontryagin's Maximum Principle.

Keywords: HIV/AIDS, optimal control, unaware infective, Pontryagin's maximum principle.

1. INTRODUCTION

HIV (Human Immunodeficiency) and AIDS (Acquired Immune Deficiency Syndrome) is one of the health problems. Recently, there is no country that is free of HIV/AIDS and HIV/AIDS has led to a multidimensional crisis, especially in the health field.

Mathematical models have been used to explain the behavior of the disease and strategies for optimal control. [6] presented sensitivity analysis of the impact of screening and therapy on the dynamics of HIV transmission in Malang. [7] assessing the impact of optimal control on the treatment of HIV/AIDS and screening of unaware infectives and [3] presented optimal control of an HIV immunology model. A book written by [4] shows how to adjust controls in biological systems in order to achieve proper outcomes.

One of the programs in order to minimize the prevalence of HIV/AIDS is using the condom, HIV screening and antiretroviral therapy for people who tested HIV positive.

2. METHODS

In this paper, we consider the HIV model used in [6]. This model is governed by the following nonlinear system of differential equations. We introduce into the model in [6], condom use (u_1), screening of unaware infectives (u_2) and antiretroviral therapy (u_3) as a time-dependent control to reduce the spread of HIV/AIDS. The compartment diagram in Figure 1 illustrates the interactions of the different population.

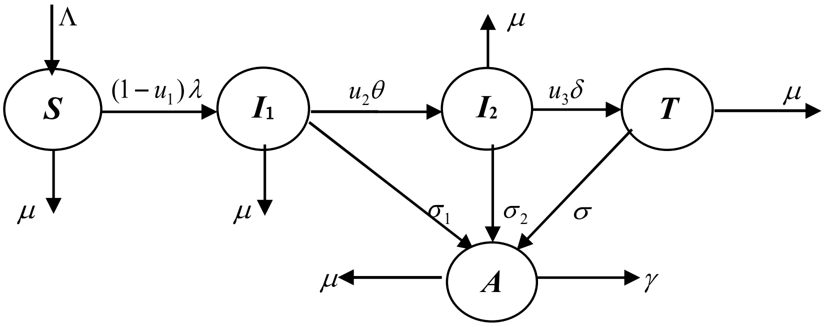

Figure 1 The Compartmental diagram for HIV/AIDS model with condom use, screening and therapy

We formulate an optimal control problem subject to the model dynamics, characterize the optimal control and the necessary conditions for the disease control in order to determine the role of unaware infective in the spread of HIV/AIDS using of condom, screening of unaware infective and antiretroviral therapy are used as the control items and constitute its optimality using Pontryagin's Maximum Principle. We solve the resulting optimality system numerically using a fourth-order iterative Runge-Kutta scheme (forward-backward sweep method).

3. RESULTS AND DISCUSSION

3.1 Mathematical Model

We consider a sexually active population N (t) is divided into five compartments: S(t), I_1(t), I_2(t), T(t) and A(t). S(t) represents the number of susceptible individuals; I_1(t) represents the number of HIV-positive individuals in the asymptomatic stage of HIV infection (unaware infective); I_2(t) represents the number of HIV-positive individuals in the pre-AIDS stage but not receiving antiretroviral therapy (screening infective); T(t) represents the number of individuals who are receiving antiretroviral therapy (therapy infective) and A(t) represents the number of individuals with full-blown AIDS but not receiving antiretroviral therapy (AIDS patient). We assume that an individual can be infected only through the sexual contacts with third types of infective. In view of the assumptions and the compartment diagram we obtain the following system of nonlinear ordinary differential equations

$$\begin{aligned}
\frac{dS}{dt} &= \Lambda - (1-u_1)\lambda S - \mu S \\
\frac{dI_1}{dt} &= (1-u_1)\lambda S - (u_2\theta + \sigma_1 + \mu)I_1 \\
\frac{dI_2}{dt} &= u_2\theta I_1 - (u_3\delta + \sigma_2 + \mu)I_2 \\
\frac{dT}{dt} &= u_3\delta I_2 - (\sigma + \mu)T \\
\frac{dA}{dt} &= \sigma_1 I_1 + \sigma_2 I_2 + \sigma T - (\gamma + \mu)A
\end{aligned} \tag{1}$$

where

$$\lambda = \frac{(c_1\beta_1 I_1 + c_2\beta_2 I_2 + c_3\beta_3 T)}{N}, \; N(t) = S(t) + I_1(t) + I_2(t) + T(t) + A(t)$$
$$\text{and } S(0) = S_0, I_1(0) = I_{10}, I_2(0) = I_{20}, T(0) = T_0, A(0) = A_0. \tag{2}$$

Here, the condom use control is bounded ($0 \le u_1 \le 1$), the control on the screening of unaware infective is bounded ($0 \le u_2 \le 1$) and the control on antiretroviral therapy is bounded ($0 \le u_3 \le 1$). The coefficient, $1-u_1$ represents the effort that prevents HIV infection in order to reduce the contact between the infectious and unaware infective.

3.2 The Optimal Control Problem

The problem is to minimize the objective functional

$$J(u_1,u_2,u_3) = \min_{u_1,u_2,u_3} \int_0^{t_f} [w_1 I_1 + \tfrac{1}{2}(w_2 u_1^2 + w_3 u_2^2 + w_4 u_3^2)]\, dt \tag{3}$$

subject to the system of equations (1) with appropriate state initials conditions (2) and t_f is the final time, while the control set U is defined

$$U = \{(u_1,u_2,u_3) \,|\, 0 \le u_1 \le 1, 0 \le u_2 \le 1, 0 \le u_3 \le 1 \text{ for } t \in t_f\} \tag{4}$$

and the weight constants w_1, w_2, w_3 and w_4 are positive weights. The weight constants, w_1, is the relative measure of the importance of reducing the unaware infective on the spread of HIV/AIDS, while w_2, w_3 and w_4 are the relative measures of the cost or effort required to implement each of the associated controls. Our target is to minimize the objective functional defined in equation (3) by minimizing the number of the unaware infective, while minimizing the cost of controls u_1^*, u_2^* and u_3^* such that

$$J(u_1^*,u_2^*,u_3^*) = \min\{J(u_1,u_2,u_3) \,|\, u_1,u_2,u_3 \in U\} \tag{5}$$

The necessary conditions that an optimal control problem must satisfy come from Pontryagin's Maximum Principle [4]. This principle converts (1), (2) and (3) into a problem of minimizing an Hamiltonian with respect to u_1, u_2 and u_3

$$\begin{aligned}
H = {} & w_1 I_1 + \tfrac{1}{2}(w_2 u_1^2 + w_3 u_2^2 + w_4 u_3^2) + \lambda_S \left[\Lambda - (1-u_1)\frac{(c_1\beta_1 I_1 + c_2\beta_2 I_2 + c_3\beta_3 T)S}{S + I_1 + I_2 + T + A} + \mu S\right] \\
& + \lambda_{I_1}\left[(1-u_1)\frac{(c_1\beta_1 I_1 + c_2\beta_2 I_2 + c_3\beta_3 T)S}{S + I_1 + I_2 + T + A} - (u_2\theta + \sigma_1 + \mu)I_1\right] + \lambda_{I_2}\left[u_2\theta I_1 - (u_3\delta + \sigma_2 + \mu)I_2\right] \\
& + \lambda_T\left[u_3\delta I_2 - (\sigma + \mu)T\right] + \lambda_A\left[\sigma_1 I_1 + \sigma_2 I_2 + \sigma T - (\gamma + \mu)A\right]
\end{aligned} \tag{6}$$

where $\lambda_S, \lambda_{I_1}, \lambda_{I_2}, \lambda_T$ and λ_A are adjoint (costate) variables. By applying Pontryagin's Maximum Principle and the existence result for the optimal control from [2], we obtain the following theorem

Theorem 1. There exists an optimal control u_1^*, u_2^* and u_3^* and corresponding solution $S^*(t), I_1^*(t), I_2^*(t), T^*(t)$ and $A^*(t)$, that minimizes $J(u_1, u_2, u_3)$ over u_1, u_2 and u_3. Then, there exists adjoint functions $\lambda_S, \lambda_{I_1}, \lambda_{I_2}, \lambda_T$ and λ_A satisfying the equations

$$\frac{d\lambda_S}{dt} = (\lambda_S - \lambda_{I_1})\left[\frac{(1-u_1)(c_1\beta_1 I_1^* + c_2\beta_2 I_2^* + c_3\beta_3 T^*)}{S^* + I_1^* + I_2^* + T^* + A^*} - \frac{(1-u_1)(c_1\beta_1 I_1^* + c_2\beta_2 I_2^* + c_3\beta_3 T^*)S^*}{(S^* + I_1^* + I_2^* + T^* + A^*)^2} - \right] - \lambda_S \mu$$

$$\frac{d\lambda_{I_1}}{dt} = -w_1 + (\lambda_S - \lambda_{I_1})\left[\frac{(1-u_1)c_1\beta_1 S^*}{S^* + I_1^* + I_2^* + T^* + A^*} - \frac{(1-u_1)(c_1\beta_1 I_1^* + c_2\beta_2 I_2^* + c_3\beta_3 T^*)S^*}{(S^* + I_1^* + I_2^* + T^* + A^*)^2}\right]$$
$$+ (\lambda_{I_1} - \lambda_{I_2})u_2\theta + (\lambda_{I_1} - \lambda_A)\sigma_1 + \lambda_{I_1}\mu.$$

$$\frac{d\lambda_{I_2}}{dt} = (\lambda_S - \lambda_{I_1})\left[\frac{(1-u_1)c_2\beta_2 S^*}{S^* + I_1^* + I_2^* + T^* + A^*} - \frac{(1-u_1)(c_1\beta_1 I_1^* + c_2\beta_2 I_2^* + c_3\beta_3 T^*)S^*}{(S^* + I_1^* + I_2^* + T^* + A^*)^2}\right] \quad (7)$$
$$+ (\lambda_{I_1} - \lambda_T)u_3\theta + (\lambda_{I_2^*} - \lambda_{A^*})\sigma_2 + \lambda_{I_2^*}\mu.$$

$$\frac{d\lambda_T}{dt} = (\lambda_S - \lambda_{I_1})\left[\frac{(1-u_1)c_3\beta_3 S^*}{S^* + I_1^* + I_2^* + T^* + A^*} - \frac{(1-u_1)(c_1\beta_1 I_1^* + c_2\beta_2 I_2^* + c_3\beta_3 T^*)S^*}{(S^* + I_1^* + I_2^* + T^* + A^*)^2}\right]$$
$$+ (\lambda_T - \lambda_A)\sigma + \lambda_T\mu.$$

$$\frac{d\lambda_A}{dt} = (\lambda_{I_1} - \lambda_S)\left[\frac{(1-u_1)(c_1\beta_1 I_1^* + c_2\beta_2 I_2^* + c_3\beta_3 T^*)S^*}{(S^* + I_1^* + I_2^* + T^* + A^*)^2}\right] + \lambda_A(\gamma + \mu).$$

and transversality conditions

$$\lambda_S(t_f) = \lambda_{I_1}(t_f) = \lambda_{I_2}(t_f) = \lambda_T(t_f) = \lambda_A(t_f) = 0. \quad (8)$$

Furthermore, the optimal control u_1^*, u_2^* and u_3^* is given by

$$u_1^* = \max\left\{0, \min\left(1, \frac{(\lambda_{I_1} - \lambda_S)(c_1\beta_1 I_1^* + c_2\beta_2 I_2^* + c_3\beta_3 T^*)S^*}{w_2(S^* + I_1^* + I_2^* + T^* + A^*)}\right)\right\}$$
$$u_2^* = \max\left\{0, \min\left(1, \frac{(\lambda_{I_1} - \lambda_{I_2})\theta I_1^*}{w_3}\right)\right\} \quad (9)$$
$$u_3^* = \max\left\{0, \min\left(1, \frac{(\lambda_{I_2} - \lambda_T)\delta I_2^*}{w_4}\right)\right\}.$$

3.3 Numerical Results

We numerically solved the resulting optimality system (a two-point boundary value problem) using a fourth-order iterative Runge-Kutta scheme (forward-backward sweep method). The state equations with an initial guess for u_1, u_2 and u_3 solved by forward in time, the adjoint equations solved by backward in time and the controls are updated using equations (9). This computational procedure is done iteratively until convergence is attained. Furthermore, to solve the problem of control, use Sweep Forward-Backward algorithm.

The numerical simulations are carried out using MATLAB. Model parameters obtained from [6] and [8] and the initial population using HIV/AIDS cases in Malang (2012).

$$\beta_1 = 0.96, \beta_2 = 0.22, \beta_3 = 0.20, \theta = 0.6, \mu = 0.143, \delta = 0.99, c_1 = 3,$$
$$c_2 = 2, c_3 = 1, \ \sigma_1 = 0.20, \sigma_1 = 0.01, \sigma = 0.001, \gamma = 1, \Lambda = 434981.$$

The cost coefficients $w_1 = 100, w_2 = 35, w_3 = 55$ and $w_4 = 75$ and the initial conditions are taken to be $S(0) = 2.912.403$, $I_1(0) = 2408$, $I_2(0) = 539$, $T(0) = 519$ and $A(0) = 1024$.. Using model parameter values (11) is obtained the effective reproduction number, R_e=3.9996. Because $R_e > 1$, the HIV infection will persist in Malang.

Figure 1, we remark that in the absence of prevention (without control condom use, screening and therapy) the number of unaware infective initially increases rapidly with time then reaches the maximum number of I_1 would be 2.106x10^6 (t=3.9) in the case without control and start to decreases then reaches 1.119x10^6 at the final time (t=20). Whereas, in the presence of prevention (with control), the number of unaware infective from the initial value (2408) initially decreases with time leads to 3.832x10^{-3} at the final time.

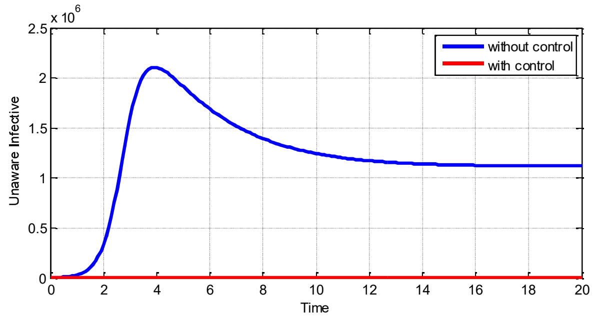

Figure 1. The number of unaware infective with the optimal control and no control

The control profile of the combination of the control strategies is shown in Figure 2. The control of condom use (u_1) is at the upper bound till t=19.9 and then decreases gradually to zero at the final time (Figure 2(a)); the screening control (u_2) dropped gradually from the upper bound to the lower bound after t=8.8 (Figure 3(b)) to zero at the final time and the antiretroviral therapy control (u_3) is at 7.268x10^{-12} at the beginning of the period then oscillates up to t=19.9 and increases rapidly reaches the maximum at 0.1066 and then decreases gradually to zero at the final time (Figure 2(c)).

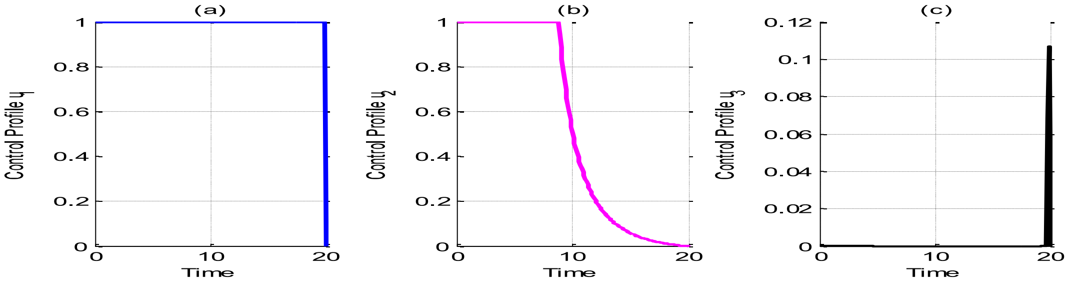

Figure 2. The optimal control profiles of u_1, u_2 and u_3

4. CONCLUSIONS

We derived and analyzed the necessary conditions for the optimal control of the HIV/AIDS model that includes the condom use, screening of unaware infective and therapy of infective. The numerical simulation of both the systems i.e. with control and without control, shows that the combination of the three strategies helps to reduce the number of unaware infective.

REFERENCES

[1]. N. Chitnis, J.M., Hyman and J.M. Cushing, (2008), Determining Important Parameter in the Spread of Malaria Through the Sensitivity Analysis of Mathematical Model, *Department of Public Health and Epidemiology,* **Vol. 70**, pp. 1272-1296.

[2]. W.H. Fleming and R.W. Rishel (1975), *Deterministic and Stochastic Optimal Control,* Spinger Verlag, New York

[3]. H.R. Joshi, (2002), Optimal control of an HIV immunology model, *Optimal Control Application Mathematics,* **Vol 23**, pp. 199-213.

[4]. S. Lenhart, and J.T. Workman, (2007) *Optimal Control Applied to Biological Model*, Chapman and Hall, London.

[5]. Marsudi, Marjono and A. Andari, (2014), Sensitivity Analysis of Effect of Screening and HIV Therapy on the Dynamics of Spread of HIV,*Applied Mathematical Sciences*, **Vol. 8**, no. 155, 7,749-776.

[6]. Marsudi, Marjono and A. Andari, (2015), Modeling the Effect of Screening and Therapy on the Dynamics of HIV Transmission in Malang, *Proceeding The 5th Annual Basic Science International Conference,* **Vol. 5**, 310-313.

[7]. K.O. Okosun, O.D. Makinde and I. Takaidza, (2013), Impact of Optimal Control on The Treatment of HIV/AIDS and Screening of unaware Infectives. *Applied Mathematical Modelling,* **Vol. 37**, pp. 3802-3820.

[8]. R. Safiel, E.S. Massawe and O.D. Makinde (2012), Modelling the Effect Screening and Treatment on Transmission of HIV/AIDS Infection in a Population, *American Journal of Mathematics and Statistics* **2** (4)**:** 75–88.

An Example of Terwilliger Algebras of Same Degree with Different Dimension

Nur Hamid[1]

[1] Sekolah Tinggi Teknologi Nurul Jadid, Probolinggo, Indonesia
*Corresponding authors: [hamidelfath@gmail.com]

Abstract -Let $T(G)$ be the Terwilliger algebra of group association of group G. Let S_n be symmetric group of degree n. It is known that the dimension of Terwilliger algebra of S_5 is 120. In this paper, we give an example of Terwilliger algebra whose degree is equal to degree of $T(S_5)$ but the dimension is different. We also continue the investigation by determining the structure of that algebra.

1. INTRODUCTION

The association scheme is a very fundamental concept in Algebraic Combinatorics. The reference [2] can be our foundation for association scheme. One of material that plays an important role in association schemes is Terwilliger Algebra.

The Terwilliger algebra was introduced in [5]. We refer to [6,7] for more complete explanation. The investigation on Terwilliger algebra then developed more [8]. In case of groups S_5 and A_5, the investigation was done in [3] along the line of work [1]. The continuation investigation was done in [4], special case for S_6, A_6, and $PSL(2,7)$.

In this paper, we show two groups that have the same degree. However, the dimension of Terwilliger algebra of these groups is different. Those groups are S_5 (symmetric group of degree 5) and $SL(2,5)$ (a special linear group of degree 2 over finite field of size 5. Here, we continue the investigation and give the example of Terwilliger algebras of same degree with different basis.

We start the discussion with the definition of group association scheme.

Definition 1.1

Let G be a finite group $C_0 = \{e\}$, $C_1, \dots, C_d$ be the conjugacy classes of G where e is the identity of G. Define the relations $R_i(i = 0, 1, \dots, d)$ on G by

$$(x, y) \in R_i \Leftrightarrow yx^{-1} \in C_i.$$

Then $\mathfrak{X}(G) = (G, \{R_i\}\_(0 \leq i \leq d)$ forms a commutative association scheme class d called the *group association scheme.*

We define the adjacency matrix A_i of the relation R_i as

$$(A_i)_{x,y} = \begin{cases} 1, \text{if } (x, y) \in R_i, \\ 0, \quad \text{otherwise.} \end{cases}$$

Then we have

$$A_i A_j = \sum_{i=0}^{d} p_{\{ij\}}^{k} A_k$$

and $A_0, \dots, A_d$ generate an algebra called Bose-Mesner algebra, denoted by $\mathfrak{A}$. The Intersection numbers $p_{\{ij\}}^{k}$ of the group association scheme $\mathfrak{X}(G)$ are given by

$$\left|\{(x, y) \in C_i \times C_j \middle| xy = z, z \in C_k\}\right|$$

The Bose-Mesner algebra $\mathfrak{A}$ has a second basis, that is primitive idempotents $E_0, E_1, \dots, E_d$, and

$$E_i \circ E_j = \frac{1}{|G|} q_{ij}^{k} E_k,$$

Where $\circ$ denotes Hadamard multiplication. Let E_i^* be the diagonal matrices of size $|G| \times |G|$ and defined by

$$(E_i^*)_{x,y} = \begin{cases} 1, & \text{if } x \in C_i, \\ 0, & \text{otherwise} \end{cases} (x \in G).$$

Then $E_0^*, \dots, E_d^*$ form a basis for the another algebra called dual Bose-Mesner algebra and denoted by $\mathfrak{A}^*$.

Definition 1.2

Let G be a finite group. The Terwilliger algebra $T(G)$ of the group association scheme $\mathfrak{X}(G)$ is sub-algebra of $\mathcal{M}_{|G|}$ generated by $\mathfrak{A}$ and $\mathfrak{A}^*$ where $\mathcal{M}_{|G|}$ denotes matrix algebra of degree $|G|$.

We sometimes write the Terwilliger algebra by T. In our investigation, we show the dimensions of $T(S_5)$ and $T(SL(2,5))$. In the last of our discussion, we will show the structure theorem of these algebra.

2. METHOD

The main parts to obtain the the structure theorem of the Terwilliger algebra can be divided into steps as follows. First we denote by $Z(T)$ the center of Terwilliger algebra.

1. Obtain the dimension of T.
2. Obtain the dimension of center $Z(T)$ of T
3. Obtain the primitive central idempotents ε_i of T.
4. Obtain the structure theorem of T.

The steps above follows what Balmaceda and Oura [3] done.

1. Dimension of T

The dimension of T can be computed by finding a set of linearly independent elements among $E_i^* A_j E_k^*$ and $E_i^* A_j E_k^* A_l E_m^*$.

2. Center $Z(T)$ of T

The dimension of $Z(T)$ can be obtained by solving a linear equation system $\{x_i y = y x_i\}$ ranging over all elements x_i in the basis of T and $y = \sum c_j b_j$ where c_j is any scalar and b_j are the elements of basis of T. In this case, we denote e_i for the basis elements of $Z(T)$. Generally, we can use

$$\{e_i | 1 \le i \le s\}$$

as a basis of $Z(T)$.

3. Primitive Central Idempotents ε_i

In the previous point, we get $\{e_i | 1 \le i \le s\}$ as a basis of $Z(T)$. Then we have

$$e_i e_j = \sum t_{ij}^k e_k.$$

We then put

$$B_i = (t_{ij}^k).$$

The matrices B_i are mutually commute. It means that they are simultaneously diagonalizable. We then denote the diagonal entries of diagonalized matrix of B_i by $v_1(i), \dots, v_s(i)$. Define the matrix M by

$$(M)_{i,j} := v_i(j).$$

The primitive central idempotents ε_i of $T(G)$ can be obtained by multiplication

$$(\varepsilon_1, \dots, \varepsilon_s) = (e_1, \dots, e_s) M^{-1}.$$

4. The Structure Theorem of T

The main part to obtain the structure theorem of T is obtaining the degrees of irreducible complex representation afforded by every idempotents ε_i. The degrees can be got by finding the number of linearly independent elements in the set $\{x_j \varepsilon_i\}$ where x_j are the basis elements of T.

By recalling

$$T(G)\varepsilon_i \cong \mathcal{M}_{d_i}$$

and

$$d_i^2 = \dim T(G)\varepsilon_i,$$

we can arrange the structure theorem of T.

3. RESULTS AND DISCUSSION

We recall two groups used, those are S_5 and $SL(2,5)$. The result for $T(S_5)$ has been published in [3]. We only recall that the dimension of $T(S_5)$ is 155. Here we show the result for $T(SL(2,5))$. The cardinality of $SL(2,5)$ is 120, it is same with the cardinality of S_5. The group $SL(2,5)$ has 9's conjugacy classes. We use SageMath for computation.

First we fix the ordering of the conjugacy classes of $SL(2,5)$ as follows:

	C_0	C_1	C_2	C_3	C_4
u_i:	$\begin{pmatrix}1 & 0\\0 & 1\end{pmatrix}$	$\begin{pmatrix}0 & 4\\1 & 3\end{pmatrix}$	$\begin{pmatrix}0 & 3\\3 & 3\end{pmatrix}$	$\begin{pmatrix}4 & 0\\0 & 4\end{pmatrix}$	$\begin{pmatrix}0 & 4\\1 & 2\end{pmatrix}$
$\lvert u_i\rvert$:	1	12	12	1	12

	C_5	C_6	C_7	C_8
u_i:	$\begin{pmatrix}0 & 3\\3 & 2\end{pmatrix}$	$\begin{pmatrix}0 & 4\\1 & 4\end{pmatrix}$	$\begin{pmatrix}0 & 4\\1 & 1\end{pmatrix}$	$\begin{pmatrix}3 & 0\\0 & 2\end{pmatrix}$
$\lvert u_i\rvert$:	12	20	20	30

By this ordering, we use the step to obtain the dimension and we get the following theorem.

Theorem 3.1 *The dimension of Terwilliger algebra of group association scheme of* $T\big(SL(2,5)\big)$ *is*

$$\dim\Big(T\big(SL(2,5)\big)\Big) = 262.$$

Proof. The dimension mentioned is obtained by step 2 in section Method. □

We provide matrix indexed by conjugacy classes of $SL(2,5)$. This matrix shows where the dimension of $T\big(SL(2,5)\big)$ got. For example, the entry 7 in the (C_7, C_8) position indicates that the basis arise from the set $\{E_7^* A_j E_8\}_{0\le j\le 8}$. The matrix is

$$\left|\begin{array}{ccccccccc}
1 & 1 & 1 & 1 & 1 & 1 & 1 & 1 & 1\\
 & 4 & 4 & 1 & 4 & 4 & 4 & 4 & 5\\
 & & 4 & 1 & 4 & 4 & 4 & 4 & 5\\
 & & & 1 & 1 & 1 & 1 & 1 & 1\\
 & & & & 4 & 4 & 4 & 4 & 5\\
 & & & & & 4 & 4 & 4 & 5\\
 & & & & & & 6 & 6 & 7\\
 & & & & & & & 6 & 7\\
 & & & & & & & & 10
\end{array}\right|$$

We omit the entries below diagonal because this matrix is symmetric. The number 262 is from the summation of all entries.

By basis element obtained in Theorem 3.1 and using step 3, we make the following lemma.

Lemma 3.2 *The dimension of* $Z(T(SL(2,5))$ *is* 7.

By Lemma 3.2, we can find the set of primitive central idempotents. It consists of 7 elements. By step 3, we can obtain the primitive central idempotents. We do not show the matrices as its big size. However, we the following theorem shows the degrees of irreducible complex representation afforded by every idempotent.

Theorem 3.3 *The degrees of irreducible complex representation afforded by every idempotent of* $T\big(SL(2,5)\big)$ *are given by*

ε_i	ε_1	ε_2	ε_3	ε_4	ε_5	ε_6	ε_7
$\deg \varepsilon_i$	1	3	3	8	7	7	9

Proof. The result is from combination step 3 and 4. □

We can combine the Theorem 3.1 and Theorem 3.3 as

$$1^2 + 3^2 + 3^2 + 8^2 + 7^2 + 7^2 + 9^2 = 262 = \dim T\big(SL(2,5)\big).$$

Since

$$T(G)\varepsilon_i \cong \mathcal{M}_{d_i},$$

we get the structure theorem of $T\big(SL(2,5)\big)$ in the following corollary.

Corollary 3.4 *We have that*

$$T\big(SL(2,5)\big) \cong \mathcal{M}_1 \oplus \mathcal{M}_3 \oplus \mathcal{M}_3 \oplus \mathcal{M}_8 \oplus \mathcal{M}_7 \oplus \mathcal{M}_7 \oplus \mathcal{M}_9.$$

where $\mathcal{M}_{d_i}$ *denotes matrix algebra over* $\mathbb{C}$ *of degree* d_i.

4. CONCLUSION

The dimension of $T\big(SL(2,5)\big)$ is 252. This means that there are algebras that have same degree but the dimensions of them are different. By Corollary 3.4, we have that the structure theorem of $T\big(SL(2,5)\big)$ is

$$T\big(SL(2,5)\big) \cong \mathcal{M}_1 \oplus \mathcal{M}_3 \oplus \mathcal{M}_3 \oplus \mathcal{M}_8 \oplus \mathcal{M}_7 \oplus \mathcal{M}_7 \oplus \mathcal{M}_9.$$

In the future, we hope that there are another examples of some algebra of same degree with different dimension.

5. REFERENCES

[1]. E. Bannai, A. Munemusa, 1995, The Terwilliger Algebras of Group Association Schemes, *Kyushu J. Math.*, **49**, 93-102

[2]. E. Bannai, T. Ito, 1984, Algebraic Combinatorics I: Association Schemes, Benjamin/Cummings, California.

[3]. J. M. P. Balmaceda, M. Oura, 1994, The Terwilliger Algebras of the Group Association Schemes of S_5 and A_5, *Kyushu J. Math.*, **48**, 221-231

[4]. N. Hamid, M. Oura, 2016, The Terwilliger Algebras of Some Group Association Schemes, pre-print.

[5]. P. Terwilliger, 1992, The Subconstituent Algebra of an Association Scheme I, *J. Algebraic Combin.*, **1**, 363-388.

[6]. P. Terwilliger, 1992, The Subconstituent Algebra of an Association Scheme II, *J. Algebraic Combin.*, **2**, 73-103.

[7]. P. Terwilliger, 1992, The Subconstituent Algebra of an Association Scheme III, *J. Algebraic Combin.*, **2**, 177-210.

[8]. W. Martin, H. Tanaka, 2009, Commutative Association Schemes, *European J. Comb.*, **30**, 1397-1525.

Choice Based Conjoint for Preferences of Statistics Teaching Methods

Utami Dyah Syafitri[1*], Farit M Afandi[1], Septian Putri Palupi[1]

[1]Department of Statistics, Faculty of Mathematics and Natural Sciencies,
Bogor Agricultural University, Bogor, Indonesia
*Corresponding authors: [utamids@apps.ipb.ac.id]

Abstract -Conjoint analysis is an analysis that used to determine the preferences of consumers. Choice-Based Conjoint Analysis (CBC) is a conjoint analysis which is based on the choice and used to determine the concept of products or services that consumers preferred. The concept of the product is constructed from a combination of levels of attributes using experimental design concept. Teaching and learning activities system is an important thing that affects the effectiveness of student learning. This study examines how undergraduate Statistics students of IPB preference to the concept of teaching and learning system. The fractional factorial design was used to construct the concepts of the product. As the response was binary (choose or not), logistic regression was used to get the utility function and the relative importance of each attribute. There were five attributes with two levels on each attribute. The results show that the teaching method that students preferred were delivering methods in two ways, using whiteboard and projector, no matter material sources, existing rewards and motivations in the class. Teaching equipment was the most important attribute whereas the source of materials was the less important attribute.

1. INTRODUCTION

Conjoint analysis is a common method in marketing research for preference analysis of consumers. Traditional conjoint uses rating or ranking as a response for evaluating a set of preferences which combine levels of attributes. Practically, it will be easier for consumers to choose one option among several choices. This is a basic idea of Choice Based Conjoint (CBC) analysis [1].

Attributes are factors that influence respondents to decide their choice. An attribute consists of several levels. Combinations of levels of attributes are called a concept. A set of choices or concepts is called a task. The different task is meaning that different version. Hence, there are several versions of choices for a whole survey. The choices of respondents are analyzed by a certain method in order to get a hypothetic product that respondents prefer.

In this paper, CBC analysis was implemented to evaluate preferences of students on statistics teaching methods. Statistics is a difficult subject for most of students. When delivering the materials, therefore, lecturers need some strategies to consider the preference of students.

In general, there were three steps in Conjoint Analysis. First, the combinations of attributes are developed using a certain experimental design method. Second, the responses of combinations of attributes are collected to respondents. Third, data are analyzed based on the measurement scale of response. In CBC problem in which the response is binary, logistic regression is used to analyze the data.

2. METHODS

The methodology of the research in this paper were divided into three steps:

1. Constructing four tasks with fractional factorial design in which each task is a combination of several profiles and embedded to the questionnaire. Five attributes used in this research were delivering methods (one way or two ways), teaching equipment (whiteboard or whiteboard + projector, material sources (slides or textbooks), giving rewards (exist or no exist), and giving motivation (exist or no exist). The code of each level of each attribute can be seen in Table 1.

Table 1. Levels of each attribute and the codes

Attributes	Levels	Codes
1. Delivering methods	One way	-1
	Two ways	1
2. Teaching equipment	Whiteboard	-1
	Whiteboard + projectors	1

Attributes	Levels	Codes
3. Material sources	Slides	-1
	Projectors	1
4. Motivation in the class	Exist	-1
	Not exist	1
5. Rewards in the class	Exist	-1
	Not exist	1

1. A combination of the level of attributes is called a profile. A set of profiles that give to respondents is called a task. Four different tasks were designed using fractional factorial. The four tasks with four different generators are shown in Table 2-5. A task is a blocking effect. Hence, there were four blocking levels.

Table 2. Task 1 with generators D = AB, E = ABC

No	A	B	C	D	E
1	1	1	1	1	1
2	1	1	-1	1	-1
3	1	-1	1	-1	-1
4	1	-1	-1	-1	1
5	-1	1	1	-1	-1
6	-1	1	-1	-1	1
7	-1	-1	1	1	1
8	-1	-1	-1	1	-1

Table 3. Task 2 with generators D = -AB, E = ABC

No	A	B	C	D	E
1	1	1	1	-1	1
2	1	1	-1	-1	-1
3	1	-1	1	1	-1
4	1	-1	-1	1	1
5	-1	1	1	1	-1
6	-1	1	-1	1	1
7	-1	-1	1	-1	1
8	-1	-1	-1	-1	-1

Table 4. Task 3 with generators D = -AB, E = -ABC

No	A	B	C	D	E
1	1	1	1	-1	-1
2	1	1	-1	-1	1
3	1	-1	1	1	1
4	1	-1	-1	1	-1
5	-1	1	1	1	1
6	-1	1	-1	1	-1
7	-1	-1	1	-1	-1
8	-1	-1	-1	-1	1

Table 5. Task 4 with generators D = AB, E = -ABC

No	A	B	C	D	E
1	1	1	1	1	-1
2	1	1	-1	1	1
3	1	-1	1	-1	1
4	1	-1	-1	-1	-1
5	-1	1	1	-1	1
6	-1	1	-1	-1	-1
7	-1	-1	1	1	-1
8	-1	-1	-1	1	1

2. Collecting samples using stratified random sampling. The population was statistic students of Department of Statistics, Faculty of Mathematics and Natural Sciences, Bogor Agricultural University. In total, there were 150 samples which were divided into three strata: 2nd batch, 3rd batch, and 4th batch. The composition of samples of each batch can be seen in Table 6.

Table 6. Distribution samples based on batches and tasks

Batch	Task				Total
	1	2	3	4	
2nd bacth	12	12	14	15	53
3rd batch	11	12	12	12	50
4th bacth	12	14	12	12	47
Total	35	38	38	39	150

3. Analyzing data using logistic linear regression because the response is binary. Next, calculating utility values and relative important value of each attribute. The logistic regression model is

$$\pi(x) = \frac{e^{\beta_0+\beta_1 x_1+\ldots+\beta_p x_p+\varepsilon}}{1+e^{\beta_0+\beta_1 x_1+\ldots+\beta_p x_p+\varepsilon}}$$

And the utility function of attributes of whole respondents is formulated as

$$U(X) = \sum_{i=1}^{m}\sum_{j=1}^{k_i} a_{ij}x_{ij}$$

Where U(X) is total utility value of whole respondent, a_{ij} is a utility value of i-th attribute and j-th level of the attribute, x_{ij} is a dummy variable of i-th attribute and j-th level of the attribute, m is the number of attributes, and k_i is j-th level of i-th attribute.

Orme (2010) stated that the important value of each attribute (I_i) is defined as the difference between maximum utility value and minimum utility value. The important value of i-th attribute is formulated as

$$I_i = \{\max(a_{ij}) - \min(a_{ij})\}$$

Where I_i is the important value of i-th attribute and aij is the utility function of i-th attribute and j-th level of the attribute. Furthermore, the relative important value (W_i) is defined as

$$W_i = \frac{I_i}{\sum_{i=1}^{m} I_i}$$

3. RESULTS AND DISCUSSION

3.1 Characteristics respondents

Figure 1 shows characteristic respondents based on gender meanwhile Figure 2 shows that characteristic respondents based on activity on the organization in the campus. The respondents consisted of 29.33% male and 70.67% female. Majority students had experiences in the organization (90%).

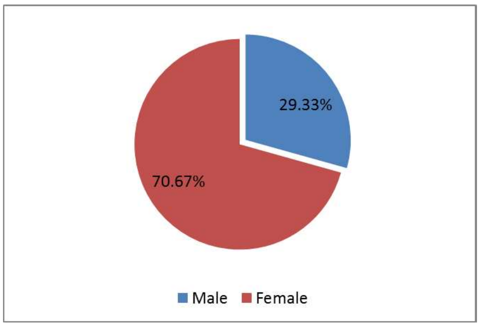

Figure 1. Characteristic respondent based on gender

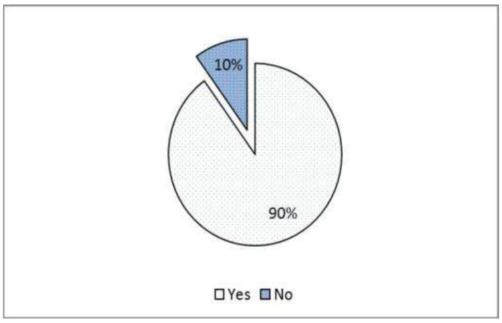

Figure 2. Distribution organization activity of respondents

3.2 Choice based conjoint analysis

There were eight parameters in the logistic model: five parameters of five attributes and three parameters of three dummy variables of tasks. Four attributes were significant at $\alpha = 5\%$. Only attribute source of materials was not significant at $\alpha = 5\%$. All dummy variables were not significant. Table 7 shows the results of the logistic model.

Table 7 shows the results of the logistic model.

Attributes	Coefficient	Wald statistics	p_value
Delivering methods	-1.370	41.730	0.000**
Teaching equipments	-1.884	65.006	0.000**
Material sources	-.022	.013	0.908
Motivation in the class	.809	16.125	0.000**
Rewards in the class	1.344	41.224	0.000**
Block 2 vs Block 1	.125	.199	0.655
Block 3 vs Block 1	.127	.205	0.651
Block 4 is Block 1	.000	.000	1.000

*significant at α 5%

Figure 1 shows the important value of each level of the attribute. A positive value means that the level of attribute is preferable compared to another level. Vice versa, a negative value meaning that the level of attribute is not preferable compared to another level. Based on utility values which are shown in Figure 1, the preferable teaching method for statistics students was: delivering methods in two ways, using whiteboard and projector, no matter material sources, existing rewards and motivations in the class. Figure 2 shows the most important attribute was teaching equipment. The next two important attributes were delivering methods and motivation. Source of materials was not important attribute at all.

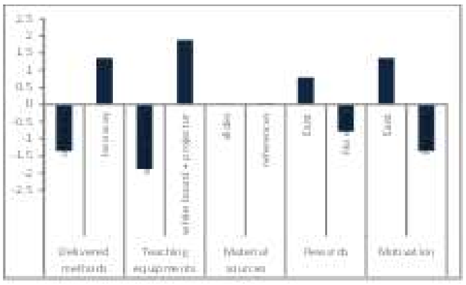

Figure 3. The utility value of each level of each attribute.

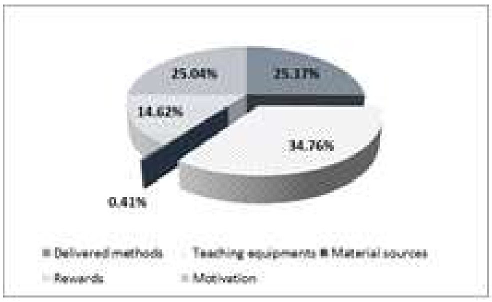

Figure 4. Important relative values of attributes.

4. CONCLUSIONS

The preferable teaching method for statistics students was: delivering methods in two ways, using whiteboard and projector, no matter material sources, existing rewards and motivations in the class. The most important attribute was teaching equipment. The next two important attributes were delivering methods and motivation. Source of materials was not important attribute at all.

5. REFERENCES

[1] D Raghavarao, JB Wiley, P Chitturi. 2011. Choice-based Conjoint Analysis, Models and Design. Boca Raton (US) : CRC Press.

[2] BK Orme. 2010. Getting Started with Conjoint Analysis: Strategies for Product Design and Pricing Research Second Edition. Madison (US): Research Publishers LLC.

Dynamics Analysis of a Rotavirus Infection Model with Saturated Incidence Rate

Anna Silvia Purnomo[1*], Isnani Darti[1]

[1] Department of Mathematics, Faculty of Mathematics and Natural Sciences, University of Brawijaya,
Jl. Veteran, Malang-Indonesia
* Corresponding authors: [annapurnomo240195@gmail.com]

Abstract – In this paper, a mathematical model of rotavirus infection incorporating vaccination with saturated incidence rate has been developed and comprehensively analyzed. The basic reproduction number R_v and R_0 has been established. The model has two equilibrium points, i.e. disease free and endemic equilibrium. Based on analysis, it has been shown that those equilibrium points are locally asymptotically stable with some specific conditions. Based on simulation, it has been shown that the disease free and endemic equilibrium are globally asymptotically stable if the value of basic reproduction number $R_0 < 1$ and $R_v < 1$, respectively.

1. INTRODUCTION

Rotavirus is a pathogen that causes acute gastroenteritis and diarrhea in infants and young children of below five years of age worldwide [1]. The spread of this virus can be through the feces, contaminated hands, the wind, and surfaces [2 - 4]. In real life, 90% of children worldwide are infected by rotavirus with mortality in excess of 600,000 among children [5]. In Kenya, the deaths of more 7,500 children were caused by rotavirus infection [6].

In 2009, WHO (World Health Organization) recommended rotavirus vaccine as one of effort the preventing spread of rotavirus infection. Omondi and friends have developed and comprehensively analyzed a mathematical model of a rotavirus infection incorporating vaccination with bilinear incidence rate [7].

In this paper, a mathematical model of a rotavirus infection incorporating vaccination with saturated incidence rate has been developed and comprehensively analyzed. The saturated incidence rate more reasonable than bilinear incidence rate because it includes the behavioral change and crowding effect of the infective individuals and prevents the unboundedness of the contact rate by choosing suitable parameters [8].

2. FORMULATION OF THE MODEL

A modified $SVIR$ model for rotavirus infection, which incorporates vaccination will be studied qualitatively and quantitatively. The total population is divided into four classes; i.e. $S(t)$ represents susceptible individuals, $V(t)$ represents vaccinated individuals, $I(t)$ represents infectious individuals, and $R(t)$ represents recovered individuals. The model is presented in the following form:

$$\begin{aligned}
\frac{dS}{dt} &= (1-\rho)\Lambda - \frac{\beta SI}{1+\alpha I} - \gamma S + \omega V - \mu S,\\
\frac{dV}{dt} &= \rho\Lambda + \gamma S - \varepsilon\beta VI - (\omega+\mu)V,\\
\frac{dI}{dt} &= \frac{\beta SI}{1+\alpha I} + \varepsilon\beta VI - (\tau+\kappa+\mu)I,\\
\frac{dR}{dt} &= \kappa I - \mu R,
\end{aligned} \tag{1}$$

where Λ is the recruitment rate of children (by birth) into the population (assumed susceptible), ρ is the proportion of recruited individuals who are vaccinated; β is the disease contact rate; μ is the natural death rate; τ is the disease induced death rate; γ is the rate of vaccination in susceptible individuals; ω is the rate at which vaccine wanes; ε is reflects the effects of vaccine reducing the infection rate; κ is recovery rate; and α is the saturation constant. The compartment diagram of model is Figure 1. All the model parameters and variables are assumed to be non-negative.

Since $N = S + V + I + R$, we get

$$\frac{dN}{dt} = \Lambda - \mu N - \tau I. \tag{2}$$

In the absence of infection, equation (2) becomes

$$\frac{dN}{dt} = \Lambda - \mu N. \tag{3}$$

So that N will approach capacity $\frac{\Lambda}{\mu}$.

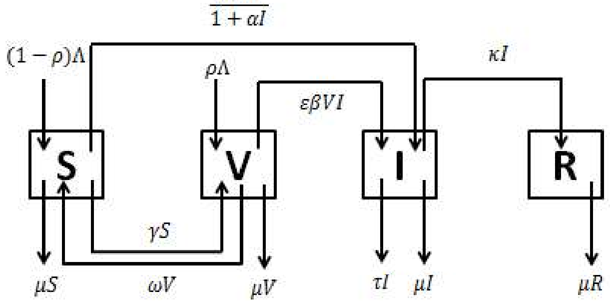

Figure 1 Compartment diagram of a rotavirus infection model with saturated infection rate

3. RESULTS AND DISCUSSION

The disease-free equilibrium points of (1) is defined by

$$E^0 = (S^0, V^0, I^0, R^0) = \left(\frac{\mu(1-\rho)\Lambda + \omega\Lambda}{\mu(\gamma+\omega+\mu)}, \frac{(\rho\mu+\gamma)\Lambda}{\mu(\gamma+\omega+\mu)}, 0, 0\right),$$

and, the endemic equilibrium points of (1) is given by $E^* = (S^*, V^*, I^*, R^*)$ where

$$S^* = \frac{(\Lambda - (\tau+\kappa+\mu)I^*)(\varepsilon\beta I^* + \mu + \omega) - \mu\rho\Lambda}{\mu(\gamma + \varepsilon\beta I^* + \mu + \omega)}, V^* = \frac{\gamma(\Lambda - (\tau+\kappa+\mu)I^*) + \mu\rho\Lambda}{\mu(\gamma + \varepsilon\beta I^* + \mu + \omega)}, R^* = \frac{\kappa I^*}{\mu}.$$

Determining of basic reproduction number is important to analyze disease spread. Basic reproduction number is defined as an average number of secondary infections an infectious individual would cause over his infectious period in an entirely susceptible population [9,10]. In this paper, the basic reproduction number R_v of the model (1) is defined as the number of secondary rotavirus infections caused by a single rotavirus infected individual in the presence of vaccination. When in the vaccination-free, the basic reproduction number is defined by R_0. If $R_0 < 1$ then the disease free equilibrium is stable. But, if $R_0 > 1$ the endemic equilibrium exists and thus the disease invades and persist in the population. Using the next-generation operator approach [8, 9], the basic reproduction number is define by

$$R_v = \frac{\beta\Lambda}{\mu(\tau+\kappa+\mu)}\left[\frac{\mu(1-\rho+\rho\varepsilon) + \omega + \varepsilon\gamma}{\mu+\omega+\gamma}\right] \tag{3}$$

$$R_0 = \frac{\beta\Lambda}{\mu(\tau+\kappa+\mu)}. \tag{4}$$

The local stability of E^0 is then determined based on the signs of the eigenvalues of the Jacobian of (1) at E^0. The equilibrium E^0 is locally asymptotically stable if the real parts of these eigenvalues are all negative. The Jacobian of (1) at E^0 is

$$J_0 = \begin{bmatrix} -(\gamma+\mu) & \omega & -\beta S^0 \\ \gamma & -(\omega+\mu) & -\varepsilon\beta V^0 \\ 0 & 0 & R_V - 1 \end{bmatrix}$$

Evaluating the J_0 gives the following characteristic polynomial:

$$\begin{aligned} F(\lambda) = \lambda^3 + [\omega + 2\mu + \gamma + (1 - R_V)]\lambda^2 + [\mu(\omega+\mu+\gamma) + (\omega+2\mu+\gamma)(1-R_V)]\lambda \\ + \mu(\omega+\mu+\gamma)(1-R_V). \end{aligned}$$

Using the Routh-Hurwitz criterion [10], that the roots of $F(\lambda)$ have negative real parts if $R_V < 1$. Thus, the disease-free equilibrium E^0 is locally asymptotically stable if $R_V < 1$.

Next, we establish the local stability of E^*. The Jacobian of (1) at E^* is

$$J^* = \begin{bmatrix} -(\gamma+\mu)-\dfrac{\beta I^*}{1+\alpha I^*} & \omega & -\dfrac{\beta I^*}{(1+\alpha I^*)^2} \\ \gamma & -\varepsilon\beta I^* - (\omega+\mu) & -\varepsilon\beta V^* \\ \dfrac{\beta I^*}{1+\alpha I^*} & \varepsilon\beta I^* & \dfrac{\beta S^*}{(1+\alpha I^*)^2} + \varepsilon\beta V^* - (\tau+\kappa+\mu) \end{bmatrix}.$$

By elementary row operation, we obtain following matrix J^*

$$J^* = \begin{bmatrix} -\mu & -\mu & -(\tau+\kappa+\mu) \\ 0 & -\mu(\varepsilon\beta I^* + \gamma + \omega + \mu) & -\mu\varepsilon\beta V^* - \gamma(\tau+\kappa+\mu) \\ 0 & \mu\left(\varepsilon\beta I^* - \dfrac{\beta I^*}{(1+\alpha I^*)}\right) & \mu\left(\dfrac{\beta S^*}{(1+\alpha I^*)^2} + \varepsilon\beta V^* - (\tau+\kappa+\mu)\right) - \dfrac{\beta I^*}{(1+\alpha I^*)}(\tau+\kappa+\mu) \end{bmatrix}.$$

Clearly, if $\frac{\beta S^*}{(1+\alpha I^*)^2} + \varepsilon\beta V^* < (\tau+\kappa+\mu)$ and $\frac{1}{1+\alpha I^*} < \varepsilon$ endemic equilibrium point is locally asymptotically stable.

4. NUMERICAL SIMULATIONS

In this section, we provide numerical simulations to illustrate model with the parameter values shown in Table 1.

Table 1 Parameter values used in Figures 2 and 3

Parameter	Symbol	Value	Dimension
Recruitment rate of humans	Λ	4.109×10^3	people
Recruitment rate of vaccinated individuals	ρ	1.884×10^{-1}	day^{-1}
Natural death rate of humans	μ	1.5×10^{-1}	day^{-1}
Rotavirus-induced deaths	τ	2×10^{-2}	day^{-1}
Disease contact rate	β	9×10^{-6}	day^{-1}
Recovery rate	κ	10^{-2}	day^{-1}
Reflects the effects of vaccine reducing the infection rate	ϵ	5×10^{-5}	day^{-1}
Vaccine efficacy waning rate	ω	5×10^{-10}	day^{-1}
Vaccination rate	γ	10^{-4}	day^{-1}
Saturation constant	α	3×10^{-3}	day^{-1}

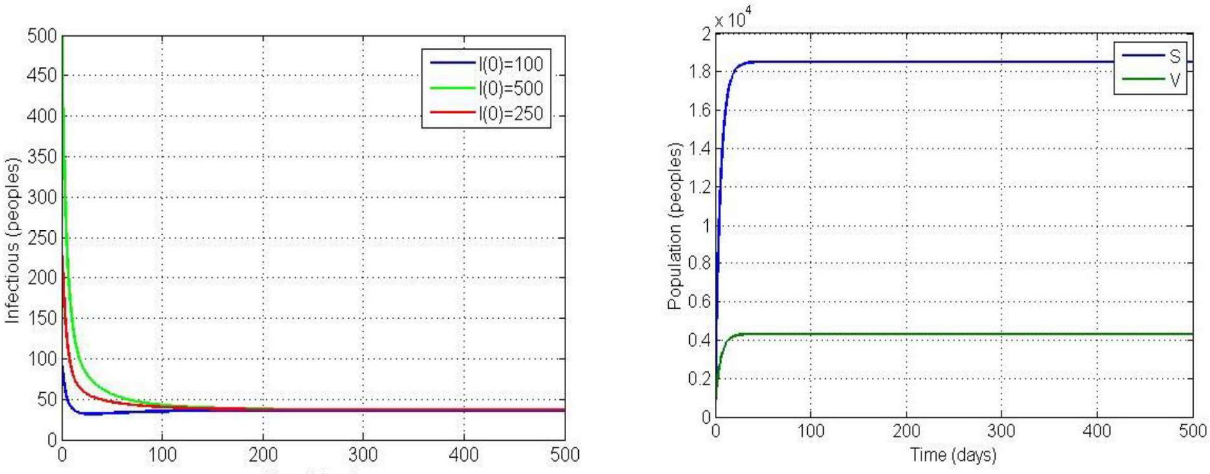

(a) (b)

Figure 2 Simulation of model (1) when $\mu = 0.18, R_v = 0.7936$ and $R_0 = 0.9783$ (a) and when $R_v = 1.1109$ and $R_0 = 1.3697$ (b).

From the numerical simulation results, Figure 2(a) shows that the disease-free equilibrium point is locally asymptotically stable when $R_v = 0.1735 < 1$ and $R_0 = 0.3028 < 1$. In that figure shown that $S(t) \geq V(t)$. This maybe because the fact that vaccination is not needed at this time since absence of infectious; that is $I(t) = 0$. Figure 2(b) shows that the endemic equilibrium is locally asymptotically stable when $R_v = 3.4113 > 1$ and $R_0 = 3.4242 > 1$.

Figure 3 shows the effects of saturation constant in the model (1). When $\alpha = 3 \times 10^{-3}$ the value of I^*= 36 peoples and when $\alpha = 3 \times 10^{-5}$ the value of I^*= 1,233 peoples. If the value of α increases then the value of I^* decreases. Similarly, if the self-protect of susceptible individuals increases then the spread of rotavirus infection decreases.

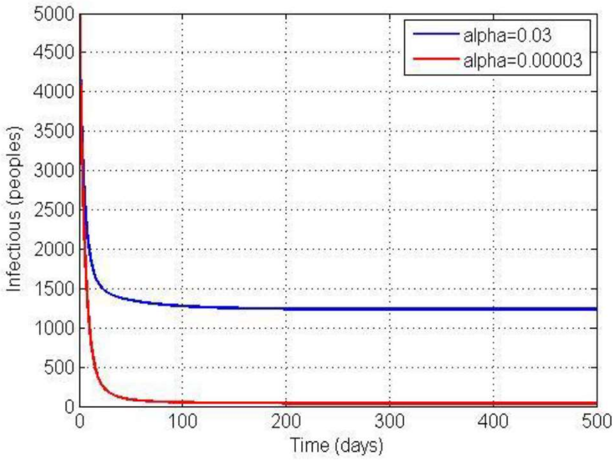

Figure 3 Simulation of model (1) at various values of α when $R_v = 1.1109$ and $R_0 = 1.3697$.

5. CONCLUSIONS

The model has two equilibrium points, i.e. disease free and endemic equilibrium. Based on analysis and simulation, it has been shown that the disease-free equilibrium is locally asymptotically stable if the value of basic reproduction number $R_v < 1$. The endemic equilibrium is locally asymptotically stable with some specific conditions. If the value of α increases then the value of I^* decreases. Similarly, if the self-protect of susceptible individuals increases then the spread of rotavirus infection decreases.

6. REFERENCES

[1] L. J. White, J. Buttery, B. Cooper, D. J. Nokes, and G. Medley, 2008, *J. The Royal Society Interface*, **5**, 1481.

[1]. P.H. Dennehy, 2000, *The Pediatric Infectious Disease Journal*, **19**, S103.
[2]. L. W. Nitiema, J. Nordgren, D. Ouermi, D. Dianou, A. S. Traore, L. Svensson, and J. Simpore, 2011, 2011, *International Society for Infectious Diseases*. **15(9)**, e646-e652.
[3]. T. Sneliling, P. Markey, J. Carapetis, and R. Andrews, 2012, *Microbiology Australia*, **33(2)**, 61-63.
[4]. U. D. Parashar, J. S. Bresee, J. R. Gentsch, and R. I. Glass, 1998, *Emerging Infectious Diseases*. **4(4)**, 561-570.
[5]. N. M. Kiulia, J. K. Nyaundi, I. Peenze, A. Nyachieo, R. N. Musoke, A. D. Steele, and J. M. Mwenda, 2009, *Journal of Tropical Pediatrics*, **55(5)**, 318-323.
[6]. O. L. Omondi, C. C. Wang, X. P. Xue, and O. G. Lawi, 2015, *Advances in Difference Equations*, **2015**, 381.
[7]. G. P. Sahu and J. Dhar, 2012, *Applied Mathematical Modelling*, **36**, 908-923.
[8]. J. Heffernan, R. Smith, and L. Wahl, 2005, *J. The Royal Society Interface*, **2**, 281-293.
[9]. O. Diekmann, J. Hessterbeek, and J. A. Metz, 1990, *J. Math. Biol.,* **28**, 365-382.

Homomorphism on Direct Product of Fuzzy Modules over Fuzzy Rings

Vira Hari Krisnawati[1*], Bayu Setyabudi[2]

1,2 Department of Mathematics, Faculty of Science, University of Brawijaya, Malang, Indonesia
Corresponding authors: [virahari@ub.ac.id]

Abstract – In this paper, the new concept of homomorphism on Direct Product of Fuzzy Modules over Fuzzy Rings is studied by using the definition fuzzy module over fuzzy ring which is introduced in [1]. By some particular condition, the direct product of kernel and image is submodule from direct product of fuzzy module. Moreover, some properties of this new concept are proven analogs to ordinary module theory.

1. INTRODUCTION

The concept of the fuzzy set was introduced by Zadeh in 1965. Then, the first concept of fuzzy group was introduced by Rosenfeld in 1971. Many researchers have established the theory of fuzzy algebra. In the development of fuzzy concept, [6] get the definition of fuzzy group based on fuzzy binary operation which is different from Rosenfeld. Also according to [1] and [2], we have some properties about module homomorphism and the direct product of fuzzy module over fuzzy ring.

In this article, we combine the fuzzy module theory such that forming some analog theorems about homomorphism on direct product of fuzzy module over fuzzy ring.

2. PRELIMINARIES

In this section, we give some preliminary definitions and theorems about fuzzy module over fuzzy ring, $R-fmodule$ homomorphism, and direct product of fuzzy modules over fuzzy rings.

Definition 1 [3]. Let X and Y be nonempty sets and f be a fuzzy subset of $X \times Y$. f is called a fuzzy function X into Y if the following conditions hold.

(i) For all $x \in X$, there exist $y \in Y$, such that $f(x,y)$.

(ii) For all $x \in X$, for all $y_1, y_2 \in Y$, $f(x,y_1) > \theta$ and $f(x,y_2) > \theta$ imply $y_1 = y_2$.

Definition 2 [4]. Let M be a nonempty set and G be a fuzzy subset of $M \times M \times M$. G is called a fuzzy binary operation on M if the following conditions hold.

(i) For all $a, b \in M$, there exist $z \in M$ such that $G(a,b,z) > \theta$.

(ii) $G(a,b,z_1) > \theta$ and $G(a,b,z_2) > \theta$, then $z_1 = z_2$, for all $a,b,z_1,z_2 \in M$.

Let G be a fuzzy binary operation on M, then we have a mapping

$$G: F(M) \times F(M) \longrightarrow F(M)$$
$$(A,B) \longmapsto G(A,B)$$

where $F(M) = \{A \mid A: X \to [0,1]\}$ and $G(A,B)(c) = \vee_{a,b \in M}\big(A(a), B(b), G(a,b,c)\big)$.
Let $A = \{a\}$, $B = \{b\}$, and $G(A,B)$ be donated as $a \circ b$, then $(a \circ b)(c) = G(a,b,c)$, for all $c \in M$.

$$\big((a \circ b) \circ c\big)(z) = \vee_{d \in M}\big(G(a,b,d) \wedge G(d,c,z)\big), \text{ there exist } z \in M,$$
$$\big(a \circ (b \circ c)\big)(z) = \vee_{d \in M}\big(G(b,c,d) \wedge G(a,d,z)\big), \text{ there existz } \in M.$$

Definition 3 [5]. Let M is a nonempty set, $\theta \in [0,1]$ and G be a fuzzy binary operation on M. (M,G) is called a fuzzy group if the following conditions hold.

(i) If $\big((a \circ b) \circ c\big)(z_1) > \theta$ and $\big(a \circ (b \circ c)\big)(z_2) > \theta$, then $z_1 = z_2$, for all $a,b,c,z_1,z_2 \in M$.

(ii) There exist $e_0 (is\ called\ an\ identity\ element\ of\ M) \in M$, such that $(e_0 \circ a)(a) > \theta$ and $(a \circ e_0)(a) > \theta$, for any $a \in M$.

(iii) For all $a \in M$, there exist $a^{-1} (is\ called\ an\ inverse\ element\ of\ a) \in M$ such that $(a \circ a^{-1})(e_0) > \theta$ and $(a^{-1} \circ a)(e_0) > \theta$.

Definition 4 [6]. Let (M,G) be a fuzzy group and H be a nonempty subset of M. H is called fuzzy subgroup of M if H be a fuzzy group.

Theorem 5 [6]. H is a fuzzy subgroup of M if and only if for all $a, b \in H$,for all $c \in H$, $(a \circ b)(c) > \theta$ implies $c \in H$, and $a \in H$ implies $a^{-1} \in H$.

Definition 6 [2]. Let R is a nonempty set, $\theta \in [0,1]$ and G, H are two fuzzy binary operation on R, with same θ. Let $G(a,b)$ and $H(a,b)$ be donated as $a \circ b$ and $a \cdot b$, defined some operation,

$$(a \cdot b)(c) = H(a,b,c),$$
$$\big(a \cdot (b \circ c)\big)(z) = \vee_{d \in M}\big(G(b,c,d) \wedge H(a,d,z)\big),$$
$$\big((a \cdot b) \circ (a \cdot c)\big)(z) = \vee_{d \in M}\begin{pmatrix} H(a,b,d) \wedge H(a,c,e) \\ \wedge G(d,e,z) \end{pmatrix}, \text{ for all } a, b, , c \in R \text{ and } z \in R.$$

(R, G, H) is called fuzzy ring if the following conditions hold.

(i) (R, G) is an Abelian fuzzy group.

(ii) If $\big((a \cdot b) \cdot c\big)(z_1) > \theta$ and $\big(a \cdot (b \cdot c)\big)(z_2) > \theta$ then $z_1 = z_2$, for all $a, b, c, z_1, z_2 \in R$.

(iii) If $\big((a \circ b) \cdot c\big)(z_1) > \theta$ and $\big((a \cdot c) \circ (a \cdot b)\big)(z_2) > \theta$ then $z_1 = z_2$; if $\big(a \cdot (b \circ c)\big)(z_1) > \theta$ and $\big((a \cdot b) \circ (a \cdot c)\big)(z_2) > \theta$ then $z_1 = z_2$, for all $a, b, c, z_1, z_2 \in R$.

Definition 7 [1]. Let (R, G, H) is a fuzzy ring and (M, J) is an Abelian fuzzy group and p is a fuzzy function on $R \times M$ to M. Then we have a mapping

$$p: F(R) \times F(M) \longrightarrow F(M),$$
$$(A, N) \longmapsto p(A, N),$$
$$p(A, N)(x) = \vee_{(a,n) \in A \times N}\big(A(a) \wedge N(n) \wedge p(a,n,x)\big),$$

where $F(R) = \{A | A: R \to [0,1]\}$ and $F(M) = \{N | N: M \to [0,1]\}$, also A and N are fuzzy subsets of R and M. Let $A = \{r\}$ and $N = \{m\}$, also let $p(A, N)$ and $J(a,b)$ be donated as $r \odot m$ and $r \oplus m$, then

$$(r \odot m)(x) = p(r, m, x),$$
$$\big(r \odot (m_1 \oplus m_2)\big)(x) = \vee_{m \in M}\big(J(m_1, m_2, m) \wedge p(r, m, x)\big)$$
$$\big((r_1 \circ r_2) \odot m\big)(x) = \vee_{r \in R}\big(G(r_1, r_2, r) \wedge p(r, m, x)\big),$$
$$\big((r_1 \cdot r_2) \odot m\big)(x) = \vee_{r \in R}\big(H(r_1, r_2, r) \wedge p(r, m, x)\big),$$
$$\big(r_1 \odot (r_2 \odot m)\big)(x) = \vee_{m_1 \in R}\big(p(r_2, m, m_1) \wedge p(r_1, m_1, x)\big),$$
$$\big((r \odot m_1) \oplus (r \odot m_2)\big)(x) = \vee_{x_1, x_2 \in M}\big(p(r, m_1, x_1) \wedge p(r, m_2, x_2) \wedge J(x_1, x_2, x)\big),$$

$$\text{for all } r, r_1, r_2 \in R, \text{ and } x, m, m_1, m_2 \in M.$$

Let (R, G, H) be a fuzzy ring and (M, J) be an Abelian fuzzy group. M is called a (left) fuzzy module over fuzzy ring R or notated R–fmodule, with fuzzy function $p: R \times M \to M$, if the following conditions hold.

(i) (M, J) Abelian fuzzy group,

(ii) $\big(r \odot (m_1 \oplus m_2)\big)(x) > \theta$ and $\big((r \odot m_1) \oplus (r \odot m_2)\big)(y) > \theta$, imply $x = y$,

(iii) $\big((r_1 \circ r_2) \odot m\big)(x) > \theta$ and $\big((r_1 \odot m) \oplus (r_2 \odot m)\big)(y) > \theta$, impy $x = y$,

(iv) $\big((r_1 \cdot r_2) \odot m\big)(x) > \theta$ and $\big(r_1 \odot (r_2 \odot m)\big)(y) > \theta$, impy $x = y$,

Definition 8 [1]. Let (R, G, H) is a fuzzy ring and (M, J) be a fuzzy module and N is a nonempty subset of $M. N$ is called a fuzzy submodule of M if (N, J) is an $R - fmodule$.

Theorem 9 [1]. Let (R, G, H) be a fuzzy ring, (M, J) be an R–fmodule, and N is a nonempty subset of $M. N$ is a fuzzy submodule of M if and only if

(i) (N, J) is a fuzzy subgroup of (M, J),

(ii) for all $r \in R, b \in N, (r \odot b)(c) > \theta$, implies $c \in N$.

Definition 10 [1]. Let A and B be two fuzzy modules over a fuzzy ring (R, G, H) with a function $p: R \times M \to M$. A function $h: A \to B$ is an $R - fmodule$ homomorphism if the following conditions hold.

i) $G(a, b, x) > \theta$ implies $G\big(h(a), h(b), h(x)\big) > \theta$.

ii) $p(r, a, x) > \theta$ implies $p\big(r, h(a), h(x)\big) > \theta$.

For all $a, b \in A$ and $r \in R$, then h is fuzzy module homomorphism.

Theorem 11 [1].Let M and N be two fuzzy modules over fuzzy ring (R, G, H). Let $h: M \to N$ is an $R - fmodule\ homomorphism$. Then

(i) $Ker\ h = \{ m \in M \mid h(m) = e_N \}$ is a *fuzzy submodule* of M,

(ii) $Im\ h = \{n \in N | n = h(m), m \in M\}$ is a *fuzzy submodule* of N,

(iii) If C is any *fuzzy submodule* of N, then $h^{-1}(C) = \{m \in M | h(m) \in C\}$ is a *fuzzy submodule* of M.

Theorem 12 [1]. Let (R, G, H) be a *fuzzy* ring and M and N be two fuzzy modules over fuzzy ring R. Let $h: M \to N$ be an $R - fmodule\ homomorphism$. Then,

(i) h is an $R - fmodule\ monomorphism$ if and only if $Ker\ h = \{e_M\}$,

(ii) $h: M \to N$ is an $R - fmodule\ isomorphism$ if and only if there exists a *fuzzy module* homomorphism $g: N \to M$ such that $gh = e_M$ and $hg = e_N$.

Definition 11 [2]. Let (R_1, G_1, H_1) and (R_2, G_2, H_2) be fuzzy rings, (M, J_M) and (N, J_N) are fuzzy module over fuzzy rings R_1 and R_2 respectively. Let J be a fuzzy binary operation on $M \times N$. Then, we have a mapping

$$J: F(M \times N) \times F(M \times N) \to F(M \times N),$$
$$(A_1 \times B_1, A_2 \times B_2) \mapsto J(A_1 \times B_1, A_2 \times B_2),$$

where $F(M \times N) = \{A \times B | A \times B: M \times N \to [0,1]\}$, A and B are fuzzy subsets of M and N.
Let $A_1 \times B_1 = \{(x_1, y_1)\}$ and $A_2 \times B_2 = \{(x_2, y_2)\}$, and $J(A_1 \times B_1, A_2 \times B_2)$ be donated as $(x_1, y_1) \boxplus (x_2, y_2)$, then

$$\big((x_1, y_1) \boxplus (x_2, y_2)\big)(x, y) = J_M(x_1, x_2, x) \wedge J_N(y_1, y_2, y),$$

$$\big((x_1, y_1) \boxplus (x_2, y_2) \boxplus (x_3, y_3)\big)(x, y) = \bigvee_{\substack{u \in M \\ v \in N}} \begin{pmatrix} J_M(x_1, x_2, u) \wedge J_N(y_1, y_2, v) \\ \wedge J_M(u, x_3, x) \wedge J_N(v, y_3, y) \end{pmatrix},$$

$$\Big((x_1, y_1) \boxplus \big((x_2, y_2) \boxplus (x_3, y_3)\big)\Big)(x, y) = \bigvee_{\substack{u \in M_1 \\ v \in M_2}} \begin{pmatrix} J_M(x_2, x_3, u) \wedge J_N(y_2, y_3, v) \\ \wedge J_M(x_1, u, x) \wedge J_N(y_1, v, y) \end{pmatrix},$$

Similarly, we can define fuzzy product as follows :

$$p: F(R_1 \times R_2) \times (M \times N) \to F(M \times N),$$
$$(K \times L, A \times B) \mapsto \tau(K \times L, A \times B),$$

where $F(R_1 \times R_2) = \{K \times L | K \times L: R_1 \times R_2 \to [0,1]\}$, K and L are fuzzy subsets of R_1 and R_2, and $F(M_1 \times M_2) = \{A \times B | A \times B: M \times N \to [0,1]\}$, A and B are fuzzy subsets of M_1 and M_2, therefore

$$p(K \times L, A \times B)(x, y) = \bigvee_{\substack{m \in M, n \in N \\ r_1 \in R_1, r_2 \in R_2}} \begin{pmatrix} A(m) \wedge B(n) \wedge K(r_1) \wedge L(r_2) \\ \wedge p(r_1, m, x) \wedge p(r_2, n, y) \end{pmatrix}.$$

Let $A \times B = \{(m, n)\}$ and $K \times L = \{(r_1 \times r_2)\}$, and $p(K \times L, A \times B)$ be donated as $(r_1, r_2) \boxdot (m, n)$, then

$$\big((r_1, r_2) \boxdot (m, n)\big)(x) = p(r_1, m, x) \wedge p(r_2, n, y),$$

$$\Big((r_1, r_2) \boxdot \big((m_1, n_1) \boxplus (m_2, n_2)\big)\Big)(x, y) = \bigvee_{\substack{m \in M \\ n \in N}} \begin{pmatrix} J_M(m_1, m_2, m) \wedge J_N(n_1, n_2, n) \\ \wedge p(r_1, m, x) \wedge p(r_2, n, y) \end{pmatrix},$$

$$\Big(\big((r_1, r_2) \boxplus (r_3, r_4)\big) \boxdot (m, n)\Big)(x, y) = \bigvee_{\substack{r \in R_1 \\ s \in R_2}} \begin{pmatrix} G_1(r_1, r_3, r) \wedge G_2(r_2, r_4, s) \\ \wedge p(r, m, x) \wedge p(s, n, y) \end{pmatrix},$$

$$\Big(\big((r_1, r_2) \boxdot (r_3, r_4)\big) \boxdot (m, n)\Big)(x, y) = \bigvee_{\substack{r \in R_1 \\ s \in R_2}} \begin{pmatrix} H_1(r_1, r_3, r) \wedge H_2(r_2, r_4, s) \\ \wedge p(r, m, x) \wedge p(s, n, y) \end{pmatrix},$$

$$\Big((r_1, r_2) \boxdot \big((r_3, r_4) \boxdot (m, n)\big)\Big)(x, y) = \bigvee_{\substack{x_1 \in M \\ y_1 \in N}} \begin{pmatrix} p(r_3, m, x_1) \wedge p(r_4, n, y_1) \\ \wedge p(r_1, x_1, x) \wedge p(r_2, x_2, y) \end{pmatrix},$$

$$\Big(\big((r_1, r_2) \boxdot (m_1, n_1)\big) \boxplus \big((r_1, r_2) \boxdot (m_2, n_2)\big)\Big)(x, y) =$$

$$\bigvee_{\substack{x_1, x_2 \in M \\ y_1, y_2 \in N}} \begin{pmatrix} p(r_1, m_1, x_1) \wedge p(r_2, n_1, y_1) \\ \wedge p(r_1, m_2, x_2) \wedge p(r_2, n_2, y_2) \\ \wedge J_M(x_1, x_2, x) \wedge J_N(y_1, y_2, y) \end{pmatrix},$$

therefore, $M \times N$ is called direct product of fuzzy modules over fuzzy rings $R_1$and R_2.

Theorem 13 [2]. $M \times N$ is a fuzzy module over fuzzy ring $R_1 \times R_2$.

3. RESULTS AND DISCUSSION

In this section, we give some analog theorems about homomorphism on direct product of fuzzy modules over fuzzy rings.

Theorem 15. Let $M_1 \times N_1$ and $M_2 \times N_2$ are fuzzy modules over fuzzy ring $R_1 \times R_2$ respectively. Let $h: M_1 \times N_1 \to M_2 \times N_2$ is an $R_1 \times R_2 - fmodule\ homomorphism$. Then

(i) $Ker\ h$ is a *fuzzy submodule* of $M_1 \times N_1$,
(ii) $Im\ h$ is a *fuzzy submodule* of $M_2 \times N_2$,
(iii) if $C \times D$ is any *fuzzy submodule* of $M_2 \times N_2$, then $h^{-1}(C \times D) = \{(m_1, n_1) \in M_1 \times N_1 | h(m_1, n_1) \in C \times D\}$ is a *fuzzy submodule* of $M_1 \times N_1$.

Proof.

(i) $Ker\ h = \{(a, b) \in M_1 \times N_1 | h(a, b) = (e_{m_2}, e_{n_2})\}$ is a fuzzy subgroup of the Abelian fuzzy group $M_1 \times N_1$. Let $(a, b) \in Ker\ h$, $(r_1, r_2) \in R_1 \times R_2$, and $(m_1, n_1) \in M_1 \times N_1$ such that $p\big((r_1, r_2), (a, b), (m_1, n_1)\big) > \theta$. Since h is an $R_1 \times R_2 - fmodule\ homomorphism$, $p\big((r_1, r_2), h(a, b), h(m_1, n_1)\big) > \theta$. On the other hand, $(a, b) \in Ker\ h$ we have $f(a, b) = (e_{m_2}, e_{n_2})$. Hence, $p\Big((r_1, r_2), (e_{m_2}, e_{n_2}), h(m_1, n_1)\Big) > \theta$ and so $h(m_1, n_1) = (e_{m_2}, e_{n_2})$ from Proposition 19 in [1]. Therefore, $(m_1, n_1) \in Ker\ h$ is obtained.

(ii) $Im\ h = \{(x, y) \in M_2 \times N_2 | (x, y) = h(a, b), (a, b) \in M_1 \times N_1\}$ is a fuzzy subgroup of the Abelian fuzzy group. Let $(x, y) \in Im\ h$, $(r_1, r_2) \in R_1 \times R_2$, and $(m_1, n_1) \in M_1 \times N_1$such that $(x, y) = h(a, b)$. Let $(c, d) \in M_1 \times N_1$ such that $p\big((r_1, r_2), (a, b), (c, d)\big) > \theta$. Since h is an $R_1 \times R_2 - fmodule\ homomorphism$, $p\big((r_1, r_2), h(a, b), h(c, d)\big) > \theta$ which mean $p\big((r_1, r_2), (x, y), h(c, d)\big) > \theta$ and so $h(c, d) \in M_2 \times N_2$.

(iii) $h^{-1}(C \times D)$ is a fuzzy subgroup of the Abelian fuzzy group from theorem 5.2 in [6]. Let $(r_1, r_2) \in R_1 \times R_2$ and $(c, d) \in h^{-1}(C \times D)$ such that $p\big((r_1, r_2), (c, d), (u, v)\big) > \theta$. Since $p\big((r_1, r_2), h(c, d), h(u, v)\big) > \theta$ and $h(c, d) \in C \times D$, we have that $h(u, v) \in C \times D$ and $(u, v) \in h^{-1}(C \times D)$.

Theorem 14. Let $M_1 \times N_1$ and $M_2 \times N_2$ are fuzzy modules over fuzzy ring $R_1 \times R_2$. Let $h: M_1 \times N_1 \to M_2 \times N_2$ be an $R_1 \times R_2 - fmodule\ homomorphism$. Then,

(i) h is an $R_1 \times R_2 - fmodule\ monomorphism$ if and only if $Ker\ h = \left\{\left(e_{M_1}, e_{N_1}\right)\right\}$,

(ii) h is an $R_1 \times R_2 - fmodule\ isomorphism$ if and only if there exists a *fuzzy module* homomorphism $g: M_2 \times N_2 \to M_1 \times N_1$ such that $gh = i_{M_1 \times N_1}$ and $hg = i_{M_2 \times N_2}$, where $i_{M_1 \times N_1}$ and $i_{M_2 \times N_2}$ are an identity function.

Proof.

(i) $(\Rightarrow)$ For any $(a,b) \in Ker\ h$ that means $h(a,b) = \left(e_{M_2}, e_{N_2}\right)$. Since h is a $R_1 \times R_2 - fmodule\ monomorphism,\ h\left(e_{M_1}, e_{N_1}\right) = \left(e_{M_2}, e_{N_2}\right)$. Thus, $(a,b) = \left(e_{M_1}, e_{N_1}\right)$ and so $Ker\ h = \left\{\left(e_{M_1}, e_{N_1}\right)\right\}$

$(\Leftarrow)$ Let $Ker\ h = \left\{\left(e_{M_1}, e_{N_1}\right)\right\}$ and $(a,b),(c,d) \in M_1 \times N_1$ such that $h(a,b) = h(c,d)$. We have $G\left(h(a,b), h(a,b)^{-1}, h\left(e_{M_1}, e_{N_1}\right)\right) > \theta$ and $G\left(h(c,d), h(a,b)^{-1}, h\left(e_{M_1}, e_{N_1}\right)\right) > \theta$. Thus, based on Proposition 2.1 in [6], $h(a,b) = h(c,d)$ and $(a,b) = (c,d)$, so h injektif . Because h homomorphism and injektif, then h is monomorphism.

(ii) It is clearly that we can find $g = h^{-1}$, so $gh = h^{-1}h = i_{M_1 \times N_1}$ and $hg = hh^{-1} = i_{M_2 \times N_2}$. where $i_{M_1 \times N_1}$ and $i_{M_2 \times N_2}$ are an identity function.

Example 15. We have $\mathbb{Z}_4 \times \mathbb{Z}_4$ and $N_1 \times N_2$ are fuzzy modules over fuzzy ring $\mathbb{Z}_4 \times \mathbb{Z}_4$ respectively where $N_1 = N_2 = (\bar{0}, \bar{2})$

Tabel 1. The value of function on G and H in $\mathbb{Z}_4$ with $\boldsymbol{\theta = 0.7}$

$\boldsymbol{G(a,b,c)}$	$\bar{\mathbf{0}}$	$\bar{\mathbf{1}}$	$\bar{\mathbf{2}}$	$\bar{\mathbf{3}}$
$(\bar{\mathbf{0}}, \bar{\mathbf{0}})$	0.8	0.3	0.6	0.7
$(\bar{\mathbf{0}}, \bar{\mathbf{1}})$	0.2	0.8	0.1	0.0
$(\bar{\mathbf{0}}, \bar{\mathbf{2}})$	0.5	0.2	0.9	0.6
$(\bar{\mathbf{0}}, \bar{\mathbf{3}})$	0.4	0.1	0.2	0.8
$(\bar{\mathbf{1}}, \bar{\mathbf{0}})$	0.6	0.9	0.6	0.4
$(\bar{\mathbf{1}}, \bar{\mathbf{1}})$	0.0	0.2	0.9	0.1
$(\bar{\mathbf{1}}, \bar{\mathbf{2}})$	0.1	0.7	0.3	0.8
$(\bar{\mathbf{1}}, \bar{\mathbf{3}})$	0.8	0.5	0.4	0.6
$(\bar{\mathbf{2}}, \bar{\mathbf{0}})$	0.6	0.3	0.8	0.1
$(\bar{\mathbf{2}}, \bar{\mathbf{1}})$	0.2	0.0	0.5	0.9
$(\bar{\mathbf{2}}, \bar{\mathbf{2}})$	0.8	0.7	0.3	0.1
$(\bar{\mathbf{2}}, \bar{\mathbf{3}})$	0.7	0.8	0.7	0.0
$(\bar{\mathbf{3}}, \bar{\mathbf{0}})$	0.6	0.3	0.5	0.8
$(\bar{\mathbf{3}}, \bar{\mathbf{1}})$	0.9	0.4	0.6	0.7
$(\bar{\mathbf{3}}, \bar{\mathbf{2}})$	0.6	0.8	0.0	0.4
$(\bar{\mathbf{3}}, \bar{\mathbf{3}})$	0.1	0.3	0.9	0.5

$\boldsymbol{H(a,b,c)}$	$\bar{\mathbf{0}}$	$\bar{\mathbf{1}}$	$\bar{\mathbf{2}}$	$\bar{\mathbf{3}}$
$(\bar{\mathbf{0}}, \bar{\mathbf{0}})$	0.8	0.1	0.3	0.7
$(\bar{\mathbf{0}}, \bar{\mathbf{1}})$	0.9	0.2	0.4	0.1
$(\bar{\mathbf{0}}, \bar{\mathbf{2}})$	0.9	0.7	0.3	0.5
$(\bar{\mathbf{0}}, \bar{\mathbf{3}})$	0.8	0.4	0.0	0.1
$(\bar{\mathbf{1}}, \bar{\mathbf{0}})$	0.9	0.3	0.1	0.2
$(\bar{\mathbf{1}}, \bar{\mathbf{1}})$	0.8	0.5	0.6	0.1
$(\bar{\mathbf{1}}, \bar{\mathbf{2}})$	0.8	0.0	0.7	0.5
$(\bar{\mathbf{1}}, \bar{\mathbf{3}})$	0.9	0.3	0.1	0.6
$(\bar{\mathbf{2}}, \bar{\mathbf{0}})$	0.9	0.2	0.4	0.0
$(\bar{\mathbf{2}}, \bar{\mathbf{1}})$	0.8	0.5	0.1	0.7
$(\bar{\mathbf{2}}, \bar{\mathbf{2}})$	0.9	0.3	0.1	0.5
$(\bar{\mathbf{2}}, \bar{\mathbf{3}})$	0.8	0.0	0.4	0.2
$(\bar{\mathbf{3}}, \bar{\mathbf{0}})$	0.8	0.6	0.2	0.0
$(\bar{\mathbf{3}}, \bar{\mathbf{1}})$	0.9	0.7	0.3	0.4
$(\bar{\mathbf{3}}, \bar{\mathbf{2}})$	0.9	0.0	0.5	0.6
$(\bar{\mathbf{3}}, \bar{\mathbf{3}})$	0.8	0.3	0.2	0.5

Then, we have $\mathbb{Z}_4 \times \mathbb{Z}_4 - fmodule\ homomorphism$ $h: \mathbb{Z}_4 \times \mathbb{Z}_4 \longrightarrow N_1 \times N_2$ where $h = (2x, 2y)$. Therefore, $Ker\ h = \{(\bar{0}, \bar{0}), (\bar{0}, \bar{2}), (\bar{2}, \bar{0}), (\bar{2}, \bar{2})\}$ $= Im\ h$ is a fuzzy submodule from $N_1 \times N_2$.

4. CONCLUSIONS

Some theorems from homomorphism on direct product of fuzzy modules over fuzzy rings have proven that have analogs with homomorphism fuzzy module over fuzzy ring. Also, we give a related example. We can extend definition and theorems about direct product of *n* number of fuzzy modules over fuzzy rings (*n* > 2) and so we can develop some related examples.

5. REFERENCES

[1] E. Yetkin and N. Olgun, 2014, New Type Fuzzy Module over Fuzzy Rings. *The Scientific Wold Journal*, **1**, 1.

[2] E. Yetkin, 2014, A Note on Direct Product of Fuzzy Modules over Fuzzy Rings, *International Journal of Algebra*, **8**, 129

[3] H.Aktaş, and Çağman.N, 2007, A type of Fuzzy Rings, *Article Math Logic*, **46**, 165.

[4] J. N. Mordeson, and Malik. D. S, 1998, **Fuzzy Commutative Algebra**, World Scientific Publishing. New York.

[5] M.Uçkun, 2004, Homomorphism Theorems in The View of Fuzzy Ring. *Annals of Fuzzy Mathematics and Informatic*, **7**, 879.

[6] Yuan. X. and Lee E.S., 2014, Fuzzy Group Based on Fuzzy Binary Operation, *Computers and Mathematics with Application*, **47**, 631.

Homotopy Analysis Method to Solve The Generalized Fisher's Equation

D. A. Hamzah[1*], E. M. Rocha[2], Y. Soeharyadi[3]

[1,3]Analysis and Geometry Research Division, Faculty of Mathematics and Natural Science, Institut Teknologi Bandung, Jl. Ganesha 10 Bandung 40132, Indonesia
[2] Center for Research and Development in Mathematics and Applications(CIDMA), Department of Mathematics, University of Aveiro, 3810-193 Aveiro, Portugal
* Corresponding authors: [dadang.amir12@gmail.com]

Abstract – In this Paper the Homotopy Analysis Method (HAM) is employed to solve the Generalized Fisher's Equation. This method contains auxiliary parameter h which provides us a simple way to adjust and control the convergence of the solution series. The solution determined by this method is then compared with the exact solution. We found that the numerical solution agrees with the exact solution.

1. INTRODUCTION

A reaction-diffusion models a competition phenomena between reaction which brings growth (bounded or may be unbounded), and diffusion which suppresses the quantity in considerations; reaction terms tend to form singularities, in some sense, and diffusion term brings regularity.

Reaction-diffusion systems appear as models in many engineering and science applications, e.g. reactor model in chemical production, chemotaxis and chemo-kinetic, populations dynamics and many others. The system is coupled with appropriate initial data.

Several methods are available to solve this system numerically, for example finite difference methods [2], sinc collocation method [1], operator-splitting methods [4], and iterative splitting method [4] (see [8] for other methods). In this paper we will use homotopy analysis method which first introduced by Liao[5]. This method provides us a simple way to adjust and control the convergence region of the solution series by varying the auxiliary parameter h.

More specifically we consider the generalized Fisher's equation of the form

$$\frac{\partial u}{\partial t} = u(1 - u^s) + Du_{xx} \tag{1.1}$$

where $s \in \mathbb{N}$. It is a logistic diffusion process with nonlinearity s. This paper is organized as follows, in section 2 the outline of the Homotopy Analysis Method (HAM) are presented. Application of (HAM) to the Fisher's equation are presented in section 3. The numerical results and conclusion are presented in section 4.

2. HOMOTOPY ANALYSIS METHOD (HAM)

In this section the basic idea of the homotopy analysis method [5] is introduced. Let $x \in [0,1], t \in \mathbb{R}^+ \cup \{0\}$ and $u : [0,1] \subset \mathbb{R} \times \mathbb{R}^+ \cup \{0\} \to \mathbb{R}$ be a real smooth function. Consider the problem

$$\frac{\partial}{\partial t} u(x,t) = L_1[u(x,t)] + L_2[u(x,t)] + N[u(x,t)] \tag{2.1}$$

with initial condition

$$u(x,0) = f(x) \tag{2.2}$$

where L_1, L_2 are differential linear operators with respect to x and $N: \mathbb{R} \to \mathbb{R}$ is a nonlinear (analytic) function.

We transform the nonlinear equation (2.1) into an infinite (triangular) system of linear differential equation by using the Homotopy method. For such consider the problem of finding the solution $v \in X$, with X a real Banach space, of the general differential equation

$$L[v(x,t)] = N[v(x,t)], \;\; v(x,0) = f(x) \tag{2.3}$$

where L is a linear differential operator, N is a nonlinear operator and $v \equiv v(x,t)$. Define the (formal) function ϕ_q, depending on a parameter q, as

$$\phi_q(x,t) = \sum_{m=0}^{+\infty} v_m(x,t)q^m \qquad \text{for all } q \in [0,1] \tag{2.4}$$

for some given function $v_m \in X, m \geq 0$. We now consider the (homotopic) equation

$$(1-q)L[\phi_q - v_0] = qh\big(L[\phi_q] - N[\phi_q]\big), \qquad \text{for all } q \in [0,1] \tag{2.5}$$

where $h \in \mathbb{R}$ is a real value, which is useful to control the convergence of the series (2.4). The arbitrary function $v_0 \in X$ behaves as a guess for the solution $v \in X$. From (2.5) we have

$$\begin{gathered} L[\phi_q - v_0] = 0, \quad q = 0 \\ L[\phi_q] - N[\phi_q] = 0, \quad q = 1. \end{gathered} \tag{2.6}$$

This means that the solution of equation (2.1) can be obtained as

$$v(x,t) = \phi_q(x,t)|_{q=1} = \sum_{m=0}^{+\infty} v_m(x,t). \tag{2.7}$$

and ϕ_q gives us a continuous deformation from v_0 to v. In order to ensure that the initial condition $v(x,0) = f(x)$ holds, we assume $v_0(x,0) = f(x)$ and $v_m(x,0) = 0$ for all $m \geq 1$.

For any function g, consider the derivative

$$D_m[g(\phi_q)] := \frac{1}{m!}\frac{\partial^m}{\partial q^m} g(\phi_q)|_{q=0} \tag{2.8}$$

For any linear operator L and $k \in \mathbb{N}$, we have: (a) $D_m(\phi_q) = v_m$; (b) $D_m(q^k\phi_q) = D_{m-k}(\phi_q)$; (c) $D_m(L[\phi_q]) = L[D_m(\phi_q)]$; (d) $D_m(q^k L[\phi_q]) = L[D_{m-k}(\phi_q)]$. If $N(r) = r^s$ for $s \in \mathbb{N}$, Molabahrami and Khani [7] showed that, for $m \geq 0$, we have

$$D_m[\phi_q^s] = \sum_{r_1=0}^{m} v_{m-r_1} \sum_{r_2=0}^{r_1} v_{r_1-r_2} \cdots \sum_{r_{s-2}=0}^{r_{s-3}} v_{r_{s-3}-r_{s-2}} \sum_{r_{s-1}=0}^{r_{s-2}} v_{r_{s-2}-r_{s-1}} v_{r_{s-1}} \tag{2.9}$$

which has the representation

$$D_m[\phi_q^s] = \sum_{r_1=0}^{r_0} v_{\gamma(1)} \sum_{r_2=0}^{r_1} v_{\gamma(2)} \cdots \sum_{r_{s-1}=0}^{r_{s-2}} v_{\gamma(s-1)} v_{\gamma(s)} \tag{2.10}$$

by setting $\gamma(i) = r_{i-1} - r_i$, $r_0 = m$ and $r_s = 0$.

Set $\chi_m = 0$, if $m < 1$ and $\chi_m = 1$, if $m \geq 1$. Applying the derivative m times with respect to q, set $q = 1$ and divide by $m!$ to equation (2.5) we have

$$\begin{gathered} L[v_m - \chi_m v_{m-1}] = hD_{m-1}\big(L[\phi_q] - N[\phi_q]\big) \\ \Rightarrow L[v_m] = (\chi_m + h)L[v_{m-1}] - hD_{m-1}N[\phi_q]. \end{gathered} \tag{2.11}$$

By induction, we see that the components of the series (2.11) satisfy

$$L[v_m(x,t)] = \alpha_m L[v_0] - \sum_{k=0}^{m-1} \alpha_{m-k} D_k N[\phi_q], \qquad m \geq 1 \tag{2.12}$$

where $\alpha_k = h(1+h)^{k-1}$, for $k \geq 1$. Note that $D_k N[\phi_q]$ only depend on the values of $v_k, \ldots, v_0$. Therefore, if we define

$$\xi_m(x,t) := \alpha_m L[v_0(x,t)] - \sum_{k=0}^{m-1} \alpha_{m-k} D_k N[\phi_q(x,t)], \tag{2.13}$$

we have to solve the infinite system of linear differential equations

$$L[v_m(x,t)] = \xi_m(x,t), \qquad m \geq 1, \tag{2.14}$$

and the solution of equation (2.3) will be given (formally) by (2.7).

Applying these ideas to the general problem (2.1) i.e. with $L[u] = \frac{\partial}{\partial t}u - L_1[u] - L_2[u]$, we have a numerical approximation scheme if we approximate the solution $u \in X$ by truncating the series (2.7), for some $n_H \in \mathbb{N}$, so

$$u \approx u_0 + \sum_{m=1}^{n_H} u_m, \tag{2.15}$$

and from (2.11), each $u_m, m \in \mathbb{N}$, satisfies the linear inhomogeneous Cauchy problem

$$\frac{\partial}{\partial t}u_m = L_1[u_m] + L_2[u_m] + \alpha_m g^u - \sum_{k=0}^{m-1} \alpha_{m-k} h_k^u, \qquad u_m(x,0) = 0.$$

With

$$g^u := \frac{\partial}{\partial t}u_0 - L_1[u_0] - L_2[u_0] \quad \text{and} \quad h_k^u := D_k N[\phi_q].$$

If we assume that u_0 satisfies

$$\frac{\partial}{\partial t}u_0 = L_1[u_0] + L_2[u_0], \quad u_0(x,0) = f(x) \tag{2.16}$$

then $g^u \equiv 0$ and each $u_m, m \in \mathbb{N}$, satisfies the linear inhomogeneous Cauchy problem

$$\frac{\partial}{\partial t}u_m = L_1[u_m] + L_2[u_m] - \sum_{k=0}^{m-1}\alpha_{m-k}h_k^u, \qquad u_m(x,0) = 0 \tag{2.17}$$

3. FISHER'S EQUATION

Let us consider the initial value problem of (1.1) for $s = 1$. Then we obtain the Cauchy problem as follows

$$\frac{\partial}{\partial t}u = \frac{\partial^2 u}{\partial t^2} + u - u^2, \quad t \in (0,T], \ x \in (0,1)$$

$$u(x,0) = f(x), \quad x \in [0,1]. \tag{3.1}$$

Where u_0 is continuous real valued function from $[0,1]$ to $\mathbb{R}$. Then, we have $L_1[u] := u_{xx}$, $L_2[u] := u$ and $N(r) = r^2$. From relation (2.9), we have

$$D_m[\phi_q^2] = \sum_{r_1=0}^{m} u_{m-r_1}u_{r_1}$$

and from relation (2.12) we have

$$L[u_m(x,t)] = \alpha_m L[u_0] - \sum_{k=0}^{m-1}\alpha_{m-k}D_k N[\phi_q^2], \qquad m \geq 1 \tag{3.2}$$

Let be given the value $n_H, N_X, N_T \in \mathbb{N}$ and $T > 0$. We consider the uniform spatial grid $\{x^j\}_{j=0}^{N_X}$ of the interval $[0,1]$, so $x^j := \frac{j}{N_X}$ with step $h_X := \frac{1}{N_X}$. The spatial discretization of L_1 may be made by standard (finite differences) second order centered approximation which is given by

$$L_1[u](x^j,t) = \frac{\partial^2 u}{\partial t^2}(x^j,t) \approx \frac{1}{(h_X)^2}\Big(u(x^{j+1},t) - 2u(x^j,t) + u(x^{j-1},t)\Big).$$

We also consider the uniform temporal grid $\{t^n\}_{n=0}^{N_T}$ of the time interval $[0,T]$, so $t^n := \frac{n}{N_T}$ with step $h_T := \frac{1}{N_T}$. We denote u_j^n as the numerical approximation of $u(x^j,t^n)$. The initial condition is defined as $u_j^0 := f(x^j)$. Now solve for each u_m in equation (3.2) we use Iterative Splitting Method with $i = 1$ (see [4]).

The initial solution is of the form $u_0(x,t) = l(t)\eta(x) + r(t)$ with $l(0) = 1$ and $r(0) = 0$. This selection is reasonable since the initial condition of (3.1) only depend on variable x.

4. NUMERICAL RESULTS

In this section we consider the Fisher's equation (3.1) subject to initial condition $\psi(x) = \frac{1}{\left(1+e^{\sqrt{\frac{1}{6}}x}\right)^2}$ where Bastani in [3] proposed the exact solution as

$$u(x,t) = \frac{1}{\left(1+e^{\sqrt{\frac{1}{6}}x-\frac{5}{6}t}\right)^2}.$$

We compare this results with the numerical solution constructed by series (2.15) which for every m satisfies eq. (3.2) and then solved Iterative Splitting Method. For the initial solution we use $u_0(x,t) = \frac{e^{-0.12t}}{\left(1+e^{\sqrt{\frac{1}{6}}x}\right)^2} + 0.221t$.

The result is given in Figure 1.

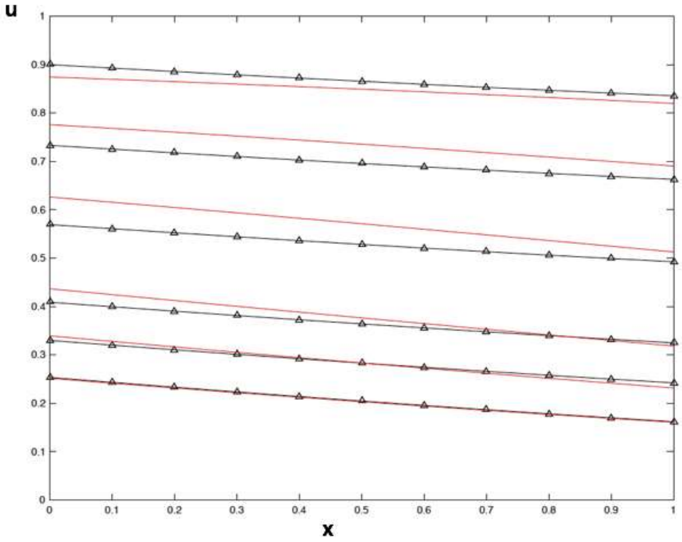

Figure 1: Comparison between numerical solution and Exact solution of Fisher's Equation where numerical solution denoted by triangle line and exact solution by straight line with $\Delta t = 0.008$, $\Delta x = 0.1$, $h = -2$, $n_H = 5$, and $t = 0, 0.4, 0.8, 1.6, 2.4, 3.2$.

We found that the numerical solution agrees with the exact solution. However if we plot for longer time the error varies due to the value of n_H and h. We can increase the accuracy by adding more n_H and varying the value of h.

5. REFERENCES

[1]. Al-Khaled, K. Numerical study of Fisher's reaction-diffusion equation by the sinc collocation method, *Journal of Computational and Applied Mathematics* **137 (2001)** 245-255.

[2]. A. Tveito and R. Winther. Introduction to Partial Differential Equations: A Computational Approach, Springer, 2009.

[3]. Bastani, M. and Salkuyeh, D. K., A highly accurate method to solve Fisher's equation, PRAMANA *journal of physics*, **Vol. 78**, No. 3, 2012 pp. 335-436.

[4]. Geiser, J. Decomposition Methods for Differential Equations: Theory and Application, CRC Press, Taylor and Francis Group, 2008.

[5]. Liao, S., Beyond Perturbation: Introduction to the Homotopy Analysis Method, Chapman & Hall/CRC Press, Boca Raton, 2003.

[6]. Molabahrami, A. and Khani, F., The homotopy analysis method to solve the Burgers-Huxley equation, *Nonlinear Analysis: Real World Applications* **10 (2009)** 589-600.

[7]. Singh, B. J. and Arora, G., A new numerical scheme to solve Fisher-type reaction diffusion equations, *MESA* **Vol. 5**, No. 2, 2014, pp. 153-164.

Application Correlation Order at Dependency Problem on Joint Life Status

Endang Wahyu Handamari[1*] , Fawzan Rinaldy[2] ,

[1, 2,]Mathematics Department, Brawijaya University Malang Indonesia

*Corresponding authors:[ewahyu-math@ub.ac.id]

Abstract-Dependency is one of the factors that affect the premium of the actuarial function joint life status. In the premium calculation of the actuarial function joint life status normally negligible influence of dependency due to limitations in the way of counting. In this paper discussed the effect of dependencies on the amount of premium in each state by using correlation order and use the definitions and theorems related. Then lower and upper bound of premiums built using the Fréchet-Hoeffding bounds. The lower and upper bound is the premium that different in dependency. Based on numerical example that created using case of married couples, it can be seen the dependency problem. The older age between husband and wife, then the dependencies between them has increased, but decreased when it reaches a certain age.

Keyword: dependency, joint life status, correlation order, Frechet-Hoeffding bounds.

1. INTRODUCTION

Determining the value of the multiple-life premiums, especially on joint life status. with the assumption that the variable remaining life of an individual is incorporated in that state are independent. If such an assumption, then the individual will have the same risk of death. However, if observed in real life, there are several factors that affect dependencies, such as family or genetic factors. for example in the case of families who have twins, in general, have an attachment to one another. So it is said to have an influence on the actuarial model of multiple life status.

This research will be discussed the issue of dependency on the rest of the age of the individual random variables is incorporated in the model of joint life status. The main references used in this research is the paper Dhaene et al. (2000) "A Note On Dependencies In Multiple Lives Statuses".[1]. Order correlation will be introduced as a tool to understand the dependencies in case of a joint life status. Order Correlation is a partial order for the distribution of two random variables. Besides used Frechet-Hoeffding bounds which are the boundaries of Copula function.

2. METHOD

The research uses correlation order to determine the dependency problem of variable remaining life. Order this correlation is a partial order for the distribution of two variables. The following definitions are given order correlation.

Definition:

$(T(x),T(y)),(S(x),S(y)) \in R(F,G)$, with marginal distribution function successive F and G. $(T(x),T(y))$ said less correlated compare with $(S(x),S(y))$, denoted by $(T(x),T(y)) \leq_c (S(x),S(y))$ if:

$Kov\left[f\big(T(x)\big),g\big(T(y)\big)\right] \leq Kov\left[f\big(S(x)\big),g\big(S(y)\big)\right]$ for all f and g which *non decreasing* and covariance exist.

From Definitions obtained Theorems on the relationship-order correlations and comparisons joint distribution function of the random variable different dependencies.

Theorem:

Suppose $(T(x),T(y))$ and $(S(x),S(y)) \in R(F,G)$. These statement are equivalent:

$\big(T(x),T(y)\big) \leq_c \big(S(x),S(y)\big)$.

$\mathrm{P}[T(x) \leq t, T(y) \leq s] \leq \mathrm{P}[S(x) \leq t, S(y) \leq s]$ for all $t, s \geq 0$.

Lemma

Suppose $(T(x),T(y))$ and $(S(x),S(y))$ are random variables from remaining life $\in R(F,G)$. If $\big(T(x),T(y)\big) \leq_c (S(x),S(y))$, so that these statement about stochastic orde satisfy:

$T(xy) \leq_{st} S(xy),$

$T(\overline{xy}) \geq_{st} S(\overline{xy}).$

From Lemma can be concluded that in the case of a joint-life status: if the remaining life of the random variable increases its dependencies, then probability of life at the joint-life status also increased. In other words the probability of death the joint-life status decreased. Furthermore, annuities and insurance premiums comparison with the remaining life of random variable different age dependencies expressed in the following theorem

Theorem

Suppose $(T(x), T(y))$ and $(S(x), S(y))$ are random variables from remaining life $\in R(F, G)$. If $\big(T(x), T(y)\big) \leq_c (S(x), S(y))$ then premiums comparison of different dependencies as follow:

Types of premium	Premium Comparison
Whole life annuity	$\ddot{a}_{xy}^{T} \leq \ddot{a}_{xy}^{S}$
Whole life insurance	$A_{xy}^{T} \geq A_{xy}^{S}$

In this research was used Frechet-Hoeffding bounds to determine the lower boundary and the upper boundary of annuities and insurance premiums. Frechet-Hoeffding bounds built using random variables remaining life $T(x)$ dan $T(y)$. For $\forall\ (T(x), T(y)) \in R(F, G)$,

$$\max\{F_{T(x)}(t) + G_{T(y)}(s) - 1, 0\} \leq C\left(F_{T(x)}(t), G_{T(y)}(s)\right) \leq \min\{F_{T(x)}(t), G_{T(y)}(s)\},$$

3. RESULTS AND DISCUSSION

Dependency problem on joint life status using the case of married couples. Discussion of the dependencies remain on the lower and upper limits of annuities and insurance premiums formed by Frechet-Hoeffding bounds. The lower limit and the upper limit $F_{T(x)}(t)$ and $G_{T(y)}(t)$ are not known for certain value. Therefore, use some assumptions that can be made numerical illustration:

$$F_{T(x)}(t) \leq G_{T(y)}(t) \qquad \text{For } t \geq 0$$

Where $F_{T(x)}(t)$ is a function of the distribution of the remaining life husband and $G_{T(y)}(t)$ is a distribution function of the remaining life wife. The previous, in case of a joint life status obtained :

$$\mathrm{P}(T_U(xy) \leq t) = \max\{F_{T(x)}(t), G_{T(y)}(t)\}$$

Because $F_{T(x)}(t) \geq G_{T(y)}(t)$ so that $P\big(T_{ij}(x) \leq t\big) = F_{T(x)}(t)$. For boundary annuities and insurance premiums formed by Frechet-Hoeffding lower bounds, used assumptions random variable independent of the remaining life.

Joint life status for a whole life annuity is :

$$\ddot{a}_{xy}^{T_L} \leq \ddot{a}_{xy} \leq \ddot{a}_{xy}^{T_U}$$

$$\ddot{a}_{xy}^{ind} \leq \ddot{a}_{xy} \leq \ddot{a}_{x}$$

and joint life status for whole life insurance is:

$$A_{xy}^{T_L} \geq A_{xy} \geq A_{xy}^{T_U}$$

$$A_{xy}^{ind} \geq A_{xy} \geq A_{x}$$

Numerical examples of the lower and upper boundary annuities and insurance are based on mortality tables Belgium. Belgian mortality tables are divided into two, namely MR (male) and FR (female). The table is constructed using the formula Makeham, shown in the following equation:

$$l_x = k s^x g^{c^x},$$

Value of parameters are shown in table below.

Table value of parameter Makeham models.

Parameter	MR	FR
k	1000266,63	1000048,56
s	0,999441703848	0,999669730966
g	0,999733441115	0,999951440172
c	1,101077536030	1,116792453830

This numerical example using the same condition in which the age of husband and wife with age. This numerical illustration is given in table below:

Table. Boundary the premium of a whole life annuity with $x = y$

x	$\ddot{a}_{xx}$		$\ddot{a}_{\overline{xx}}$		Difference Boundary
	Lower Boundary	Upper Boundary	Lower Boundary	Upper Boundary	
20	19,7349	20,1667	20,6574	21,0891	0,4318
30	18,6667	19,2597	19,9384	20,5313	0,5929
40	17,0871	17,9114	18,8316	19,6559	0,8243
50	14,8691	15,9929	17,1768	18,3005	1,1238
60	11,9987	13,4408	14,8254	16,2675	1,4421
70	8,7147	10,3706	11,7577	13,4136	1,6559
75	7,0797	8,7516	10,0300	11,7018	1,6719
76	6,7640	8,4296	9,6770	11,3427	1,6656
77	6,4536	8,1096	9,3233	10,9793	1,6560
80	5,5606	7,1679	8,2646	9,8719	1,6073

The difference between the lower and upper boundaryof whole life annuity increases with age of husband and wife. But when the husband and wife reached the age of 76, the difference between the lower and upper boundary begins to decrease. Thus, it can be said the husband and wife will be even greater if the husband and wife dependencies reach the age of 75, but the dependencies become smaller when the husband and wife age exceeding 75 years.

4. REFERENCES

[1]. Dhaene, J., Vanneste, M., dan Wolthuis, H. 2000. A Note on Dependencies in Multiple- Lives Statuses. *Bulletin of the Swiss Association of Actuaries*, **2000 (1)**, 19-34.

[2]. Dhaene, J. dan Goovaerts, M. 1996. Dependency of Risks and Stop-Loss Order. *ASTIN Bulletin* **26 (2)**. 201-212.

[3]. Lehmann, E. 1966. Some Concepts of Dependence. *Annals of Mathematical Statistics* **37**, 1137-1153.

The Interface-Fluid Coupled Model with Free Boundary at Triple Line

[1*]Nur Shofianah

[1]Department of Mathematics, Faculty of Mathematics and Natural Sciences, University of Brawijaya, Malang, Indonesia
[*]Corresponding authors: [nur_shofianah@ub.ac.id]

Abstract – In this paper, we focus on finding the boundary condition at static triple line in the interface-fluid coupled model. The triple line is a free boundary in the interface-fluid coupled model which consists of interface model and fluid model. Based on the result, we get the boundary condition at static triple line of the coupled model, that is the balance of forces which is equivalent to the Young's equation as the well-known condition at static triple line.

1. INTRODUCTION

The triple line is arise when we consider three immiscible fluids whose interfaces meet at one triple point / triple line. Triple line has a number of impacts on material behaviors which is of great interest in material science. Its specific boundary conditions arise based on the fact that the thin membrane boundary of the fluid domain is moving, i.e., interface. Here, we focus on finding boundary condition at static triple line. The previous researches show that the condition at static triple line of three immiscible fluids can be described by Young's equation. In this paper, we show that it also true in the interface-fluid coupled model. Understanding the dynamical of the triple line is very useful in the interface-fluid coupled model since this model is interesting in both concept and applications. The coupled model consists of interface model and fluid model. The numerical solution of interface model can be obtained in [3,2] and the numerical solution of the fluid model can be obtained in [2,6]. To couple these two models we need to analyze the triple line dynamics which is very useful to realize some important motions such as the motion of small droplet or bubbles [1,2] which has important applications in nanotechnology, the two-phase flow in microfluidic devices, inkjet printing, etc [1,2].

2. METHODS

In order to find the specific boundary condition at static triple line of the interface-fluid coupled model, we consider interface as a thin membrane that has mass and its motion is described by the Newton's second law. After we know the kind of interface motion from this analysis, we consider a system that described the evolution of triple line under condition that we got such that we get the suitable boundary condition at static triple line in this coupled model.

3. RESULTS AND DISCUSSION

Let $\Omega_t \in R^2$ be the fluid domain with boundary Γ_t at time $t \in [0, T]$. The Navier-Stokes equation for incompressible flow in moving domain can be written as

$$\rho\left(\frac{\partial \boldsymbol{u}}{\partial t} + \boldsymbol{u}.\nabla \boldsymbol{u} - \boldsymbol{f}\right) - \nabla.\boldsymbol{\sigma} = \boldsymbol{0}\text{ , in } \cup_{t\in[0,T]} \Omega_t \; x \; \{t\},$$

$$\nabla. u = 0, \text{ in } \cup_{t\in[0,T]} \Omega_t \; x \; \{t\},$$

where $\rho, \boldsymbol{u}, \boldsymbol{f}$ are the density, velocity and the external force, respectively. We consider only gravity as an external force. The stress tensor $\boldsymbol{\sigma}$ can be represented as

$$\boldsymbol{\sigma}(p, \boldsymbol{u}) = -p\boldsymbol{I} + 2\mu\varepsilon(\boldsymbol{u})$$

where p is pressure, $\boldsymbol{I}$ is the identity tensor, μ is viscosity, $\boldsymbol{\varepsilon}(\boldsymbol{u})$ is the strain-rate tensor,

$$\boldsymbol{\varepsilon}(\boldsymbol{u}) = \frac{\mathbf{1}}{\mathbf{2}}((\nabla \boldsymbol{u}) + (\nabla \boldsymbol{u})^{\boldsymbol{T}})$$

The initial condition consists of a specified divergence-free velocity field

$$\boldsymbol{u}(\boldsymbol{x}, \mathbf{0}) = \boldsymbol{u}_{\mathbf{0}}$$

and hydrostatic pressure

$$p(\boldsymbol{x},0) = \boldsymbol{P_0} + \rho g h$$

where $\boldsymbol{P_0}$ is atmospheric pressure, g is gravitational acceleration, and h is the depth.

Specific boundary conditions arise based on the fact that the boundary of the fluid domain is moving, i.e., interface. We consider the interface as a thin membrane that has mass and its motion is described by the Newton's second law,

$$m\mathbf{a} = \mathbf{F}$$

$$m\frac{d\mathbf{v}}{dt} = \widehat{\boldsymbol{\sigma}} \cdot \mathbf{n} + \sigma\kappa\mathbf{n} - \mathbf{f}_{fr},$$

where the third term of the right-hand side is the friction force. The first and second terms are the influence from the fluid and interface, respectively. Writing out the components of stress tensor and the proportionality of the friction force to the velocity,

$$m\frac{d\mathbf{v}}{dt} = -p\mathbf{I} \cdot \mathbf{n} + 2\mu\epsilon(\mathbf{u}) \cdot \mathbf{n} + \sigma\kappa\mathbf{n} - C\mathbf{v}$$

where C is a constant. In this case, we assume that $C >> m$ and that both the membrane and the fluid are composed of the same material, we obtain

$$C\mathbf{v} = -p\mathbf{I} \cdot \mathbf{n} + \sigma\kappa\mathbf{n},$$

which implies that by the absence of the pressure term, the motion of the interface according to mean curvature flow.

At this stage, we have the boundary condition on the interface. We need another boundary condition on the moving triple line as free boundary in this problem. Based on the analysis above, the interface evolves according to mean curvature flow. Such kind of motion is derived as the gradient flow of surface energy. Thus, we consider a system that describes the evolution of triple junction under gradient flow of surface energy as explained in the next section.

We write the total surface energy of a curve network and compute its first variation to get the normal velocity for each interface and the condition that has to be satisfied at triple junction. In particular, we consider three evolving curves

$$\gamma_i(s) = (\gamma_{i1}(s), \gamma_{i2}(s)),\ s \in [p_i, q_i], i = 1, 2, 3,$$

which lie inside a fixed smooth region $\Omega \in R^2$, meet the outer boundary at a right angle and get together at triple line. Each curve has different surface tension σ_i.

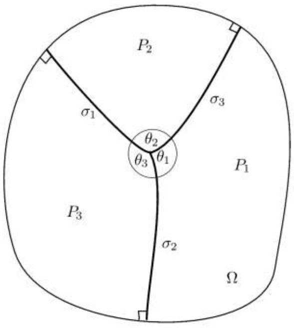

Figure 1 Setting of the triple line

Then the surface energy of all curves is given by

$$L(\gamma) = \sum_{i=1}^{3} \int_{\gamma_i} \sigma_i \, \mathrm{d}l = \sum_{i=1}^{3} \int_{p_i}^{q_i} \sigma_i \, |\gamma_i'(s)| \mathrm{d}s = \sum_{i=1}^{3} \int_{p_i}^{q_i} \sigma_i \, \sqrt{(\gamma_{i1}')^2 + (\gamma_{i2}')^2} \mathrm{d}s$$

The gradient flow of surface energy can be found from its variation. For a smooth vector field $\varphi = (\varphi_1, \varphi_2)$ vanishing the near boundary,

$$
\begin{aligned}
&\frac{d}{d\epsilon}L(\gamma+\epsilon\varphi(\gamma))\\
&=\frac{d}{d\epsilon}\sum_{i=1}^{3}\int_{p_i}^{q_i}\sigma_i\,|\gamma_i'+\epsilon\frac{d}{ds}(\varphi(\gamma))|\,\mathrm{d}s\\
&=\frac{d}{d\epsilon}\sum_{i=1}^{3}\int_{p_i}^{q_i}\sigma_i\,\sqrt{\left(\gamma_{i1}'+\epsilon\frac{d}{ds}(\varphi_1(\gamma))\right)^2+\left(\gamma_{i2}'+\epsilon\frac{d}{ds}(\varphi_2(\gamma))\right)^2}\,\mathrm{d}s\\
&=\frac{d}{d\epsilon}\sum_{i=1}^{3}\int_{p_i}^{q_i}\sigma_i\,\sqrt{(\gamma_{i1}'+\epsilon(\varphi_1(\gamma))')^2+(\gamma_{i2}'+\epsilon(\varphi_2(\gamma))')^2}\,\mathrm{d}s
\end{aligned}
$$

Then we can find,

$$
\begin{aligned}
\frac{d}{d\epsilon}L(\gamma+\epsilon\varphi(\gamma))|_{\epsilon=0}&=\sum_{i=1}^{3}\int_{p_i}^{q_i}\sigma_i\frac{(\gamma_{i1}'(\varphi_1(\gamma))'+\gamma_{i2}'(\varphi_2(\gamma))')}{\sqrt{(\gamma_{i1}')^2+(\gamma_{i2}')^2}}\,\mathrm{d}s\\
&=\sum_{i=1}^{3}\int_{p_i}^{q_i}\sigma_i\frac{\gamma_i'\cdot(\varphi(\gamma))'}{|\gamma_i'|}\,\mathrm{d}s\\
&=\sum_{i=1}^{3}\int_{p_i}^{q_i}\sigma_i\boldsymbol{t}_i\cdot(\varphi(\gamma))'\,\mathrm{d}s\\
&=\sum_{i=1}^{3}\left(\sigma_i\boldsymbol{t}_i\cdot\varphi(x_{TL})-\int_{\gamma_i}\sigma_i\kappa_i\mathbf{n}_i\cdot\varphi(\gamma)\,\mathrm{d}l\right)
\end{aligned}
$$

Where the tangential vector, curvature and outer normal of curve, respectively, are given by

$$
\boldsymbol{t}_i=\frac{\gamma_i'}{|\gamma_i'|},\quad \kappa_i=-\frac{\gamma_{i1}'\gamma_{i2}''-\gamma_{i2}'\gamma_{i1}''}{|\gamma_i'|^3},\quad \boldsymbol{n}_i=\frac{1}{|\gamma_i'|}(\gamma_{i2}',-\gamma_{i1}').
$$

From this result, the motion by gradient flow satisfies

1. The normal velocity of the interface,

$$
v_i=\sigma_i\kappa_i.
$$

2. The boundary condition at static triple line,

$$
\sum_{i=1}^{3}\sigma_i\boldsymbol{t}_i=0.
$$

The boundary condition at static triple line is the balance of forces whixh is wll-known to be equivalent to the Young’s equation.

4. CONCLUSIONS

From the Newton’s second law, we get that the motion of the interface according to mean curvature flow. It means that we have got the boundary on the interface that can be useful information to consider the suitable system to find the boundary condition at static triple line. Based on the result, in this case, we get the specific boundary condition at static triple line, that is the balance of forces

$$
\sum_{i=1}^{3}\sigma_i\boldsymbol{t}_i=0.
$$

and well-known to be equivalent to the Young’s equation.

5. REFERENCES

[1]. N. Shofianah, R. Mohammad, K. Svadlenka, 2014, On a Numerical Method for The Simulation of Contact Angle Dynamics, *JSCES 19*, Japan.

[2]. N. Shofianah, 2014, Simulation of Triple Line Dynamics by Interface-Fluid Coupling, Ph.D Thesis, Kanazawa University, Japan.

[3]. N. Shofianah, R. Mohammad, K. Svadlenka, 2015, *IAENG International Journal of Applied Mathematics*, **45**, 3, 235.

[4]. T. E. Tezduyar, 2003, Lecture Notes on Finite Element Simulation of Flow Problems, *Japan Society of Computational Engineering and Sciences.*

[5]. T. E. Tezduyar, S. Sathe, 2003, *Journal of Computation and Applied Mechanics*, **4**, 1, 71.

[6]. N. Shofianah, 2016, Numerical Solution of Incompressible Navier-Stokes Equation in Interface-Fluid Coupled Model, **BASIC 6th**, Indonesia

A Convolved Gaussian Process for Multiple Dependent Processes

A'yunin Sofro[1*], Jian Qing Shi[2]

[1] Mathematics Department, Surabaya State University and Kampus Ketintang, Surabaya, Indonesia
[2] School of Mathematics and Statistics, Newcastle University and Herschel Building, NE1 7RU, United Kingdom
*Corresponding authors: [ayuninsofro@unesa.ac.id]

Abstract – Multiple dependent Gaussian processes have developed rapidly in last decade. Dealing with multiple processes is not easy task. We have some difficulty in this case, such as how we construct the cross correlation between two responses and covariance matrix need to be positive definite. Convolution is one method providing easy way how to construct dependency between two responses. In this paper, we will discuss how several covariance structures and their mixed build the cross-correlation. Simulation study will be provided as well.

1. INTRODUCTION

Gaussian process has been famous recently, particularly spatial analysis and machine learning. It is because the process offers flexibility on the choosing the covariance structure. The benefit of using a Gaussian process is that it enables us to extend the idea to address multiple dependent Gaussian processes. During the last decade, many researchers have been developing this method for multiple processes. The vast majority of approaches have attempted to handle the difficulty of capturing inter-dependence between two processes and to ensure that the covariance matrix is positive definite [4]. Now, we can estimate the parameters from observed data to model multiple dependent processes instead of specifying and controlling the parameters of the positive covariance structure. An alternative way is to use a convolution method. In this chapter we will focus on constructing multiple dependent Gaussian processes, i.e the definition of the cross-correlation structure. We extend the method proposed by [1], [3] and consider a broader range of problems by comparing models with different covariance functions. Therefore, we are able to test sensitivity when choosing different covariance structures. We first investigate briefly look at the problem of constructing a convolved Gaussian process for multiple dependent processes using different covariance functions in the section as well. The last section will explore how we analyze multivariate nonlinear data with convolved Gaussian process as priors as comprehensive simulation study.

2. METHODS

2.1 Multiple Dependent Processes

Now we provide a general framework to derive the set of $\boldsymbol{k_{ab}(d)}$ from any stationary covariance kernel. We can express it in a closed form by applying the proposition as follows.

Proposition

Assume that $\boldsymbol{S_m}$is an isotropic covariance function on $\boldsymbol{\mathcal{R}^p}$, for any $\boldsymbol{p} \in \mathbb{N}$. Then the covariance $\boldsymbol{k_{ab}(d)}$ is given by

$$\boldsymbol{k_{ab}(d) = \frac{v_a v_b 2\pi^{p/2}}{|A_a + A_b|} S(\sqrt{Q_{ab}(d)}}$$

where

$$\boldsymbol{Q_{ab}(d) = d^T (A_a + A_b)^{-1} A_b d}$$

$$\boldsymbol{v_a, v_b} \in \mathbb{R}$$

and arbitrary positive matrices $A_a; a = 1,2$ and $k_{ab}(d)$ is a positive definite function on $\mathcal{R}^p$, p =1,2,... for a,b = {1,2}.

The proof of the proposition uses similar arguments to the one used in [1] and [4] although Proposition only focuses on two outputs. From the Proposition, we are able to obtain closed forms of the kernel function for the model and provide flexibility regarding the choice of the stationary covariance structure. We can apply the proposition by taking any isotropic covariance function to build multiple dependent Gaussian processes. There are several stationary kernels which can be extended by Proposition, such as gamma exponential, exponential, Matern and rational quadratics as we will discuss in this paper.

Different covariance functions can be used to model specific characteristics for each component in convolved Gaussian processes. The idea here is to set up dependent Gaussian processes by using mixed kernels.

3. Result and Discussion

In this subsection, two different examples are considered. We first generate a set of data as training and test data, $\boldsymbol{y}$ given the latent variable $\boldsymbol{x}$, by assuming that $\boldsymbol{y}$ and are $\boldsymbol{x}$, nonlinearly related. We estimate hyper-parameters using training data with an empirical Bayesian approach and then calculate the prediction mean and variance. As a measure of goodness of fit, the values of root mean squared error (RMSE) between predictions and their true values are used.

The aim of this scenario is to test the sensitivity of the proposed model with different covariances functions, considering mixed squared exponential and gamma exponential covariance functions.

The true model used to generate the process is

$$\begin{pmatrix} f_{1i} \\ f_{2i} \end{pmatrix} = \begin{pmatrix} \sin(6\boldsymbol{x}) \\ \cos(6\boldsymbol{x}) \end{pmatrix} + \begin{pmatrix} \tau_{1i} \\ \tau_{2i} \end{pmatrix}$$

Here (τ_{1i}, τ_{2i}) follows multivariate normal with mean zero and covariance structure as in the previous section. Also $\boldsymbol{x}$ are equally spaced points in [0,1]. We consider a mixed squared exponential and gamma exponential covariance functions which have been discussed in the previous section. The details of covariance structures is η_1 (the first independent process) is generated from a squared exponential covariance function with the true values of (w_1=0.04, B_1=1); η_2 (the second independent process) follows from a Gamma exponential covariance functions with true values of the hyper- of (w_2=0.04, B_2=1);. The shared processes, $\boldsymbol{\zeta}$ have squared exponential covariance functions with true values of (v_1=0.04, A_1=1, v_2=0.04, A_2=1). Two component processes, each containing 30 data points, are generated and used as training data. We generate also the same number of data points for test data. We use the nonlinear regression model and the convolved Gaussian process priors as discussed in previous section. To test the sensitivity of the choice of covariance functions, several models are considered and compared.

1. Model 1, we assume that it has the same covariance structure as the true model, ie ζ_1, ζ_2, η_1 have a squared exponential covariance function while η_2 has a Gamma exponential covariance function.
2. Model 2, similar to Model 1 but η_2 has a rational quadratic covariance function
3. Model 3, similar to Model 1 but η_2 has a Matern covariance function
4. Model 4, similar to Model 1 but η_2 has a a squared exponential covariance function
5. Model 5, We also compare with exist model proposed by [2] namely the CD model.

Now, we define CD model in [2]. Suppose that y_1 and y_2 are two dependent processes that can be written as follows

$$y_2 | y_1 \sim N(\alpha y_1, \sigma_\epsilon^2)$$

where y_1 is a Gaussian process with zero mean and any stationary covariance functions. In this setting, we define the model with squared exponential covariance function in y_1.

The average values of the root of mean squared errors (RMSE) between y at test data points and estimated y are calculated based on one hundred repetitions for different models and are reported in Table 1

Table 1 : Average of RMSE prediction between y and estimated y from various models for one hundred replications

Type of Model	Average RMSE
Model 1	0.01145
Model 2	0.01220
Model 3	0.01185
Model 4	0.01222
Model 5	0.16470

The figures show that the average RMSE by all the proposed models are quite close to zero. It also can be seen from the table that Model 2, Model 3 and Model 4 also perform reasonably well, even though misspecified covariance functions are used. This is possibly because the empirical Bayesian approach can select the best member from each covariance function family respectively for η_1, η_2 and the shared processes $\boldsymbol{\zeta}$. Although it cannot beat the true model, the flexibility can still guarantee a reasonably good solution. In contrast, the dependency across the component processes Model 5 is determined by a covariance structure. It fails to capture the individual characteristics. The above findings are confirmed by a simulation study.

One of the most significant advantages is that the proposed model provided huge flexibility regarding the choice of covariance functions. The proposed model is very robust because it still provides a reasonably good result even if a misspecified covariance function is used. Furthermore, the model is also able to perfectly capture the main features of each processes and provides a way to tackle individual characteristics of each response component in multivariate nonlinear regression

4. CONCLUSION

In this paper, we proposed the extension of convolved Gaussian processes for multivariate nonlinear regression analysis by investigating many stationary covariance functions and their mixed forms as convolved kernels. We considered covariance functions such as squared exponential, gamma exponential, rational quadratic and Matern. Furthermore, we also explored a way to apply mixed covariance functions for constructing multiple dependent Gaussian processes and used them as priors in a multivariate nonlinear model. During our investigation, we were able to identify several advantages using a convolved Gaussian process for multiple dependent processes. One of the most significant advantages is that the proposed model provided huge flexibility regarding the choice of covariance functions. From the scenario, it has been shown that the model is very robust because it still provides a reasonably good result even if a misspecified covariance function is used. Furthermore, this proposed method is also able to perfectly capture the main features of each processes As a result, the extension model with convolved Gaussian process priors provides a way to tackle individual characteristics of each response component in multivariate nonlinear regression. But their model fails to do so.

5. REFERENCES

[1]. Andriluka, M., Weizsacker, L. & Hofmann, T. 2006 Multi-class classification with dependent gaussian process. Darmstadt University of Technology.

[2]. Crainiceanu, C. M., Diggle, P. J. & Rowlingson, B. 2008 Bivariate binomial spatial modeling of loa loa prevalence in tropical africa. *Journal of the American Statistical Association* **103**, 21-37.

[3]. Boyle, P. & Frean, M. 2005 Multiple output Gaussian process regression. Technical Report, Victoria University of wellington

[4]. A'yunin, S, 2016, A convolved Gaussian Process Regression for Multivariate Non-Gaussian Regression, thesis, Newcastle University,U K

[5]. Paciorek, C. J. 2003 Nonstationary gaussian processes for regression and spatial mod- elling. Dissertation, Carnegie Mellon University.

Dealing with Feller Condition Under Heston Model

Abe Vallerian Siswanto[1*], Giovani Gracianti[1], Helena Margaretha[1]

[1] Department of Applied Mathematics, Pelita Harapan University, Tangerang, Indonesia
* Corresponding authors: abe.vallerian@hotmail.com

Abstract – Heston model provides better modelling compared to Black Scholes, since it has non-constant volatility, which is more approachable to the market. However, *Feller Condition* limits the model since it is a sufficient condition for always-positive volatility. If the volatility goes below zero, then the model would below up. In fact, in the market, not every security obeys the Feller Condition. In this paper, I provide a method to deal with Feller Condition to price American call option using numerical simulation.

1. INTRODUCTION

In 1973, Fisher Black and Myron Scholes [1] developed a successful option pricing model which is still widely used nowadays. However, the Black-Scholes model has a constant volatility. In reality, the volatility curve resembles a ‘smile’, often called ‘volatility smile’, and not constant. Heston [5] extended the model by adding one more Stochastic Differential Equation (SDE). In his paper, Heston derived the closed solution to price European Call option. However, the closed solution for American Call option is not yet available, thus numerical approach has to be taken.

Ait-Sahalia and R. Kimmel [7] developed the likelihood function for the Heston model to estimate the Heston parameters, in order to do numerical simulation. However, most of the stocks do not follow the *Feller Condition* [2]. Consequently, the simulation might be ruined since the variance will most likely go below 0. In this paper, I developed a solution to deal with this limitation.

2. METHODS

2.1 Stochastic Model

Heston Model, or Heston SDE (Stochastic Differential Equation) [5] satisfies the following equations:

$$dS_t = \mu S_t dt + \sqrt{v_t} S_t dB_t^{(1)},$$
$$dv_t = \kappa(\theta - v_t)dt + \sigma\sqrt{v_t} dB_t^{(2)},$$

where

- S_t the price of the stock at time t,
- $\sqrt{v_t}$ the volatility of the stock at time t,
- μ the rate of return of the stock,
- θ the long run variance v_t,
- κ the rate of mean reversion to the long term variance θ,
- σ the volatility of volatility v_t,
- $dB_t^{(1)}$ and $dB_t^{(2)}$ the Brownian motion with correlation ρ, and
- $S_t, v_t, \theta, \kappa, \sigma \geq 0$.

Although this model is more consistent to the market due to its dynamic volatility, it has a limitation stated in the *Feller Condition* [2]:

Assume that $v_0 > 0$. *If Feller Coefficient,* $\xi = \frac{2\kappa\theta}{\sigma^2} \geq 1$, *then the process* v_t *can never reach zero. Otherwise, the origin is accessible and strongly reflecting.*

It means that if this condition is not satisfied, v_t can go below 0 and it will cause issue in the simulation. Unfortunately, this condition is rarely satisfied in the market. To deal with this limitation, modification $v_t = \max(0, v_t)$ in the simulation was utilized.

2.2 Simulation Process

The simulation process is divided into 5 steps:

1. Find the Heston Parameters using *Maximum Likelihood Estimator*.

   Ait-Sahalia and R. Kimmel [7] developed the likelihood function for the Heston model to estimate the Heston parameters. Using the historical stock price and its variance, Heston parameters are estimated using *Steepest Descend* method [3]. The initial values of the parameters are estimated using the data as follows:

   - κ : absolute slope between the change in variance (Δv_t) with the variance (v_t),
   - θ : mean of the variance,
   - σ : standard deviation of the variance, and
   - ρ : correlation between stock price and its variance.

   Also assume that $\mu = 0$ to simplify the model, since it is not significant for the simulation.

2. Modify the Heston SDE

   To do the simulation using Monte Carlo method [4], the Heston SDE has to be discretize by substituting $dt = \frac{1}{h}$, where h is the number of intervals and $dX_t = X_{k/h} - X_{(k-1)/h}$ for $X_t = S_t, v_t, B_t^{(1)}, B_t^{(2)}$. Moreover, substitute $B_t^{(1)} = \sqrt{1-\rho^2} Z_t^{(1)} + \rho Z_t^{(2)}$, so that $corr\left(B_t^{(1)}, B_t^{(2)}\right) = \rho$. To deal with *Feller Condition*, substitute $v_t = \max(0, v_t)$ in the simulation to prevent the v_t from going negative.

3. Simulate using Monte Carlo method to find the expected future stock price

   The simulation is run to find the expected value of S_T, where T is the time until maturity. Assume that the stock has initial values of S_0 and v_0. First, calculate the expected value of $\widetilde{v_1}$ and $\widetilde{S_1}$ by generating the variable m times and taking the average. The process continues for $\widetilde{v_2}$, $\widetilde{S_2}$, …, until $\widetilde{v_T}$, $\widetilde{S_T}$.

4. Calculate the option price

   After obtaining the expected future stock price from $t = 1$ to $t = T$, calculate the option price using the formula $C = \max(0, S_s - K)$, where K is the strike price and $0 \le s \le T$.

5. Compare the simulated price with the market price

   The simulated price is compared to the market price to check the consistency of the model.

3. RESULTS AND DISCUSSION

The simulation was run using the data of 4 different stocks – AAPL, C, GE and KO – from 21 Nov 2013 until 21 Nov 2014. The goal of the simulation is to price an American Call option with the maturity date 28 Nov 2014, or $T = 5$ (workdays). $m = 1000$ and $h = 100$ were used for the simulation.

The Heston parameters estimation resulted from the simulation is shown in the *Table 1*. It can be observed that all those 4 stocks did not follow the Feller Condition or $\xi < 1$. Thus, the modification $\max(0, v_t)$ was critical in this case. Moreover, the comparison between market and simulation price of the option is shown in the *Figure 1*. From the simulation result, it can be observed that the simulation result is consistent to the market, although there are significant discrepancies when the strike price is high, due to the limitation of the model which prices the option as 0 if the strike price is higher than the maximum expected stock price. In the real case, there is no such free lunch.

Table 1 (Parameters Estimation)

Parameter	AAPL		C		GE		KO	
	Initial	**MLE**	**Initial**	**MLE**	**Initial**	**MLE**	**Initial**	**MLE**
κ	0.01150	0.21130	0.02298	0.02439	0.00534	0.00686	0.00198	0.00256
θ	70.91481	70.91480	6.53637	6.53637	2.00808	2.00808	2.11457	2.11457
σ	28.62092	28.64959	4.17678	4.17664	0.87437	0.87470	0.60062	0.60030
ρ	0.92822	0.17199	0.36383	0.36320	-0.01441	-0.01440	0.46976	0.46836
ξ	0.00199	0.03651	0.01722	0.01828	0.02805	0.03600	0.02326	0.03004

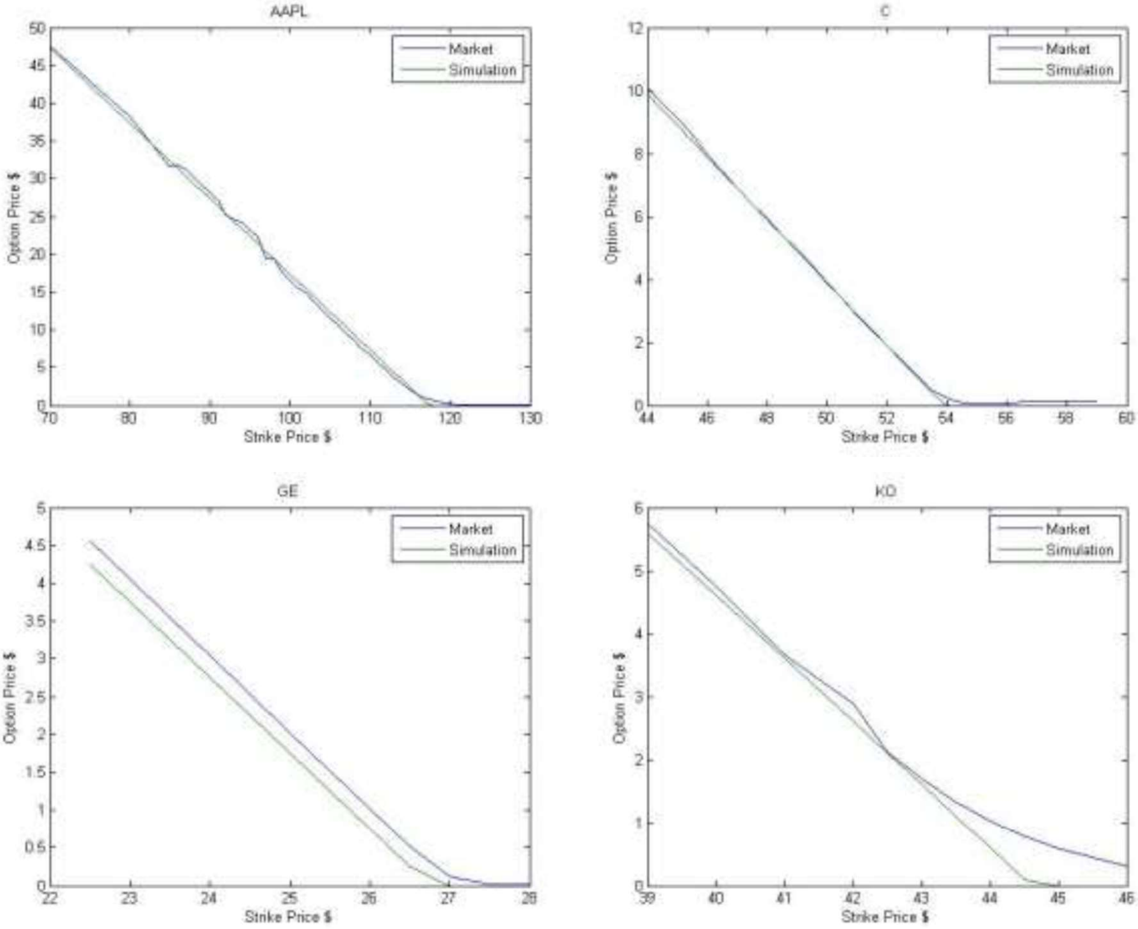

Figure 1 (Market vs Simulation Price)

4. CONCLUSIONS

To conclude, the stochastic model with modification $v_t = \max(0, v_t)$ in the simulation produced the result which is consistent to the market. However, this model has a limitation in case when the strike price is higher than the maximum expected stock price.

5. REFERENCES

[1] F. Black, M. Scholes, 1973, *The Journal of Political Economy*, **81**, 637–654

[2] I. Gikhman, 2011, A Short Remark on Feller's Square Root Condition, https://ssrn.com/abstract=1756450, accessed on 10 October 2014.

[3] J. H. Mathews, K. D. Fink, 1999, Numerical Methods using MATLAB, 3 ed, Prentice Hall, New Jersey.

[4] M. H. Kalos, P. A. Whitlock, 2004, Monte Carlo Methods. Wiley-VCG, Weinheim

[5] S. Heston, 1993, *The Review of Financial Studies*, **6**, 327–343.

[6] T. Mikosch, 1998, Elementary Stochastic Calculus, with Finance in View, World Scientific, Singapore.

[7] Y. Ait-Sahalia, R. Kimmel, 2007, *Journal of Financial Economics*, **83**, 413–452.

Properties of Various Smoothing Functions for Smoothed Particle Hydrodynamics

Kenny Wiratama[12*], Helena Margaretha[1], Pujianto Yugopuspito[2]

[1] Department of Applied Mathematics, Faculty of Science and Technology, Universitas Pelita Harapan, Tangerang, Indonesia
[2] Department of Informatics, Faculty of Science and Technology, Universitas Pelita Harapan, Tangerang, Indonesia
* Corresponding authors: [kenny.wiratama@outlook.com]

Abstract – In this paper, we address some of the smoothing functions used in Smoothed Particle Hydrodynamics approximations. We also discuss the widely used general properties of the smoothing functions, and we mathematically prove that the concerned smoothing functions obey the desired properties.

1. INTRODUCTION

Smoothed Particle Hydrodynamics (SPH) is a method for obtaining approximate numerical solutions of the equations of fluid dynamics by replacing the fluid with a set of particles [1]. SPH was initially developed to solve astrophysical problems. Currently, it has been applied to solve various engineering problems such as coastal hydrodynamics and fluid simulation for computer graphics. The meshfree nature of SPH is its main advantage. It enables treatment of complex geometries comfortably. On the other hand, the main disadvantage of SPH is the difficulty of dealing with solid boundaries.

An essential part of SPH is smoothing functions. Smoothing functions determine the influence area of each particle and also the shape of the interpolation. There are various smoothing functions published in SPH literature. This paper will discuss the smoothing functions proposed by [4]. Many kinds of properties have been applied as requirements for the smoothing functions as described in different literature. The most general ones are summarized by [2].

2. METHODS

2.1 SPH Approximations

We briefly discuss SPH approximations. Further details are presented in [2] and [3]. Let f be a scalar function of a three-dimensional position vector $\mathbf{r}$, and let V be the whole three-dimensional space. The fundamental property of the Dirac delta function $\delta(\mathbf{r})$ can be written as

$$f(\mathbf{r}) = \int_V f(\mathbf{r}')\delta(\mathbf{r}-\mathbf{r}')\,d\mathbf{r}',$$

where $d\mathbf{r}'$ is the differential volume element. We define another function called the smoothing function $W(\mathbf{r}-\mathbf{r}', h)$, where h is the smoothing length. The smoothing length h defines the influence area of the smoothing function. Replacing the Dirac delta function by the smoothing function, we obtain the kernel approximation of a function,

$$f(\mathbf{r}) \approx \int_V f(\mathbf{r}')\delta(\mathbf{r}-\mathbf{r}')\,d\mathbf{r}'.$$

The discretization process of the kernel approximation is called particle approximation. Particle approximation begins with representing the entire system with a finite number of particles. Suppose there are N particles, where particle j has mass m_j, density ρ_j, and volume ΔV_j. We replace the differential volume element $d\mathbf{r}'$ with the finite volume ΔV_j, and write the integral as a summation. We obtain

$$f(\mathbf{r}) \approx \sum_{j=1}^{N} f(\mathbf{r}_j)W(\mathbf{r}-\mathbf{r}_j, h)\Delta V_j = \sum_{j=1}^{N} \frac{m_j}{\rho_j} f(\mathbf{r}_j)W(\mathbf{r}-\mathbf{r}_j, h).$$

Hence, the value of a function at particle i can be written as

$$f(\mathbf{r}_i) = \sum_{j=1}^{N} \frac{m_j}{\rho_j} f(\mathbf{r}_j) W(\mathbf{r}_i - \mathbf{r}_j, h).$$

2.2 Smoothing Functions

There are various smoothing functions that can be used for applications. We consider three smoothing functions proposed by [4]. We denote the length of $\mathbf{r}$ as $r = |\mathbf{r}|$.

1. Sixth-degree polynomial kernel.

   The sixth-degree polynomial kernel is

$$W_p(\mathbf{r}, h) = \frac{315}{64\pi h^9} \begin{cases} (h^2 - r^2)^3 & 0 \leq r \leq h, \\ 0 & \text{otherwise.} \end{cases}$$

2. Debrun's spiky kernel

   The Debrun's spiky kernel is

$$W_s(\mathbf{r}, h) = \frac{15}{\pi h^6} \begin{cases} (h - r)^3 & 0 \leq r \leq h, \\ 0 & \text{otherwise.} \end{cases}$$

3. Viscosity kernel.

   The viscosity kernel is

$$W_v(\mathbf{r}, h) = \frac{15}{2\pi h^3} \begin{cases} -\frac{r^3}{2h^3} + \frac{r^2}{h^2} + \frac{h}{2r} - 1 & 0 < r \leq h, \\ 0 & \text{otherwise.} \end{cases}$$

3. RESULTS AND DISCUSSION

There are different kinds of properties for smoothing functions as described in different literature. We discuss the common ones summarized by [2].

- Unity
  The smoothing function must be normalized,
$$\int_V W(\mathbf{r}, h)\, d\mathbf{r} = 1.$$
- Compact support
  The value of the smoothing function must be zero outside its influence area.
  $W(\mathbf{r}, h) = 0$, for $r > kh$, where k is the scaling factor.
- Non-negativity.
  The value of the smoothing function must be nonnegative inside its influence area.
  $W(\mathbf{r}, h) \geq 0$, for all $\mathbf{r}$.
- Decay.
  The smoothing function is monotonically decreasing as the distance from a particle is increasing.
  If $r_1 < h, r_2 < h, r_1 > r_2$, then $W(\mathbf{r}_1, h) < W(\mathbf{r}_2, h)$.
- Delta function property.
  The smoothing function must be approximately identical to the Dirac delta function if the smoothing length approaches zero.
$$\lim_{h \to 0} W(\mathbf{r}, h) = \delta(\mathbf{r}).$$
- Symmetric property.
  The smoothing function must be radially symmetric.
$$r_1 = r_2 \Rightarrow W(\mathbf{r}_1, h) = W(\mathbf{r}_2, h).$$
- Smoothness
  The smoothing function must be an at least twice differentiable function.

We prove that the smoothing functions defined in section 2.2 obey the above properties.

1. Sixth degree polynomial kernel.
   We evaluate the integral using spherical coordinates. We have
$$\int_V W_p(\mathbf{r}, h)\, d\mathbf{r} = \int_0^{2\pi} \int_0^{\pi} \int_0^{h} \frac{315}{64\pi h^9} (h^2 - r^2)^3 (r^2 \sin\phi)\; dr\, d\phi\, d\theta = 1.$$
   Choose $k = 1$. We have $W_p(\mathbf{r}, h) = 0$ for $r > h$. If $r \leq h$, we obtain

$$r^2 \leq h^2,$$
$$\frac{315}{64\pi h^9}(h^2 - r^2)^3 \geq 0,$$
$$W_p(\mathbf{r}, h) \geq 0.$$

From the compact support property, if $r > h$, $W_p(\mathbf{r}, h) = 0$. If $r_1 < h, r_2 < h, r_1 > r_2$,

$$r_1^2 > r_2^2,$$
$$\frac{315}{64\pi h^9}(h^2 - r_1^2)^3 < \frac{315}{64\pi h^9}(h^2 - r_2^2)^3,$$
$$W_p(\boldsymbol{r}_1, h) < W_p(\boldsymbol{r}_2, h).$$

If $\mathbf{r} \neq \mathbf{0}, \lim_{h\to 0} W_p(\mathbf{r}, h) = 0$. If $\mathbf{r} = \mathbf{0}$,

$$\lim_{h\to 0} W_p(\mathbf{r}, h) = \lim_{h\to 0^+} \frac{315}{64\pi h^3} = +\infty.$$

If $r_1 = r_2$,

$$W_p(\mathbf{r}_1, h) = \frac{315}{64\pi h^9}(h^2 - r_1^2)^3 = \frac{315}{64\pi h^9}(h^2 - r_2^2)^3 = W_p(\mathbf{r}_2, h).$$

Since $W_p(\mathbf{r}, h)$ is a polynomial function, it follows that $W_p(\mathbf{r}, h)$ is at least twice differentiable. Hence, the sixth degree polynomial kernel obeys the desired properties.

2. Debrun's spiky kernel.

   We evaluate the integral using spherical coordinates. We have

$$\int_V W_s(\mathbf{r}, h)\, d\mathbf{r} = \int_0^{2\pi}\int_0^{\pi}\int_0^{h} \frac{15}{\pi h^6}(h - r)^3(r^2 \sin\phi)\ dr\ d\phi\ d\theta = 1.$$

Choose $k = 1$. We have $W_s(\mathbf{r}, h) = 0$ for $r > h$. If $r \leq h$, we obtain

$$-r \geq -h,$$
$$\frac{15}{\pi h^6}(h - r)^3 \geq 0,$$
$$W_s(\mathbf{r}, h) \geq 0.$$

From the compact support property, if $r > h$, $W_s(\mathbf{r}, h) = 0$. If $r_1 < h, r_2 < h, r_1 > r_2$,

$$-r_1 > -r_2,$$
$$\frac{15}{\pi h^6}(h - r_1)^3 < \frac{15}{\pi h^6}(h - r_2)^3,$$
$$W_s(\boldsymbol{r}_1, h) < W_s(\boldsymbol{r}_2, h).$$

If $\mathbf{r} \neq \mathbf{0}, \lim_{h\to 0} W_s(\mathbf{r}, h) = 0$. If $\mathbf{r} = \mathbf{0}$,

$$\lim_{h\to 0} W_s(\mathbf{r}, h) = \lim_{h\to 0^+} \frac{15}{\pi h^6} = +\infty.$$

If $r_1 = r_2$,

$$W_s(\mathbf{r}_1, h) = \frac{15}{\pi h^6}(h - r_1)^3 = \frac{15}{\pi h^6}(h - r_2)^3 = W_s(\mathbf{r}_2, h).$$

Since $W_s(\mathbf{r}, h)$ is a polynomial function, it follows that $W_s(\mathbf{r}, h)$ is at least twice differentiable. Hence, the Debrun's spiky kernel obeys the desired properties.

3. Viscosity kernel.

   We evaluate the integral using spherical coordinates. We have

$$\int_V W_v(\mathbf{r}, h)\, d\mathbf{r} = \int_0^{2\pi}\int_0^{\pi}\int_0^{h} \frac{15}{2\pi h^3}\left(-\frac{r^3}{2h^3} + \frac{r^2}{h^2} + \frac{h}{2r} - 1\right)(r^2 \sin\phi)\ dr\ d\phi\ d\theta = 1.$$

Choose $k = 1$. We have $W_v(\mathbf{r}, h) = 0$ for $r > h$. If $r \leq h$, we obtain

$$r^2 \geq h^2,$$
$$h^2 - r^2 \geq 0,$$
$$(h^2 - r^2)(h - r)^2 \geq 0,$$
$$h^4 - r^4 - 2h^3 r + 2hr^3 \geq 0,$$
$$\frac{-r^4 + 2hr^3 + h^4 - 2h^3 r}{2h^3 r} \geq 0,$$
$$\frac{15}{2\pi h^3}\left(-\frac{r^3}{2h^3} + \frac{r^2}{h^2} + \frac{h}{2r} - 1\right) \geq 0,$$
$$W_v(\mathbf{r}, h) \geq 0.$$

From the compact support property, if $r > h$, $W_v(\mathbf{r}, h) = 0$. Fix $h > 0$. Define

$$f(r) = -\frac{r^3}{2h^3} + \frac{r^2}{h^2} + \frac{h}{2r} - 1,$$

for all $r < h$.

$$f'(r) = -\frac{3r^2}{2h^3} + \frac{2r}{h^2} - \frac{h}{2r^2}.$$

Since $r < h$,

$$-r > -h,$$
$$(h - r)^2 > 0,$$
$$(h - r)^2(3r^2 + 2rh + h^2) > 0,$$
$$3r^4 - 4r^3h + h^4 > 0,$$
$$\frac{-3r^4 + 4r^3h - h^4}{2r^2h^3} < 0,$$
$$-\frac{3r^2}{2h^3} + \frac{2r}{h^2} - \frac{h}{2r^2} < 0,$$
$$f'(r) < 0.$$

It follows that f is decreasing. Hence, if $r_1 < h, r_2 < h, r_1 > r_2$,

$$f(r_1) < f(r_2),$$
$$\frac{15}{2\pi h^3}\left(-\frac{r_1^3}{2h^3} + \frac{r_1^2}{h^2} + \frac{h}{2r_1} - 1\right) < \frac{15}{2\pi h^3}\left(-\frac{r_2^3}{2h^3} + \frac{r_2^2}{h^2} + \frac{h}{2r_2} - 1\right),$$
$$W_v(\mathbf{r}_1, h) < W_v(\mathbf{r}_2, h).$$

If $\mathbf{r} \neq \mathbf{0}, \lim_{h\to 0} W_v(\mathbf{r}, h) = 0$. If $\mathbf{r} \to \mathbf{0}$,

$$\lim_{r\to 0} W_v(\mathbf{r}, h) = \lim_{r\to 0^+} \frac{15}{2\pi h^3}\left(-\frac{r^3}{2h^3} + \frac{r^2}{h^2} + \frac{h}{2r} - 1\right) = +\infty.$$

If $r_1 = r_2$,

$$W_v(\mathbf{r}_1, h) = \frac{15}{2\pi h^3}\left(-\frac{r_1^3}{2h^3} + \frac{r_1^2}{h^2} + \frac{h}{2r_1} - 1\right) = \frac{15}{2\pi h^3}\left(-\frac{r_2^3}{2h^3} + \frac{r_2^2}{h^2} + \frac{h}{2r_2} - 1\right) = W_v(\mathbf{r}_2, h).$$

$W_v(\mathbf{r}, h)$ is at least twice differentiable when $\mathbf{r} \neq \mathbf{0}$. Hence, the viscosity kernel obeys the desired properties.

4. CONCLUSIONS

We have proven that the smoothing functions proposed by [4] obey the properties summarized by [2].

5. REFERENCES

[1]. J.J. Monaghan, 2005, *Reports on Progress in Physics*, **68**, 1703.

[2]. G.R. Liu, M.B. Liu, 2003, *Smoothed Particle Hydrodynamics: A Meshfree Particle Method*. World Scientific, Singapore.

[3]. S. Li, W.K. Liu, 2007, *Meshfree Particle Methods*, Springer, New York.

[4]. M. Müller, D. Charypar, M. Gross, 2003, *Particle-based fluid simulation for interactive applications*, ACM SIGGRAPH, USA.

Application Ant Colony Optimization on Weight Selection of Optimal Control SEIR Epidemic Model

Dinita Rahmalia[1], Teguh Herlambang[2]

[1] Universitas Islam Darul Ulum. Jalan Airlangga 3 Sukodadi Lamongan, Indonesia
[2] Universitas Nahdlatul Ulama Surabaya, Indonesia
* Corresponding authors: [dinitarahmalia@gmail.com, teguh@unusa.ac.id]

Abstract – Nowadays, there are many contagious diseases which have been found. Disease with SEIR (Susceptible-Exposed-Infected-Recovered) type is a disease which can be contagious through contact with an infected individual. Optimal control is used for minimizing the number of infected individuals, the cost of vaccination, and the cost of treatment. The cost of an objective function depends on weight. In this research, we use an heuristic method like Ant Colony Optimization (ACO) to select weight so that minimizing the cost of objective function. It can be seen that the number of infected individual with control is lower than without control. Furthermore, we also obtain optimal weight related to cost of vaccination and treatment.

1. INTRODUCTION

The bad habit of lifestyle, food consuming, sanitation can raise the various of disease. In contagious disease, generally there are susceptible individual, exposed individual, infected individual, and recovered individual. A susceptible individual can be infected individually after making contact with an infected individual based on disease transmission rate. However, before being infected individually, the susceptible individual becomes exposed individual who doesn't show the symptom of a disease during latent time. When the symptom of the disease appears, the exposed individual becomes an infected individual. Then, the infected individual becomes a recovered individual when the symptom of the disease have lost [5]. In this research, we will control the number of susceptible individual by vaccination and the number of infected individual by treatment. However, both vaccination and treatment can affect cost. The cost of objective function also depends on weight.

Ant Colony Optimization (ACO) is optimization method which is inspired by the behavior of ant colony which can find the best path from a nest to food source. This method was discovered by Dorigo in 1990. At the early time, ants start to travel from their home to food source by selecting path randomly. Before returning to their home, ants deposit pheromone on a path which has visited. After returning to their home, pheromone information is updated based on evaporation rate. At the optimization process, a pheromone is updated until all ants choose the similar path as the best path [1]. In this research, we will apply ACO algorithm on weight selection of optimal control SEIR epidemic model. The weight used is related to cost of vaccination and treatment for controlling the number of susceptible and infected individual respectively. From the simulation, we can obtain comparison the number of individual with and without control. Furthermore, we also obtain optimal weight related to cost of vaccination and treatment.

2. METHODS

2.1 Optimal Control SEIR Epidemic Model

Consider the SEIR epidemic model with vaccination and treatment as follows [5]:

$$\dot{S} = \Lambda - \beta SI - \mu S - u_1 S \qquad \dot{E} = \beta SI - \mu E - \pi E \qquad \dot{I} = \pi E - \alpha I - \mu I - \gamma I - u_2 I$$

$$\dot{R} = \gamma I - \mu R + u_1 S + u_2 I \qquad S(0) \geq 0 \quad E(0) \geq 0 \quad I(0) \geq 0 \quad R(0) \geq 0$$

With the parameters: recruitment rate Λ, disease transmission rate β, natural death rate μ, death by disease rate α, recovery rate γ, and disease mutation rate π. We also add control function of susceptible who is vaccinated u_1 and control function of infected who is treated u_2. For the model, the objective function which is minimized is:

$$J(u_1, u_2) = \int_0^T \left(A_1 I + A_2 \frac{u_1^2}{2} + A_3 \frac{u_2^2}{2} \right) dt$$

with $A_1 > 0, A_2 > 0, A_3 > 0$, where we want to minimize the number of infected individuals, the cost of vaccination, and the cost of treatment. The goal is to find optimal control u_1^*, u_2^* such that

$$J(u_1^*, u_2^*) = \min(J(u_1, u_2) : (u_1, u_2) \in U)$$

Where U is the set of admissible controls defined by : $U = \{(u_1, u_2) : 0 < u_1 < 1, 0 < u_2 < 1\}$ u_1, u_2 are Lebesgue measurable [5].

2.2 Pontryagin's Maximum Principle

Theorem and Proof. If u_1^*, u_2^* is an optimal control corresponding state system, there exist adjoint variables $(\lambda_S \quad \lambda_E \quad \lambda_I \quad \lambda_R)$ which satisfy the following [3]:

$$\dot{\lambda}_S = -\frac{\partial H}{\partial S} = -\lambda_S(-\beta I - \mu - u_1) - \lambda_E \beta I - \lambda_R u_1 \qquad \dot{\lambda}_E = -\frac{\partial H}{\partial E} = -\lambda_E(-\mu - \pi) - \lambda_I \pi$$

$$\dot{\lambda}_I = -\frac{\partial H}{\partial I} = -A_1 - \lambda_S(-\beta S) - \lambda_E \beta S - \lambda_I(-\alpha - \mu - \gamma - u_2) - \lambda_R(\gamma + u_2)$$

$$\dot{\lambda}_R = -\frac{\partial H}{\partial R} = -\lambda_R(-\mu) \qquad \lambda_S(T) = \lambda_E(T) = \lambda_I(T) = \lambda_R(T) = 0$$

where the Hamiltonian equation is:

$$H(S,E,I,R) = \left(A_1 I + A_2 \frac{u_1^2}{2} + A_3 \frac{u_2^2}{2} \right) + \begin{pmatrix} \lambda_S & \lambda_E & \lambda_I & \lambda_R \end{pmatrix} \begin{pmatrix} \Lambda - \beta SI - \mu S - u_1 S \\ \beta SI - \mu E - \rho E \\ \rho E - \alpha I - \mu I - \gamma I - u_2 I \\ \gamma I - \mu R + u_1 S + u_2 I \end{pmatrix}$$

Furthermore, we find optimal control u_1^*, u_2^*:

$$\frac{\partial H}{\partial u_1} = A_2 u_1 - \lambda_S S + \lambda_R S = 0 \qquad \frac{\partial H}{\partial u_2} = A_3 u_2 - \lambda_I I + \lambda_R I = 0$$

$$\Leftrightarrow u_1 = \min\left(\max\left(0, \frac{(\lambda_S - \lambda_R)S}{A_2} \right), 1 \right) \qquad \Leftrightarrow u_2 = \min\left(\max\left(0, \frac{(\lambda_I - \lambda_R)I}{A_3} \right), 1 \right)$$

2.3 Discrete Form and Ant Colony Optimization

To solve optimal control SEIR epidemic model, we need discretization using forward-backward difference approximation where initial conditions for the state equations and terminal conditions for the adjoint equations [4][5]. The weight used are A_2, A_3 related to cost of vaccination and treatment for controlling the number of susceptible and infected individual respectively.

$SEIR(A_2, A_3)$

1. Set $S_0, E_0, I_0, R_0, \lambda_{S,T} = 0, \lambda_{E,T} = 0, \lambda_{I,T} = 0, \lambda_{R,T} = 0, u_{1,0} = u_{2,0} = 0$
2. Calculate state equations $S_{k+1}, E_{k+1}, I_{k+1}, R_{k+1}$, adjoint equations $\lambda_{S,T-k-1}, \lambda_{E,T-k-1}, \lambda_{I,T-k-1}, \lambda_{R,T-k-1}$, and optimal control $u_{1,k+1}, u_{2,k+1}$ iteratively with $h = 1$.

   for $k = 0 : T-1$

$$\frac{S_{k+1} - S_k}{h} = \Lambda - \beta S_{k+1} I_k - \mu S_{k+1} - u_{1,k} S_{k+1}$$

$$\frac{E_{k+1} - E_k}{h} = \beta S_{k+1} I_k - \mu E_{k+1} - \pi E_{k+1}$$

$$\frac{I_{k+1} - I_k}{h} = \pi E_{k+1} - \alpha I_{k+1} - \mu I_{k+1} - \gamma I_{k+1} - u_{2,k} I_{k+1}$$

$$\frac{R_{k+1} - R_k}{h} = \gamma I_{k+1} - \mu R_{k+1} + u_{1,k} S_{k+1} + u_{2,k} I_{k+1}$$

$$\frac{\lambda_{S,T-k} - \lambda_{S,T-k-1}}{h} = -\lambda_{S,T-k-1}(-\beta I_{k+1} - \mu - u_{1,k}) - \lambda_{E,n-k}(\beta I_{k+1}) - \lambda_{R,n-k}(u_{1,k})$$

$$\frac{\lambda_{E,T-k}-\lambda_{E,T-k-1}}{h}=-\lambda_{E,T-k-1}(-\mu-\pi)-\lambda_{I,T-k}(\pi)$$

$$\frac{\lambda_{I,T-k}-\lambda_{I,T-k-1}}{h}$$

$$=-A_1-\lambda_{S,T-k-1}(-\beta S_{k+1})-\lambda_{E,T-k-1}(\beta S_{k+1})-\lambda_{I,T-k-1}(-\alpha-\mu-\gamma-u_{2,k})-\lambda_{R,T-k}(\gamma+u_{2,k})$$

$$\frac{\lambda_{R,T-k}-\lambda_{R,T-k-1}}{h}=-\lambda_{R,T-k-1}(-\mu)$$

$$u_{1,k+1}=\min\left(1,\max\left(0,\frac{(\lambda_{S,T-k-1}-\lambda_{R,T-k-1})S_{k+1}}{A_2}\right)\right)$$

$$u_{2,k+1}=\min\left(1,\max\left(0,\frac{(\lambda_{I,T-k-1}-\lambda_{R,T-k-1})I_{k+1}}{A_3}\right)\right)$$

end

3. Set A_1 then calculate the objective function as fitness function

$$J(u_1,u_2)=\sum_{k=0}^{T-1}\left(A_1I_k+A_2\frac{{u_{1,k}}^2}{2}+A_3\frac{{u_{2,k}}^2}{2}\right)$$

The algorithm of determining optimal weight using ACO can be constructed as follows [1]:

1. Set the number of ants N and the pheromone decay factor ρ.
2. Generate the set of possible weight $A_2=\{1,2,...,m\},A_3=\{1,2,...,n\}$ and give the probability uniformly.
$$p(A_{2_i},A_{3_j})=\frac{1}{mn},\quad i=1,2,...,m\quad j=1,2,...,n$$
3. Calculate cumulative probability range C_{ij}
4. Generate random variable $r_s\sim U(0,1)$ $s=1,2,...,N$.
5. Determine selected weight $A_{2_i},i\in\{1,2,...,m\}$ and $A_{3_j},j\in\{1,2,...,n\}$ for every ant s.
6. Calculate objective function $SEIR(A_{2_i},A_{3_j})$ for every ant s.
7. Choose minimum fitness function $f_{best}=\min\left(SEIR(A_{2_i},A_{3_j}),i\in\{1,2,...,m\},j\in\{1,2,...,n\}\right)$, and count N_{best}, the number of f_{best}
8. Set constant Q and calculate $\sum\Delta\tau(A_{2_i},A_{3_j})$, $i=1,2,...,m$ $j=1,2,...,n$
$$\sum\Delta\tau\left(A_{2_i},A_{3_j}\right)=\begin{cases}N_{best}\cdot\dfrac{Q}{f_{best}}, & \text{if } A_{2_i},A_{3_j} \text{ is the best weight}\\ 0, & \text{otherwise}\end{cases}$$
9. Update the pheromone
$$\tau_{ij}=(1-\rho)\tau_{ij}+\sum\Delta\tau\left(A_{2_i},A_{3_j}\right)\quad i=1,2,...,m\quad j=1,2,...,n$$
10. Update the pheromone probability
$$p(A_{2_i},A_{3_j})=\frac{\tau_{ij}}{\sum\tau_{ij}}\quad i=1,2,...,m\quad j=1,2,...,n$$
11. Repeat step 3-10 until process converges.

3. RESULTS AND DISCUSSION

Parameters used in ACO simulation are: the number of ants $N=100$, the range of weight is [1-10], pheromone decay factor $\rho=0.1$, maximum iteration is 200.

Parameters used for optimal control SEIR epidemic model are: recruitment rate $\Lambda=3$, disease transmission rate $\beta=0.05$, natural death rate $\mu=0.01$, death by disease rate $\alpha=0.3$, recovery rate $\gamma=0.1$, and disease mutation rate $\pi=0.2$.

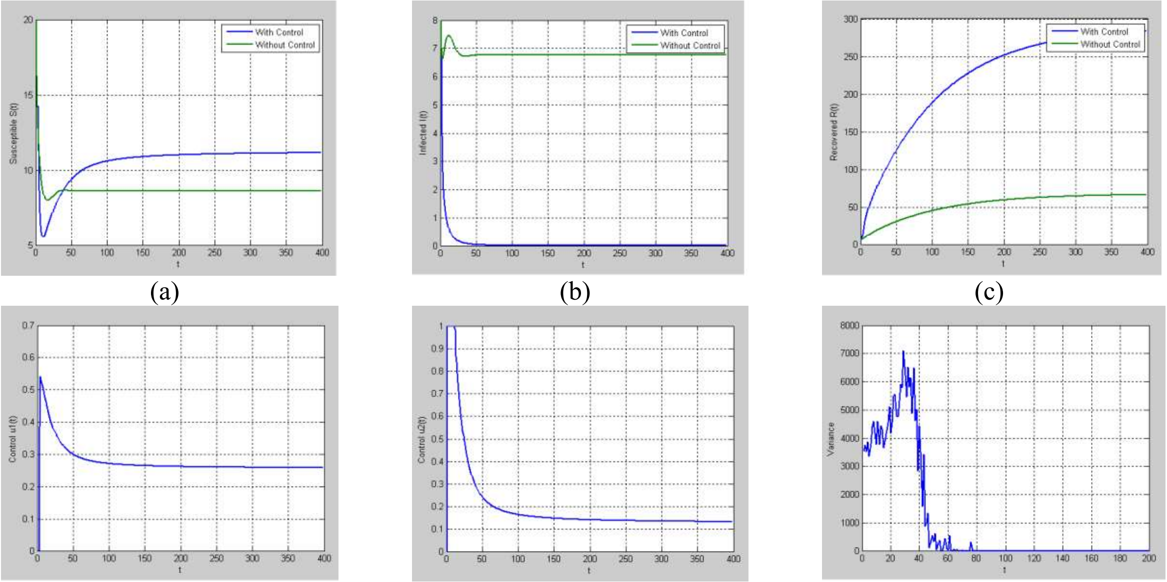

(a) (b) (c)

(d) (e) (f)

Figure 1 (a)-(f)

The simulation of optimal control SEIR epidemic model can be seen at figure 1(a)-(e) while figure 1(f) is ACO simulation. Figure 1(a) shows the numerical solution of a susceptible individual with and without control. At the early time, the number of susceptible individual with control is lower than without control because vaccination effect which decreases the number of the susceptible individuals. However, as time goes on, the number of susceptible individual with control can be higher than without control because recruitment rate effect. Figure 1(b) shows the numerical solution of an infected individual. The number of infected individual with control is lower than without control because treatment effect which decreases the number of infected individual. Figure 1(c) shows numerical solution of recovered individual. The number of recovered individuals with control is higher than without control because of both vaccination and treatment effect which increases the number of recovered individual. Figure 1(d) shows control function of susceptible vaccinated. Figure 1(e) shows control function of infected treated. Figure 1(f), on the first iteration, all ants choose weight randomly so that variance is relatively high. At the optimization process, we update pheromone until all ants choose the similar weight so that process converges and variance approaches zero.

4. CONCLUSIONS

ACO method can select the optimal weight of optimal control SEIR epidemic model. From the simulation, on the first iteration, all ants choose weight randomly. At the optimization process, we update pheromone until all ants choose the similar weight so that process converges and variance approaches zero. At the SEIR simulation, based on aparameter : recruitment rate, disease transmission rate, natural death rate, death by disease rate, recovery rate, disease mutation rate, can be seen comparison the number of individual with and without control. Furthermore, we also obtain optimal weight related to cost of vaccination and treatment.

5. REFERENCES

[1] S. Rao, 2009, Engineering Optimization. Theory and Practice, Canada : John Wiley and Sons.
[2] Z. Michalewicz, J.B. Krawczyk, C.Z. Janikow, 1992, A Modified Genetic Algorithm for Optimal Control Problems, *Computers Math Applic*, **12**, pp. 83-94
[3] E.A. Bakare, A. Nwagwo, E. Danso-Addo, 2014, Optimal Control Analysis of an SIR Epidemic Model with Constant Recruitment, *International Journal of Applied Mathematical Research*, **3**, pp. 273-285.
[4] O. Sharomi, T. Malik, 2015, Optimal Control in Epidemiology, *Springer Science+Business Media*.
[5] M. El Hia, O. Balatif, M. Rachik, J. Bouyaghroummi, 2013, Application of Optimal Control Theory to an SEIR Model with Immigration of Infectives, *International Journal of Computer Science Issues*, **10**, pp. 230-236

Structural Modeling of Half-Through Steel Arch Bridge On Buckling Effect

Ussy Andawayanti[1], Evi Nur Cahya[1*]

[1] Water Resources Engineering Dept. Universitas Brawijaya
* Corresponding authors: [evi_nc@ub.ac.id]

Abstract – This paper presents the structural modeling of a half-through steel arch bridge to observed buckling behavior. The bridge model is analyzed by applying an imperfection to observe the existence of global buckling or local buckling in some parts of the structures when subjected to different loading direction to cause in-plane buckling or out of plane buckling. The static pushover analysis was carried out using three loading cases which are considering the dead load, live load, impact load and earthquake load, according to JSHB loading condition. According to the analytical results, it was found that the lateral loading resulted in the global buckling in the beam element in diagonal brace member near the support at the springing arch rib and these members are the critical members under loading in a transverse direction. The longitudinal loading resulted in the local buckling in the shell element regions near the intersection of the arch rib and the side girder only but showed no local buckling for the shell element regions near the support of the springing arch rib. It revealed that the critical members are around the intersection in this model.

1. INTRODUCTION

When arch bridges or steel piers are subjected to a strong earthquake, it is crucial for these structures to have enough stability and higher ductility by preventing the failure caused by local buckling of component plates, Mohamed et al [1-3]. Although there may be some types of failures in all kinds of steel structures, local buckling is always the key factor governing failure of thin-walled civil engineering steel structures, as illustrated by previous investigators, Zheng et al, JHSB 2012 [4, 5]. Stiffened steel plates with longitudinal stiffeners are used widely in steel structures such as steel box girders, box columns and pylons for cable bridges. When compressed or bent, the longitudinally stiffened plate may buckle in either local buckling mode or distortional buckling mode, Mohamed et al [1]. The critical buckling modes of the longitudinally stiffened plates depend mainly on the in-plane flexural rigidity of the longitudinal stiffener and the width-to-thickness ratio of the subpanels.

Buckling behavior and seismic ductility design for of a single element structure or simple structures were discussed in most buckling studies by many researchers. However, buckling failure behaviors for the half-through type arch bridge model, as a whole structure, have not been clarified yet and only few studies concerning buckling studies have been reported. It is still necessary to establish a method concerning the effect of local buckling to check the performance developed from pushover analysis with load distribution based on seismic design force for arch bridges design.

2. METHODS

2.1 Theoretical model

The theoretical arch model studied herein is representative for actual half-through type arch bridges as shown in Fig. 1, in which 11 vertical columns are hinged to arch ribs at both ends. The arch has a span length (*l*) of 106 m and the arch rise (*f*) is 22 m, giving a rise-span ratio 0.2, while *b* and *L* represent the width of a stiffened girder and the deck span, respectively. Arch ribs of the bridge consist of steel box-section members, connected by lateral bracing and diagonals. The longitudinal girders and arch ribs are connected with a vertical column. The cross sectional profiles of arch ribs, stiffened box-section, vertical members and lateral members are rectangular and I-sections as shown in Fig. 2.

Two types of steels, SM490Y (yield stress, σy = 355 MPa, Young's modulus, E = 206 GPa and Poisson's ratio, ν = 0.3) and SS400 (yield stress, σy = 245 MPa, Young's modulus, E = 206 GPa and Poisson's ratio, ν = 0.3) are adopted. The first type of steel, SM490Y is used for the main members of the bridge, while SS400 is used for diagonal brace member which connected two stiffened girder and diagonal brace member between two arch ribs.

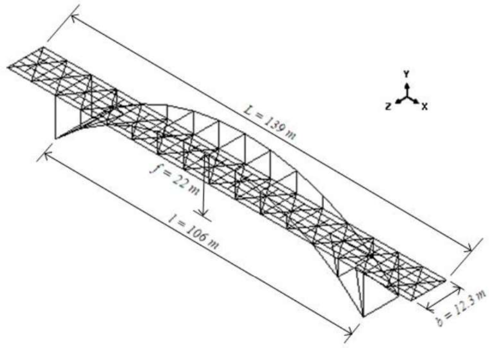

Figure 1 Theoretical arch model

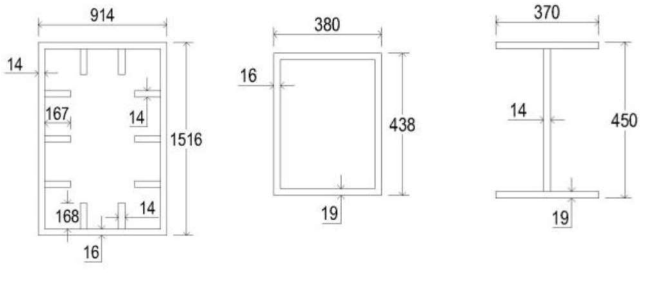

a) Arch rib b) Vertical column c) Lateral member

Figure 2 Cross sectional profiles of members

2.2 Procedures

The static nonlinear pushover analysis in this study is performed with increased lateral force distribution based on seismic design force in each joint node in the stiffened girder and arch rib in the arch bridge model. The loading is applied in a longitudinal direction of the bridge axis. An imperfection in a lateral direction of the arch bridge model as $\delta_0.\sin\pi x/l$ with maximum initial displacement $l/1000$ is applied in bridge span with l equal to total span length, is given in the center of the bridge span. The critical nodes, Point A and Point B are determined by the most significant displacement in the model by the case of an arch bridge model consists of beam elements only. Point A was at the arch crown while the Point B was at the intersection of stiffened girder and the arch rib which had the largest displacement from the first buckling case.

The beam elements were replaced by shell element region by consideration from the result from the first case of using beam elements only in the whole arch bridge model. The critical elements for buckling case in the arch structure usually occurred in the element near springing arch rib and the element near the intersection between the stiffened girder and the arch rib. Thus, the beam elements in those regions are chosen to be replaced by shell element members to investigate the local buckling behavior of its element. The shell elements and beam elements are connected by constraint with rigid body type since the rigid body is expected not to sustain any stress, strain, nor load as it should be sustained by the shell itself to see the local buckling that possibly occurs on it. Pushover analysis of bridge model is carried out by applying the increased seismic design force in each joint node in the stiffened girder and arch rib in the arch bridge model. The ultimate displacement is determined from the result of this analysis.

In the case of local buckling, the buckling behavior in stiffened plate is ruled by the structural parameter of the model in R-mode buckling and F-mode buckling, Kanai and Ang [8]. The width to thickness ratio parameter of the plate panel surrounded by the longitudinal stiffeners, RR were checked for this model and defined by Eq. (1)

$$R_R = \frac{b}{t}\sqrt{\frac{\sigma_y}{E}\cdot\frac{12(1-\nu^2)}{\pi^2 k_R}} \tag{1}$$

Where:

R_R = equivalent width to thickness ratio for the R-mode buckling (R-mode buckling is buckling of subpanels between straight stiffeners)
b = width of plate
t = thickness of plate
E = Young's modulus
σy = yield point of material
ν = Poisson's ratio
k_R = buckling coefficient (k_R = 4n2, n = number of panels).

Observe that for R_R = 1.0, the R-mode elastic buckling strength is equal to the yield point of the material. The equivalent width to thickness ratio parameter of the plate panel surrounded by the longitudinal stiffeners, R_F defined by Eq. (3)

$$R_F = \frac{b}{t}\sqrt{\frac{\sigma_y}{E}\cdot\frac{12(1-\nu^2)}{\pi^2 k_F}} \tag{2}$$

$$k_F = \frac{(1+\alpha^2)^2+n\gamma}{\alpha^2(1+n\delta)};\alpha < \sqrt[4]{1+n\gamma} \qquad k_F = \frac{2\left(1+\sqrt{1+n\gamma}\right)}{1+n\delta};\alpha > \sqrt[4]{1+n\gamma} \tag{3}$$

In which:

R_F = equivalent width to thickness ratio for the F-mode buckling (F-mode buckling is the general buckling of the entire stiffened panel)
γ = ratio of stiffener stiffness to panel stiffness
α = aspect ratio of a panel
δ = ratio of the area of a stiffener to area of a panel

3. RESULTS AND DISCUSSION

In the case of pushover analysis with the loading direction in transverse and longitudinal direction of the bridge model, the load versus displacement in corresponding direction is shown in Fig. 3. And the deformation modes of the structure are shown in Fig. 4 in 3D view Y-Z plane, while Fig. 5 in 3D view X-Y plane.

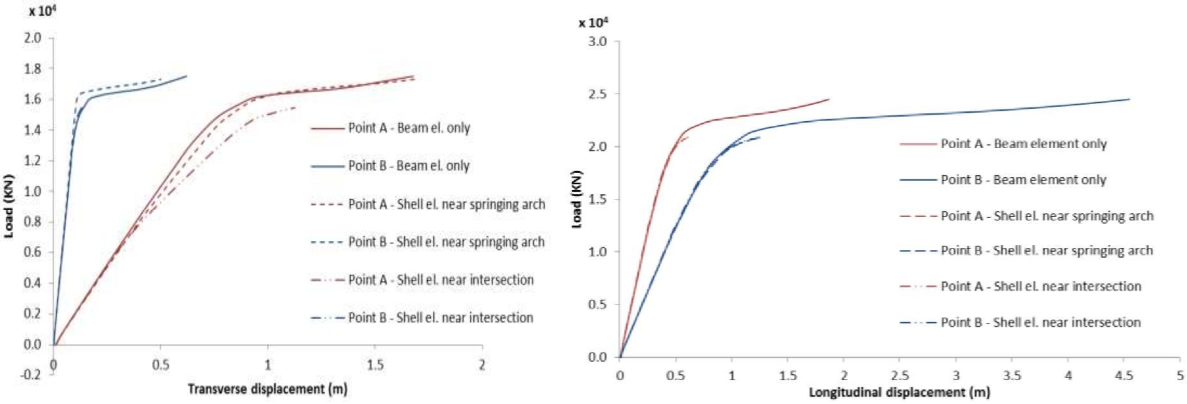

Figure 3 Load-displacement response for loading in transverse and longitudinal direction

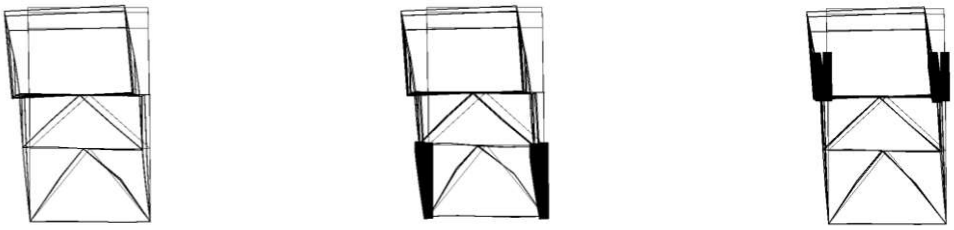

a) Beam element **b) Shell element in the springing arch** **c) Shell element in the intersection**

Figure 4 The deformation in Y-Z view for loading in transverse direction of the bridge model

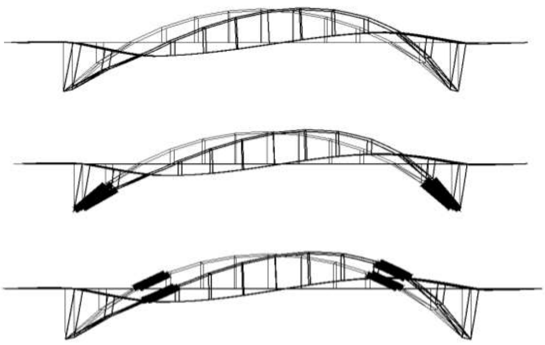

a) Beam element

b) Shell element in the springing arch

c) Shell element in the intersection

Figure 5 The deformation in X-Y view for loading in longitudinal direction of the model

From the load versus displacement response for this case, Point A shows larger displacement than Point B. This is affected by the loading direction in a transverse direction that led to the displacement growth greatly in Point A. From the result of the analysis in this case as shown in Fig. 4, it also can be seen that global buckling occurred in all case of these problems in a different amount at the diagonal brace under the deck connected the two arch ribs. Otherwise, local buckling was not found in any of shell element region, neither near springing arch rib nor near the intersection.

In the bridge studied, from the load-displacement response, it is shown that the behavior of the model which consists of beam elements only or the model that also has the shell element regions have quite the same trends, so this response behavior can be drawn by using beam element only for simplification of the analysis. But in the next case, for observing the further behavior of the local buckling behavior, the shell element regions are needed to be included.

From the results of the analysis, it is also shown that no global buckling occurred in any case of these problems. In the other hand, local buckling was found in the case of shell element region near the intersection (c). The deformation mode of this phenomenon is shown in Fig. 6 for shell element region in the left side and the right side of the bridge model, which is led by the direction of the loading. It is also shown the cross-sectional deformation of the shell element region.

The width to thickness ratio parameter of the stiffened box plate for arch rib which occur local buckling, R_R and R_F were checked for this arch bridge model and the value is defined by Eq. (1) and Eq. (2) respectively. These values are calculated in the web and flange of the stiffened plate. From the analysis, it was found that for flange plate, R_R and R_F were equal to 0.42 and 0.55. Meanwhile, for the web plate, R_R and R_F were equal to 0.59 and 1.00 respectively for the arch rib element members which occurs local buckling. This value shows that the R_F is determined as the Rmax as $R_F > R_R$, and it also can be a judge that the F-buckling mode governs the buckling deformation of the element member which shows the same behavior, as shown in Fig 6. In the analysis considering local buckling on the flange plate, it can be seen that it occurs under a very low R_F, which is equal to 0.55. While the local buckling on the web plate occur under R_F equal to 1.00, which is an intermediate Rmax value in the local buckling case in stiffened plate.

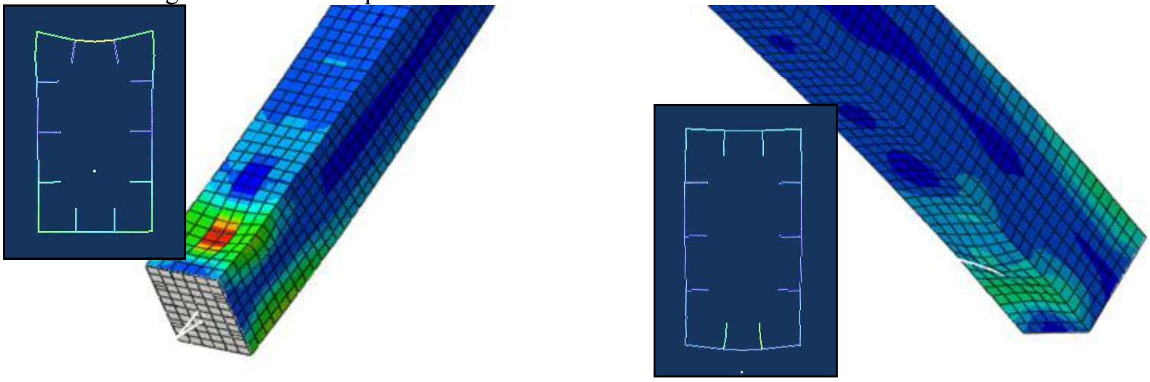

a) Local buckling in the left shell element region of the bridge model

b. Local buckling in the right shell element region of the bridge model

Figure 6 The deformation mode of the shell element region in the case of shell elements are placed near the intersection (case (c) for loading in longitudinal direction)

4. CONCLUSIONS

The following main conclusions were drawn:

1. In the bridge studied, from the load-displacement response, it is shown that the behavior of the model which consists of beam elements only or the model that also has the shell elements have quite the same trends, so it the load-displacement response behavior can be drawn by the beam element only for simplification of the analysis.
2. The longitudinal loading resulted in the local buckling in the shell element regions near the intersection of the arch rib and the side girder only but showed no local buckling for the shell element regions near the support of the springing arch rib. It showed that the critical members are around the intersection in this model.
3. The longitudinal loading resulted in the local buckling in the different side of the shell elements near the intersection of the arch rib and the side girder. One showed that in the direction of loading, local buckling occurs in the upper side of the shell member, but in the other side of the arch rib shell elements, local buckling occurs in the lower side of the shell member near intersection of the arch rib and the side girder.

5. REFERENCES

[1] Mohamed, O., Sakimoto, T. and Yamao, T., “Ductility of stiffened plates after buckling as a component of a box cross-section”. The 2nd International Conference on Steel & Composite Structures (ICSCS’04), Seoul, Korea, 2004.

[2] Mohamed, O., Sakimoto, T. and Yamao, T., “Ductility of Stiffened Steel Box Member”. *Proceedings of Advances in Steel Structures*, **Vol. 1**, pp. 179-184

[3] Mohamed, O., Yamao, T., Kawabe, T. and Sakimoto, T., “Ultimate Behavior and a Seismic Design of Steel Arch Bridge*”. The 4th International Symposium on Steel Structures*, Seoul, Korea, 2006.

[4] Japan Road Association, Specifications for Highway Bridges, Part V-Seismic Design, Japan, 2012.

[5] Japan Society of Civil Engineering (1999), The 1999 Ji-Ji Earthquake, Taiwan–Investigation into Damage to Civil Engineering Structures.

[6] Kanai, M. and Ang, A.H-S., “A Study of Safety of Box Girder Bridges in Japan”, *Technical Report of Research, National Science Foundation*, Departement of Civil Engineering, University of Illinois ar Urbana-Champaign, June, 1979.

Analysis of Potential Evaporation Calculation Method at Karangploso, Malang Regency, East Java

Donny Harisuseno[1*], Ery Suhartanto[1], Ersty Nurul Frida Asmara[1]

[1] Department of Water Resources Engineering, Faculty of Engineering, University of Brawijaya, Malang
* Corresponding authors: [donnyhari@ub.ac.id]

Abstract – The approach to measure evapotranspiration was variated, either for potential or actual occurrences of evapotranspiration. There were some methods available to estimate evapotranspiration rates, and these methods were applied at the Climatology Station Class II Karangploso, Malang Regency. It was assumed that the availability of water was plentiful, and therefore, the measurement was directed to estimate potential evaporation rate. The methods for this measurement included Blaney-Criddle Method, Radiation Method, FAO-Modification Penman Method, Penman-Monteith Method, Thornthwaite Method, and Multiple Linear Regression Method. All these methods were used climate-related data, such as air temperature, air humidity, sunbeam length, and wind speed. An analysis was done to understand the compatibility between the result of measurement methods and the result of observation on a field. The outcome of this analysis could be the most compatible method. This analysis itself involved several tests such as Nash-Sutcliffe Efficiency Test (ENS), Stationary Test, Mean Absolute Error (MAE), Coefficient of Determination (R^2), and Relative Error (Kr). The result of the analysis indicated that the selected method with the best compatibility was Multiple Linier Regression Method, proved by Nash Sutcliffe Efficiency (NSE) 0,797 and coefficient of determination (R^2) 84,01%.

1. INTRODUCTION

The Evaporation is an essential process in the climate system because it provides moisture to the atmosphere, which indicates the beginning of the hydrological cycle [1]. Generally, most of method for calculating evaporation were used to estimate evapotranspiration based on assumption that water availability was abundant, thus the term of evapotranspiration was commonly refer to the term of evaporation. Many methods for estimating evaporation losses from free water surfaces have been conducted, and overall the methods could be classified into several categories including: methods based on empirical approach, methods based on water budget, energy budget concept, mass-transfer concept; and methods of combination [2]. Accuracy of evaporation estimation are important for supporting water balance studies, reservoir operation, water crop requirement in irrigation field, water management and hydraulic construction planning as well [3]. Comparison studies on several evaporation methods have been conducted previously, and most of them have objective to find the best method which most suitable at certain location. The comparison study concerning potential evaporation between observation evaporation and one obtained from ReGCM software, the result showed that evaporation estimated from ReGCM software exhibited relatively high deviation from the observed one [4]. A study on comparison between Penman Modified and Penman Monteith method at Irrigation Area Muara Jalai, Kampar Regency, Riau Province was carried on as well and the result showed that Penman Monteith more accurate than Penman Modified [5]. The variance of methods previously explained to estimate potential evaporation rate must lead to the variance of potential evaporation rate that resulted. Therefore, the aim of this study was to evaluate the applicability and validity of different evaporation methods, each of them requiring different meteorological data sets for their application and determine their applicability in the research location.Thus, the selected evaporation method could be considered as method to estimate the evaporation which high accuracy particularly at research location.

2. METHODS

2.1 Reserch Location

The current research was located at Ngijo Village, Karangploso District, Malang regency which is geographically lies between 07°45’48” LS - 112°35’48” BT, and elevation 575 mdpl. Figure 1 showed the research location.

Figure 1 Karangploso Climate Station

2.2 Supporting Data

The supporting meteorological data were derived from Karangploso Climate Station managed by BMKG; which were namely air temperature, relative humidity, wind velocity, solar radiation, and evaporation. Those data were collected in monthly based for 10 years period of observation (2004 – 2013) .

2.3 Procedure

The methods of evaporation used in the present study consist of five methods, namely Blaney Criddle method, Radiation method, Penmann Modified FAO method, Penmann Monteith method and Thornthwaite method. Those five methods require different meteorological data sets for their application, geographical location (latitude and longitude) and elevation data as well. In addition, Multiple Regression Analysis was conducted in order to gain relationship between Observed Evaporation as Dependent Variable and Climate Data (Solar Radiation, Air Temperature, Wind Velocity, Relative Humidity) as Independent Variable. The Multiple Regression Analysis was developed using the following equation:

$$\hat{Y} = A_0 + A_1X_1 + A_2X_2 + A_3X_3 + A_4X_4$$

Where Y is evaporation, (mm/day) X_1 is air temperature, X_2 is relative humidity, X_3 is solar radiation, and X_4 is wind velocity; A_0 is line intercept, A_1, A_2, A_3, A_4 are direct coefficient of regression. In order to determine which evaporation method will be selected, several methods of evaluation were implemented in the present study. Those were namely Nash Sutcliffe Efficiency method, Stationary Test method (mean and variance stability test), Mean Absolute Error (MAE), Relative Error, and Coefficient of Determination (R^2). The evaluation process was performed by evaluating appropriateness between several evaporation methods compared with observed data statistically, hence the chosen evaporation method is derived, subsequently, the verification test upon the chosen evaporation method is conducted by comparing with the observed data. Further, meteorological data used in the evaluation process was divided into two groups based on a period of meteorological data collecting. First group data (period 2004-2010) was used in evaluation process to determine which best evaporation methods has good agreement with the evaporation data from direct measurement (observation data), and the second group data (period 2011-2013) was used to examine accuracy and validity of the chosen evaporation method according to the result of evaluation from the first group data.

3. RESULTS AND DISCUSSION

As previously explained that all of the evaporation methods evaporation need different meteorological data sets in their application. The evaporation analysis was performed in monthly based where monthly meteorological data during period 2004-2010 used as an input to each evaporation method and subsequently the evaporation calculation resulted was averaged to obtain a monthly average. Direct measurement of evaporation (Obs) was carried on monthly based for same year duration and assumed as the valid evaporation value. Compararison analysis was performed by comparing between the evaporation resulted from the five methods of evaporation and the valid one resulted from direct measurement. Tabel 1 gives the result of monthly average of evaporation based on period 2004-2010 for the five evaporation methods. Based on the recapitulation of the monthly evaporation displayed in Tabel 1, it could be demonstrated that there is a fluctuation of evaporation calculation resulted among each month for all of methods of evaporation. It is simply understood that the fluctuation of evaporation most likely caused by difference of monthly meteorological data which were employed in each method of evaporation. Further, if compared with the evaporation from direct measurement (Obs), the result exhibited that the Penmann Modified FAO displayed highest of evaporation value, whereas the lowest one showed by the Thornthwaite method.

Table 1 Recapitulation of Monthly Average ET$_0$

Method	Recapitulation of Monthly Average ET$_0$ (mm/day)											
	Jan	Feb	Mar	Apr	May	Jun	Jul	Ags	Sept	Okt	Nov	Des
BC	4.33	4.28	4.01	3.62	3.55	3.46	3.42	3.69	4.05	4.33	4.36	4.38
R	4.64	4.61	4.24	4.71	4.60	4.44	4.63	5.23	5.80	6.01	5.70	4.81
PFAO	4.61	4.59	4.42	4.97	4.84	4.54	4.86	5.17	6.00	6.25	5.85	4.69
PM	4.01	4.00	3.88	4.19	4.05	3.80	4.02	4.31	4.96	5.22	4.92	4.07
T	3.48	3.83	3.41	3.53	3.29	2.95	2.72	2.65	3.20	3.65	3.96	3.70
Obs	3.70	3.82	3.74	4.25	4.18	4.12	4.25	4.65	5.57	5.61	4.63	3.68

*) BC : Blaney Criddle ; R : Radiation ; PFAO: Penmann Modified FAO; PM : Penmann Monteith ; T : Thornwaite; Obs : Observed

By concerning that there is a close relationship between evaporation and the meteorological data, accordingly the multiple regression analysis was developed in the present study. The multiple regression analysis (RLB) was carried on using data analysis in MS Excel software, and the equation shown as follow:

$$\hat{Y} = 7,677 + 0,170X_1 - 10,577X_2 + 1,144X_3 + 0,033X_4$$

Where Y is evaporation, (mm/day) X_1 is air temperature, X_2 is relative humidity, X_3 is solar radiation, and X_4 is wind velocity. The cofficient of determination (R^2) of the multiple regression equation demonstrated value of 65,82%.

Figure 2 demonstrated monthly average ET$_0$ for the evaporation methods applied in the present study. Refer to Figure 2, it was found that the similar trend of the monthly evaporation was shown by all of the evaporation methods except the Thornthwaite method. The highest evaporation takes place during September until Oktober which is normally in the period of a dry season. While the lowest evaporation appeared during November until May, which is normally in a period of a wet season. During period of the dry season, normally much solar radiation transfer to earth surface, and directly will influence latent heat process particularly in increasing evaporation from free surface water. On the contrary, during wet season, normally less solar radiation transfer to earth surface, and as a consequence less evaporation process will take place. This explains why evaporation tends to decrease during wet season and increase during dry season.

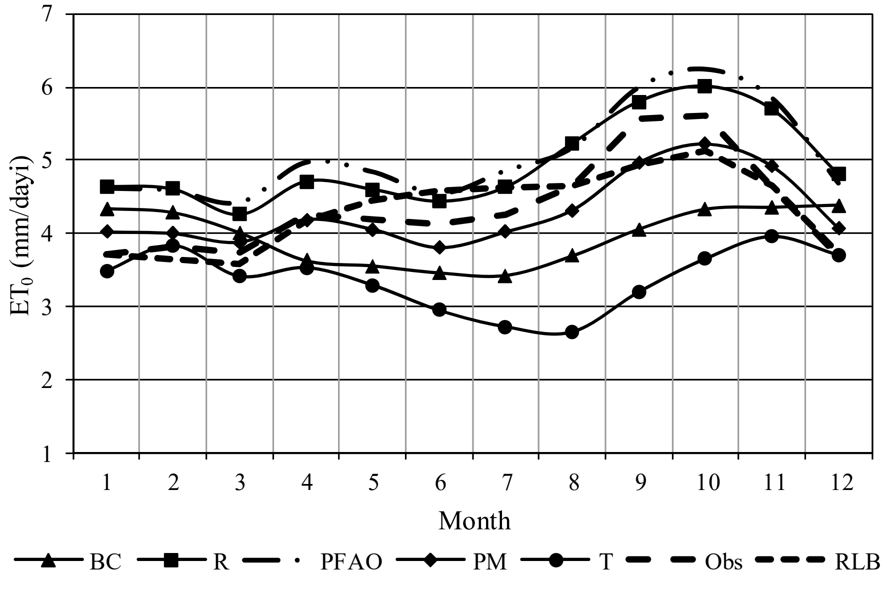

Figure 2 Monthly average ET$_0$ for each evaporation method

Evaluation of each evaporation method was performed based on data period 2004-2010 (7 years) by comparing between calculated from the methods of evaporation and evaporation from direct measurement (Obs). The methods of evaluation comprise with Nash Sutcliffe Efficiency method, Stationary Test method (mean and variance stability test), Mean Absolute Error (MAE), Relative Error, and Coefficient of Determination (R^2). The evaluation results showed that the Penmann Monteith method had a good agreement with evaporation from direct measurement (Obs). The chosen evaporation method will be proceeded to a validation process to ensure the validity and reliability of the chosen method of estimating evaporation in research location. The validation process was running based on data period 2011-2013 (3 years), and the chosen model will be accompanied by the evaporation equation derived from the Multiple Regression Linear Analysis (RLB). Figure 3 showed a monthly average of ET0 for Penmann Monteith, Multiple Linear Regression, and Observed evaporation (Obs). The validation process was performed in the same way with the methods considered in the evaluation process. The result of validation process demonstrated that both methods showed less difference the validation resuls, however the Multiple Linier Regression give the best result which indicated with Nash Sutcliffe Efficiency (NSE) 0,797 and coefficient of determination (R^2) 84,01%. Thereby, those methods could be used as an approach to estimate evaporation in the research location.

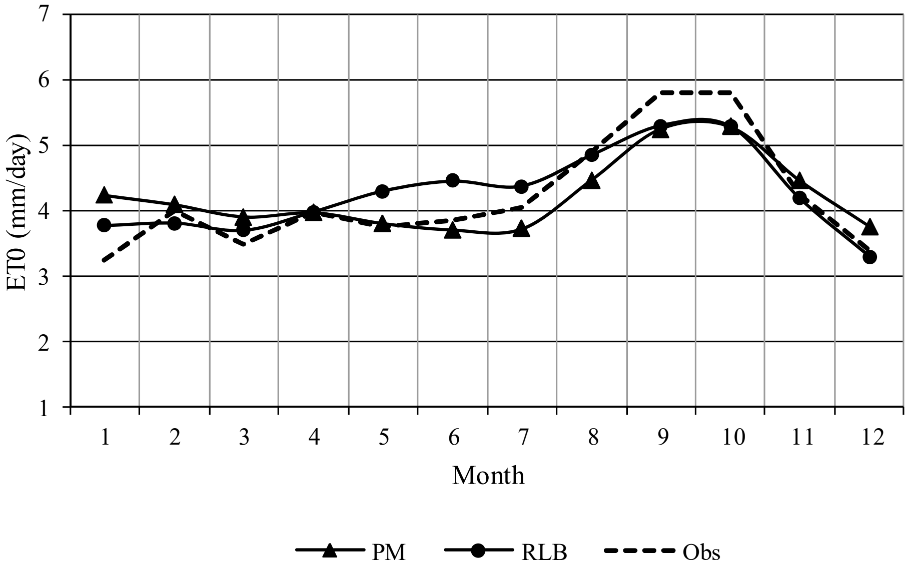

Figure 3 Monthly average ET₀ for Penmann Monteith (PM), Multiple Regression Linier (RLB) and Observed data (Obs)

4. CONCLUSIONS

Based on an appropriateness evaluation, Penmann Monteith and Multiple Linier Regression showed a good result. Thus, those methods could be used as an approach to estimate evaporation in the research location. However, considering that the Penmann Monteith has been known widely and generally applied for evaporation estimation in many locations with various climate characteristic, hence the method was strongly recommended to be used in the research location.

5. REFERENCES

[1] Z.W. Shilenje, Murage P, Ongoma V, 2015, *Pakistan Journal of Meteorology*, **23**, pp.33-42.
[2] F. Malika, B. Abdenour, M. Saighi, 2013, *International Journal of Application or Innovation in Engineering & Management*, **2**, pp.376-381
[3] G.K. Soultana, A.Z. Vassilis, 2007, *Journal of Hydrology*, **345**, pp.212-223.
[4] J.B. Lu, G. Sun, S.G. McNulty, D.M. Amataya, 2005, *Journal of the American Water Resources Association*, **41**, 621-633
[5] D. Panjaitan, 2014, *e-journal.upp.ac.id*

Service Satisfaction Level (Study Case in Gojek and Grab Bike)

Yulinda Rizky Pratiwi[1*], Edy Widodo[2]

[1,2]Department of Statistics, Faculty of Mathematics and Natural Science, Universitas Islam Indonesia, Yogyakarta, Indonesia
*Corresponding authors: [yulindarizkypratiwi@gmail.com]

Abstract-Globalization has become a motor for the current technological developments. The presence of the Virtual Space provides an opportunity for the community to actualization with access to a wider world, quickly and easily. Transport which is part of the existence of life, civilization needs over time that also has been the object vital to technological developments. Some android apps are emerging as Gojek and Grab Bike application that can fulfill the public demand for transportation services more easily. Methods for obtaining the data is done by using secondary data. Secondary data are user comments for Gojek and Grab Bike that obtained through a search on the internet media. The analytical methods are descriptive analysis, Clustering, Association Rules, and Wordcloud. These are performed by software open source R adding packages such as "tm", "twitteR", "wordcloud", and "ggplot". By text mining, can be seen the number of followers of the official account of Gojek and Grab Bike by looking at the spread map of the followers of the account to consider the expansion of sales to be widespread. Moreover, it can be known how any talks that are often associated with Gojek and Grab Bike in twitter account.

Keywords–Gojek, Grab Bike, Logistic Regression, Twitter, Talks

1. INTRODUCTION

One of the communication media is now the fast-growing social media. One part of the social media is a social networking site, which is a web-based service that allows users to create profiles, see the list of available users, as well as invite or accept friends to join the site. Generally, there are two types of textual information on the web, ie facts and opinions. The fact is the objective statement about entities and events in the world, while opinions are subjective statements that reflect the sentiment or perception of people about an entity or world events. Currently, the organization has many uses information from social media to conduct surveys than through conventional survey that will cost quite a lot. Twitter is one of the social networks that are popular today.

Twitter is a website owned and operated by Twitter Inc. which offers a form of micro-blogging social network that allows the users to send and read messages called tweets. In twitter, followers and following are the terms in which it is very important for some twitter users. Due to the popularity of twitter accounts owned by several persons or institutions be seen from the number of followers.

Informatics business is a work by individuals or groups to benefit like a business that utilizes informatics techniques, such as the Internet or applications on the mobile phone. What we know today informatics business rapidly growing, one of the capital city of Indonesia being 'invaded' by green troops who created a stir among the urban community. When down the road, wherever you are, you will see one or two motors that passengers wearing a green jacket with writing Gojek or Grab in tow. Seeing the development of Gojek and Grab Bike are very interesting because Gojek and Grab Bike are startup pioneer in the field of online motorcycle, it is expected that Gojek and Grab Bike development can become a success story that can be taken as lesson learned for other startups.

2. THEORICAL BASIS

2.1 Data Mining

Data mining is the extraction of interesting patterns from large amounts of data. A pattern is said to be interesting if the pattern was "not trivial", implicit, previously unknown, and useful. Patterns presented should be easy to understand, apply to the data to be predicted with a degree of certainty, useful, and new. Data mining is a process that uses statistical techniques, mathematics, artificial intelligence, and machine learning to extract and to identify useful information and related knowledge from a variety of large databases (Turban, et al., 2005). Extracting data required when the available data are too many (for example, data obtained from the company's database system, e-commerce, share data, and bioinformatics data), but do not know what pattern can be obtained. Examples of discovery patterns in data mining is supposed a company that will increase the credit card facility of the customer, the company will look for patterns of customers to know your potential customers and potential customers who do not. In addition, data mining plays an important role in the fields of industry, finance, weather, climate, science, and technology.

2.2 Text Mining

Doing the work of the prediction of what will happen to a student based on previous historical data relating to the performance index to be reached last semester, and jobs like this in the scientific world is often referred to as pattern recognition. Pattern recognition is part of the data Mining. So pattern recognition is a discipline that studies how we group objects to the various classes and how data mining can be found the inclined. Data mining plays an important role in the fields of industry, finance, weather, science and technology. Data mining with regard to the processing of data on a large scale.

2.3 WordCloud

Word cloud is one of the results of text mining methods that feature popular words associated with internet keywords and text data. Word cloud is often used to highlight popular terms or trend based on the word frequency of users (PBC, 2013). Word cloud is an approach that can explain the research questions very quickly and easily, we can explore word cloud briefly and can perform comprehensive analysis (Graham, I. Milligan, & S. Weingart).

2.4 Association Rules

Association rules analysis is a data mining techniques to discover the rules of associative between a combination of items. Association rules want to provide information in the form of "if-then”. Functions association rules are often referred to as market basket analysis which is used to find a relation or correlation between the set of items.

2.5 Text Clustering

Text clustering assists in a decision by making a connection between the same document, which in turn allows the relevant documents be taken after one of the documents has been considered relevant to the request [Martin, 1995]. The main applications of clustering in text mining are as follows:

a. Simple clustering. This refers to the formation of clusters feature text. For example: the grouping of hits generated by search engine.

b. Taxonomy generation. This refers to the generation of a hierarchical group. For example: a cluster that contains the text of the automaker is the parent of the child cluster that contains the text of car models.

c. Topic extraction. This refers to the extraction of the most distinctive features of a group. For example the most distinctive characteristics of the documents in each topic of the document.

2.6 Gojek and Grab Bike

Gojek and Grab Bike are social enterprises that partners with a group of experienced and trustworthy ojek drivers to deliver a one-stop-shop convenience service for Indonesians. GoJek and Grab Bike are a motorcycle taxi that can be reached through phone and mobile application. As another ordinary taxi, the fare is fixed depends on the distance. People love it because GoJek and Grab Bike are cheap and easy to access. They feel delighted with the fair pay-what-you-get service. Moreover, they do not have to walk to find the closest motorcycle taxi since GoJek and Grab Bike driver offers door-to-door service. Generally, there are 3 main services: transport service, instant courier, and shopping & delivery.

3. RESULTS AND DISCUSSION

3.1 Population

The population in this study are active Twitter users are on a tweet with the mentions in account “@GojekIndonesia” and “@GrabID” taken the data as many as 3000 tweets.

3.2 Data analysis method

There are several methods of data analysis used in this study, among other things:

1. Descriptive Analysis is used to describe the condition tweet of the account “@GojekIndonesia” and “@GrabID” .

2. Clustering used to view groups of words have in common.

3. The Association rules used to identify patterns or relationships of words that is often discussed in conjunction with the account “@GojekIndonesia” and “@GrabID”.

4. Wordcloud used to see how the public comments or words that are often associated with account “@GojekIndonesia” and “@GrabID”.

5. Logistic regression is used to determine the factors that influence the use of selection between gojek or grab bike.

3.3 WordCloud

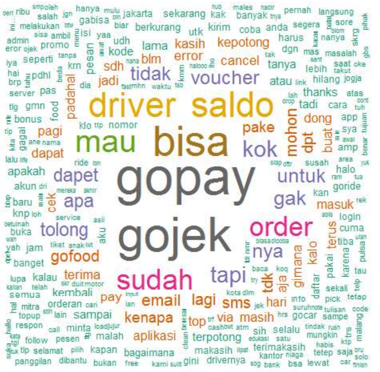

Figure 3.3.1. WordCloud about words that appear most frequently in account Gojek

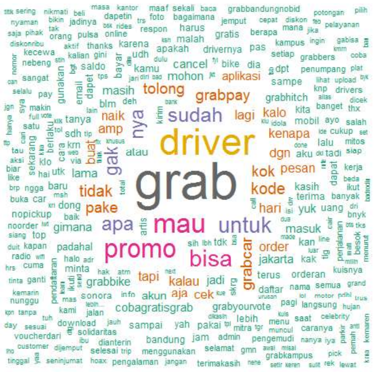

Fig 3.3.2. WordCloud about words that appear most frequently in account Grab Bike

In the results obtained from the word cloud @GojekIndonesia, the most popular tweet is about "gopay" and "gojek". But in the account @GrabID, the most popular tweet is about “grab” and “driver”. It reinforces the analysis that the words that often appear when people talk about @GojekIndonesia and @GrabID through social media twitter is different. Moreover the people are also talking about “driver”. Based on these results mean that everybody twitter users associate the @GojekIndonesia with “gopay” and associate the @GrabID with “driver”. While the “promo” means that tariffs on Grab Bike also be considered a person in choosing transportation that will be used. Beside that, in account @GojekIndonesia people are also talking about “saldo”. It means that the payment also affect the interests of the Gojek users.

3.4 Dendogram Clustering

Words that have been obtained then being clustered in the dendogram below, after eliminating the words that rarely go out. Thus, in this dendrogram raised only words that most often come out.

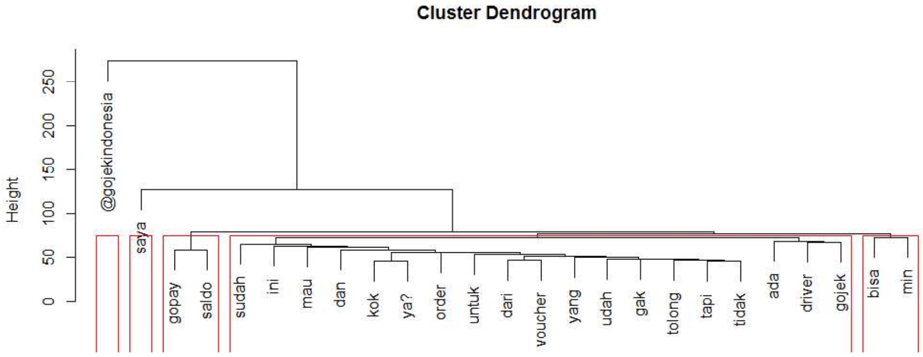

Figure 3.4.1 Dendrogram @GojekIndonesia

Based on the Figure 3.4.1, the result grouped into five clusters. For example, the results shows that the word “gopay” and “saldo” to be one group, so it means that the tweet about gopay will be followed by the word “saldo”.

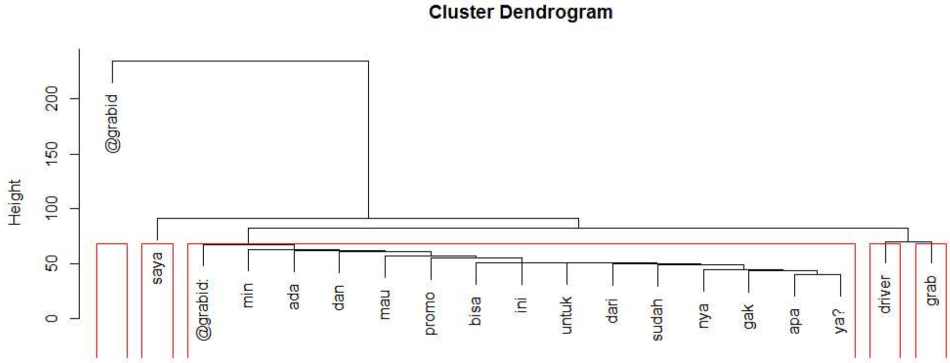

Fig 3.4.2 Dendrogram @GrabID

Based on the Figure 3.4.2, the result grouped into five clusters. For example, the results shows that the word “driver” and “grab” to be one group, so it means that the tweet about grab will be followed by the word “driver”.

3.5 Assosiation Rules

To find the word most associated with XYZ word, use the following command:

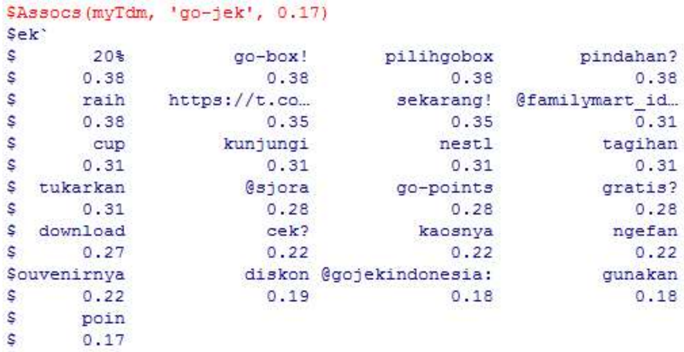

```
$Assocs(myTdm, 'go-jek', 0.17)
$ek`
$       20%          go-box!       pilihgobox        pindahan?
$      0.38             0.38             0.38             0.38
$      raih    https://t.co…        sekarang!  @familymart_id…
$      0.38             0.35             0.35             0.31
$       cup         kunjungi            nestl          tagihan
$      0.31             0.31             0.31             0.31
$  tukarkan           @sjora        go-points          gratis?
$      0.31             0.28             0.28             0.28
$  download             cek?          kaosnya           ngefan
$      0.27             0.22             0.22             0.22
$ouvenirnya           diskon @gojekindonesia:          gunakan
$      0.22             0.19             0.18             0.18
$      poin
$      0.17
```

Based on the results, the word “go-jek” has the highest association with the word “20%” as much as 0:38 or 38% and the rest follow the number of words that are often associated by someone if writing words on social media twitter @GojekIndonesia.

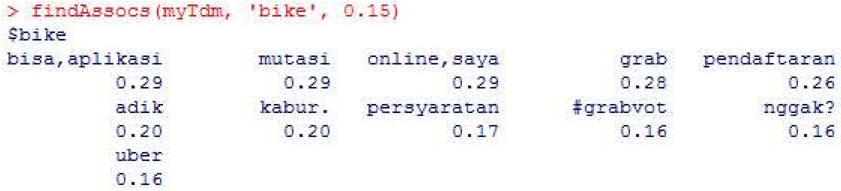

```
> findAssocs(myTdm, 'bike', 0.15)
$bike
bisa,aplikasi       mutasi  online,saya           grab    pendaftaran
         0.29         0.29         0.29           0.28           0.26
         adik       kabur.  persyaratan       #grabvot         nggak?
         0.20         0.20         0.17           0.16           0.16
         uber
         0.16
```

Based on the results, the word “bike” has the highest association with the word “bisa,aplikasi” as much as 0,29 or 29% and the rest follow the number of words that are often associated by someone if writing words on social media twitter @GrabID.

4. CONCLUSION

Based on the analysis and the twitter account @GojekIndonesia can be concluded that the words were much discussed regarding “go-jek” are “gopay”, “gojek”, and “saldo”. Based on the analysis and the twitter account @GrabID can be concluded that the words were much discussed regarding “bike” are “grab”, “driver”, and “promo”.

In addition to the Gojek and Grab Bike word, the pattern is the word most often occurs with the explanation and said that word is rare. The results obtained in the cluster analysis form of some words that are used by users of Twitter, one of which is a twitter account Gojek and Grab Bike itself.

5. REFERENCES

[1]. Buntoro, Ghulam Asrofi. 2014. Sentiment Analysis Twitter dengan Kombinasi Lexicon Based dan Double Propagation. Pada CITEE 2014 7-8 Oktober 2014. Yogyakarta, Indonesia.

[2]. Elex Media Komputindo. Friendster Tempat Gaul Gaya. IslandScrpt.Net.

[3]. Fairuji, Dede. 2014. Makalah Manajemen Strategik Sejarah, Visi, Misi, dan Strategi yang Digunakan PT XYZ Golden Missisippi. Teknologi Pangan dan Gizi Politeknik Negeri Jember.

[4]. Gopego. Ketahui Lokasi Followers Twitter dengan Aplikasi Tweepsmap. http://gopego.com/news/a/2011/12/ketahui-lokasi-followers-twitter-dengan-aplikasi-tweepsmap [17 Oktober 2015]

[5]. Manalu, Boy Utomo. Analisis Sentimen Pada Twitter Menggunakan Text Maining. http://repository.usu.ac.id/bitstream/123456789/41904/7/Cover.pdf [17 Oktober 2015]

[6]. NN. 2013. Jejaring sosial. https://id.wikipedia.org/wiki/Jejaring_sosial [04 Oktober 2015].

[7]. Prabawati, Ari. 2010. Marketing Gratis dengan Facebook. Yogyakarta: ANDI.

[8]. Santosa, Budi. 2007. Data Mining : Teknik Pemanfaatan Data untuk Keperluan Bisnis. Yogyakarta : GRAHA ILMU.

[9]. Ukhwah, Ernin Niswatul. 2007. Text Mining. http://ernin.wordpress.com/2007/09/21/text-mining/ [04 Oktober 2015].

[10].Waloeyo, Yohan Jati. 2010. Twitter Best Social Networking. Yogyakarta: ANDI.

Generalized formulae for instantaneous nonlinear susceptibilty in the presence of excitation and ionization

Muhammad Nurhuda[1*]

[1] Physics Department, Faculty of Mathematics and Natural Sciences, Brawijaya University, Jl. Veteran 2, Malang, 65145, Indonesia.
* Corresponding authors: [mnurhuda@ub.ac.id]

Abstract – We theoretically investigate the nonlinear susceptibility of an atomic hydrogen irradiated by an intense laser field by solving numerically the respective time dependent Schrödinger equation . The instantaneous dipole oscillations are identified from that of (i) the ground-state to excited states transition and (ii) from the ground-state to continuous states transition. By adding the two dipole oscillation components and also considering the depletion of the ground state due to the excitation and ionization processes, it is found that the total instantaneous susceptibility of the atom can be simply written as $\chi(\omega) = P_g\left[\chi^{(1)}(\omega) + I\chi^{(3)}(\omega)\right]$, where P_g is the probability of the electron remaining in the ground-state level.

1. INTRODUCTION

There has been great interest in the nonlinear susceptibility of atoms or molecules to an external electric field. The understanding of nonlinear susceptibility is important in the field of nonlinear optics; i.e., to quantitatively describe the dynamics of short laser pulses propagating in the transient nonlinear medium [1] as well as propagation of the high harmonic waves (see, e.g., Ref. [2]), and to design better nonlinear optical materials for technological development [3]. Traditionally, the nonlinear response is truncated to the cubic term of applied electric field. With the development of high-intensity laser pulses, experiments on laser-material interaction with nonlinear responses higher than third becomes possible.

Analysis of the high-order nonlinear susceptibility are usually based on the perturbation theory. In most calculations, only the third-order term is considered (see, e.g., Refs. [4,5]). The computations of higher order terms χ^k , where $k > 3$, in general are very difficult to perform and need special treatment to overcome singularities due to overlaps between the intermediate states. It is well known that perturbation theory fails when the intensity of the applied electric field is greater than 1 X 10^{13} W/cm^2 [6]. Current laser technology has enable one to generate laser peak intensities in the level atomic intensity I_0= 3.5X 10^{16} W/cm^2 . Therefore, when atoms are exposed to very high-intensity, it is expected that higher-order nonlinear susceptibilities becomes apparent.

Recently, the origin of the nonlinear susceptibility of atom interacting with intense laser field has been deeply studied [6]. It is found that the instantaneous susceptibly is mainly contributed by the dipole oscillation of electron in ground state that is coupled to the both excited or continuum states. Electrons that are occupying continuum states do not contribute the instantaneous nonlinear susceptibility. In this paper, we discuss the contribution of each component to the instantaneous susceptibility.

2. METHODS

The numerical method underlying the simulation is based on the TDSE that can be written as (we use the Hartree atomic units $e = m = \hbar = 1$):

$$i\frac{\partial}{\partial t}\psi(\mathbf{r},t) = \left[-\frac{\nabla^2}{2} + V(r) + \mathbf{E}(t)\cdot\mathbf{r}\right]\psi(\mathbf{r},t), \tag{1}$$

where $\mathbf{E}(t) = \hat{\mathbf{k}}\mathrm{E}(t)\sin(\omega t)$ is the electric field, given in the dipole approximation, and $\mathrm{E}(t)$ is the electric field envelope. We assume that the electric field is linearly polarized along the z-axis, such that only the magnetic quantum number $m = 0$ is required. Equation (1) is solved by expanding the wave function in a set of spherical basis function.

$$\psi(\mathbf{r},t) = \sum_l R_l(r,t)Y_{l,m}(\theta,\vartheta) \tag{2}$$

The resulting coupled set of partial differential equations is integrated numerically using the split operator method, described elsewhere [7]. Following [6], the wavepacket $\psi(\mathbf{r},t)$ can be decomposed into terms belonging to the ground state, bound-excited wavepackets and continuum wavepacket:

$$\begin{aligned}\psi_{\mathrm{g}}(\mathbf{r},t) &= <\phi_{1s}(\mathbf{r})|\psi(\mathbf{r},t)>\phi_{1s}(\mathbf{r}),\\ \psi_{\mathrm{B}}(\mathbf{r},t) &= \sum_{n\neq 1s}\langle\phi_n(\mathbf{r})|\psi(\mathbf{r},t)\rangle\phi_n(\mathbf{r}),\\ \psi_{\mathrm{C}}(\mathbf{r},t) &= \psi(\mathbf{r},t)-\psi_{\mathrm{B}}(\mathbf{r},t)-\psi_{\mathrm{g}}(\mathbf{r},t).\end{aligned} \tag{3}$$

The probability density of the electron in the ground state or the corresponding wavepacket can be easily obtained using $\rho_j = <\psi_j(\mathrm{r})|\psi_j(\mathrm{r})>$, where the subscript j refers to the ground, excited or continuum state. To track the origin of the saturation, the time-dependent dipole oscillation, $d(t)$, and its components $d_{\mathrm{gB}}(t)$, $d_{\mathrm{gC}}(t)$ and $d_{\mathrm{CC}}(t)$ are evaluated using the following form:

$$\begin{aligned}d(t) &= \langle\psi(\mathbf{r},t)|z|\psi(\mathbf{r},t)\rangle\\ d_{\mathrm{gB}}(t) &= 2\langle\psi_{\mathrm{g}}(\mathbf{r},t)|z|\psi_{\mathrm{B}}(\mathbf{r},t)\rangle\\ d_{\mathrm{gC}}(t) &= 2\langle\psi_{\mathrm{g}}(\mathbf{r},t)|z|\psi_{\mathrm{C}}(\mathbf{r},t)\rangle\\ d_{\mathrm{CC}}(t) &= \langle\psi_{\mathrm{C}}(\mathbf{r},t)|z|\psi_{\mathrm{C}}(\mathbf{r},t)\rangle,\end{aligned} \tag{4}$$

One can immediately see that $d(t) \approx d_{\mathrm{gB}}(t) + d_{\mathrm{gC}}(t) + d_{\mathrm{CC}}(t)$.The induced dipole polarization is related to the electric field by $d_j(\omega) = \chi_j(I, \omega)E(\omega)$, where $d_j(\omega)$ is the Fourier transform of the respective dipole moment, $E(\omega)$ is the Fourier transform of the electric field and $\chi_j(I,\omega)$ is the respective susceptibility. One can immediately see that the total susceptibility, $\chi^T(I\ \omega)$, can be written as $\chi^T(I, \omega) \approx \chi_{\mathrm{gB}}(I, \omega) + \chi_{\mathrm{gC}}(I, \omega) + \chi_{\mathrm{CC}}(I, \omega)$.

In simulation, the pulse envelope was chosen to have the form $\sin^2(\pi t/T\mathrm{max})$, with Tmax is the total pulse duration. The laser field is chosen to have the central frequency of a Ti:sapphire of $\omega 0$ = 1.55 eV (or laser wavelength of 800 nm). The total pulse duration T_{max} was taken to be 24 and 12 optical cycles, and each cycle was discretized into 512 temporal grids. In order to ensure the accuracy of the solution, we utilized a very fine radial grid Δr = 0.04 au, a large radial boundary $r$max = 2500 au. The maximum number of the angular momentum Lmax = 60. The accuracy of the wavepacket separation was controlled using the identity $|\rho g + \rho B + \rho C - 1| = \varepsilon$. We observed that by including 45 bound states, the error in the wavepacket separation, ε was less than $10^{-6.}$

3. RESULTS AND DISCUSSION

The instantaneous susceptibility is defined as the behavior of the dipole moment that follows the electric field. In Fig. 1, the total time-dependent dipole oscillation $d(t)$, and its components $d_{gB}(t)$ and $d_{gB}(t)$ are shown from the top to bottom, respectively. The left panels stand for results obtained using intensity of 6.4 × 10^{13} W cm^{-2}, while the right panels show those obtained using an intensity of 1.47 × 10^{14} W cm^{-2}. In both panels, the total pulse durations are 24 cycles.

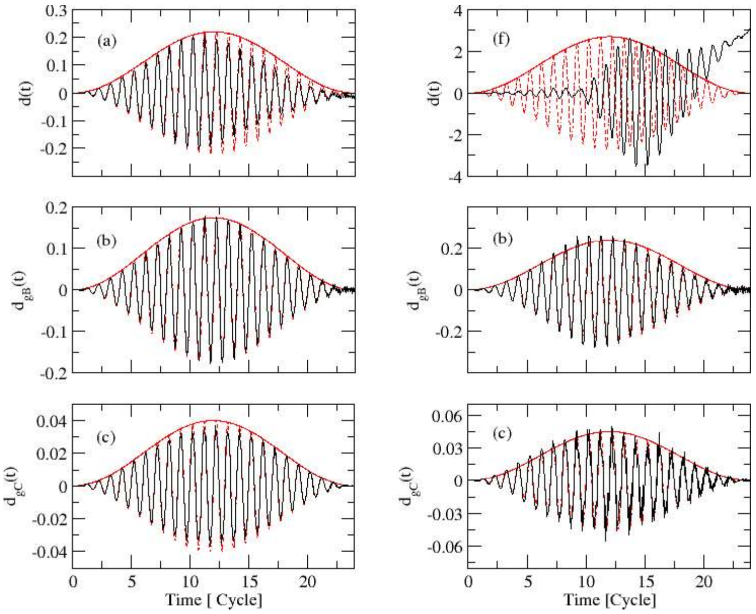

Figure 1. Plots of the various dipole oscillations, *d(t)* and their components, $d_{gB}(t)$ and $d_{gC}(t)$. In left panels, the intensity is 6.4 ×10^{13} W cm^{-2}, while in right panels the intensity is 1.47 ×10^{14} W cm^{-2}. The red-dotted curves stand for the rescaled electric fields while the red-thin curves the respective electric field envelopes.

It is seen that at low intensity, $d(t)$, $d_{gB}(t)$ and $d_{gC}(t)$ show relatively better overlap with both the electric field and its envelope, which indicates the instantaneous responses property. Other indication is lying in the similarity in the phase of the electric field and the dipole oscillation. At high intensity, however, the rise of the oscillation amplitude of $d(t)$ trails behind that of the electric field. Furthermore, at the beginning, the electric field and dipole moment are in phase but then reverted to be anti-phase in the rest time. This reveals that at short times when the ionization is still low, $d(t)$ is instantaneous, but then is predominately induced by ionization at later times.

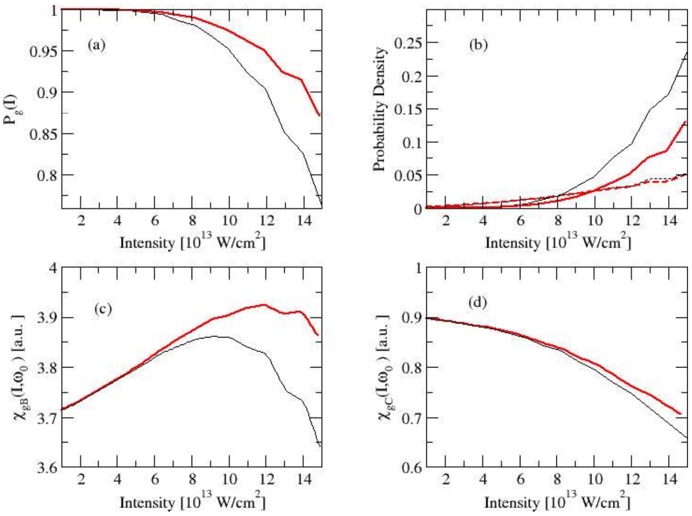

Figure 2: Plot of the electron probability density in the ground state (a), in (b) the electron probability density in the excited wavepacket is depicted as a dotted curve, while the solid curve stands for those in the continuum wavepacket. (c) and (d) The nonlinear susceptibility components extracted from the dipole oscillation $d_{gB}(t)$ and $d_{gC}(t)$, respectively. In all the panels, the thin-black curves represent simulation results obtained using pulse duration $T = 24$ cycles, whereas the thick red curve represents those using $T = 12$ cycles.

In order to further investigate the effect of ground state depletion, we carried out additional simulations with a total pulse duration equal to 12 cycles. It is expected that by using shorter pulses, the ground state becomes less depleted. The results are ground state depletion are displayed in Fig. 2(a). The results generated using $T = 24$ cycles are shown as thin black curves while those of 12 cycles are depicted as thick red curves. In Fig 2(b), the results of probability density of electron in the excited states and ionization states are shown. We can see that at low intensity ($I < 6 \times 10^{13}$ W cm^{-2}), the excitation process is dominant, whereas ionization dominates at high intensity. The growth of the electron density occupying the excited states seems to be linear and stabilizes with respect to the pulse duration, while that of the ionization seemly increases exponentially. Comparing Fig. 2(a) and 2(b), one may conclude that that the ground-state depletion is eventually due to an ionization rather than an excitation process.

In Fig. 2(c) and 2(d), we demonstrate the results of susceptibility components $\chi_{gB}(\omega_0)$ and $\chi_{gC}(\omega_0)$, respectively. At small intensity, the two curves coincide with each other, indicating that at low intensity, all responses are purely instantaneous, independent of the pulse shape and duration. At high intensity, $\chi gB(\omega 0)$ becomes saturated. However, the saturation from the simulation using $T = 24$ cycles occurs at relatively lower intensity than that of $T = 12$ cycles. Because $dgB(t)$ is determined from the coupling between the ground state and the bound- excited wavepacket, and on the other hand, the excitation probability density remains unchanged (figure 2(b)), we can conclude that the saturation of the $\chi gB(\omega 0)$ must be originated from the ground state depletion.

On the other contrary, $\chi gC(\omega 0)$ already shows saturation even at small intensity. This is a strong indication that the nonlinear susceptibility components generated by the electronic transition from the ground state to the continuum have a negative sign. Higher ionization probability seems to bring only irrelevant small effects. This finding is a strong indication that the instantaneous component, $\chi gC(\omega 0)$, is not much influenced by the onset of ionization, but is mainly the result of ground state depletion. This is due the fact that the continuum wavepacket is spatially removed away from the atomic core, such that its contribution to the instantaneous susceptibility is negligible.

Based on the above findings, the total instantaneous susceptibility can now be approximately written in the form:

$$\chi_{\text{inst}}(I,\omega) = \hat{P}_{\text{g}}(I)\left\{\chi^{(1)}(\omega) + \chi^{(3)}(\omega) I\right\} \tag{5}$$

And the corresponding nonlinear part hence has the form:

$$\chi_{\rm inst}^{\rm NL}(I,\omega) = \hat{P}_{\rm g}(I)\left\{\chi^{(1)}(\omega) + \chi^{(3)}(\omega)I\right\} - \chi^{(1)} \tag{6}$$

At low intensity where the depletion of the ground state is negligible such that $\hat{P}_{\rm g}(I) = 1$, then Eq. (6) is simply the Kerr nonlinearity. Equation (6) thus generalizes the well known Kerr nonlinearity formulae for high intensity and ultrashort laser pulses.

4. CONCLUSIONS

In conclusion, we have investigated the saturation of the nonlinear susceptibility of atomic hydrogen induced by intense ultrashort laser pulses, by solving the time dependent Schrödinger equation. The electronic wavepacket is separated into terms belonging to the ground, bound-excited and the continuum states, such that the dipole oscillation components contributing to the instantaneous susceptibility can be well identified. We found that the instantaneous susceptibly is predominantly determined by the electron in ground state, and the saturation is found to be originated from the depletion of the electron in the ground state.

5. REFERENCES

[1]. M.D. Feit, J.A. Fleck, 1974, Appl. Phys. Lett. **24**, 169; E.T.J. Nibbering, P.F. Curley, G. Grillon, B.S. Prade, M.A. Franco, F. Salin, A. Mysyrowicz, 1996, Opt. Lett. **21**, 62; Q. Feng, J.V. Moloney, A.C. Newell, E.M. Wright, K. Cook, P.K. Kennedy, D.X. Hammer, R.C. Thompson, 1997, IEEE J. Quantum Electron. **33**, 127; M. Mlejnek, E.M. Wright, J.V. Moloney, 1997, Opt. Lett. **23**, 382.

[2]. A. L'Huillier *et.al.,* 1992, *Atoms in Intense Laser Fields*, edited by M. Gravrila (Academic Press, New York, p. 139); M.W.Wasler, C.H. Keitel, A. Scrinzi,, T. Brabec, 2000, Phys. Rev. Lett. **85**, 5082 ; N.H. Shon, A. Suda, Y. Tamaki,, K. Midorikawa, 2001, Phys. Rev. A **63**, 063806

[3]. G.T. Boyd, 1989, J. Opt. Soc. Am. B **6**, 685; J.W. Wu, J.R Heffin, R.A. Norwood, K.Y. Wong, O. Zamani-Khamiri, A.F. Garito, P. Kalyanaraman, J. Sounik, *ibid.* **6**, 1990, 707.

[4]. P.N. Butcher and D. Cotter, 1990, The Elements of Nonlinear Optics (Cambridge University Press, Cambridge,.

[5]. R.W. Boyd, *Nonlinear Optics,1992,* (Academic Press, San Diego .

[6]. M. Nurhuda, A. Suda , K. Midorikawa, 2008, *New Journal of Physics* **10** , 053006

[7]. Saul Teukolsky, 1992, Numerical Recipes, Cambridge University Press, UK

Study of Optimization of Cropping Pattern to Maximize The Profit of Agricultural Production at Jati Ampuh Irrigation Area

Lily Montarcih Limantara[1*], Rini Wahyu Sayekti[1], M. A. Sajali[1], Dipta Pramana S.[1]

[1] Universitas Brawijaya, Jl. MT. Haryono No. 165 Malang
* Corresponding authors: [lilymont2001@gmail.com]

Abstract – Jati Ampuh irrigation area has faced a problem of water capacity shortage at the existing cropping pattern, which occurred at the beginning of cultivation on November period I to December Period I and June period III. This resulted in incompatibility between the amount of water supply and the crop water demand and decreased its agricultural production. In order to solve the problem, cultivation season has carried out by shifting the pattern from November period I to December period II and optimize the cropping pattern. The purpose of this research is to obtain the appropriate cropping pattern by using the linear program so that the water discharge provided in the intake can be fully utilized.

1. INTRODUCTION

Along with the development and growth of the community, always carry highly complex influences, especially regarding the fulfillment of food needs. Therefore, it is necessary to set and to use water effectively and efficiently in irrigation network system in order to obtain maximum results. In this study, it will be examined the maximum area of crops and the maximum profits derived from linear programming optimization (solver).

2. METHODS

Administratively, Jati Ampuh irrigation area located in the district of Pajarakan. it included in the authority of regional level ii Probolinggo regency and managed by the department of public works, Pekalen branch observer. The total irrigation area is 497 hectares.

The data required in this study are in the form of rainfall data, intake discharge, climatology, cropping patterns existing data and agricultural profits existing data.

This study did optimization using five alternative cropping pattern layouts. Besides, the planting season has shifted from the beginning in November period I into December Period II. Planting area was the same as planting area in the Jati Ampuh Irrigation area in the amount of 497 Ha. Mathematical models or scenarios can be seen in the following descriptions

2.1 Target function

In this optimization, the targets are to maximize the profit and the total area of crops (paddy, corn, and Sugarcane) for each season during one year, and resolve the imbalance of water supply.

$$Z = A.X_{1a} + B.X_{1b} + C.X_{1c} + A.X_{2a} + B.X_{2b} + C.X_{2c} + A.X_{3a} + B.X_{3b} + C.X_{3c}$$

Where:

Z = Target function to be achieved in the form of maximum profit (Rp)

A,B,C = production profit each crop

X_{1a}, X_{1b},…,X_{3C} = crop area in each season

2.2 Constraint functions

Constraint function is an equation, which limits the usefulness of the main function, which are the total area of the research study, the volume of water supply, and the maximum area of Sugarcane. The function can be seen respectively in the following:

$$X_{1a} + X_{1b} + X_{1c} \leq Xt_1$$

$$X_{2a} + X_{2b} + X_{2c} \leq Xt_2$$

$$X_{3a} + X_{3b} + X_{3c} \leq Xt_3$$

Where:

X_{t1}, x_{t2}, x_{t3} = total area in each planting season

X_{1a}, x_{1b},…,X_{3c} = crop area in each season

For dependable volume the function is:

$$V_{p1}.X_{1a} + V_{j1}.X_{1b} + V_{t1}.X_{1c} \leq Vs_1$$

$$V_{p2}.X_{2a} + V_{j2}.X_{2b} + V_{t2}.X_{2c} \leq Vs_2$$

$$V_{p3}.X_{3a} + V_{j3}.X_{3b} + V_{t3}.X_{3c} \leq Vs_3$$

Where:

V_{S1}, V_{S2}, V_{S3} = dependable volume of water supply in each 10 days (m^3/ha)

V_{P1}, V_{P2},…,X_{t3} = crops water demand in each 10 days (m^3/ha)

For Sugarcane total area function can be seen as follow:

$$X_{1c} \leq Xte_1$$

$$X_{2c} \leq Xte_2$$

$$X_{3c} \leq Xte_3$$

Where:

V_{te1}, V_{te2}, V_{te3} = total area of Sugarcane in each season

V_{1c}, V_{2c},…,X_{3c} = area of Sugarcane in each season

3. RESULTS AND DISCUSSION

The optimization are divided into three criteria to determine which pattern will be used in the Jati Ampuh irrigation are which are the water demand is fulfilled in each scenario, the intensity of the crops, and the total profit. Based on the water balance calculation results shown that the water demand of each scenario is below the water supply, which means the water needs is fulfilled. One of the results can be seen in Figure 1.

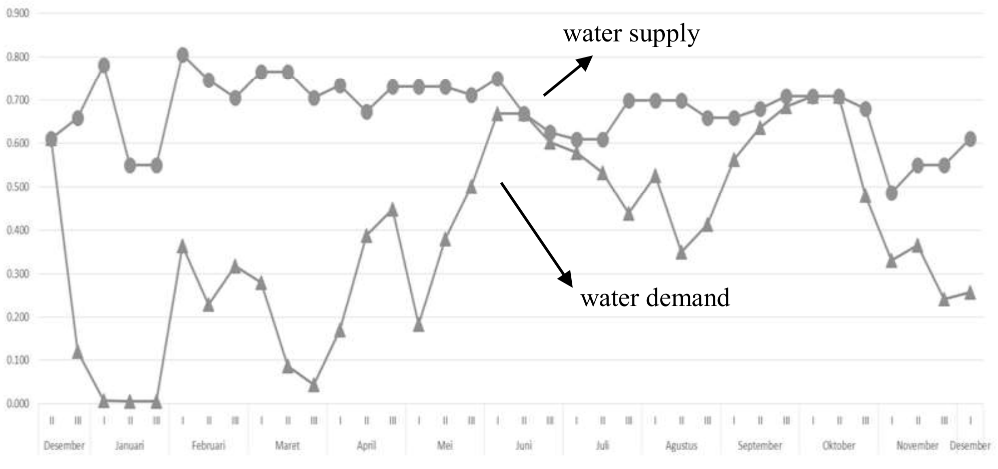

Figure 1 water balance in the scenario I

For the intensity of the crops (Table 1), the highest intensity is scenario II with the total percentage is 271.76 %, following by scenario IV, scenario V, scenario I, and scenario III.

Table 1 Intensity of the crops

Cropping Pattern	Period	Crops	Total Area (Ha)	Intensity Percentage (%)
Scenario I	I	Paddy, Sugarcane	376.000	257.66
	II	Paddy, Corn, Sugarcane	497.000	
	III	Paddy, Corn, Sugarcane	407.587	
Scenario II	I	Paddy, Corn, Sugarcane	497.000	271.76
	II	Paddy, Sugarcane	497.000	
	III	Corn, Sugarcane	356.672	
Scenario III	I	Paddy, Sugarcane	371.503	235.45
	II	Paddy, Sugarcane	497.000	
	III	Paddy, Sugarcane	301.696	
Scenario IV	I	Corn, Sugarcane	497.000	271.76
	II	Paddy, Sugarcane	497.000	
	III	Corn, Sugarcane	356.672	
Scenario V	I	Paddy, Corn, Sugarcane	497.000	260.70
	II	Paddy, Sugarcane	497.000	
	III	Paddy, Sugarcane	301.696	

The total profit is expressed as Indonesian Rupiah (IDR) with the highest profit can be seen in Table 2 below.

Table 2 Total profit of each scenario

Cropping Pattern	Period	Crops	Total Area (Ha)	Profit (IDR)
Scenario I	I	Paddy, Sugarcane	376.000	14,641,829,329
	II	Paddy, Corn, Sugarcane	497.000	
	III	Paddy, Corn, Sugarcane	407.587	
Scenario II	I	Paddy, Corn, Sugarcane	497.000	15,495,380,341
	II	Paddy, Sugarcane	497.000	
	III	Corn, Sugarcane	356.672	
Scenario III	I	Paddy, Sugarcane	371.503	14,526,090,445
	II	Paddy, Sugarcane	497.000	
	III	Paddy, Sugarcane	301.696	
Scenario IV	I	Corn, Sugarcane	497.000	14,786,753,688
	II	Paddy, Sugarcane	497.000	
	III	Corn, Sugarcane	356.672	
Scenario V	I	Paddy, Corn, Sugarcane	497.000	15,593,316,933
	II	Paddy, Sugarcane	497.000	
	III	Paddy, Sugarcane	301.696	

Subsequently, each cropping pattern is ranked from the highest score to the lowest score based on the number of cropping intensity and profits. The cropping pattern is given a score of 5 for the highest, and score of 1 for the lowest and can be seen in Table 3. Based on the result the best cropping pattern with the highest total score is scenario II (total score is 9).

Table 3 Total score of each scenario

Cropping Pattern	Intensity Score	Profit score	Total
Scenario I	**2**	**2**	**4**
Scenario II	**5**	**4**	**9**
Scenario III	**1**	**1**	**2**
Scenario IV	**4**	**3**	**7**
Scenario V	**3**	**5**	**8**

4. CONCLUSIONS

To determine the best scenario of the cropping pattern, each scenario is assessed by looking at the percentage of crop intensity and the amount of profit gained of each scenario. Based on Table 1, the cropping pattern with the highest score is scenario II (Period I: Paddy-Corn-Sugarcane; Period II: Paddy-Sugarcane; Period III: Corn-Sugarcane), which has the intensity for one year is 271.76 % and the profit is Rp. 15,495,380,341.

5. REFERENCES

[1] L.M. Limantara, 2008, Pengaruh Perubahan Cuaca terhadap Optimasi Irigasi dengan Program Linier, Bandung.
[2] L.M. Limantara, S. Widandi, 2009, Pengantar Manajemen Teknik Sumber Daya Air, Malang.

Clustering Analysis for Incomplete Data (Study Case of Composing Zone of User Rights Radio Frequency Cost)

Erfiani[1*]

[1] Department of Statistics, Faculty of Mathematics and Natural Sciences, Bogor Agricultural University, Bogor, Indonesia[2] Author's institution and address
* Corresponding authors: [erfiani_ipb@yahoo.com]

Abstract – Cluster analysis is one of exploration data techniques which is widely used and has an extensive application. Initially, the clustering method is only used on cases with complete data. Nowadays, cluster analysis also covers incomplete data. This paper discusses two approaches to overcome incomplete data in cluster analysis: a marginalization and a special algorithm approach. Radio frequency spectrum is a limited natural resource; therefore, it should be considered that radio frequency spectrum is strategic and economical for holding telecommunications. Hence, it is important to develop zones for optimizing the market interest of the service frequency band.

1. INTRODUCTION

In statistical analysis approach, clustering data is generally carried out by cluster method. The principle of cluster method is classifying objects, based on the similarity of certain characteristics, into a cluster so that objects have a high homogeneity in one cluster and has a high heterogeneity among clusters. Cluster method has been widely used in the case of complete data. Problems will arise, however, in the case of incomplete data.

The radio frequency is a limited natural resource that has economic and strategic value in telecommunication operations. For its effective and optimal use, accordingly, , this must be regulated by the government. Thus, it is the government that has the authority to determine the User Rights Fee (Biaya Hak Penggunaan/BHP) of radio frequency. BHP determination indicator is based on several certain variables; as a result, BHP in Indonesia will vary from one area to another. Area with the same cost of BHP is called a zone.

In around 2012 there were a lot of divisions of a city/district, so problems appeared when developing zones of BHP, as new cities/ districts that do not have data indicators were included to construct a zone. This study will explore the formation of BHP zones for cities/districts in Indonesia using marginalization approach and A partial distance (PDS) algorithm.

2. METHODS

2.1 Data

Data in this study were taken from the Ministry of Communication and Informatics as well as from Central Bureau of Statistics. The observation was conducted in 514 cities/districts in Indonesia. There are seven Observed variables, which are similar to those used by the Ministry of Communication and Informatics to construct cost of frequency band: 1. Gross Regional Domestic Product (billion rupiah) 2. Population density (people/km2) 3. Total labor force (thousands of souls) 4. Percentage of economic growth 5. Income from the cost of user rights radio frequency (million rupiah) 6. the number of Base Transceiver Station (BTS) 7. consumer price index.

2.2 Methods

A marginalization approach was excluded observations which was not complete and then clustered observations by hierarchical and non-hierarchical method (i.e. k-means algorithm). A partial distance (PDS) algorithm is a special algorithm to cluster incomplete data. This means that the PDS algorithm includes incomplete observations. Those methods were applied on a cost of user rights radio frequency.

Marginalization method is the simplest technique to be used as a solution for incomplete data clustering. There are two possibilities to do, first, removing objects from the collection of incomplete data, second, deleting incomplete attribute, but it should be noted that marginalization approach can make information existing data will be lost [1].

PDS method is a clustering algorithm with incomplete data by calculating the distance of the object to the center of cluster based on existing data [2]. The first step of the clustering process data using PDS method is to construct an initial value for the center of cluster, which is generally randomly generated. The number of the cluster was specified at the beginning of the process.

To evaluate the results of clusters, Davies Bouldin Index (DBI) and mapping approach were used. DBI is used to determine the amount of the optimal cluster. DBI measurement maximizes the distance between clusters and minimizes the distance between objects in a cluster. If the distance between cluster is maximum, a variance between cluster was high; so the difference between clusters is clearly visible. If the distance between object in a cluster minimum, the variance of objects in a cluster is small, so objects in each cluster has the same characteristics. Optimal cluster scheme is according to the DBI is having a value of DBI minimal [3].

3. RESULTS AND DISCUSSION

Of 514 cities/districts, there were 50 (10%) new citiest districts due to the new area expansion . These new cities/districts usually have several variables with incomplete data. A cluster analysis with marginalization approach, however, needs complete data, so that 464 cities/districts were extremely useful. Otherwise, PDS algorithm could be applied for all of the ies/districts (514 cities /districts).

With 464 cities/districts, the marginalization approach constructed 4 clusters, meanwhile, the PDS approach constructed 5 clusters of zones from 514 cities/districts. The number of clusters of the PDS algorithm was larger than that in the marginalization approach because the former had more observations than the later. Using PDS algorithm, there is no loss of information from new cieties/districts. Figure 1 shows the clustering result of marginalization approach, and Figure 2 reveals the clustering result of PDS. DBI value generated by the PDS approach is 0.989, while on marginalization approach is 0.705. Thus, there is no significant different in the Value of DBI's approach.

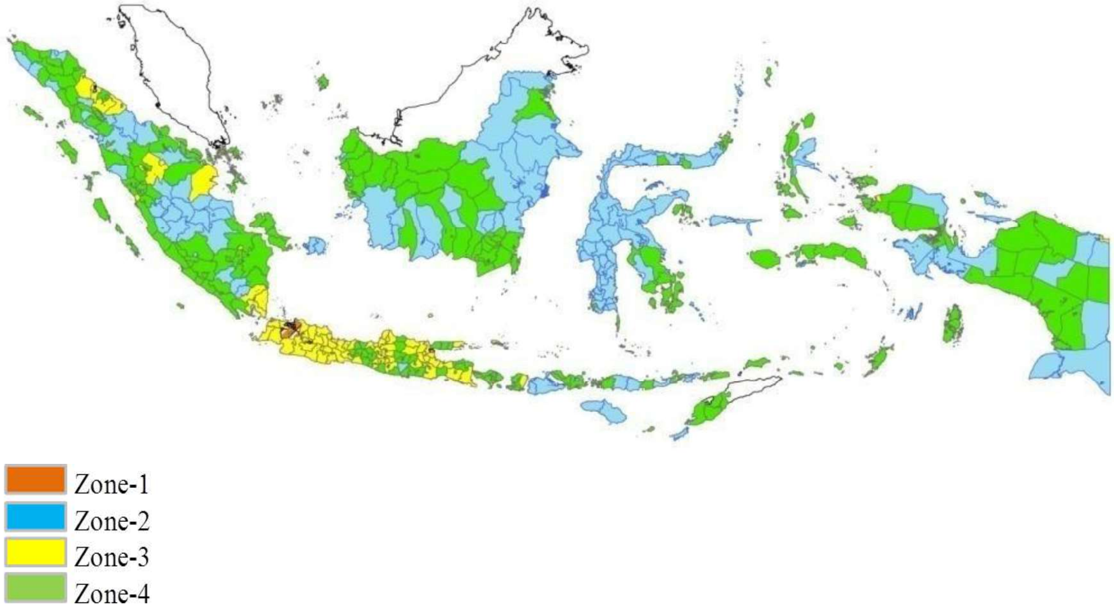

Figure 1 Clustering Result of Marginalization Approach

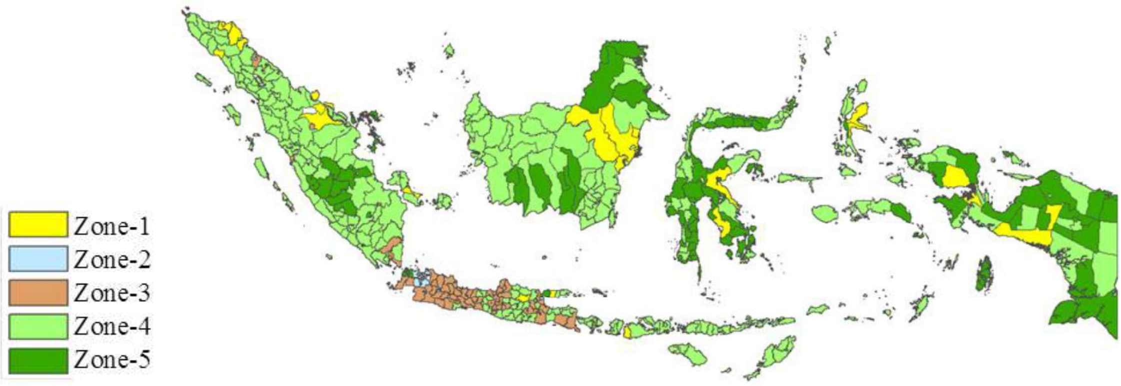

Figure 2 Clustering Result of PDS

CONCLUSIONS

Clustering incomplete data with PDS approach is better than the one with marginalization approach. The application of PDS utilizes all data. Value DBI of PDS results is relatively small, which means that it has an optimal cluster

5. REFERENCES

[1] Wagstaff, K. and Laidler V. 2005. Making the most of missing values: Object clustering with partial data in astronomy. *Proceedings of Astronomical Data Analysis Software and Systems* **XIV** 347: 172–176. California,USA

[2] Matyja A. and Simiński, K. 2014. Comparison of algorithms for clustering incomplete data. *Journal Foundations of Computing and Decision Sciences* **39**: 107–127.

[3] Yatkiv, I. and Gusarova, L. 2004. The Method of Cluster Analysis Result Validation. *Proceedings of International Conference RelStat*'**04part 1**: 75-8

An $L(2,1)$-Labeling of Corona Product of Ladder and K_1

Rismawati Ramdani[1*], Indah Hastuti[1]

[1] Department of Mathematics Faculty of Sciences and Technologies UIN Sunan Gunung Djati Bandung
* Corresponding authors: [rismawatiramdani@gmail.com]

Abstract – An $L(2,1)$-labeling of a simple graph G is a nonnegative integer-valued function $f{:}V(G)\rightarrow\{0,1,2,....\}$ such that, whenever x and y are two adjacent vertices in $V(G)$, then $|f(x)\text{-}f(y)| \geq 2$, and, whenever the distance between x and y is 2, then $|f(x)\text{-}f(y)| \geq 1$. The $L(2,1)$-labeling number of G, denoted by $\lambda(G)$, is the smallest number m such that G has an $L(2,1)$-labeling with no label greater than m. In this paper, we determine an $L(2,1)$-labeling of Corona product of ladder and K_1.

Keywords: Graph labeling, $L(2,1)$-labeling, $L(2,1)$-labeling number, complete graph, Corona product, ladder, path

1. INTRODUCTION

An $L(2,1)$-labeling of a simple graph G is a nonnegative integer-valued function $f{:}V(G)\rightarrow\{0,1,2,....\}$ such that, whenever x and y are two adjacent vertices in $V(G)$, then $|f(x)\text{-}f(y)| \geq 2$, and, whenever the distance between x and y is 2, then $|f(x)\text{-}f(y)| \geq 1$. The $L(2,1)$-labeling number of G, denoted by $\lambda(G)$, is the smallest number m such that G has an $L(2,1)$-labeling with no label greater than m.

A graph G is called complete graph if every two different vertices of G are adjacent. A complete graph with order n denoted by $K_{n.}$

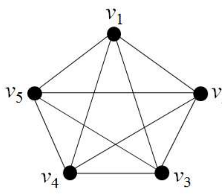

Figure 1. A graph K_5

Path with order n, denoted by P_n, is a graph with two vertices of degree 1, and n-2 vertices of degree 2.

Figure 2. A graph P_4

Let G be a graph with order n and H be a graph with order m. The corona product $G \odot H$ is obtained by taking one copy of G and n copies of H; and by joining each vertex of the i-th copy of H to the i-th vertex of G, where $1 \leq i \leq n$.

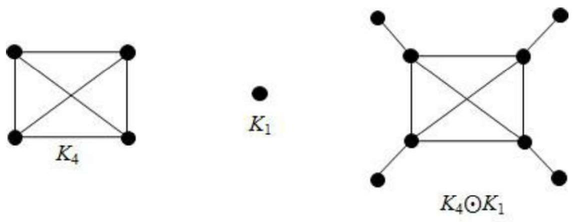

Figure 1. The illustration of Corona product graph

The Cartesian product $G \square H$ of graphs G and H is a graph such that the vertex set of $G \square H$ is the Cartesian product $V(G)\mathrm{x}V(H)$ and any two vertices (u_i,v_j) and (u_k,v_l) are adjacent in $G \square H$ if and only if either u_i=u_k and $v_jv_l \in E(H)$, or v_i=v_k and $u_ju_k \in E(G)$.

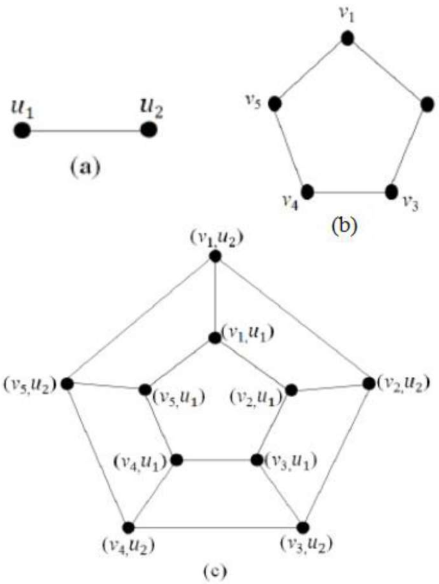

Figure 4. (a) Path P_2 ; (b) Cycle C_5 ; (c) Cartesian product $P_2 \square C_5$

2. SOME RESULTS ABOUT *L*(2,1)-LABELING

Some results about $L(2,1)$-labeling are given by propositions as follows.

Proposition 2.1 [1]

If H is a subgraph of G, then $\lambda(H) \leq \lambda(G)$.

Proposition 2.2 [2]

Let K_n be a complete graph with order n, then $\lambda(K_n) = 2n-2$.

Proposition 2.3 [3]

Let G be a graph with maximum degree $\Delta \geq 1$. If G contains three vertices of degree Δ such that one of them is adjacent to the other two, then $\lambda(G) \geq \Delta+2$.

Proposition 2.4 [2]

The L(2,1)-labeling number of a star $K_{1,\Delta}$ is $\Delta+1$, where Δ is the maximum degree.

3. THE MAIN RESULT

In this paper, we determine an $L(2,1)$-labeling of Corona product of ladder and K_1. Ladder is the Cartesian product of P_n and P_2, denoted by $P_n \square P_2$. The ilustration of ladder $P_n \square P_2$ could be seen in Figure 5.

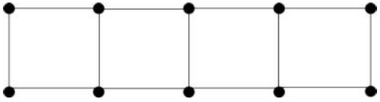

Figure 5. A ladder graph $P_5 \square P_2$

Corona product of ladder and K_1, denoted by $(P_n \square P_2) \odot K_1$, is a graph with vertex set

$$V((P_n \square P_2) \odot K_1)=\{x_1, x_2, x_3, \ldots ,x_n\} \cup \{v_1, v_2, v_3, \ldots ,v_n\} \cup \{w_1, w_2, w_3, \ldots ,w_n\} \cup \{y_1, y_2, y_3, \ldots ,y_n\}$$

and edge set

$$E((P_n \square P_2) \odot K_1)=\{(x_1, v_1), (x_2, v_2), \ldots , (x_n, v_n)\} \cup \{(v_1, w_1), (v_2, w_2), \ldots , (v_n, w_n)\} \cup \{(w_1, y_1), (w_2, y_2), \ldots , (w_n, y_n) \cup \{(v_1, v_2), (v_2, v_3), \ldots , (v_{n-1}, v_n)\} \cup \{(w_1, w_2), (w_2, w_3), \ldots , (w_{n-1}, w_n)\}.$$

An illustration of $(P_n \square P_2) \odot K_1$ could be seen in Figure 6.

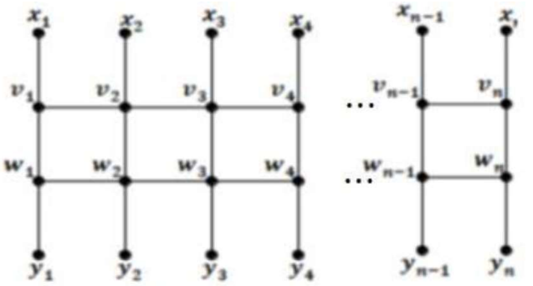

Figure 6. A graph $(P_n \square P_2) \odot K_1$

The L(2,1)-labeling number of $(P_n \square P_2) \odot K_1$ is given in Theorem 1.

Theorem 1. Let P_n be a path with order n and K_1 be a complete graph with order 1, then

$$\lambda((P_n \square P_2) \odot K_1) = \begin{cases} 5 & \text{if } n \in \{2,3\}; \\ 6 & \text{if } n \geq 4. \end{cases}$$

Proof.

Will be shown that

$$\lambda((P_n \square P_2) \odot K_1) = \begin{cases} 5 & \text{if } n \in \{2,3\}; \\ 6 & \text{if } n \geq 4. \end{cases}$$

Case 1. For n=2.

An illustration of $(P_2 \square P_2) \odot K_1$ could be seen in Figure 7.

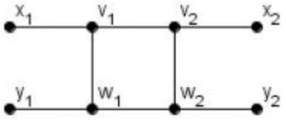

Figure 7. A graph $(P_2 \square P_2) \odot K_1$

The maximum degree of $(P_2 \square P_2) \odot K_1$ is Δ=3. Graph $(P_2 \square P_2) \odot K_1$ contains three vertices of degree Δ such that one of them is adjacent to the other two, the vertices are v_1, v_2, and w_1. Then, from Proposition 2.3, we have

$$\lambda((P_2 \square P_2) \odot K_1) \geq \Delta+2=5 \text{ .... } (3.1)$$

Next, will be shown that $\lambda((P_2 \square P_2) \odot K_1) \leq 5$. Define an L(2,1)-labeling f of $(P_2 \square P_2) \odot K_1$ as follows:

$$f(v_2) = f(y_1) = 0,\ f(x_1) = 1,\ f(x_2) = f(w_1) = 2,\ f(y_2) = 3,\ f(v_1) = 4,\ f(w_2) = 5.$$

The maximum label of labeling f above is 5. So that, we have

$$\lambda((P_2 \square P_2) \odot K_1) \leq 5 \text{ .... } (3.2)$$

From (3.1) and (3.2), we have $\lambda((P_2 \square P_2) \odot K_1) = 5$.

Case 2. For n=3.

In the Figure 8, could be seen an illustration of $(P_3 \square P_2) \odot K_1$.

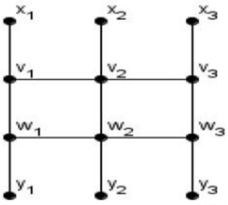

Figure 8. A graph $(P_3 \square P_2) \odot K_1$

Graph $(P_3 \square P_2) \odot K_1$ has a subgraph isomorf with $K_{1,4}$. The subgraph is induced by vertices x_2, v_1, v_2, v_3, and w_2. From Proposition 2.4, $\lambda(K_{1,4}) = 4+1 = 5$. Because of a graph isomorf with $K_{1,4}$ is a subgraph of $(P_3 \square P_2) \odot K_1$, by Proposition 2.1, we have

$$\lambda((P_3 \square P_2) \odot K_1) \geq \lambda(K_{1,4}) = 5 \text{ .... } (3.3)$$

Define an L(2,1)-labeling f of $(P_3 \square P_2) \odot K_1$ as follows:

$f(v_2) = f(y_1) = 0$, $f(x_1) = f(w_3) = 1$, $f(x_2) = f(w_1) = 2$, $f(y_2) = f(v_3) = 3$, $f(v_1) = f(y_3) = 4$, $f(w_2) = f(x_3) = 5$.

The maximum label of labeling f above is 5. So that, we have

$$\lambda((P_3 \square P_2) \odot K_1) \leq 5 \text{ .... } (3.4)$$

From (3.3) and (3.4), we have $\lambda((P_3 \square P_2) \odot K_1) = 5$.

Case 3. For $n \geq 4$.

An ilustration of $(P_n \square P_2) \odot K_1$ could be seen in The Figure 6. From the Figure, we can see that, for $n \geq 4$, $(P_n \square P_2) \odot K_1$ has a subgraph isomorf with $(P_4 \square P_2) \odot K_1$. The maximum degree of graph $(P_4 \square P_2) \odot K_1$ is $\Delta=4$ and the graph contains three vertices of degree Δ such that one of them is adjacent to the other two. So, from Proposition 2.3, we have $\lambda((P_4 \square P_2) \odot K_1) \geq \Delta+2=6$. Since a graph isomorf with $(P_4 \square P_2) \odot K_1$ is a subgraph of $(P_n \square P_2) \odot K_1$ for $n \geq 4$, so from Proposition 2.1, we have

$$\lambda((P_n \square P_2) \odot K_1) \geq \lambda((P_4 \square P_2) \odot K_1) = 6 \text{ for } n \geq 4 \text{ .... } (3.5)$$

To show that $\lambda((P_n \square P_2) \odot K_1) \leq 6$ for $n \geq 4$, define an L(2,1)-labeling f of $(P_n \square P_2) \odot K_1$ as follows:

$$f(x_i) = \begin{cases} 0 \text{ if } i \equiv 6 \pmod 7; \\ 1 \text{ if } i \equiv 4 \pmod 7; \\ 2 \text{ if } i \equiv 2 \pmod 7; \\ 3 \text{ if } i \equiv 0 \pmod 7; \\ 4 \text{ if } i \equiv 5 \pmod 7; \\ 5 \text{ if } i \equiv 3 \pmod 7; \\ 6 \text{ if } i \equiv 1 \pmod 7; \end{cases} \quad f(v_i) = \begin{cases} 0 \text{ if } i \equiv 2 \pmod 7; \\ 1 \text{ if } i \equiv 0 \pmod 7; \\ 2 \text{ if } i \equiv 5 \pmod 7; \\ 3 \text{ if } i \equiv 3 \pmod 7; \\ 4 \text{ if } i \equiv 1 \pmod 7; \\ 5 \text{ if } i \equiv 6 \pmod 7; \\ 6 \text{ if } i \equiv 4 \pmod 7; \end{cases} \quad f(w_i) = \begin{cases} 0 \text{ if } i \equiv 5 \pmod 7; \\ 1 \text{ if } i \equiv 3 \pmod 7; \\ 2 \text{ if } i \equiv 1 \pmod 7; \\ 3 \text{ if } i \equiv 6 \pmod 7; \\ 4 \text{ if } i \equiv 4 \pmod 7; \\ 5 \text{ if } i \equiv 2 \pmod 7; \\ 6 \text{ if } i \equiv 0 \pmod 7; \end{cases} \quad f(y_i) = \begin{cases} 0 \text{ if } i \equiv 1 \pmod 7; \\ 1 \text{ if } i \equiv 6 \pmod 7; \\ 2 \text{ if } i \equiv 4 \pmod 7; \\ 3 \text{ if } i \equiv 2 \pmod 7; \\ 4 \text{ if } i \equiv 0 \pmod 7; \\ 5 \text{ if } i \equiv 5 \pmod 7; \\ 6 \text{ if } i \equiv 3 \pmod 7. \end{cases}$$

The labeling f is an L(2,1)-labeling f of $(P_n \square P_2) \odot K_1$ with the maximum label 6. So that, we have

$$\lambda((P_n \square P_2) \odot K_1) \leq 6 \text{ for } n \geq 4 \text{ .... } (3.6)$$

From (3.5) and (3.6), we conclude that $\lambda((P_n \square P_2) \odot K_1) = 6$ for $n \geq 4$.

4. CONCLUSIONS

In section 3, we define an L(2,1)-labeling f of $(P_2 \square P_2) \odot K_1$ and an L(2,1)-labeling f of $(P_3 \square P_2) \odot K_1$ with the maximum label 5. We also define an L(2,1)-labeling f of $(P_n \square P_2) \odot K_1$ for $n \geq 4$ with the maximum label 6. So, we have $\lambda((P_n \square P_2) \odot K_1) \leq 5$ for $n \in \{2,3\}$ and $\lambda((P_n \square P_2) \odot K_1) \leq 6$ for $n \geq 4$. In other hand, we use some propositions about L(2,1) labeling number given in Section 2 such that we have $\lambda((P_n \square P_2) \odot K_1) \geq 5$ for $n \in \{2,3\}$ and $\lambda((P_n \square P_2) \odot K_1) \geq 6$ for $n \geq 4$. So that, we conclude that $\lambda((P_n \square P_2) \odot K_1) = 5$ for $n \in \{2,3\}$ and $\lambda((P_n \square P_2) \odot K_1) = 6$ for $n \geq 4$.

5. REFERENCES

[1] G. Chang and D. Kuo, (1996), The L(2,1)-labeling problem on graphs, *SIAM J.Discrete Math*. **9(2)**, 309-316.

[2] J. Griggs and R. Yeh, (1992), Labeling graphs with a condition at distance 2, *SIAM J.Discrete Math.* **5**, 586-595.

[3] P. Jha, (2001), Optimal L(2, 1)-labeling of strong products of cycles, *IEEE Trans-actions on Circuits and System-1: Fundamenal Theory and Applications* **48(4)**, 498-500.

Indonesia Life Table Derivation Based On Indirect Estimation Data with Logit Model Life Table System

Stephen[1*], Helena Margaretha[1], Ferry Vincenttius Ferdinand[1]

[1] Department of Applied Mathematics, Faculty of Science and Technology, Universitas Pelita Harapan, Tangerang, Indonesia
* Corresponding authors: stephen2703.sx@gmail.com

Abstract – In this paper, we discuss how to derived a Life Table for Indonesia population using data from indirect estimation method. We also conduct a Life Table comparison and hypothesis testing between our derived Life Table and WHO 1999 Life Table also 2000 Indonesia Life Table.

1. INTRODUCTION

Life Table can be defined as a table of numerical values of $S_X(x)$ (the survive probability) for a certain value of x [1]. The rapid growth of insurance industry allows actuaries to use the Life Table to calculate most of typical actuarial terminologies such as death probability, complete life expectation at birth and survival probability. Although there is a limitation of data [2], it's important to regularly update the Life Table since its many functions. This paper offers a method to construct the Life Table by Indirect Estimation with Logit Model Life Table System.

The main idea of Logit Model Life Table System is one can derive a new Life Table using another existing Life Table (Standard Life Table) [3]. The new Life Table and the Standard Life Table is related to Linear System with special Logit Transformation. In this Linear System, our input is child mortality estimation, adult mortality estimation and a list of Logit value of existing Life Table. So in order to use Logit Model Life Table System, child and adult mortality estimation will be essential. We're using an Indirect Estimation Method to obtain this terminology.

2. METHODS

2.1 Indirect Estimation Method

2.1.1 Child Mortality

Child mortality estimation was calculated using Brass Method Trussel Version which is expressed by the following equation

$$q\big(x(i)\big) = k(i)D(i)$$

where $q\big(x(i)\big)$ define child mortality for group i, $k(i)$ define a constant term with different value depends on the chosen Standard Life Table and $D(i)$ define the proportion of death child in each group i. $D(i)$ is expressed by the following equation

$$D(i) = \frac{CD(i)}{CEB(i)}$$

$CD(i)$ stands for a number of children had died at group i, and $CEB(i)$ stands for a number of child ever born in group i. $k(i)$ is expressed by the following equation

$$k(i) = a(i) + b(i)\frac{P(1)}{P(2)} + c(i)\frac{P(2)}{P(3)}$$

the value of $a(i)$, $b(i)$ and $c(i)$ can be obtained from [2] and it depends on the chosen Standard Life Table. $P(1)$, $P(2)$and $P(3)$ or in general $P(i)$ define the average parity of women in age group i and expressed by the following equation

$$P(i) = \frac{CEB(i)}{FP(i)}$$

where $FP(i)$ stands for total number of women in age group i.

Since we're using an indirect estimation mether, there is also a terminology called Reference Year which means the actual year that our mortality estimation is valid, expressed as

$$Reference\ Year = Survey\ Year - t\big(x(i)\big)$$

$$t\big(x(i)\big) = d(i) + e(i)\frac{P(1)}{P(2)} + f(i)\frac{P(2)}{P(3)}$$

$d(i)$, $e(i)$ and $f(i)$ are constants, have different value depends on chosen Standard Life Table and its value can be obtain from [2].

2.1.2 Adult Mortality

Adult mortality estimation is calculate using Brass Method which is expressed by the following equation

$${}_{n}p_{25} = \frac{l(25+n)}{l(25)} = W(n)S(n-5) + \big(1 - W(n)\big)S(n)$$

${}_{n}p_{25}$ define an adult mortality estimation for each value of n, $W(n)$ defines a weighting factor and $S(n)$ defines a proportion of children that have a mother. In order to calculate $W(n)$, we have to calculate the mean age at maternity M which is expressed by

$$M = \frac{\sum_{i=1}^{7} a(i)B(i)}{\sum_{i=1}^{7} B(i)}$$

$a(i)$ means the median age of group age i and $B(i)$ means total number of birth from group age i. The value of $W(n)$ with M is integer available in [4], otherwise we need to calculate $W(n)$ as follows

$$\theta = \frac{\lceil M \rceil - M}{\lceil M \rceil - \lfloor M \rfloor}$$

$$W(n) = \theta W(n)|_{M=\lfloor M \rfloor} + (1-\theta)W(n)|_{M=\lceil M \rceil}$$

then, $S(n)$ or $S(n-5)$ can be calculated as follows

$$S(n) = \frac{number\ of\ child\ without\ mother, age\ n\ until\ n+4}{total\ number\ of\ child, age\ n\ until\ n+4}$$

Just like the previous child mortality, we also have Reference Year for adult mortality estimation which is expressed by the following equation

$$Reference\ Year = Survey\ Year - t(n)$$

$$t(n) = \frac{n\big(1 - u(n)\big)}{2}$$

$$u(n) = 0.3\ln(\ {}_{10}S_{n-5}) + Z(M+n) + 0.0037(27 - M)$$

${}_{10}S_{n-5}$ stands for proportion of number of children with age $n-5$ until $n+4$ which have mother with total of children with age $n-5$ until $n+4$ and $Z(M+n)$ is a Standard Function with available value at [4] for M is the element of integer, otherwise we need to calculate $Z(M+n)$ as follows

$$Z(M+n) = \theta Z(\lfloor M+n \rfloor) + (1-\theta)Z(\lceil M+n \rceil)$$

with the same value of θ as before.

2.2 Life Table Derivation

In order to derive a Life Table after we got the child and adult mortality, we need to determine our target year D. Then we will be using the system of

$$\begin{cases} Y(x) = \alpha + \beta Y^{s}(x) \\ Y(x) = logit\big(l(x)\big) = \frac{1}{2}\ln\left(\frac{1-l(x)}{l(x)}\right) = -\frac{1}{2}\ln\left(\frac{1-q(x)}{q(x)}\right) \end{cases}$$

with $Y(x)$ stands for the value of logit $l(x)$, α and β are the model parameters. Now to estimate the parameter, we will be using iteration technique with the following equations

$$\alpha^{child} = Y(x) - Y^{s}(x)$$

in the first iteration, β is equal to 1 then we proceed with Least Square Method and fill this equation

$$\alpha^{*} = Z(\alpha) + DS(\alpha)$$

To estimate β we will use the following equations

$$\beta = \frac{Y(60) - Y(15)}{Y^s(60) - Y^s(15)}$$

$$Y(15) = \alpha^* + \beta Y^s(15)$$

$$Y(60) = -\frac{1}{2}\ln\left(\frac{l(15)_{45}p_{15}}{1 - l(15)_{45}p_{15}}\right)$$

$$l(15) = \frac{1}{1 + \exp\big(2Y(15)\big)}$$

$${}_{45}p_{15} = \frac{1 + \exp\Big(2\big(\alpha^{adult} + \beta Y^s(15)\big)\Big)}{1 + \exp\Big(2\big(\alpha^{adult} + \beta Y^s(60)\big)\Big)}$$

$$\alpha^{adult} = \frac{1}{2}\ln\left(\frac{1 - {}_n p_x}{{}_n\, p_x \exp\big(2Y^s(x+n)\big) - \exp\big(2Y^s(x)\big)}\right)$$

then perform the Least Square Method to fill this equation

$$\beta^* = Z(\beta) + DS(\beta)$$

For the next iteration, we need to calculate the new α^{child} with the following equation

$$\alpha^{child} = logit(q_x) - \beta^* Y^s(x)$$

with $Y^s(x)$ stands for logit value of Standard Life Table. Its value can be obtained from http://demographicestimation.iussp.org/

2.3 Life Table Comparison & Hypothesis Testing

In order to verify our Life Table credibility, we conduct a comparison with the previous Indonesia Life Table such as WHO 1999 Life Table [5] and the 2000 Indonesia Life Table by Kosen et al [2]. We also perform a hypothesis testing with these Life Table. We used Kolmogorov-Smirnov 2 Sample Independent Test under the null hypothesis : Both Life Table are derive from the same population data.

3. RESULTS AND DISCUSSION

Here are the result from this paper

- Child Mortality Estimation
  Child mortality shows a fluctuation between age 1 – 3. This is due to common symptoms of human behavior pattern. See Table 1.
- Adult Mortality Estimation
  Adult mortality start increasing from $n = 25$ until $n = 45$. This is due to the data we're using. It's not a cohort population data. See Table 1.
- Life Table
  Logit Model Life Table System provides a credible Life Table only for the first 60 ages. Our derived Life Table shows a first significant decrease at age 50 which indicate that complete life expectation at birth for Indonesia population fall at age above 50. See Table 2.
- Life Table Comparison
  Our Life Table shows a similar mortality pattern with WHO 1999 Indonesia Life Table. The average of $l(x)$ value deviation is 4241. Our Life Table shows a slight similarity mortality pattern with the 2000 Indonesia Life Table with the average of $l(x)$ value deviation about 5619.
- Hypothesis Testing
  Under the null hypothesis of both of life table are derive form the same population data, we perform Kolmogorov-Smirnov 2 Sample Independent Test. The result shows that our Life Table are derive from the same population data with 1999 WHO Life Table and the 2000 Indonesia Life Table each with 0.01 significance level. The test statistic for 1999 WHO Life Table test is $36\ (< 180)$ and test statistic for the 2000 Indonesia Life Table is $48 (< 160)$.

5. CONCLUSIONS

We have derived the 2012 Indonesia Life Table using Logit Model Life Table System .

Table 1 Child and Adult Mortality

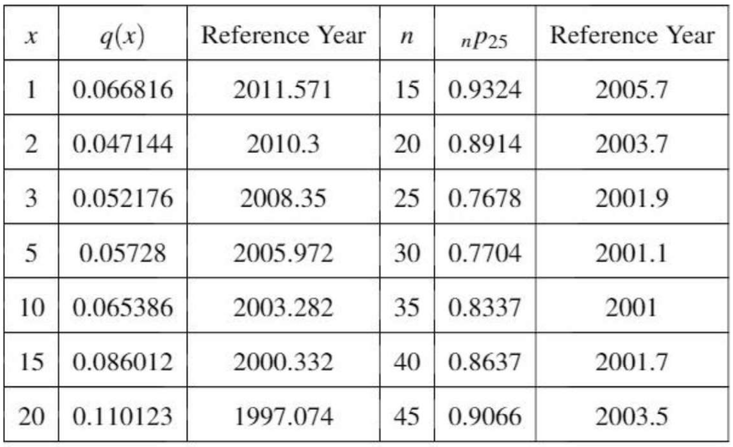

x	$q(x)$	Reference Year	n	${}_{n}p_{25}$	Reference Year
1	0.066816	2011.571	15	0.9324	2005.7
2	0.047144	2010.3	20	0.8914	2003.7
3	0.052176	2008.35	25	0.7678	2001.9
5	0.05728	2005.972	30	0.7704	2001.1
10	0.065386	2003.282	35	0.8337	2001
15	0.086012	2000.332	40	0.8637	2001.7
20	0.110123	1997.074	45	0.9066	2003.5

Table 2 Indonesia 2012 Life Table

x	l(x)
0	1
1	0.95681023
2	0.95025552
3	0.947431729
4	0.945553066
5	0.944222578
10	0.940336061
15	0.937843522
20	0.934174851
25	0.92922768
30	0.923576144
35	0.917079264
40	0.909446648
45	0.900408585
50	0.888868968
55	0.872702867
60	0.848874371

6. REFERENCES

[1]. Cunningham, R., Herzog, T., and London. R. L. *Models for Quantifying Risks.* ACTEX Publications, Inc., 2006

[2]. Kosen, S., Soemantri, S., and Agung, I. N., eds. *The 2000 Indonesia Life Table*. 2002.

[3]. Moultrie, T., Dorrington, R., Hill, A., eds. *Tools for Demographic Estimation.* International Union for the Scientific Study of Population, 2013.

[4]. United Nations, *Manual X : Indirect Techniques for Demographic Estimation.* United Nations Publication, 1983.

[5]. Lopez, A. D., Salomon, J., eds. *Life Table for 191 Countries : Data, Methods, and Results.* 2000

Semiparametric Mixed Model for Small Area Estimation under Informative Sampling

Angela Nina R. C.[1*], Sri Haryatmi[2], Danardono[2]

[1]Student of Department of Mathematics, Faculty of Science and Mathematics, University of Gadjah Mada, Yogyakarta, Indonesia
[1]Departement of Mathematics Education, Faculty of Teaching and Education, University of Pancasakti Tegal, Tegal, Indonesia
[2]Department of Mathematics, Faculty of Science and Mathematics, University of Gadjah Mada, Yogyakarta, Indonesia
* Corresponding authors: [angela.nina.r@mail.ugm.ac.id]

Abstract – Small area estimation has received attention due to growing demand for reliable small estimators and has been extensively studied under unit level linear mixed model. Under informative sampling design, model holding the sample may differ from model holding in the population. Ignoring an informative sample may lead to erroneous inference. On the other hand, the function of the parametric mean model may restrictive in practice. This paper describes a concept idea to obtain an estimator of mean small area using nested error regression model approach under informative sampling with parametric mean function that can not be predetermined. The sample model in this paper is extended by adding a function of unit selection probability as an auxiliary variable to account the informativeness. Mean model and the extended term are approached then with a nonparametric function respectively. By using penalized splines as the representation of the nonparametric term in the model, it is possible to express the small area estimation problem as a mixed effect regression model. Estimation of model parameters was derived by Henderson's method. The estimation of variance components of the model was derived by using moment approach. Mean square prediction error of mean area prediction was derived by using a bootstrap method.

1. INTRODUCTION

Sample surveys have been used widely to produce estimates for the quantity of observed population or subpopulation (domain). The term of a small area is used in statistics to denote the population domain where the sample domain is not large enough to produce a direct estimation for domains with adequate precision. Suppose that the population of interest consists of M non-overlapping areas (as small area) with N_i elements in the i^{th} area, $i = 1, ..., M$. By using a specified sampling scheme with inclusion probabilities π_i , m number of areas are selected first. Subsamples of specified sizes n_i are then independently selected from the sampled areas i with inclusion probabilities $\pi_{j|i}$.

An indirect estimator, i.e. estimator based on a model, often used in small area estimation to obtain sufficient precision. In this paper, it assumed that y_{ij} based on covariate $\boldsymbol{x}_{ij}$ follows a nested error regression model [4],

$$y_{ij} = \mathbf{x}'_{ij}\beta + v_i + e_{ij}, \qquad . \ i = 1, \ldots, M \ ; j = 1, \ldots, N_i. \qquad (1)$$

Where $\boldsymbol{x}'_{ij}$ is model covariate, β is a vector of coefficients of regression, v_i stating the effect of small random area that calculates variations in y that is not explained by the covariate variables and e_{ij} stating the error unit. It is often assumed that $v_i \overset{iid}{\sim} N(0, \sigma_v^2)$ and $e_{ij} \overset{iid}{\sim} N(0, \sigma_e^2)$.

In practice, the functional relationships between the observed variable and covariate variables may not be predetermined, so the nonparametric approach is required. One way of nonparametric approach that can be used is penalized spline regression approach (p-spline). [3] stated that p-spline has a close link with the linear mixed model, so p-spline is also a naturally nonparametric approach for the establishment of small area estimators. On the other hand, efficient model-based estimators may be obtained if the sampling design is noninformative for the model, which implies that the sample and the population models coincide, [2]. Data used in applications often result from informative sampling design, that is the complex sampling design with correlation between the inclusion probability and the observed outcome variable. A correlation between inclusion probability and observed variable must be considered in the process of inference. Failure to take into account or ignoring the effects of informativeness sample inference can lead to poor inference results by obtaining biased estimates [1], [6], [7].

This paper describes the concept of the idea of obtaining an estimator for the average small area, $\overline{Y}_i$, under informative sampling designs using nested error regression model approach where the mean function in model can not be predetermined. Nested error regression model in this paper expanded by adding a function of inclusion probability of unit j in area i, $g(\pi_{j|i})$, as covariates to reduce the effects of informativeness sampling. In this paper, additional parts and mean functions in the model will be approached by p-spline function.

2. METHODS

Estimator for fixed effects and predictors for the random effects in the model obtained by determine a solution for Henderson mixed model equations. The variance components of model will be estimated using restricted maximum likelihood estimators and estimation accuracy is determined by a bootstrap mean square prediction error.

3. RESULTS AND DISCUSSION

The focus of this paper is a case when m = M and the probabilities $\pi_{j|i}$ may be related to the associated y_{ij} even after conditioning on the covariates x_{ij}. Set a augmented sample model as

$$y_{ij} = \boldsymbol{x}_{ij}\gamma + g(\pi_{j|i})\alpha + v_i + e_{ij}, \qquad i = 1,\ldots, m; \quad j = 1,\ldots, n_i . \tag{2}$$

with unknown coefficients α. [2] determined $g(\pi_{j|i})$ by choosing one suitable function from three possible choices. In this paper, it is assumed that $\boldsymbol{x}_{ij}\gamma$ and $g(\pi_{j|i})\alpha$ in the model are unknown smooth functions and can be approximated by a p-spline function respectively. Also, $\boldsymbol{x}_{ij} = (1, x_{ij})$. In the form of a p-spline mixed model, (2) can be expressed by

$$y_{ij} = \beta_0 + \sum_{k=1}^{p}\beta_k x_{ij}^k + \sum_{k=1}^{K_1} t_k (x_{ij} - q_k)_+^p + \sum_{k=1}^{p}\delta_k \pi_{ij}^k + \sum_{k=1}^{K_2} r_k (\pi_{ij} - Q_k)_+^s + v_i + e_{ij} \tag{3}$$

with p and s are respectively the order p-spline for $\mathbf{x}'\boldsymbol{\beta}$ and $g(\pi_{j|i})\alpha$; β_0 is a constants; β_k and δ_k are respectively a row of vector coefficients of the parametric for $\boldsymbol{x}'\beta$ and $g(\pi_{j|i})\alpha$; t_k and r_k are respectively vector of coefficients of the spline for $\boldsymbol{x}'\beta$ and $g(\pi_{j|i})\alpha$; $q_1 < \cdots < q_{K_1}$ and $Q_1 < \cdots < Q_{K_2}$ are respectively a row of knots in $\boldsymbol{x}$ and $\pi_{j|i}$.

In matrix notation, (3) can be written as

$$\mathbf{y} = \mathbf{Uw} + \mathbf{Ct} + \mathbf{Dr} + \mathbf{Zv} + \mathbf{e}. \tag{4}$$

where $\mathbf{y} = \underset{1\le i\le m}{\mathrm{col}}(\mathbf{y}_i)$ and $\mathbf{y}_i = \begin{bmatrix} y_{i1} & \cdots & y_{in_i} \end{bmatrix}'$; $\mathbf{U} = [\mathbf{x} \vdots \pi]$ where $\mathbf{x} = \underset{1\le i\le m}{\mathrm{col}}(\mathbf{x}_i)$, $\mathbf{x}_i$ is n_i x (1+p) matrix with rows $x_{ij} = \begin{bmatrix} 1 & x_{ij} & \cdots & x_{ij}^p \end{bmatrix}'$, $\boldsymbol{\pi} = \underset{1\le i\le m}{\mathrm{col}}(\boldsymbol{\pi}_i)$, $\boldsymbol{\pi}_i$ is n_i x s matrix with rows $\pi_{ij} = \begin{bmatrix} \pi_{ij} & \cdots & \pi_{ij}^s \end{bmatrix}$; $\mathbf{w} = [\boldsymbol{\beta}' \vdots \boldsymbol{\delta}']'$ where $\boldsymbol{\beta} = \begin{bmatrix} \beta_0 & \cdots & \beta_p \end{bmatrix}'$, $\boldsymbol{\delta} = \begin{bmatrix} \delta_1 & \cdots & \delta_s \end{bmatrix}'$; $\mathbf{t} = \begin{bmatrix} t_1 & \cdots & t_{K_1} \end{bmatrix}'$; $\mathbf{r} = \begin{bmatrix} r_1 & \cdots & r_{K_2} \end{bmatrix}'$; $\mathbf{C} = \underset{1\le i\le m}{\mathrm{col}}(\mathbf{C}_i)$ and $\mathbf{C}_i$ is n_i x K_1 matrix with rows $\mathbf{C}_{ij} = \begin{bmatrix} (x_{ij} - q_1)_+^p & \cdots & (x_{ij} - q_{K_1})_+^p \end{bmatrix}$; $\mathbf{D} = \underset{1\le i\le m}{\mathrm{col}}(\mathbf{D}_i)$ where $\mathbf{D}_i$ is n_i x K_2 matrix with rows $\mathbf{D}_{ij} = \begin{bmatrix} (\pi_{ij} - Q_1)_+^p & \cdots & (\pi_{ij} - Q_{K_2})_+^p \end{bmatrix}$; $\mathbf{Z} = \underset{1\le i\le m}{\mathrm{diag}}(\mathbf{Z}_i)$ where $\mathbf{Z}_i = \mathbf{1}_{n_i}$; $\mathbf{v} = \begin{bmatrix} v_1 & \cdots & v_m \end{bmatrix}'$; $\mathbf{e} = \underset{1\le i\le m}{\mathrm{col}}(\mathbf{e}_i)$ and $\mathbf{e}_i = \begin{bmatrix} e_{i1} & \cdots & e_{in_i} \end{bmatrix}'$. Assumed, $\mathbf{t} \overset{\mathrm{iid}}{\sim} N(0, \mathbf{G}_1)$, $\mathbf{r} \overset{\mathrm{iid}}{\sim} N(0, \mathbf{G}_2)$, $\mathbf{v} \overset{\mathrm{iid}}{\sim} N(0, \mathbf{G}_3)$ where $\mathbf{G}_1 = \sigma_t^2 \mathbf{I}_{K_1}$, $\mathbf{G}_2 = \sigma_r^2 \mathbf{I}_{K_2}$, $\mathbf{G}_3 = \sigma_v^2 \mathbf{I}_m$, $\mathbf{G}_4 = \sigma_e^2 \mathbf{I}_n$, $n = \sum_{i=1}^{m} n_i$. It is also assumed that **t**, **r**, **v**, and **e** are mutually independent.

Henderson's mixed model equations obtained by assuming $\mathbf{(y\,|\,t, r, v)} \lrcorner \mathrm{N}\mathbf{(Uw+Ct+Dr+Zv, G_4)}$. The logarithmic function for the joint density of **y**, **t**, **r**, **v** is

$$\log \mathbf{f} = -\tfrac{1}{2}\{(\mathbf{y - Uw - Ct - Dr - Zv})'\,\mathbf{G}_4^{-1}(\mathbf{y - Uw - Ct - Dr - Zv}) \\ + \mathbf{t}'\mathbf{G}_1^{-1}\mathbf{t} + \mathbf{r}'\mathbf{G}_2^{-1}\mathbf{r} + \mathbf{v}'\mathbf{G}_3^{-1}\mathbf{v}\}^{\cdot} \tag{5}$$

Derived (5) against **w**, **t**, **r**, and **v** respectively, and then equated with zero lead to Henderson's model equation,

$$\begin{bmatrix} \mathbf{U'G_4^{-1}U} & \mathbf{U'G_4^{-1}C} & \mathbf{U'G_4^{-1}D} & \mathbf{U'G_4^{-1}Z} \\ \mathbf{C'G_4^{-1}U} & \mathbf{C'G_4^{-1}C+G_1^{-1}} & \mathbf{C'G_4^{-1}D} & \mathbf{C'G_4^{-1}Z} \\ \mathbf{D'G_4^{-1}U} & \mathbf{D'G_4^{-1}C} & \mathbf{D'G_4^{-1}D+G_2^{-1}} & \mathbf{D'G_4^{-1}Z} \\ \mathbf{Z'G_4^{-1}U} & \mathbf{Z'G_4^{-1}C} & \mathbf{Z'G_4^{-1}D} & \mathbf{Z'G_4^{-1}Z+G_3^{-1}} \end{bmatrix} + \begin{bmatrix} \hat{\mathbf{w}} \\ \hat{\mathbf{t}} \\ \hat{\mathbf{r}} \\ \hat{\mathbf{v}} \end{bmatrix} = \begin{bmatrix} \mathbf{U'G_4^{-1}y} \\ \mathbf{C'G_4^{-1}y} \\ \mathbf{D'G_4^{-1}y} \\ \mathbf{Z'G_4^{-1}y} \end{bmatrix} \tag{6}$$

The obvious advantage computationally of (6) is that no need to calculate the inverse matrix of y which has the order nxn. Related inverse calculation are $\mathbf{G}_1^{-1}, \mathbf{G}_2^{-1}, \mathbf{G}_3^{-1}, \mathbf{G}_4^{-1}$ but these are diagonal matrix.

Estimator for **w**, and predictors for **t**, **r**, and **v** are obtained simultaneously by solving the Henderson's model equation, that is

$$\begin{bmatrix} \hat{\mathbf{w}} \\ \hat{\mathbf{t}} \\ \hat{\mathbf{r}} \\ \hat{\mathbf{v}} \end{bmatrix} = \mathbf{J} \begin{bmatrix} \mathbf{U'G_4^{-1}y} \\ \mathbf{C'G_4^{-1}y} \\ \mathbf{D'G_4^{-1}y} \\ \mathbf{Z'G_4^{-1}y} \end{bmatrix} = \begin{bmatrix} \mathbf{H}_1' \\ \mathbf{H}_2' \\ \mathbf{H}_3' \\ \mathbf{H}_4' \end{bmatrix} \mathbf{y}. \tag{7}$$

where **J** is an inverse of coefficients matrix**,**

$$\mathbf{J} = \begin{bmatrix} \mathbf{U'G_4^{-1}U} & \mathbf{U'G_4^{-1}C} & \mathbf{U'G_4^{-1}D} & \mathbf{U'G_4^{-1}Z} \\ \mathbf{C'G_4^{-1}U} & \mathbf{C'G_4^{-1}C+G_1^{-1}} & \mathbf{C'G_4^{-1}D} & \mathbf{C'G_4^{-1}Z} \\ \mathbf{D'G_4^{-1}U} & \mathbf{D'G_4^{-1}C} & \mathbf{D'G_4^{-1}D+G_2^{-1}} & \mathbf{D'G_4^{-1}Z} \\ \mathbf{Z'G_4^{-1}U} & \mathbf{Z'G_4^{-1}C} & \mathbf{Z'G_4^{-1}D} & \mathbf{Z'G_4^{-1}Z+G_3^{-1}} \end{bmatrix}^{-1}.$$

Following [5], by using the relationship

$$\mathbf{G}_4^{-1}\begin{bmatrix}\mathbf{U} & \mathbf{C} & \mathbf{D} & \mathbf{Z}\end{bmatrix}'\begin{bmatrix}\mathbf{U} & \mathbf{C} & \mathbf{D} & \mathbf{Z}\end{bmatrix} = \mathbf{J}^{-1} - \mathrm{diag}\begin{bmatrix}\mathbf{0} & \mathbf{G}_1^{-1} & \mathbf{G}_2^{-1} & \mathbf{G}_3^{-1}\end{bmatrix}'$$

and

$$\begin{bmatrix}\mathbf{H}_1 & \mathbf{H}_2 & \mathbf{H}_3 & \mathbf{H}_4\end{bmatrix}'\begin{bmatrix}\mathbf{U} & \mathbf{C} & \mathbf{D} & \mathbf{Z}\end{bmatrix} = \mathbf{J}^{-1} - \mathrm{diag}\begin{bmatrix}\mathbf{0} & \mathbf{G}_1^{-1} & \mathbf{G}_2^{-1} & \mathbf{G}_3^{-1}\end{bmatrix}',$$

it can be obtained that $\mathrm{E}(\hat{\mathbf{w}}) = \mathbf{w}$, $\mathrm{E}(\hat{\mathbf{t}} - \mathbf{t}) = 0$, $\mathrm{E}(\hat{\mathbf{r}} - \mathbf{r}) = \mathbf{0}$, $\mathrm{E}(\hat{\mathbf{v}} - \mathbf{v}) = \mathbf{0}$, in other words, $\hat{\mathbf{w}}, \hat{\mathbf{t}}, \hat{\mathbf{r}}, \hat{\mathbf{v}}$ are unbiased. Further, using (7) and along with $\mathrm{E}(\mathbf{t}\,|\,\mathbf{y}) = \mathbf{G}_1\mathbf{C}'(\mathbf{C}\mathbf{G}_1\mathbf{C}' + \mathbf{G}_4)^{-1}(\mathbf{y - Uw - Dr - Zv})$ it can be proved that $\hat{\mathbf{t}} = \mathrm{E}(\mathbf{t}\,|\,\mathbf{y})$, $\hat{\mathbf{r}} = \mathrm{E}(\hat{\mathbf{r}}\,|\,\mathbf{y})$ and $\hat{v} = \mathrm{E}(v\,|\,y)$, in other words $\hat{\mathbf{t}}$, $\hat{\mathbf{r}}$ and $\hat{\mathbf{v}}$ are the best predictor.

Further, using (7) and the relationship $\mathbf{JJ}' = \mathbf{I}$, it can be derived the fixed point equation,

$$\sigma_t^2 = \sum_{k=1}^{K_1} \frac{\hat{t}_k^2}{(K_1 - t_1)};\quad \sigma_r^2 = \sum_{k=1}^{K_2} \frac{\hat{r}_k^2}{(K_2 - t_2)};\quad \sigma_v^2 = \sum_{k=1}^{K_3} \frac{\hat{v}_k^2}{(m - t_3)}. \tag{8}$$

where $t_1 = \sigma_{\mathbf{t}}^{-2}\mathrm{tr}\,\mathbf{J}_{33}$, $t_2 = \sigma_{\mathbf{r}}^{-2}\mathrm{tr}\,\mathbf{J}_{44}$, $t_3 = \sigma_{\mathbf{v}}^{-2}\mathrm{tr}\,\mathbf{J}_{55}$. By using the similar way with $\hat{\mathbf{e}} = \mathbf{y} - \mathbf{U}\hat{\mathbf{w}} - \mathbf{C}\hat{\mathbf{t}} - \mathbf{D}\hat{\mathbf{r}} - \mathbf{Z}\hat{\mathbf{v}} = [\mathbf{I}_n - \sigma_e^2\mathbf{MJM}']\,\mathbf{y}$ where $\mathbf{M} = \begin{bmatrix}\mathbf{U} & \mathbf{C} & \mathbf{D} & \mathbf{Z}\end{bmatrix}$, it can be found that

$$\sigma_e^2 = \sum_{k=1}^{K_1} \frac{\hat{e}_k^2}{(n - t_4)},. \tag{9}$$

where $t_4 = \sigma_{\mathbf{e}}^{-2}\mathrm{tr}\,\mathbf{MJM}'$. Estimation for the components of variance $\hat{\theta} = (\sigma_t^2, \sigma_r^2, \sigma_v^2, \sigma_e^2)$ can be count iteratively using (8) and (9), with the following steps: Specifies the initial value for the variance components;

determining and using the (7); counting each right side of (8) and (9) using the results of the second step to obtain the latest value; repeating the third step to obtain a convergent value estimator. Values were then substituted in (7) to obtain empirical estimations and predictions for **u** and predictors for **t**, **r**, **v**.

Predictor for $\overline{Y}_i$ calculated by $\overline{Y}_i = \frac{1}{N_i}\left\{\sum_{i\in s} y_{ij} + \sum_{i\in \overline{s}} \hat{y}_{ij}\right\}$. Mean square prediction error for $\overline{Y}_i$ calculated by step as follows: generate random variable values of **t**, **r**, **v** and **e** from normal distributions respectively with mean **0** and variance $\hat{\theta}$; obtain bootstrap response y^*_{ij}; $j = 1,\cdots,N_i$; $i = 1,\cdots, m$ using results from (7) and the first step; obtain bootstrap estimates for fixed and random effect using the corresponding bootstrap sample data y^*_{ij} and x_{ij}; $j \in s_i$, $i = 1,\cdots,m$; obtain the predicted value $\hat{y}_{ij}$ for $j \in \overline{s}_i$; calculating bootstrap empirical predictions for $\overline{Y}_i$ by $\tilde{Y}^*_i = \frac{1}{N_i} = \{\sum_{j\in s_i} y_{ij} + \sum_{j\in \overline{s}_i} y^*_{ij}\}$ and bootstrap mean population using $\overline{Y}^*_i = N_i^{-1}\sum_{j=1}^{j=N_i} y_{ij}$; repeating the bootstrap operation B times; obtain bootstrap MSPE for $\overline{Y}_i$ using $\hat{M}_{boot}(\tilde{Y}_i) = \frac{1}{B}\sum_{b=1}^{B}\{\tilde{Y}^*_i(b) - \overline{Y}^*_i(b)\}^2$.

4. CONCLUSIONS

The approach in this paper, as a starting study, may develop to resolve small area estimation in a model-based framework under informative sampling. The close link between p-spline and mixed model enable to solve spline mixed model in the mixed model framework. This mixed model simultaneously generates a best linear unbiased estimator for **w**, namely for **β** and **δ**, and best linear unbiased predictors for **t**, **r** and **v**. Further study to analyze the significance of the addition of the function $g(\pi_{j|i})$ in the model to reduce the effect of informativeness be required.

5. REFERENCES

[1]. C. J. Skinner, D. Holt and T. M. F. Smith, 1989, **Analysis of Complex Surveys**, Wiley and Sons, New York.

[2]. F. Verret, J. N. K. Rao, M. A. Hidiroglou, 2015, *Survey Methodology*, **41**, 333-347.

[3]. J. D. Opsomer, F. J. Breidt, S. G. Claensken, G. Kauermann and M. G. Ranalli, 2008, *Journal of the Royal Statistical Society Series B*. **70**, 265-286.

[4]. J. N. K Rao, 2003, **Small Area Estimation**, John Wiley and Sons, Inc., New Jersey.

[5]. J. N. K Rao, S. K. Sinha and L. Dumitrescu, 2014, *The Canadian Journal of Statistics,* **42**, 126-141.

[6]. J. P. Burgard, T. Zimmermann, 2014, *Journal of Official Statistics*, **30,** 749-771.

[7]. L. E. Chambless and K. E. Boyle, 1985, *Communications in Statistics Theory and Methods*, **14**,1377-1392.

The Influences of Weber Trench to Tsunami Simulation in Banda Sea

Nisrina Ikbar Rahmawati[1*], Bagus Jaya Santosa[1], Wiko Setyonegoro[2], Supriyanto Rohadi[2], Urip Haryoko[2]

[1]Fisika, Faculty of Mathematics and Science, Institut Teknologi Negeri Sepuluh Nopember, Surabaya, Indonesia
[2]Research and Development Center, Meteorological Climatological and Geophysical Agency, Jl. Angkasa I No.2 Kemayoran Jakarta Pusat 10720
*Corresponding authors: [nara.rina@gmail.com, wiko.setyonegoro@bmkg.go.id]

Abstract-The tsunami modeling in Banda Sea had conducted with aim to answer hypothesis of influences the weber trench to tsunami modeling. Due to tsunami propagation, bathymetri data is the main influences parameter, and we probably knowing and obtains the answer of weber trench as an extreem bathymetri with has a large influences to tsunami modeling. The methode in this research is to identify the maximum run-up area which it affected around Banda Sea. We do also ocean modeling with tsunami travel time to indicate the accumulation of maximum tsunami height in the ocean. The result is obtain by result of models and references that maximum tsunami height has accumulated in "Thiel (Tual) which the nearest affected area from the weber trench. The ratio potentially of maximum flooded up to 15.806% and amounted to 84.194% safe from inundation in Buru Island. In the figure 4 is probably the main key to explained the hypothesis that in the minutes 48 the tsunami height and run up increasing again after obtain the accumulation energy from weber trench, where in the previous tsunami propagation (in the minutes 29) the tsunami height it has a minimum wave.

1. INTRODUCTION

Increased frequency of tsunamis occurence in Indonesia is quite a lot, especially in the eastern part of Indonesia. Complexity of tectonic structure in this area holds large potential tsunami, as in research of (Puspito, 2007) shows the characteristics of the earthquake generating tsunami in Indonesia is 67% happen in the eastern part of Indonesia. Recent studies prove there is Indonesia's deepest trench in Banda Sea, Maluku with the depth of 7.2 kilometers and has size of 120 kmx450 km. Trench was a fault zone formed from a giant plate collision (megathrust) Australia and Asia which has a massive earthquake and tsunami threat. As events crushes Seram Island and Ambon in 1674. From the analysis of events in 1674, needs to be created scenario tsunami that occurred in the Banda Sea and surrounding area, especially around the Weber trench. Mass conservation equation of tsunami (Equation 1, equation 2 and equation 3) (Nakamura, M. 2006).

$$\frac{\partial \eta}{\partial t}+\frac{\partial M}{\partial x}+\frac{\partial N}{\partial y}=0 \tag{1}$$

Momentum equation of tsunami propagation (Nakamura, M. 2006).

$$\frac{\partial M}{\partial t}+\frac{\partial}{\partial x}\left(\frac{M^2}{D}\right)+\frac{\partial}{\partial y}\left(\frac{MN}{D}\right)+gD\frac{\partial \eta}{\partial x}+\frac{gn^2}{D^{7/3}}M\sqrt{M^2+N^2}=0 \tag{2}$$

$$\frac{\partial N}{\partial t}+\frac{\partial}{\partial x}\left(\frac{MN}{D}\right)+\frac{\partial}{\partial y}\left(\frac{N^2}{D}\right)+gD\frac{\partial \eta}{\partial y}+\frac{gn^2}{D^{7/3}}N\sqrt{M^2+N^2}=0 \tag{3}$$

h : vertical displacement of water surface above the still water surface.

D : total water depth (D= h +h), g : gravitational acceleration, x, y : horizontal axes.

t : time, M, N : discharge fluxes in the x- and y- directions, n : Coefficient of bottom friction.

Purposes of Study

1. Create a simulation of tsunami in Banda sea, including source modeling, ocean modeling and run-up and inundation modeling.

2. Make analysis and hyphotesis that weber trench is has influences to propagation of ocean modeling, run-up and inundation modeling in related with affected area in the coasline.

2. METHODOLOGY

Bathymetrical data etopo2 in Maluku area (Banda Sea) obtain from web address for downloading Bathymetri data Etopo 2 through Global Mapper. 2017. Data fochal mechanism of the earthquake that occurred around trench Weber dated March 19, 2001 based on three scenarios earthquake event sources by using simulation software tsunami L-2008 Setyonegoro, W. 2011, to map the regions affected by the tsunami. For the length and width parameters and fault slip is obtained based on the relationship between the empirical formula Papazachos, et al, 2004, Hank and Kanamori, 1979, and Wells, DL, & Coppersmith, KJ, 1994 (figure 1).

3. RESULTS

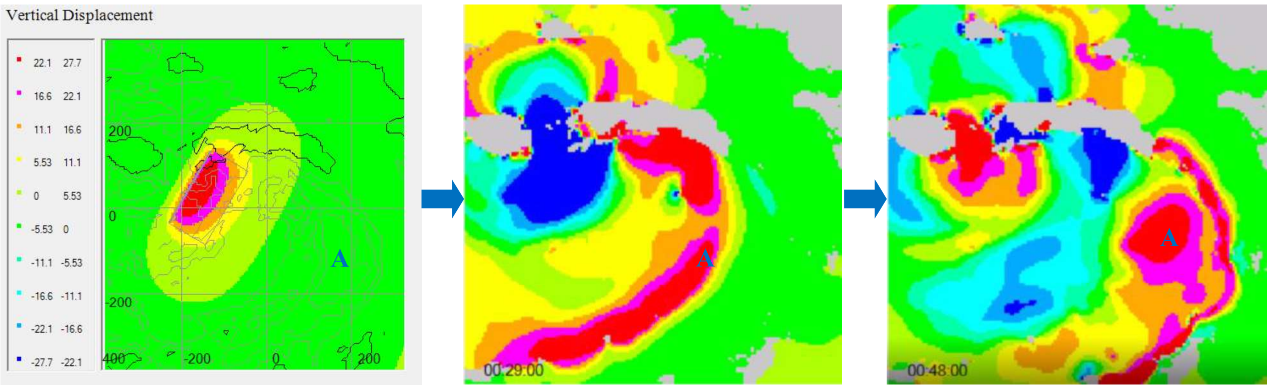

Figure 1. Source modeling by showing the vertical displacement for tsunami simulation. Sequently from 1 to 3, where A is weber trench location.

Shown in figure 1, we probably had answered our hypothesis that weber trench is potentially affected the tsunami propagation in around Banda Sea. Also through tsunami time, 29 minutes after earthquake, the tsunami height in the near of epicenter has a minus waves (valley), and it has increasing after the propagation obtain the accumulation of momentum energy form weber trench at minute 48.

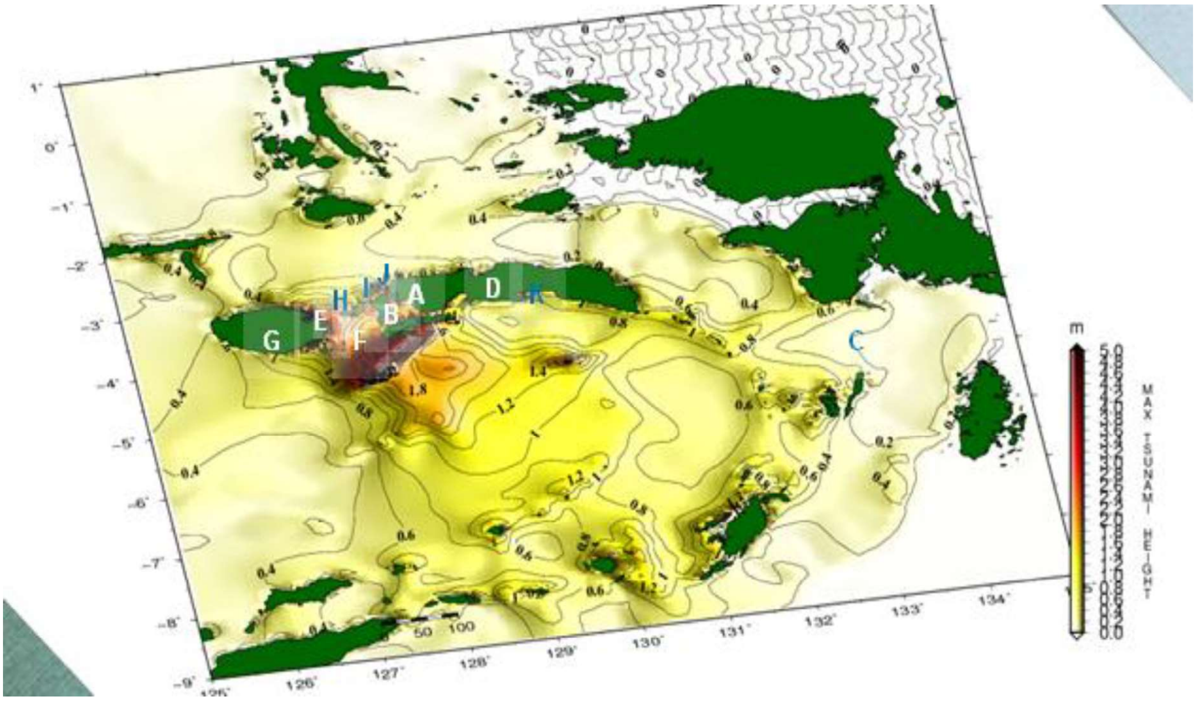

Figure 2. Tsunami height and run-up in Weber trench, Banda Sea.

Shown in figure 2 the location of affected area around Weber trench. It shown by tsunami height and run-up for 29 minutes after earthquake occurred. Affected area including ; A : Hitu Lama Ambon City, B : Larike, Western of Ambon Island, C : Thiel, Maluku, D : Nusa Laot, E : Buru Island, F : Ambelau Island, G : South of

Buru Island, H: Manipa Island, I: Kelang Island, J : Boano Island, K : Seram Island. For detail value of run-up in the each affected area shown in figure 3 and table 1 below.

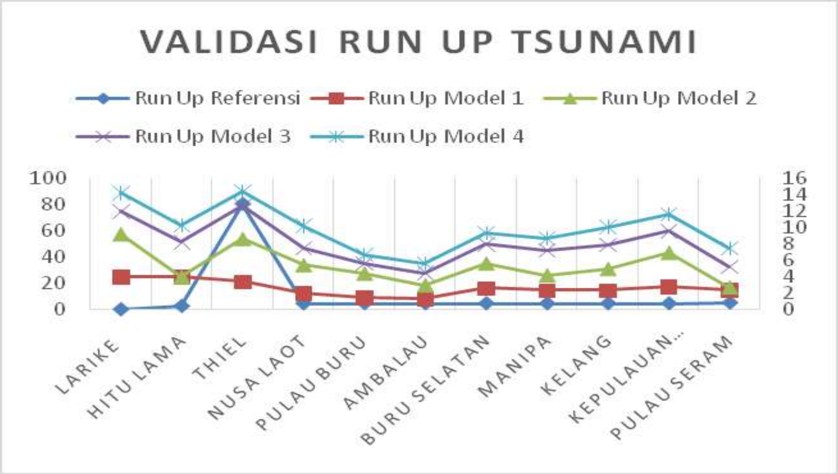

Figure 3. Correlation between tsunami wave height to the length of the inundation of the area affected tsunami.

To knowing the accuracy of tsunami modeling, it was needed a validation to survey result. The validation refferences were used as a comparation in this research is referring to a view journal ; Seyfart, 1756; Perrey, 1857; Wichmann, 1918; Heck, 1934; Ponyavin, 1965; Iida et al, 1967; Berninghausen, 1969) in Soloviev dan Go, 1974.

4. DISCUSSION

From the results of the run-up modeling (figure 3) shows that a tsunami propagates along the coast around Central Maluku, Western of Seram and Shouthern of Buru. Where as shown in Figure 6 run up the highest value based on a model first place in Central Maluku district, precisely in the area Hitulama has a value of 3.99 meters. In table 1, the highest in Central Maluku district, precisely in the area Thual is reaching 5.215 meters. Meanwhile the highest value of the run up in the area of Central Maluku Hitulama is 4.198 meters, and highest run up in Central Maluku regency precisely in the area of Nusa laot as high as 2.75 meters. Spread run up a different value is affected by the tsunami wave height which resulted in inundation length which affects the number of casualties in the area. In Table 1 shows the impact of the tsunami wave height to estimate the ratio of the population.

Tabel 1. Correlation between tsunami height andKorelasi Antara Tinggi Gelombang Tsunami dengan Panjang Inundasi Terhadap Populasi Penduduk

No.	Affected Area	Longitude	Latitude	Hs (m)	Xmax For Building Area (m)	Wide Area in the district in affected area (m)	Estimation of Maximum range on affected area(m)	Estimation of ratio between maximum inundation area to wide of affected area (%)
1	Larike	127.94138	3.719425	2.52457	228.4641207	7953810000	89184.13536	0.256
2	Hitu lama	128.20316	3.582075	6.12791	743.0776586	7953810000	89184.13536	0.833
3	Thiel	128.33238	3.62645	3.65435	373.6338606	7953810000	89184.13536	0.418
4	Nusa Laot	128.78916	3.6641056	3.49961	352.7401327	7953810000	89184.13536	0.395
5	Pulau Buru	126.77249	3.3927778	2.09092	177.8105418	1265500	1124.944443	15.806
6	Ambalau	127.19298	3.8605444	2.22169	192.7514896	3780560000	6148625.863	0.003
7	Buru Selatan	126.69572	3.7273972	1.12807	78.25564711	3780560000	61486.25863	0.127
8	Manipa	127.57475	3.3086167	1.99217	166.7296534	3780560000	61486.25863	0.271
9	Kelang	127.74498	3.2038306	4.56965	502.9827003	3780560000	61486.25863	0.818
10	Kepulauan Boano	127.99804	2.0092694	1.72293	137.4499838	5033380000	70946.31773	0.193
11	Pulau Seram	129.49065	2.9326083	1.59495	124.0401686	7953810000	89184.13536	0.139

Based on table 1, it can be seen that the percentage of area affected by the tsunami inundation for Larike area is 0.256%, so that the secure area of tsunami inundation is equal to 99.744%. For areas that were flooded Hitulama tsunami is 0,833% and is safe from inundation of 99.167%, while for areas that are likely Tial tsunami inundated by 0.418%, and safe from inundation is 99.582%. Nusa laot potentially flooded by only 0.395% and amounted to 99.605% safe from inundation. In areas that were flooded Buru amounted to 15.806%, 84.194% remaining safe from inundation. To estimate the ratio of the affected area in Ambalau is very small area only 0.003% waterlogged areas, amounting to 99.997% safe from inundation. South Buru has a possibility of 0.127% for an area flooded, while 99.873% safe from inundation. Amounting to 0.271% area Manipa tsunami inundated, while 99.729% safe from tsunami inundation. For areas Kelang area that can be flooded tsunami of 0.818%, while 99.182% safe from inundation. The ratio of the islands Boano experienced inundation of 0.193% and 99.807%. And for Seram island flooded area is estimated at only 0.139% of the area of Central Maluku, remaining safe from inundation, amounting to 99.861%.

5. CONCLUSIONS

1. The comparation result between tsunami simulation in model 1 and references is -0.768992771, whereas model 2, model 3 and model 4 each is -0.364516788, -0.395177147 and -0.287686521. Through this result probably we were mention that the tsunami simulation had estimated as the references .
2. *We had an analysis and hyphotesis that weber trench is has inluences to propagation of ocean modeling, run-up and inundation modeling in related with affected area in the coastline.* The prove is obtain by result of models and references that maximum tsunami height has accumulated in “Thiel (Tual) which the nearest affected area from the weber trench. The ratio potentially of maximum flooded up to 15.806% and amounted to 84.194% safe from inundation in Buru Island. In the figure 4 is probably the main key to explained the hypothesis that in the minutes 48 the tsunami height and run up increasing again after obtain the accumulation energy from weber trench, where in the previous tsunami propagation (in the minutes 29) the tsunami height it has a minimum wave.

6. REFERENCES

[1]. Global Mapper. 2017. Bathymetri Data. Accessed at http://www.bluemarblegeo.com/products/global-mapper-formats-elevation.php, February 2017.

[2]. Hanks, Thomas C.; Kanamori, Hiroo. 1979. "Moment magnitude scale*". Journal of Geophysical Study* **84 (B5):** 2348–2350. Retrieved 2007-10-06.

[3]. Nakamura, M. 2006. Source fault model of the 1771 Yaeyama Tsunami- Southern Ryukyu island Japan Inferred from Numerical Simulation, *Pure Appl. Geophys*., **163**, 41-54.

[4]. Papazachos, B.C., Scordilis, E.M., Panagiotopoulos, D.G., Papazachos, C.B., and Karakaisis, G.F., 2004. Global Relations between Seismic Fault Parameters and Moment Magnitude of Earthquakes. Bull. Geol. Soc. Greece, Vol. XXXVI. *Proceedings of the 10 International Congress, Thessaloniki*, April 2004$^{\text{Th}}$.

[5]. Puspito, N. T., Karakteristik Gempa Pembangkit Tsunami di Kepulauan Indonesia dan sekitarnya. *Jurnal Segara*, **3(2),** pp. 49-65. 2007.

[6]. Setyonegoro, W. 2011. Tsunami Numerical Simulation Applied to Tsunami Early Warning System, *Jurnal Meteorologi dan Geofisika*, **Vol.12.No.1**, p.:21-32.

[7]. Wells, D.L., & Coppersmith, K.J. 1994. New Empirical Relationships among Magnitude, Rupture Length, Rupture Width, Rupture Area, and Surface Displacement. *Bulletin of the Seismological Society of America*, **84(4)**. 974-1002.

[8]. Wallansha, R dan Setyonegoro, W. 2015. "Skenario Tsunami Menggunakan Data Parameter Gempabumi Berdasarkan Kondisi Batimetri (Studi Kasus : Gempabumi Maluku 28 Januari 2004)". *Jurnal Segara Kementrian Kelautan dan Perikanan (KKP)*, ISSN : 1907-0659, **11(2)**, hal : 159-168.

Modeling Catastrophic Deaths In Indonesia With Extreme Value Theory

Henry Kurniawan[1]*, Helena Margaretha[1], Ferry Vincenttius Ferdinand[1]

[1] Department of Mathematics, Faculty of Science and Technology, Universitas Pelita Harapan, Tangerang, Indonesia
* Corresponding authors: henkur_phana@yahoo.com

Abstract – In this paper, we model the catastrophic death data that acquired from BNPB (Badan Nasional Penanggulangan Bencana) using Extreme Value Theory. We also extend the application of the model to calculating VaR (Value-at-Risk) and ES (Expected Shortfall) that can be used to describe the risk that will happen days ahead.

1. INTRODUCTION

Indonesia is a country located in the meeting area of four tectonic plates and in the line of the pacific ring of fire where series of active volcanoes are located. Furthermore, the country have more than 5000 big and small rivers with 30% of it have the potential to make floods risk [2]. The future potential of catastrophic death risk in Indonesia needs to be further evaluated and analyzed to give a more accurate representation of the risk. The assessment of catastrophic death risk is very important for life insurers writing accidental death covers. A good view from insurance companies to the catastrophic death risk is needed to assess loss that will occur [1]. This will ensure better damage anticipation, Therefore, this paper provides a model that can be applied to the catastrophic death risk in Indonesia to assess a better risk.

Extreme Value Theory (EVT) is a theory from statistics that discuss deviation of data from the average value within a distribution and it's focus is the tail of the distribution [4]. Catastrophic events can be classified as extreme events which are events that rarely occur, hard to predict, and have a high risk when those events happen. EVT here can be used to calculate the risk of catastrophic events by looking catastrophic events that already happen before. There are two distributions for extreme data: Generalized Extreme Value (GEV) distribution and Generalized Pareto Distribution (GPD). The extreme data can be determine and follow either of these two distribution using these three methods, which is block maxima – GEV, r-largest order statistics – GEV, peaks over threshold – GPD. This paper will be used the peaks over threshold method because of the accurate and efficient of this method rather than the other two methods.

The outline of this paper is as follows, firstly, we determine the extreme data using peaks over the threshold by selecting the threshold. Secondly, from the extreme data we model the time dimension using time-homogeneous Poisson process approach. Thirdly, we calculate the parameter that needed for the model using Maximum Likelihood Estimation (MLE). Finally, we calculate the value of VaR and ES as the application of the model that we used to describe the risk that will happen within days ahead [3].

2. METHODS

2.1 Threshold Selection

To determine the extreme data using peaks over the threshold, we need to select the appropriate threshold value. In peaks over threshold method, the catastrophic death data that is above the threshold value will be determined as extreme value or extreme data and the extreme data follow GPD. One of the main challenges in extreme value modeling is the selection of an appropriate threshold for fitting the model. There is inevitably a trade-off between bias and variance, as setting the threshold too low will lead to invalidity of the GPD approximation of the excess distribution, hence bias in estimated parameters. Meanwhile, setting the threshold too high will leave only a few observations for the statistical model estimation, leading to high variance in parameter estimates, or even failure of the numerical estimates to converge [1]. The selection for the proper threshold value is done by using two main tools, excess plot and parameter of stability plot.

2.1.1 Mean Excess Plot

Mean excess plot is a visual tool that will help select the proper threshold value based on the mean or average of the GPD using mean excess function. Mathematically, the mean excess function can be defined as:

$$\boldsymbol{e(u) = E(X - u | X > u)}$$

With X is loss or death data and u is a threshold value. Mean excess function or $e(u)$ of a random variable X means the average of the excess that exceeds the threshold value, which conditional for $X > u$. However, in the application of the data we will use the empirical mean excess function which can be defined as:

$$\boldsymbol{e_n(u) = \frac{1}{N_u}\sum_{i=1}^{N_u}(X_i - u)}$$

With X_i is loss or data at i, u is a threshold value, and N_u is the amount of data that exceed threshold value. This tool needs many iteration and threshold value u to plot the mean excess plot. After that, we draw the plot $(u,e_n(u))$ and see if the initial of the threshold value on the plot linear roughly. If it is linear, we take the initial threshold value as our threshold value to determine the extreme data. In practical applications, we usually try to set the threshold as low as possible, subject to the GPD providing an acceptable fit [1]. The problem of this tool is that there will be many threshold values that can be used to determine the extreme data. Therefore, using the other tool, that is a parameter of stability plot will help the selection of the proper threshold.

2.1.2 Parameter of Stability Plot

The parameter of stability plot is a plot that used to estimate the parameter from the threshold that we have. After the selection of the threshold, using mean excess plot, the parameter of stability plot will help to select the true threshold value for the extreme data. Each of the threshold value will be determined its parameter (shape parameter and scale parameter) and see if the plot is stable for each threshold value. The method that will be used to calculate the parameter is Maximum Likelihood Estimation (MLE). One thing about GPD is that GPD is a distribution that has a unique property, that is if GP is a model that fit for the data that exceeds the threshold value u, then GP also a model that fit for every threshold value $v > u$ [1]. By definition, if data that exceeds the threshold value u follow GPD model with parameter ξ and σ_u, then for every threshold value v, where $v > u$, the data that exceeds threshold value still follow GPD with shape parameter, but the scale parameter:

$$\boldsymbol{\sigma_v = \sigma_u + \xi(v - u)}$$

By reparameterize the scale parameter σ_v we get the equation:

$$\boldsymbol{\sigma^* = \sigma_v - \xi v}$$

Choosing the true and appropriate threshold value can be done by looking at the plot for the initial threshold value where the parameter stabilization start. After selecting the threshold value, we can get the extreme data which is above the threshold value from the catastrophic data.

2.2 Time-Homogeneous Poisson Process Approach

After we model the size or mark distribution, now we include the time dimension in our model. The time of the catastrophic events that exceeds the threshold value follow the time-homogeneous Poisson process. Time-homogeneous Poisson process model is a model that the time between catastrophic events i.i.d (independent and identically distributed) based on exponential distribution with parameter λ. The points of the process N consists of points $(T_j, \tilde{X}_j) \in E = (0, n] \times (u, \infty)$ from the underlying sequence of rvs $(X_1, \ldots, X_n)$ that exceed the chosen threshold u. This model has one constant parameter which is intensity (λ). The realization of the point process N is a set of points $\{(T_j, \tilde{X}_j) : j = 1, \ldots, N_u\}$, where N_u is the number of exceedances and T_j and $\tilde{X}_j$ represent the time and size of an exceedance, respectively [1]. This paper will use the intensity of Poisson process based on GP model, which will fit the model that we want, that is GP-Poisson.

The intensity of Poisson process N on point (t,x) element of E is:

$$\lambda(t,x) = \frac{1}{\sigma}(1 + \xi\frac{x-\mu}{\sigma})^{-\frac{1}{\xi}-1}$$

and the likelihood of the intensity, that is:

$$L(\theta;\tilde{x}) = \exp\{-\Lambda\big((0,n]\times(u,\infty)\big)\}\prod_{i=1}^{k}\lambda(\tilde{x}_i)$$

$$L(\theta;\tilde{x}) = \exp\{-n\tau(u)\}\prod_{i=1}^{k}\lambda(\tilde{x}_i)$$

next we generate the log-likelihood function:

$$lnL(\theta;\tilde{x}) = -n\ \left(1 + \xi\frac{x-\mu}{\sigma}\right)^{\frac{1}{\xi}} + \sum_{i=1}^{k}\ln\{\frac{1}{\sigma}\left(1 + \xi\frac{x-\mu}{\sigma}\right)^{-\frac{1}{\xi}-1}\}$$

After that, the estimation of parameter GP-Poisson will be done by maximizing the log-likelihood function above. Both of the model (GP and GP-Poisson) need to check the relationship parameter using this equation:

$$\sigma^* = \sigma + \xi(u - \mu)$$

With σ^* is the scale parameter of GP model, σ is the scale parameter of GP-Poisson model, ξ is the shape parameter of GP-Poisson, and μ is location parameter of GP-Poisson model.

2.3 Parameter Estimation of GP Model

The estimating of GP parameter is needed for the checking relationship parameter for the GP-Poisson model and GP model and also the calculation of VaR and ES. The parameters in GP model are shape parameter (ξ) and scale parameter (σ). Method that will be used to estimate these parameters is MLE (Maximum Likelihood Estimation). First, the PDF of the GP distribution is:

$$\boldsymbol{g(x) = \frac{1}{\sigma}(1 + \xi\frac{x}{\sigma})^{-\frac{1}{\xi}-1},\ \xi \neq 0}$$

And now we derive the equation above to get the GP log-likelihood function:

$$\begin{aligned}
L\left(\xi,\sigma \middle| x_1, x_{2,\dots,}x_n\right) &= \prod_{i=1}^{n} g(x) \\
&= \prod_{i=1}^{n} \frac{1}{\sigma}(1 + \xi\frac{x_i}{\sigma})^{-\frac{1}{\xi}-1} \\
&= (\frac{1}{\sigma})^n \prod_{i=1}^{n}(1 + \xi\frac{x_i}{\sigma})^{-\frac{1}{\xi}-1} \\
ln\ L\left(\xi,\sigma \middle| x_1, x_{2,\dots,}x_n\right) &= \ln[(\frac{1}{\sigma})^n \prod_{i=1}^{n}(1 + \xi\frac{x_i}{\sigma})^{-\frac{1}{\xi}-1}] \\
&= -nln\sigma - (\frac{1}{\xi} + 1)\sum_{i=1}^{n} \ln(1 + \xi\frac{x_i}{\sigma})
\end{aligned}$$

Next, we derive the log-likelihood function to each of the parameter (shape and scale parameter). First, for the calculation of shape parameter (ξ) we get the equation:

$$\hat{\xi} = \frac{\sum_{i=1}^{n} \ln(1+\hat{\xi}\frac{x_i}{\sigma})}{(1+\hat{\xi})\sum_{i=1}^{n}\frac{x_i}{\sigma+\hat{\xi}x_i}}$$

Second, for the scale parameter (σ) we get the equation:

$$n = (1 + \xi)\sum_{i=1}^{n}\frac{x_i}{\sigma+\xi x_i}$$

2.4 Calculation of VaR and ES

The calculation of VaR and ES is the extended application of the model GP. VaR is the loss value that will happen with probability *(1-α)%* and ES is the average value of loss if the loss exceeds VaR level [3]. The value of VaR and ES can be acquired from the parameter scale, parameter shape, threshold value, and alpha or significance level. The parameters can be acquired using MLE method for GP model. Formula for VaR value can be seen from the equation below:

$$VaR_\alpha = u + \frac{\sigma}{\xi}((\frac{1-\alpha}{\tilde{F}(u)})^{-\xi} - 1)$$

To know the VaR value will be for the *T* days ahead, we can use this equation:

$$VaR_T = VaR \times \sqrt{T}$$

For the ES calculation, we use this expression of formula:

$$ES_\alpha = \frac{1}{1-\alpha}\int_\alpha^1 VaR_s ds$$

$$ES_\alpha = \frac{VaR_\alpha}{1-\xi} + \frac{\sigma-\xi u}{1-\xi}$$

Where $\boldsymbol{\xi}$ is shape parameter, $\boldsymbol{\sigma}$ is scale parameter, $\boldsymbol{VaR_\alpha}$ is Value-at-Risk at confidence level α, and $\boldsymbol{s = 1 - \frac{1}{t}}$ or the confidence level.

3. RESULTS AND DISCUSSION

Here are the results for this paper:

- Threshold selection

  The threshold selection has been done and we get the true threshold for this model, that is u = 150 and can be seen from the probability plot and quantile-quantile plot below that the extreme data or the data that exceeds the threshold value 150 is very fit to GP model.

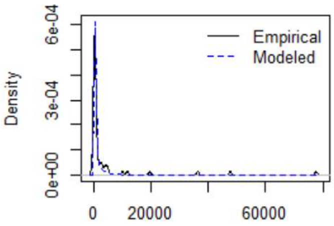

Figure 1 Probability Plot for Threshold Value 150

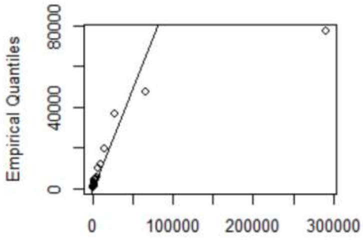

Figure 2 Quantile Plot for Threshold Value 150

Parameter estimation of GP model and GP-Poisson model

The parameter estimation using MLE for both models have been done and the results in the table below. There are two results for the threshold which is 0 and 150. These two thresholds done because of the situation of the data, hence when the threshold value is 150, the shape parameter > 1 which will make the value of ES be negative and we want the positive result for ES [1]. For that, we give another solution which the threshold value is 0 and make the shape parameter < 1. This threshold value 0 will be used only to see the value of ES positive. We also provide the fitting of the data to the GP-Poisson model using the probability plot and quantile-quantile plot for threshold 150 below.

Table 1. Parameter Estimator for Threshold 0

Threshold	0
Amount of Data Above Threshold	2433
Shape Parameter	0.8363704
Scale Parameter	2.5404930

Table.2. Parameter for Threshold 150

Threshold	150
Amount of Data Above Threshold	56
Shape Parameter	2.141386
Scale Parameter	108.358358

Table 3. Parameter Estimator for GP Poisson Model

Threshold	150
Amount of Data Above Threshold	56
Shape Parameter	2.072185
Scale Parameter	123.047237
Location Parameter	148.401147

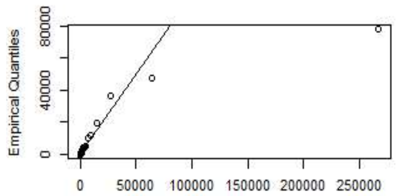

Figure 3 Quantile Plot for GP-Poisson Model

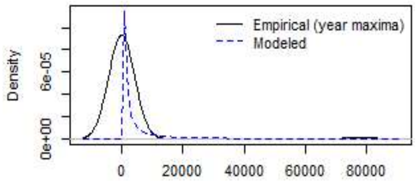

Figure 4 Probability Plot for GP-Poisson Model

Testing the relationship between the models (GP-Poisson and GP)

The testing for the relationship will be using the equation from section 2.2. The result is that the relationship between GP and GP-Poisson model have an error parameter relationship, which means there are an error in the relationship between size distribution and time. The result can be seen below.

$$\begin{aligned} &\sigma^* = \sigma + \xi(u - \mu) \\ &= 124.047237 + 2.072185(150 - 148.401147) \\ &= 127.360356204 \end{aligned}$$

Calculation of VaR and ES

The calculation of VaR and ES for threshold 0 and threshold 150 is done and can be seen the results in the table below. For T days, we set the $T = 365$ days or 1 year.

Table 4. VaR and ES Value for Threshold value 0

α	0,90	0,95	0,99	0,995	0,999
VaR_α	18	34	140	251	974
ES_α	124	224	871	1.551	5.967

Table 5. VaR and ES Value for Threshold value 150

α	0,90	0,95	0,99	0,995	0,999
VaR_α	439	1.596	47.709	207.365	6.505.795,41
ES_α	-198	-1.212	-41.060	-181.493	-5.699.721,71

Table 6 VaR_T Value for Threshold Value 0

α	0,90	0,95	0,99	0,995	0,999
VaR_α	18	34	140	251	974
VaR_T	343	649	2.674	4.795	18.608

Table 7 VaR_T Value for Threshold Value 150

α	0,90	0,95	0,99	0,995	0,999
VaR_α	439	1.596	47.709	207.365	6.505.795
VaR_T	8.387	30.491	911.479	3.961.702	124.293.039

4. CONCLUSIONS

The final result of this modeling is the death data followed GP-Poisson (modeled separately) model with relationship parameter error on GP-Poisson model and GP model, which means there are error in the relationship between size distribution and time. Also, the value of VaR and ES as seen from the table 4-7, the result can be used to describe the risk that will happen in several days ahead with certain probability each. The equation for the GP model (mark size distribution) is:

$$G_{\xi,\sigma}(x) = \begin{cases} 1-(1+\xi\frac{x}{\sigma})^{-\frac{1}{\xi}}, & \xi \neq 0, \\ 1-e^{\frac{-x}{\sigma}}, & \xi = 0. \end{cases}$$

and the equation for the time distribution (Poisson) is:

$$\lambda(t,x) = \frac{1}{\sigma}(1+\xi\frac{x-\mu}{\sigma})^{-\frac{1}{\xi}-1}$$

5. REFERENCES

[1]. Matias Leppisaari. Modeling Catastrophic Deaths using EVT With a Microsimulation Approach to Reinsurance Pricing. *Scandinavian Actuarial Journal* **2016(2)**: 113-145, 2016.

[2]. Depkes, R. Pedoman Teknis Penanggulangan Krisis Kesehatan Akibat Bencana. Jakarta: Departemen Kesehatan RI (2007).

[3]. Yamai, Y. And Yoshiba, T. Value-at-Risk Versus Expected Shortfall: A Practical Perspective. *Journal of Banking & Finance* **29**, 4 (2005), 997–1015.

[4]. Wijaya, Y. Estimasi Volatilitas dan Value at Risk dengan Generalized Pareto Distribution. *Seminar Nasional Matematika* 10(2015), MT 7–14.

Elliptic Curve Cryptosystem (ECC) USED in Encryption and Decryption Text.txt with C# Programming

Akik Hidayat[1*], Mira Suryani[2], Intan Nurma Yunita[3], Rudi Rosyadi[4]

1 Department of Computer Engineering, Faculty of Mathematic and Science, Padjadaran University, Bandung, Indonesia
*Corresponding Author: [akik@unpad.ac.id]

Abstract – Encryption was a method that changes the message data (plaintext) to a code data (chipertext). While decryption was a method that change chippertext to a plaintext. There is two types algorithm that used, symmetrical algorithm and assymetrical algorithm. Symmetrical algorithm was an algorithm that used the same code in the encryption and decryption process. While asymmetrical algorithm was an algorithm that used a public code for encryption process and private code for decryption process. Elliptic Curve Cryptosystem (ECC) was cryptosystem that using a symmetrical algorithm. Xor logic used for the Implementation of this ECC, with the length of code between 8 to 72 bits. The objective was applying elliptic Curve Cryptosystem (ECC) method using C# programming.

***Keywords**: encryption, decryption, Cryptosystem, public code, private code.*

1. INTRODUCTION

Elliptic Curve Cryptosystem is using discrete algorithm problem on elliptic curve points called Elliptic Curves Discrete Logarithm Problem (ECDLP). To form *elliptic curve cryptoystem* (ECC), the sum of two points on the elliptic curve $E(Z_p)$ that produce the third point on the elliptic curve needed [7]. The algorithm that used is Dieffie – Hellman code exchange algorithm [3], while for encryption algorithm illustrate by two users (user1 and user2). User1 choosing randomly a big X Integer number then send it to User2 with $X = g^x \bmod n$, User2 choosing randomly a big X Integer number, then send it to User1 with $Y = g^y \bmod n$, User_1 calculate value of $k_1 = Y^x \bmod n$, User_2 calculate value of $k_2 = X^y \bmod n$. Whereas decryption Algorithm that Illustrated by two users (User_1 and User_2): User_1 will send the message $x \in Zp$, then he must choose a random number for k, that is $k \in Z^*_{p-1}$ and send the encrypted message to User_2 with the equation: $(y_1,y_2) = (\alpha^k \bmod p, x\ \beta^k \bmod p)$, for the decryption, User_2 calculating : $y_2(y_1^{a_J})^{-1} \bmod p$ where a_J is the private code of User_2 [1].

2. METHOD

The method in this article is encryption and decryption the text file with .txt extension using Elliptic Curve Cryptosystem algorithm. Whereas to enhance the speed of the process, C# Programming is using.

3. RESULT AND DISCUSSION

3.1 Elliptical Curve Equation

Determining the equation of $y^2=x^3+ax+b$ and value of a, b are randomly for the coefficient

Table 1. Determining Coefficient

Iteration	$y^2=x^3+ax+b$		
	a	b	Mod ($4a^3 + 27b^2$, 23)
1	5	6	0
2	11	7	0
3	1	1	8

Random value for third Iteration is $a = 1$ and $b = 1$, $4a^3 + 27b^2 = 4+27 = 31 \pmod{23} = 8 \neq 0 \pmod{23}$. If the discriminant is not equal to zero, then the equation is $y^2 = x^3 + 1x + 1$.

3.3 Choosing the Random Point

Table 2. Determining Element E23 (1,1)

$x \in Z_{23}$	$y^3 = x^2 + x + 1 (mod\ 23)$	$y^2 \in QR_{23}$	$(x, y) \in E_{23}(1, 1)$
0	1	Yes	(0,1) and (0,22)
1	3	Yes	(1,7) and (1,16)
2	11	No	-
3	8	Yes	(3,10) and (3,13)
4	0	Yes	(4,0)
5	16	Yes	(5,4) and (5,19)
6	16	Yes	(6,4) and (6,19)
7	6	Yes	(7,11) and (7,12)
8	15	No	-
9	3	Yes	(9,7) and (9,16)
10	22	No	-
11	9	Yes	(11,3) and (11,20)
12	16	Yes	(12,4) and (12,19)
13	3	Yes	(13,7) and (13,16)
14	22	No	-
15	10	No	-
16	19	No	-
17	9	Yes	(17,3) and (17,20)
18	9	Yes	(18,3) and (18,20)
19	2	Yes	(19,5) and (19,18)

Determine the random value of private code of user1 (private1) and user2 (private2), with private1, private2 element {2,3,..., p-1} in Zp. For example private1 = 2 and private2 = 3.

3.4 Calculating public 1 and public 2

Both of the user calculates the public key respectively, and user 1 generates public code (publik1) = private1*P

Table 3. Determining Invers

Divider	44
Iteration	Mod (Divider*iteration, p)
1	21
2	19
3	17
4	15
5	13
6	11
7	9
8	7
9	5
10	3
11	1

3.5 Encryption and decryption result using C# programming

Cryptosystem which saved inside file *kunci.txt* is key component ranging from prime number (p) = 17, Elliptical curve coefficient a=1, b=0, selected random point (P) = (14,2), public key user1 (publik1) = (4,0), public key user2 (publik2) = (0,0), private key user 1 (private1) = 2 and private key user2 (pravate2) = 4. All components of the public key may be known by another party, except both of their private key. From the agreement above, both user1 and user2 can use the key component for encryption and decryption of the data as shown in figure_1

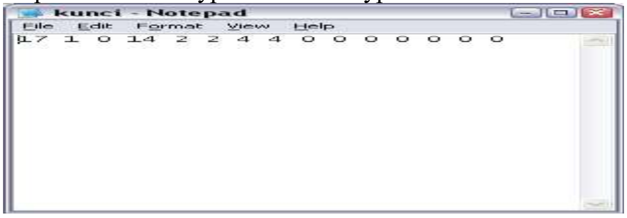

```
17  1  0  14  2  2  4  4  0  0  0  0  0  0  0
```

Figure 1. Key file

Plaintext data named *pesan.txt* (Figure_3) will be encrypted by user1 using the program as shown in (Figure_2) so that produce a file named *sandi_pesan.txt* as shown in (Figure _4).

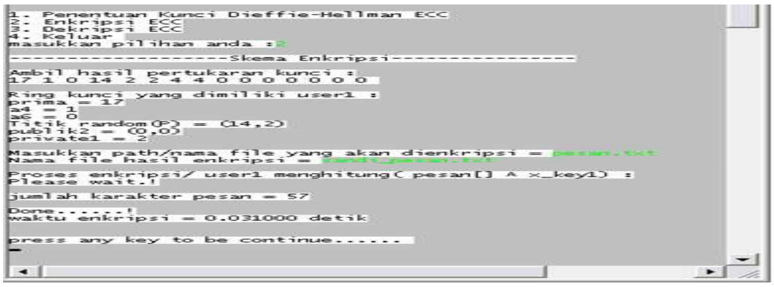

```
1. Penentuan Kunci Dieffie-Hellman ECC
2. Enkripsi ECC
3. Dekripsi ECC
4. Keluar
masukkan pilihan anda :2
--------------------Skema Enkripsi-------------------

Ambil hasil pertukaran kunci :
17 1 0 14 2 2 4 4 0 0 0 0 0 0 0

Ring kunci yang dimiliki user1 :
prima = 17
a4 = 1
a6 = 0
Titik random(P) = (14,2)
publik2 = (0,0)
private1 = 2

Masukkan path/nama file yang akan dienkripsi = pesan.txt
Nama file hasil enkripsi = sandi_pesan.txt

Proses enkripsi/ user1 menghitung( pesan[] ^ x_key1) :
Please wait.!

jumlah karakter pesan = 57

Done......!
waktu enkripsi = 0.031000 detik

press any key to be continue......
_
```

Figure 2. Encryption scheme Form

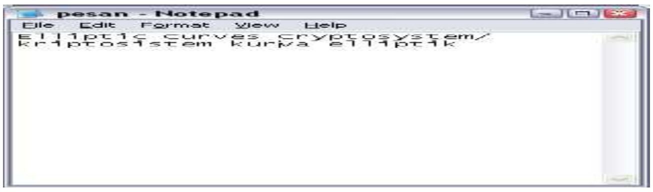

```
Elliptic curves cryptosystem/
kriptosistem kurva elliptik
```

Figure 3. ***Pesan.txt*** **file**

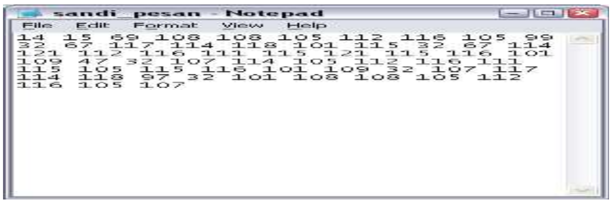

```
14 15 69 108 108 105 112 116 105 99
32 67 117 114 118 101 115 32 67 114
121 112 116 111 115 121 115 116 101
109 47 32 107 114 105 112 116 111
115 105 115 116 101 109 32 107 117
114 118 97 32 101 108 108 105 112
116 105 107
```

Figure 4. sandi_pesan.txt file

Cipertext data named *sandi_pesan.txt* (Figure _4) will decrypt by user2 using the program as shown in (Figure 5) so that produce a file named *pesan_sandi_pesan.txt* as shown in (Figure _6).

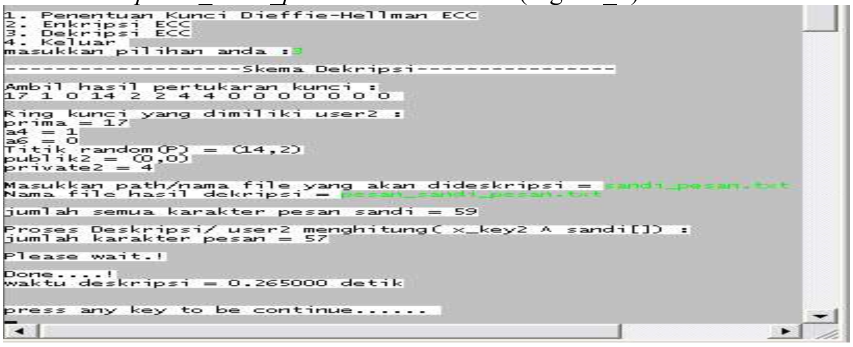

```
1. Penentuan Kunci Dieffie-Hellman ECC
2. Enkripsi ECC
3. Dekripsi ECC
4. Keluar
masukkan pilihan anda :3
--------------------Skema Dekripsi------------------

Ambil hasil pertukaran kunci :
17 1 0 14 2 2 4 4 0 0 0 0 0 0 0

Ring kunci yang dimiliki user2 :
prima = 17
a4 = 1
a6 = 0
Titik random(P) = (14,2)
publik2 = (0,0)
private2 = 4

Masukkan path/nama file yang akan dideskripsi = sandi_pesan.txt
Nama file hasil dekripsi = pesan_sandi_pesan.txt

jumlah semua karakter pesan sandi = 59

Proses Deskripsi/ user2 menghitung( x_key2 ^ sandi[]) :
jumlah karakter pesan = 57

Please wait.!

Done....!
waktu deskripsi = 0.265000 detik

press any key to be continue......
_
```

Figure 5. Decryption Shceme Form

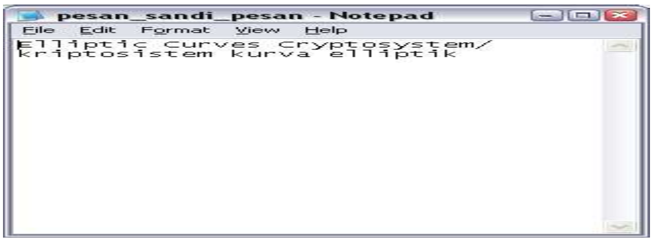

```
Elliptic curves cryptosystem/
kriptosistem kurva elliptik
```

Figure 6. Pesan_sandi_pesan file

4. CONCLUSION

Elliptic curve cryptosystem (ECC) is a cryptosystem that using an asymmetric algorithm. The Advantage of the asymmetric algorithm is not requiring the secrecy when the key distribution process using no safe media such as using the internet. Because the distributed key is a public key. So, if this key is lost or known by the party who are not reserving the right, the message code still kept safe. While the private key remains stored (not distributed). *Elliptic curve cryptosystem* (ECC) have other advantages in the efficiency of the public code number. If there are n user, then it only takes one public code, so the system so efficient when there a lot of users. When using C# programming, encryption and Decryption extention.txt file will be easily obtained.

6. REFFERENCE

[1]. A. Foster, (2004) A polynomial-time probabilistic algorithm for the minimum distance of an arbitrary linear error-correcting code, Mathematics Honors Report,.
[2]. A. Meneezes, P. Van Oorschot, and S. Vanstone, (1996) Handbook of Applied Cryptography**.** CRC Press,.
[3]. C.A. Van TILBORG, Henk, (2000). Fundamentals of Cryptology, Kluwer Academic Publishers,
[4]. KOBLITZ, Neal, (1987) A Course in Number Theory & Cryptography, Springer-Verlag New York Inc.,.
[5]. R. J. McEliece, (1978). A public-key crypto system based on algebraic coding theory, Vol.42-44, DSN Progress Rep.,
[6]. Shala, Mahmet. (2004). Primes Number In Cryptography. University of Greenwich.
[7]. Stinson, Douglas R. (1956). Cryptography: Theory and Practice. CRC Press. Boca Raton. Florida.
[8]. W. Irons, (2005). A polynomial-time probabilistic algorithm for the minimum distance of a non-binary linear error-correcting code Mathematics Honors Report.

Calculation of Insurance Premium of Rice Plants In Citarum Watershed

Endang Soeryana Hasbullah [1*], Sukono[2], Muhammad Faiz Rifqi[3], Sudrajat Supian[4]

[1,2,3,4] Mathematics Department of FMIPA of Padjadjaran University,
Raya Bandung-Sumedang Street Km 21,
Jatinangor 45363
Telp/Fax: 022-7794696
* Corresponding authors: [endangsoeryana@yahoo.co.id]

Abstract – Determination of crop insurance premiums in the Citarum Watershed can be calculated by mathematical methods. One of the premium calculation methods is the method of the normal curve of plant productivity data is assumed to be normally distributed. In this paper discussed the calculation of crop insurance premiums in the Citarum Watershed West Bandung regency with the normal curve method involves a level of coverage. The method is used for crop productivity data obtained a normal distribution. Normal curve method is used without using the assumption that the value of the coefficient of variation and tried for some level of coverage. Application materials used are rice crop productivity data in the Citarum Watershed West Bandung District from 2008-2014. This research resulted in the value of the rice crop insurance premiums for farmers in the region based on a certain level of coverage.

Keywords : Agricultural Insurance, Premium, The Normal Curve Method, Coverage Level

1. INTRODUCTION

Watershed Area (Daerah Aliran Sungai – "DAS") Citarum is the biggest and longest DAS in West Java Province. This basin passes through 5 DAS such as DAS Citarum, DAS Cipunegara, DAS Cilamaya, DAS Cikalanang, and DAS Ciasem which pass through 9 Districts and 3 Cities include Bandung, Bekasi, and Cimahi City. There are a lot of inhabitants who utilize the land around DAS Citarum as their livelihood. The use of land in DAS Citarum from year to year has been changing and classified as exploitative where the primary forest extension from year to year continuously decreasing. The use of land in DAS Citarum itself is dominated by residential area, mixed garden, and agriculture. This research is focused on the discussion on the use of land in Watershed (DAS) Citarum at agriculture sector.

Agriculture sector is one of the sectors which has important role in national economies. It includes the agriculture sector in Watershed (DAS) Citarum. One of the roles of agriculture sector is as foreign exchange when the products of agriculture are being exported abroad ([1]). However, on the other side the agricultural sector has a high risk on nature dynamics or pests attack which is caused the decreasing of production result and the farmers will take all the risks. On the other side, the level of farmer's welfare tends to be under the poverty line. To deal with the risks, the farmers have done some things to minimalize the loss. However, the farmers' ability in dealing those risks are often constrained by lack of capital.

So far the government has been issued the policies and programs to help farmers deal with the risks. Some of them are seed subsidy, fertilizer subsidy, saprodi helps, also credit of farming sector. Nevertheless, the help still has not enough to prevent some problems in farming sector especially problems of nature condition. Therefore, one of the efforts that needs to be done to reduce the risk of loss is by introducing plants insurance in agriculture sector. This strategy has been widely adopted by farmers in developed countries, or some farmers in developing countries ([2]) to prevent the loss. Consequently, agricultural insurance is one strategy to face the damage risks in a farming sector including agricultural sector in DAS Citarum. Agricultural sector is one of sectors which has important role in national economic. This includes agricultural sector in Watershed (DAS) Citarum.

2. RESEARCH METHODS

This research will discuss the calculation of premium insurance of rice plants by using the normal curve method and the calculation of spared value with the method of Unearned Premium Reserve (UPR). Normal Curve Method is a method to calculate premium insurance of agriculture by using the help of curve at normal distribution. This method firstly introduced by Ralph R. Botts and James N. Boles in 1958, it was used by

Federal Crop Insurance Corporation (FCIC) as a method to find plants premium insurance in United States of America, and Manitoba Crop Insurance (MCIC) in Canada. This method was used because the frequency of distribution of rice plants productivity in Watershed (DAS) Citarum normally distributed. This method is assumed the coefficient parameter of variation value 0,25 or on the other words the value of standard deviation parameter of crop results 25% of the average parameter value. While, unearned Premium Reserve is a calculation value of premium spare which has not got the income.

2.1 Normal Curve Method

In normal curve methods with the same coverage level *C (0 < C < 1)*, rice productivity Y is distributed normally with the average μ of and variations of σ^2. The compensation I for the yields Y less than coverage level C can be written as follows:

$$\mathrm{I} = \begin{cases} C\mu - Y; Y \le C\mu \\ 0 \qquad ; Y \ge C\mu \end{cases}$$

The compensation above can be calculated with the expectation as follows:

$$E(I) = \left[E(C\mu - Y \mid Y \le C\mu\right]\left[P(Y \le C\mu)\right]$$

$$= \left[C\mu - \left(\mu - \sigma \frac{\phi\left(\frac{C\mu-\mu}{\sigma}\right)}{\phi\left(\frac{C\mu-\mu}{\sigma}\right)}\right)\right]\left[\phi\left(\frac{C\mu-\mu}{\sigma}\right)\right]$$

$$= \left[\phi\left(\frac{C\mu-\mu}{\sigma}\right)\right](C\mu-\mu) + \left[\phi\left(\frac{C\mu-\mu}{\sigma}\right)\right](\sigma)$$

The equations above is a formula used to calculate the premium value of normal curve method, so it can be written:

$$PREMIUM = \left[\phi\left(\frac{C\mu-\mu}{\sigma}\right)\right](C\mu-\mu) + \left[\phi\left(\frac{C\mu-\mu}{\sigma}\right)\right](\sigma)$$

Unearned Premium Reserve (UPR)

There are some methods used in calculation of an Unearned Premium Reserve. The one will be used in this thesis is methods 1/24, where this method each polis will be issued in early month and middle of the month.

Because this research used 1/24 method so the premium value will be conversed first in each plants period until per middle month. One season of planting has 4 months' average, then there is spared value with the formula as follows :

$$UPR = P_0 \cdot F(t) \cdot (1-k)$$

Where,

P_0 = Premium value, $F(t)$ = Time Period, K= 1/24

3. RESULTS AND DISCUSSION

3.1 Premium Insurance of Rice Crops in Citarum River Watershed

The data which is used in this research is secondary data Productivity Data of Rice Plants in Citarum River Watershed of West Bandung Regency from the year 2010 until 2014 attached in attachment 1. Then the data will be used to estimate plants premium insurance value in Citarum Watershed. This is the productivity data of rice plants in Citarum River Watershed in West Bandung Regency.

Table 1 Rice Plants Productivity Data in DAS Citarum from 2010 to 2014

YEAR	HARVEST BOARD (Ha)	PRODUCTION (Ton)	PRODUCTIVITY (Ku/Ha)
2008		175,646	55,48
2009		214,702	59,84

YEAR	HARVEST BOARD (Ha)	PRODUCTION (Ton)	PRODUCTIVITY (Ku/Ha)
2010	46,915	267,348	56,99
2011	38,998	222,899	57,16
2012	39,338	230,692	58,64
2013	41,631	252,712	60,70
2014	42,999	256,687	59,70

Using IBM SPSS 23 application is done data distribution test with one-sample Kolmogorov-Smirnov test methods get the result like the picture below

From the result above can be seen that *sig* = 0,068 > 0,05, so Ho is not rejected or accepted which means the productivity data of rice plants in Citarum DAS is normally distributed.

This research will involve some adaptation related to compensation system and coverage level involvement. In this matter farmer who just maximum harvest 25% of the planted area will get full compensation of IDR6,000,000.00. While for other cases depends on the damage level and planting age.

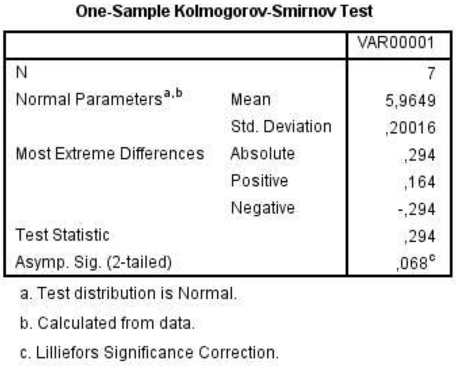

One-Sample Kolmogorov-Smirnov Test

		VAR00001
N		7
Normal Parameters[a,b]	Mean	5,9649
	Std. Deviation	,20016
Most Extreme Differences	Absolute	,294
	Positive	,164
	Negative	-,294
Test Statistic		,294
Asymp. Sig. (2-tailed)		,068[c]

a. Test distribution is Normal.

b. Calculated from data.

c. Lilliefors Significance Correction.

Picture 1. The result of the method of one-sample Kolmogorov-Smirnov test

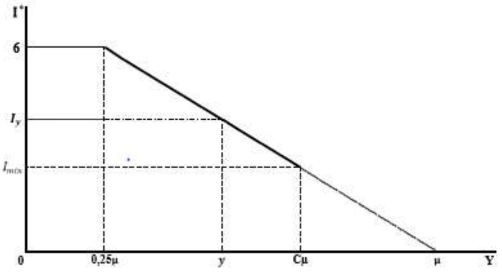

Picture 2. Compensation system with compliance

So the compensation for farmers can be designed as follows:

$$I^* = \begin{cases} 6 & ; \quad Y \le 0.25\mu \\ \dfrac{8}{\mu} & ; \quad 0.25\mu < y \le C\mu \\ 0 & ; \quad Y > C\mu \end{cases}$$

The next step is seeking compensation expectation in the Equations. The result of harvest or productivity of rice is the same with Y, can be normally distributed with the average of μ variants σ^2

So, the compensation expectation can be calculated as follows:

$$E(I) = E(\frac{8}{\mu}(\mu - Y) \mid 0,25\mu < Y < C\mu)P(0,25\mu < Y \le C\mu)$$

$$E(I) = \frac{8}{\mu}\left[\mu - \left(\mu + \sigma\frac{\phi\left(\frac{0,25\mu-\mu}{\sigma}\right) - \phi\left(\frac{C\mu-\mu}{\sigma}\right)}{\phi\left(\frac{C\mu-\mu}{\sigma}\right) - \phi\left(\frac{0,25\mu-\mu}{\sigma}\right)}\right)\right]\left[\phi\left(\frac{C\mu-\mu}{\sigma}\right) - \phi\left(\frac{0,25\mu-\mu}{\sigma}\right)\right]$$

This thesis will involve some adaptation related to compensation system and coverage level involvement. In this matter farmer who just maximum harvest 25% of the planted area will get full compensation of IDR6,000,000.00. While for other cases depends on the damage level and planting age.

$$Premium = 6\phi\left(\frac{-0,75\overline{Y}}{S}\right) + \frac{8S}{\overline{Y}}\left(\phi\left(\frac{C\overline{Y}-\overline{Y}}{S}\right) - \left(\frac{-0,75\overline{Y}}{S}\right)\right)$$

with the average of Y = 5,9649 and standard deviation of S = 1,491225, to coverage level 40%, 50%, 60%, 65%, 70%, 75%. The premium insurance value of plants in Citarum Watershed is calculated by using equation number (2) and the result is as follows; 88.200, 243.800, 551.040, 1.412.400, 1.935.600 is the total premium. Based on government regulation is valid that 80% premium is burdened by the government so the farmers only take 20%, namely; 17.640, 60.960, 137.760, 282.480, 387.120.

If a farmer buys crop insurance polis with coverage level of 60%, so a farmer only pay IDR 137.760,00 each hectare of the land for one planting season. If the harvest season the harvest result of the farmer less than 25% of average result of harvest of long term crop, so a farmer can get full compensation, for IDR 6.000.000,00. If the result is on 25% and 60% average result of long term harvest, so a farmer can get compensation according with the result of the harvest. If the result of rice plants harvest is more than 60% average result of long term harvest, so a farmer will not get compensation. The same explanation is applied to coverage level other than 60%.

3.2 The Backup Value of Rice Plants Insurance in Citarum Watershed

The calculation of backup value in this thesis use 1/24 method, based on formulation, where polis of insurance is assumed to be issued every month. It must be converted first with premium value in each periods of planting until it becomes premium polis in this method. Then with the formulation:

$$UPR = P_0 \cdot F(t) \cdot (1-k)$$

Searched value for its premium to coverage level. The result can be obtained as follows: 91.282, 254.450, 576.107, 1.461.748, 2.013.222 to premium with coverage level of 40%, 50%, 60%, 70% and 75%.

4. CONCLUSIONS

The insurance premium of rice plants in Citarum River Watershed in West Bandung Regency with a coverage level of 40%, 50%, 60%, 70% and 75% are:

1. IDR 88.200,00 with premium charged to farmers for IDR 17.640,00 per one planting period.
2. IDR 243.800,00 with premium charged to farmers for IDR 60.960,00 per one planting period.
3. IDR 551.040,00 with premium charged to farmers for IDR 137.760,00 per one planting period.
4. IDR 1.412.400,00 with premium charged to farmers for IDR 282.480,00 per one planting period.
5. IDR 1.935.600,00 with premium charged to farmers for IDR 387.120,00 per one planting period.

The value of reserves rice plants insurance in Citarum River Watershed in West Bandung Regency with each level of coverage 40%, 50%, 60%, 70% and 75% are:

1. IDR 91.282,00 each insurance polis issued
2. IDR 154.450,00 each insurance polis issued
3. IDR 576.107,00 each insurance polis issued
4. IDR 1.461.748,00 each insurance polis issued
5. IDR 2.013.222,00 each insurance polis issued

5. REFERENCES

[1]. Booth P., Chadburn, R.,Cooper, D., Haberman, S., James, D., 1999, Modern Actuarial Theory and Practice. Chapman & Hall / CRC

[2]. Kaas, R., Goovaerts, M., Dhaene, J., Denuit, M., 2008, Modern Actuarial Risk Theory: Using R. Springer, Berlin / Heidelberg

[3]. Insyafiah dan Wardhani, Indria, 2014, Kajian Persiapan Implementasi Asuransi Pertanian Secara Nasional. Kementrian Keuangan Badan Kebijakan Fiskal, Pusat Pengelolaan Risiko Fiskal.

[4]. Muhammad, Abdulkadir, 2006, Hukum Asuransi Indonesia. Bandung: Citra Aditya Bakti.

[5]. Octaviani, Rini, 2011, Menaksir Parameter pada Distribusi Eksponensial Bivariat Dengan Metode Maksimum Likelihood. Skripsi. FMIPA. Universitas Sumatra Utara. Medan

[6]. Purnomo, Bambang, 2007, Penyakit Biotik dan Abiotik. Faperta. UNIB.

[7]. Sumaryanto dan Nurmanaf, A. R., 2007, Simpul-Simpul Strategis Pengembangan Asuransi Pertanian untuk Usahatani Padi di Indonesia. *Forum Penelitian Agro Ekonomi*, **25 (2)**: 89-103.

[8]. Untung, Kasumbogo, 2010, Diklat Dasar-Dasar Ilmu Hama Tanaman, Fakultas Pertanian UGM, Yogyakarta.

[9]. Yasin, S., 2015, Perhitungan Premi Asuransi Usaha Tani Padi Menggunakan Metode Kurva Normal dengan Melibatkan Tingkat Cakupan, Fakultas MIPA UNISBA. Bandung.

COMMERCIAL SUPPORT

PT ANDALAN TUNAS MANDIRI
Supplier for survey and laboratory euipments
BizPark2 Commercial Estate Ruko R2 No 1
Penggilingan Cakung Jakarta Timur
Phone: 021-29062020
www.ptandalan.com
Email: sales@ptandalan.com

SAKTI MOBILE
Graha Bima Juara
Jl. Utan kayu 42, Jakarta
Email: eric@saktimobile.com
Phone: 021- 83796763 s/d 83796768
Fax: 021 83796762

PT. MITRA INTIMARGA
Bekasi Square - Kanto No. 70,
Pekayon Jaya, Bekasi Selatan 17148
Indonesia
Phone No. (021) 8243 4829
Fax No. (021) 8243 4831
Website: www.ptmitra.com

MALANG STRUDEL
Jl. Semeru No.47, Oro-oro Dowo, Klojen,
Kota Malang, Jawa Timur 65115
Phone : (0341) 480242
Website : www.malangstrudel.com

Supported by

Faculty of Mathematics and Natural Sciences

Brawijaya University

Organized by:

BaSiC 2017
INTERNATIONAL CONFERENCE

Sponsored by:

sakti
MOBILE.COM

PT. MITRA INTIMARGA
SUPPLIER FOR LABORATORIES & RESEARCH INSTITUTES

PT. ANDALAN TUNAS MANDIRI
SUPPLIER FOR SURVEY & LABORATORY EQUIPMENTS
www.ptandalan.com

Malang Strudel

Faculty of Science
Brawijaya University
Jl. Veteran, Malang 65145
Phone : +62-341-571142
Site : basic.ub.ac.id
e-mail : basicscience@ub.ac.id
basicscience2017@gmail.com